

nature

GETTING A GRIP

An all-in-one method for creating programmable soft robots



Uncomfortable truths
Caltech confronts its past to build a more equitable future

Meet the ancestors
Genomes shed light on lineage of Bronze Age mummies

Counting the cost
Nature's salary survey reveals how COVID has affected the workplace

Vol. 595 No. 7876

Nature.2021.11.13

[Sat, 13 Nov 2021]

- [This Week](#)
- [News in Focus](#)
- [Books & Arts](#)
- [Opinion](#)
- [Work](#)
- [Research](#)

This Week

- **[COVID is disrupting scientific careers around the world](#)** [10 November 2021]
Editorial • Earlier generations faced fallout from the global financial crisis and a boost from emerging economies. Today, COVID-19 and concerns about diversity dominate.
- **[Simplify drug labelling to show benefits clearly](#)** [09 November 2021]
World View • Regulators and researchers should give patients and physicians meaningful information to guide decisions.
- **[Maps reveal surprising details of Mongols' ancient capital](#)** [04 November 2021]
Research Highlight • Sensors that peer underground chart the unexpected sprawl of Karakorum, established by the heir to Genghis Khan.
- **[Deadline divide: women shy away from asking for extensions](#)** [03 November 2021]
Research Highlight • Even when deadlines are flexible, women are less likely than men to seek extra time for assignments.
- **[Dressed-up tumour cells make up a personalized cancer vaccine](#)** [04 November 2021]
Research Highlight • A dose of silica-coated cancer cells helps to rally the immune system against malignancies in mice.
- **[Worker ants vault to queenly rank after just one gene turns on](#)** [05 November 2021]
Research Highlight • One master switch controls a wide range of behaviours in an ant that undergoes a radical makeover.
- **[Scientists glimpse little galactic clusters on their way to greatness](#)** [05 November 2021]
Research Highlight • Light from 11 billion years ago provides a view of galactic ‘protoclusters’ that could grow into behemoths.
- **[Line in the sand: the physics of halting a dune on the march](#)** [05 November 2021]

Research Highlight • A laboratory ‘roundabout’ helps scientists to determine the types of barrier that can halt an underwater dune’s travels.

- **‘Flash’ droughts are quick-drying farm fields globally** [03

November 2021]

Research Highlight • Important crop-growing regions, such as Brazil, are susceptible to droughts that strike with alarming speed.

- EDITORIAL
- 10 November 2021

COVID is disrupting scientific careers around the world

Earlier generations faced fallout from the global financial crisis and a boost from emerging economies. Today, COVID-19 and concerns about diversity dominate.



The pandemic has hit researchers in Brazil particularly hard. Credit: Maria Magdalena Arrellaga/Bloomberg/Getty

“Pay them and they will stay. Keep them and it will pay.” Sudanese mathematician Mohamed Hassan’s summary of *Nature*’s first international survey tracking scientists’ salaries and how they feel about their jobs in 2010

was both pithy and prescient ([M. H. A. Hassan *Nature* 465, 1006–1007; 2010](#)).

Hassan, who was then the president of the African Academy of Sciences in Nairobi, was cheering the leaders of the then-emerging science countries, such as Brazil, India and China, that were properly paying their researchers despite the ongoing economic fallout from the global financial crisis. He urged others to do the same to avoid a brain drain.

Nature has since conducted a salary survey every two to three years. The results of our sixth one, [Nature's 2021 Salary and Job Satisfaction Survey](#), are published this week. The impact of the ongoing COVID-19 pandemic on careers looms large, alongside salaries, job satisfaction and issues of workforce diversity and inclusion, which we'll be reporting on over the next four weeks.



[Scientists count the career costs of COVID](#)

The respondents are self-selecting, but the surveys provide a regular snapshot of scientific careers worldwide and enable comparisons to be made across regions, genders, career stages and disciplines. As well as highlighting the highs and lows of researchers' professional lives, the findings can reveal how career trajectories are shaped by both world events and those closer to home. In the 2014 survey, for example, the global

financial crisis was still casting a shadow, with 44% of respondents saying the resulting recession had negatively affected their job satisfaction.

This year, 12% of the survey's respondents said they have lost a job offer because of COVID-19. Among early-career researchers, 53% of respondents said that the pandemic has negatively impacted their career prospects.

The total number of respondents this year (3,209) was lower than in previous years and was less than half of the 7,670 who responded to our survey of postdoctoral researchers last year. This perhaps reflects a jaded workforce as pandemic-related disruptions to daily life continue.

When, in 2010, Hassan singled out Brazil, India and China, they were among a handful of nations predicted to dominate the global economy by 2050. This optimism was reflected in that year's *Nature*'s survey: job satisfaction in those nations, particularly in India and China, had increased that year, compared with that in other countries.



[Collection: Coronavirus and scientific careers](#)

But this year, the mood seems to be especially bleak in Brazil and India, which the pandemic has hit particularly hard. Some 72% of respondents in Brazil and 61% in India, which received 107 and 89 responses, respectively, said the pandemic has slowed their careers. "We don't have the technology

to do anything other than basic research. Brazil is just chaos,” says Jucelaine Haas, a plant-science researcher at the Federal University of Technology in Paraná, Brazil.

Regardless of where they work, researchers point to lost productivity caused by data-collection challenges (57% of respondents) and an inability to conduct lab-based experiments (55%). One clear message from *Nature*'s survey and other recent studies is that it is still too early to say how lost productivity during the pandemic will affect future careers. But the early signs are not good.

A study of two surveys — with a combined total of almost 7,000 responses from principal investigators in Europe and the United States — found that around 27% of respondents did not initiate any new research projects in 2020, a dramatic rise from 9% in the previous year ([J. Gao et al. *Nature Commun.* 12, 6188; 2021](#)). The authors also report an analysis of some 9.5 million articles and preprints published in 2019 and 2020; they found that when research on COVID-19 is taken out of the equation, the number of published co-authored papers dropped by 5% in 2020.

But *Nature*'s latest survey also speaks to other global concerns. Since 2018, the surveys have proactively sought researchers' experiences of discrimination in science, and of attempts to improve diversity, equity and inclusion in response to movements such as #MeToo and #BlackLivesMatter. This year, 34% of women who responded said they have experienced discrimination, in contrast to 21% of men. Among women reporting discrimination, 50% said they have experienced gender-based discrimination.



'Does anyone have any of these?': Lab-supply shortages strike amid global pandemic

Like previous surveys, this year's suggests that the gender pay gap is most stark in later career stages, with 40% of men but just 36% of women reporting annual salaries of more than US\$110,000. The gap is especially apparent in the United States, where 68% of senior men have crossed the \$110,000 mark, compared with 55% of senior women.

In both the United States and the United Kingdom, respondents who are non-white were more likely than their white colleagues to report experiencing harassment or discrimination.

One happier and recurrent theme of all six surveys is that, despite the challenges of financial crises and a pandemic, scientists broadly love what they do, although satisfaction rates have fallen from 68% to 58% since 2018.

As pandemic-related disruptions abate in many parts of the world, it is important that funders and employers remember the power of world events to shape scientists' careers and fortunes. Now is the time to consider how to rekindle the desire to embark on new projects and to encourage a positive research culture that fosters inclusive collaboration and acknowledges that everyone in the research ecosystem has a part to play.

Nature **599**, 179 (2021)

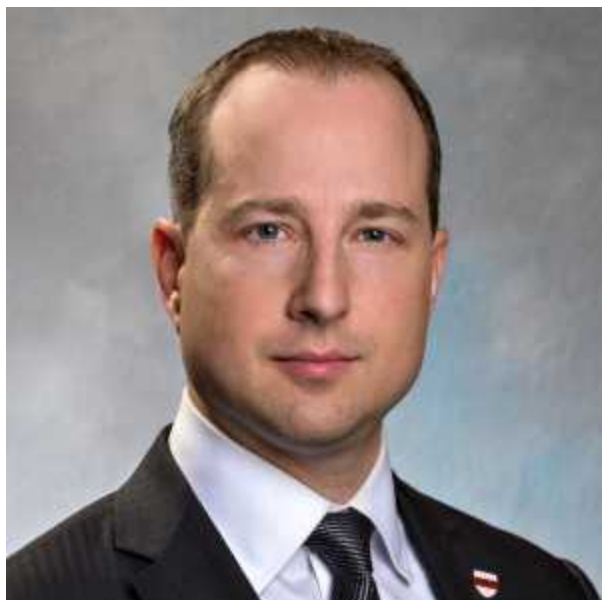
doi: <https://doi.org/10.1038/d41586-021-03049-6>

This article was downloaded by **calibre** from <https://www.nature.com/articles/d41586-021-03049-6>

| [Section menu](#) | [Main menu](#) |

- WORLD VIEW
- 09 November 2021

Simplify drug labelling to show benefits clearly



Regulators and researchers should give patients and physicians meaningful information to guide decisions.

- [Jonathan J. Darrow](#) 0

Aducanumab, an Alzheimer's disease treatment, was approved by the US Food and Drug Administration (FDA) in June this year despite a lack of robust evidence that it actually slows cognitive decline. In protest, three experts quit an advisory panel. Amid all the soul-searching over how FDA approvals should work, something has been largely missing: a clear description of benefits.

The FDA (and the relevant community of scholars) knows that most new drugs offer only modest incremental benefit over drugs already available.

But although its thorough analyses of submitted clinical-trial data are disclosed, the relevant documents are impenetrable to nearly everyone. Drug labelling should clearly state what effectiveness was demonstrated and how. The metrics should have real-world relevance, such as how a patient feels, functions or survives.

The FDA's statute requires "substantial evidence" of efficacy, but that term is flexible. Clinical trials are increasingly using 'surrogate end points', or non-clinical measures that are 'reasonably likely' to predict clinical benefit. But one study found that 52% of 65 oncology-drug correlations were not strong ([V. Prasad et al. JAMA Intern. Med. 175, 1389–1398; 2015](#)).

Aducanumab's label reports "Amyloid Beta PET Composite SUVR", a confusing measure that is hard to translate into, for example, a patient's ability to recognize loved ones. If a trial outcome cannot be reasonably explained in patient-relevant terms, the FDA should reconsider whether that end point is acceptable for drug approval.



Show drugs work before selling them

There is also no requirement for substantial efficacy, leaving patients guessing at a drug's therapeutic value. I have scoured FDA documents underlying drug approvals that have been described in lay media as "life-saving", "dramatically effective" or "curative". That is rarely what the evidence demonstrates. In 2021, I identified ten reports by multiple authors,

each examining the evidence of benefit of a range of newly approved drugs ([*J. J. Darrow J. Manag. Care Spec. Pharm.* **27**, 685–688; 2021](#)).

Collectively, these papers concluded that only 2–31% had better than modest benefits over existing treatments. Aducanumab might therefore be an extreme example, but it is hardly alone.

The medical community attempted to fix a related labelling problem more than a decade ago. In the 1990s, practitioners protested that drug labelling was so lengthy and complex that they found it difficult to locate crucial information. Now the FDA requires that drug labelling include a half-page box at the top of package inserts, called ‘highlights of prescribing information’. It requires warnings and precautions to be included, as well as dosage and administration, but not, alas, how well the drug actually works.

In a report to Congress in 2010, the FDA concluded that clear efficacy labelling in a space-limited box might often be impossible for drugs because medical information is too complex and variable. Unlike me, few patients or physicians can devote full-time efforts to researching a drug’s value and its regulation, and might therefore be tempted to use price as a proxy for value. In my view, meaningful improvement is possible, and the dramatic increase in drug costs means that it is past time to revisit the issue.

The few drugs that provide understandable statements of efficacy offer a hint of just how useful such information could be. For example, the FDA labelling for Yasmin (drospirenone/ethinyl oestradiol), a birth-control product, explains that “pregnancy rates in the clinical trials were less than one per 100 woman-years of use”. Sunscreen — regulated in the United States as an over-the-counter drug — bears quantitative benefit information in the form of a single number: sun protection factor, or SPF. Although SPF is not a perfect measure and few people understand how it is calculated, repeated use allows consumers to learn over time what SPF they require to avoid burning.



Demand cancer drugs that truly help patients

Benefit cannot always be described with a single figure such as SPF or pregnancies per 100 woman-years. But nutrition labels could serve as a model. Their clear columns and uncluttered text show key information, such as calories and vitamin and mineral content, at a glance.

Two randomized controlled trials involving 450 people suggested that an analogous drug-facts box could greatly improve patients' comprehension of drug benefits and risks ([L. M. Schwartz et al. Ann. Intern. Med. 150, 516–527; 2009](#)). Without it, 65% of patients overestimated benefits tenfold or more. For instance, most participants not given the facts box thought that the absolute risk reduction in heart attacks from a hypothetical drug was between 6% and 70%, whereas 72% of participants given the drug-fact box correctly perceived the actual value of 0.8%.

The European Medicines Agency has acknowledged the need to “provide more information on benefits in understandable terms”, but regulators around the world have been slow to deliver. I think part of the problem is that showcasing limited drug benefits would be awkward for regulators, health-care providers and manufacturers while also dashing patient hopes, however unrealistic. But there is an ethical duty to inform patients of benefits and risks.

Clearer labelling could also change drug companies' incentives. Radical transparency would favour drugs that work best over those approved despite only marginal benefits.

Nature **599**, 181 (2021)

doi: <https://doi.org/10.1038/d41586-021-03050-z>

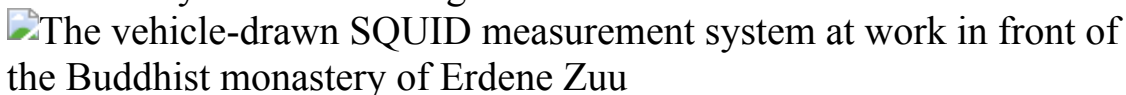
This article was downloaded by **calibre** from <https://www.nature.com/articles/d41586-021-03050-z>

| [Section menu](#) | [Main menu](#) |

- RESEARCH HIGHLIGHT
- 04 November 2021

Maps reveal surprising details of Mongols' ancient capital

Sensors that peer underground chart the unexpected sprawl of Karakorum, established by the heir to Genghis Khan.



Truck-drawn sensors map the Mongolian empire's ancient capital, which is now partially concealed beneath farm fields and a Buddhist monastery.

Credit: Jan Bemmann

During his travels through the Mongol empire in the 1250s, a Flemish friar described the capital, Karakorum, as an enclosed city with four gates. Now, researchers have fully mapped the city — and called the friar's picture into question¹.

Access options

Subscribe to Journal

Get full journal access for 1 year

\$199.00

only \$3.90 per issue

[Subscribe](#)

All prices are NET prices.
VAT will be added later in the checkout.
Tax calculation will be finalised during checkout.

Rent or Buy article

Get time limited or full article access on ReadCube.

from \$8.99

[Rent or Buy](#)

All prices are NET prices.

Additional access options:

- [Log in](#)
- [Learn about institutional subscriptions](#)

Nature **599**, 182 (2021)

doi: <https://doi.org/10.1038/d41586-021-03013-4>

References

1. 1.

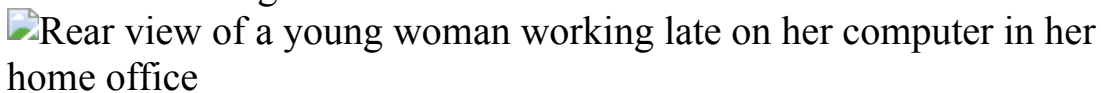
Bemmamn, J. Linzen, S., Reichert, S. & Munkhbayar, L. *Antiquity* <https://doi.org/10.15184/aqy.2021.153> (2021).

This article was downloaded by **calibre** from <https://www.nature.com/articles/d41586-021-03013-4>

- RESEARCH HIGHLIGHT
- 03 November 2021

Deadline divide: women shy away from asking for extensions

Even when deadlines are flexible, women are less likely than men to seek extra time for assignments.



Survey data suggest that women feel more time stress than men in part because they are more reluctant to ask for deadline extensions. Credit: Getty

Sometimes, there simply aren't enough hours in the day to get everything done on time. But women are less likely than men to ask for deadline extensions, a new study suggests¹.

Access options

Subscribe to Journal

Get full journal access for 1 year

\$199.00

only \$3.90 per issue

[Subscribe](#)

All prices are NET prices.
VAT will be added later in the checkout.

Tax calculation will be finalised during checkout.

Rent or Buy article

Get time limited or full article access on ReadCube.

from \$8.99

[Rent or Buy](#)

All prices are NET prices.

Additional access options:

- [Log in](#)
- [Learn about institutional subscriptions](#)

Nature **599**, 182 (2021)

doi: <https://doi.org/10.1038/d41586-021-03014-3>

References

1. 1.

Whillans, A. V., Yoon, J., Turek, A. & Donnelly, G. E. *Proc. Natl Acad. Sci. USA* <https://doi.org/10.1073/pnas.2105622118> (2021).

This article was downloaded by **calibre** from <https://www.nature.com/articles/d41586-021-03014-3>

- RESEARCH HIGHLIGHT
- 04 November 2021

Dressed-up tumour cells make up a personalized cancer vaccine

A dose of silica-coated cancer cells helps to rally the immune system against malignancies in mice.



Ovarian cancer cells. An individualized vaccine made from similar cells can slow ovarian-tumour growth in laboratory animals. Credit: Steve Gschmeissner/Science Photo Library

Coating a person's cancer cells with silica might one day yield personalized cancer treatments, according to a study in mice¹.

Access options

Subscribe to Journal

Get full journal access for 1 year

\$199.00

only \$3.90 per issue

[Subscribe](#)

All prices are NET prices.

VAT will be added later in the checkout.

Tax calculation will be finalised during checkout.

Rent or Buy article

Get time limited or full article access on ReadCube.

from \$8.99

[Rent or Buy](#)

All prices are NET prices.

Additional access options:

- [Log in](#)
- [Learn about institutional subscriptions](#)

Nature **599**, 182 (2021)

doi: <https://doi.org/10.1038/d41586-021-03021-4>

References

1. 1.

Guo, J. *et al.* *Nature Biomed. Eng.* <https://doi.org/10.1038/s41551-021-00795-w> (2021).

This article was downloaded by **calibre** from <https://www.nature.com/articles/d41586-021-03021-4>

- RESEARCH HIGHLIGHT
- 05 November 2021

Worker ants vault to queenly rank after just one gene turns on

One master switch controls a wide range of behaviours in an ant that undergoes a radical makeover.

 A Harpegnathos saltator worker ant captured in an aggressive display with open mandibles.

Gamergate-in-waiting: a Jerdon's jumping ant worker can attain queenly status if it vanquishes other workers in fights. Credit: Karl Glastad/Berger Lab

A single gene can determine whether an ant is a worker or royalty, by triggering a cascade of brain changes that alter the insect's behaviour¹.

Access options

Subscribe to Journal

Get full journal access for 1 year

\$199.00

only \$3.90 per issue

[Subscribe](#)

All prices are NET prices.

VAT will be added later in the checkout.

Tax calculation will be finalised during checkout.

Rent or Buy article

Get time limited or full article access on ReadCube.

from \$8.99

[Rent or Buy](#)

All prices are NET prices.

Additional access options:

- [Log in](#)
- [Learn about institutional subscriptions](#)

Nature **599**, 182 (2021)

doi: <https://doi.org/10.1038/d41586-021-03024-1>

References

1. 1.

Gospocic, J. *et al.* *Cell* <https://doi.org/10.1016/j.cell.2021.10.006> (2021).

This article was downloaded by **calibre** from <https://www.nature.com/articles/d41586-021-03024-1>

- RESEARCH HIGHLIGHT
- 05 November 2021

Scientists glimpse little galactic clusters on their way to greatness

Light from 11 billion years ago provides a view of galactic ‘protoclusters’ that could grow into behemoths.

The Large Binocular Telescope Interferometer surrounded by trees.

Data from the Large Binocular Telescope in Safford, Arizona, has helped researchers to study the rapid star formation inside young clumps of galaxies. Credit: NASA/JPL-Caltech

Galaxies like to group together. The Milky Way and its nearest neighbours, for example, are part of the Virgo Cluster, which has more than 1,000 member galaxies. Now, in a bit of astronomical time travel, researchers have had a peek at how the cluster’s core might have looked around 11 billion years ago¹.

Access options

Subscribe to Journal

Get full journal access for 1 year

\$199.00

only \$3.90 per issue

[Subscribe](#)

All prices are NET prices.
VAT will be added later in the checkout.
Tax calculation will be finalised during checkout.

Rent or Buy article

Get time limited or full article access on ReadCube.

from \$8.99

[Rent or Buy](#)

All prices are NET prices.

Additional access options:

- [Log in](#)
- [Learn about institutional subscriptions](#)

Nature **599**, 183 (2021)

doi: <https://doi.org/10.1038/d41586-021-03022-3>

References

1. 1.

Polletta, M. *et al.* *Astron. Astrophys.* **654**, A121 (2021).

This article was downloaded by **calibre** from <https://www.nature.com/articles/d41586-021-03022-3>

- RESEARCH HIGHLIGHT
- 05 November 2021

Line in the sand: the physics of halting a dune on the march

A laboratory ‘roundabout’ helps scientists to determine the types of barrier that can halt an underwater dune’s travels.



Piles of glass beads simulate underwater sediment in an experiment on dune migration and what can stop it. Credit: Karol Bacik, Nathalie Vriend/University of Cambridge

When pushed by the wind, sand dunes can travel across the ground — potentially leading to buried infrastructure. Similarly, ocean currents can shift an underwater dune onto a sea-floor pipeline or cable. Experiments have now shown that the outcome of such encounters depends on the obstacle’s size and shape¹.

Access options

Subscribe to Journal

Get full journal access for 1 year

\$199.00

only \$3.90 per issue

[Subscribe](#)

All prices are NET prices.
VAT will be added later in the checkout.
Tax calculation will be finalised during checkout.

Rent or Buy article

Get time limited or full article access on ReadCube.

from \$8.99

[Rent or Buy](#)

All prices are NET prices.

Additional access options:

- [Log in](#)
- [Learn about institutional subscriptions](#)

Nature **599**, 183 (2021)

doi: <https://doi.org/10.1038/d41586-021-03023-2>

References

1. 1.

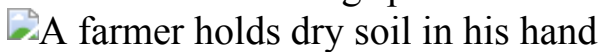
Bacik, K. A., Canizares, P., Caulfield, C. P., Williams, M. J. & Vriend, N. M. *Phys. Rev. Fluids* **6**, 10438 (2021).

This article was downloaded by **calibre** from <https://www.nature.com/articles/d41586-021-03023-2>

- RESEARCH HIGHLIGHT
- 03 November 2021

‘Flash’ droughts are quick-drying farm fields globally

Important crop-growing regions, such as Brazil, are susceptible to droughts that strike with alarming speed.



A farmer holds soil from his arid field in Logan, Kansas, during a flash drought that baked the US Midwest in 2012. Credit: John Moore/Getty

Scientists have identified global hotspots for ‘flash droughts’, which develop with unusual swiftness and quickly parch the land¹.

Access options

Subscribe to Journal

Get full journal access for 1 year

\$199.00

only \$3.90 per issue

[Subscribe](#)

All prices are NET prices.

VAT will be added later in the checkout.

Tax calculation will be finalised during checkout.

Rent or Buy article

Get time limited or full article access on ReadCube.

from \$8.99

[Rent or Buy](#)

All prices are NET prices.

Additional access options:

- [Log in](#)
- [Learn about institutional subscriptions](#)

Nature **599**, 183 (2021)

doi: <https://doi.org/10.1038/d41586-021-03009-0>

References

1. 1.

Christian, J. I. *et al.* *Nature Commun.* <https://doi.org/10.1038/s41467-021-26692-z> (2021).

This article was downloaded by **calibre** from <https://www.nature.com/articles/d41586-021-03009-0>

| [Section menu](#) | [Main menu](#) |

News in Focus

- **‘Brumby’ cull, carbon rebound and a giant research index**

[10 November 2021]

News Round-Up • The latest science news, in brief.

- **Why hundreds of scientists are weighing in on a high-stakes US abortion case**

[26 October 2021]

News • Studies suggest that a reversal of the landmark Roe v. Wade decision would be detrimental for many.

- **Why scientists worldwide are watching UK COVID infections**

[02 November 2021]

News Explainer • The country’s relaxation of measures such as masking — especially in England — is showing the limits of relying on vaccines alone.

- **The search for people who never get COVID**

[29 October 2021]

News • An international team of researchers wants to find people who are genetically resistant to SARS-CoV-2, in the hope of developing new drugs and treatments.

- **US astronomy's 10-year plan is super-ambitious**

[04 November 2021]

News • Its ‘decadal survey’ pitches big new space observatories, funding for large telescopes and a reckoning over social issues plaguing the field.

- **Sponge cells hint at origins of nervous system**

[05 November 2021]

News • Synapse genes help cells to communicate in sponge’s digestive chambers.

- **Caltech confronted its racist past. Here’s what happened**

[10 November 2021]

News Feature • With a push from students and alumni, the university faced up to a legacy of support for eugenics. As it renames buildings and programmes, can its story serve as a model for others?

- NEWS ROUND-UP
- 10 November 2021

‘Brumby’ cull, carbon rebound and a giant research index

The latest science news, in brief.



Brumbies roam a wintry landscape near Yarangobilly in Australia’s Kosciuszko National Park. Credit: Perry Duffin/EPA-EFE/Shutterstock

Australia’s ‘brumby’ cull doesn’t go far enough

Up to 10,000 feral horses might be killed or removed from Australia’s largest alpine national park under a [draft plan to control the rapidly growing population of non-native animals](#). Scientists have welcomed the idea, but are

alarmed that the plan allows for thousands of horses to remain, threatening endangered species and habitats.

The proposed cull, in Kosciuszko National Park, New South Wales (NSW), contrasts with a ban on lethal control measures in the United States, where large populations of wild horses, known as mustangs, also cause problems.

The plan, released in October, recommends reducing the park's population of wild horses, known in Australia as brumbies, from about 14,000 to 3,000 through ground-based shooting and rehoming.

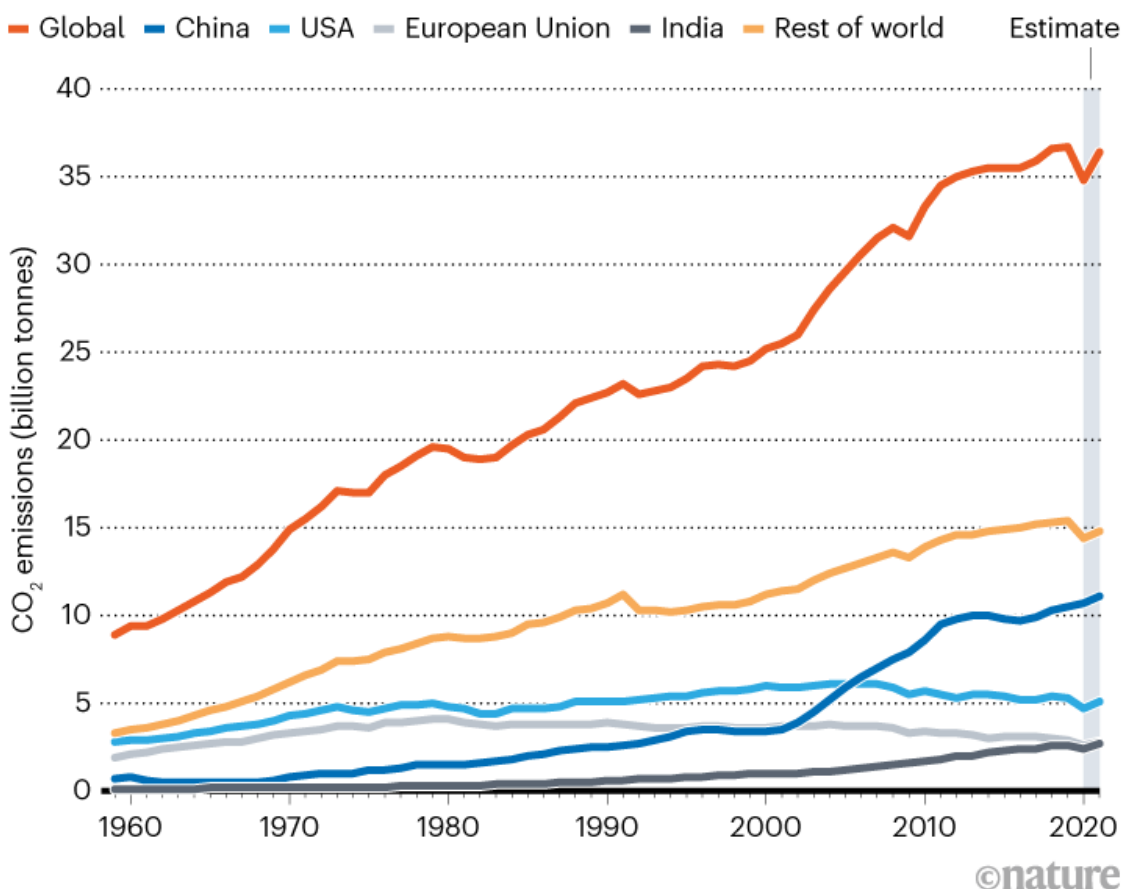
But the Australian Academy of Science argues for a rapid reduction to below 3,000. In an open letter with 69 signatories, including both scientists and institutions, sent to the NSW environment minister on 29 October, it notes that "alpine wetlands continue to degrade even with very small numbers of feral horses. Kosciusko cannot begin to recover from drought, extensive bush fires and overgrazing if, as currently proposed, 3,000 feral horses remain."

Carbon emissions rebounded rapidly following COVID pandemic dip

The abrupt decline in global carbon dioxide emissions during the COVID-19 pandemic, caused by government-mandated lockdowns, will be all but erased by the end of this year, a consortium of scientists reports. The group predicts that carbon emissions from burning fossil fuels will rise to 36.4 billion tonnes in 2021 — an increase of 4.9% compared with last year (see 'Pandemic rebound'). That's faster than many scientists expected. The rapid rebound, driven in part by the increasing demand for coal in China and India, suggests that emissions will begin to rise anew next year unless governments make substantial efforts to bend the curve, the researchers warn.

PANDEMIC REBOUND

After a drop of more than 5% during the first year of the COVID-19 pandemic, global carbon emissions will rebound in 2021, researchers predict. Among nations that are the largest emitters, the strongest growth compared with pre-pandemic levels is projected for China and India.



Source: Global Carbon Project

“This is a reality check,” says Corinne Le Quéré, a climate scientist at the University of East Anglia in Norwich, UK, and a member of the Global Carbon Project. The group presented the report last week at the United Nations climate summit in Glasgow, UK, where nations are debating the pledges they will make to curb greenhouse-gas emissions. “I’m expecting that it will really hit home with the negotiators and make it very obvious that action is needed.”

Carbon emissions from fossil fuels fell by 5.4% in 2020, as pandemic restrictions shut down restaurants and factories, grounded planes and closed borders, the Global Carbon Project estimates. Most scientists expected emissions to rebound to some extent, but questions remained about the how much and how fast they would do so.

“What we’ve seen is that the demand that’s bouncing back now has been met largely by fossil fuels,” says Steven Davis, an Earth systems scientist at the University of California, Irvine, and a member of Carbon Monitor, another consortium that tracks global carbon emissions.

But the report is not all doom and gloom. Le Quéré sees hope in the data: some 23 countries curbed fossil-fuel emissions over the course of more than a decade before the pandemic. “We have the technology and we know what to do,” she says.



Technologist Carl Malamud.Credit: Smita Sharma

Index to world's research papers released online

A US technologist has released a [gigantic online index of 355 billion words and short phrases contained in more than 100 million journal articles](#) —

including many paywalled papers. This ‘General Index’, which was made public on 7 October and is free to use, holds tables of words and sentence fragments listed next to the articles in which they appear. It is an effort to help scientists use software to glean insights from published work even if they have no legal access to the underlying papers, says creator Carl Malamud.

Malamud says that because the index doesn’t contain the full text of articles, but only snippets up to five words long, releasing it does not breach publishers’ copyright restrictions on the reuse of paywalled articles.

Some researchers who have had early access to the index say that it has helped them to search the literature with software — a procedure known as text mining.

The database’s release is a “major development for the wealth of information it has unlocked from those 107 million journal articles”, says Arul George Scaria, a legal researcher at the National Law University, Delhi.

Nature **599**, 185 (2021)

doi: <https://doi.org/10.1038/d41586-021-03051-y>

This article was downloaded by **calibre** from <https://www.nature.com/articles/d41586-021-03051-y>.

- NEWS
- 26 October 2021

Why hundreds of scientists are weighing in on a high-stakes US abortion case

Studies suggest that a reversal of the landmark *Roe v. Wade* decision would be detrimental for many.

- [Amy Maxmen](#)



Access to abortion is one of the most polarizing issues in the United States.Credit: Stefani Reynolds/Bloomberg/Getty

An upcoming case in the US Supreme Court might hasten the end of abortion across roughly half of the United States — a right that the country has defended for nearly 50 years. More than 800 scientists and several scientific organizations have provided evidence to the court showing that abortion access is an important component of reproductive health care.

The researchers, some of whom have studied the impact of abortion for many years, are rebutting arguments made to the court that abortion has no beneficial effect on women's lives and careers — and might even cause them harm. "The scientific community is eager to weigh in on such an important issue, especially given five decades of evidence concerning the importance of abortion access," says Stephanie Toti, a director at the New York City-based Lawyering Project, a group that advocates for abortion access in the United States. She adds, "This case is a big deal."



[What Trump's Supreme Court pick could mean for science](#)

The case, to be heard by the Supreme Court on 1 December, is between the state of Mississippi, which has issued a ban on abortion after 15 weeks of pregnancy, and the Jackson Women's Health Organization, the only clinic in the state that provides abortions. In lower US courts, the clinic has successfully argued that the ban violates *Roe v. Wade*, the landmark 1973 Supreme Court decision that enshrined the federal right to an abortion until

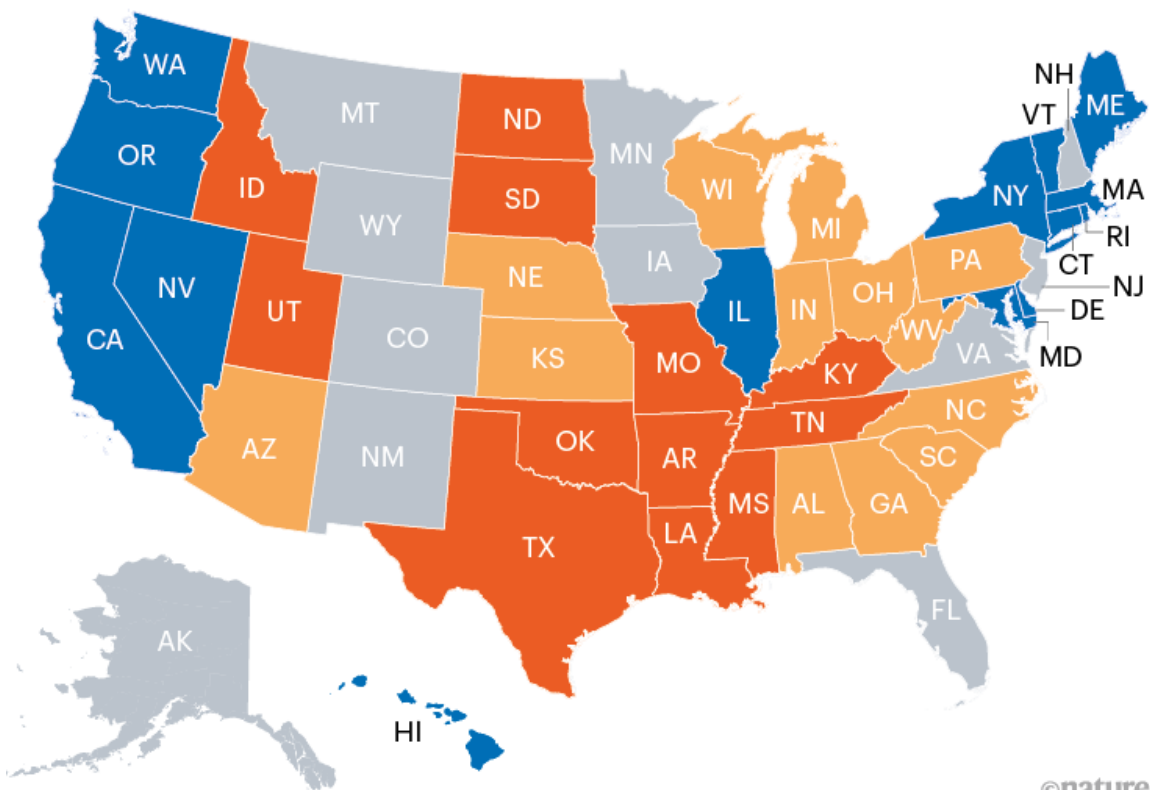
the point that a fetus can live outside the womb — a ‘viability standard’ typically set at 22 or 24 weeks of pregnancy. But state officials are now taking the case to the highest court, seeking to end the precedent set by *Roe* so that individual states can set their own rules on the legality of abortion. In a surprise move last week, the Supreme Court announced that it would also hear a separate case on an abortion ban in Texas on 1 November; that decision has the potential to hobble *Roe* by allowing states to ignore the viability standard.

Since *Roe*, many states have diminished abortion access by, collectively, [issuing more than 1,000 restrictions](#) on the procedure, the majority in midwestern and southern states (see ‘Abortion regulations’). But legal analysts say the Mississippi case is the first in the Supreme Court in 30 years that could directly overturn or significantly undermine that long-standing precedent. Some analysts think that is likely to happen, judging from the court’s current composition. Former US president Donald Trump promised to appoint Supreme Court justices who would reverse *Roe*, and [succeeded in replacing three justices](#) during his presidency: there are now six conservative justices who have said that they disagree with abortion precedents, and three liberal justices. Should the court effectively end *Roe*, 12 states have policies designed to ban most abortions immediately, and — on the basis of existing and pending policies — researchers predict that another 8 to 10 could follow suit.

ABORTION REGULATIONS

Many states have passed policies that restrict abortion access, including mandating waiting periods before the procedure and onerous licensing requirements that have shut down clinics. Twelve of these states also have pre-emptive ‘trigger bans’ that would make abortion illegal if *Roe v. Wade* is overturned.

- States with trigger bans and restrictions
- With several types of abortion restriction
- With a law to protect abortion access
- With few or no types of abortion restriction



©nature

Source: Guttmacher Institute

With much at stake, many people on both sides of the abortion debate — including scientists, religious leaders and athletes — have filed a total of more than 130 ‘amicus’, or ‘friend of the court’, briefs to the Supreme Court in advance of the Mississippi case, *Dobbs v. Jackson Women’s Health Organization*. A handful of the briefs are authored by hundreds of researchers in public health, social science, health equity and economics, who urge the court to uphold abortion rights on the basis of dozens of peer-reviewed studies examining the effects of abortion on well-being.

Rosie Griffin, an attorney at the law firm Feldesman Tucker Leifer Fidell in Washington DC, which [filed an amicus brief](#) signed by almost 550 researchers in public-health, reproductive-health and health policy, along with the American Public Health Association and two research institutes, says her firm felt it was important for scientists to weigh in, even though the justices aren't obliged to rely on this type of report.

"This is a coalition of folks who have spent their working lives looking at objective measures of maternal and child health," says Griffin, "and who read Mississippi's court filings, as well as those in favour of its argument, and said, 'These claims are not at all supported by the data.'"

Reliable data

State restrictions, dictating, for instance, that teenagers must obtain parental consent for abortion, have been fought in courts for decades. The most recent major Supreme Court decision on abortion — *Planned Parenthood v. Casey* in 1992 — determined that judges must weigh the reasons for new regulations against the obstacles they create for people seeking abortions. But data to help inform such decisions have been lacking.

This gap was noted by former conservative Supreme Court justice Anthony Kennedy in a 2007 case that upheld a ban on one abortion procedure. Ruling in favour of the restriction, Kennedy decided that it was protecting women from depression and a loss of self-esteem. "While we find no reliable data to measure the phenomenon, it seems unexceptionable to conclude some women come to regret their choice," he said in his opinion.



A technician checks a person's blood pressure at Jackson Women's Health Organization in Mississippi.Credit: Bonnie Jo Mount/The Washington Post/Getty

But as he wrote those words, studies to supply such data were in the works. Chief among them was an initiative to compare women who had abortions with those who wanted them, but were turned away from clinics for various reasons, including state restrictions or a lack of doctor availability. Called the Turnaway Study, the effort followed about 1,000 women in the United States for five years after they sought abortions. The women were similar in terms of physical, mental and economic well-being initially, but diverged over time¹.

In more than 40 reports published in peer-reviewed scientific journals, researchers analysed what happened to the women, adjusting for potential confounding factors such as age. The overall finding was that, on average, receiving an abortion didn't harm women's mental or physical health, but

being denied an abortion resulted in some negative financial and health outcomes.

“The science clearly shows that abortion is incredibly common, and it is important to women living full lives,” says Diana Greene Foster, leader of the Turnaway Study and a reproductive-health researcher at the University of California, San Francisco. Recent years have seen the Turnaway and other studies referenced in abortion court cases. For example, judges [have cited a 2018 National Academies of Sciences, Engineering, and Medicine report](#) finding that abortion is safe. This and other reports find that mortality rates are nearly 4 times as high for colonoscopies — and 14 times as high for childbirth² — as for legal abortion procedures.

Phillip Levine, an economist at Wellesley College in Massachusetts who studies social issues, but didn’t sign an amicus brief because he refrains from abortion-policy advocacy, says the Turnaway Study represents an important advance because it’s designed to answer questions about the long-term effects of abortion and abortion denial on individuals. “That is a very hard thing to do,” he explains. He adds that his confidence in the study’s results is bolstered by similar findings in Sweden, Finland and the former Czechoslovakia. “Answering these questions perfectly is essentially impossible,” he explains, because researchers can’t conduct clinical trials on the subject. “But the Turnaway Study is some of the best evidence we have.”

The health argument

The amicus briefs authored by hundreds of scientists ahead of the Mississippi case address a particular line of argument made by state attorney-general Lynn Fitch and her colleagues in their court filing — namely, that abortion is unnecessary and possibly harmful to women. “*Roe* and *Casey* block the States and the people from fully protecting unborn life, women’s health, and their professions,” Fitch and her colleagues write.

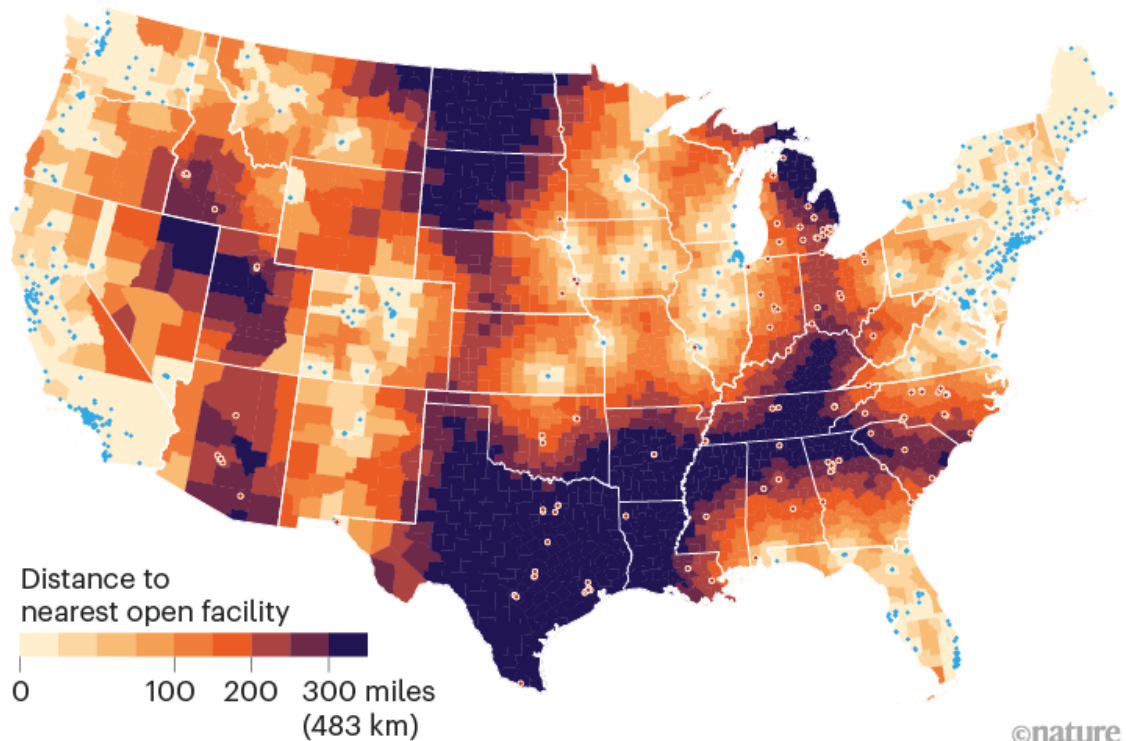
They argue that abortion access is no longer necessary because women have the ability to succeed in their professional lives without it. This, the brief explains, is due to the availability of highly effective contraceptives; state assistance, such as adoption services; and policies including those that

prevent employers from discriminating on the basis of pregnancy. [In a September interview](#), Fitch said that banning abortion would actually empower women to raise children while pursuing careers.

IF ROE IS OVERTURNED

Twelve states with 'trigger bans' and ten others with multiple restrictions might ban abortion almost entirely if *Roe v. Wade* is undermined. In this scenario, an economist estimates that, on average, a woman in the affected states will need to travel 280 miles (450 kilometres) to have the procedure, which would prevent around 100,000 women from accessing abortion care each year owing to economic and other hardships.

- Abortion facility likely to close
- Abortion facility likely to remain open



©nature

Source: Caitlin Myers/Middlebury College

But half a century of evidence — much of it accumulating in the past decade — runs contrary to these claims, Foster says. Those data appear in [the amicus brief that she helped draft](#) with about 100 social scientists who study abortion. It cites, for example, a 2017 report³ finding that women who had abortions were no more depressed or anxious than those who wanted one but couldn't get it, and a 2019 study⁴ of nearly 900 revealing that women who

sought but were unable to get abortions reported higher rates of chronic headaches and joint pain five years later, compared with those who got an abortion.

Allowing states to ban abortion might even increase maternal and infant mortality rates, [according to the brief signed by about 550 public-health and reproductive-health researchers](#). Unwanted pregnancies are [associated with worse health outcomes for several reasons](#), including that people who plan their pregnancies tend to change their behaviour — drinking less alcohol, for example — and receive prenatal medical care long before those who are surprised by their pregnancy and don't want it.



[Pregnancy and COVID: what the data say](#)

In addressing whether contraceptives obviate the need for abortion, the research briefs point out that abortion is still common — nearly one in four women in the United States will have an abortion by age 45⁵. The briefs also discuss how birth control is fallible, and that young people and poor people have less access to it. That is one reason why, in the United States as of 2011, women living below the federal poverty level [had five times the rate of unintended pregnancies](#) seen in women with high incomes.

About one-quarter of people in poverty in the United States are Black. Joia Crear-Perry, president of the National Birth Equity Collaborative in

Washington DC, warns that banning abortion would disproportionately harm the physical, mental and economic well-being of Black people with the capacity for pregnancy. In particular, Crear-Perry is concerned that abortion bans will raise the already dire rates of maternal mortality for Black women in the United States — which currently stand at 44 deaths per 100,000 births, four times the global average for high-income countries. [The amicus brief that she co-signed](#) with other health-equity researchers and advocates states: “Black women, in particular, who continue to experience the effects of racially-motivated policies and practices that impact their maternal health, must have the right to decide whether to continue a pregnancy to term.”

The empowerment argument

Mississippi’s assertion that abortion access has nothing to do with women’s ability to pursue careers, higher education and financial stability is supported by an [amicus brief](#) signed by anti-abortion organizations and a group that describes itself as 240 women scholars and professionals, who have degrees in law, medicine and other subjects. “Women do not need abortions to achieve,” says Michele Sterlace-Accorsi, the executive director of the organization Feminists Choosing Life of New York, and a signatory on the brief. It criticizes the Turnaway Study and others that link the right to abortion to women’s health and empowerment, saying that researchers have mistaken correlation for causation.

More than 150 economists disagree with this criticism [in an amicus brief of their own](#). They write that statistical methods developed over the past 30 years allow researchers to isolate and measure the effects of abortion policies. “The field of causal inference focuses precisely on figuring out when correlation does equal causation,” their brief argues.



Jackson Women's Health Organization is the only abortion clinic in Mississippi. Credit: Evelyn Hockstein/Reuters

Some of the studies described in the economists' brief find that abortion legalization in the 1970s helped to increase women's educational attainment, participation in the labour force and earnings — especially for single Black women⁶. That remains true, the brief says. For example, one study⁷ posted last year assessed about 560 women of comparable age and financial standing periodically after they either got an abortion or were unable to get an abortion they sought. After five years, the group that was turned away from an abortion had experienced a 78% increase in overdue debt and an 81% increase in publicly recorded financial events, such as bankruptcies and evictions. Meanwhile, the overdue debt of women who had received an abortion remained stable, and their financial events had declined modestly.

[Will COVID force public health to confront America's epic inequality?](#)

“Mississippi is arguing that there is no evidence that abortion access matters to people’s lives, and that is just wrong,” says Caitlin Myers, an applied macroeconomist at Middlebury College in Vermont, and a signatory on the brief.

Finally, the economists supply evidence to counter Fitch’s argument that abortion is no longer necessary because support is available from the state. The United States is alone among wealthy nations in not mandating paid maternity leave, the brief points out. It also provides figures indicating that a single parent earning the minimum wage would need to spend more than two-thirds of their income on childcare, with care for the average infant costing about US\$10,400 per year. These figures matter, the researchers argue, because two main reasons that women give for seeking abortions are concerns about money and caring for existing children. About 75% of women who choose to have abortions are in a low-income bracket, and 59% already have children, according to the economists’ brief.

A post-*Roe* world

The Supreme Court will decide the case by the end of June 2022. Even if the justices don’t overturn *Roe*, they could effectively end the precedent by erasing its viability standard, which permits abortion up until a fetus can survive outside of the womb. If the court shifts this standard on the basis of arguments about when a fetus becomes a person, the research filed to the justices might not matter. Because this question is not something that science clearly defines, Toti says, courts generally haven’t debated it. But that could change.

If *Roe*’s viability standard ceases to exist, states will be able to block abortion at early stages of pregnancy, as Texas did last month with a law that bans abortions after six weeks of pregnancy, before most people know they are pregnant. On 21 October, Texas joined Mississippi in asking the Supreme Court to reverse *Roe*.

With this in mind, some researchers are forecasting what the future might look like in the United States if *Roe* is overturned or significantly curtailed by the Supreme Court. In one unpublished analysis, Myers modelled what

will happen if abortions are banned in 12 states with pre-emptive ‘trigger bans’ — which will automatically block abortion if *Roe* is overturned — and in 10 other states with several types of abortion restrictions in place. She estimates that, on average, a woman in these states who seeks an abortion will need to travel 280 miles (450 kilometres) to reach a clinic (see ‘If *Roe* is overturned’), and each year the distance will present an insurmountable obstacle for around 100,000 of them, who don’t have the means to travel far.

Laurie Sobel, a researcher at KFF, a non-partisan health-policy research organization based in San Francisco, California, is working on a similar assessment. KFF refrains from taking political positions, but Sobel says the evidence for the potential repercussions of this court decision is clear. “This could have a devastating impact on women that would be real and very severe in many states.”

Nature **599**, 187–189 (2021)

doi: <https://doi.org/10.1038/d41586-021-02834-7>

Editor’s note: Nature recognizes that transgender men and non-binary people might become pregnant and seek abortion care. We use ‘women’ in this story to reflect how participants are reported in the studies we cite, and how people are referred to in court briefs.

References

1. 1.

Foster, D. G. *The Turnaway Study: Ten Years, a Thousand Women, and the Consequences of Having — or Being Denied — an Abortion* (Simon & Schuster, 2021).

2. 2.

Raymond, E. G. & Grimes, D. A. *Obstet. Gynecol.* **119**, 215–219 (2012).

3. 3.

Biggs, M. A., Upadhyay, U. D., McCulloch, C. E., & Foster, D. G. *JAMA Psychiatry* **74**, 169–178 (2017).

4. 4.

Ralph, L. J., Schwarz, E. B., Grossman, D. & Foster, D. G. *Ann. Intern. Med.* **171**, 238–247 (2019).

5. 5.

Jones, R. K. & Jerman, J. *Am. J. Public Health* **107**, 1904–1909 (2017).

6. 6.

Kalist, D. E. *J. Labor Res.* **25**, 503–514 (2004).

7. 7.

Miller, S., Wherry, L. R. & Foster, D. G. *NBER working paper No. 26662* <https://doi.org/10.3386/w26662> (2020).

This article was downloaded by **calibre** from <https://www.nature.com/articles/d41586-021-02834-7>

- NEWS EXPLAINER
- 02 November 2021

Why scientists worldwide are watching UK COVID infections

The country's relaxation of measures such as masking — especially in England — is showing the limits of relying on vaccines alone.

- [Luke Taylor](#)



A wall in London commemorates people who died of COVID-19.Credit: Toby Melville/Alamy/Reuters

The COVID-19 pandemic in the United Kingdom has often foreshadowed what came later elsewhere. The highly contagious Alpha variant was first

detected there, and the country then reported high caseloads of the more-contagious Delta strain before this variant dispersed around the rest of the world. The United Kingdom also saw a wave of infections that seems to have preceded a similar glut now sweeping Western Europe.

Furthermore, England was among the first regions in Western Europe to lift almost all of its COVID-19 restrictions, following one of the world's fastest vaccine roll-outs. It ended the legal requirements for social distancing and mask use on 19 July, with Wales and Scotland — which set their own public-health policies — lifting most of their restrictions on 7 and 9 August, respectively. Northern Ireland followed on 31 October.

As one of the first countries to trust high vaccine coverage and public responsibility alone to control the spread of SARS-CoV-2, the United Kingdom has become a control experiment that scientists across the world are studying. “We are watching the increase in cases closely, trying to dissect what is going on and how that might influence our situation right now,” says Rafael Radi, a biochemist and coordinator of Uruguay’s COVID-19 Scientific Advisory Group.

Nature spoke to scientists around the world about what they hope to learn from the UK experience.

Can vaccines alone prevent infections from surging?

The United Kingdom was hit by three million infections between July and October this year — comparable to when the country was under a strict lockdown in late 2020. This is despite 79.5% of those aged 12 years and older having received two vaccine doses as of 31 October.

UK infection rates are higher than those in countries in continental Europe, where COVID-19 restrictions were relaxed later or remain in place. In the 7 days between 17 October and 23 October, Spain recorded 286 infections per one million people, and Germany 1,203. The United Kingdom registered 4,868 over the same week.

The surge in infections shows that vaccines alone cannot contain the virus, say scientists calling for the introduction of ‘soft’ public-health measures to avoid another lockdown.

“The vaccines are amazing and doing exactly what they’re supposed to do,” says Susan Butler-Wu, director of medical microbiology at the LAC+USC Medical Center in Los Angeles, California. “But why don’t we want to give them the best chance by combining them with other measures?”

Was the behaviour of individuals responsible for the recent surge?

The surge in infections is not the result of the public suddenly abandoning caution, researchers say. “We have not seen a continuous rise [in social interaction], but rather a small increase and then fluctuations driven by whether schools are open and how many people are attending work,” says Christopher Jarvis, a statistician who heads the London School of Hygiene & Tropical Medicine’s CoMix Social Contact Survey.

The average adult now has [contact with three to four other people per day](#), compared with more than ten before the pandemic. For children, the numbers are much higher now that schools have reopened. Mask use dropped once the mandate was lifted, but this is harder to measure.

The gradual pace of behaviour readjustment could explain why the country has experienced a sustained high level of infections rather than the spike that models predicted in August or September. Ongoing high transmission suggests that measures such as free rapid COVID-19 testing will not contain infections while high-risk events in crowded indoor environments are permitted, says William Hanage, an epidemiologist at the Harvard T. H. Chan School of Public Health in Boston, Massachusetts.

“This shows how cautious we need to be with the return to normality,” says Radi. “Increasing human interactions, even with a high proportion of the population fully vaccinated, may lead to new surges, hospitalizations and death.” Uruguay is using the United Kingdom’s rise in infections as a

cautionary tale to warn people of the risk of easing restrictions prematurely, Radi says.

Is vaccine protection waning?

The United Kingdom had one of the fastest COVID-19 vaccination campaigns in Europe. But that strength now seems to be its Achilles heel. The country's first COVID-19 vaccines were administered ten months ago, and antibodies have had time to decline.

Vaccine effectiveness against infection, hospitalization and death fell considerably after six months, particularly in older people, a UK-based study has found¹. A separate study in Israel — another country that deployed vaccines early — found similar results².

One of the driving forces behind this might have been dropping antibody levels, says Paul Hunter, who studies health protection and medicine at the University of East Anglia in Norwich, UK. Despite high infection rates and the ongoing vaccination campaign, antibody levels plateaued in May and then began to drop, according to the UK Office for National Statistics.

A decline in infection-blocking, or ‘neutralizing’, antibodies does not mean that someone is susceptible to infection, because memory immune cells also play a part, “but we do know that the level of neutralizing antibodies early on is a good indicator of protection”, Hunter says.

But are vaccines still holding up against death and serious illness?

The Delta variant's mutations — combined with waning vaccine antibodies — are causing more breakthrough infections. But vaccines are still offering remarkable protection against hospitalization and death. A study at the University of Edinburgh, UK, found that the Pfizer–BioNTech and Oxford–AstraZeneca vaccines were 90% and 91% effective, respectively, at preventing death³. Furthermore, around 75,000 people required hospital treatment for COVID-19 in the United Kingdom between the start of July

and early October this year, compared with 185,000 between October 2020 and January 2021, when the number of infections was comparable but vaccines were less available.

Relative to the size of its population, the United Kingdom has around three times as many infections as the United States, but only two-thirds the daily deaths. “The amount of infection that is currently going on in the UK would be expected to have much worse consequences if replicated elsewhere,” says Hanage.

Can boosters help to control future surges?

UK authorities began offering a third dose of the COVID-19 vaccines to residents aged 50 years and older, and to those in high-risk groups, on 16 September. Although the precise impact of booster doses has not been established, “the emerging evidence is that they are a lot more effective at reducing infections than we were expecting”, says Hunter.

A study at the Weizmann Institute of Science in Rehovot, Israel, found that people who received a third dose of the Pfizer–BioNTech vaccine were almost 20 times less likely to get seriously ill from COVID-19, and 10 times less likely to be infected, than were people who had received their second and last dose at least 5 months before⁴.

The World Health Organization has criticized the roll-out of third doses in wealthy nations when many people in poorer ones are yet to receive their first. But boosters could get the United Kingdom through the coming winter without new restrictions being imposed, says Marc Baguelin, who models COVID-19 infections for the UK government at Imperial College London. His team’s most optimistic models — based on assumptions regarding behaviour and the effectiveness of immunity — predict a sustained high number of infections between October 2021 and March 2022, leading to around 43,000 hospital admissions and more than 5,000 deaths.

High circulation of the virus, as the cold pushes people indoors where the virus spreads more easily, and as immunity wanes, means that marginal increases in vaccine protection should have “a significant impact on

hospitalizations and deaths”, Baguelin says. “Now everything relies on the boosters.”

Nature **599**, 189–190 (2021)

doi: <https://doi.org/10.1038/d41586-021-03003-6>

References

1. 1.

Andrews, N. *et al.* Preprint at medRxiv
<https://doi.org/10.1101/2021.09.15.21263583> (2021).

2. 2.

Bar-On, Y. M. *et al.* *N. Engl. J. Med.* **385**, 1393–1400 (2021).

3. 3.

Sheikh, A. *et al.* *N. Engl. J. Med.*
<https://doi.org/10.1056/NEJMc2113864> (2021).

4. 4.

Barda, N. *et al.* *Lancet* [https://doi.org/10.1016/S0140-6736\(21\)02249-2](https://doi.org/10.1016/S0140-6736(21)02249-2) (2021).

This article was downloaded by **calibre** from <https://www.nature.com/articles/d41586-021-03003-6>

- NEWS
- 29 October 2021

The search for people who never get COVID

An international team of researchers wants to find people who are genetically resistant to SARS-CoV-2, in the hope of developing new drugs and treatments.

- [Smriti Mallapaty](#)



A couple walk on the streets of Istanbul, Turkey.Credit: Ibrahim Oner/SOPA Images/Shutterstock

Imagine being born naturally resistant to SARS-CoV-2, and never having to worry about contracting COVID-19 or spreading the virus. If you have this superpower, researchers want to meet you, to enrol you in their study.

As described in a paper in *Nature Immunology*¹ this month, an international team of scientists has launched a global hunt for people who are genetically resistant to infection with the pandemic virus. The team hopes that identifying the genes protecting these individuals could lead to the development of virus-blocking drugs that not only protect people from COVID-19, but also prevent them from passing on the infection.

“It’s a terrific idea,” says Mary Carrington, an immunogeneticist at the Frederick National Laboratory for Cancer Research in Bethesda, Maryland. “Really, a wise thing to do.”

But success isn’t guaranteed. If genetic resistance to the coronavirus SARS-CoV-2 exists, there may be “only a handful” of people with this trait, says Isabelle Meyts, a paediatric immunologist and physician at the Catholic University of Leuven in Belgium, who is part of the consortium behind the effort.

“The question is how to find those people,” says Sunil Ahuja, an infectious-diseases specialist at the University of Texas Health Science Center at San Antonio. “It’s very challenging. This is not for the faint of heart.”

Discordant couples

Nevertheless, the study authors, including Evangelos Andreakos, an immunologist at the Biomedical Research Foundation of the Academy of Athens, say they are confident of tracking down their quarry. “Even if we identify one, it will be really major,” he says.

The first step is to narrow the search to people who have been exposed, without protection, to a sick person over an extended period, and have not tested positive or mounted an immune response against the virus. Of particular interest are people who shared a home and bed with an infected partner — pairs known as discordant couples.



The quest to find genes that drive severe COVID

The team of co-authors from 10 research centres across the world, from Brazil to Greece, have already recruited some 500 potential candidates, who might fit these criteria. And since the publication of their paper less than 2 weeks ago, another 600 people, including some from Russia and India, have contacted them, nominating themselves as possible candidates.

The response was a real surprise, says Jean-Laurent Casanova, a geneticist and study co-author at the Rockefeller University in New York City. “I did not think for one second that people themselves, exposed and apparently not infected, would contact us.”

The goal is to have at least 1,000 recruits; Andreakos says they’ve already started analysing data.

A huge challenge ahead

But the researchers might have an almost impossible task, given the difficulties of proving that candidates were highly exposed to the virus, argues Ahuja. They will have to confirm that the sick partner was shedding high doses of live virus when the couple were interacting closely with one another.

Discordant couples are not uncommon, but it is rare to find those that meet these criteria and have been regularly tested, he says. The fact that many people have now been vaccinated, potentially masking any genetic resistance to the virus, further limits the pool of people to study, Ahuja adds.

Once they have identified possible candidates, the researchers will compare the individuals' genomes with those of people who have been infected, in search of genes associated with resistance. Any contender genes will be studied in cell and animal models to confirm a causal link to resistance and establish the mechanism of action.

Casanova's team has previously identified rare mutations that make people more susceptible to [severe COVID-19](#), but the researchers are now shifting gears from susceptibility to resistance.

In genetic surveys called genome-wide association studies (GWAS), other groups have scoured the DNA of tens of thousands of people in search of single-nucleotide changes — which typically only have a weak biological effect — and identified some possible candidates associated with reduced susceptibility to infection.

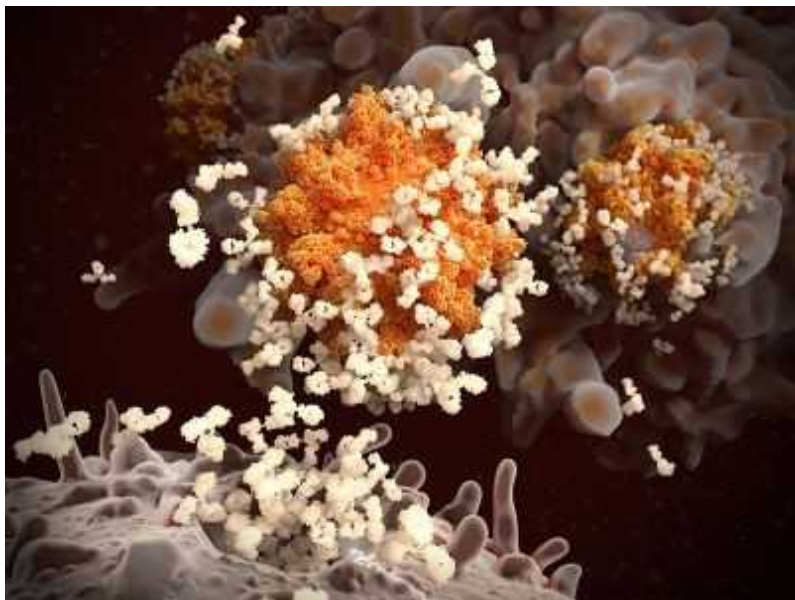
One of these is found in the gene responsible for the type O blood group, but its protective effect is small, says Carrington, and it's not clear how it is conferred.

Mechanisms of resistance

The researchers behind the new project have hypothesized the kind of resistance mechanisms they might find. The most obvious could be that some people don't have a functioning ACE2 receptor, which SARS-CoV-2 uses to enter cells. In one GWAS, posted as a preprint², and therefore not peer reviewed, researchers identified a possible link between a rare mutation that probably reduces expression of the *ACE2* gene and a diminished risk of infection.

This type of mechanism has previously been observed with HIV, the virus behind AIDS. Beginning in the 1990s, Ahuja and Carrington were involved

in work that helped to identify a rare mutation that disables the CCR5 receptor on white blood cells, preventing HIV from entering them.



[COVID super-immunity: one of the pandemic's great puzzles](#)

“That knowledge has been really useful,” says Carrington. It led to a class of HIV-blocking drugs and two people were also apparently cleared of HIV after receiving bone-marrow transplants from donors with two copies of the resistant genes.

Other people resistant to SARS-CoV-2 might have very powerful immune responses, especially in the cells lining the insides of their noses. Andreakos says some people might have mutations that ramp up genes that stop the virus from replicating and repackaging into new viral particles, or that break down viral RNA in the cell.

Despite the challenges ahead, he is optimistic about discovering people who are naturally resistant. “We are confident that we will find them,” he says.

Nature **599**, 191 (2021)

doi: <https://doi.org/10.1038/d41586-021-02978-6>

References

1. 1.

Andreakos, E. *et al.* *Nature Immunol.* <https://doi.org/10.1038/s41590-021-01030-z> (2021).

2. 2.

Horowitz, J. E. *et al.* Preprint at medRxiv
<https://doi.org/10.1101/2020.12.14.20248176> (2021).

This article was downloaded by **calibre** from <https://www.nature.com/articles/d41586-021-02978-6>

| [Section menu](#) | [Main menu](#) |

- NEWS
- 04 November 2021
- Correction [04 November 2021](#)

US astronomy's 10-year plan is super-ambitious

Its ‘decadal survey’ pitches big new space observatories, funding for large telescopes and a reckoning over social issues plaguing the field.

- [Alexandra Witze](#)



With input from many astronomers, ‘decadal surveys’ periodically help to set the priorities for US astronomy.Credit: Stan Honda/AFP via Getty

A long-anticipated road map for the next ten years of US astronomy is here — and it's nothing if not ambitious.

It recommends that NASA coordinate, build and launch three flagship space observatories capable of detecting light over a broad range of wavelengths. It suggests that the US National Science Foundation (NSF) fund two enormous ground-based telescopes in Chile and possibly Hawaii, to try to catch up with an advanced European telescope that's under construction. And for the first time, it issues recommendations for how federal agencies should fight systemic racism, sexism and other structural issues that drive people out of astronomy, weakening the quality of the science.

“There are tremendous scientific opportunities before us — twenty-first-century astrophysics is incredibly rich,” says Fiona Harrison, an astrophysicist at the California Institute of Technology in Pasadena and co-chair of the steering committee that wrote the report, known as *Astro2020*. The plan, [released on 4 November](#), attempts to capitalize on some of those opportunities while also being realistic about budget and schedule constraints, she says.



[How the fight over a Hawaii mega-telescope could change astronomy](#)

US astronomy has sometimes taken a haphazard approach to building research facilities. *Astro2020* is “imposing order on the field in a way that

probably hasn't been done before", says Matt Mountain, president of the Association of Universities for Research in Astronomy in Washington DC. For instance, *Astro2020* describes how the NSF could consider withdrawing its support from either of the large ground-based telescopes if they fail to reach certain milestones. It also sets out the deliberate steps NASA should take to develop technology for its ambitious space missions.

NASA, the NSF, the US Department of Energy (DOE) and the US Air Force commissioned the US National Academies of Sciences, Engineering, and Medicine to research and produce *Astro2020*. It is the latest in a series of 'decadal surveys' that aim to guide the direction of US astronomy and astrophysics, by gathering input from thousands of astronomers every ten years. "They're influential because they really do let the whole community speak their voice," says Aki Roberge, an astrophysicist at NASA's Goddard Space Flight Center in Greenbelt, Maryland. Funding agencies generally follow the decadal survey's recommendations, which means that billions of dollars are at stake.

Many astronomers welcome the vision laid out in the new report. "They really set the whole framework for how we can go about doing this ambitious science," says Scott Gaudi, an astronomer at The Ohio State University in Columbus. "It's a very balanced view," adds Priyamvada Natarajan, an astrophysicist at Yale University in New Haven, Connecticut. "I like that they really acknowledge that it takes time for the science and technology for missions to mature."

A forced partnership

Astronomers have been worried about the United States falling behind Europe, which is building the [Extremely Large Telescope](#) in Chile. Slated to come online in 2028, that facility is larger and further along than either of the extremely large US telescope projects under way. The 24.5-metre-wide Giant Magellan Telescope (GMT) is under construction in Chile, and the Thirty Meter Telescope (TMT) is planned for the Hawaiian mountain of Maunakea; *Astro2020* recommends that the NSF buy into both of them, to help the country catch up.



The Giant Magellan Telescope (artist's rendering shown) is under construction in Chile. Credit: Giant Magellan Telescope – GMTO Corporation

Under this arrangement, the GMT and the TMT, once bitter rivals, would partner to cover skies in both the Northern and Southern hemispheres, which the European telescope cannot do. Together, they could make new types of astronomical discovery in galaxy evolution, exoplanet studies and other fields. “The only way to have astronomy in the United States be competitive at this scale is with this kind of capability,” says John O’Meara, chief scientist at the W. M. Keck Observatory in Kamuela, Hawaii.

The decadal survey’s recommendation would deliver a much-needed boost in funding: the GMT is estimated to cost at least US\$2 billion and the TMT \$2.6 billion, but neither has all the money it needs. Both began as privately funded projects. Buy-in from the US federal government — the NSF might consider investing \$800 million in each — would give all US astronomers a chance to compete for a portion of observing time on both telescopes.

But it’s not clear whether the NSF could afford to support both facilities. So *Astro2020* lays out a process for deciding whether to jettison one of the telescopes if need be.



NASA won't rename James Webb telescope — and astronomers are angry

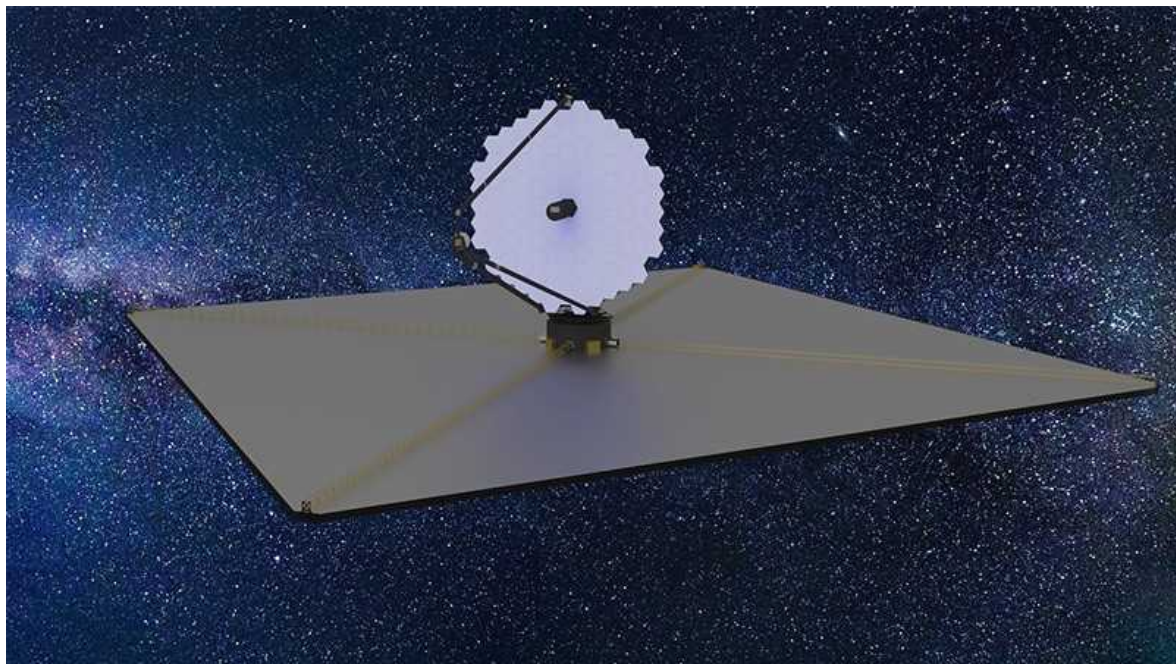
It remains to be seen how the TMT might move forward, however. The project is planned for Maunakea — one of the best sites in the world for stargazing — but construction there has been halted since 2015 owing to [protests from Native Hawaiians](#), to whom the mountain is sacred. The TMT's back-up site, on the island of La Palma in Spain's Canary Islands, seemed to be knocked out of the running in July, when a court annulled the agreement that the TMT would need to build there. The project is appealing against the decision, but remains focused on building relationships at the preferred site in Hawaii, says Kerry Slater, the TMT's vice-president of communications.

Other priorities on *Astro2020*'s wishlist for ground-based projects are a next-generation cosmology experiment in Antarctica and Chile that would probe the cosmic microwave background, commonly known as the afterglow of the Big Bang, and a major upgrade to the existing Very Large Array radio telescopes scattered across North America.

Triple threat

In addition to ground-based astronomy, the report provides guidance on the future of space-based missions, typically the most expensive and highest-

profile astronomical observatories. Recommendations from previous decadal surveys have led to iconic spacecraft such as the Hubble Space Telescope. This time around, the top recommendation is to launch not one, but three flagship observatories, spanning different wavelengths of light to enable a variety of discoveries. The last time NASA coordinated projects in this way was between 1990 and 2003, when the agency launched four satellites dubbed the Great Observatories, beginning with Hubble.



A future NASA space telescope, recommended by *Astro2020*, could be a scaled-down version of this one, shown as an artist's illustration. Credit: NASA GSFC

First out of the gate in the next set of missions, which some astronomers are calling the 'New Great Observatories', would be a space telescope similar to Hubble, but with a mirror more than twice the width of Hubble's. It would detect light in ultraviolet, visible and near-infrared wavelengths, and be able to discover objects of astrophysical interest ranging from habitable planets to violent black holes. It would cost around \$11 billion and launch in the early 2040s.

Second and third would be missions detecting X-rays, a sector of the electromagnetic spectrum in which some of the most powerful astrophysical

phenomena can be observed, and far-infrared radiation, which can penetrate the shrouds of dust around newborn stars. These missions would cost \$3 billion to \$5 billion each, and a decision on whether to build them would be made five years after the start of the first Hubble-like mission.

Lurking behind these ambitious spacecraft is the spectre of previous space missions whose budgets have blown out of control. Neither of the top recommendations for large space-based missions from the past two decadal surveys are operational yet. The James Webb Space Telescope, the leading recommendation in the 2000 survey, is set to launch on 18 December, [years later than intended](#), at a cost of nearly \$10 billion — well above its original budget. The Nancy Grace Roman Space Telescope, the main recommendation in the 2010 survey, had to accommodate a 2.4-metre primary mirror donated by a spy-satellite programme, which was supposed to save money but required design changes and extra processing that drove up the cost. The COVID-19 pandemic added costs and delays, and Roman is now targeted to launch no earlier than 2027, at a cost of \$4.3 billion.



[Astronomy impasse: What's next for the Thirty Meter Telescope?](#)

“We’ve learned a lot in the course of the last 10–20 years about how to do large missions,” says Gaudi. “For me, it’s almost inconceivable that we couldn’t do better the next time, because we’ve learned from our past mistakes.”

Astro2020 recommends that NASA save money by, among other things, terminating the Stratospheric Observatory for Infrared Astronomy, a telescope-on-a-plane that has [come under criticism](#) for its relatively high operational price tag — nearly as much as Hubble’s — and relatively low scientific output so far, although that is improving. At the same time, the report advises that the agency fund mid-sized space missions, such as astrophysics spacecraft on the order of \$1.5 billion each.

A human endeavour

Astro2020 also attempts to grapple with the importance of equity and inclusion to the health of US astronomy. “Astrophysics is done by humans,” says Jane Rigby, an astrophysicist at the Goddard centre. “How these humans treat each other, how they are led, how they hold each other accountable, what the policies and the systems are that they’re working in — this makes so much of a difference to the quality of the science that gets done.”



Native Hawaiians have been protesting the construction of a new, extremely large telescope at Maunakea for years. Credit: Ronit Fahl/Zuma Press

US astronomy has found itself at the forefront of many social issues, such as the ethics of doing science on lands seized from Indigenous groups — such as Maunakea. The field has also faced widespread problems of sexism and racism in science, including [a sexual harassment scandal](#) surrounding prominent astronomer Geoff Marcy.

The report lays out some recommendations for reducing the systemic barriers that block many people from entering and staying in science. They include increasing federal funding for student and early-career researchers, making diversity a criterion in awarding grants, and gathering data to better track the lack of equity in funding. Collecting such data is the first crucial step towards distributing resources equitably, Natarajan says.

“Racial/ethnic diversity among astronomy faculty remains, in a word, abysmal,” the report says. Indigenous people are even more under-represented in astronomy than in other physical sciences, it notes, while calling for “a new model for respectful, collaborative decision-making in partnership with Indigenous and other local communities”.



[NASA won't rename James Webb telescope — and astronomers are angry](#)

Attention will now turn to how the survey's recommendations might become reality. Pandemic-related delays in the report's release mean that the NSF, NASA and the DOE have already missed their chance to incorporate the findings into the budgets they are drawing up for the 2023 fiscal year. As a result, *Astro2020* priorities will not start receiving funding until 2024 at the earliest. NASA says it will respond in detail to the recommendations within about ten weeks.

"It is now the community's job to translate these words into actions," says Tony Beasley, director of the National Radio Astronomy Observatory in Charlottesville, Virginia.

Nature **599**, 192-193 (2021)

doi: <https://doi.org/10.1038/d41586-021-03027-y>

Updates & Corrections

- **Correction 04 November 2021:** An earlier version of this story listed the credit on the image of the Giant Magellan Telescope as GMTO Corporation/M3 Engineering. It is Giant Magellan Telescope – GMTO Corporation.

This article was downloaded by **calibre** from <https://www.nature.com/articles/d41586-021-03027-y>.

| [Section menu](#) | [Main menu](#) |

- NEWS
- 05 November 2021

Sponge cells hint at origins of nervous system

Synapse genes help cells to communicate in sponge's digestive chambers.

- [Max Kozlov](#)



This freshwater sponge (*Spongilla lacustris*) may hold clues about the evolution of the nervous system. Credit: Willem Kolvoort/Nature Picture Library

Sponges are simple creatures, yet they are expert filter feeders, straining tens of thousands of litres of water through their bodies every day to collect their

food. Their mastery of this complex behaviour is all the more remarkable because they have no brain, nor even a single neuron to their name.

A study published on 4 November in *Science* now reveals that sponges use an intricate cell communication system to regulate their feeding and to potentially weed out invading bacteria¹. The findings could help to understand how animals' nervous systems evolved, says Casey Dunn, an evolutionary biologist at Yale University in New Haven, Connecticut, who studies marine invertebrates. "This is a really exciting study that allows us to see sponges in a new light," he says.



Sponge-like fossil could be Earth's earliest known animal

Cells frequently communicate with one another, and neurons do so by passing electrical or chemical signals through tiny, targeted connections called synapses. Previous research² has found that sponges possess genes encoding proteins that typically help synapses to function, despite the animals' lack of neurons.

To discover which cells were expressing these genes, Detlev Arendt, an evolutionary biologist at the European Molecular Biology Laboratory (EMBL) in Heidelberg, Germany, and colleagues sequenced the RNA in various individual cells from a freshwater sponge (*Spongilla lacustris*).

They found that the sponge has 18 distinct cell types. Synaptic genes were active in a few of these types, which were clustered around the sponges' digestive chambers. This suggests that some form of cellular communication might coordinate the animal's filter-feeding behaviour.

The researchers then used X-ray imaging and electron microscopy to study one of these cell types, which they called secretory neuroid cells. The scans revealed that neuroids send out long arms to reach choanocytes, a type of cell with hair-like protrusions that drive sponges' water-flow systems and capture most of their food.

Electron microscopy reveals that neuroid cells (purple and red) can stretch out their arms to communicate with digestive cells (blue, green and yellow).

Nervous-system precursor

On the basis of the proximity of the two cell types and the expression of genes that might allow for the secretion of chemicals, the researchers think that these arms enable neuroids to communicate with choanocytes, so that they can pause the water-flow system and clear out any debris or foreign microbes. However, these neuroid cells are not nerves, and there is no sign of the synapses that enable neurons to communicate so quickly. Instead, this cell type might represent an evolutionary precursor to a true nervous system, says Jacob Musser, an evolutionary biologist at EMBL, who co-authored the study. "We're at an intermediate point, where you've gone from having all these independent pieces to bringing them together more broadly, but you haven't gotten all the interconnectivity needed to create a fast synapse," he says.

Some scientists say that calling these cells a precursor to a nervous system is a stretch. "It's tantalizing, but it's hardly definitive," says Linda Holland, an evolutionary developmental biologist at the University of California, San Diego. She says it will be difficult to prove whether nervous systems evolved from this cellular communication system or arose earlier or even multiple times, as some groups have proposed. Indeed, many other organisms, including unicellular eukaryotes³, contain the same synaptic

genes, says Sally Leys, a marine biologist at the University of Alberta in Edmonton, Canada.

April Hill, a developmental geneticist at Bates College in Lewiston, Maine, hopes that scientists will use this study and its methods as a “launchpad” for further investigation of this ubiquitous sponge. Whether other sponges use a similar cellular communication system, she adds, remains a key unanswered question.

Nature **599**, 193 (2021)

doi: <https://doi.org/10.1038/d41586-021-03015-2>

References

1. 1.

Musser, J. *et al.* *Science* <https://doi.org/10.1126/science.abj2949> (2021).

2. 2.

Srivastava, M. *et al.* *Nature* **466**, 720–726 (2010).

3. 3.

Burkhardt, P. & Sprecher, S. G. *BioEssays* **39**, 1700024 (2017).

This article was downloaded by **calibre** from <https://www.nature.com/articles/d41586-021-03015-2>

- NEWS FEATURE
- 10 November 2021

Caltech confronted its racist past. Here's what happened

With a push from students and alumni, the university faced up to a legacy of support for eugenics. As it renames buildings and programmes, can its story serve as a model for others?

- [Nidhi Subbaraman](#)



The Robert A. Millikan Memorial Library was this week renamed Caltech Hall. Credit: Sam Comen for *Nature*

After a few hours leafing through documents in the basement of a research building, Jane Panangaden was shaking with rage. It was 2017 and she was reading case records for hundreds of people who had been sterilized, usually without their consent, in the 1920s and 1930s. The physician reports had been collected to support the eugenics movement, a racist, pseudoscientific ideology with a history, Panangaden now realized, that was deeply entwined with that of her university, the California Institute of Technology — or Caltech — in Pasadena.

She was a first-year graduate student in mathematics at the time, but had always been interested in how people have co-opted or twisted science to support unjust policies. She knew a little about eugenics, but had only just learnt of the Human Betterment Foundation (HBF), one of the most prominent eugenics groups of its time, begun in Pasadena in the same decade that Caltech transformed from a sleepy small-town technical school into a science and engineering powerhouse. When Panangaden found out — through the university's own library website — that hundreds of records from the group were neatly preserved on campus, she had to see them for herself.

“It was really upsetting,” she remembers. She told everyone she knew, anyone who would listen, that Caltech’s past was linked to this group. “I could talk about nothing else for days and days afterward,” she says.

In June 2020, shortly after the killing of George Floyd by police in Minneapolis, Minnesota, student groups including the Socialists of Caltech, a group to which Panangaden belongs, put the spotlight on Caltech’s most famous former president — Nobel-prizewinning physicist Robert Millikan — and his involvement with the Human Betterment Foundation as a trustee.

The students wanted name changes for several campus buildings, professorships and programmes that memorialize people linked to the eugenics movement. This included the imposing nine-storey library named after Millikan. “It seems very straightforward: we shouldn’t be idolizing people with horrible views of the world,” says Daniel Mukasa, a graduate student who is currently the president of Black Scientists and Engineers of Caltech (BSEC), the student group that led the call for change. “Then we’re setting a horrible standard for all society.”

The students were eventually joined by faculty members and alumni, prompting Caltech administrators to reconsider the people it venerates.

Caltech is not alone. Across the United States and around the world, administrations at wealthy institutions have been peeling away name plates and putting statues into storage. In June 2020, the University of Mons in Belgium removed a bust of King Leopold II, who in the late 1800s established a bloody colonial rule in what is now the Democratic Republic of the Congo. Princeton University in New Jersey had decided in 2016 to preserve the name of former US president Woodrow Wilson for a residential college and a public-affairs school — despite his support of segregation in the federal government. It reversed course last June, announcing that it would rename the buildings. Last month, a group commissioned by Imperial College London recommended removing the names of scientists who supported eugenics and of university benefactors who became wealthy through arms sales or mining in colonized territories. The university's administrators are consulting with staff and students while they consider their next steps.



Graduate student Jane Panangaden was horrified to learn about Caltech's links to eugenics. Credit: Sam Comen for *Nature*

Many others are conducting excavations of their histories. At the [Universities Studying Slavery \(USS\) project](#), based at the University of Virginia in Charlottesville, historians and administrators from dozens of institutions around the world are sharing best practices for researching their pasts. Each is looking for ways to reconcile previous injustices with present-day ideals of inclusion and equality.

At Caltech, events progressed quickly last year. The institute assigned a committee to investigate its links to eugenics advocacy. And after a months-long process that sometimes pitted students against administrators, leaders decided in January to remove Millikan's name and several others from prominence on campus. This week, they announced some of the names that will replace them.

It's a meaningful move for Panangaden, who identifies as multiracial and disabled. "I find it important to rename the buildings just because I don't want to have that constant reminder that the people who built this institution didn't want me to be there, and didn't even want me to exist."

But she says it would be a hollow effort without further steps to address the institution's diversity gaps. Many US universities that focus on science and engineering acknowledge that Black, Hispanic, Native American and Native Hawaiian students are under-represented. At Caltech, the figures have been especially stark: only 1.2% of the graduate-student body in 2020–21 identified as Black.

Others agree that investigating the past is just part of the process. "If we're going to acknowledge this history and atone for it, we're then going to have to tilt to something that involves repair," says Kirt von Daacke, a historian at the University of Virginia who heads the USS project. "That's where the real hard work begins."

Lore and legacy

Caltech alumnus Michael Chwe first learnt about Millikan in 1981, in the big undergraduate seminar for physics students.

Millikan gained fame for his 'oil drop' experiment, which helped to measure the magnitude of an electron's charge. Chwe, now a political scientist at the University of California, Los Angeles, remembers following these historic experiments through the scanned pages of Millikan's own notebooks, with rows of recordings and notes in a neat, regular cursive script.



Caltech alumnus Michael Chwe stands in front of the institution's Kerckhoff Laboratories, where the Human Betterment Foundation used to have an office. Credit: Sam Comen for *Nature*

Millikan was a towering figure in US culture and politics. "With the exception of Einstein, no scientist was better known to Americans," former Caltech archivist Judith Goodstein wrote in a 2015 essay (see go.nature.com/3mtmgbj). Over 30 years, he transformed the institute to a revered scientific centre with US\$40 million in private funding.

"What he did is extraordinary," Goodstein says. "In one generation, he took a school that was really just a local school, and turned it into a powerhouse."

Before 1920, it was known as Throop College of Technology. By the time Millikan arrived in 1921, it had been renamed the California Institute of Technology. When Millikan won the Nobel Prize in Physics two years later, it boosted the institute's reputation and helped him to recruit rising scientific

stars and build state-of-the-art labs for electrical engineering and seismology.

When he died in 1953, the Associated Press lauded him as “a prophet of a new age, educator, humanitarian, philosopher” and “one of the world’s outstanding scientists”.

The links between the Human Betterment Foundation and the institute were forged in the same years that Caltech was growing into an academic heavyweight. But Chwe doesn’t remember hearing about Millikan’s ties to the group or to eugenics when he was a student.

He first became aware of that last June, on a Facebook thread about campus histories. Someone had linked to Princeton University’s decision to stop honouring Woodrow Wilson’s name because of his support for segregation, and because he had discouraged the enrolment of Black students at the university. Someone else commented that because Millikan had supported eugenics, perhaps it was time to rethink his legacy, too.

“I thought, ‘Wow, I’d never known that at all,’” Chwe says. He began googling, and the information was all easy to find, some of it in Caltech’s own records.



[Black scientist network celebrates successes — but calls for more support](#)

Before the start of the Second World War, Millikan had joined the Human Betterment Foundation as a trustee, just as the group was redoubling its efforts to advocate the forced sterilization of people whom doctors deemed ‘feeble-minded’ and therefore unfit to have children. California was one of more than 30 states to carry out state-sanctioned sterilization, and would grow to be the most prolific in the country. More than 20,000 people, including young teenagers, underwent forced sterilization surgery in California before the law allowing it was dismantled in 1979 ([A. M. Stern](#) *Am. J. Public Health* **95**, 1128–1138; 2005). African Americans and immigrants were chosen for sterilization at rates that were higher than their proportion in the population.

Chwe was crushed. He had come to view Millikan’s achievements as part of Caltech’s lore. “We saw ourselves as very much a part of that scientific institutional tradition and we were proud of it,” Chwe says. The revelations felt like a betrayal, as if his relatives had buried a dark family secret.

In late June 2020, as students on campus began putting together their call for Millikan’s name to be removed, Chwe began circulating a petition among alumni, highlighting Caltech’s links to the Human Betterment Foundation.

Weeks earlier, two students had written a letter explicitly calling for the removal of names. Members of BSEC drafted a petition that included a demand to rename memorials to Millikan, alongside a list of steps to diversify the student body.

Chwe’s petition and BSEC’s letter swiftly gathered more than 1,000 signatures each, and the calls were covered by US national and local newspapers.

Assertive action

Within weeks, Caltech president Thomas Rosenbaum announced a slew of changes. These included funding to expand research and recruitment programmes involving students from under-represented groups. The president also pledged to provide funding for students to attend scientific conferences such as the Annual Biomedical Research Conference for

Minority Students and the Society for Advancement of Chicanos/Hispanics and Native Americans in Science.

Caltech affirmed that it would share diversity data covering staff, students and faculty members; send out a survey to document the experience of students on campus; and provide unconscious-bias training for recruitment committees. “The initial interventions and areas of focus were informed by what the administration heard and learned from the community, and included a mixture of immediate and long-term measures,” a Caltech spokesperson told *Nature* by e-mail.



Sarah Sam was the only graduate student on Caltech’s Committee on Naming and Recognition. Credit: Sam Comen for *Nature*

Sarah Sam, a neurobiology graduate student then in her fifth year, and president of BSEC at the time, was pleased by the news, but wary. Since her first week on campus, when she felt like the only Black woman in her

incoming graduate class, she had devoted time to speaking at graduate-student panels and recruitment events and leading BSEC to build better support for Black students on campus. It seemed, now, that the administration was listening.

“None of the ideas in the petition are new,” Sam said at the time. “These things have been requested by me or other people for years, and so a lot of the changes are long overdue.”

As for renaming buildings, Rosenbaum announced last July that he would convene a committee to consider the question. He asked Sam to join a 15-member group, the Committee on Naming and Recognition, that included administrators, faculty members and trustees.

Like many Black students and academics who balance efforts to increase diversity with their own career goals, Sam recognized the time and emotional cost of being part of such a group. She had already sunk hours into crafting and promoting the petition, and wasn’t sure she was ready to do more. But she had assurances from Rosenbaum that it wouldn’t be too much of a drain. “I was there mostly to lend my perspective,” Sam says.

Past and future

The committee met weekly from July to December. Its main task was to consider the links that Millikan and six other Caltech benefactors and affiliates had to eugenics broadly, or to the Human Betterment Foundation specifically. Beyond considering whether those names were still fit to be memorialized, the group was to propose general principles for choosing names to honour in the future, to make Caltech “a destination of choice for a diverse community of exceptional scholars”.

Scholars of history and racism were invited to advise the committee — including Harvard University historian Evelyn Hammonds, who researches race and science, and Daniel Kevles, an emeritus professor at Caltech and Yale University who has studied the history of the eugenics movement.

Some of the evidence was already on campus. Caltech archivist Peter Collopy combed the university’s collections, including Millikan’s letters to

other scientists, as well as posters, pamphlets and administrative records from the Human Betterment Foundation itself. He scanned, saved and distributed electronic copies of decades-old letters, meeting notices and memos, so the group could see the primary documents.



Evan Haze Nuñez (left), Jean Badroos (centre) and Daniel Mukasa (right) are members of Black Scientists and Engineers of Caltech, the student group that led the call for change. Credit: Sam Comen for *Nature*

The group also posted a survey and invited Caltech faculty members and students to send in their views. Nicolás Wey Gómez, a Caltech historian who studies science and colonialism, joined the committee alongside Sam. He says, “One of the questions, to me, was: was not Millikan a man of his time?”

In 1909, California had become the third US state to pass a bill that authorized doctors in prisons and asylums to sterilize inmates and residents.

About 15 years later, Pasadena businessman Ezra Gosney was laying the groundwork for what would eventually become the Human Betterment Foundation.

Biologist Paul Popenoe headed the research operation for the foundation, speaking at conferences and events. He also sent out surveys to thousands of doctors who had carried out the procedure. They responded, describing the people they'd operated on. Others sent observations about the practice. "I believe sterilizations should be performed more freely," one wrote. Another said she thought "sterilization is the best, if not the only, important treatment for hereditary insanity". There were a few more-sceptical responses, too: "I am not convinced that eugenics makes or mars civilization," one California doctor wrote, pointing out that the idea was still being debated, and urging "extreme caution".

Popenoe converted these medical dispatches into a series of pamphlets that advocated the sterilization policy.



The hashtags that brought Black scientists together

These publications were "sloppy and biased research", says historian Alexandra Minna Stern, founder and co-director of the Sterilization and Social Justice Lab at the University of Michigan in Ann Arbor. Yet the efforts lent a false sheen of 'scientific' support for forced sterilization, in the

United States and beyond. When California proposed extending its sterilization programme, the Human Betterment Foundation backed the bills (the legislation did not pass). In 1934, an exhibition in Pasadena supported by the foundation praised the emerging ‘racial hygiene’ theory of the Third Reich in Germany. German eugenicists visited California and corresponded with the big eugenics groups in that state, looking to its laws as a model before Germany adopted a nationwide sterilization policy for people deemed to have certain conditions that were assumed to be hereditary — among them schizophrenia, chronic alcoholism and ‘feeble-mindedness’.

Of the 25 founding members of the Human Betterment Foundation, several were scientists. This wasn’t unusual at the time — eugenics was “a feature of the American academy in the age of segregation”, says von Daacke. Its main principles grew out of older ideas of ‘race science’ that wrongly sought to categorize people on the basis of the colour of their skin, and falsely argued that biological differences set them apart.

Pasadena itself was deeply segregated. Rules adopted by businesses and home owners blocked people who were Jewish, Latino, Black or immigrants from living and working in the city.

The 2020 Caltech committee also saw evidence of racism and sexism in Millikan’s correspondence, even before he became involved with the foundation. In a 1924 letter, he described southern California and Caltech’s location as “the westernmost outpost of Nordic civilization”, adding that the “problem of the relations of our race to the Asiatic races is the big race problem of the future”, and that California’s massive “Anglo-Saxon” population compared to that of east-coast cities such as New York made it an attractive destination. In 1936, he wrote to the president of Duke University in Durham, North Carolina, advising against recruiting a female physicist and arguing that it would be better to hire young men.

During the Second World War, as the United States began a nationwide effort to imprison civilians living in the country who had Japanese ancestry, Millikan collected the names and addresses of Japanese students who had studied at Caltech in the previous two decades and passed the list to the US military.



[Universities scrub names of racist leaders — students say it's a first step](#)

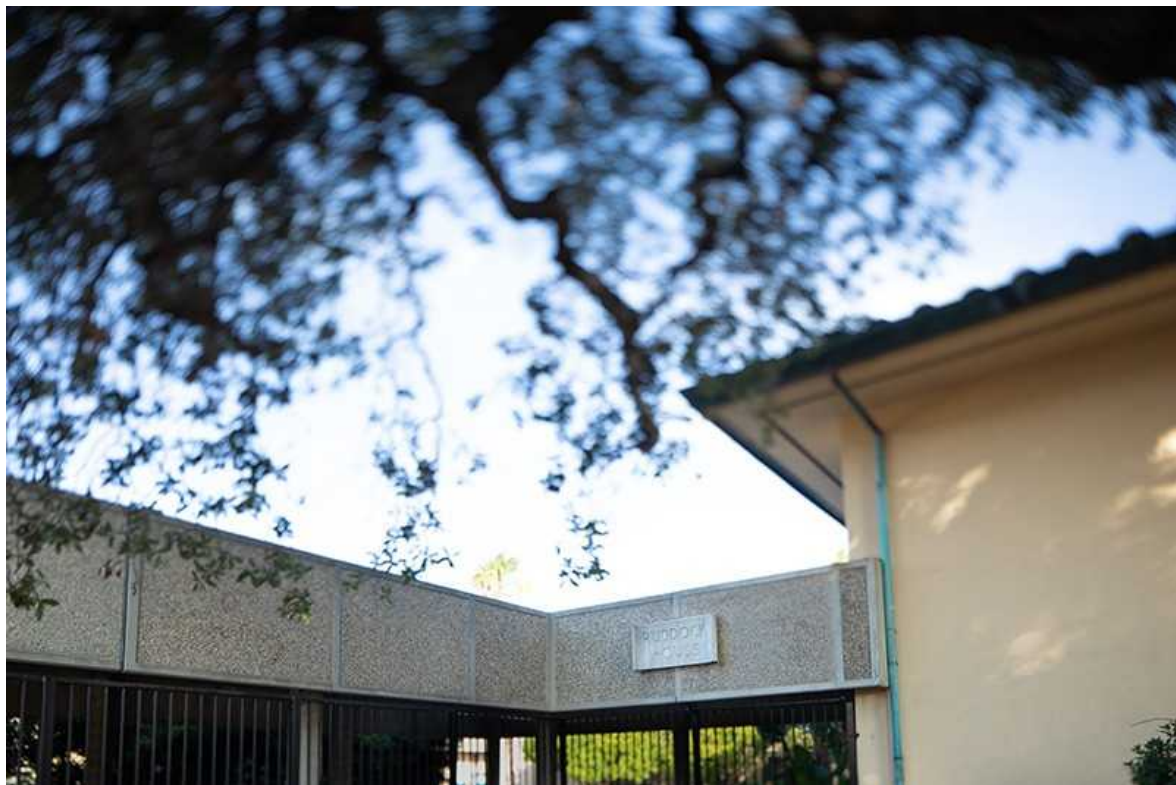
Millikan became a trustee of the Human Betterment Foundation in 1937. Records show that he often did not attend meetings and instead let other trustees vote on matters on his behalf. But documents also show that his support for the group persisted even when his peers had abandoned eugenics as a viable scientific ideology. “It was not inevitable in Millikan’s time to espouse eugenics,” Wey Gómez says. “In fact, the academic community and scientists had pronounced themselves already very strongly against eugenics. It was also not inevitable to be sexist or racist or xenophobic. So we have to be very careful what it is that we mean when we talk about contextualizing people in their own time.”

The Caltech community was divided at the start about renaming buildings, however. Of the 1,500 faculty members and students who replied to the committee’s survey, only about 45% supported removing the names of people associated with the Human Betterment Foundation. And about 37% of respondents explicitly opposed the idea.

One big argument from this latter group was that the recognition of Millikan on campus was for his scientific work and “not for their social activities or wrongdoings”, according to a summary included in the committee’s report. There was some concern that renaming “amounts to an erasure of history”, and separately that Caltech was swept up in “cancel culture”, according to one community member’s response quoted in the report. “If we were to

‘cancel’ Millikan for his views on eugenics, we should most certainly ‘cancel’ every scientist involved in the Manhattan Project, for their deleterious effects on life,” one person wrote. Whether responders supported or opposed removing names, there was broad agreement that Caltech needed to better recognize Millikan’s past defence of bigoted ideas and eugenics.

Goodstein supported preserving Millikan’s name. She also says that the committee was wrong to scrutinize Millikan’s private letters as public statements. “To judge him on the basis of his personal comments — I’m not sure it’s fair.” But she acknowledges that Millikan made a wrong call in not considering how firmly the tide had turned against eugenics and its spurious foundation in science. “He wanted the money, and he made a terrible compromise,” Goodstein says.



Ruddock House, a student residence hall at Caltech, has been renamed to honour Grant Venerable, the first Black student to graduate from the university. Credit: Sam Comen for *Nature*

When Gosney died in 1942, Caltech accepted the foundation’s assets of about \$171,500, equivalent to about \$3 million today. The committee’s

report states that “the California Institute of Technology clearly distanced itself from the HBF’s program” but used the money to support basic research in genetics, establishing a postdoctoral programme that was named the Gosney Research Fellowship.

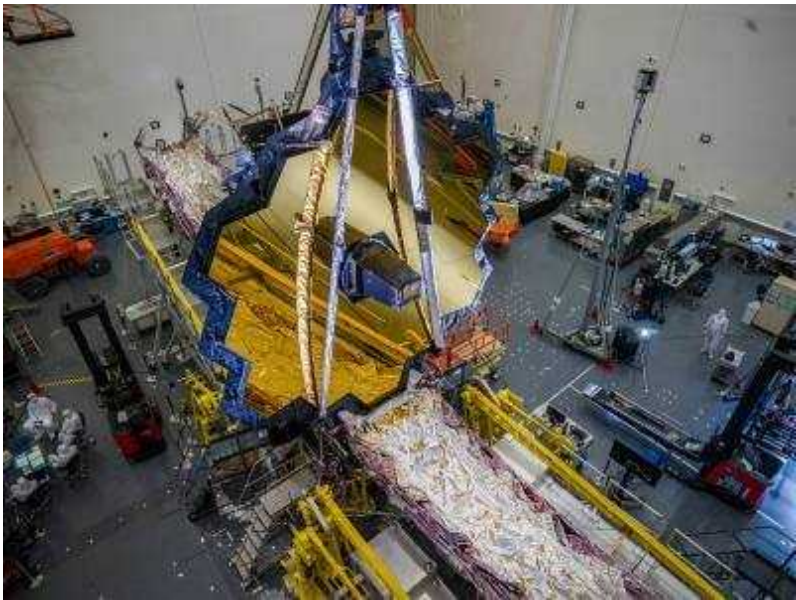
The committee heard a variety of arguments. “What emerges is a very complex picture of Millikan,” Wey Gómez says, “And the committee felt very strongly that we needed to continue to remember Millikan, in all of his complexity.”

Bumpy path

Sam was concerned by how things were progressing. In September last year, she announced that she was quitting the committee.

In a letter later shared online, she listed a series of grievances. Chief among them, she felt that the committee was questioning the part that racism played in the activities of the Human Betterment Foundation. Also, she was disturbed that discussion focused on the extent of Millikan’s involvement with the foundation, rather than the horror in the case reports preserved by the foundation.

When she tried to challenge the arguments from the inside, she says, she was shut down or ignored. She worried that the group would gloss over the racism in Caltech’s history, and didn’t want her name on such a report. So she quit. Within days, the *Los Angeles Times* covered her exit, describing it as a stumble in an otherwise swift response from the institute.



[NASA investigates renaming James Webb telescope after anti-LGBT+ claims](#)

Rosenbaum sent an e-mail to the community that week, not mentioning Sam by name, but insisting that Caltech and the naming group were “committed as an institution to the open exchange of ideas as a means to discover truth”.

“We were very sorry to see her leave,” says Wey Gómez. But he did not elaborate on the specific criticisms Sam had outlined in her resignation letter, saying that the committee had agreed to keep deliberations confidential.

Panangaden and other student activists who had watched Sam’s public exit were bracing for a fight with the administration. So what happened next came as a surprise. In December, the Committee on Naming and Recognition recommended to the Caltech president and trustees that memorials to Millikan and five other benefactors to Caltech be removed. These included *Los Angeles Times* publisher and Caltech board member Harry Chandler, HBF founder Ezra Gosney, and trustees William Munro, Henry Robinson and Albert Ruddock.

“Millikan’s affiliation with eugenics and the HBF as well as his stances on gender, race, and ethnicity constitute a significant breach of Caltech’s core commitments and its efforts toward diversity and inclusion,” the group

wrote in its final report. It also recommended that Caltech present the university's links with eugenics in a more public and open way.

Wey Gómez thinks this was the right decision — the recommendations were unanimous. “Memorialization means that you put an idea or a person in public view, as somebody who represents present values, and who represents the future that we aspire to,” he says. Millikan’s actions fell woefully short of that mark.

On 15 January, Rosenbaum announced that the board of trustees had agreed to all the recommendations of the group.



Caltech renamed the Linde + Robinson Laboratory in August to remove the association with eugenics supporter Henry Robinson. Credit: Sam Comen for *Nature*

Some changes in the student body have occurred already. As of September, 2% of the graduate-student body identifies as Black — nearly double the proportion from the previous year. A programme to bring undergraduates from groups under-represented in science to campus for the summer has

tripled, from 25 fellows in 2020 to 80 this year. And graduate record examinations, which have biases against women and people of colour, are no longer required for admission to graduate studies, following a BSEC recommendation.

This week, Caltech's Board of Trustees authorized the new names that will replace many of the contested memorializations, a process that required the university to contact descendants of donors affected by the changes, and to make legal petitions to the state. The nine-storey library will become Caltech Hall, and professorships named after Millikan now bear the name of Shirley Hufstedler, a judge, former trustee and advocate for diversity at Caltech. The Harry Chandler Dining Hall will be named after Lee Browne, who cultivated relationships between Caltech and local secondary schools. Ruddock House, a residence hall, will be named after Grant Venerable, the first Black student to graduate from the university. Departments are reconsidering fellowships and funds named after Millikan and Munro, and the Division of Biology and Biological Engineering has stopped using the Gosney name for fellowships.

Future focus

Mukasa, who has served on a committee advising on Caltech student admissions, is hopeful about the progress so far. "Normally with these diversity efforts, you really spend your entire time trying to make these efforts happen, but then you don't really see the fruits of your labour until three, four years after you're gone," he says. "Now I still have three, maybe four, years at Caltech and I still get to actually enjoy seeing this process actually happen."

His next focus is making sure the changes have staying power, by way of securing permanent endowments for some of the expanded programmes. "So far, that has gone well, but again the most important thing is that it continues to go well."

Student activists tracking Caltech's progress are pleased, but would like to see the institute improve on some other requests. These include a requirement for diversity statements, community service and outreach by faculty members in tenure applications, and asking all departments to define

clear rules on how prospective graduate students can apply for waivers to the application fees that sometimes serve as a barrier to people from disadvantaged backgrounds.

A Caltech spokesperson pointed to information on the institute's website that describes fee-waiver requirements. She adds: "The current administration has long been fully committed to doing the difficult work of creating a more diverse and inclusive community."

Panangaden is relieved about the outcome and thinks it will make the campus more welcoming to students, but she wonders whether the institute would have enacted such change if student groups had challenged Millikan's legacy in previous years. Activists at other institutions have observed that [universities were swayed by last year's groundswell of public opinion](#) against visible symbols of bigotry, whereas a few years ago they might have been reluctant to adopt change.

Sam was similarly relieved about the outcome, but says she was "devastated" to see that the committee had credited another student, who was not a member of BSEC, with writing the petition that she had co-written with other BSEC members. Caltech corrected the error but failed, in Sam's view, to give her adequate credit for her role in the process. Sam left the university shortly thereafter. A spokesperson wrote in an e-mail to *Nature* that "Sarah's input and contributions to the Caltech community have been and will continue to be of significant value". Six months later, Sam returned to campus, and she is now looking ahead to a new cohort of students that will find a different Caltech from the one she was introduced to in 2016. "We all did this work so that people in the future wouldn't have to think about how much it takes to get there," she says.

Caltech's story might prompt change beyond its own campus. Von Daacke says that, when an elite institution such as Caltech publicly acknowledges its history and begins dealing with it, it has ripple effects with other universities. It "has to be moving the needle", he says. The USS project, which launched with just a handful of institutes in Virginia, was built on that principle, he says, and over 4 years, it snowballed to include 80 institutions across 5 countries.

It was always going to be a challenge to come to grips with Caltech's history and Millikan's towering legacy, says Shirley Malcom, a Caltech trustee who served on the renaming committee with Sam. Malcom also leads the SEA Change programme, an initiative from the American Association for the Advancement of Science that aims to make science and engineering at US higher-education institutions more diverse, equitable and inclusive.

But in striving for a more equitable future, it was essential that Caltech looked to the facts of its past. "History affects your values, your traditions, your culture," Malcom says. Scores of US universities have been built on land taken from Indigenous residents. Many were built and run by people the institutions enslaved, so there is more reckoning to come, she says. "This was not the first institution that had to confront its history, and it won't be the last."

Nature **599**, 194-198 (2021)

doi: <https://doi.org/10.1038/d41586-021-03052-x>

This article was downloaded by **calibre** from <https://www.nature.com/articles/d41586-021-03052-x>

| [Section menu](#) | [Main menu](#) |

Books & Arts

- **[Are mothers too easy to blame?](#)** [08 November 2021]
Book Review • A book critiques the evidence for epigenetic inheritance of trauma.
 - **[Lessons from history on climate and pandemics: Books in brief](#)** [22 October 2021]
Book Review • Andrew Robinson reviews five of the week's best science picks.
-

- BOOK REVIEW
- 08 November 2021

Are mothers too easy to blame?

A book critiques the evidence for epigenetic inheritance of trauma.

- [Anna Nowogrodzki](#)



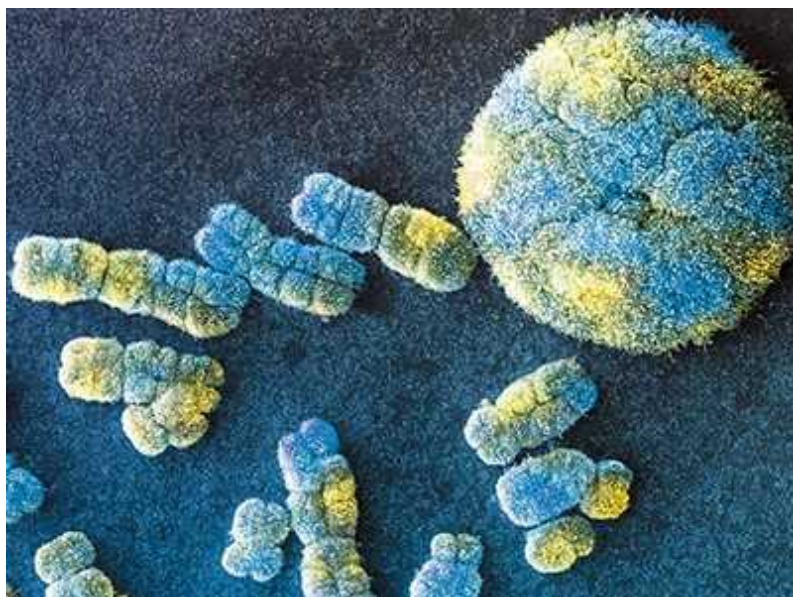
Refugees trying to cross the Croatian border into the European Union in 2015. Credit: Sanja Vrzic/Shutterstock

The Maternal Imprint: The Contested Science of Maternal-Fetal Effects
Sarah S. Richardson Univ. Chicago Press (2021)

Like me, my grandmother lived with anxiety, although she wouldn't have described it like that. Unlike me, she fled Poland under forged papers at the outset of the Second World War, knowing that her twin sister and beloved stepmother remained in the occupied country.

When I read news coverage of Rachel Yehuda's 2016 study claiming that the children of Holocaust survivors have epigenetic changes at a particular site in the genome, and those changes make them more susceptible to stress ([R. Yehuda et al. *Biol. Psychiatry* 80, 372–380; 2016](#)), it set me wondering. Did my grandmother's traumatic experiences cause changes to the regulation of her DNA that her body transmitted to my father when she was pregnant, ultimately contributing to my anxiety? Or was my anxiety due to genetics, culture, upbringing or the chilling knowledge that something terrible had happened to my relatives? Or was it all of the above?

Yehuda's study has been criticized often for its small sample size, tiny control group and outsize claims of causality, although you might not know it from media coverage. Sarah Richardson's book *The Maternal Imprint* broadens this criticism to the field of human transgenerational epigenetics more generally. She argues that social assumptions about maternal responsibility lend ideas in this field more credibility than they deserve on the basis of the data. Her argument will be interesting to researchers, pregnant nerds and policymakers, although she could have done a better job of showing her working.



Heredity beyond the gene

Epigenetics concerns chemical changes to DNA that don't alter the sequence itself, but do affect how genes are regulated; one such change is called methylation. Richardson discusses only transgenerational epigenetics, the kind that can be passed down to a gamete or embryo. This is distinct from epigenetic changes relayed between cells in a person's body. The latter is solidly supported and has a significant effect on the genomes of cancer cells, for example.

The first half of the book is an overlong tour of theories of maternal and paternal contributions to heredity since the late nineteenth century. Richardson, a historian of science, shows how each era's beliefs shaped its theories.

Prevailing thought has flip-flopped several times. In the 1880s, 'germ plasm' theory held that the sperm and egg contributed equally to heredity. Between the 1880s and early 1900s, a subgroup of eugenicists in the United States rejected these ideas and thought that a mother's mental state during pregnancy would be permanently imprinted on her child. For instance, an 1882 book by educational reformer Georgiana Bruce Kirby told pregnant women that to properly influence their fetuses, they should do mathematics and play music every day instead of taking part in "household drudgery" such as "making jam" and "hemming skirts". Then, in the 1910s, men were thought to bring the lion's share of risk to the offspring, owing to their more dangerous jobs and greater likelihood of drinking alcohol.

Finally, Richardson gets to her central critique of human epigenetics work. She pokes many holes in three groups of studies: Suzanne King's work on babies gestated during a 1998 ice storm in Quebec, Canada; Yehuda's studies of Holocaust survivors and their children; and research on babies gestated during the Dutch Hunger Winter famine of 1944–45.



The Avon Longitudinal Study of Parents and Children (also known as Children of the 90s) is part of an epigenetics consortium that hopes to plug knowledge gaps, using millions of biological samples including umbilical-cord blood and placentas. Credit: Children of the 90s

The ice-storm studies looked at only 34 children, and had no control group. The Holocaust work had only eight parental controls and nine offspring controls. The Dutch studies involved 811 offspring — a large enough sample size, including plenty of controls. Yet Richardson points out that the effect sizes they found were low: differences in DNA methylation levels of between 0.7% and 2.7%. None of the studies took biological samples from the children at birth. Without those, Richardson argues, they can't rule out 'reverse causation'. In other words, they can't pin down whether epigenetic changes caused, say, increased susceptibility to stress, or whether susceptibility to stress caused the epigenetic changes.



Genetic determinism rides again

Epigenetics studies typically use blood samples, but epigenetics varies by cell type, so if you're interested in effects in the brain, it's not clear that you would learn anything from changes in blood. And studies rarely collect much, if any, information about paternal contributions to the studied effects. One theory holds that maternal obesity during pregnancy causes higher rates of obesity in children; studies that expanded the research have found that paternal size explains the variation better.

Richardson makes many good points, but references and counterpoints are too thin on the ground. Most problematic, she doesn't engage with the growing body of work designed to address some of the gaps in the Dutch studies — efforts such as the Avon Longitudinal Study of Parents and Children in the United Kingdom, and at least seven others covered by the Pregnancy And Childhood Epigenetics Consortium that have sample sizes in the thousands and collect umbilical-cord blood to address reverse causation. Richardson never explains how she selected the three groups of studies that she focuses on to the exclusion of others.

Her key contention is that weak epigenetics findings can exert too tenacious a hold because our culture teaches us to assume that mothers bear responsibility. It's true — women are much too easy to blame. But to make a strong case, other interpretations need to be addressed, such as the general

frenzy for DNA-based explanations, or the cult of personal over societal responsibility.

Richardson is right, however, about how cultural assumptions diminish possibilities. As public-health specialist Liana Winett has written: “Asking, ‘What would a woman do today if she wanted to help her baby avoid chronic disease?’ is very different from, and much more limiting than asking, ‘What would our society do and provide if we wanted to be the healthiest place to be born?’”

Nature **599**, 199-200 (2021)

doi: <https://doi.org/10.1038/d41586-021-03053-w>

This article was downloaded by **calibre** from <https://www.nature.com/articles/d41586-021-03053-w>

| [Section menu](#) | [Main menu](#) |

- BOOK REVIEW
- 22 October 2021

Lessons from history on climate and pandemics: Books in brief

Andrew Robinson reviews five of the week's best science picks.

- [Andrew Robinson](#) 0

BRIAN FAGAN

NEW YORK TIMES-BESTSELLING AUTHOR OF THE GREAT WARMING

& NADIA DURRANI

CLIMATE CHAOS

LESSONS ON SURVIVAL

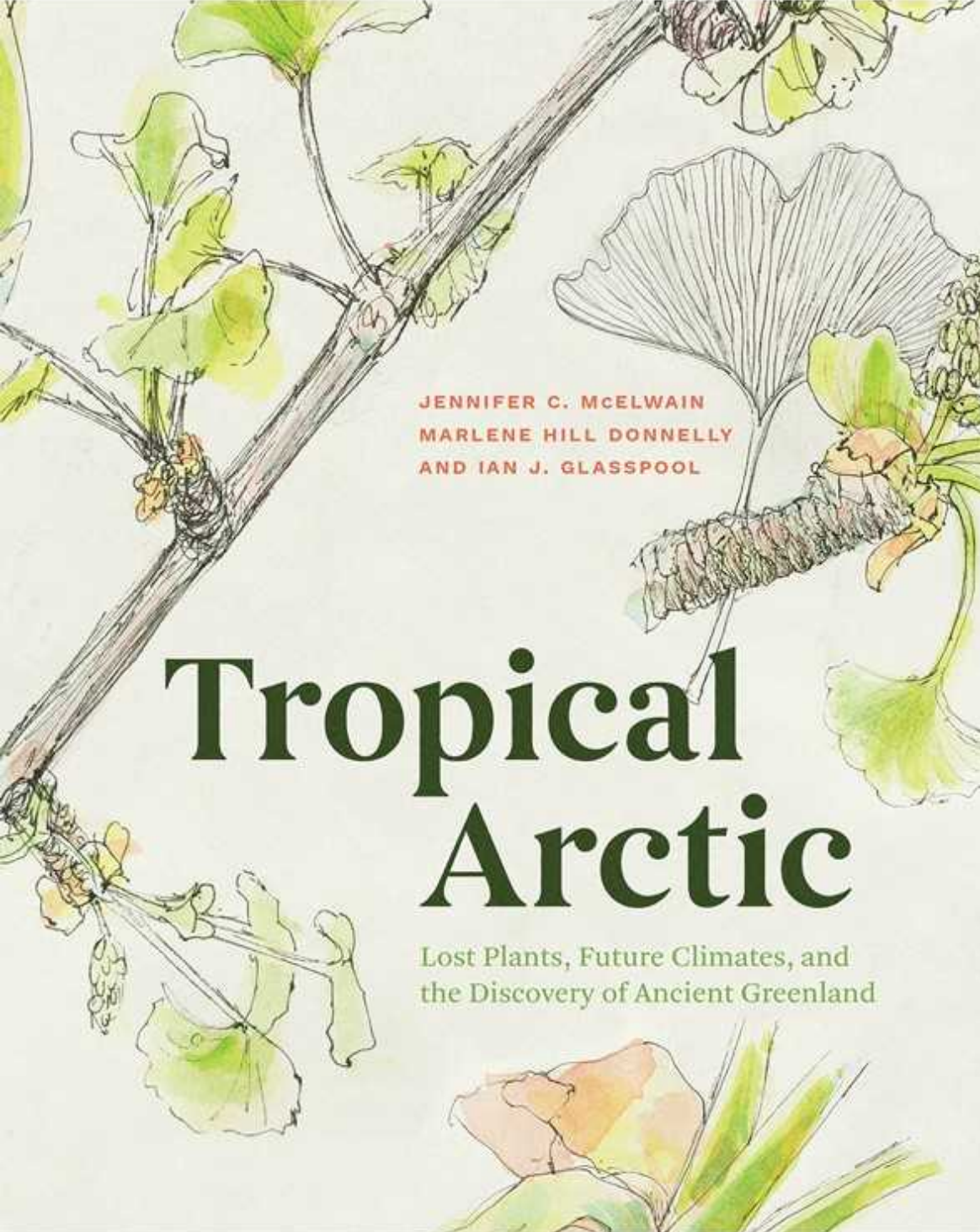
from OUR ANCESTORS



Climate Chaos

Brian Fagan & Nadia Durrani *Public Affairs* (2021)

Earlier civilizations' responses to natural climate shifts are often assumed to be irrelevant to the current crisis. Not so, argue archaeologists Brian Fagan and Nadia Durrani in their rich survey of the past 30,000 years. A global drought from 2200 to 1900 bc first destabilized Egypt, then strengthened it, after pharaohs in supposed divine control of the Nile were replaced by provincial leaders who invested in dams and irrigation. Egypt's "organized oasis" flourished for two millennia, becoming ancient Rome's granary.



JENNIFER C. McELWAIN
MARLENE HILL DONNELLY
AND IAN J. GLASSPOOL

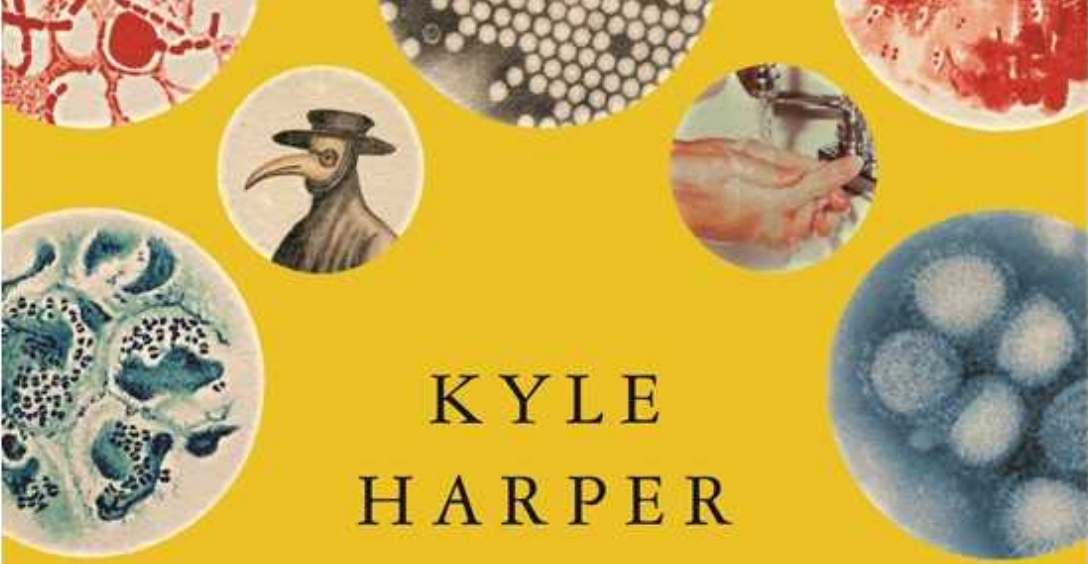
Tropical Arctic

Lost Plants, Future Climates, and
the Discovery of Ancient Greenland

Tropical Arctic

Jennifer C. McElwain *et al.* *Univ. Chicago Press* (2021)

Ice-covered Greenland was named misleadingly by tenth-century Norse settlers hoping to attract others. But at the time of the dinosaurs, the label would have been accurate, judging from the fossilized plants intricately reconstructed and pictured in this fascinating study by palaeobotanists Jennifer McElwain and Ian Glasspool, with scientific illustrator Marlene Donnelly. They warn that current greenhouse-gas emissions are becoming comparable in impact to the volcanic emissions that triggered the collapse of Triassic Greenland's flora.



KYLE
HARPER

Plagues Upon the Earth

*Disease and the
Course of Human
History*

Plagues upon the Earth

Kyle Harper *Princeton Univ. Press* (2021)

Classicalist Kyle Harper's absorbing global history of disease from prehistoric times to today emerged from a study of ancient Roman plagues. Their details left him asking why the empire suffered giant epidemics; why these particular diseases; and why then? He explores how human history has shaped disease ecology and the evolution of pathogens, and vice versa — both predictably and unpredictably. The COVID-19 pandemic is part of this “deep pattern”, he concludes: “expect the unexpected”.

The End of Bias

Jessica Nordell

The
of
A Beginning

THE SCIENCE
AND PRACTICE OF
OVERCOMING
UNCONSCIOUS BIAS

The End of Bias

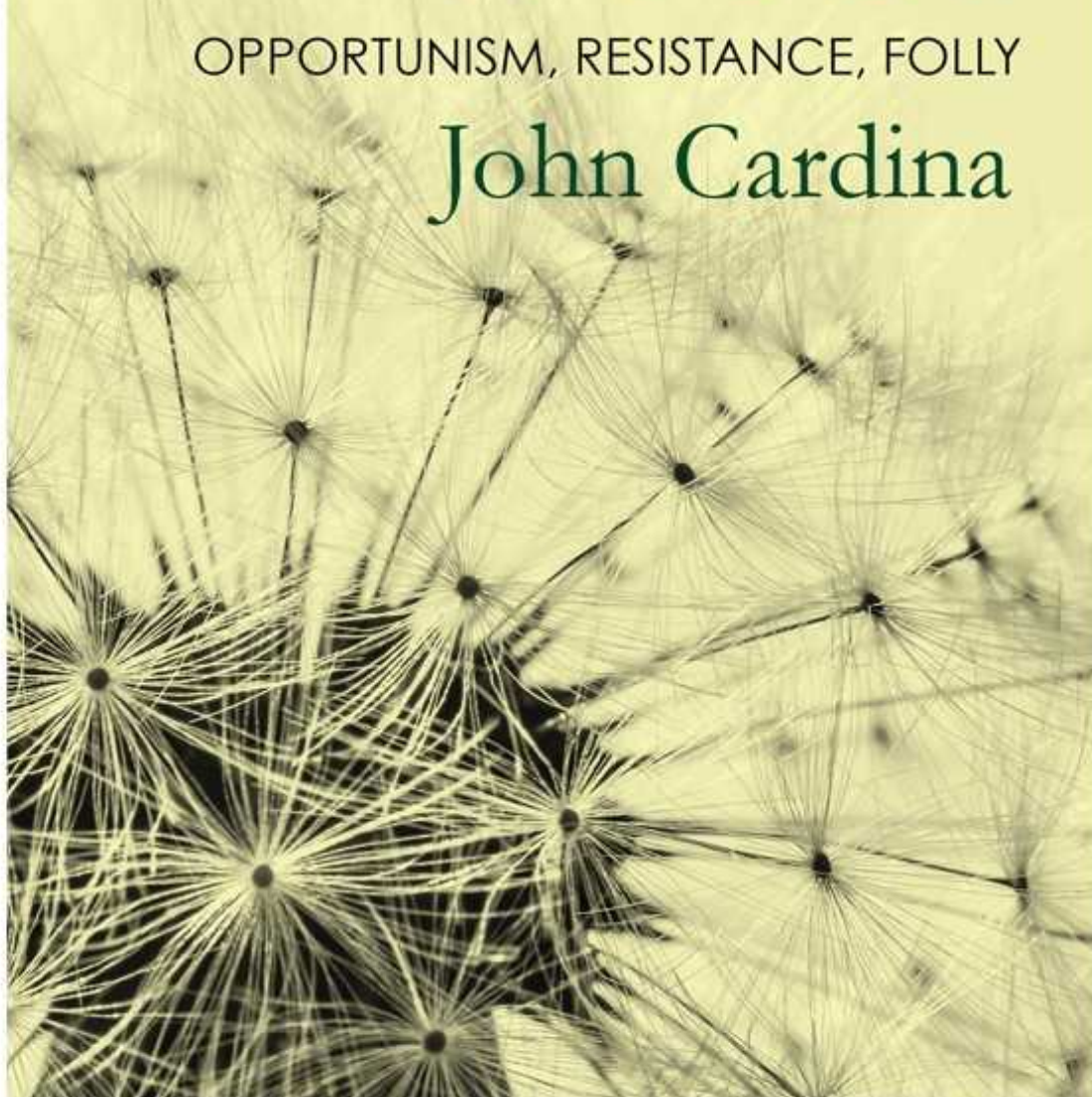
Jessica Nordell *Metropolitan/Henry Holt* (2021)

When she was trying to break into journalism, Jessica Nordell had no response from editors — until she used a man's name on her pitches. Her first book (shortlisted for the 2021 Royal Society Science Book Prize) skilfully and sensitively explores ways to eradicate bias in society and oneself. Interviewing cognitive scientists and social psychologists, mostly in the United States, she covers a huge range of methods, such as doctors' diagnostic check lists for gender equality, and a police unit practising mindfulness to diminish its use of force.

Lives *of* Weeds

OPPORTUNISM, RESISTANCE, FOLLY

John Cardina



Lives of Weeds

John Cardina *Cornell Univ. Press* (2021)

Of the roughly 400,000 species of flowering plants, how many are weeds? The answer depends on who, where and when you ask. “One person’s weed is another’s wildflower, food or medicine,” notes plant ecologist John Cardina; think of cannabis. His penetrating analysis disentangles botany from history by offering eight interwoven stories, each focused on one weed, some familiar, others less so: dandelion, Florida beggarweed, velvetleaf, nutsedge, marestail, pigweed, ragweed and foxtail.

Nature **599**, 200 (2021)

doi: <https://doi.org/10.1038/d41586-021-02929-1>

This article was downloaded by **calibre** from <https://www.nature.com/articles/d41586-021-02929-1>

| [Section menu](#) | [Main menu](#) |

Opinion

- **Replication efforts have limited epistemic value** [09 November 2021]
Correspondence •
- **Remembering a great friend of Nature** [09 November 2021]
Correspondence •
- **Japan: prize diversity, not conformity, to boost research**
[09 November 2021]
Correspondence •

- CORRESPONDENCE
- 09 November 2021

Replication efforts have limited epistemic value

- [Kauê Machado Costa](#) ORCID: <http://orcid.org/0000-0002-5562-6495>⁰ &
- [Geoffrey Schoenbaum](#) ORCID: <http://orcid.org/0000-0001-8180-0701>¹

Olavo Amaral and Kleber Neves argue that collaborative projects to confirm other researchers' experimental results could help to resolve the reproducibility crisis (see [Nature 597, 329–331; 2021](#)). In our view as laboratory researchers, it would be more effective in the long term to test the limits of a paper's conclusions.

Access options

Subscribe to Journal

Get full journal access for 1 year

\$199.00

only \$3.90 per issue

[Subscribe](#)

All prices are NET prices.

VAT will be added later in the checkout.

Tax calculation will be finalised during checkout.

Rent or Buy article

Get time limited or full article access on ReadCube.

from \$8.99

[Rent or Buy](#)

All prices are NET prices.

Additional access options:

- [Log in](#)
- [Learn about institutional subscriptions](#)

Nature **599**, 201 (2021)

doi: <https://doi.org/10.1038/d41586-021-03068-3>

This article was downloaded by **calibre** from <https://www.nature.com/articles/d41586-021-03068-3>

| [Section menu](#) | [Main menu](#) |

- CORRESPONDENCE
- 09 November 2021

Remembering a great friend of *Nature*

- [Peter Newmark](#) 0

Walter Gratzer, a biophysicist with a distinguished research career, who died on 20 October at the age of 89, was for many years also a writer for and adviser to *Nature*. In 1967, then-editor John Maddox offered Walter a position on the journal on the recommendation of eminent biochemist Paul Doty, with whom Walter had been a postdoc at Harvard University in Cambridge, Massachusetts. Walter turned down the opportunity in favour of continuing his research at King's College London (see go.nature.com/2ydpvyn).

Access options

Subscribe to Journal

Get full journal access for 1 year

\$199.00

only \$3.90 per issue

[Subscribe](#)

All prices are NET prices.

VAT will be added later in the checkout.

Tax calculation will be finalised during checkout.

Rent or Buy article

Get time limited or full article access on ReadCube.

from \$8.99

[Rent or Buy](#)

All prices are NET prices.

Additional access options:

- [Log in](#)
- [Learn about institutional subscriptions](#)

Nature **599**, 201 (2021)

doi: <https://doi.org/10.1038/d41586-021-03069-2>

This article was downloaded by **calibre** from <https://www.nature.com/articles/d41586-021-03069-2>

| [Section menu](#) | [Main menu](#) |

- CORRESPONDENCE
- 09 November 2021

Japan: prize diversity, not conformity, to boost research

- [Guojun Sheng](#) ORCID: <http://orcid.org/0000-0001-6759-3785>⁰,
- [Piero Carninci](#) ORCID: <http://orcid.org/0000-0001-7202-7243>¹,
- [Mikiko C. Siomi](#) ORCID: <http://orcid.org/0000-0002-6149-4396>²,
- [Toshio Suda](#) ORCID: <http://orcid.org/0000-0001-7540-1771>³ &
- [Cantaz Alev](#) ORCID: <http://orcid.org/0000-0002-4879-8782>⁴

Fuelled by the economic rise of China and South Korea, East Asia's influence in global research and innovation is growing. But with Japan's economy flagging and its international research ranking slipping to tenth this year (see go.nature.com/2ygwy3), the country risks being left behind (see [Nature 543, S7; 2017](#)). Its new government must reform science policy and research infrastructure, and revitalize its base of next-generation scientists, before it loses more ground.

Access options

Subscribe to Journal

Get full journal access for 1 year

\$199.00

only \$3.90 per issue

[Subscribe](#)

All prices are NET prices.
VAT will be added later in the checkout.
Tax calculation will be finalised during checkout.

Rent or Buy article

Get time limited or full article access on ReadCube.

from \$8.99

[Rent or Buy](#)

All prices are NET prices.

Additional access options:

- [Log in](#)
- [Learn about institutional subscriptions](#)

Nature **599**, 201 (2021)

doi: <https://doi.org/10.1038/d41586-021-03070-9>

This article was downloaded by **calibre** from <https://www.nature.com/articles/d41586-021-03070-9>

| [Section menu](#) | [Main menu](#) |

Work

- **Scientists count the career costs of COVID** [10 November 2021]
Career Feature • As the pandemic continues, researchers are coming to terms with what they've learnt and lost so far, finds Nature's global survey.
- **An expanding molecular toolbox untangles neural circuits** [09 November 2021]
Technology Feature • Scientists are developing ways to probe the activity, function and organization of neurons in real time with increasing precision.
- **'I have to use a torch and watch my step': netting seabirds at night** [08 November 2021]
Where I Work • Kendrew Colhoun tracks the movements of migratory birds in Ireland.

- CAREER FEATURE
- 10 November 2021

Scientists count the career costs of COVID

As the pandemic continues, researchers are coming to terms with what they've learnt and lost so far, finds *Nature*'s global survey.

- [Chris Woolston](#) ✉

[Find a new job](#)



Illustration by Antonio Rodríguez

Martha Nelson was in her element in early 2020. As the world grappled with the outbreak of the coronavirus SARS-CoV-2, Nelson, who studied viruses with pandemic potential at the US National Institutes of Health (NIH), felt her work was suddenly more urgent and relevant than ever. Friends and family assumed that she had ultimate job security. “People were telling me that I must be on top of the world because my work is so important,” she says.

In reality, Nelson says she was barely hanging on. Balancing work and family life was often a struggle even before the pandemic, and that was when she had paid childcare support and nearby help from her young son’s grandparents. The pandemic removed that support system, and it became harder to keep pace at work. In October 2020, her annual contract wasn’t renewed. In turbulent times, even important jobs can disappear.

Nelson was one of more than 3,200 self-selected scientists around the world who took *Nature*’s 2021 Salary and Job Satisfaction Survey, which ran from June until early July. *Nature* is presenting the survey results in a series of articles that will shed light on the state of science at a pivotal time (see ‘*Nature*’s salary and job survey’). As with [last year’s survey of postdoctoral researchers](#), this year’s included a series of questions about the impact of the pandemic on lives and careers.

Nature’s salary and job survey

This article is the first of four linked to *Nature*’s global salary and job satisfaction survey. Further articles are scheduled for the following weeks, exploring job satisfaction, compensation, career prospects, diversity and inclusion, and other aspects of scientific life.

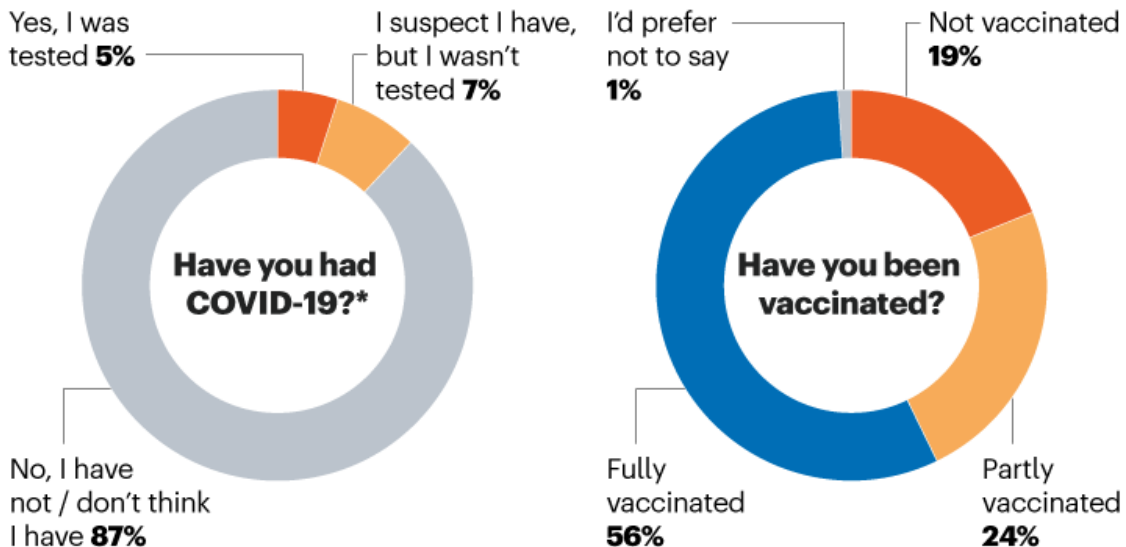
The salary survey runs every three years and [last took place in 2018](#). It was created together with Shift Learning, a market-research company in London, and was advertised on nature.com, in Springer Nature digital products and through e-mail campaigns. It was offered in English, Mandarin Chinese, Spanish, French and Portuguese. The full survey data sets are available at go.nature.com/3eqcpk9.

After more than a year of lockdowns and delays, scientists everywhere are still coming to terms with what they've learnt and what they've lost, says Alessandra Minello, a demographer at the University of Padua in Italy. "We have more information now about what really happened during the pandemic," says Minello, who co-authored an August 2020 interview-based study showing that female academics often had to de-emphasize their careers during the pandemic ([*A. Minello et al. Eur. Soc. 23 \(Suppl. 1\), S82–S94; 2020*](#)). "We all suffered from the social isolation, but it will take years to know the full impact on careers."

Even though relatively few respondents reported having COVID-19 (see 'Geography of a pandemic'), the outbreak transformed workplaces and careers. Overall, 12% of respondents said they had lost a job offer because of COVID-19, and 43% said that the pandemic had negatively impacted their career prospects. The majority of respondents (57%) said that it had impaired their ability to collect data. Similar proportions said that it hampered collaborations with internal colleagues (56%) and the ability to conduct laboratory-based experiments (55%; see 'Careers at risk').

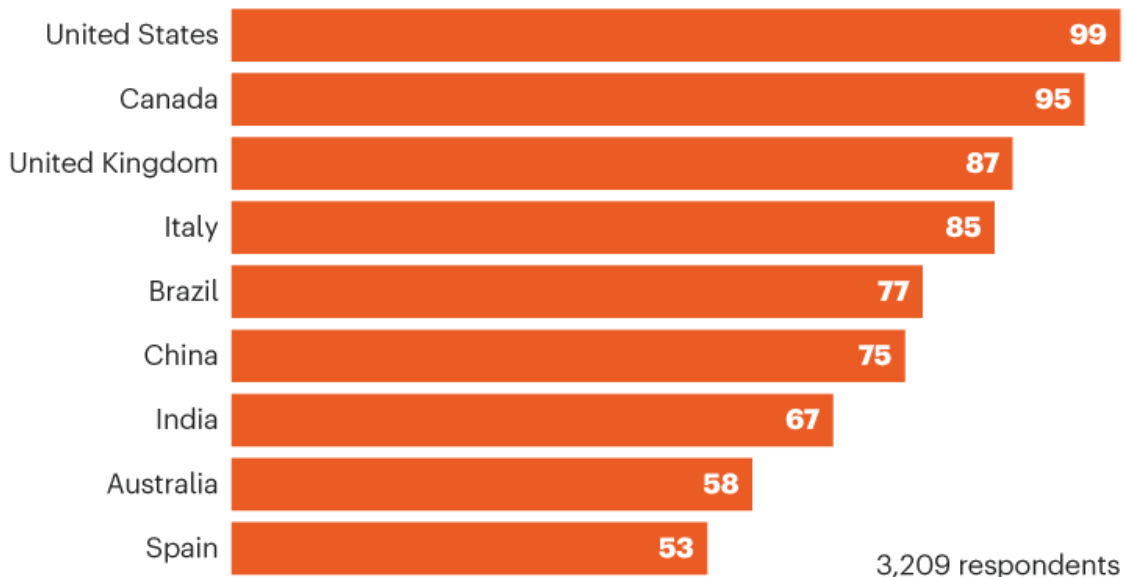
GEOGRAPHY OF A PANDEMIC

Despite wide geographical disparities in vaccination rates, relatively few respondents reported having been infected with COVID-19.



*Percentage does not add to 100% because of rounding.

Proportion partly or fully vaccinated by region (%)



©nature

Only time will tell how this lost productivity during the pandemic will affect future careers, says Tiffany Reese, an immunologist at the University of Texas Southwestern Medical Center in Dallas. Ideally, she says, funding

agencies and hiring committees won't penalize scientists whose work was disrupted through no fault of their own. "What worries me is that memories are short," she says. "There's been a lot of talk about how you should take COVID into account when you review a grant. Is that going to be true two or three years from now? It's going to be hard for reviewers to consider the fact that there was so much lost productivity."

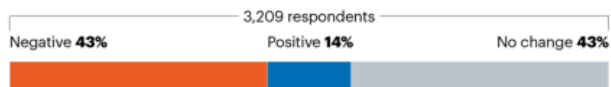
Researchers at risk

Junior researchers were especially vulnerable. More than half (53%) of early-career researchers — including 65% of all postdoctoral researchers — said that the pandemic had hampered their prospects. Those results are in line with [last year's survey of postdoctoral researchers](#), in which 61% of respondents shared that concern. In this year's survey, respondents who described themselves as 'late career' scientists were the outliers: just over one-quarter (26%) felt that the pandemic had negatively impacted their career prospects.

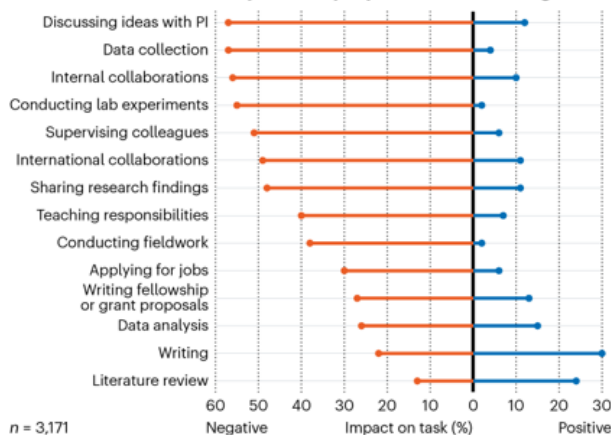
CAREERS AT RISK

Whereas some scientists — especially those in health-care fields — saw a career-related upside to the pandemic, many more felt professionally threatened by shutdowns, supply shortages and strained collaborations. Most foresee long-term impacts, for better or worse.

What effect has the COVID-19 pandemic has on your career prospects?



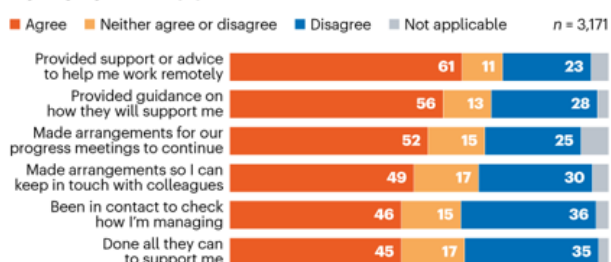
How has COVID-19 affected your ability to perform the following work?



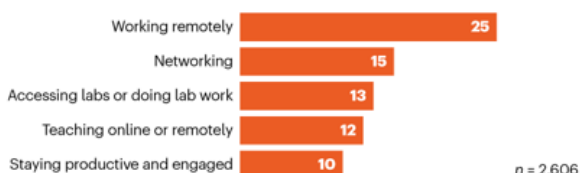
Have you faced problems getting lab or workplace supplies during the pandemic?



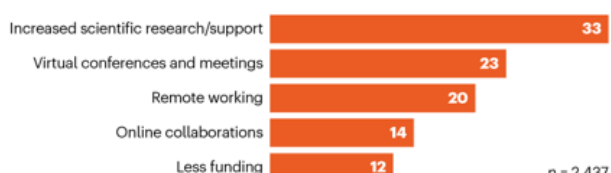
My employer has ... (%)



What is your biggest professional challenge during the pandemic? (%)*



How do you think the pandemic will change science? (%)*



*Bars do not add to 100%: respondents could provide multiple answers.

Men and women were equally likely to report that the pandemic negatively affected their careers, but other factors also came into play. For instance, researchers in the fields of ecology and evolution (51%) and physics (49%) were especially hard hit. This is perhaps because ecology and evolution is a discipline that depends largely on fieldwork, and because physics, similarly, often requires lab-based experiments that might have been difficult to conduct during lockdowns. Geography mattered, too. Researchers in the United States (38%), China (41%) and the United Kingdom (43%) were much less likely than those in Brazil (72%) and India (61%) to say that the pandemic had slowed down their careers.

Edmond Sanganyado, an environmental chemist at Shantou University in Guangdong province in China, says the pandemic brought his research to a halt. “In China, we hire outside labs to do routine analysis,” he says. “Most of those labs closed because they weren’t considered essential.” Travel restrictions stopped him from visiting his home country of Zimbabwe and attending international conferences, an important opportunity for networking and career advancement. “In China, you are evaluated by the conferences you attend, and online conferences are rarely recognized.”



[COVID is disrupting scientific careers around the world](#)

Likewise, the pandemic put the brakes on Jucelaine Haas’s plant-science research at the Federal University of Technology in Paraná, Brazil. Haas

says the research system in her home country was already fragile. “We don’t have the technology to do anything other than basic research,” she says. Like many Brazilian scientists, she had to count on the labour of graduate students and others to do tasks that could have been automated. In her case, that meant watering plants by hand. “In Brazil, even growing plants is difficult,” she says. When graduate students and others had to stay at home, those plants didn’t get watered and the research couldn’t move forward. “Some colleagues continued asking some students to do this and that, but I thought that was not good for their health,” she says.

Haas left Brazil in November 2020 for a sabbatical as a visiting researcher at the Helmholtz Centre for Environmental Research in Leipzig, Germany. She returned to Brazil last month, a move that she had been dreading. “Brazil is just chaos,” Haas says. Referring to the spread of COVID-19 there, she explains: “The government never took action and it snowballed. The president [Jair Bolsonaro] says it’s just the flu and won’t wear a mask. That makes it easy for others to not take it seriously. I don’t feel safe there.” Last month, the Brazilian Senate recommended charging Bolsonaro with “crimes against humanity” over his handling of the pandemic.

Short supplies

In one sign of far-reaching effects, the pandemic also [disrupted supply chains of basic lab materials](#), forcing scientists to scramble. “Obtaining supplies has been the biggest challenge, hands down,” wrote a South African researcher in the biomedical field. “We are waiting 3–6 months for any one order to arrive in the lab.” In the United Kingdom, a researcher in the field of food and agriculture lamented that he was waiting much longer than usual for supplies, although he couldn’t be sure how much of the delay was pandemic-related and how much was caused by well-documented supply problems as a result of the country’s departure from the European Union. Overall, nearly half (49%) of all respondents reported having trouble getting materials for the lab. Those problems were especially common in India (63%) and Australia (57%), but notably less so in China (27%).

Scientists are resourceful, and they found ways to work around shortages. Slightly over half of respondents who faced supply problems said they were

able to find materials from alternative suppliers. Another 42% said they were able to make substitutions using materials that were more readily available. But 17% said they weren't able to obtain supplies, no matter what they tried.



[Collection: Coronavirus and scientific careers](#)

For some, the pandemic and the flood of related research that followed provided an opportunity. Twenty-seven per cent of researchers in the health-care field said that the pandemic improved their career prospects, the highest of any field. Overall, 14% of respondents saw a silver lining for their careers.

Sören Lukassen was working as a postdoc in bioinformatics at Charité — University Medicine Berlin when the pandemic sent his workload into overdrive. As part of his research into lung cancer, he had data on lung cells that would prove crucial to understanding the pathology of SARS-CoV-2 infections. “We knew we had to get the information out as quickly as possible,” he says. “Our first COVID publication took ten days from conception to submission.”

Lukassen’s work on COVID-19 proved pivotal to his career. He racked up several high-profile publications, including a June 2020 report in *Nature Biotechnology* that found a correlation between the severity of COVID-19

infections and interactions with immune cells in the airway ([R. L. Chua *et al.* *Nature Biotechnol.* **38**, 970–979; 2020](#)), and he worked directly with the head of Charité on various projects. He says that connection came in handy when he applied to become a group leader there, a position he started in January. “My work on COVID definitely increased my chances,” he says.

For Lukassen, however, his career progress came at a cost. From April to June 2020, he says he was working up to 16 hours a day, wiping out any hope of attaining a work–life balance. “In hindsight, I’m glad I did, but there were moments when that wasn’t the case,” he says.

The frantic speed of pandemic science proved overwhelming for Nelson, especially when she spent so much time caring for her young son. “I could barely handle the pace of science before,” she says. “The pandemic put it on steroids. I realized I was very vulnerable.”

Evidence is mounting that the pandemic was especially challenging for researchers with childcare responsibilities. In a survey of 1,347 researchers conducted in February and March by UKRI, the UK government research body, 61% of all respondents and 88% of respondents with childcare responsibilities said that the pandemic had reduced the amount of time they could spend on research (see [go.nature.com/3chq7jt](#)).



[Satisfaction in science](#)

“It just amplified some of the problems that already existed for women,” Reese says. In February, she co-authored an editorial in *Science Advances* calling for universities to support women in academia and eliminate gender inequities ([T. A. Reese et al. *Sci. Adv.* 7, eabg9310; 2021](#)).

In *Nature*’s survey, women (40%) were more likely than men (34%) to report that their employer hadn’t done all they could do to support them during the pandemic. Female respondents were also more likely than male respondents to say that they hadn’t received clear guidelines for navigating changes in their ability to work: 32% to 26%.

Men had their share of complaints about institutional support. A male biomedical researcher at a state university in California wrote: “I never stopped coming to work during COVID; there was a three-month period at the beginning where I worked from home three days a week and in the lab two days a week, but after that, it was back to full-time lab work. The institution did nothing for all the lab staff that kept the labs across the university running during COVID.”

Many scientists anticipate that the pandemic will change their careers and lives for years to come (see ‘How do you think the pandemic will change science?’). One-third of respondents predicted that the pandemic will lead to increased scientific research; nearly one in four anticipated more virtual conferences; and 14% foresee more online collaborations. However, about one in three predicted that science wouldn’t change at all, for better or worse. “Everything will return to the status quo soon enough,” wrote a UK staff scientist who works in the biomedical field.

How do you think the pandemic will change science?

Free-text comments in *Nature*’s salary and job satisfaction survey highlight many of the issues scientists are grappling with during the pandemic. Comments have been edited for length and clarity and, when necessary, translated into English.

- Eighteen months ago, I would have told you that I could not work away from my desk for a prolonged period of time. Now I wonder whether it is necessary to go into the office one day per week. I have a two-hour Zoom

meeting with colleagues in China and Poland (almost) every morning. *Staff scientist in the steel industry, Belgium.*

- Science will be more focused on issues that make headlines. *Postdoc in physics, Poland.*
- I hope remote seminars are here to stay. I have attended more and a greater diversity of seminars than ever before without leaving my desk. *Postdoc in biomedicine, United States.*
- The cost of lab and research supplies in Brazil skyrocketed. We will have to rethink how to perform experiments using cheaper methodologies. One positive aspect is that the team members are less selfish and are helping colleagues. *Staff scientist in biomedicine, Brazil.*
- We are already an overworked and underpaid sector, especially considering our high level of education. COVID has increased childcare burdens and paused some field and lab work. Our careers are fast-paced and I fear COVID might cause some women scientists and under-represented groups to be further pushed out of the field. *Postdoc in geology and environmental science, United States.*
- I am very concerned about the huge negative impact on early-career researchers, who were unable to get papers out or to generate data for grant applications at this crucial stage in our careers. *Assistant professor in biomedicine, United States.*
- I hope I'm wrong, but I'm deeply concerned about those of us in our first couple of years of a tenure-track position. I have not seen much understanding from reviewers or many senior colleagues of the enormous impact the pandemic has had on those of us. I worry that many of us might ultimately leave or be forced out of science. *Assistant professor in chemistry, United States.*
- Perhaps the investment in online international collaborations will be a good thing. However, I now attend meetings and seminars at all hours of the day and night, so it has done nothing to address the lack of work-life balance in

academia. *Professor in geology and environmental sciences, United Arab Emirates.*

- I thought science would change for the better, but I'm not so optimistic any more; I see the same petty attitudes as always. *Technician in the health-care industry, Argentina. (Translated from Spanish.)*
- Hopefully people will realize biomedical research in the twenty-first century is similar to physics research in the twentieth century, which has completely changed the world and the course of history. *Biomedical consultant, United States. (Translated from Chinese.)*
- I hope it will make people realize the importance of global issues, and the absolute requirement for rich countries to give better support to research and the implementation of solutions in poorer countries. I also hope it will result in more requirements for research institutions to include and support researchers from countries that are less well-resourced. *Staff scientist in agriculture and food, United Kingdom.*

For Nelson, the future looks promising. After losing her contract job at the NIH, she was able to find a permanent position with the same agency. She is now an evolutionary biologist in the Intramural Research Program at the US National Institute of Allergy and Infectious Diseases in Rockville, Maryland. After settling for a series of one-year contracts, she finally took charge of her career. All she needed was a nudge from a pandemic. “All of these years I was just focusing on the science and I wasn’t a good self-advocate,” she says. “I had the CV and publication record. But I came so close to falling off, it made me realize how many other people were also in vulnerable positions. The pandemic takes you to a tipping point.”

Nature **599**, 331-334 (2021)

doi: <https://doi.org/10.1038/d41586-021-03040-1>

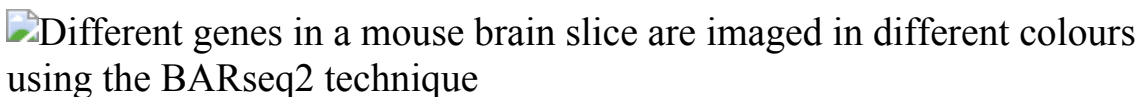
This article was downloaded by **calibre** from <https://www.nature.com/articles/d41586-021-03040-1>

- TECHNOLOGY FEATURE
- 09 November 2021

An expanding molecular toolbox untangles neural circuits

Scientists are developing ways to probe the activity, function and organization of neurons in real time with increasing precision.

- [Esther Landhuis](#) 



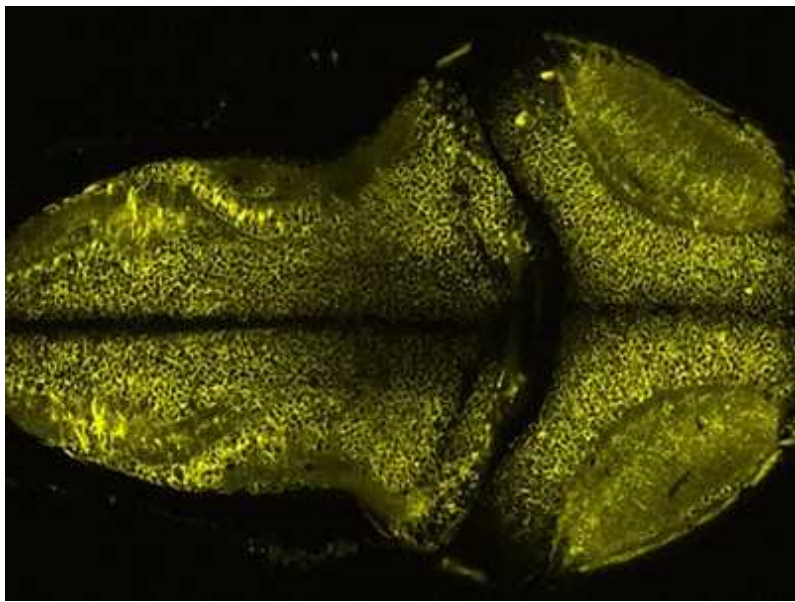
The BARseq2 technique can identify snippets of messenger RNA (colours) and help researchers see which brain layers those snippets are in. Credit: Yu-Chi Sun *et al.*/*Nature Neurosci.*

Life is full of nervous reactions — a head snaps towards a voice, leg muscles tense at the sound of a starting gun and thirsty mice scamper towards a squirt of water when trained to respond to a certain tone.

The mechanisms behind such reward-related behaviours are notoriously difficult to unpick. Nerve cells often snake through multiple brain areas, and their long axons and dense, tree-like dendrites can spark cellular conversations with thousands upon thousands of neighbours. Neural filaments can be exceptionally fine, and their positioning is crucial: disruptions in neural networks can lead to a range of neurological conditions. Yet, “If you want to label more than a few neurons at the same time and then trace where their axons go, it’s really difficult”, says Xiaoyin Chen, a neuroscientist at the Allen Institute for Brain Science in Seattle, Washington.

Still, researchers are slowly creating the tools to untangle that complexity, harnessing the power of sequencing, optogenetics and protein engineering to trace neuronal connections, record their activity, measure their inputs and outputs and map their networks.

The conventional way to label cells is to tag them with fluorescent dyes and then look at them under the microscope. But this technique can typically track only a few handfuls of cells, so Anthony Zador and his co-workers at Cold Spring Harbor Laboratory in New York developed a tool to trace thousands of individual neurons in parallel. Rather than dyes, they used viruses to insert a unique RNA sequence, or barcode, into each neuron. They could then map how the neurons connected with each another by taking samples from regions close to where the virus was injected, grinding them up and extracting the RNA, then sequencing it to look for the barcodes.



Genetic light bulbs illuminate the brain

The technique, known as multiplexed analysis of projections by sequencing (MAPseq), was published in 2016¹, and was widely regarded as a technological breakthrough for high-throughput mapping of neural connectivity, Chen says. But the method could indicate only roughly where the axons were going, like providing county-level detail, rather than a street address. And Chen, who had recently joined Zador's laboratory as a postdoctoral researcher, wanted more detail. For example, Chen says,

MAPseq could tell him that the neurons he was studying were in the auditory cortex, but not which of the region's six layers they were in.

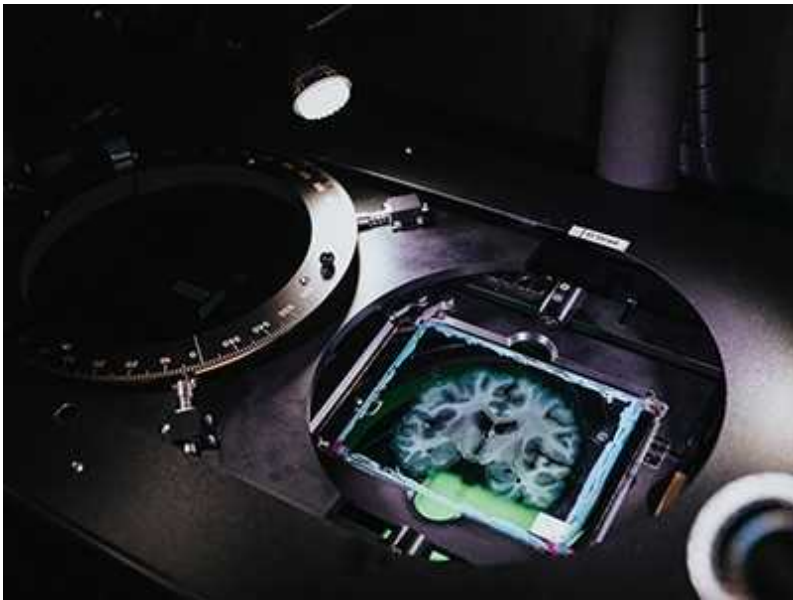
So Chen made a key modification to the technique. Rather than sequencing barcodes from ground-up brain slices, he sequenced them directly in fixed tissue, thereby retaining spatial information. "You still get the same projection patterns, but in this case you can see where the cells are," Chen says.

Called BARseq (barcoded anatomy resolved by sequencing)², the method helps researchers to correlate projection patterns with other properties, such as expression of specific genes. Chen and his colleagues, for example, combined it with a method known as fluorescence *in situ* hybridization (FISH) as well as targeted protein labelling, to identify different types of neuron.

Imaging update

Earlier this year, Chen and his colleagues took the technique a step further, adding in the ability to profile gene expression throughout the genome³. They then used BARseq2 to map the expression of 20 proteins known as cadherins, which help to guide the development of neuronal projections, and found that similar types of projection express similar sets of cadherins even when they originate in different areas of the brain. "The fact that we find the same signature in two cortical areas supports that we found something that may reflect general organization of the cortex, and not just peculiarity in certain cortical areas or artefacts in the data," says Chen. Applying BARseq2 earlier in development could also give insight into how these molecules "are actually directing the establishment of these projections", he adds.

The ability to correlate spatial mapping with gene expression means that scientists can now start to tackle a long-standing question: do groups of neurons that share a molecular profile have similar connectivity? In other words, "can you use gene-expression patterns to predict where the cells would project to?" says Allen Institute director Hongkui Zeng.



How the world's biggest brain maps could transform neuroscience

Other researchers are using barcoded viruses to answer different questions. Researchers led by neuroimmunologist Francisco Quintana at Harvard Medical School in Boston, Massachusetts, for instance, developed a method called RABID-seq (rabies barcode interaction detection followed by sequencing) to investigate mechanisms of cell–cell interaction *in vivo*⁴. The technique uses a virus that is engineered to infect only cells of interest and express a barcode as it spreads from cell to cell. That helps researchers to identify which cells are interacting and then to identify molecular pathways that might mediate those interactions. They also engineered the virus to express the red fluorescent protein mCherry so that they could isolate infected cells in a cell sorter and investigate the mechanisms involved in follow-up experiments. “You can go all the way from ‘which cells interact’ to ‘what mechanisms’ and potential targets,” says Quintana.

At the Allen Institute, Zeng and her colleagues have created ‘enhancer viruses’ to drive expression of target genes in specific cell types^{5,6}. The researchers used single-cell RNA sequencing and a technique known as single-cell ATAC-seq to identify stretches of DNA that are accessible to the proteins that regulate gene transcription. They could then insert the relevant regulatory regions into viruses to drive expression of specific genes in specific cell types — in brain slices and even in other species, Zeng says, including tissues that are not typically amenable to genetic methods.

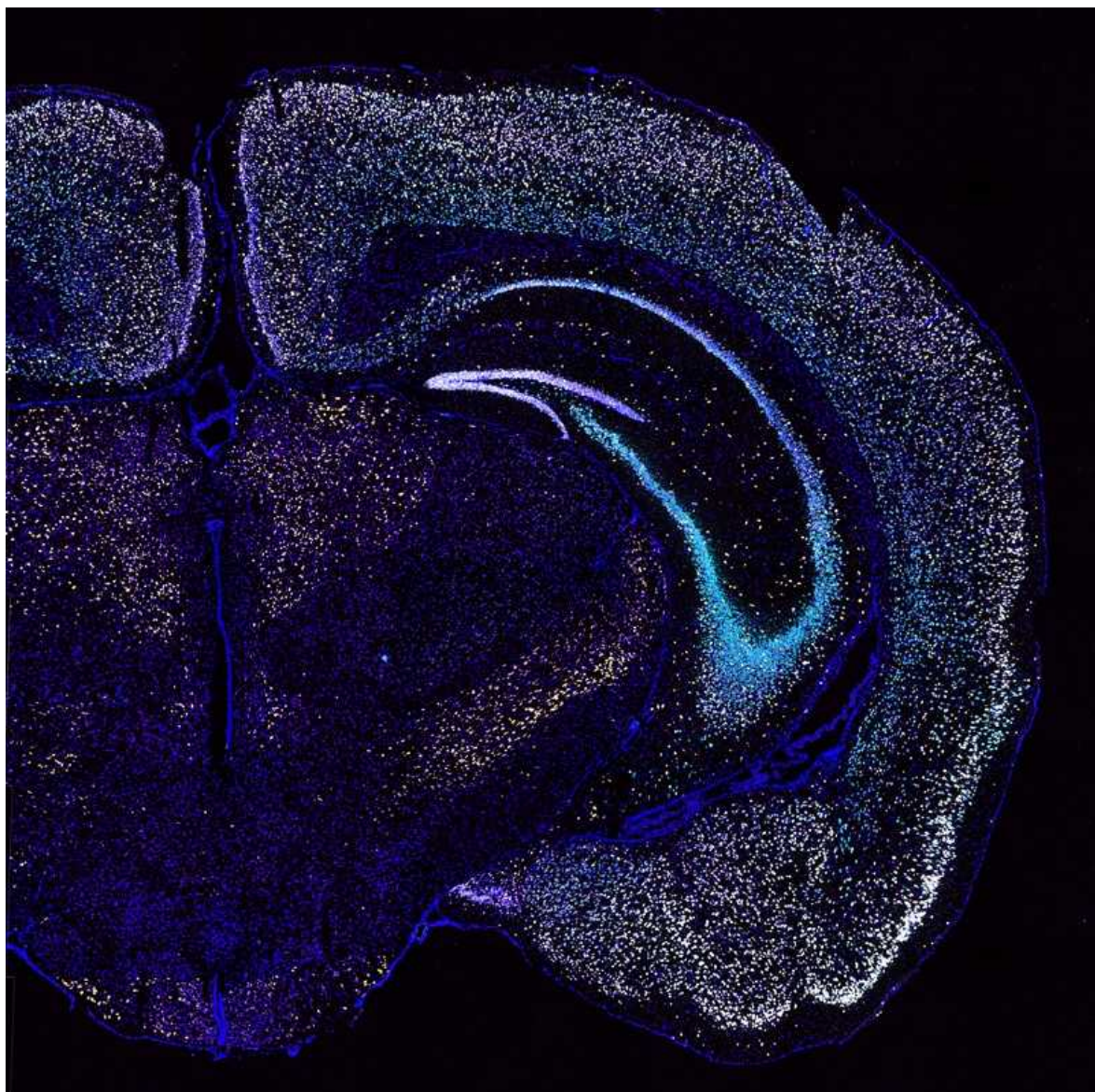
Neuroscientist Rui Costa at Columbia University in New York City plans to use enhancer viruses to tease out the roles of mouse neurons that respond to the neurotransmitter dopamine in learning, reward and movement, as well as to investigate different susceptibilities to degeneration. Such ‘dopaminergic’ neurons are lost in conditions such as Parkinson’s disease.

Light work

Other scientists are developing innovative ways to probe neuronal activity using optogenetics — techniques that use light to control cells.

Typically, researchers use an enzyme known as Cre recombinase to turn genes on or off in specific cell types or in response to genetic or chemical cues. In 2016, two independent research teams put Cre under the control of light. The approach, in both cases, was to split the enzyme into two pieces that would become active only when reassembled in blue light^{7,8}. However, that meant that tissues needed to be injected with two separate engineered genes, and those genes needed to be expressed at comparable levels for the technique to work. “If you could control Cre with a single-chain protein, then you could potentially be more efficient and rapid,” says Gaël Yvert, a molecular geneticist at the École Normale Supérieure de Lyon in France.

To create a more powerful system, Yvert’s team pored over the crystal structure of Cre, looking for pieces of the enzyme that they might be able to make use of to control the protein with light. They were looking for things that they “could unblock or play on to have a switch”, Yvert says. They identified several helices that were crucial to the enzyme’s activity and fused a light-responsive domain from oat plants into these positions. The result was LiCre: an enzyme that can be activated within minutes and reach a much greater intensity than previous systems⁹.

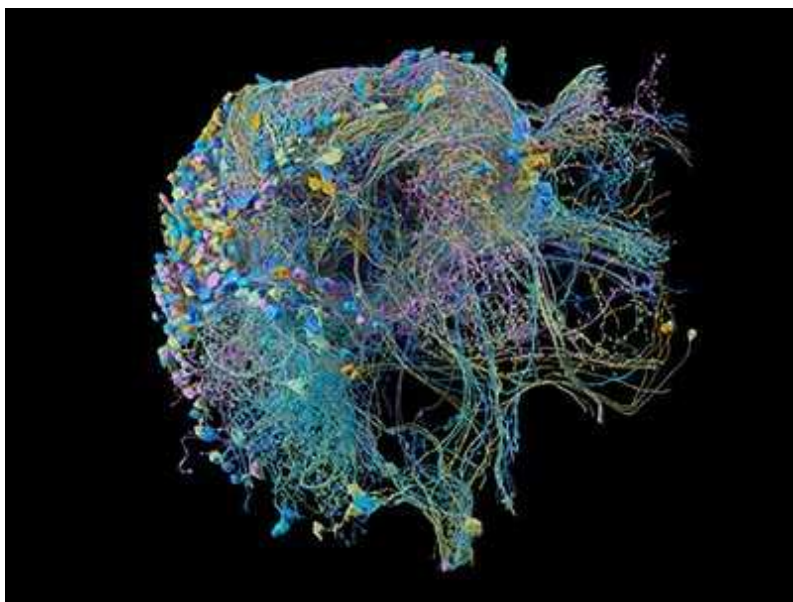


Gene expression in a slice of mouse brain, captured with BARseq2.Credit: Yu-Chi Sun *et al./Nature Neurosci.*

Steven Wyler, a postdoctoral researcher at the University of Texas Southwestern Medical Center in Dallas, wants to use LiCre to investigate groups of neuronal cell bodies called ganglia to understand more about how information from various tissues helps the brain to stay metabolically stable. But ganglia are delicate structures that are easily damaged. “LiCre would hopefully allow us to have both spatial and temporal control of Cre activity without causing physical damage to the neurons,” says Wyler.

Researchers have also created sensors that measure the calcium dynamics inside living cells. Calcium levels are crucial to biological decisions — they can determine when a muscle cell contracts or initiates programmed cell death (apoptosis), for instance — so quantifying them accurately helps scientists to model cell behaviour. Most of the existing tools can determine whether calcium levels are rising or falling, “but it’s close to impossible to quantify the actual concentrations”, says Joachim Goedhart, a cell biologist at the University of Amsterdam.

These techniques generally use proteins that fluoresce in the presence of calcium, but the level of fluorescence can also be affected by experimental conditions such as pH, how much of the probe is present or the thickness of the sample. A way to get around such complications is to use fluorescence lifetime — how long the fluorophores spend in the excited state after absorbing a photon — instead of intensity.



Probing fine-scale connections in the brain

To harness this property, Goedhart and his colleagues modified the structure of a turquoise fluorescent protein to optimize its lifetime and brightness, and added a calcium-sensitive protein domain¹⁰. The result was a probe that could provide robust measurements of the calcium levels in both individual cells and multicellular tissue.

Helmut Kessels, a neuroscientist at the University of Amsterdam, and his co-workers plan to use the probe in slices of mouse brain to test whether intracellular calcium levels drop with age or as cells and tissues start to show characteristics of Alzheimer's disease. He's particularly keen to get a measurement that doesn't vary with the thickness of the sample. "Since its signal is measured using lifetime imaging, this should be independent of tissue depth," he says.

One potential constraint on the use of such fluorescent markers is the speed of many microscopes. At present, Goedhart's microscopy system cannot take measurements faster than once every 1.6 seconds, which could limit some applications in neuroscience, given that fluctuations in calcium levels correlate with a neuronal firing rate of around 200 per second. But faster microscopes do exist: some labs have built their own, and commercial versions are available through suppliers such as Leica Microsystems in Wetzlar, Germany, and Picoquant in Berlin.

Converging signals

There's another, broader, limitation, too. Calcium indicators allow researchers only to "read out the neural activity in real time", says Christina Kim, a neuroscientist who started her lab at the University of California, Davis, last month. That's a problem, Kim says, because if you want to manipulate neurons or delve into their molecular make-up, you need to be able to identify which neurons are relevant for a particular behaviour.

When she was in Alice Ting's chemical-biology lab at Stanford University in California, Kim and fellow postdoc Mateo Sanchez developed a method that can do just that.

The tool builds on an earlier technique created in Ting's lab, called fast light- and activity-regulated expression, or FLARE. Like many genetically encoded sensors, FLARE combines calcium and light sensing to identify groups of neurons that are active during a defined time window. But it goes a step further: on detecting elevated calcium concentrations and the presence of blue light, it causes one of the proteins in the membrane to move into the nucleus and start driving transcription of a fluorescent reporter protein¹¹.

This provides a lasting record of which cells were active and allows those same cells to be subsequently analysed for other properties.



[NatureTech hub](#)

But, Ting says, FLARE has “considerable background leak”, giving a signal even in the absence of light and calcium. And because neurons need to be exposed to it for at least ten minutes, it is too slow to apply to fast behaviours *in vivo*, says Ting.

Kim and Sanchez made two key improvements. First, they made the signal stronger by using a more efficient enzyme to control the translocation of the transcription factor. Second, they optimized the light-sensing molecule to further reduce the amount of leak.

The improved tool, called fast light- and calcium-regulated expression, or FLiCRE, can label neurons that are activated for as little as one minute. In a paper¹² published last December, Kim and her colleagues used the method in mice to tag and identify cells that help regulate aversive behaviours, such as avoidance of an electric shock or unpleasant odour, then stimulate the relevant neurons without actually subjecting the mice to unpleasant stimuli.

Deeper understanding

Still, as much as calcium levels and other cellular properties can reveal about neural circuitry, some of the deepest questions in neuroscience demand other methods. “Calcium imaging tells you which neuron fires during a particular task, but it doesn’t tell you why it fires,” says Kaspar Podgorski, a neuroscientist at the Howard Hughes Medical Institute’s Janelia Research Campus in Ashburn, Virginia. Understanding what makes a given neuron fire requires measuring the inputs going into that cell.

A suite of sensors is now helping researchers to measure these inputs. The dLight1¹³ and GRAB_{DA}¹⁴ sensors, for instance, detect changes in dopamine. The GACH family of sensors monitor transmission of acetylcholine, a key neurotransmitter involved in dilating blood vessels and slowing heart rate¹⁵. And red-shifted dopamine sensors (RdLight1)¹⁶ can be combined with green fluorescent protein-based sensors to provide scientists a more nuanced view of neuronal systems.

Neuronal communication, Podgorski says, is fascinating. “Neurons receive thousands of inputs. They’re just bombarded.” Somehow, the cells parse all those signals to meaningful effect, translating them into an appropriate action. “Neural computation is the question: How does information flow through the network? How do inputs get transformed into outputs? And where does the activity go? I think we’re really at the cusp of being able to very richly study neural computation,” he says.

Nature **599**, 335–337 (2021)

doi: <https://doi.org/10.1038/d41586-021-03054-9>

References

1. 1.

Kebischull, J. M. *et al.* *Neuron* **91**, 975–987 (2016).

2. 2.

Chen, X. *et al.* *Cell* **179**, 772–786 (2019).

3. 3.

Sun, Y.-C. *et al.* *Nature Neurosci.* **24**, 873–885 (2021).

4. 4.

Clark, I. C. *et al.* *Science* **372**, eabf1230 (2021).

5. 5.

Graybuck, L. T. *et al.* *Neuron* **109**, 1449–1464 (2021).

6. 6.

Mich, J. K. *et al.* *Cell Rep.* **34**, 108754 (2021).

7. 7.

Taslimi, A. *et al.* *Nature Chem. Biol.* **12**, 425–430 (2016).

8. 8.

Kawano, F., Okazaki, R., Yazawa, M. & Sato, M. *Nature Chem. Biol.* **12**, 1059–1064 (2016).

9. 9.

Duplus-Bottin, H. *et al.* *eLife* **10**, e61268 (2021).

10. 10.

van der Linden, F. H. *et al.* Preprint at bioRxiv
<https://doi.org/10.1101/2021.06.21.449214> (2021).

11. 11.

Wang, W. *et al.* *Nature Biotechnol.* **35**, 864–871 (2017).

12. 12.

Kim, C. K. *et al.* *Cell* **183**, 2003–2019 (2020).

13. 13.

Patriarchi, T. *et al.* *Science* **360**, eaat4422 (2018).

14. 14.

Sun, F. *et al.* *Cell* **174**, 481–496 (2018).

15. 15.

Jing, M. *et al.* *Nature Biotechnol.* **36**, 726–737 (2018).

16. 16.

Patriarchi, T. *et al.* *Nature Methods* **17**, 1147–1155 (2020).

This article was downloaded by **calibre** from <https://www.nature.com/articles/d41586-021-03054-9>

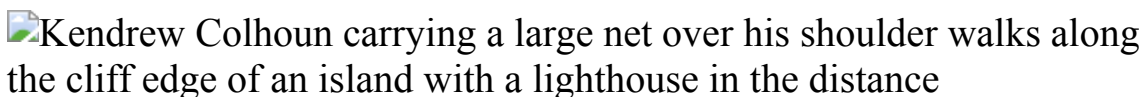
| [Section menu](#) | [Main menu](#) |

- WHERE I WORK
- 08 November 2021

‘I have to use a torch and watch my step’: netting seabirds at night

Kendrew Colhoun tracks the movements of migratory birds in Ireland.

- [Chris Woolston](#) 0



Kendrew Colhoun is a seabird biologist with MarPAMM (Marine Protected Area Management and Monitoring), funded by the European Union. Credit: Chris Maddaloni for *Nature*

Netting seabirds is great fun. And it’s crucial for science and conservation.

In this photo, taken in July, I’m heading out to capture birds on Inishtrahull, Ireland’s northernmost island. Lying about 10 kilometres northeast of the mainland, the island is home to thousands of seabirds during the summer nesting season, including storm petrels (*Hydrobates pelagicus*), Manx shearwaters (*Puffinus puffinus*) and fulmars (*Fulmarus glacialis*). The fulmars are experiencing a population crash, which I’m investigating.

Migratory birds are protected here, but we need to know where they go when they leave their nests. I attach an identification band and a light-level geolocator — a sensor that helps to estimate location from day length — to every bird I catch. A few birds get GPS monitors, but we dole those out carefully, because each costs about £1,000 (US\$1,368).

The birds tend to nest on cliffs, and on a bad day I'll catch just three. Some days I get as many as 12. Shearwaters are a challenge, because they nest only at night: I have to use a torch and watch my step.

The birds don't enjoy getting caught, but the stress is only temporary. The data they provide help us to understand their migration patterns. Fulmars spend almost their entire lives at sea. I'm interested in finding out how often they share waters with long-line fishers, which would be a potentially fatal scenario for the birds. That's not the only threat: a study has found that more than half of beached North Sea fulmars have large amounts of plastic in their stomachs (see go.nature.com/3cosy8j).

The lighthouse behind me is now home to the Inishtrahull Bird Observatory, a base for birdwatchers. I'm the founding chairman, but the observatory, part of a network of monitoring spots stretching 1,200 kilometres from Scotland to southern Ireland, will outlive me. It will be a centre for science and education for years to come.

Nature **599**, 340 (2021)

doi: <https://doi.org/10.1038/d41586-021-03055-8>

This article was downloaded by **calibre** from <https://www.nature.com/articles/d41586-021-03055-8>

Research

- **[Bryozoan fossils found at last in deposits from the Cambrian period](#)** [27 October 2021]

News & Views • Molecular evidence has long indicated that aquatic animals called bryozoans should be found among the fossils of the Cambrian period, around 541 million years ago. Yet they have been conspicuously absent, until now.

- **[The unexpected ancestry of Inner Asian mummies](#)** [27 October 2021]

News & Views • The genomes of Bronze Age mummies from the Tarim Basin in northwest China suggest that these individuals were descended from an ancient Asian population that was genetically isolated, despite extensive cultural interactions in the region.

- **[Diet comparison suggests a lipid imbalance can slow tumour growth](#)** [20 October 2021]

News & Views • Understanding how diet affects tumour growth could lead to better treatments. Analysis in mice reveals that a low-calorie diet, but not a ketogenic diet, slows the growth of pancreatic cancer. This effect is mediated by lipid changes.

- **[From the archive](#)** [09 November 2021]

News & Views • Nature's pages feature a textbook that takes a new approach for covering science, and an obituary of Charles Babbage.

- **[Global temperature changes mapped across the past 24,000 years](#)** [10 November 2021]

News & Views • Palaeoclimate data and models have been used to produce a comprehensive report of Earth's temperature changes over the past 24 millennia. The results suggest that modern warming differs from the gradual rise of the past 10,000 years.

- **[Rhinoceros genomes uncover family secrets](#)** [19 October 2021]

News & Views • Genomes from living and extinct rhinos reveal that different species evolved as a result of geographic isolation. A comparison of DNA from different species also shows that rhinos have long displayed low genetic variability.

- **[An optical lattice with sound](#)** [10 November 2021]

Article • An optical lattice for trapping a Bose–Einstein condensate reported here includes photon-mediated atom–atom interactions that replicate acoustic modes in real crystals.

- **Cascade of correlated electron states in the kagome superconductor CsV₃Sb₅** [29 September 2021]

Article • A study reveals a temperature-dependent cascade of different symmetry-broken electronic states in the kagome superconductor CsV₃Sb₅, and highlights intriguing parallels between vanadium-based kagome metals and materials exhibiting similar electronic phases.

- **Roton pair density wave in a strong-coupling kagome superconductor** [29 September 2021]

Article • A study reports unconventional superconductivity and a pair density wave in the kagome superconductor CsV₃Sb₅, and provides a basis for understanding the microscopic origin of correlated electronic states and superconductivity in vanadium-based kagome metals.

- **Bubble casting soft robotics** [10 November 2021]

Article • An all-in-one methodology for fabricating soft robotics reported here uses interfacial flows in elastomers that cure to produce actuators that can be tailored to suit applications from artificial muscles to grippers.

- **In situ formation of ZnO_x species for efficient propane dehydrogenation** [10 November 2021]

Article • Propene is obtained through propane dehydrogenation using catalysts that are toxic, expensive or demanding to regenerate with ecologically harmful compounds, but the ZnO-based alternative reported here is cheap, clean and scalable.

- **Globally resolved surface temperatures since the Last Glacial Maximum** [10 November 2021]

Article • Paleoclimate datasets are integrated with a climate model to reconstruct global surface temperature since the Last Glacial Maximum, showing sustained warming until the mid-Holocene.

- **Dynamic slab segmentation due to brittle–ductile damage in the outer rise** [10 November 2021]

Article • Numerical subduction models used to determine the consequences of bending-induced plate damage show that slab weakening and segmentation can occur at the outer-rise region of the subducting plate.

- **Fossil evidence unveils an early Cambrian origin for Bryozoa** [27 October 2021]

Article • Interpretation of the early Cambrian fossil Protomelission gatehousei⁹ as a potential stem-group bryozoan realigns the fossil record with molecular clock estimations of the origins of Bryozoa.

- **The genomic origins of the Bronze Age Tarim Basin mummies** [27 October 2021]

Article • A genomic analysis of human remains from the Bronze Age provides insights into the origin of the Tarim Basin mummies from the Xinjiang region.

- **Neural control of affiliative touch in prosocial interaction**

[13 October 2021]

Article • Neurons in the medial amygdala regulate prosocial comforting behaviour towards distressed social partners in mice.

- **Human neural tube morphogenesis in vitro by geometric constraints**

[27 October 2021]

Article • Stem cells cultured in a micropattern-constrained platform form a quantitative and robust model of human neural tube morphogenesis.

- **Cell surface and intracellular auxin signalling for H⁺ fluxes in root growth**

[27 October 2021]

Article • Auxin rapidly modulates root growth through simultaneous activation of two opposing mechanisms—TMK1-mediated apoplast acidification and TIR1/AFB-mediated apoplast alkalinization.

- **TMK-based cell-surface auxin signalling activates cell-wall acidification**

[27 October 2021]

Article • Auxin induces transmembrane-kinase-dependent activation of H⁺-ATPase in the plasma membrane through phosphorylation of its penultimate threonine residue, promoting apoplastic acidification and hypocotyl cell elongation in Arabidopsis.

- **Virus-induced senescence is a driver and therapeutic target in COVID-19**

[13 September 2021]

Article • Virus-induced senescence is a central pathogenic feature in COVID-19, and senolytics, which promote apoptosis of senescent cells, can reduce disease severity in hamsters, mice, as well as humans infected with SARS-CoV-2.

- **Shigella evades pyroptosis by arginine ADP-riboboxanation of caspase-11**

[20 October 2021]

Article • This study reports the identification of a new post-translational modification, termed ADP riboxanation, which is mediated by the Shigella effector OspC3 and inactivates the cytosolic LPS sensing pathway of caspase-4 and caspase-11.

- **Glycogen metabolism links glucose homeostasis to thermogenesis in adipocytes**

[27 October 2021]

Article • Increased glycogen metabolism in adipocytes leads to expression of uncoupling protein 1, thereby linking glucose metabolism to thermogenesis.

- **Low glycaemic diets alter lipid metabolism to influence tumour growth**

[20 October 2021]

Article • Lien et al. show that low glycemic diets can reduce tumour growth by deregulating lipid metabolism.

- **eccDNAs are apoptotic products with high innate immunostimulatory activity** [20 October 2021]

Article • By developing a new eccDNA purification and profiling method, the study revealed close-to-random genomic origination, mechanism of biogenesis and function of eccDNAs.

- **The structure of neurofibromin isoform 2 reveals different functional states** [27 October 2021]

Article • Cryo-EM structure of Nf1 protein is reported, revealing closed and open conformations that regulate interaction with Ras oncogene, setting the stage for understanding the mechanistic action of Nf1 and how disease mutations lead to dysfunction.

- **Dispatched uses Na⁺ flux to power release of lipid-modified Hedgehog** [27 October 2021]

Article • Cryo-electron microscopy studies show that dynamic coordination of Na⁺ in the ion channel of Dispatched homologue 1 and the transmembrane Na⁺ gradient have key roles in exporting lipid-modified Hedgehog protein signal.

- **Kainate receptor modulation by NETO2** [22 September 2021]

Article • The authors report the structures of glutamate-gated kainate receptors in complex with NETO2 in both the resting and the desensitized states and reveal how kainate receptors in the brain are regulated by NETO2.

- NEWS AND VIEWS
- 27 October 2021

Bryozoan fossils found at last in deposits from the Cambrian period

Molecular evidence has long indicated that aquatic animals called bryozoans should be found among the fossils of the Cambrian period, around 541 million years ago. Yet they have been conspicuously absent, until now.

- [Andrej Ernst](#)⁰ &
- [Mark A. Wilson](#)¹

Multicellular animals called metazoans underwent a profound diversification of their forms during what is known as the Cambrian radiation, which began about 541 million years ago. This resulted in the formation of most of the main animal groupings (phyla) known today in a geologically relatively short time of less than 15 million years. Some phyla seem to have missed this biodiversification event, as judged from their absence in the fossil record for the Cambrian period (which ran from 541 million to 485 million years ago). However, genetic evidence, based on a ‘molecular clock’ to estimate when they emerged, suggests that they were present in this Cambrian ‘kitchen’. The most prominent animal phylum missing from the Cambrian record until now has been the Bryozoa, a group of aquatic animals that exist as individual organisms connected by tissue to form colonies. These animals are abundantly present later in the fossil record. [Writing in Nature](#), Zhang *et al.*¹ present a collection of fossils from early Cambrian deposits of China and Australia that are unequivocally bryozoans, and thus present evidence that solves one of the mysteries regarding the early diversification of animals.

Access options

Subscribe to Journal

Get full journal access for 1 year

\$199.00

only \$3.90 per issue

[Subscribe](#)

All prices are NET prices.

VAT will be added later in the checkout.

Tax calculation will be finalised during checkout.

Rent or Buy article

Get time limited or full article access on ReadCube.

from \$8.99

[Rent or Buy](#)

All prices are NET prices.

Additional access options:

- [Log in](#)
- [Learn about institutional subscriptions](#)

Nature **599**, 203-204 (2021)

doi: <https://doi.org/10.1038/d41586-021-02874-z>

References

1. 1.

Zhang, Z. *et al.* *Nature* **599**, 251–255 (2021).

2. 2.

Schwaha, T. in *Phylum Bryozoa* (ed. Schwaha, T.) 1–10 (de Gruyter, 2020).

3. 3.

Xia, F.-S., Zhang, S.-G. & Wang, Z.-Z. *J. Paleontol.* **81**, 1308–1326 (2007).

4. 4.

Ma, J., Taylor, P. D., Xia, F. & Zhan, R. *Palaeontology* **58**, 925–934 (2015).

5. 5.

Budd, G. E. & Jackson, I. S. C. *Phil. Trans. R. Soc. B* **371**, 20150287 (2016).

6. 6.

Erwin, D. H. *Development* **147**, dev182899 (2020).

This article was downloaded by **calibre** from <https://www.nature.com/articles/d41586-021-02874-z>

- NEWS AND VIEWS
- 27 October 2021

The unexpected ancestry of Inner Asian mummies

The genomes of Bronze Age mummies from the Tarim Basin in northwest China suggest that these individuals were descended from an ancient Asian population that was genetically isolated, despite extensive cultural interactions in the region.

- [Paula N. Doumani Dupuy](#) ORCID: <http://orcid.org/0000-0003-0505-0480> 0

Discoveries of 4,000-year-old naturally mummified individuals in the remote deserts of the Tarim Basin in the south of present-day Xinjiang, northwest China, have prompted decades of speculation about the individuals' ancestry. [Writing in Nature](#), Zhang *et al.*¹ resolve the question of the genetic origins of the mummies, and suggest that they were descended from an ancient, genetically isolated population. The authors' conclusions have implications for future studies of Inner Asian prehistory that must address the complex relationship between cultural exchange and genetic ancestry.

Access options

Subscribe to Journal

Get full journal access for 1 year

\$199.00

only \$3.90 per issue

Subscribe

All prices are NET prices.
VAT will be added later in the checkout.
Tax calculation will be finalised during checkout.

Rent or Buy article

Get time limited or full article access on ReadCube.

from \$8.99

Rent or Buy

All prices are NET prices.

Additional access options:

- [Log in](#)
- [Learn about institutional subscriptions](#)

Nature **599**, 204-206 (2021)

doi: <https://doi.org/10.1038/d41586-021-02872-1>

References

1. 1.

Zhang, F. *et al.* *Nature* **599**, 256–261 (2021).

2. 2.

Mallory, J. P. & Mair, V. H. *The Tarim Mummies: Ancient China and the Mystery of the Earliest Peoples from the West* (Thames & Hudson, 2000).

3. 3.

Chen, K. & Hiebert, F. T. *J. World Prehist.* **9**, 243–300 (1995).

4. 4.

Betts, A., Jia, P. & Abuduresule, I. *Archaeol. Res. Asia* **17**, 204–213 (2019).

5. 5.

Narasimhan, V. M. *et al. Science* **365**, eaat7487 (2019).

6. 6.

Anthony, D. W. *The Horse, the Wheel, and Language: How Bronze-Age Riders from the Eurasian Steppes Shaped the Modern World* (Princeton Univ. Press, 2007).

7. 7.

Wilkin, S. *et al. Nature* <https://doi.org/10.1038/s41586-021-03798-4> (2021).

8. 8.

Li, C. *et al. BMC Genet.* **16**, 78 (2015).

9. 9.

Wang, W. *et al. Sci. Adv.* **7**, eabd6690 (2021).

10. 10.

Ning, C. *et al. Front. Genet.* **12**, 740167 (2021).

11. 11.

Hermes, T. R. *et al. Proc. R. Soc. B* **286**, 20191273 (2019).

12. 12.

Taylor, W. T. T. *et al.* *Nature Hum. Behav.* **5**, 1169–1179 (2021).

13. 13.

Zhou, X. *et al.* *Nature Plants* **6**, 78–87 (2020).

14. 14.

Frachetti, M. D. *Curr. Anthropol.* **53**, 2–38 (2012).

This article was downloaded by **calibre** from <https://www.nature.com/articles/d41586-021-02872-1>

| [Section menu](#) | [Main menu](#) |

- NEWS AND VIEWS
- 20 October 2021

Diet comparison suggests a lipid imbalance can slow tumour growth

Understanding how diet affects tumour growth could lead to better treatments. Analysis in mice reveals that a low-calorie diet, but not a ketogenic diet, slows the growth of pancreatic cancer. This effect is mediated by lipid changes.

- [Giulia Salvadori](#)⁰ &
- [Valter D. Longo](#)¹

Various diets, such as those that periodically restrict calorie intake and thereby drive metabolic changes associated with fasting (periodic fasting-mimicking diets)¹, or ones that are low in carbohydrates and high in fat (ketogenic diets), are emerging as nutritional interventions that can delay cancer growth and perhaps boost the effect of anticancer drugs^{1,2}. Whereas long-term calorie restriction is not feasible for people on most cancer therapies because it leads to weight loss and lean body mass³, ketogenic diets and periodic fasting-mimicking diets are beginning to be tested in a series of clinical trials, and are particularly promising when used in combination with standard therapies^{1,2,4–6}. [Writing in Nature](#), Lien *et al.*⁷ fill in some of the missing details about how diet affects cancer growth.

Access options

Subscribe to Journal

Get full journal access for 1 year

\$199.00

only \$3.90 per issue

[Subscribe](#)

All prices are NET prices.

VAT will be added later in the checkout.

Tax calculation will be finalised during checkout.

Rent or Buy article

Get time limited or full article access on ReadCube.

from \$8.99

[Rent or Buy](#)

All prices are NET prices.

Additional access options:

- [Log in](#)
- [Learn about institutional subscriptions](#)

Nature **599**, 206-207 (2021)

doi: <https://doi.org/10.1038/d41586-021-02775-1>

References

1. 1.

de Groot, S. *et al.* *Nature Commun.* **11**, 3083 (2020).

2. 2.

Zahra, A. *et al.* *Radiat. Res.* **187**, 743–754 (2017).

3. 3.

Dirks, A. J. & Leeuwenburgh, C. *Mech Ageing Dev.* **127**, 1–7 (2006).

4. 4.

Nencioni, A., Caffa, I., Cortellino, S. & Longo, V. D. *Nature Rev. Cancer* **18**, 707–719 (2018).

5. 5.

Hopkins, B. D. *et al.* *Nature* **560**, 499–503 (2018).

6. 6.

Douris, N. *et al.* *Biochim. Biophys. Acta* **1852**, 2056–2065 (2015).

7. 7.

Lien, E. C. *et al.* *Nature* **599**, 302–307 (2021).

8. 8.

Hay N. *Nature Rev. Cancer* **16**, 635–649 (2016).

9. 9.

Lee, C. *et al.* *Sci. Transl. Med.* **4**, 124ra27 (2012).

10. 10.

Caffa, I. *et al.* *Nature* **583**, 620–624 (2020).

11. 11.

Di Tano, M. *et al.* *Nature Commun.* **11**, 2332 (2020).

12. 12.

D'Aronzo, M. *et al.* *Oncotarget* **6**, 18545–18457 (2015).

This article was downloaded by **calibre** from <https://www.nature.com/articles/d41586-021-02775-1>

| [Section menu](#) | [Main menu](#) |

- NEWS AND VIEWS
- 09 November 2021

From the archive

Nature's pages feature a textbook that takes a new approach for covering science, and an obituary of Charles Babbage.

50 years ago

Access options

Subscribe to Journal

Get full journal access for 1 year

\$199.00

only \$3.90 per issue

[Subscribe](#)

All prices are NET prices.

VAT will be added later in the checkout.

Tax calculation will be finalised during checkout.

Rent or Buy article

Get time limited or full article access on ReadCube.

from \$8.99

[Rent or Buy](#)

All prices are NET prices.

Additional access options:

- [Log in](#)
- [Learn about institutional subscriptions](#)

Nature **599**, 207 (2021)

doi: <https://doi.org/10.1038/d41586-021-03012-5>

This article was downloaded by **calibre** from <https://www.nature.com/articles/d41586-021-03012-5>

| [Section menu](#) | [Main menu](#) |

- NEWS AND VIEWS
- 10 November 2021

Global temperature changes mapped across the past 24,000 years

Palaeoclimate data and models have been used to produce a comprehensive report of Earth's temperature changes over the past 24 millennia. The results suggest that modern warming differs from the gradual rise of the past 10,000 years.

- [Shaun A. Marcott](#) ^⑨ &
- [Jeremy D. Shakun](#) ^①

John E. Kutzbach, a pioneer of palaeo-climate modelling, had a grand vision for how we might better understand past climate changes — and better predict the climatic future^①. In his view, climate research should seamlessly combine models and proxy data, which provide an indirect measure of the palaeo-climate when direct data are unavailable, using certain chemical species preserved in the environment that provide an estimate of past temperatures. A geologist could tease out a climate record from a stalagmite in China, for example, while a modeller simulated its growth, drip by drip, in a digital cave. [Writing in Nature](#), Osman *et al.*^② bring us a step closer to realizing Kutzbach's vision by pairing proxy data with models to reconstruct the evolution of the global temperature over the past 24,000 years, extending back to a period called the Last Glacial Maximum.

Access options

[Subscribe to Journal](#)

Get full journal access for 1 year

\$199.00

only \$3.90 per issue

[Subscribe](#)

All prices are NET prices.

VAT will be added later in the checkout.

Tax calculation will be finalised during checkout.

Rent or Buy article

Get time limited or full article access on ReadCube.

from \$8.99

[Rent or Buy](#)

All prices are NET prices.

Additional access options:

- [Log in](#)
- [Learn about institutional subscriptions](#)

Nature **599**, 208-209 (2021)

doi: <https://doi.org/10.1038/d41586-021-03011-6>

References

1. 1.

Kutzbach, J. E. *EOS Trans. Am. Geophys. Un.* **89**, Fall Meet. Suppl., abstr. U22A-04 (2008).

2. 2.

Osman, M. B. *et al. Nature* **599**, 239–244 (2021).

3. 3.

Marcott, S. A., Shakun, J. D., Clark, P. U. & Mix, A. C. *Science* **339**, 1198–1201 (2013).

4. 4.

Shakun, J. D. *et al. Nature* **484**, 49–54 (2012).

5. 5.

He, C. *et al. Sci. Adv.* **7**, eabh1007 (2021).

6. 6.

Liu, Z. *et al. Science* **325**, 310–314 (2009).

7. 7.

Tardif, R. *et al. Clim. Past* **15**, 1251–1273 (2019).

8. 8.

Malevich, S. B., Vetter, L. & Tierney, J. E. *Paleoceanogr. Paleoclimatol.* **34**, 1292–1315 (2019).

9. 9.

Clark, P. U., Pisias, N. G., Stocker, T. F. & Weaver, A. J. *Nature* **415**, 863–869 (2002).

10. 10.

Jones, P. D., Osborn, T. J. & Briffa, K. R. *J. Clim.* **10**, 2548–2568 (1997).

11. 11.

Kaufman, D. *et al.* *Sci. Data* **7**, 201 (2020).

12. 12.

IPCC. *Climate Change 2021: The Physical Science Basis. Contribution of Working Group I to the Sixth Assessment Report of the Intergovernmental Panel on Climate Change* (eds Masson-Delmotte, V. *et al.*) (Cambridge Univ. Press, 2021).

13. 13.

Annan, J. D. & Hargreaves, J. C. *Clim. Past* **9**, 367–376 (2013).

This article was downloaded by **calibre** from <https://www.nature.com/articles/d41586-021-03011-6>

| [Section menu](#) | [Main menu](#) |

- NEWS AND VIEWS
- 19 October 2021

Rhinoceros genomes uncover family secrets

Genomes from living and extinct rhinos reveal that different species evolved as a result of geographic isolation. A comparison of DNA from different species also shows that rhinos have long displayed low genetic variability.

- [Desire Lee Dalton](#) ⁰ &
- [Stefan Prost](#) ¹

Historically, rhinos were once abundant throughout Europe, Asia and Africa¹. Today, five species of rhinoceros survive as small populations in Asia and Africa, and are all threatened with extinction². Although well studied, there is debate in the literature about evolutionary relationships between modern and extinct rhinos, with three hypotheses being proposed (Fig. 1a–c). [Writing in Cell](#), Liu *et al.*³ analyse contemporary and ancient rhinoceros DNA to piece together the puzzle of the rhino's evolutionary history.

Access options

Subscribe to Journal

Get full journal access for 1 year

\$199.00

only \$3.90 per issue

Subscribe

All prices are NET prices.
VAT will be added later in the checkout.
Tax calculation will be finalised during checkout.

Rent or Buy article

Get time limited or full article access on ReadCube.

from \$8.99

Rent or Buy

All prices are NET prices.

Additional access options:

- [Log in](#)
- [Learn about institutional subscriptions](#)

Nature **599**, 209-210 (2021)

doi: <https://doi.org/10.1038/d41586-021-02777-z>

References

1. 1.

Tissier, J. *et al.* *PLoS One* **13**, e0193774 (2018).

2. 2.

Ashley, M. V., Melnick, D. J. & Western, D. *Conserv. Biol.* **4**, 71–77 (1990).

3. 3.

Liu, S. *et al.* *Cell* **184**, 4874–4885.e16 (2021).

4. 4.

Van Couvering, J. A. & Delson, E. *J. Vert. Paleontol.* **40**, e1803340 (2020).

5. 5.

Tougard, C., Delefosse, T., Hänni, C. & Montgelard, C. *Mol. Phylogenet. Evol.* **19**, 34–44 (2001).

6. 6.

Von Seth, J. *et al.* *Nature Commun.* **12**, 2393 (2021).

7. 7.

van der Valk, T., Díez-Del-Molino, D., Marques-Bonet, T., Guschanski, K. & Dalén, L. *Curr. Biol.* **29**, 165–170.e6 (2019).

8. 8.

Antoine, P.-O. *et al.* *Zool. J. Linn. Soc.* **160**, 139–194 (2010).

9. 9.

Cappellini, E. *et al.* *Nature* **574**, 103–107 (2019).

10. 10.

Steiner, C. C. & Ryder, O. A. *Zool. J. Linn. Soc.* **163**, 1289–1303 (2011).

11. 11.

Antoine, P.-O. *et al.* *Zool. J. Linn. Soc.* <https://doi.org/10.1093/zoolinnean/zlab009> (2021).

12. 12.

Welker, F. *et al.* *PeerJ* **5**, e3033 (2017).

13. 13.

Margaryan, A. *et al.* *Zool. J. Linn. Soc.* **190**, 372–383 (2020).

This article was downloaded by **calibre** from <https://www.nature.com/articles/d41586-021-02777-z>

| [Section menu](#) | [Main menu](#) |

- Article
- [Published: 10 November 2021](#)

An optical lattice with sound

- [Yudan Guo^{1,2},](#)
- [Ronen M. Kroeze^{1,2},](#)
- [Brendan P. Marsh^{2,3},](#)
- [Sarang Gopalakrishnan⁴,](#)
- [Jonathan Keeling](#) ORCID: orcid.org/0000-0002-4283-552X⁵ &
- [Benjamin L. Lev](#) ORCID: orcid.org/0000-0001-9163-185X^{1,2,3}

Nature volume **599**, pages 211–215 (2021)

- 314 Accesses
- 62 Altmetric
- [Metrics details](#)

Subjects

- [Bose–Einstein condensates](#)
- [Quantum simulation](#)

Abstract

Quantized sound waves—phonons—govern the elastic response of crystalline materials, and also play an integral part in determining their thermodynamic properties and electrical response (for example, by binding electrons into superconducting Cooper pairs)^{1,2,3}. The physics of lattice phonons and elasticity is absent in simulators of quantum solids constructed of neutral atoms in periodic light potentials: unlike real solids, traditional

optical lattices are silent because they are infinitely stiff⁴. Optical-lattice realizations of crystals therefore lack some of the central dynamical degrees of freedom that determine the low-temperature properties of real materials. Here, we create an optical lattice with phonon modes using a Bose–Einstein condensate (BEC) coupled to a confocal optical resonator. Playing the role of an active quantum gas microscope, the multimode cavity QED system both images the phonons and induces the crystallization that supports phonons via short-range, photon-mediated atom–atom interactions. Dynamical susceptibility measurements reveal the phonon dispersion relation, showing that these collective excitations exhibit a sound speed dependent on the BEC–photon coupling strength. Our results pave the way for exploring the rich physics of elasticity in quantum solids, ranging from quantum melting transitions⁵ to exotic ‘fractonic’ topological defects⁶ in the quantum regime.

Access options

Subscribe to Journal

Get full journal access for 1 year

\$199.00

only \$3.90 per issue

[Subscribe](#)

All prices are NET prices.

VAT will be added later in the checkout.

Tax calculation will be finalised during checkout.

Rent or Buy article

Get time limited or full article access on ReadCube.

from \$8.99

[Rent or Buy](#)

All prices are NET prices.

Additional access options:

- [Log in](#)
- [Access through your institution](#)
- [Learn about institutional subscriptions](#)

Fig. 1: Transverse, double-pumped confocal cavity quantum electrodynamics system coupled to a BEC.

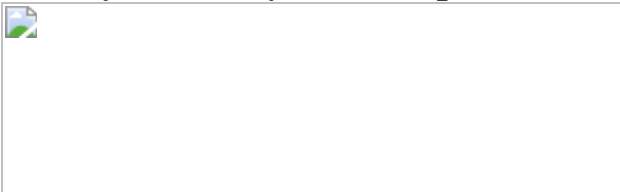


Fig. 2: Efficacy of double-pumping scheme.



Fig. 3: Soft-mode dispersion of density-wave polaritons below threshold.

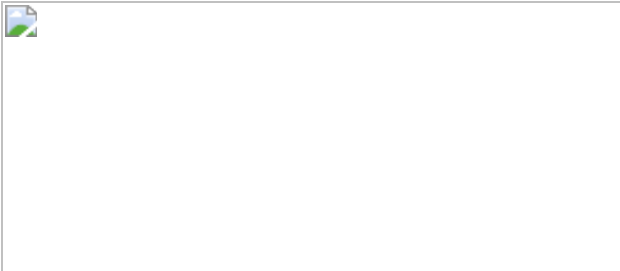
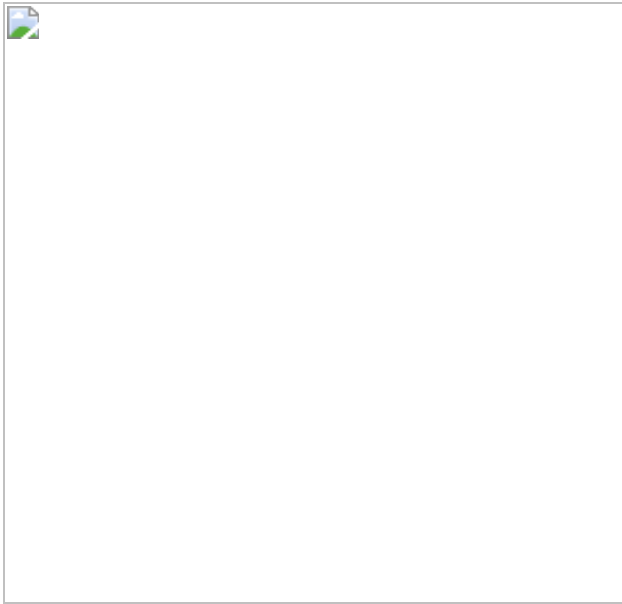


Fig. 4: Goldstone dispersion relation $\{\boldsymbol{\omega}\}$ ($\{\boldsymbol{k}\}_{\perp}$).



Data availability

The datasets generated during the current study are available in the Harvard Dataverse Repository, <https://doi.org/10.7910/DVN/LGT5O6>.

References

1. 1.

Kittel, C. *Introduction to Solid State Physics* (Wiley, 2004).

2. 2.

Chaikin, P. M. & Lubensky, T. C. *Principles of Condensed Matter Physics* (Cambridge Univ. Press, 1995).

3. 3.

Tinkham, M. *Introduction to Superconductivity* (Dover, 2004).

4. 4.

Grimm, R., Weidemüller, M. & Ovchinnikov, Y. B. in *Advances In Atomic, Molecular, and Optical Physics* Vol. 42 (eds. Bederson, B. & Walther, H.) 95–170 (Elsevier, 2000).

5. 5.

Beekman, A. J. et al. Dual gauge field theory of quantum liquid crystals in two dimensions. *Phys. Rep.* **683**, 1–110 (2017).

6. 6.

Pretko, M. & Radzhovsky, L. Fracton-elasticity duality. *Phys. Rev. Lett.* **120**, 195301 (2018).

7. 7.

Bloch, I., Dalibard, J. & Zwerger, W. Many-body physics with ultracold gases. *Rev. Mod. Phys.* **80**, 885–964 (2008).

8. 8.

González-Cuadra, D., Grzybowski, P. R., Dauphin, A. & Lewenstein, M. Strongly correlated bosons on a dynamical lattice. *Phys. Rev. Lett.* **121**, 090402 (2018).

9. 9.

Stamper-Kurn, D. M. et al. Excitation of phonons in a Bose-Einstein condensate by light scattering. *Phys. Rev. Lett.* **83**, 2876–2879 (1999).

10. 10.

Pethick, C. & Smith, H. *Bose-Einstein Condensation in Dilute Gases* (Cambridge Univ. Press, 2002).

11. 11.

Patel, P. B. et al. Universal sound diffusion in a strongly interacting Fermi gas. *Science* **370**, 1222–1226 (2020).

12. 12.

Brown, P. T. et al. Bad metallic transport in a cold atom Fermi-Hubbard system. *Science* **363**, 379–382 (2018).

13. 13.

Carusotto,, I. & Ciuti, C. Quantum fluids of light. *Rev. Mod. Phys.* **85**, 299–366 (2013).

14. 14.

Kirton, P., Roses, M. M., Keeling, J. & Dalla Torre, E. G. Introduction to the Dicke model: from equilibrium to nonequilibrium, and vice versa. *Adv. Quantum Technol.* **2**, 1800043 (2018).

15. 15.

Mivehvar, F., Piazza, F., Donner, T. & Ritsch, H. Cavity QED with quantum gases: new paradigms in many-body physics. Preprint at <https://arxiv.org/abs/2102.04473> (2021).

16. 16.

Klinder, J., Keßler, H., Bakhtiari, M. R., Thorwart, M. & Hemmerich, A. Observation of a superradiant Mott insulator in the Dicke-Hubbard model. *Phys. Rev. Lett.* **115**, 230403 (2015).

17. 17.

Landig, R. et al. Quantum phases from competing short- and long-range interactions in an optical lattice. *Nature* **532**, 476–479 (2016).

18. 18.

Kollár, A. J. et al. Supermode-density-wave-polariton condensation with a Bose–Einstein condensate in a multimode cavity. *Nat. Commun.* **8**, 14386 (2017).

19. 19.

Kroeze, R. M., Guo, Y. & Lev, B. L. Dynamical spin-orbit coupling of a quantum gas. *Phys. Rev. Lett.* **123**, 160404 (2019).

20. 20.

Gopalakrishnan, S., Lev, B. L. & Goldbart, P. M. Emergent crystallinity and frustration with Bose Einstein condensates in multimode cavities. *Nat. Phys.* **5**, 845–850 (2009).

21. 21.

Gopalakrishnan, S., Lev, B. L. & Goldbart, P. M. Atom-light crystallization of Bose–Einstein condensates in multimode cavities: Nonequilibrium classical and quantum phase transitions, emergent lattices, supersolidity, and frustration. *Phys. Rev. A* **82**, 043612 (2010).

22. 22.

Mivehvar, F., Ostermann, S., Piazza, F. & Ritsch, H. Driven-dissipative supersolid in a ring cavity. *Phys. Rev. Lett.* **120**, 123601 (2018).

23. 23.

Schuster, S., Wolf, P., Ostermann, S., Slama, S. & Zimmermann, C. Supersolid properties of a Bose-Einstein condensate in a ring resonator. *Phys. Rev. Lett.* **124**, 143602 (2020).

24. 24.

Léonard, J., Morales, A., Zupancic, P., Esslinger, T. & Donner, T. Supersolid formation in a quantum gas breaking a continuous translational symmetry. *Nature* **543**, 87–90 (2017).

25. 25.

Léonard, J., Morales, A., Zupancic, P., Donner, T. & Esslinger, T. Monitoring and manipulating Higgs and Goldstone modes in a supersolid quantum gas. *Science* **358**, 1415–1418 (2017).

26. 26.

Ballantine, K. E., Lev, B. L. & Keeling, J. Meissner-like effect for a synthetic gauge field in multimode cavity QED. *Phys. Rev. Lett.* **118**, 045302 (2017).

27. 27.

Rylands, C., Guo, Y., Lev, B. L., Keeling, J. & Galitski, V. Photon-mediated Peierls transition of a 1D gas in a multimode optical cavity. *Phys. Rev. Lett.* **125**, 010404 (2020).

28. 28.

Vaidya, V. D. et al. Tunable-range, photon-mediated atomic interactions in multimode cavity QED. *Phys. Rev. X* **8**, 011002 (2018).

29. 29.

Guo, Y., Kroese, R. M., Vaidya, V. D., Keeling, J. & Lev, B. L. Sign-changing photon-mediated atom interactions in multimode cavity quantum electrodynamics. *Phys. Rev. Lett.* **122**, 193601 (2019).

30. 30.

Guo, Y. et al. Emergent and broken symmetries of atomic self-organization arising from Gouy phase shifts in multimode cavity QED. *Phys. Rev. A* **99**, 053818 (2019).

31. 31.

Lewenstein, M. et al. in *AIP Conference Proceedings* Vol. 869 (eds Roos, C., Häffner, H. & Blatt, R.) 201–211 (AIP, 2006).

32. 32.

Ostermann, S., Piazza, F. & Ritsch, H. Spontaneous crystallization of light and ultracold atoms. *Phys. Rev. X* **6**, 021026 (2016).

33. 33.

Dimitrova, I. et al. Observation of two-beam collective scattering phenomena in a Bose-Einstein condensate. *Phys. Rev. A* **96**, 051603 (2017).

34. 34.

Monroe, C. et al. Programmable quantum simulations of spin systems with trapped ions. *Rev. Mod. Phys.* **93**, 025001 (2021).

35. 35.

Siegman, A. E. *Lasers* (University Science Books, 1986).

36. 36.

Mottl, R. et al. Roton-type mode softening in a quantum gas with cavity-mediated long-range interactions. *Science* **336**, 1570–1573 (2012).

37. 37.

Papageorge, A. T., Kollár, A. J. & Lev, B. L. Coupling to modes of a near-confocal optical resonator using a digital light modulator. *Opt. Express* **24**, 11447–11457 (2016).

38. 38.

Devreese, J. T. & Alexandrov, A. S. Fröhlich polaron and bipolaron: recent developments. *Rep. Prog. Phys.* **72**, 066501 (2009).

39. 39.

Hu, M.-G. et al. Bose polarons in the strongly interacting regime. *Phys. Rev. Lett.* **117**, 055301 (2016).

40. 40.

Jørgensen, N. B. et al. Observation of attractive and repulsive polarons in a Bose-Einstein condensate. *Phys. Rev. Lett.* **117**, 055302 (2016).

41. 41.

Yan, Z. Z., Ni, Y., Robens, C. & Zwierlein, M. W. Bose polarons near quantum criticality. *Science* **368**, 190–194 (2020).

42. 42.

Werman, Y., Kivelson, S. A. & Berg, E. Nonquasiparticle transport and resistivity saturation: a view from the large-N limit. *npj Quant. Mater.* **2**, 7 (2017).

43. 43.

Kollár, A. J., Papageorge, A. T., Baumann, K., Armen, M. A. & Lev, B. L. An adjustable-length cavity and Bose-Einstein condensate apparatus for multimode cavity QED. *New J. Phys.* **17**, 043012 (2015).

44. 44.

Kroeze, R. M., Guo, Y., Vaidya, V. D., Keeling, J. & Lev, B. L. Spinor self-ordering of a quantum gas in a cavity. *Phys. Rev. Lett.* **121**, 163601 (2018).

Acknowledgements

We thank S. Kivelson, S. Hartnoll and V. Khemani for stimulating discussions. We acknowledge funding support from the Army Research Office. Y.G. and B.M. acknowledge funding from the Stanford Q-FARM Graduate Student Fellowship and the NSF Graduate Research Fellowship, respectively. S.G. acknowledges support from NSF grant no. DMR-1653271.

Author information

Affiliations

1. Department of Physics, Stanford University, Stanford, CA, USA
Yudan Guo, Ronen M. Kroeze & Benjamin L. Lev
2. E. L. Ginzton Laboratory, Stanford University, Stanford, CA, USA
Yudan Guo, Ronen M. Kroeze, Brendan P. Marsh & Benjamin L. Lev
3. Department of Applied Physics, Stanford University, Stanford, CA, USA
Brendan P. Marsh & Benjamin L. Lev
4. Department of Physics, The Pennsylvania State University, University Park, PA, USA
Sarang Gopalakrishnan
5. SUPA, School of Physics and Astronomy, University of St Andrews, St Andrews, UK
Jonathan Keeling

Contributions

All authors contributed to the work and contributed to writing the paper.

Corresponding author

Correspondence to [Benjamin L. Lev](#).

Ethics declarations

Competing interests

The authors declare no competing interests.

Additional information

Peer review information *Nature* thanks Francesco Piazza and the other, anonymous, reviewer(s) for their contribution to the peer review of this work.

Publisher's note Springer Nature remains neutral with regard to jurisdictional claims in published maps and institutional affiliations.

Extended data figures and tables

Extended Data Fig. 1 DMD momentum probes.

a–g, Measured DMD probe transmission cavity field and their phase profile line cuts. The values of $\langle k \rangle_{\perp} / \langle k \rangle_r$ in panels **a–f** are $[0.2, 1.4, 2.6, 3.8, 5.10, 6.6]$ (times 10^{-3}), respectively. The white dashed line in panel **a** shows the length of the cuts in panel **g**. Additional features around the main probe field are due to imperfections of the confocal cavity and stray light from the DMD probe beam. The grey area is the half plane that contains the mirror image of the probe field, and we do not show this redundant portion of the image in the main text figures.

Supplementary information

Supplementary Information

Supplementary Information sections 1–9, including Supplementary Figs. 1–5 and references.

Supplementary Video 1 Phonon dynamics animation

Phonon dynamics animation illustrating the phonon dynamics via change in the atomic density in a chequerboard lattice with lattice constant $\sqrt{2}\lambda$. The k_{\perp} used, $0.3k_r$, has been exaggerated in magnitude for clarity in showing the lattice motion in which the maximum excursion of a lattice site is 0.2λ .

Rights and permissions

[Reprints and Permissions](#)

About this article

Cite this article

Guo, Y., Kroeze, R.M., Marsh, B.P. *et al.* An optical lattice with sound. *Nature* **599**, 211–215 (2021). <https://doi.org/10.1038/s41586-021-03945-x>

- Received: 27 April 2021
- Accepted: 23 August 2021
- Published: 10 November 2021
- Issue Date: 11 November 2021
- DOI: <https://doi.org/10.1038/s41586-021-03945-x>

Share this article

Anyone you share the following link with will be able to read this content:

[Get shareable link](#)

Sorry, a shareable link is not currently available for this article.

[Copy to clipboard](#)

Provided by the Springer Nature SharedIt content-sharing initiative

This article was downloaded by **calibre** from <https://www.nature.com/articles/s41586-021-03945-x>

| [Section menu](#) | [Main menu](#) |

- Article
- [Published: 29 September 2021](#)

Cascade of correlated electron states in the kagome superconductor CsV₃Sb₅

- [He Zhao](#)¹,
- [Hong Li](#)¹,
- [Brenden R. Ortiz](#)²,
- [Samuel M. L. Teicher](#)²,
- [Takamori Park](#)³,
- [Mengxing Ye](#)⁴,
- [Ziqiang Wang](#) [ORCID: orcid.org/0000-0001-7617-2886](#)¹,
- [Leon Balents](#)^{4,5},
- [Stephen D. Wilson](#) [ORCID: orcid.org/0000-0003-3733-930X](#)² &
- [Ilija Zeljkovic](#) [ORCID: orcid.org/0000-0001-9966-2140](#)¹

[Nature](#) volume 599, pages 216–221 (2021)

- 4619 Accesses
- 6 Citations
- 45 Altmetric
- [Metrics details](#)

Subjects

- [Electronic properties and materials](#)

- [Superconducting properties and materials](#)

Abstract

The kagome lattice of transition metal atoms provides an exciting platform to study electronic correlations in the presence of geometric frustration and nontrivial band topology^{1,2,3,4,5,6,7,8,9,10,11,12,13,14,15,16,17,18}, which continues to bear surprises. Here, using spectroscopic imaging scanning tunnelling microscopy, we discover a temperature-dependent cascade of different symmetry-broken electronic states in a new kagome superconductor, CsV_3Sb_5 . We reveal, at a temperature far above the superconducting transition temperature $T_c \sim 2.5$ K, a tri-directional charge order with a $2a_0$ period that breaks the translation symmetry of the lattice. As the system is cooled down towards T_c , we observe a prominent V-shaped spectral gap opening at the Fermi level and an additional breaking of the six-fold rotational symmetry, which persists through the superconducting transition. This rotational symmetry breaking is observed as the emergence of an additional $4a_0$ unidirectional charge order and strongly anisotropic scattering in differential conductance maps. The latter can be directly attributed to the orbital-selective renormalization of the vanadium kagome bands. Our experiments reveal a complex landscape of electronic states that can coexist on a kagome lattice, and highlight intriguing parallels to high- T_c superconductors and twisted bilayer graphene.

Access options

Subscribe to Journal

Get full journal access for 1 year

\$199.00

only \$3.90 per issue

[Subscribe](#)

All prices are NET prices.
VAT will be added later in the checkout.
Tax calculation will be finalised during checkout.

Rent or Buy article

Get time limited or full article access on ReadCube.

from \$8.99

[Rent or Buy](#)

All prices are NET prices.

Additional access options:

- [Log in](#)
- [Access through your institution](#)
- [Learn about institutional subscriptions](#)

Fig. 1: Surface identification.

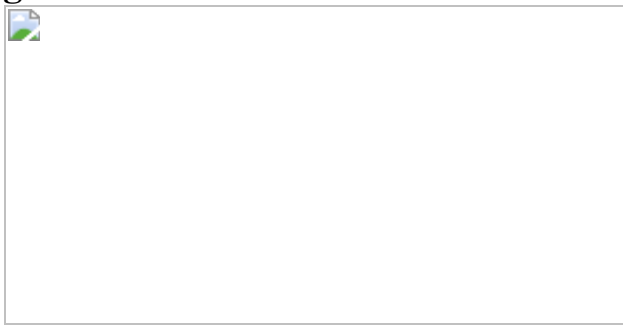


Fig. 2: Large-scale electronic characterization.

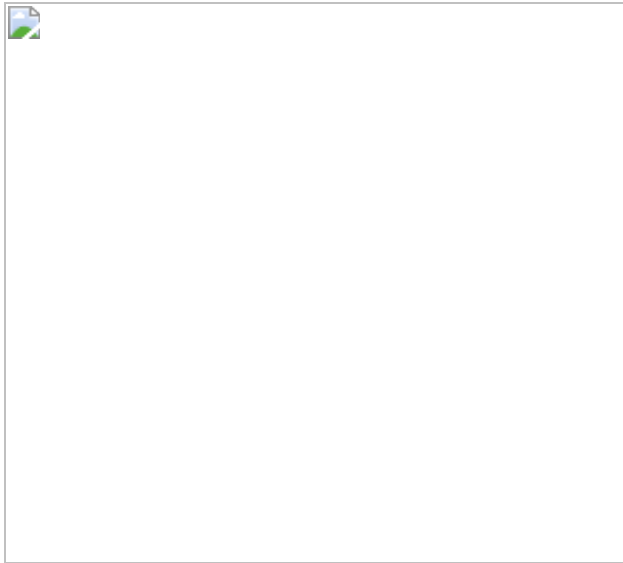
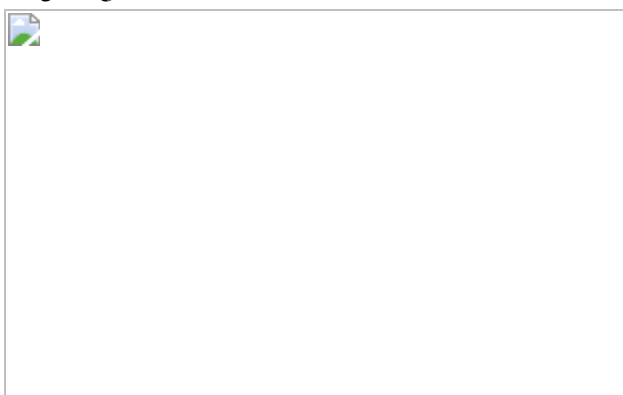


Fig. 3: Charge ordering at low temperature.



Fig. 4: Visualizing rotational symmetry breaking in the QPI of CsV₃Sb₅.



Data availability

The data supporting the findings of this study are available upon request from the corresponding author. [Source data](#) are provided with this paper.

Code availability

The computer code used for data analysis is available upon request from the corresponding author.

References

1. 1.

Sachdev, S. Kagome- and triangular-lattice Heisenberg antiferromagnets: ordering from quantum fluctuations and quantum-disordered ground states with unconfined bosonic spinons. *Phys. Rev. B* **45**, 12377–12396 (1992).

2. 2.

Mazin, I. I. et al. Theoretical prediction of a strongly correlated Dirac metal. *Nat. Commun.* **5**, 4261 (2014).

3. 3.

Guo, H.-M. & Franz, M. Topological insulator on the kagome lattice. *Phys. Rev. B* **80**, 113102 (2009).

4. 4.

Bilitewski, T. & Moessner, R. Disordered flat bands on the kagome lattice. *Phys. Rev. B* **98**, 235109 (2018).

5. 5.

Balents, L., Fisher, M. P. A. & Girvin, S. M. Fractionalization in an easy-axis kagome antiferromagnet. *Phys. Rev. B* **65**, 224412 (2002).

6. 6.

Neupert, T., Santos, L., Chamon, C. & Mudry, C. Fractional quantum Hall states at zero magnetic field. *Phys. Rev. Lett.* **106**, 236804 (2011).

7. 7.

Plat, X., Alet, F., Capponi, S. & Totsuka, K. Magnetization plateaus of an easy-axis kagome antiferromagnet with extended interactions. *Phys. Rev. B* **92**, 174402 (2015).

8. 8.

Wen, J., Rüegg, A., Wang, C.-C. J. & Fiete, G. A. Interaction-driven topological insulators on the kagome and the decorated honeycomb lattices. *Phys. Rev. B* **82**, 075125 (2010).

9. 9.

Yu, S.-L. & Li, J.-X. Chiral superconducting phase and chiral spin-density-wave phase in a Hubbard model on the kagome lattice. *Phys. Rev. B* **85**, 144402 (2012).

10. 10.

Kiesel, M. L., Platt, C. & Thomale, R. Unconventional Fermi surface instabilities in the kagome Hubbard model. *Phys. Rev. Lett.* **110**, 126405 (2013).

11. 11.

Sun, K., Gu, Z., Katsura, H. & Das Sarma, S. Nearly flatbands with nontrivial topology. *Phys. Rev. Lett.* **106**, 236803 (2011).

12. 12.

Tang, E., Mei, J.-W. & Wen, X.-G. High-temperature fractional quantum Hall states. *Phys. Rev. Lett.* **106**, 236802 (2011).

13. 13.

O'Brien, A., Pollmann, F. & Fulde, P. Strongly correlated fermions on a kagome lattice. *Phys. Rev. B* **81**, 235115 (2010).

14. 14.

Rüegg, A. & Fiete, G. A. Fractionally charged topological point defects on the kagome lattice. *Phys. Rev. B* **83**, 165118 (2011).

15. 15.

Yan, S., Huse, D. A. & White, S. R. Spin-liquid ground state of the $S=1/2$ kagome Heisenberg antiferromagnet. *Science* **332**, 1173–1176 (2011).

16. 16.

Isakov, S. V., Wessel, S., Melko, R. G., Sengupta, K. & Kim, Y. B. Hard-core bosons on the kagome lattice: valence-bond solids and their quantum melting. *Phys. Rev. Lett.* **97**, 147202 (2006).

17. 17.

Wang, W.-S., Li, Z.-Z., Xiang, Y.-Y. & Wang, Q.-H. Competing electronic orders on kagome lattices at van Hove filling. *Phys. Rev. B* **87**, 115135 (2013).

18. 18.

Jiang, H.-C., Devereaux, T. & Kivelson, S. A. Holon Wigner crystal in a lightly doped kagome quantum spin liquid. *Phys. Rev. Lett.* **119**, 067002 (2017).

19. 19.

Wang, Q. et al. Large intrinsic anomalous Hall effect in half-metallic ferromagnet $\text{Co}_3\text{Sn}_2\text{S}_2$ with magnetic Weyl fermions. *Nat. Commun.* **9**, 3681 (2018).

20. 20.

Morali, N. et al. Fermi-arc diversity on surface terminations of the magnetic Weyl semimetal $\text{Co}_3\text{Sn}_2\text{S}_2$. *Science* **365**, 1286–1291 (2019).

21. 21.

Yin, J.-X. et al. Negative flat band magnetism in a spin–orbit-coupled correlated kagome magnet. *Nat. Phys.* **15**, 443–448 (2019).

22. 22.

Jiao, L. et al. Signatures for half-metallicity and nontrivial surface states in the kagome lattice Weyl semimetal $\text{Co}_3\text{Sn}_2\text{S}_2$. *Phys. Rev. B* **99**, 245158 (2019).

23. 23.

Liu, E. et al. Giant anomalous Hall effect in a ferromagnetic kagome-lattice semimetal. *Nat. Phys.* **14**, 1125–1131 (2018).

24. 24.

Lin, Z. et al. Dirac fermions in antiferromagnetic FeSn kagome lattices with combined space inversion and time-reversal symmetry. *Phys. Rev. B* **102**, 155103 (2020).

25. 25.

Kang, M. et al. Dirac fermions and flat bands in the ideal kagome metal FeSn. *Nat. Mater.* **19**, 163–169 (2020).

26. 26.

Lin, Z. et al. Flatbands and emergent ferromagnetic ordering in Fe_3Sn_2 kagome lattices. *Phys. Rev. Lett.* **121**, 096401 (2018).

27. 27.

Yin, J.-X. X. et al. Giant and anisotropic many-body spin–orbit tunability in a strongly correlated kagome magnet. *Nature* **562**, 91–95 (2018).

28. 28.

Ortiz, B. R. et al. New kagome prototype materials: discovery of KV_3Sb_5 , RbV_3Sb_5 , and CsV_3Sb_5 . *Phys. Rev. Mater.* **3**, 094407 (2019).

29. 29.

Ortiz, B. R. et al. CsV_3Sb_5 : a Z_2 topological kagome metal with a superconducting ground state. *Phys. Rev. Lett.* **125**, 247002 (2020).

30. 30.

Yang, S.-Y. et al. Giant, unconventional anomalous Hall effect in the metallic frustrated magnet candidate, KV_3Sb_5 . *Sci. Adv.* **6**, eabb6003 (2020).

31. 31.

Ortiz, B. R. et al. Superconductivity in the Z_2 kagome metal KV_3Sb_5 . *Phys. Rev. Mater.* **5**, 034801 (2021).

32. 32.

Wang, D. et al. Evidence for Majorana bound states in an iron-based superconductor. *Science* **362**, 333–335 (2018).

33. 33.

Zhang, P. et al. Observation of topological superconductivity on the surface of an iron-based superconductor. *Science* **360**, 182–186 (2018).

34. 34.

Wang, Y. et al. Proximity-induced spin-triplet superconductivity and edge supercurrent in the topological Kagome metal. Preprint at <https://arxiv.org/abs/2012.05898> (2020).

35. 35.

Zhao, C. C. et al. Nodal superconductivity and superconducting dome in the topological Kagome metal CsV_3Sb_5 . Preprint at <https://arxiv.org/abs/2102.08356> (2021).

36. 36.

Jiang, Y.-X. et al. Unconventional chiral charge order in kagome superconductor KV_3Sb_5 . *Nat. Mater.* <https://doi.org/10.1038/s41563-021-01034-y> (2021).

37. 37.

Kostin, A. et al. Imaging orbital-selective quasiparticles in the Hund's metal state of FeSe. *Nat. Mater.* **17**, 869–874 (2018).

38. 38.

Nakayama, K. et al. Multiple energy scales and anisotropic energy gap in the charge-density-wave phase of kagome superconductor CsV_3Sb_5 . Preprint at <https://arxiv.org/abs/2104.08042> (2021).

39. 39.

Xiang, Y. et al. Twofold symmetry of c -axis resistivity in topological kagome superconductor CsV_3Sb_5 with in-plane rotating magnetic field. Preprint at <https://arxiv.org/abs/2104.06909> (2021).

40. 40.

Chen, H. et al. Roton pair density wave in a strong-coupling kagome superconductor. *Nature* <https://doi.org/10.1038/s41586-021-03983-5> (2021).

41. 41.

Ratcliff, N., Hallett, L., Ortiz, B. R., Wilson, S. D. & Harter, J. W. Coherent phonon spectroscopy and interlayer modulation of charge density wave order in the kagome metal CsV_3Sb_5 . Preprint at <https://arxiv.org/abs/2104.10138> (2021).

42. 42.

Fradkin, E., Kivelson, S. A. & Tranquada, J. M. Colloquium: Theory of intertwined orders in high temperature superconductors. *Rev. Mod. Phys.* **87**, 457–482 (2015).

43. 43.

Lawler, M. J. et al. Intra-unit-cell electronic nematicity of the high- T_c copper-oxide pseudogap states. *Nature* **466**, 347–351 (2010).

44. 44.

Kresse, G. & Hafner, J. Ab initio molecular-dynamics simulation of the liquid-metal–amorphous-semiconductor transition in germanium. *Phys. Rev. B* **49**, 14251–14269 (1994).

45. 45.

Kresse, G. & Furthmüller, J. Efficient iterative schemes for ab initio total-energy calculations using a plane-wave basis set. *Phys. Rev. B* **54**, 11169–11186 (1996).

46. 46.

Kresse, G. & Furthmüller, J. Efficiency of ab-initio total energy calculations for metals and semiconductors using a plane-wave basis set. *Comput. Mater. Sci.* **6**, 15–50 (1996).

47. 47.

Blöchl, P. E. Projector augmented-wave method. *Phys. Rev. B* **50**, 17953–17979 (1994).

48. 48.

Kresse, G. & Joubert, D. From ultrasoft pseudopotentials to the projector augmented-wave method. *Phys. Rev. B* **59**, 1758–1775 (1999).

49. 49.

Perdew, J., Burke, K. & Ernzerhof, M. Generalized gradient approximation made simple. *Phys. Rev. Lett.* **77**, 3865–3868 (1996).

50. 50.

Grimme, S., Ehrlich, S. & Goerigk, L. Effect of the damping function in dispersion corrected density functional theory. *J. Comput. Chem.* **32**, 1456–1465 (2011).

51. 51.

Mostofi, A. A. et al. An updated version of wannier90: a tool for obtaining maximally-localised Wannier functions. *Comput. Phys. Commun.* **185**, 2309–2310 (2014).

52. 52.

Hu, Y. et al. Charge-order-assisted topological surface states and flat bands in the kagome superconductor CsV_3Sb_5 . Preprint at <https://arxiv.org/abs/2104.12725> (2021).

Acknowledgements

We thank K. Fujita and A. Pasupathy for valuable discussions. I.Z. gratefully acknowledges the support from the National Science Foundation grant no. NSF-DMR-1654041 and Boston College startup. S.D.W., B.R.O., L.B., S.M.L.T. and T.P. gratefully acknowledge support via the University of California Santa Barbara NSF Quantum Foundry funded via the Q-AMASE-i programme under award DMR-1906325. B.R.O. also acknowledges support from the California NanoSystems Institute through the Elings Fellowship programme. We acknowledge use of the shared computing facilities of the Center for Scientific Computing at University of California Santa Barbara, supported by NSF CNS-1725797, and the NSF Materials Research Science and Engineering Center at University of California Santa Barbara, NSF DMR-1720256. M.Y. is supported in part by the Gordon and Betty Moore Foundation through Grant GBMF8690 to UCSB. S.M.L.T. has been supported by the National Science Foundation Graduate Research Fellowship Program under grant no. DGE-1650114. Any opinions, findings, and conclusions or recommendations expressed in this material are those of the authors and do not necessarily reflect the views of the National Science Foundation. Z.W. acknowledges the support of US Department of Energy, Basic Energy Sciences grant no. DE-FG02-99ER45747.

Author information

Affiliations

1. Department of Physics, Boston College, Chestnut Hill, MA, USA

He Zhao, Hong Li, Ziqiang Wang & Ilijia Zeljkovic

2. Materials Department and California Nanosystems Institute,
University of California Santa Barbara, Santa Barbara, CA, USA

Brenden R. Ortiz, Samuel M. L. Teicher & Stephen D. Wilson

3. Department of Physics, University of California Santa Barbara, Santa Barbara, CA, USA

Takamori Park

4. Kavli Institute for Theoretical Physics, University of California, Santa Barbara, Santa Barbara, CA, USA

Mengxing Ye & Leon Balents

5. Canadian Institute for Advanced Research, Toronto, Ontario, Canada

Leon Balents

Contributions

STM experiments and data analysis were performed by H.Z. and H.L. B.R.O. synthesized and characterized the samples under the supervision of S.D.W. S.M.L.T. performed band structure calculations. T.P., M.Y., L.B. and Z.W. provided theoretical input on the underlying physics and the interpretation of data. H.Z., S.D.W., Z.W. and I.Z. wrote the paper, with input from all authors. I.Z. supervised the project.

Corresponding author

Correspondence to [Ilija Zeljkovic](#).

Ethics declarations

Competing interests

The authors declare no competing interests.

Additional information

Peer review information *Nature* thanks the anonymous reviewers for their contribution to the peer review of this work. Peer reviewer reports are available.

Publisher's note Springer Nature remains neutral with regard to jurisdictional claims in published maps and institutional affiliations.

Extended data figures and tables

Extended Data Fig. 1 Cs clustering on as-cleaved Sb-terminated surface.

(a) 3D portrayal of a large-scale morphology of the Sb layer from an STM topograph. Inset is a 3D zoom-in of a small square region covering three Cs atoms. (b) As-cleaved STM topograph with several Cs atoms scattered on the surface. The apparent height of Cs atoms in (b) is approximately 2 Angstroms, and the color scale is saturated to emphasize the $4a_0$ -CO modulation. STM setup condition: (a) $V_{sample} = 200$ mV, $I_{set} = 10$ pA; (b) $V_{sample} = 200$ mV, $I_{set} = 50$ pA. T = 4.5 K in all panels.

Extended Data Fig. 2 Large-scale STM topograph of the Sb-terminated surface.

High resolution STM topograph over a large region encompassing the topograph from Fig. 3c. Inset shows a zoom-in on two defects that serve as main scattering sites for the wave-like QPI modulations, with different atoms superimposed on top (Cs – green, Sb – gray and V – red spheres). As it can be seen in the inset, the defects are located at the Cs site. STM setup condition: $V_{sample} = -20$ mV, $I_{set} = 20$ pA, T = 4.5 K; (inset) $V_{sample} = 20$ mV, $I_{set} = 60$ pA, T = 4.5 K.

Extended Data Fig. 3 Quasiparticle interference imaging of the electron pocket around Γ .

(a-f) Differential conductance ($dI/dV(\mathbf{r}, V)$) maps over the same region of the sample used for the analysis of the dispersion in Fig. 2, and (g-l) corresponding Fourier transforms (FTs). Green, brown and blue circles denote the atomic Bragg peaks, $2a_0$ charge ordering peaks $\mathbf{q}_{2a_0\text{-CO}}$ and unidirectional stripe charge order peaks $\mathbf{q}_{4a_0\text{-CO}}$ in momentum-transfer space, respectively. The red and orange arrows indicate the QPI wave vectors that we attribute to the intra-electron pocket scattering around Γ . (m) Radially-averaged FT linecut as a function of STM bias V showing the presence of \mathbf{q}_1 across Fermi energy. STM setup condition: (a) $V_{sample} = -400$ mV, $I_{set} = 800$ pA, $V_{exc} = 5$ mV; (b) $V_{sample} = -300$ mV, $I_{set} = 600$ pA, $V_{exc} = 4$ mV; (c) $V_{sample} = -200$ mV, $I_{set} = 400$ pA, $V_{exc} = 4$ mV; (d) $V_{sample} = -100$ mV, $I_{set} = 200$ pA, $V_{exc} = 4$ mV; (e) $V_{sample} = -50$ mV, $I_{set} = 100$ pA, $V_{exc} = 4$ mV; (f) $V_{sample} = 200$ mV, $I_{set} = 400$ pA, $V_{exc} = 4$ mV; (m) $V_{sample} = 10$ mV, $I_{set} = 100$ pA, $V_{exc} = 1$ mV; $T = 4.5$ K.

Extended Data Fig. 4 Identification of additional peaks in the Fourier transform linecut along the charge stripe direction.

Fourier transform linecut of $L(\mathbf{r}, V)$ maps along the $\mathbf{q}_{4a_0\text{-CO}}$ (charge stripe) direction at 4.5 K (same as Fig. 3g). The green dashed lines are visual guides showing the most prominent additional non-dispersive peaks. Green arrows denote all the satellite peaks we observe, approximately equally spaced from the dominant peaks. The black, blue and brown arrows indicate the dominant peaks: the low-frequency peak (\mathbf{q}_{low}) likely associated with the satellite peaks, unidirectional charge order peak ($\mathbf{q}_{4a_0\text{-CO}}$) and tri-directional charge order peak ($\mathbf{q}_{2a_0\text{-CO}}$), respectively. STM setup condition: $V_{sample} = 100$ mV, $I_{set} = 600$ pA, $V_{exc} = 4$ mV, $T = 4.5$ K.

Extended Data Fig. 5 Data reproducibility across different CsV_3Sb_5 single crystals.

(a-c) STM topographs acquired over different CsV_3Sb_5 samples. (d,e) Differential conductance ($dI/dV(\mathbf{r}, V)$) maps obtained on sample #1 and #3, respectively. Panels (f-j) are the corresponding Fourier transforms of the

images above. STM setup condition: (a) $V_{sample} = -20$ mV, $I_{set} = 20$ pA; (b) $V_{sample} = 300$ mV, $I_{set} = 90$ pA; (c) $V_{sample} = -40$ mV, $I_{set} = 110$ pA; (d) $V_{sample} = -4$ mV, $I_{set} = 50$ pA, $V_{exc} = 1$ mV; (e) $V_{sample} = 4$ mV, $I_{set} = 40$ pA, $V_{exc} = 1$ mV.

Extended Data Fig. 6 Bias dependence of STM topographs.

(a-d) STM topographs acquired over an identical region at 60 K under different biases. (e-h) STM topographs acquired over another region at 4.5 K under different biases. Insets in (a-h) are the associated Fourier transforms. Green, brown and blue circles denote the atomic Bragg peaks, tri-directional charge order peaks and unidirectional stripe charge order peaks in momentum-transfer space, respectively. STM setup condition: (a) $V_{sample} = 90$ mV, $I_{set} = 30$ pA; (b) $V_{sample} = 50$ mV, $I_{set} = 30$ pA; (c) $V_{sample} = -30$ mV, $I_{set} = 40$ pA; (d) $V_{sample} = -90$ mV, $I_{set} = 40$ pA; (e) $V_{sample} = 200$ mV, $I_{set} = 400$ pA; (f) $V_{sample} = 50$ mV, $I_{set} = 100$ pA; (g) $V_{sample} = 10$ mV, $I_{set} = 20$ pA; (h) $V_{sample} = -50$ mV, $I_{set} = 100$ pA.

Extended Data Fig. 7 Density functional theory(DFT) calculation of the electronic band structure.

(a) DFT calculated band structure of CsV_3Sb_5 along high symmetry directions across the Brillouin zone, visualized by SUMO (Supplementary Section 1). The blue and red colors represent the contributions from Sb and V orbitals, respectively. (b) Schematic of different high-symmetry points.

Extended Data Fig. 8 Energy dependence of the quasiparticle interference (QPI) near Fermi level.

(a-g) Two-fold symmetrized Fourier transforms (FTs) of differential conductance ($dI/dV(\mathbf{r}, V)$) maps acquired over the same field-of-view on an Sb-terminated surface of sample 1. The dispersive QPI stripes are denoted by magenta (along \mathbf{q}_a) and blue (along $\mathbf{q}_{b,c}$) rectangles. At bias lower than 12 mV, the stripe features along \mathbf{q}_a are clearly visible (solid magenta

rectangles), while the equivalent features along \mathbf{q}_b and \mathbf{q}_c are absent (dashed blue rectangles). The trend is reversed at a bias higher than 12 mV. Green circles denote the atomic Bragg peaks. For visual purposes, noise streaks in (c-e) along ~45 degree direction with respect to the horizontal are removed by subtracting a polynomial from each row of the raw dI/dV map before the map is rotated, FT is performed and the FT is two-fold symmetrized. (h,i) Linecuts in FTs of $dI/dV(\mathbf{r}, V)$ maps as a function of bias along the magenta and blue dashed lines in (d). Orange curves in (h,i) are visual guides showing the dispersion of QPI wave vectors. STM setup condition: (a) $V_{sample} = 18$ mV, $I_{set} = 90$ pA, $V_{exc} = 1$ mV; (b) $V_{sample} = 16$ mV, $I_{set} = 200$ pA, $V_{exc} = 1$ mV; (c) $V_{sample} = 14$ mV, $I_{set} = 100$ pA, $V_{exc} = 1$ mV; (d) $V_{sample} = 12$ mV, $I_{set} = 90$ pA, $V_{exc} = 1$ mV; (e) $V_{sample} = 10$ mV, $I_{set} = 70$ pA, $V_{exc} = 1$ mV; (f) $V_{sample} = 5$ mV, $I_{set} = 60$ pA, $V_{exc} = 1$ mV; (g) $V_{sample} = -5$ mV, $I_{set} = 60$ pA, $V_{exc} = 1$ mV; T = 4.5 K.

Extended Data Fig. 9 Additional temperature-dependent STM data.

(a,b) STM topographs of an identical area of the sample at (a) 4.5 K, and (b) 50 K, and (c,d) corresponding spatially-averaged dI/dV spectra. As it can be seen from (b), the $4a_0$ charge ordering is nearly completely absent at this elevated temperature. The low-temperature dI/dV spectrum in (c) shows two shoulders at ± 20 mV (black arrows) and gap-like features closer to Fermi energy around ± 5 to 10 mV (orange arrows). dI/dV spectrum at higher temperature in (d) (just before entering the $4a_0$ -CO state) only shows the broad shoulders at higher energy. (e) Large-scale STM topograph and (f) Fourier transform of simultaneous $dI/dV(\mathbf{r}, V=-6$ mV) map showing the presence of $4a_0$ -CO peak and the absence of QPI (\mathbf{q}_2 and \mathbf{q}'_2 enclosed by dashed rectangles) seen at low temperature in Fig. 4 and Fig. S1. STM setup condition: (a-d) $V_{sample} = 50$ mV, $I_{set} = 50$ pA, $V_{exc} = 1$ mV; (e,f) $V_{sample} = -8$ mV, $I_{set} = 80$ pA, $V_{exc} = 1$ mV.

Extended Data Fig. 10 Magnetization and magnetotransport measurements of CsV_3Sb_5 single crystals.

(a) Temperature (T) dependence of magnetization $M=4\pi\chi$ (χ is magnetic susceptibility). Zero-field cooled (field cooled at 5 Oe field) magnetization is denoted by a black solid (dashed) line. (b) Angle-dependent magnetotransport measurements, plotting resistivity $\langle\rho\rangle$ along the c-axis as a function of angle $\langle\theta\rangle$, which is the direction of magnetic field $H=14$ T applied in the ab-plane, as denoted in the inset. (c) Resistivity anisotropy as a function of temperature, calculated from the three data sets in (b) as $\langle\delta\rangle=\frac{2(\rho(0^\circ)+\rho(180^\circ))}{\{\rho(60^\circ)+\rho(120^\circ)+\rho(240^\circ)+\rho(300^\circ)\}}$.

Supplementary information

[Supplementary Information](#)

This file contains Supplementary Information, including Supplementary Figs. 1–6 and references.

[Peer Review File](#)

Source data

[Source Data Fig. 2](#)

[Source Data Fig. 3](#)

Rights and permissions

[Reprints and Permissions](#)

About this article

Cite this article

Zhao, H., Li, H., Ortiz, B.R. *et al.* Cascade of correlated electron states in the kagome superconductor CsV₃Sb₅. *Nature* **599**, 216–221 (2021).
<https://doi.org/10.1038/s41586-021-03946-w>

- Received: 13 March 2021
- Accepted: 24 August 2021
- Published: 29 September 2021
- Issue Date: 11 November 2021
- DOI: <https://doi.org/10.1038/s41586-021-03946-w>

Share this article

Anyone you share the following link with will be able to read this content:

[Get shareable link](#)

Sorry, a shareable link is not currently available for this article.

[Copy to clipboard](#)

Provided by the Springer Nature SharedIt content-sharing initiative

Further reading

- [Roton pair density wave in a strong-coupling kagome superconductor](#)
 - Hui Chen
 - , Haitao Yang
 - , Bin Hu
 - , Zhen Zhao
 - , Jie Yuan
 - , Yuqing Xing

- , Guojian Qian
- , Zihao Huang
- , Geng Li
- , Yuhang Ye
- , Sheng Ma
- , Shunli Ni
- , Hua Zhang
- , Qiangwei Yin
- , Chunsheng Gong
- , Zhijun Tu
- , Hechang Lei
- , Hengxin Tan
- , Sen Zhou
- , Chengmin Shen
- , Xiaoli Dong
- , Binghai Yan
- , Ziqiang Wang
- & Hong-Jun Gao

Nature (2021)

Roton pair density wave in a strong-coupling kagome superconductor

- Hui Chen
- Haitao Yang
- Hong-Jun Gao

Article 29 Sept 2021

This article was downloaded by **calibre** from <https://www.nature.com/articles/s41586-021-03946-w>

- Article
- [Published: 29 September 2021](#)

Roton pair density wave in a strong-coupling kagome superconductor

- [Hui Chen](#) ORCID: orcid.org/0000-0002-3369-8113^{1,2,3,4 na1},
- [Haitao Yang](#) ORCID: orcid.org/0000-0003-4304-9835^{1,2,3,4 na1},
- [Bin Hu](#)^{1,2 na1},
- [Zhen Zhao](#)^{1,2},
- [Jie Yuan](#)^{1,2},
- [Yuqing Xing](#) ORCID: orcid.org/0000-0002-8646-6631^{1,2},
- [Guojian Qian](#)^{1,2},
- [Zihao Huang](#)^{1,2},
- [Geng Li](#) ORCID: orcid.org/0000-0002-3347-7222^{1,2,3},
- [Yuhan Ye](#)^{1,2},
- [Sheng Ma](#)^{1,2},
- [Shunli Ni](#)^{1,2},
- [Hua Zhang](#)^{1,2},
- [Qiangwei Yin](#)⁵,
- [Chunsheng Gong](#)⁵,
- [Zhijun Tu](#)⁵,
- [Hechang Lei](#) ORCID: orcid.org/0000-0003-0850-8514⁵,
- [Hengxin Tan](#)⁶,
- [Sen Zhou](#)^{2,3,7},
- [Chengmin Shen](#)^{1,2},
- [Xiaoli Dong](#) ORCID: orcid.org/0000-0002-6268-2049^{1,2},
- [Binghai Yan](#) ORCID: orcid.org/0000-0003-2164-5839⁶,
- [Ziqiang Wang](#) ORCID: orcid.org/0000-0001-7617-2886⁸ &

- [Hong-Jun Gao](#) [ORCID: orcid.org/0000-0001-9323-1307^{1,2,3,4}](#)

[*Nature*](#) volume **599**, pages 222–228 (2021)

- 5404 Accesses
- 7 Citations
- 2 Altmetric
- [Metrics details](#)

Subjects

- [Superconducting properties and materials](#)
- [Topological matter](#)

Abstract

The transition metal kagome lattice materials host frustrated, correlated and topological quantum states of matter^{1,2,3,4,5,6,7,8,9}. Recently, a new family of vanadium-based kagome metals, AV_3Sb_5 ($\text{A} = \text{K}$, Rb or Cs), with topological band structures has been discovered^{10,11}. These layered compounds are nonmagnetic and undergo charge density wave transitions before developing superconductivity at low temperatures^{11,12,13,14,15,16,17,18,19}. Here we report the observation of unconventional superconductivity and a pair density wave (PDW) in CsV_3Sb_5 using scanning tunnelling microscope/spectroscopy and Josephson scanning tunnelling spectroscopy. We find that CsV_3Sb_5 exhibits a V-shaped pairing gap $\Delta \sim 0.5$ meV and is a strong-coupling superconductor ($2\Delta/k_{\text{B}}T_{\text{c}} \sim 5$) that coexists with $4a_0$ unidirectional and $2a_0 \times 2a_0$ charge order. Remarkably, we discover a 3Q PDW accompanied by bidirectional $4a_0/3$ spatial modulations of the superconducting gap, coherence peak and gap depth in the tunnelling conductance. We term this novel quantum state a roton PDW associated with an underlying vortex–antivortex lattice that can account for the observed conductance modulations. Probing the

electronic states in the vortex halo in an applied magnetic field, in strong field that suppresses superconductivity and in zero field above T_c , reveals that the PDW is a primary state responsible for an emergent pseudogap and intertwined electronic order. Our findings show striking analogies and distinctions to the phenomenology of high- T_c cuprate superconductors, and provide groundwork for understanding the microscopic origin of correlated electronic states and superconductivity in vanadium-based kagome metals.

Access options

Subscribe to Journal

Get full journal access for 1 year

\$199.00

only \$3.90 per issue

[Subscribe](#)

All prices are NET prices.

VAT will be added later in the checkout.

Tax calculation will be finalised during checkout.

Rent or Buy article

Get time limited or full article access on ReadCube.

from \$8.99

[Rent or Buy](#)

All prices are NET prices.

Additional access options:

- [Log in](#)

- [Access through your institution](#)
- [Learn about institutional subscriptions](#)

Fig. 1: Atomic structures and the surface identification of the CsV_3Sb_5 .



Fig. 2: V-shaped pairing gap and the Josephson effect observed using a SC STM tip on the Cs and Sb surfaces.

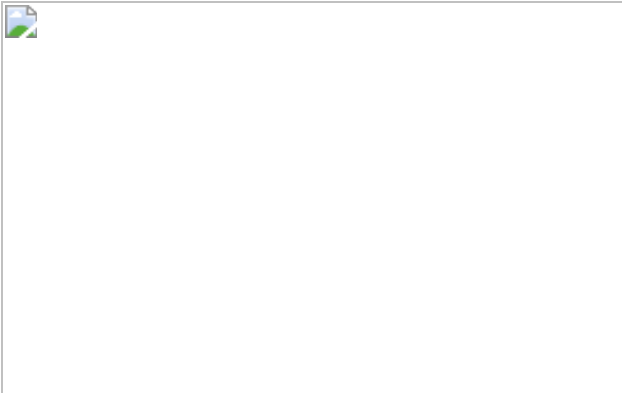


Fig. 3: STM topography, dI/dV map and linecut at 300 mK revealing CDW, PDW and spatial modulations of superconductivity on Sb surfaces.

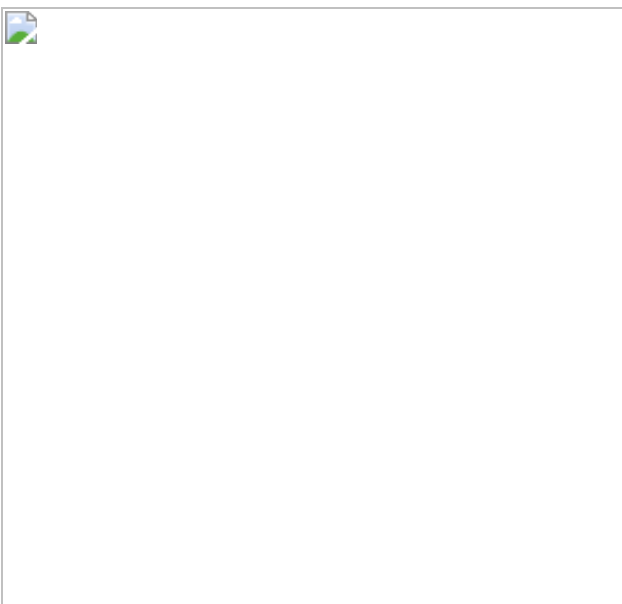


Fig. 4: PDW and pseudogap in CsV_3Sb_5 in magnetic fields at 300 mK and in zero field at 4.2 K.



Data availability

Data measured or analysed during this study are available from the corresponding author on reasonable request.

References

1. 1.
Ye, L. D. et al. Massive Dirac fermions in a ferromagnetic kagome metal. *Nature* **555**, 638–642 (2018).
2. 2.
Yin, J. X. et al. Giant and anisotropic many-body spin–orbit tunability in a strongly correlated kagome magnet. *Nature* **562**, 91–95 (2018).
3. 3.
Liu, Z. et al. Orbital-selective Dirac fermions and extremely flat bands in frustrated kagome-lattice metal CoSn. *Nat. Commun.* **11**, 4002

(2020).

4. 4.

Morali, N. et al. Fermi-arc diversity on surface terminations of the magnetic Weyl semimetal $\text{Co}_3\text{Sn}_2\text{S}_2$. *Science* **365**, 1286–1291 (2019).

5. 5.

Liu, D. F. et al. Magnetic Weyl semimetal phase in a Kagomé crystal. *Science* **365**, 1282–1285 (2019).

6. 6.

Kuroda, K. et al. Evidence for magnetic Weyl fermions in a correlated metal. *Nat. Mater.* **16**, 1090 (2017).

7. 7.

Yin, J. X. et al. Quantum-limit Chern topological magnetism in TbMn_6Sn_6 . *Nature* **583**, 533–536 (2020).

8. 8.

Yin, J.-X. et al. Negative flat band magnetism in a spin–orbit-coupled correlated kagome magnet. *Nat. Phys.* **15**, 443–448 (2019).

9. 9.

Xing, Y. et al. Localized spin-orbit polaron in magnetic Weyl semimetal $\text{Co}_3\text{Sn}_2\text{S}_2$. *Nat. Commun.* **11**, 5613 (2020).

10. 10.

Ortiz, B. R. et al. New kagome prototype materials: discovery of KV_3Sb_5 , RbV_3Sb_5 , and CsV_3Sb_5 . *Phys. Rev. Mater.* **3**, 094407 (2019).

11. 11.

Ortiz, B. R. et al. CsV_3Sb_5 : a Z_2 topological kagome metal with a superconducting ground state. *Phys. Rev. Lett.* **125**, 247002 (2020).

12. 12.

Yin, Q. et al. Superconductivity and normal-state properties of kagome metal RbV_3Sb_5 Single Crystals. *Chin. Phys. Lett.* **38**, 037403 (2021).

13. 13.

Jiang, Y. X. et al. Unconventional chiral charge order in kagome superconductor KV_3Sb_5 . *Nat. Mater.* **20**, 1353–1357 (2021).

14. 14.

Zhao, H. et al. Cascade of correlated electron states in a kagome superconductor CsV_3Sb_5 . *Nature* <https://doi.org/10.1038/s41586-021-03946-w> (2021).

15. 15.

Liang, Z. et al. Three-dimensional charge density wave and surface-dependent vortex-core states in a kagome superconductor CsV_3Sb_5 . *Phys. Rev. X* **11**, 031026 (2021).

16. 16.

Yang, S.-Y. et al. Giant, unconventional anomalous Hall effect in the metallic frustrated magnet candidate, KV_3Sb_5 . *Sci. Adv.* **6**, eabb6003 (2020).

17. 17.

Yu, F. H. et al. Concurrence of anomalous Hall effect and charge density wave in a superconducting topological kagome metal. *Phys. Rev. B* **104**, L041103 (2021).

18. 18.

Wang, Y. et al. Proximity-induced spin-triplet superconductivity and edge supercurrent in the topological Kagome metal, $K_{1-x}V_3Sb_5$. Preprint at <https://arxiv.org/abs/2012.05898> (2020).

19. 19.

Zhao, C. C. et al. Nodal superconductivity and superconducting dome in the topological Kagome metal CsV_3Sb_5 . Preprint at <https://arxiv.org/abs/2102.08356> (2021).

20. 20.

Chen, H. et al. Evidence for ultralow-energy vibrations in large organic molecules. *Nano Lett.* **17**, 4929–4933 (2017).

21. 21.

Hirjibehedin, C. F. et al. Large magnetic anisotropy of a single atomic spin embedded in a surface molecular network. *Science* **317**, 1199–1203 (2007).

22. 22.

Fischer, Ø., Kugler, M., Maggio-Aprile, I., Berthod, C. & Renner, C. Scanning tunneling spectroscopy of high-temperature superconductors. *Rev. Mod. Phys.* **79**, 353–419 (2007).

23. 23.

Jiao, L. et al. Chiral superconductivity in heavy-fermion metal UTe_2 . *Nature* **579**, 523–527 (2020).

24. 24.

Lawler, M. J. et al. Intra-unit-cell electronic nematicity of the high- T_c copper-oxide pseudogap states. *Nature* **466**, 347–351 (2010).

25. 25.

Fujita, K., Hamidian, M. H., Sprau, P. O., Edkins, S. D. & Davis, J. C. S. in *Springer Handbook of Microscopy* (eds Hawkes, P. W. & Spence, J. C. H.) 1369–1390 (Springer, 2019).

26. 26.

Kivelson, S. A., Fradkin, E. & Emery, V. J. Electronic liquid-crystal phases of a doped Mott insulator. *Nature* **393**, 550–553 (1998).

27. 27.

Emery, V. J., Fradkin, E., Kivelson, S. A. & Lubensky, T. C. Quantum theory of the smectic metal state in stripe phases. *Phys. Rev. Lett.* **85**, 2160 (2000).

28. 28.

Hamidian, M. H. et al. Detection of a Cooper-pair density wave in $\text{Bi}_2\text{Sr}_2\text{CaCu}_2\text{O}_{8+x}$. *Nature* **532**, 343–347 (2016).

29. 29.

Ruan, W. et al. Visualization of the periodic modulation of Cooper pairing in a cuprate superconductor. *Nat. Phys.* **14**, 1178–1182 (2018).

30. 30.

Agterberg, D. & Tsunetsugu, H. Dislocations and vortices in pair-density-wave superconductors. *Nat. Phys.* **4**, 639–642 (2008).

31. 31.

Berg, E., Fradkin, E. & Kivelson, S. A. Charge- $4e$ superconductivity from pair-density-wave order in certain high-temperature superconductors. *Nat. Phys.* **5**, 830–833 (2009).

32. 32.

Lee, P. A. Amperean pairing and the pseudogap phase of cuprate superconductors. *Phys. Rev. X* **4**, 031017 (2014).

33. 33.

Agterberg, D. F. et al. The physics of pair-density waves: cuprate superconductors and beyond. *Annu. Rev. Condens. Matter Phys.* **11**, 231–270 (2020).

34. 34.

Liu, X., Chong, Y. X., Sharma, R. & Davis, J. C. S. Discovery of a Cooper-pair density wave state in a transition-metal dichalcogenide. *Science* **372**, 1447–1452 (2021).

35. 35.

Landau, L. On the theory of superfluidity. *Phys. Rev.* **75**, 884–885 (1949).

36. 36.

Feynman, R. P. in *Progress in Low Temperature Physics* Vol. 1 (ed. Gorter, C. J.) 17–53 (Elsevier, 1955).

37. 37.

Feynman, R. P. & Cohen, M. Energy spectrum of the excitations in liquid helium. *Phys. Rev.* **102**, 1189–1204 (1956).

38. 38.

Nozières, P. Is the roton in superfluid ^4He the ghost of a Bragg spot? *J. Low Temp. Phys.* **137**, 45–67 (2004).

39. 39.

Edkins, S. D. et al. Magnetic field-induced pair density wave state in the cuprate vortex halo. *Science* **364**, 976–980 (2019).

40. 40.

Dai, Z., Zhang, Y.-H., Senthil, T. & Lee, P. A. Pair-density waves, charge-density waves, and vortices in high- T_c cuprates. *Phys. Rev. B* **97**, 174511 (2018).

41. 41.

Yu, S. L. & Li, J. X. Chiral superconducting phase and chiral spin-density-wave phase in a Hubbard model on the kagome lattice. *Phys. Rev. B* **85**, 144402 (2012).

42. 42.

Kiesel, M. L., Platt, C. & Thomale, R. Unconventional Fermi surface instabilities in the kagome Hubbard model. *Phys. Rev. Lett.* **110**, 126405 (2013).

43. 43.

Wang, W. S., Li, Z. Z., Xiang, Y. Y. & Wang, Q. H. Competing electronic orders on kagome lattices at van Hove filling. *Phys. Rev. B* **87**, 115135 (2013).

44. 44.

Cho, D., Bastiaans, K. M., Chatzopoulos, D., Gu, G. D. & Allan, M. P. A strongly inhomogeneous superfluid in an iron-based superconductor. *Nature* **571**, 541–545 (2019).

45. 45.

Pan, S. H., Hudson, E. W. & Davis, J. C. Vacuum tunneling of superconducting quasiparticles from atomically sharp scanning tunneling microscope tips. *Appl. Phys. Lett.* **73**, 2992–2994 (1998).

46. 46.

Rodrigo, J. G., Suderow, H., Vieira, S., Bascones, E. & Guinea, F. Superconducting nanostructures fabricated with the scanning tunnelling microscope. *J. Phys. Condens. Matter* **16**, R1151–R1182 (2004).

47. 47.

Naaman, O., Teizer, W. & Dynes, R. C. Fluctuation dominated Josephson tunneling with a scanning tunneling microscope. *Phys. Rev. Lett.* **87**, 097004 (2001).

48. 48.

Kimura, H., Barber, R. P., Ono, S., Ando, Y. & Dynes, R. C. Josephson scanning tunneling microscopy: a local and direct probe of the superconducting order parameter. *Phys. Rev. B* **80**, 144506 (2009).

49. 49.

Šmakov, J., Martin, I. & Balatsky, A. V. Josephson scanning tunneling microscopy. *Phys. Rev. B* **64**, 212506 (2001).

50. 50.

Proslík, T. et al. Probing the superconducting condensate on a nanometer scale. *Europhys. Lett.* **73**, 962–968 (2006).

51. 51.

Kresse, G. & Furthmüller, J. Efficiency of ab-initio total energy calculations for metals and semiconductors using a plane-wave basis set. *Comput. Mater. Sci.* **6**, 15–50 (1996).

52. 52.

Kresse, G. & Furthmüller, J. Efficient iterative schemes for ab initio total-energy calculations using a plane-wave basis set. *Phys. Rev. B* **54**, 11169–11186 (1996).

53. 53.

Perdew, J. P., Burke, K. & Ernzerhof, M. Generalized gradient approximation made simple. *Phys. Rev. Lett.* **77**, 3865–3868 (1996).

54. 54.

Grimme, S., Antony, J., Ehrlich, S. & Krieg, H. A consistent and accurate ab initio parametrization of density functional dispersion correction (DFT-D) for the 94 elements H-Pu. *J. Chem. Phys.* **132**, 154104 (2010).

55. 55.

Togo, A. & Tanaka, I. First principles phonon calculations in materials science. *Scr. Mater.* **108**, 1–5 (2015).

56. 56.

Agterberg, D. F., Melchert, D. S. & Kashyap, M. K. Emergent loop current order from pair density wave superconductivity. *Phys. Rev. B* **91**, 054502 (2015).

57. 57.

Tan, H., Liu, Y., Wang, Z. & Yan, B. Charge density waves and electronic properties of superconducting kagome metals. *Phys. Rev. Lett.* **127**, 046401 (2021).

58. 58.

Ortiz, B. R. et al. Fermi surface mapping and the nature of charge density wave order in the kagome superconductor CsV_3Sb_5 . Preprint at <https://arxiv.org/abs/2104.07230> (2021).

59. 59.

Li, H. X. et al. Observation of unconventional charge density wave without acoustic phonon anomaly in kagome superconductors AV_3Sb_5 (A=Rb,Cs). *Phys. Rev. X* **11**, 031050 (2021)

Acknowledgements

We thank I. Zeljkovic, S. Wilson, J. Yin and Z.-X. Zhao for helpful discussions. The work is supported by grants from the National Natural Science Foundation of China (61888102, 52022105, 11974422, 51771224 and 11974394), the National Key Research and Development Projects of China (2016YFA0202300, 2017YFA0206303, 2018YFA0305800 and 2019YFA0308500) and the Chinese Academy of Sciences (XDB28000000, XDB30000000, XDB33030100 and 112111KYSB20160061). Z.W. is supported by the US DOE, Basic Energy Sciences grant no. DE-FG02-99ER45747.

Author information

Author notes

1. These authors contributed equally: Hui Chen, Haitao Yang, Bin Hu

Affiliations

1. Beijing National Center for Condensed Matter Physics and Institute of Physics, Chinese Academy of Sciences, Beijing, People's Republic of China

Hui Chen, Haitao Yang, Bin Hu, Zhen Zhao, Jie Yuan, Yuqing Xing, Guojian Qian, Zihao Huang, Geng Li, Yuhan Ye, Sheng Ma, Shunli Ni, Hua Zhang, Chengmin Shen, Xiaoli Dong & Hong-Jun Gao

2. School of Physical Sciences, University of Chinese Academy of Sciences, Beijing, People's Republic of China

Hui Chen, Haitao Yang, Bin Hu, Zhen Zhao, Jie Yuan, Yuqing Xing, Guojian Qian, Zihao Huang, Geng Li, Yuhan Ye, Sheng Ma, Shunli Ni, Hua Zhang, Sen Zhou, Chengmin Shen, Xiaoli Dong & Hong-Jun Gao

3. CAS Center for Excellence in Topological Quantum Computation, University of Chinese Academy of Sciences, Beijing, People's Republic of China

Hui Chen, Haitao Yang, Geng Li, Sen Zhou & Hong-Jun Gao

4. Songshan Lake Materials Laboratory, Dongguan, People's Republic of China

Hui Chen, Haitao Yang & Hong-Jun Gao

5. Beijing Key Laboratory of Optoelectronic Functional Materials & Micro-Nano Devices, Department of Physics, Renmin University of China, Beijing, People's Republic of China

Qiangwei Yin, Chunsheng Gong, Zhijun Tu & Hechang Lei

6. Department of Condensed Matter Physics, Weizmann Institute of Science, Rehovot, Israel

Hengxin Tan & Binghai Yan

7. CAS Key Laboratory of Theoretical Physics, Institute of Theoretical Physics, Chinese Academy of Sciences, Beijing, People's Republic of China

Sen Zhou

8. Department of Physics, Boston College, Chestnut Hill, MA, USA

Ziqiang Wang

Contributions

H.-J.G. designed the experiments. H.C., B.H., Y.X., G.Q., Z.H., Y.Y., C.S. and G.L. performed STM experiments with guidance from H.-J.G. and H.Y. Z.Z. and H.L. prepared samples. Q.Y., C.G. and Z.T. also participated in sample preparation. X.D., J.Y., H.Y., S.M., H.Z. and S.N. performed the transport experiments. Z.W., S.Z., H.T. and B.Y. carried out theoretical work. All of the authors participated in analysing experimental data, plotting figures and writing the manuscript. H.-J.G. and Z.W. supervised the project.

Corresponding authors

Correspondence to [Ziqiang Wang](#) or [Hong-Jun Gao](#).

Ethics declarations

Competing interests

The authors declare no competing interests.

Additional information

Peer review information *Nature* thanks the anonymous reviewers for their contribution to the peer review of this work.

Publisher's note Springer Nature remains neutral with regard to jurisdictional claims in published maps and institutional affiliations.

Extended data figures and tables

[Extended Data Fig. 1 Detailed STM characterization of the Sb and Cs surfaces.](#)

a, Top panel: a typical STM image showing a step edge of Cs surface. Bottom panel: line profile along the white dotted arrow in **a**, indicating that the height of the step edge is ~0.95 nm, which is consistent with the

calculated interlayer distance ($V_s = -1$ V, $I_t = 0.1$ nA). **b**, Atomically-resolved STM image of Cs surface, showing a hexagonal lattice with a period of 1.0 nm, which is $\sqrt{3}$ times larger than the lattice constant ($a=b=0.55$ nm, see Fig. S1a). ($V_s = -500$ mV, $I_t = 0.5$ nA). **c**, Atomically-resolved STM image of Sb surface, showing a honeycomb lattice. The periodicity of the honeycomb lattice is about 0.56 nm, which agrees with the bulk lattice constant ($a=b=0.55$ nm, see Fig. S1a). ($V_s = -500$ mV, $I_t = 0.5$ nA). **d**, Atomically-resolved STM image of an interface between the top Cs and bottom Sb surfaces (same as in Fig. 1d). The atomic model is overlaid on the image, showing that each Cs atom sits on top of the Sb honeycomb center ($V_s = -500$ mV, $I_t = 0.5$ nA). **e**, FFT of d showing the Cs $\sqrt{3} \times \sqrt{3}R30^\circ$ reconstruction relative to the Sb 1×1 lattice. **f, g** Top panels: schematics showing STM manipulations to expose the bottom Sb surface. Bottom panels: STM images of Cs surface before (f) and after (g) STM manipulation, respectively, showing the freshly-obtained bottom Sb surface highlighted by the white dotted square ($V_s = -500$ mV, $I_t = 0.5$ nA).

Extended Data Fig. 2 STM topography and dI/dV maps over a 40 nm × 40 nm region at 300 mK.

a, Topography, dI/dV maps and the intensity of the drift-corrected Fourier transforms at the sample bias from -2 mV to 0 mV, respectively. Each map consists of 500 pixels × 500 pixels. **b**, Energy dependence of the Fourier line cuts along the three directions of the hexagonal zone. ($V_s = -5$ mV, $I_t = 2$ nA, $V_{mod} = 0.5$ mV).

Extended Data Fig. 3 Absence of $4a_0/3$ in high energy dI/dV maps at 300 mK.

a, Large-scale STM image (60 nm × 60 nm) of the Sb surface obtained at the temperature below T_c (300 mK), where a unidirectional charge order is visible ($V_s = -20$ mV, $I_t = 2$ nA). **b**, The magnitude of drift-corrected Fourier transform of a, showing clearly the \mathbf{Q}_{3q-2a} CDW and \mathbf{Q}_{1q-4a} stripe CDW peaks. **c, d** dI/dV mapping (1024 pixels × 1024 pixels) over the same

region at -20 mV and the corresponding magnitude of drift-corrected Fourier transform ($V_s = -20$ mV, $I_t = 2$ nA, $V_{mod} = 0.2$ mV). **d, f** dI/dV mapping (1024 pixels \times 1024 pixels) over the same region at -30 mV and the corresponding magnitude of drift-corrected Fourier transform ($V_s = -30$ mV, $I_t = 2$ nA, $V_{mod} = 0.2$ mV).

Extended Data Fig. 4 Schematic illustration of the roton-PDW.

Top panel: the roton dispersion and roton minimum at $\mathbf{Q}_{\text{roton}} = \mathbf{Q}_{3q-4a/3}$ in the reciprocal lattice. Bottom panel: the 3Q roton-PDW at $\mathbf{Q}_{\text{pdw}} = \mathbf{Q}_{\text{roton}}$ forming a commensurate vortex-antivortex lattice (red, blue and yellow circles) that spatially modulates the tunneling conductance spectra along a line cut.

Extended Data Fig. 5 Spatial map of pseudogap and $\mathbf{Q}_{3q-4a/3}$ modulations.

a, Spatially-averaged dI/dV spectrum obtained below T_c , exhibiting several peaks in the energy range between 1 mV and 6 mV ($V_s = -10$ mV, $I_t = 1$ nA, $V_{mod} = 0.05$ mV). The PDW pseudogap peak located near 5 mV is labelled as *P*. **b**, Waterfall and color plot of a dI/dV line cut, showing spatial modulations of the peak *P* ($V_s = -3.7$ mV, $I_t = 1$ nA, $V_{mod} = 0.05$ mV). **c**, Spatial gap map of $\Delta^*(\mathbf{r})$, showing the spatial modulations of the pseudogap ($V_s = -3.7$ mV, $I_t = 1$ nA, $V_{mod} = 0.05$ mV). **d**, Fourier transform of the pseudogap map showing peaks at the PDW vectors $\mathbf{Q}_{3q-4a/3}$ circled in magenta.

Extended Data Fig. 6 Charge ordered normal state in CsV_3Sb_5 above T_c .

a,b Large-scale STM topography of Sb surface obtained at 4.2 K and the magnitude of drift-corrected Fourier transform, showing $2a_0 \times 2a_0$ and $4a_0$ striped CDW peaks at wave vectors \mathbf{Q}_{3q-2a} and \mathbf{Q}_{1q-4a} ($V_s = -90$ mV, $I_t = 2$

nA). **c,d** dI/dV mapping of **a** at 20 mV and the magnitude of drift-corrected Fourier transform, respectively ($V_s = -90$ mV, $I_t = 2$ nA, $V_{mod} = 0.5$ mV). **e**. Energy dependence of the Fourier line cuts along \mathbf{q}_a directions, showing that peaks at \mathbf{Q}_{3q-2a} and \mathbf{Q}_{1q-4a} at 4 K are non-dispersive ($V_s = -90$ mV, $I_t = 2$ nA, $V_{mod} = 0.5$ mV).

Extended Data Fig. 7 Normal state angular-dependent magnetoresistance.

a, Schematic of the in-plane resistance measurement under a 5 T magnetic field by rotating the sample along c axis of the single crystal. **b**, Angular plot of the normalized anisotropic magnetoresistance $(\Delta R/R_{min})$, showing two-fold symmetry at the temperature below ~ 50 K. (θ) is defined in **a**. **c**, Temperature dependence of the angular-dependent of at $(\Delta R/R_{min})$ the angle of 28° , showing the onset of two-fold rotational symmetry below $T^* \sim 50 \pm 10$ K.

Supplementary information

Supplementary Information

Supplementary Figs. 1–16.

Rights and permissions

Reprints and Permissions

About this article

Cite this article

Chen, H., Yang, H., Hu, B. *et al.* Roton pair density wave in a strong-coupling kagome superconductor. *Nature* **599**, 222–228 (2021).

<https://doi.org/10.1038/s41586-021-03983-5>

- Received: 23 March 2021
- Accepted: 01 September 2021
- Published: 29 September 2021
- Issue Date: 11 November 2021
- DOI: <https://doi.org/10.1038/s41586-021-03983-5>

Share this article

Anyone you share the following link with will be able to read this content:

[Get shareable link](#)

Sorry, a shareable link is not currently available for this article.

[Copy to clipboard](#)

Provided by the Springer Nature SharedIt content-sharing initiative

Further reading

- [Cascade of correlated electron states in the kagome superconductor CsV₃Sb₅](#)
 - He Zhao
 - , Hong Li
 - , Brenden R. Ortiz
 - , Samuel M. L. Teicher
 - , Takamori Park
 - , Mengxing Ye
 - , Ziqiang Wang
 - , Leon Balents

- , Stephen D. Wilson
- & Ilija Zeljkovic

Nature (2021)

Cascade of correlated electron states in the kagome superconductor CsV₃Sb₅

- He Zhao
- Hong Li
- Ilija Zeljkovic

Article 29 Sept 2021

This article was downloaded by **calibre** from <https://www.nature.com/articles/s41586-021-03983-5>

| [Section menu](#) | [Main menu](#) |

- Article
- [Published: 10 November 2021](#)

Bubble casting soft robotics

- [Trevor J. Jones ORCID: orcid.org/0000-0003-3233-0752¹](#),
- [Etienne Jambon-Puillet¹](#),
- [Joel Marthelot^{1,2}](#) &
- [P.-T. Brun ORCID: orcid.org/0000-0002-4175-0604¹](#)

[Nature](#) volume **599**, pages 229–233 (2021)

- 819 Accesses
- 152 Altmetric
- [Metrics details](#)

Subjects

- [Fluids](#)
- [Mechanical engineering](#)
- [Polymers](#)

Abstract

Inspired by living organisms, soft robots are developed from intrinsically compliant materials, enabling continuous motions that mimic animal and vegetal movement¹. In soft robots, the canonical hinges and bolts are replaced by elastomers assembled into actuators programmed to change shape following the application of stimuli, for example pneumatic inflation^{2,3,4,5}. The morphing information is typically directly embedded within the shape of these actuators, whose assembly is facilitated by recent

advances in rapid prototyping techniques^{6,7,8,9,10,11}. Yet, these manufacturing processes have limitations in scalability, design flexibility and robustness. Here we demonstrate a new all-in-one methodology for the fabrication and the programming of soft machines. Instead of relying on the assembly of individual parts, our approach harnesses interfacial flows in elastomers that progressively cure to robustly produce monolithic pneumatic actuators whose shape can easily be tailored to suit applications ranging from artificial muscles to grippers. We rationalize the fluid mechanics at play in the assembly of our actuators and model their subsequent morphing. We leverage this quantitative knowledge to program these soft machines and produce complex functionalities, for example sequential motion obtained from a monotonic stimulus. We expect that the flexibility, robustness and predictive nature of our methodology will accelerate the proliferation of soft robotics by enabling the assembly of complex actuators, for example long, tortuous or vascular structures, thereby paving the way towards new functionalities stemming from geometric and material nonlinearities.

Access options

Subscribe to Journal

Get full journal access for 1 year

\$199.00

only \$3.90 per issue

[Subscribe](#)

All prices are NET prices.

VAT will be added later in the checkout.

Tax calculation will be finalised during checkout.

Rent or Buy article

Get time limited or full article access on ReadCube.

from \$8.99

Rent or Buy

All prices are NET prices.

Additional access options:

- [Log in](#)
- [Access through your institution](#)
- [Learn about institutional subscriptions](#)

Fig. 1: From flow to programmed actuation.

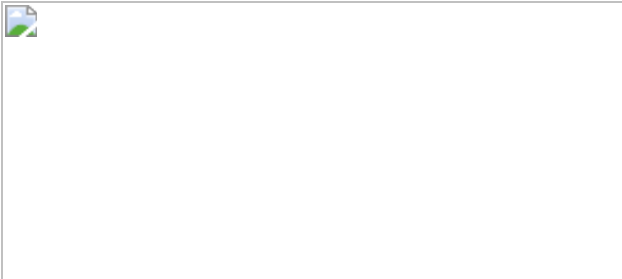


Fig. 2: Flow determines form.



Fig. 3: Pneumatic actuation produces curvature.

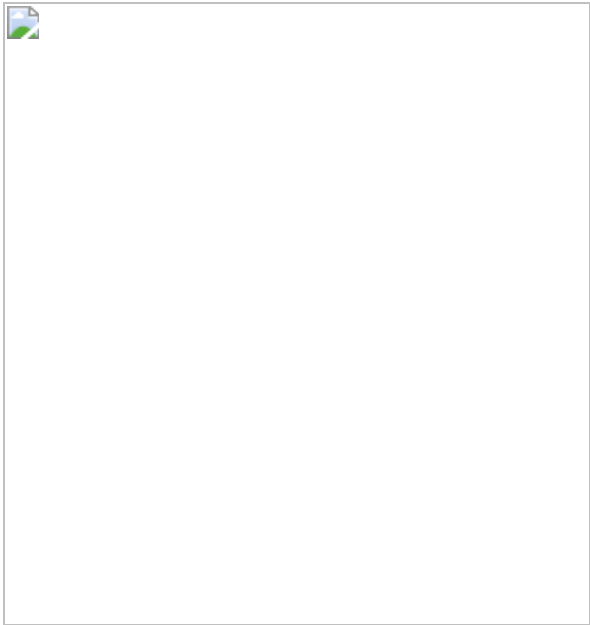
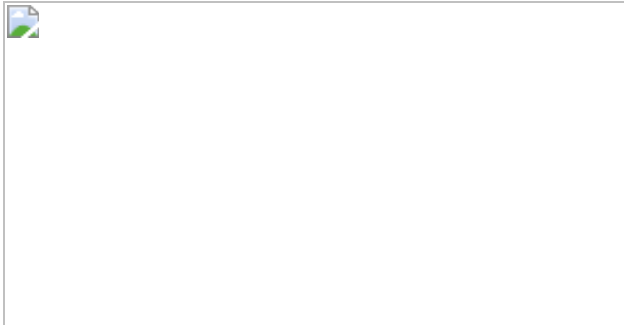


Fig. 4: Programmed mechanics from curvature.



Data availability

The data used in this study are available from the corresponding authors upon reasonable request. [Source data](#) are provided with this paper.

Code availability

The codes that support the findings of this study are available from the corresponding authors upon reasonable request.

References

1. 1.

Whitesides, G. M. Soft robotics. *Angew. Chem. Int. Ed.* **57**, 4258–4273 (2018).

2. 2.

Polygerinos, P., Wang, Z., Galloway, K. C., Wood, R. J. & Walsh, C. J. Soft robotic glove for combined assistance and at-home rehabilitation. *Rob. Autom. Syst.* **73**, 135–143 (2015).

3. 3.

Shepherd, R. F. et al. Multigait soft robot. *Proc. Natl Acad. Sci. USA* **108**, 20400–20403 (2011).

4. 4.

Martinez, R. V. et al. Robotic tentacles with three-dimensional mobility based on flexible elastomers. *Adv. Mater.* **25**, 205–212 (2013).

5. 5.

Roche, E. T. et al. A bioinspired soft actuated material. *Adv. Mater.* **26**, 1200–1206 (2014).

6. 6.

Mosadegh, B. et al. Pneumatic networks for soft robotics that actuate rapidly. *Adv. Funct. Mater.* **24**, 2163–2170 (2014).

7. 7.

Yap, H. K., Ng, H. Y. & Yeow, C.-H. High-force soft printable pneumatics for soft robotic applications. *Soft Robot.* **3**, 144–158 (2016).

8. 8.

Wehner, M. et al. An integrated design and fabrication strategy for entirely soft, autonomous robots. *Nature* **536**, 451–455 (2016).

9. 9.

Zhao, H., Li, Y., Elsamadisi, A. & Shepherd, R. Scalable manufacturing of high force wearable soft actuators. *Extreme Mech. Lett.* **3**, 89–104 (2015).

10. 10.

Paek, J., Cho, I. & Kim, J. Microrobotic tentacles with spiral bending capability based on shape-engineered elastomeric microtubes. *Sci. Rep.* **5**, 10768 (2015).

11. 11.

Jin, L., Forte, A. E., Deng, B., Rafsanjani, A. & Bertoldi, K. Kirigami-inspired inflatables with programmable shapes. *Adv. Mater.* **32**, 2001863 (2020).

12. 12.

Ilievski, F., Mazzeo, A. D., Shepherd, R. F., Chen, X. & Whitesides, G. M. Soft robotics for chemists. *Angew. Chem. Int. Ed.* **50**, 1890–1895 (2011).

13. 13.

Marchese, A. D., Onal, C. D. & Rus, D. Autonomous soft robotic fish capable of escape maneuvers using fluidic elastomer actuators. *Soft Robot.* **1**, 75–87 (2014).

14. 14.

Yang, D. et al. Buckling pneumatic linear actuators inspired by muscle. *Adv. Mater. Technol.* **1**, 1600055 (2016).

15. 15.

Overvelde, J. T. B., Kloek, T., D'haen, J. J. A. & Bertoldi, K. Amplifying the response of soft actuators by harnessing snap-through

instabilities. *Proc. Natl Acad. Sci. USA* **112**, 10863–10868 (2015).

16. 16.

Hawkes, E. W., Blumenschein, L. H., Greer, J. D. & Okamura, A. M. A soft robot that navigates its environment through growth. *Sci. Robot.* **2**, aan3028 (2017).

17. 17.

Majidi, C. Soft robotics: a perspective—current trends and prospects for the future. *Soft Robot.* **1**, 5–11 (2014).

18. 18.

Gladman, A. S., Matsumoto, E. A., Nuzzo, R. G., Mahadevan, L. & Lewis, J. A. Biomimetic 4D printing. *Nat. Mater.* **15**, 413–418 (2016).

19. 19.

Kanik, M. et al. Strain-programmable fiber-based artificial muscle. *Science* **365**, 145–150 (2019).

20. 20.

William Boley, J. W. et al. Shape-shifting structured lattices via multimaterial 4D printing. *Proc. Natl Acad. Sci. USA* **116**, 20856–20862 (2019).

21. 21.

Guseinov, R., McMahan, C., Pérez, J., Daraio, C. & Bickel, B. Programming temporal morphing of self-actuated shells. *Nat. Commun.* **11**, 237 (2020).

22. 22.

Kim, Y., Yuk, H., Zhao, R., Chester, S. A. & Zhao, X. Printing ferromagnetic domains for untethered fast-transforming soft materials.

Nature **558**, 274–279 (2018).

23. 23.

Hu, W., Lum, G. Z., Mastrangeli, M. & Sitti, M. Small-scale soft-bodied robot with multimodal locomotion. *Nature* **554**, 81–85 (2018).

24. 24.

Acome, E. et al. Hydraulically amplified self-healing electrostatic actuators with muscle-like performance. *Science* **359**, 61–65 (2018).

25. 25.

Gorissen, B. et al. Elastic inflatable actuators for soft robotic applications. *Adv. Mater.* **29**, 1604977 (2017).

26. 26.

Polygerinos, P. et al. Soft robotics: review of fluid-driven intrinsically soft devices; manufacturing, sensing, control, and applications in human-robot interaction. *Adv. Eng. Mater.* **19**, 1700016 (2017).

27. 27.

Siefert, E., Reyssat, E., Bico, J. & Roman, B. Bio-inspired pneumatic shape-morphing elastomers. *Nat. Mater.* **18**, 24–28 (2019).

28. 28.

Vasios, N., Gross, A. J., Soifer, S., Overvelde, J. T. B. & Bertoldi, K. Harnessing viscous flow to simplify the actuation of fluidic soft robots. *Soft Robot.* **7**, 1–9 (2020).

29. 29.

Jambon-Puillet, E., Piéchaud, M. R. & Brun, P.-T. Elastic amplification of the Rayleigh–Taylor instability in solidifying melts. *Proc. Natl Acad. Sci. USA* **118**, e2020701118 (2021).

30. 30.

Bretherton, F. P. The motion of long bubbles in tubes. *J. Fluid Mech.* **10**, 166–188 (1961).

31. 31.

Aussillous, P. & Quéré, D. Quick deposition of a fluid on the wall of a tube. *Phys. Fluids* **12**, 2367–2371 (2000).

32. 32.

Klaseboer, E., Gupta, R. & Manica, R. An extended Bretherton model for long Taylor bubbles at moderate capillary numbers. *Phys. Fluids* **26**, 032107 (2014).

33. 33.

Takagi, D. & Huppert, H. E. Flow and instability of thin films on a cylinder and sphere. *J. Fluid Mech.* **647**, 221–238 (2010).

34. 34.

Lee, A. et al. Fabrication of slender elastic shells by the coating of curved surfaces. *Nat. Commun.* **7**, 11155 (2016).

35. 35.

Audoly, B. & Pomeau, Y. *Elasticity and Geometry: From Hair Curls to the Non-Linear Response of Shells* (Oxford Univ. Press, 2010).

36. 36.

Gerbode, S. J., Puzey, J. R., McCormick, A. G. & Mahadevan, L. How the cucumber tendril coils and overwinds. *Science* **337**, 1087–1091 (2012).

37. 37.

Miller, J. T., Lazarus, A., Audoly, B. & Reis, P. M. Shapes of a suspended curly hair. *Phys. Rev. Lett.* **112**, 068103 (2014).

38. 38.

Yang, H. D., Greczek, B. T. & Asbeck, A. T. Modeling and analysis of a high-displacement pneumatic artificial muscle with integrated sensing. *Front. Robot. AI* **5**, 136 (2019).

39. 39.

Kaufman, J. J. et al. Structured spheres generated by an in-fibre fluid instability. *Nature* **487**, 463–467 (2012).

40. 40.

Marthelot, J., Strong, E. F., Reis, P. M. & Brun, P.-T. Designing soft materials with interfacial instabilities in liquid films. *Nat. Commun.* **9**, 4477 (2018).

41. 41.

Zhao, C. et al. Layered nanocomposites by shear-flow-induced alignment of nanosheets. *Nature* **580**, 210–215 (2020).

42. 42.

Nerger, B. A., Brun, P.-T. & Nelson, C. M. Marangoni flows drive the alignment of fibrillar cell-laden hydrogels. *Sci. Adv.* **6**, eaaz7748 (2020).

43. 43.

Cybulski, O. et al. Concentric liquid reactors for chemical synthesis and separation. *Nature* **586**, 57–63 (2020).

Acknowledgements

This work was supported by NSF CAREER award (CBET 2042930) and through the Princeton University Materials Research Science and Engineering Center (NSF Grant DMR-1420541) and the Princeton Yang Family and David T. Wilkinson Innovation Funds.

Author information

Affiliations

1. Department of Chemical and Biological Engineering, Princeton University, Princeton, NJ, USA
Trevor J. Jones, Etienne Jambon-Puillet, Joel Marthelot & P.-T. Brun
2. Aix-Marseille University, CNRS, IUSTI, Marseille, France
Joel Marthelot

Contributions

T.J.J., J.M. and P.-T.B. conceived the project. T.J.J., E.J.-P. and P.-T.B. conducted the experiments and analysed the data. T.J.J. performed the Kirchhoff rod simulations. E.J.-P. performed the finite element simulations. All authors wrote the manuscript.

Corresponding author

Correspondence to [P.-T. Brun](#).

Ethics declarations

Competing interests

The authors declare no competing interests.

Additional information

Peer review information *Nature* thanks Detlef Lohse, Orlin Velev and the other, anonymous, reviewer(s) for their contribution to the peer review of this work.

Publisher's note Springer Nature remains neutral with regard to jurisdictional claims in published maps and institutional affiliations.

Extended data figures and tables

Extended Data Fig. 1 Characterization of elastomers.

a, Oscillatory shear rheology measurements for VPS-08, 16 and 32 (strain 1%, frequencies { 1, 2.5, 2.5} Hz). The cross indicates τ_c . **b**, Rescaled time varying viscosity for $t < \tau_c$. The dashed lines are fits of equation (5). **c**, Dogbone uniaxial tensile tests data for multiple samples of VPS-32, VPS-16 and VPS-08. The black curves are fits of the various constitutive models. **d**, Table showing rheological and elastic material constants for VPS

[Source data](#).

Extended Data Fig. 2 Cross-section shape.

a, Schematic for the computation of the shape of the liquid bath. **b**, Meniscus shape profiles obtained from solving equation (9) for various values of $(R/\{\mathcal{l}\}) - (\rm{c})$ and h_i/R . **c**, Model shape profiles obtained from matching of the bath solution (equation (9)) to the film thickness solution (equation (2)) for $R = 1.6$ mm. The solid lines represent the membrane and the dashed lines represent the bath. The color codes the average membrane thickness h_f . **d**, **e**, Void fraction $\phi = (1 - h_i/R)^2$ (**d**) and average membrane thickness h_f (**e**) as a function of the axial position for a metre-long actuator (sample 1). Error bars represent propagated measurement uncertainty. **f**, Void fraction for three different samples. Uncertainty is shown as box (middle 50%) and whisker (full

range) plots overlaid on the markers. **g**, Membrane thickness for three different samples. The upward (respectively downward) facing triangles represent the maximum thickness $\langle h(0) \rangle$ (minimum thickness $\langle h(\psi_0) \rangle$), while the diamonds indicates the average thickness h_f . Uncertainty is shown as box (middle 50%) and whisker (full range) plots overlaid on the markers

[Source data.](#)

Extended Data Fig. 3 Finite element simulations.

a, Deformation of the simulated actuator shown in b for $(P \approx 23)$ kPa (experimental shape, $G = 0.36$ MPa, $(J_m) = 14$). Inset: view of the deformed cross-section. The color codes the von Mises stress while the black lines show the edges of the undeformed configuration. **b**, Curvature κ as a function of the inflation pressure P . Circles represent experimental data (VPS-32, $R = 1.57$ mm, $\langle h(0) \rangle = 52 \mu m$, $h_i/R = 0.34$), the solid curve is the finite element simulation using the experimental cross-sectional shape extracted by image analysis, the dashed curve is the simulation using the modeled cross-section using the experimental value of $\langle h(0) \rangle$. Inset: comparison between the experimental and model shapes. **c**, Curvature κ as a function of the applied pressure P for our model shapes as we vary h_f and R (see legend in **d**). **d**, Same data as **c** rescaled according to equation (17), the dashed line is a power law fit

[Source data.](#)

Extended Data Fig. 4 Pneumatic bending of actuator.

a, Schematic for the pneumatic inflation of a bubble cast actuator cross-section. **b**, Schematic for the bending of a bubble cast actuator. **c**, Actuator curvature $\langle \kappa \rangle$ as a function of applied pressure P for varied length L (i), thickness h_f (ii), radius R (iii), and shear modulus G (iv; see legend in Fig. 3a, b). **d**, Three-dimensional plot of the rescaled curvature $\langle \kappa R \rangle$ as a function of the rescaled pressure $\langle P/G \rangle$ and the rescaled membrane thickness R/h_f . Markers show the experimental data while the blue surface

is our model (equation (16)) using a Gent constitutive law with $\{\psi\}_0 = \{\pi\}/4$, $\varphi = 0.4225$, $\chi = 0.45$, $J_m = 14$)

[Source data](#).

Extended Data Fig. 5 Blocking force elastica.

a, Series of images (i) and calculated elastic curve (ii) for a bubble cast actuator inflated with one end clamped and the other end blocked by a wall (see Extended Data Fig. 7c; scale bar, 1 cm). **b**, Blocking force F as a function of the inflation pressure P for various actuators (R , G , h_f and L have been varied)

[Source data](#).

Extended Data Fig. 6 Fabrication with a twist.

a, c, Two tubes are kept tightly together with a connector (not represented here) that allows the rotation of one tube with respect to the other. Applying the rotation at the very end of the drainage step, that is, around the gelation point where the polymer is still deformable, yet would not flow significantly anymore under the action of gravity results in the actuator shown in **b** and **d**. Colours are a guide to eye; only one polymer is used. Rotating the cylinder (as shown in **a** (respectively **c**)) rotates the thin membrane and thus the direction of actuation under pressure. In this example, the 90° (180°) rotation produces two curvatures equal in magnitude but in orthogonal planes (resp. with opposite signs).

Extended Data Fig. 7 Experimental set-ups.

a, Experimental set-up for Bretherton-like flow during fabrication. The camera captures the bubble front velocity U to determine the Capillary number Ca . **b**, Experimental set-up for inflation-bending experiments. The pressure sensor records the internal–external pressure difference P while the camera records the shape of the actuator. **c**, Experimental set-up for blocking force–pressure experiments. The pressure sensor records the internal–external pressure difference P while the load cell measures the

force F . **d**, Experimental set-up for force-elongation experiments. The pressure sensor records the internal–external pressure difference P while the Instron measures the force F and displacement $\{\ell\}$.

Supplementary information

Supplementary Information

Supplementary text, Supplementary equations and Supplementary references

Supplementary Video 1

Bubble casting fabrication method. A tortuous channel in an acrylic mould is filled with a curing VPS melt. An elongated bubble is then injected through the channel. The VPS film is then given time to cure as gravity causes drainage. The resulting soft actuator bends when inflated, demonstrating the ability to grasp a blackberry.

Supplementary Video 2

High aspect ratio pneumatic muscles. Comparison between an inflated actuator at pressures P and a simulation of a Kirchhoff rod with changing natural curvature κ according to equation (3) of the main text. A human-scale actuator demonstrates coiling behaviour when inflated with air. An artificial limb mimics a human arm with a contractile force. Actuators with diameters of 12.8 mm and 1.0 mm are inflated to lift a water bottle and paper clip. A high-aspect-ratio curved actuator wraps itself around a raspberry and lifts it without any damage.

Supplementary Video 3

Sequential actuation of digits. The programming logic is depicted via schematic representation. A bubble is injected through the channel digits (1,2,3,4) in a sequential manner at various waiting times $\tau_{w,i}$. The evolving viscosity increases as the polymer melt cross-links and diverges at the

curing time τ_c as the melt cures into an elastic solid. Injecting air into the resulting actuator causes a sequential bending of the actuator digits.

Supplementary Video 4

Morphing to complex shapes. An actuator with a tortuous path is inflated in water. The actuator bends out of plane to a curve that lives on the surface of a sphere. A spiral-shaped actuator is attached to a circular membrane, transforming local curvature change of the rod to a global bending of the membrane. An actuator is attached to the edge of a membrane to perform self-folding of a five-sided box. Two branched actuators are bonded to either side of a membrane in the shape of a caudal fin. The fin actuators are alternatively inflated in a water bath with tracer particles. During fabrication a tubular mould is rotated 180 degrees at the gelation point. The resulting actuator bends in two different directions. During fabrication a three sectioned tubular mould is rotated at 180 degrees and 90 degrees at the gelation point. The resulting actuator bends in three directions and in two planes.

Supplementary Video 5

A soft machine to fetch in a constrained space. A modular soft machine made of two actuators is programmed to grip and then retrieve a ball from a cylindrical vessel using a single pressure source.

Supplementary Video 6

Programming curvature variation. A rectilinear actuator, built by bubble casting, is programmed to have three sections of varying curvatures (curvature ratio 4:2:1). The coding is accomplished by injecting the bubble through the tube in a step wise sequence such that the final film thickness is predicted. The actuator is inflated on a water bath forming a spiral with appropriate curvatures.

Source data

[**Source Data Fig. 2**](#)

[**Source Data Fig. 3**](#)

[**Source Data Fig. 4**](#)

[**Source Data Extended Data Fig. 1**](#)

[**Source Data Extended Data Fig. 2**](#)

[**Source Data Extended Data Fig. 3**](#)

[**Source Data Extended Data Fig. 4**](#)

[**Source Data Extended Data Fig. 5**](#)

Rights and permissions

[**Reprints and Permissions**](#)

About this article

Cite this article

Jones, T.J., Jambon-Puillet, E., Marthelot, J. *et al.* Bubble casting soft robotics. *Nature* **599**, 229–233 (2021). <https://doi.org/10.1038/s41586-021-04029-6>

- Received: 08 March 2021
- Accepted: 16 September 2021
- Published: 10 November 2021
- Issue Date: 11 November 2021

- DOI: <https://doi.org/10.1038/s41586-021-04029-6>

Share this article

Anyone you share the following link with will be able to read this content:

[Get shareable link](#)

Sorry, a shareable link is not currently available for this article.

[Copy to clipboard](#)

Provided by the Springer Nature SharedIt content-sharing initiative

This article was downloaded by **calibre** from <https://www.nature.com/articles/s41586-021-04029-6>

| [Section menu](#) | [Main menu](#) |

- Article
- Open Access
- [Published: 10 November 2021](#)

In situ formation of ZnO_x species for efficient propane dehydrogenation

- [Dan Zhao](#) ORCID: orcid.org/0000-0002-8301-7654^{1,2},
- [Xinxin Tian](#) ORCID: orcid.org/0000-0002-3195-3176^{2,3},
- [Dmitry E. Doronkin](#)⁴,
- [Shanlei Han](#) ORCID: orcid.org/0000-0002-6110-0203^{1,2},
- [Vita A. Kondratenko](#)²,
- [Jan-Dierk Grunwaldt](#) ORCID: orcid.org/0000-0003-3606-0956⁴,
- [Anna Perechodjuk](#)²,
- [Thanh Huyen Vuong](#) ORCID: orcid.org/0000-0001-5535-7064²,
- [Jabor Rabeah](#) ORCID: orcid.org/0000-0003-2162-0981²,
- [Reinhard Eckelt](#)²,
- [Uwe Rodemerck](#)²,
- [David Linke](#) ORCID: orcid.org/0000-0002-5898-1820²,
- [Guiyuan Jiang](#) ORCID: orcid.org/0000-0003-1464-3368¹,
- [Haijun Jiao](#) ORCID: orcid.org/0000-0002-2947-5937² &
- [Evgenii V. Kondratenko](#) ORCID: orcid.org/0000-0003-0431-6937²

Nature volume 599, pages 234–238 (2021)

- 439 Accesses
- 12 Altmetric
- [Metrics details](#)

Subjects

- [Heterogeneous catalysis](#)
- [Materials for energy and catalysis](#)
- [Process chemistry](#)

Abstract

Propane dehydrogenation (PDH) to propene is an important alternative to oil-based cracking processes, to produce this industrially important platform chemical^{1,2}. The commercial PDH technologies utilizing Cr-containing (refs. ^{3,4}) or Pt-containing (refs. ^{5,6,7,8}) catalysts suffer from the toxicity of Cr(vi) compounds or the need to use ecologically harmful chlorine for catalyst regeneration⁹. Here, we introduce a method for preparation of environmentally compatible supported catalysts based on commercial ZnO. This metal oxide and a support (zeolite or common metal oxide) are used as a physical mixture or in the form of two layers with ZnO as the upstream layer. Supported ZnO_x species are in situ formed through a reaction of support OH groups with Zn atoms generated from ZnO upon reductive treatment above 550 °C. Using different complementary characterization methods, we identify the decisive role of defective OH groups for the formation of active ZnO_x species. For benchmarking purposes, the developed ZnO–silicalite-1 and an analogue of commercial K–CrO_x/Al₂O₃ were tested in the same setup under industrially relevant conditions at close propane conversion over about 400 h on propane stream. The developed catalyst reveals about three times higher propene productivity at similar propene selectivity.

[Download PDF](#)

Main

Encouraged by the requirements of environmental sustainability, both industry and academia are searching for ecologically friendly PDH catalysts. The most promising materials are based on oxides of V (refs. ^{10,11}), Ga (ref. ¹²), Zr (refs. ^{13,14}) or Co (refs. ^{15,16}). Zn-containing catalysts were also tested but show commercially unattractive performance^{17,18,19,20,21,22,23,24,25,26,27}. A general shortcoming of practically all supported catalysts developed until now is their economic inefficiency due to the complex preparation methods often requiring expensive chemicals. In addition, the structure of active supported species can undergo irreversible reaction-induced changes causing an unalterable catalyst deactivation.

Against the above background, our intention was to offer a preparation method with a potential of large-scale applications using commercially available ZnO and oxidic supports to yield catalysts with industrially relevant activity, durability and selectivity. In contrast to previous relevant studies^{17,18,19,20,21,22,23,24,25,26,27}, we simply tested a physical mixture of ZnO (8wt%) and non-acidic SiO₂ material (silicalite-1 (S-1_1), silicalite-2 (S-2), MCM-41, SBA-15 or non-structured SiO₂) to hinder undesired side reactions. ZnO and the bare supports tested separately are practically inert. The

activity of the physical mixtures depends on the kind of support and pre-treatment (Fig. [1a](#)). Propane conversion ($X(C_3H_8)$) over oxidized ZnO-S-1_1 increases from 6% to 24% within 1.5 h on propane stream, while high conversion of about 30% is achieved directly after treatment in $H_2/N_2 = 1$ at 550 °C for 1 h before PDH (Extended Data Fig. [1a](#)). Other either oxidized or reduced mixtures show low activity (Fig. [1a](#)). Thus, when testing ZnO-S-1_1, catalytically active species must be formed upon interaction between ZnO and S-1_1 under reaction conditions or upon reductive treatment. What are these sites and how are they formed?

Fig. 1: Catalyst activity, formation of ZnO_x species and their structure.

 **figure1**

a, $r(\text{C}_3\text{H}_6)$ at 550 °C over oxidatively (open symbols) or reductively (closed symbols) treated mixtures of ZnO (blue spheres) and SiO₂-based support (orange spheres). **b**, $r(\text{C}_3\text{H}_6)$ over Zn-containing materials (dark-red spheres), prepared as shown in the

inset. **c**, H₂ and H₂O evolution upon temperature-programmed heating of a mixture of Zn⁰ and S-1_1 in Ar. **d**, In situ DRIFTS spectra of S-1_1, MCM-41, or their mixtures with 10wt% ZnO at 550 °C in H₂/Ar = 1. **e**, $r(C_3H_6)$ over reduced ZnO-silicalite-1 at 550 °C versus the concentration of OH nests in differently prepared silicalite-1. **f**, Ex situ FT EXAFS spectra (not corrected for the phase shift) of different materials. **g**, In situ XANES spectra of S-1_1(H₂) treated in 5vol% H₂ in He at different temperatures. **h**, Turnover frequency (TOF) of propene formation over Zn-based catalysts. The values of single ZnO_x/SiO₂ and single ZnO_x/TiZrO_x are reported in ref. [19](#) and ref. [24](#), respectively.

Source data

To answer these questions, we prepared a series of additional catalysts. ZnO and S-1_1, S-2 or MCM-41 were loaded into a tubular reactor in form of two layers separated by a quartz wool with the upstream layer being ZnO (inset in Fig. [1b](#)). After exposing to H₂/Ar = 1 at 550 °C for 1 h and finally cooling down to room temperature in Ar, the downstream support-containing layer was collected and abbreviated as S-1_1(H₂), S-2(H₂) and MCM-41(H₂). Although zinc is present in these materials in similar amounts, S-1_1(H₂) (1.2wt% Zn) shows higher propene formation rate ($r(C_3H_6)$) than MCM-41(H₂) (0.98wt% Zn) and S-2(H₂) (2.4wt% Zn) (Fig. [1b](#) and Extended Data Fig. [1b](#)). S-1_1(O₂) or S-1_1(Ar) prepared in 5vol% O₂/Ar or Ar do not contain zinc and are inactive (Fig. [1b](#)).

As zinc is present in S-1_1(H₂), S-2(H₂) and MCM-41(H₂), there must be a gas-phase transport of Zn-containing species to the supports because ZnO and support layers were separated by a quartz wool. To check if Zn⁰ or ZnO is transported, we heated a physical mixture of Zn⁰ and S-1_1 in Ar. H₂ evolution was observed between 300 and 400 °C (Fig. [1c](#)). Thus, H₂ should originate from the oxidation of Zn⁰ by OH groups to yield supported ZnO_x. In situ DRIFTS (diffuse reflectance infrared Fourier transform spectroscopy) measurements prove that OH nests preferentially react with Zn⁰. When treating a ZnO–S-1_1 mixture in H₂/Ar = 1 at 550 °C, the intensity of band at 3,540 cm⁻¹ characteristic^{[28](#)} for such defects in S-1_1 decreases with time on H₂ stream (Fig. [1d](#)). No such changes were observed upon reduction of the sole supports or a mixture of ZnO and MCM-41 possessing exclusively isolated OH groups.

The importance of OH nests for creation of ZnO_x species is demonstrated further. In addition to S-1_1, S-1 materials (S-1_2, S-1_3, S-1_4 and S-1_5) with different concentration of OH nests were synthesized and characterized (Extended Data Table [1](#) and Extended Data Fig. [1c–h](#)). When each of them was separately tested as a physical

mixture with ZnO, a positive linear correlation between $r(C_3H_6)$ and the number of OH nests on the support was established (Fig. 1e). A mixture of ZnO and Na-containing S-1 with exclusively isolated OH groups shows very low $r(C_3H_6)$ (Extended Data Fig. 1i). OH nests appear after removal of Na^+ and the rate increases by about 14 times. ZnO_x species formed in these materials should be of same structure because a similar apparent activation energy of propene formation was determined for ZnO–S-1 mixtures (Extended Data Fig. 1j).

To determine the local structure of ZnO_x species, the catalysts were prepared according to the inset in Fig. 1b and characterized by X-ray absorption spectroscopy. The oxidation state of Zn in S-1_1(H_2) is +2 as the absorption edge in the X-ray absorption near-edge structure (XANES) spectrum is close to 9,662 eV characteristic for ZnO. Partially reduced ZnO_x (defect structure with oxygen vacancies) should be present in MCM-41(H_2) (Extended Data Fig. 2a, b). As concluded from the Fourier transformed k^2 -weighted extended X-ray absorption fine structure (EXAFS) spectra of these catalysts (Fig. 1f), the first and the second shell scatterings at 1.5 and 2.9 Å correspond to O and Zn neighbours as in ZnO, respectively. All fitting details are summarized in Extended Data Figs. 2e–j and 3, and Extended Data Table 2. Based on the average coordination number (CN) in Zn–O of 2.5 and in Zn–Zn of 8.4, MCM-41(H_2) should contain ZnO_x nanoparticles. The corresponding CN values for S-1_1(H_2) are 3 and 1. Thus, S-1_1(H_2) should contain binuclear ZnO_x species. Using Si instead of Zn is not able to satisfactorily predict the second shell (Extended Data Fig. 2g–j). We also explored if and how the structure of such species in S-1_1(H_2) changes upon catalyst treatment in H_2 to mimic its state in PDH. The position of the Zn K-absorption edge shifts to lower energy upon heating from 100 to 500 °C (Fig. 1g). In addition, CN in the first Zn–O shell decreases from 3 to 2. The intensity in the EXAFS spectra at 1.5 Å decreases too (Extended Data Fig. 2c, d). Contrarily, the intensity in the EXAFS spectra at 2.9 Å decreases only slightly upon heating to 200 °C and does not change with a further temperature rise. Thus, no changes in CN of Zn–Zn occur upon catalyst reductive treatment.

The ability of binuclear ZnO_x species to lose lattice oxygen upon reductive treatment was independently proven by O_2 -titration tests with S-1_1(H_2) treated in H_2 at 550 °C. O_2 was consumed until all vacancies were filled (Extended Data Fig. 4a). These defects were also directly identified by in situ electron paramagnetic resonance spectroscopy as F^+ centres at a g factor of 2.005 characteristic for a trapped electron in an oxygen vacancy²⁹. Their concentration increases after reducing S-1_1(H_2) in $H_2/Ar = 1$ at 550 °C (Extended Data Fig. 4b). No F^+ centres could be seen after reductive treatment of bare S-1_1 (Extended Data Fig. 4c).

Based on the above discussion, the active site for PDH over S-1_1(H₂) should be lower coordinated binuclear ZnO_x species. It reveals about 300, 2 or 100 times higher turnover frequency of propene formation in comparison with isolated ZnO_x species present in ZnO_x/SiO₂ and ZnO_x/TiZrO_x or ZnO_x nanoparticles in ZnO_x/MCM-41 (Fig. 1h). Moreover, the developed catalysts also show higher propene productivity under industrially relevant conditions in comparison with the state-of-the-art Zn-containing catalysts (Extended Data Table 3).

Kinetically relevant step(s) in the PDH reaction were investigated using the temporal analysis of products (TAP) reactor operating with sub-millisecond resolution³⁰. C₃H₆ or C₃D₆ were detected upon pulsing of C₃H₈/Ar = 1 or C₃D₈/Ar = 1 over S-1_1(H₂) at 550 °C (Extended Data Fig. 4d,e). The amount of C₃D₆ was significantly lower. Neither H₂ nor D₂ were detected. The reason for their absence might be the lower sensitivity of mass spectrometric analysis toward these products in comparison with propene. Alternatively, when H₂ was formed very slowly, the ratio of signal to noise would be too low for proper detection. To check if H₂ formation limits the PDH reaction, H/D exchange tests were carried out at 550 °C using a D₂/Ne = 1 mixture. When this mixture was pulsed over S-1_1(H₂), HD was observed while this product was not formed in tests with bare S-1_1 and MCM-41(H₂) (Extended Data Fig. 4f-h). Thus, binuclear ZnO_x species in S-1_1(H₂) must be involved in the exchange reaction. D atoms formed from D₂ on these species react with OH groups of S-1_1(H₂) to yield HD. This process should be fast because the initial conversion of D₂ is high (Extended Data Fig. 4i). The conversion decreases with rising number of D₂ pulses due to the transformation of OH groups into OD groups. The high activity to HD exchange and the lower amount of propene formed from deuterated propane suggest that the breaking of C—H bonds in propane should be the rate-limiting step in PDH.

Molecular-level details of PDH were derived from DFT calculations. A model for binuclear ZnO_x species was created according to our characterization data mentioned above. Two Si defects were substituted by two Zn atoms in the orthorhombic MFI framework (Extended Data Fig. 5a,b). The positively charged Zn atoms are 2O- and 3O-coordinated. We considered breaking of methylene or methyl C—H bonds in C₃H₈ and successive transformations of the formed *iso*-C₃H₇ or *n*-C₃H₇ intermediates to gas-phase C₃H₆ and H₂ (Extended Data Figs. 5d and 6). The pathway starting with the heterolytic methyl C—H bond cleavage seems to be kinetically relevant. For the most preferred route (Fig. 2), the first C—H bond cleavage occurs on the low-coordinated Zn^{δ+} with a barrier of 1.35 eV. The formed *n*-C₃H₇ is in a bridged position between two Zn^{δ+} after substituting one Zn—O bond of the 3O-coordinated Zn^{δ+} by Zn—Zn

coordination. The subtracted H atom is bound to the neighbouring O atom. The cleavage of the methylene C—H bond in *n*-C₃H₇ proceeds homolytically and requires 1.22 eV. The apparent barrier of the whole process is 1.81 eV.

Fig. 2: Molecular details of PDH.

 figure2



The calculated energy profiles along the minimum energy pathways and the optimized intermediates (A–C) and transition states (TS) at the PBE + D3 + ZPE level upon PDH on the reduced binuclear ZnO_x (blue) and single ZnO_x (red) sites on the surface of S-1. Cyan, red, grey, yellow and white spheres stand for Zn, O, C, Si and H atoms, respectively.

For comparison, we also calculated PDH on single-site ZnO_x/S-1, created upon replacing one T5-site Si atom (Extended Data Fig. 5c). In comparison with the binuclear ZnO_x species, the first C—H bond cleavage is favourable on this site, but the whole energy span and the apparent activation barrier are higher, that is, 3.39 versus 2.38 eV and 2.14 versus 1.81 eV, respectively (Fig. 2). Therefore, single-site ZnO_x should be much less active, in agreement with the experimental data (Fig. 1h).

The application potential of our approach for preparation of active, selective and durable catalysts was proven in a test over about 400 h on propane stream at 550 °C using different feeds (40 or 70 vol% C₃H₈ and H₂/C₃H₈ of 0, 0.5 or 1) representative for the current large-scale PDH technologies. The test consisted of a series of PDH, regeneration (air) and reduction (50 vol% H₂ in N₂) cycles lasting for about 4–6, 0.5–1

and 0.5–1 h respectively at the same temperature. A mixture of ZnO and S-1_3 with an upstream-located ZnO layer (ZnO//ZnO–S-1_3) (Extended Data Fig. 7a) and an analogue of commercial K–CrO_x/Al₂O₃ were loaded into two reactors of the same setup and tested in parallel. To compare these catalysts fairly, we adjusted contact time to achieve similar initial propane conversion under each reaction condition.

Both catalysts restore their initial activity after regeneration (Fig. 3a). A decrease in the propane conversion over ZnO//ZnO–S-1_3 after about 250 h on propane stream is due to consumption of ZnO under reductive conditions. However, the initial conversion is completely recovered after fresh ZnO was added on top of the remaining catalyst. No visible changes in the conversion could be seen for the next 120 h on propane stream. Such behaviour proves that OH nests of the support are thermally stable at the reaction temperature and can easily form catalytically active ZnO_x species. Thus, non-interrupted PDH using our layered catalyst can be ensured on the large-scale application through periodic addition of ZnO, for example, upon non-toxic and explosive-free catalyst regeneration in air.

Fig. 3: Durability test and validation of the approach.



a, b, On-stream profiles of $X(C_3H_8)$ (**a**) and STY(C_3H_6) (**b**) over ZnO//ZnO–S-1_3 (blue, 0.09 g of ZnO and 0.09 g of ZnO–S-1_3) and K–CrO_x/Al₂O₃ (grey, 0.302 g). Only the amount of ZnO–S-1_3 was considered for calculating STY(C_3H_6). Reaction conditions: 550 °C, (0): $C_3H_8:H_2:N_2 = 4:2:4$, 10 or 6 ml min⁻¹, (I): $C_3H_8:H_2:N_2 = 4:2:4$, 6 ml min⁻¹, (II) $C_3H_8:N_2 = 4:6$, 6 ml min⁻¹, (III) $C_3H_8:H_2:N_2 = 4:4:2$, 6 ml min⁻¹.

min^{-1} , and (IV) $\text{C}_3\text{H}_8:\text{N}_2 = 7:3$, 6 ml min^{-1} . **c, d**, $r(\text{C}_3\text{H}_6)$ over ZnO -zeolite mixtures (reduced for 1 h) (**c**) or $\text{ZnO}/\text{metal oxides}$ (reduced for 2 h) (**d**). A scheme of reactor loading for **c, d** is present in Extended Data Fig. [7e and 7a](#), respectively.

Source data

In comparison with $\text{K}-\text{CrO}_x/\text{Al}_2\text{O}_3$, $\text{ZnO}/\text{ZnO-S-1}_3$ reveals higher on-stream stability particularly under conditions without co-fed H_2 . It also shows about three times higher space time yield of propene formation ($\text{STY}(\text{C}_3\text{H}_6)$) (Fig. [3b](#)) with a slightly lower propene selectivity (on average 91.9% versus 93.1%) due to a higher coke production (Extended Data Fig. [7b, c](#)). However, our catalyst produces a lower amount of cracking products at even 600°C that might be advantageous for downstream distillation processes (Extended Data Fig. [7d, f](#)). Concerning undesired coke production, this product in the Catofin process is combusted upon catalyst regeneration, thus providing heat required for the endothermic PDH reaction.

Further we demonstrate that our approach is of general character and can be applied for preparation of active Zn-containing catalysts using other SiO_2 -based zeolites, that is, dealuminated mordenite, Beta and MCM-22 or commercially available OH-rich metal oxides, such as Al_2O_3 , TiO_2 , LaZrO_x , TiZrO_x and $\text{ZrO}_2-\text{SiO}_2$. When applying these supports as a physical mixture with ZnO or in form of two layers with ZnO being the upstream layer, high $r(\text{C}_3\text{H}_6)$ is achieved (Fig. [3c, d](#)). The activity of most of our samples is higher than that of an analogue of commercial $\text{K}-\text{CrO}_x/\text{Al}_2\text{O}_3$. The mechanism of formation of ZnO_x species in the zeolites and the oxidic supports should be same because H_2 formation was observed upon heating of a physical mixture of metallic Zn and support in Ar and the intensity of band of defective OH groups decreases when such mixtures were treated at 550°C in $\text{H}_2/\text{N}_2 = 1$ (Extended Data Fig. [8](#)).

Our results demonstrate that defective OH sites in zeolites or metal oxides are crucial for the formation of certain ZnO_x species, which are relevant for the non-oxidative dehydrogenation of propane to propene. Although the concentration of such defects can be adjusted in a controlled manner through the method of support preparation, further improvements are expected when their exact structure and its impact on oxidation of Zn^0 to ZnO_x of a certain speciation will be understood. Thus, this study opens the possibility for a purposeful creation of active species and for establishing fundamentals relevant for efficient C–H bond activation in various alkanes. In addition, the catalysts prepared according to our approach might find their application in other Zn-catalysed reactions.

Methods

Synthesis of bare supports

The following chemicals were used as received. Tetraethyl orthosilicate (Sinopharm Chemical Reagent Co. Ltd or Alfa Aesar), tetrapropylammonium hydroxide (TPAOH, Shanghai Cairui Chemical Engineering Technology Co., Ltd, 25wt% water solution), cetyltrimethylammonium bromide (CTAB, Aldrich), P123 (MW = 5,800, Aldrich), ZnO (Sigma-Aldrich), metallic Zn (>98%, <65 µm, ROTH), tetrabutylammonium hydroxide solution (TBAOH, 40wt%, Sigma-Aldrich), LUDOX (Sigma-Aldrich, 30wt% suspension in H₂O), SiO₂ (Sigma-Aldrich, with 6 nm pores, 302 m² g⁻¹ S_{BET} (BET surface area)), MOR (SiO₂/Al₂O₃ = 20), MCM-22 (SiO₂/Al₂O₃ = 46), beta zeolite (SiO₂/Al₂O₃ = 25,) were purchased from NanKai university. γ-Al₂O₃ (SAINT-Gobain), TiO₂ (rutile TiO₂, Sachtleben Chemie GmbH). TiZrO_x (30wt% TiO₂) and LaZrO_x (9wt% La₂O₃) were offered by Daiichi Kigenso Kagaku Kogyo Co.

S-1_1 was exactly synthesized according to our previous study with an initial gel molar composition of 0.24 TEOS: 0.042 TPAOH: 3.67 H₂O (ref. [31](#)). S-1 supports with different concentration of OH nests were synthesized with the same procedure upon varying H₂O/SiO₂ ratio, silica source, OH⁻/H₂O ratio, crystallization temperature or adding Na⁺. Further details are given in Extended Data Table [1](#).

To prepare S-2 (S_{BET} of 362 m² g⁻¹), 27 g of silica sol (30wt%), 18 g of TBAOH solution and 40 g of deionized water were blended at room temperature for 30 min. Hereafter, the suspension was placed in a 200 ml stainless-steel autoclave with a PTFE insert at 170 °C for three days. After cooling down, the solid product was collected after filtration, washing, drying and calcination at 550 °C for 5 h. To remove any K⁺ and/or Na⁺, the S-2 zeolite was dispersed in 1 M NH₄NO₃ solution ($m_{(\text{solid})} \cdot V_{(\text{solution})} = 1 \text{ g} : 50 \text{ ml}$) at 100 °C for 10 h. After ion-exchange, the solid product was washed three times by deionized water and dried at 100 °C for 6 h. The final sample was obtained after calcination at 550 °C for 5 h.

For preparation of SBA-15 (7 nm pores, S_{BET} of 812 m² g⁻¹), 600 g of deionized water and 120 g of concentrated HCl (37wt%) were mixed at room temperature. Then, 24 g of P123 were added to the above solution followed by adding 48 g of TEOS. The clear solution was heated under stirring to 45 °C and tempered for 30 min. The solution changed to white suspension. This suspension was stirred at 45 °C for additional 24 h and then aged at 90 °C for 48 h under static conditions. After cooling down, the product was separated by filtration and washed thoroughly with deionized water. The

sample was dried at room temperature for 24 h and then calcined in air at 550 °C for 6 h with a heating rate of 5 °C min⁻¹.

MCM-41 (3 nm pores, S_{BET} of 925 m² g⁻¹) was synthesized as follows. 500 g of deionized water, 200 g of ethanol and 17 g of CTAB were mixed at room temperature. Then, 42 g of TEOS were added to the above solution. To get an acidic solution (pH value of 2), 0.4 ml of concentrated HCl was added. The solution became clear after a short time. After 30 min, the pH value was adjusted to 8–9 through adding concentrated NH₄OH (25wt%). The white solid product obtained by filtration was washed with deionized water. After drying at room temperature for 24 h, the sample was calcined at 550 °C for 5 h.

To obtain aluminium-free zeolites, 10 g of MOR, Beta or MCM-22 were treated in 200 ml of concentrated HNO₃ at 120 °C for 10 h. The washed and dried materials were dispersed and stirred in diluted HNO₃ (200 ml, $V_{(\text{HNO}_3)}:V_{(\text{H}_2\text{O})} = 3:1$) at room temperature for 5 h to remove extra-framework Al species. Afterwards, the dealuminated zeolites were washed thoroughly by deionized water until pH value reached 7. The washed samples were dried at 100 °C overnight and used without calcination.

Catalyst preparation

Physical mixtures of ZnO and a certain support were prepared as follows. 0.08 g of ZnO powder and 0.92 of SiO₂-based supports were ground in a mortar for 10 min. Afterwards, the resulting mixtures were pressed and sieved to 315–710 µm. The samples were denoted as ZnO support.

A simple method was developed for depositing ZnO_x species on the surface of various supports (inset in Fig. 1b). 0.05 g of ZnO (315–710 µm) and 0.1 g of support (315–710 µm) were loaded into continuous-flow fixed-bed quartz reactors (diameter: 6 mm), ZnO was located upstream. These two layers were separated by a layer of quartz wool (~10 mg) to avoid any physical contact between ZnO and the supports. The loaded reactors were heated up to 550 °C in Ar flow followed by feeding air flow at the same temperature for 1 h. Hereafter, the catalyst precursors were exposed to a flow (10 ml min⁻¹) of 50vol% H₂ in Ar, 5vol% O₂ in Ar, or Ar at the same temperature and kept for different time (from 5 to 240 min). Finally, they were cooled in Ar. The downstream layer was recovered from the reactors and the resulting catalysts were abbreviated as support(atmosphere). For example, S-1_1(H₂) means that S-1_1 support was used and synthesized under H₂. According to inductively coupled plasma

atomic emission spectroscopy measurements, Zn loading in S-1_1(H₂), MCM-41(H₂) and S-2(H₂) is 1.2wt%, 0.98wt% and 2.4wt%, respectively.

An analogue of commercial K–CrO_x/Al₂O₃ was synthesized according to the method described in the patent from Vladimir Fridman³². Briefly, desired amounts of CrO₃ and KOH were separately dissolved in water. Then, both solutions were mixed. Afterwards, γ-Al₂O₃ was added to the above solution. The catalyst was collected after drying and calcination at 760 °C for 4 h. The amount of Cr₂O₃ and K₂O in the resulting catalyst was 19.7wt% and 0.93wt%, respectively.

Catalyst characterization

X-ray absorption near-edge structure (XANES) and extended X-ray absorption fine structure (EXAFS) spectra at the Zn K absorption edge were recorded at the P65 beamline of the PETRA III synchrotron (DESY, Hamburg) in transmission mode. The energy of the X-ray photons was selected by a Si(111) double-crystal monochromator and the beam size was set by means of slits to 0.2 (vertical) × 1.5 (horizontal) mm². The spectra were normalized and the EXAFS spectra background was subtracted using the ATHENA program from the IFFEFIT software package³³. The k^2 -weighted EXAFS functions were Fourier transformed (FT) in the k range of 2.5–12.3 Å^{−1} (2.0–10.0 Å^{−1} for the in situ data). Then the amplitude reduction factor $\langle\{S\}_0^2\rangle = 1.08$ was obtained by fitting the ZnO reference spectrum to a wurtzite structural model as reported in the Inorganic Crystal Structure Database (ICSD; collection code is 34477). The fits of the EXAFS data were performed using Artemis³³ by a least square method in r space between 1.0 and 3.2 Å. The model with two shells from the wurtzite structure (Zn–O and Zn–Zn or Zn–Si) was used for the fits. Coordination numbers (CN), interatomic distances (r), energy shift (δE_0) and mean square deviation of interatomic distances (σ^2) were refined during fitting. The absolute misfit between theory and experiment is represented by ρ .

For ex situ catalyst characterisation, samples were diluted with cellulose and the total mass was calculated in such a way that absorbance was 2.5 absorbance units (Lambert–Beer law, the logarithm of the ratio of incident to transmitted (X-ray) photons through a sample). For in situ XANES, the S-1_1(H₂) catalyst with a sieve fraction of 100–200 µm was loaded in an in situ micro-reactor (quartz capillary, 1.5 mm diameter, 0.02 mm wall thickness³⁴). The sample was heated stepwise to 500 °C under 5vol% H₂ in He (30 ml min^{−1} flow rate). Before recording the spectra, the sample was kept at each temperature for 10 min.

In situ diffuse reflectance Fourier-transform infrared spectroscopy (DRIFTS) measurements were performed on a Bruker VERTEX 70 equipped with a ZnSe window at a resolution of 4 cm^{-1} from 600 cm^{-1} to $4,000\text{ cm}^{-1}$. Before recording spectra, the background spectrum was obtained over KBr powder at $550\text{ }^\circ\text{C}$ in $\text{H}_2/\text{Ar}=1$. For in situ DRIFTS measurements, bare support or its physical mixture with ZnO (10wt%) was heated to $550\text{ }^\circ\text{C}$ in N_2 and then exposed to $\text{H}_2/\text{Ar}=1$ for 90 min. The spectra were recorded every 5 min automatically. For comparative purposes, all spectra were normalized by the intensity of the overtone band of T-O-T lattice vibration at $1,870\text{ cm}^{-1}$ (ref. ²⁸).

In situ electron paramagnetic resonance (EPR) tests were performed on Bruker ELEXSYS 500-10/12 X-band cw-spectrometer with a microwave power of 6.3 mW , a modulation frequency of 100 kHz and modulation amplitude of 5 G . About 30 mg of catalyst were loaded into an in house-developed continuous-flow fixed-bed quartz reactor, and heated to $550\text{ }^\circ\text{C}$ in flow of Ar. Then the sample was exposed to a flow of $\text{H}_2/\text{Ar}=1$ (20 ml min^{-1}) for 1 h at $550\text{ }^\circ\text{C}$. The EPR spectra were recorded at $20\text{ }^\circ\text{C}$ before and after H_2 reduction.

Temperature-programmed measurements of physically mixed metallic Zn^0 and support were carried out in an in-house developed setup containing eight individually heated continuous-flow fixed-bed quartz reactors. 100 mg of metallic Zn^0 was mixed with 200 mg of support. The obtained mixture was then pressed and sieved to $315\text{--}710\text{ }\mu\text{m}$. 50 mg of this fraction was loaded into a quartz tube and flushed with Ar at $40\text{ }^\circ\text{C}$ for 90 min. The samples were heated in Ar from 40 to $400\text{ }^\circ\text{C}$ (the melting point of Zn is about $420\text{ }^\circ\text{C}$) with a heating rate of $10\text{ }^\circ\text{C min}^{-1}$ while recording H_2O ($m/z=18$) and H_2 ($m/z=2$) signals by an on-line mass spectrometer.

An overall concentration of OH groups in differently prepared S-1 zeolites (Extended Data Table 1) was determined from the amount of water released upon temperature-programmed catalyst treatment in Ar flow according to our previous work³⁵. Each sample (50 mg) was loaded into a quartz tubular reactor and heated up to $550\text{ }^\circ\text{C}$ in Ar and then calcined under air at same temperature for 1 h. Then, the samples were reduced in $\text{H}_2/\text{Ar}=1$ at $550\text{ }^\circ\text{C}$ for 1 h. After that, the samples were cooled down to $400\text{ }^\circ\text{C}$ to get stable mass spectrometric signals of gas-phase components. Desorption profiles of water were obtained during heating up to $900\text{ }^\circ\text{C}$ with a heating rate of $10\text{ }^\circ\text{C min}^{-1}$ in Ar and keeping at the final temperature for 75 min. The amount of released water was determined from the obtained water profiles through their integration over time.

Temporal analysis of products

Transient studies were performed in the temporal analysis of products (TAP-2) reactor, a time-resolved technique with a resolution of around 100 µs (refs. [30,36](#)). Each catalyst sample ($m = 27$ mg, sieve fraction of 315–710 µm) was packed between two layers of quartz particles (sieve fraction of 250–350 µm) within the isothermal zone of the micro-reactor made of quartz. Prior to the pulse experiments, the catalyst was treated in a flow of H₂ (5 ml min⁻¹) at 550 °C for 0.5 h. Then, it was exposed to high vacuum of about 10⁻⁵ Pa.

Pulse experiments were performed at 550 °C using D₂/Ne = 1, C₃H₈/Ar = 1, C₃D₈/Ar = 1 and O₂/Ar = 1 mixtures. D₂ (CK Special Gases Limited, 2.8), C₃H₈ (Linde, 3.5), C₃D₈ (ISOTEC INC., 99 at% D), O₂ (Air Liquide, 4.8), Ar (Air Liquide, 5.0) and Ne (Air Liquide, 4.0) were used without additional purification. Transient responses at the reactor outlet were monitored with a quadrupole mass spectrometer (HAL RD 301 Hiden Analytical) at atomic mass units (AMU) related to the reactants, reaction products and inert gases (Ar and Ne). The latter were used as reference standards. The following AMUs were recorded 52 (C₃D₈), 48 (C₃D₆), 46 (C₃H₆D₂), 45 (C₃H₇D), 44 (C₃H₇D, C₃H₈), 42 (C₃H₈, C₃H₆), 41 (C₃H₈, C₃H₆), 34(C₃D₈), 32 (O₂), 31 (C₃H₆D₂), 30 (C₃H₇D), 29 (C₃H₈), 28 (C₃H₈), 18.0 (H₂O), 4.0 (D₂), 3.0 (HD), 2.0 (H₂), 40 (Ar) and 20 (Ar, Ne). For each AMU, pulses were repeated ten times and averaged to improve the signal-to-noise ratio. The concentration of the feed components and the reaction products was determined from the respective AMU using standard fragmentation patterns and sensitivity factors determined in separate calibration tests.

Catalytic tests

PDH tests were carried out in an in-house developed setup with 15 continuous-flow tubular fixed-bed quartz reactors. The total pressure was 1.2 bar (absolute). For determining the rate of propene formation ($r(C_3H_6)$), the degree of propane conversion was below 10% when using 50 mg of catalyst and a total flow of 40 ml min⁻¹ containing 40 vol% C₃H₈ in N₂. Before the catalytic tests, the samples were initially heated up to 550 °C in N₂, and then flushed in air at the same temperature for 1 h. After 15 min purging with N₂, for oxidatively treated samples, the catalysts were directly exposed to 40 vol% C₃H₈ in N₂, while for reductively treated samples, the catalysts were additionally reduced in H₂/N₂ = 1 for 1 h followed by flushing with N₂ and finally feeding 40 vol% C₃H₈ in N₂. $r(C_3H_6)$ is calculated according to equation (1).

$$r(C_3H_6) = \frac{\dot{n}(C_3H_6)}{m_c \cdot c_a \cdot t} \quad (1)$$

where $\dot{n}(\{\mathrm{C}\})_3\{\mathrm{H}\}_6)$ and m_{cat} stand for the molar flow of propene (mmol min^{-1}) and catalyst mass, respectively.

A durability PDH test was carried out at 550°C with different feeds for about 400 h on propane stream (total time is about 600 h). A catalyst consisting of a ZnO layer on top of ZnO–S-1_3 (ZnO//ZnO–S-1_3) and an analogue of commercial K–CrO_x/Al₂O₃ were tested in the same setup in parallel. A scheme representing reactor loading in these tests is shown in Extended Data Fig. 7a. To achieve a similar degree of propane conversion, we used 0.302 g of K–CrO_x/Al₂O₃ as well as 0.09 g of ZnO and 0.09 g of ZnO–S-1_3. After about 250 h on propane stream, 0.09 g of ZnO were added on top of S-1_3 because the first ZnO layer was consumed. The test consisted of a series of dehydrogenation, regeneration cycles and reduction. The catalysts were purged with N₂ for 15 min between each step.

To determine an apparent activation energy of propene formation, $r(\mathrm{C}_3\mathrm{H}_6)$ over ZnO–S-1_1, ZnO–S-1_2, ZnO–S-1_3, ZnO–S-1_4 and ZnO–S-1_5 was determined at 500, 525 and 550°C . The desired values were obtained by plotting $\ln(r\mathrm{C}_3\mathrm{H}_6)$ versus $1/T$ (Extended Data Fig. 1j). Propane conversion was kept below 10% to ensure differential operation.

The conversion of propane and the selectivity to gas-phase products and to coke were calculated according to equations (2), (3) and (4), respectively. Equation (5) was used for calculating the space time yield (STY) of propene formation. The turnover frequency (TOF) of propene formation was calculated according to equation (6).

$$\begin{aligned}
 & \$\$ X(\{\mathrm{C}\})_3\{\mathrm{H}\}_8 = \frac{\dot{n}(\{\mathrm{C}\})_3}{\dot{n}(\{\mathrm{H}\})_8} \\
 & \$\$ S(i) = \frac{\beta_i}{\sum_i \beta_i} \\
 & \$\$ S(\text{coke}) = 1 - \sum_i S(i) \\
 & \$\$ \text{STY} = \frac{\dot{n}(\{\mathrm{C}\})_3\{\mathrm{H}\}_6}{M \cdot \{\mathrm{C}\}_3\{\mathrm{H}\}_6 \cdot 60 \cdot 1,000} \\
 \end{aligned}
 \tag{2, 3, 4, 5}$$

$$\text{TOF} = \frac{r(C) \cdot 3 \cdot \{H\}_6}{n_{Zn}} \times 60 \quad (6)$$

Where \dot{n} with superscripts ‘in’ or ‘out’ means the molar flow of gas phase components at the reactor inlet and outlet (mmol min^{-1}), respectively. β_i represents the number of carbon atoms in propane and the product i . $M(C)_3 \cdot \{H\}_6$ is the molecular weight of propene (42 g mol^{-1}). n_{Zn} means the molar loading of Zn (mmol g^{-1}).

The feed components and the reaction products were analysed by an on-line gas chromatograph (GC, Agilent 6890) equipped with flame ionization (FID) and thermal conductivity (TCD) detectors. Gas-phase components were identified by GC, which equipped with PLOT/Q (for CO_2), AL/S (for hydrocarbons) and Molsieve 5 (for H_2 , O_2 , N_2 and CO) columns. The GC analysis time of gas-phase products is 4 min.

DTF calculations

Spin-polarized and periodic density functional theory calculations were carried out with the VASP software^{37,38}. The electron exchange and correlation energies were treated using the generalized gradient approximation in the GGA-PBE functional^{39,40}. The cut-off energy was set up to 400 eV. Geometry optimization was converged until forces acting on atoms were lower than 0.02 eV \AA^{-1} , and the energy difference was lower than 10^{-4} eV . The CI-NEB method was applied for identifying transition states⁴¹. All our reported energies include dispersion (D3)⁴² and ZPE corrections (PBE + D3 + ZPE). In addition, we tested the corrections of the Hubbard term (DFT + U_{eff})⁴³ for partially reduced oxidation state of Zn atom ($U_{\text{eff}} = 4.7 \text{ eV}$ (ref. 44)) for comparison. The U_{eff} term just affects the absolute value of states in potential energy surface (PES) and does not change the reaction trend or the mechanism. Therefore, we used the PBE functional results for main discussion and the DFT + U_{eff} results for comparison.

A model with binuclear ZnO_x species inside the pores of S-1 (MFI) was used for calculating elementary pathways of PDH reaction. For comparison, we calculated the PDH reaction on isolated ZnO_x inside the pores of S-1.

Data availability

All data that led us to understand the results presented here are available with the paper or from the corresponding author upon reasonable request. [Source data](#) are

provided with this paper.

References

1. 1.

Sattler, J. J., Ruiz-Martinez, J., Santillan-Jimenez, E. & Weckhuysen, B. M. Catalytic dehydrogenation of light alkanes on metals and metal oxides. *Chem. Rev.* **114**, 10613–10653 (2014).

2. 2.

Otroschenko, T., Jiang, G., Kondratenko, V. A., Rodemerck, U. & Kondratenko, E. V. Current status and perspectives in oxidative, non-oxidative and CO₂-mediated dehydrogenation of propane and isobutane over metal oxide catalysts. *Chem. Soc. Rev.* **50**, 473–527 (2021).

3. 3.

Weckhuysen, B. M. & Schoonheydt, R. A. Alkane dehydrogenation over supported chromium oxide catalysts. *Catal. Today* **51**, 223–232 (1999).

4. 4.

Mentasty, L. R., Gorri, O. F. & Cadus, L. E. Chromium oxide supported on different Al₂O₃ supports: catalytic propane dehydrogenation. *Ind. Eng. Chem. Res.* **38**, 396–404 (1999).

5. 5.

Zhu, Y. et al. Lattice-confined Sn (IV/II) stabilizing raft-like Pt clusters: high selectivity and durability in propane dehydrogenation. *ACS Catal.* **7**, 6973–6978 (2017).

6. 6.

Sun, G. et al. Breaking the scaling relationship via thermally stable Pt/Cu single atom alloys for catalytic dehydrogenation. *Nat. Commun.* **9**, 4454 (2018).

7. 7.

Shi, L. et al. Al₂O₃ nanosheets rich in pentacoordinate Al³⁺ ions stabilize Pt-Sn clusters for propane dehydrogenation. *Angew. Chem. Int. Ed.* **54**, 13994–13998

(2015).

8. 8.

Jiang, F. et al. Propane dehydrogenation over Pt/TiO₂–Al₂O₃ catalysts. *ACS Catal.* **5**, 438–447 (2014).

9. 9.

Masoudian, S. K., Sadighi, S., Abbasi, A., Salehirad, F. & Fazlollahi, A. Regeneration of a commercial catalyst for the dehydrogenation of isobutane to isobutene. *Chem. Eng. Technol.* **36**, 1593–1598 (2013).

10. 10.

Rodemerck, U., Stoyanova, M., Kondratenko, E. V. & Linke, D. Influence of the kind of VO_x structures in VO_x/MCM-41 on activity, selectivity and stability in dehydrogenation of propane and isobutane. *J. Catal.* **352**, 256–263 (2017).

11. 11.

Zhao, Z. et al. Hydroxyl-mediated non-oxidative propane dehydrogenation over VO_x/Al₂O₃ catalysts with promoted stability. *Angew. Chem. Int. Ed.* **57**, 6791–6795 (2018).

12. 12.

Sattler, J. J. et al. Platinum-promoted Ga/Al₂O₃ as highly active, selective, and stable catalyst for the dehydrogenation of propane. *Angew. Chem. Int. Ed.* **53**, 9251–9256 (2014).

13. 13.

Otroschenko, T. et al. ZrO₂-based alternatives to conventional propane dehydrogenation catalysts: Active sites, design, and performance. *Angew. Chem. Int. Ed.* **54**, 15880–15883 (2015).

14. 14.

Zhang, Y. et al. Control of coordinatively unsaturated Zr sites in ZrO₂ for efficient C—H bond activation. *Nat. Commun.* **9**, 3794 (2018).

15. 15.

Chen, C., Zhang, S., Wang, Z. & Yuan, Z. Ultrasmall Co confined in the silanols of dealuminated Beta zeolite: a highly active and selective catalyst for direct dehydrogenation of propane to propylene. *J. Catal.* **383**, 77–87 (2020).

16. 16.

Hu, B. et al. Selective propane dehydrogenation with single-site Co^{II} on SiO₂ by a non-redox mechanism. *J. Catal.* **322**, 24–37 (2015).

17. 17.

Almutairi, S. M. T., Mezari, B., Magusin, P. C. M. M., Pidko, E. A. & Hensen, E. J. M. Structure and reactivity of Zn-modified ZSM-5 zeolites: the importance of clustered cationic Zn complexes. *ACS Catal.* **2**, 71–83 (2011).

18. 18.

Chen, C. et al. New insight into enhanced catalytic performance of ZnPt/HZSM-5 catalysts for direct dehydrogenation of propane to propylene. *Catal. Sci. Technol.* **9**, 1979–1988 (2019).

19. 19.

Schweitzer, N. M. et al. Propylene hydrogenation and propane dehydrogenation by a single-site Zn²⁺ on silica catalyst. *ACS Catal.* **4**, 1091–1098 (2014).

20. 20.

Wan, B. & Chu, H. Reaction kinetics of propane dehydrogenation over partially reduced zinc oxide supported on silicalite. *J. Chem. Soc. Faraday Trans.* **88**, 2943–2947 (1992).

21. 21.

Biscardi, J. A., Meitzner, G. D. & Iglesia, E. Structure and density of active Zn species in Zn/H-ZSM-5 propane aromatization catalysts. *J. Catal.* **179**, 192–202 (1998).

22. 22.

Gong, T., Qin, L., Lu, J. & Feng, H. ZnO modified ZSM-5 and Y zeolites fabricated by atomic layer deposition for propane conversion. *Phys. Chem. Chem. Phys.* **18**, 601–614 (2016).

23. 23.

Camacho-Bunquin, J. et al. Single-site zinc on silica catalysts for propylene hydrogenation and propane dehydrogenation: synthesis and reactivity evaluation using an integrated atomic layer deposition-catalysis instrument. *J. Catal.* **345**, 170–182 (2017).

24. 24.

Han, S. et al. Elucidating the nature of active sites and fundamentals for their creation in Zn-containing ZrO_2 -based catalysts for nonoxidative propane dehydrogenation. *ACS Catal.* **10**, 8933–8949 (2020).

25. 25.

Chen, C. et al. ZnO nanoclusters supported on dealuminated zeolite β as a novel catalyst for direct dehydrogenation of propane to propylene. *ChemCatChem* **11**, 868–877 (2019).

26. 26.

Chen, C. et al. ZnO supported on high-silica HZSM-5 as efficient catalysts for direct dehydrogenation of propane to propylene. *Mol. Catal.* **476**, 110508 (2019).

27. 27.

Liu, G. et al. Platinum-modified $\text{ZnO}/\text{Al}_2\text{O}_3$ for propane dehydrogenation: minimized platinum usage and improved catalytic stability. *ACS Catal.* **6**, 2158–2162 (2016).

28. 28.

Barbera, K., Bonino, F., Bordiga, S., Janssens, T. V. W. & Beato, P. Structure–deactivation relationship for ZSM-5 catalysts governed by framework defects. *J. Catal.* **280**, 196–205 (2011).

29. 29.

Smith, J. M. & Vehse, W. E. ESR of electron irradiated ZnO confirmation of the F^+ center. *Phys. Let. A* **31**, 147–148 (1970).

30. 30.

Morgan, K. et al. Forty years of temporal analysis of products. *Catal. Sci. Technol.* **7**, 2416–2439 (2017).

31. 31.

Zhao, D. et al. ZnO nanoparticles encapsulated in nitrogen-doped carbon material and silicalite-1 composites for efficient propane dehydrogenation. *iScience* **13**, 269–276 (2019).

32. 32.

Fridman, V. Catalyst for dehydrogenation of hydrocarbons. US Patent, 8101541 B2, Sud-Chemie Inc. (2012).

33. 33.

Ravel, B. & Newville, M. ATHENA, ARTEMIS, HEPHAESTUS: data analysis for X-ray absorption spectroscopy using IFEFFIT. *J. Synchrotron Radiat.* **12**, 537–541 (2005).

34. 34.

Grunwaldt, J. D., van Vegten, N. & Baiker, A. Insight into the structure of supported palladium catalysts during the total oxidation of methane. *Chem. Commun.* 4635–4637 (2007).

35. 35.

Rodemerck, U., Kondratenko, E. V., Otroshchenko, T. & Linke, D. Unexpectedly high activity of bare alumina for non-oxidative isobutane dehydrogenation. *Chem. Commun.* **52**, 12222–12225 (2016).

36. 36.

Pérez-Ramírez, J., & Kondratenko, E. V. Evolution, achievements, and perspectives of the TAP technique. *Catal. Today* **121**, 160–169 (2007).

37. 37.

Kresse, G. & Furthmüller, J. Efficiency of ab-initio total energy calculation for metals and semiconductors using a plane-wave basis set. *Comput. Mater. Sci.* **6**, 15–50 (1996).

38. 38.

Kresse, G. & Furthmueller, J. Efficient iterative schemes for ab initio total energy calculations using a plane-wave basis set. *Phys. Rev. B* **54**, 11169–11186 (1996).

39. 39.

Perdew, J. P., Burke, K. & Ernzerhof, M. Generalized gradient approximation made simple. *Phys. Rev. Lett.* **77**, 3865–3868 (1996).

40. 40.

Perdew, J. P., Burke, K. & Ernzerhof, M. Erratum: Generalized gradient approximation made simple. *Phys. Rev. Lett.* **78**, 1396 (1997).

41. 41.

Henkelman, G., Uberuaga, B. P. & Jónsson, H. A climbing image nudged elastic band method for finding saddle points and minimum energy paths. *J. Chem. Phys.* **113**, 9901–9904 (2000).

42. 42.

Grimme, S., Antony, J., Ehrlich, S. & Krieg, H. A consistent and accurate ab initio parametrization of density functional dispersion correction (DFT-D) for the 94 elements H-Pu. *J. Chem. Phys.* **132**, 154104 (2010).

43. 43.

Dudarev, S. L., Botton, G. A., Savrasov, S. Y., Humphreys, C. J. & Sutton, A. P. Electron-energy-loss spectra and the structural stability of nickel oxide: an LSDA+U study. *Phys. Rev. B* **57**, 1505–1509 (1998).

44. 44.

Janotti, A., Segev, D. & Van de Walle, C. G. Effects of cationdstates on the structural and electronic properties of III-nitride and II-oxide wide-band-gap semiconductors. *Phys. Rev. B* **74**, 045202 (2006).

Acknowledgements

Financial support by Deutsche Forschungsgemeinschaft (KO 2261/8-1, JI 210/1-1), the National Natural Science Foundation of China (grants 21961132026, 21878331, 91645108, 21903049 and U1510103), the National key Research and Development Program Nanotechnology Specific Project (no. 2020YFA0210900), Science

Foundation of China University of Petroleum, Beijing (C201604) and the State of Mecklenburg-Vorpommern are gratefully acknowledged. The authors thank K. Guo for synthesis of some zeolites. The authors thank A. Simmula for ICP measurement. The authors thank J. Li for IR measurements of metal oxides. The authors also thank Daiichi Kigenso Kagaku Kogyo Co., Ltd, for offering ZrO₂-based supports. D.Z. acknowledges support from the China Scholarship Council. We acknowledge DESY (Hamburg, Germany), a member of the Helmholtz Association HGF, for the provision of experimental facilities. Parts of this research were carried out at PETRA III and we would like to thank E. Welter for assistance in using beamline P65.

Funding

Open access funding provided by Leibniz-Institut für Katalyse e.V. (LIKAT Rostock).

Author information

Affiliations

1. State Key Laboratory of Heavy Oil Processing, China University of Petroleum, Beijing, P. R. China

Dan Zhao, Shanlei Han & Guiyuan Jiang

2. Leibniz-Institut für Katalyse e.V., Rostock, Germany

Dan Zhao, Xinxin Tian, Shanlei Han, Vita A. Kondratenko, Anna Perechodjuk, Thanh Huyen Vuong, Jabor Rabeah, Reinhard Eckelt, Uwe Rodemerck, David Linke, Haijun Jiao & Evgenii V. Kondratenko

3. Key Laboratory of Materials for Energy Conversion and Storage of Shanxi Province, Institute of Molecular Science, Shanxi University, Taiyuan, P. R. China

Xinxin Tian

4. Institute of Catalysis Research and Technology and Institute for Chemical Technology and Polymer Chemistry, Karlsruhe Institute of Technology (KIT), Karlsruhe, Germany

Dmitry E. Doronkin & Jan-Dierk Grunwaldt

Contributions

E.V.K. initiated and led the whole project. E.V.K. and G.J. supervised and coordinated the project. D.Z. prepared all the catalysts and carried out characterization measurements and catalytic tests. D.Z. and E.V.K. wrote the first draft. U.R. and D.L. contributed to the analysis of catalytic tests. X.T. and H.J. performed DFT calculations and wrote the corresponding part of the manuscript. D.E.D. and J.D.G. performed XAS experiments and analysed the results. S.H. performed in situ DRIFTS measurements and some catalytic tests. V.A.K. carried out temporal analysis of product tests and analysed the results. T.V. and J.R performed in situ EPR characterization and analysed the results. A.P. carried out the durability test and analysed the results. R.E. synthesized mesoporous SiO₂ materials and carried out N₂ adsorption–desorption measurements. All the authors discussed the results and improved the manuscript.

Corresponding authors

Correspondence to [Guixuan Jiang](#), [Haijun Jiao](#) or [Evgenii V. Kondratenko](#).

Ethics declarations

Competing interests

The authors declare no competing interests.

Additional information

Peer review information *Nature* thanks the anonymous reviewers for their contribution to the peer review of this work. Peer reviewer reports are available.

Publisher's note Springer Nature remains neutral with regard to jurisdictional claims in published maps and institutional affiliations.

Extended data figures and tables

[Extended Data Fig. 1 Selected catalytic performance and physicochemical characteristics.](#)

a, On-stream profiles of X(C₃H₈) over oxidatively or reductively treated ZnO–S-1_1 mixture (150 mg) at 550 °C using C₃H₈:N₂=2:3 (15 ml min⁻¹). **b**, *r*(C₃H₆) at 550 °C over S-1_1(H₂), S-2(H₂) and MCM-41(H₂) prepared at 550 °C for different reduction time according to the inset in Fig. [1b](#). **c**, XRD patterns of differently synthesized S-1

zeolites and S-2 zeolite. **d**, Magnified XRD patterns in the 2θ range of 22–25°. S-1_1, S-1_2 and S-1_3 are composed of the orthorhombic MFI phase, while the monoclinic MFI phase was identified in S-1_4 and S-1_5. The XRD patterns of S-2 are typical for the MEL topology. **e**, N_2 adsorption–desorption isotherms of S-1 zeolites. **f**, Pore size distribution of S-1 zeolites based on the BJH model. S_{BET} is given in Extended Data Table 1. **g**, DRIFTS spectra of S-1 zeolites in the OH stretching region. **h**, Temperature-programmed release of H_2O upon heating of S-1 zeolites in Ar. **i**, $r(C_3H_6)$ over $ZnO-S-1(Na)$ or $ZnO-S-1(Na, NH_4^+)$ mixtures. The bare supports differ in the concentration of OH nests (see the DRIFTS spectra in the insert), which are important for the formation of catalytically active ZnO_x species from Zn^0 . **j**, Arrhenius plots of $r(C_3H_6)$ over $ZnO-S-1$ mixtures (50 mg) tested using $C_3H_8:N_2 = 2:3$ (40 ml min⁻¹).

[Source data](#)

Extended Data Fig. 2 Ex situ, in situ XAS and fitting data.

a, XANES spectra of as-prepared catalysts and reference materials (Zn foil and commercial ZnO). **b**, The corresponding k^2 -weighted $\chi(k)$ functions (extracted fine structure in k space) to **a**. **c**, In situ FT EXAFS spectra of S-1_1(H_2) in a flow of 5 vol% H_2 in He at different temperatures. **d**, The corresponding k^2 -weighted $\chi(k)$ functions (extracted fine structure in k space) to **c**. **e**, **f**, The EXAFS fits of the ZnO reference (used to estimate amplitude reduction factor) in r (**e**) and q spaces (**f**). ZnO fit summary (based on the wurtzite structure): $\delta E_0 = 1.0 \pm 2.6$ eV; $\rho = 2.0\%$; amplitude reduction factor (S_0^{-2}) = 1.08 ± 0.2 ; $\sigma^2 = 10.1 \pm 1.8$ eV (the same for all fitted shells). First shell comprises four O atoms at 1.96 ± 0.03 Å; second shell: one O atom at 3.11 ± 0.34 Å, six Zn atoms at 3.21 ± 0.02 Å and six Zn atoms at 3.26 ± 0.02 Å. **g–j**, Comparison between the ex situ spectrum of S-1_1(H_2) and models assuming Si or Zn in the second shell in r (**g**, **h**) and q spaces (**i**, **j**). A significant misfit can be seen for the second shell peak at approx. 3.0 Å for the Si-containing model.

[Source data](#)

Extended Data Fig. 3 Fitting results.

a, **b**, The EXAFS fits for different materials in r (**a**) and q spaces (**b**).

[Source data](#)

Extended Data Fig. 4 Proving the presence of O vacancies and rate-limiting step in PDH.

a, The amount of consumed oxygen atoms ($N[O]$) upon O_2 pulsing at $550\text{ }^\circ\text{C}$ over S-1_1(H_2) reduced in $H_2/Ar = 1$ at $550\text{ }^\circ\text{C}$ for 0.5 h. **b, c**, In situ EPR spectra at $20\text{ }^\circ\text{C}$ of fresh and treated ($H_2/Ar = 1$ (20 ml min $^{-1}$) at $550\text{ }^\circ\text{C}$ for 1 h) S-1_1(H_2) (**b**) or bare S-1_1 (**c**). **d, e**, Height-normalized transient responses of C_3H_8 , C_3H_6 , C_3D_8 , C_3D_6 , D_2 and HD recorded after pulsing of $C_3H_8/Ar = 1$ (**d**) or $C_3D_8/Ar = 1$ (**e**) at $550\text{ }^\circ\text{C}$. **f-h**, Height-normalized transient responses of H_2 , D_2 and H/D recorded after pulsing of $D_2/Ne = 1$ over S-1_1 (**f**), MCM-41(H_2) (**g**), S-1_1(H_2) (**h**) at $550\text{ }^\circ\text{C}$. **i**, Conversion of D_2 ($X(D_2)$) over S-1_1(H_2) in multi-pulse $D_2/Ne = 1$ tests at $550\text{ }^\circ\text{C}$. Experimental details are given in the ‘Temporal analysis of products’ section.

[Source data](#)

Extended Data Fig. 5 Calculation DFT models and intermediates for different reaction pathways.

a-c, Top and side views of the MFI cell (S-1 support) (**a**), the binuclear $ZnO_x/S-1$ model (**b**) and the single $ZnO_x/S-1$ model (**c**). **d**, Side views of intermediates in the *n*-propyl or isopropyl paths using the $ZnO_x/S-1$ model. (Cyan, red, grey, yellow and white balls stand for Zn, O, C, Si and H atoms, respectively.) The orthorhombic MFI framework, which contains 12 distinct tetrahedral (T) centres based on a periodic slab model containing 96 T centres was used to simulate (Silicalite-1, S-1) catalyst, especially its channel structure. A $1 \times 1 \times 1$ Monkhorst–Pack k -point grid was used for sampling the Brillouin zone for this model. We randomly constructed a defective MFI catalyst, where two neighbouring Si atoms at T1 and T5 sites both located at the intersection of the channels and surrounded by six OH groups forming a OH nest were removed. Then, these two defective sites were filled with two Zn atoms with a simultaneous formation of two H_2 molecules, and then further removal the left two Si–OH groups by H_2 into two Si–H groups (mimics the additional reduction steps before carrying out the reaction). The OH location, that is, the final Si–H location, is chosen according to the Zn–Zn distance (3.32 Å, EXAFS results).

Extended Data Fig. 6 Potential energy surface of different reaction pathways in PDH.

a, The potential energy surface of PDH using the binuclear $ZnO_x/S-1$ model at the PBE + D3 + ZPE level. Two competitive PDH paths are considered: (i) propane is

initially activated upon methyl C–H heterolytic cleavage to yield *n*-C₃H₇ or (ii) propane is activated at the central methylene C–H bond heterolytically to yield *i*-C₃H₇. The calculations predict that the latter route is unlike. **b**, The U_{eff} corrected potential energy surfaces of PDH using the binuclear ZnO_{*x*}/S-1 model. The U_{eff} term only affects the absolute value of states in the potential energy surface (PES) and does not change the reaction trend or the mechanism.

[Extended Data Fig. 7 Durability of ZnO//ZnO–S-1_3 and K–CrO_{*x*}/Al₂O₃ under industrially relevant conditions.](#)

a, A schematic of reactor loading for the tests. **b–d**, On-stream profiles of the selectivity to propene (S(C₃H₆)) (**b**), coke (S(coke)) (**c**) or cracking products (S(cracking products)) (**d**) over ZnO//ZnO–S-1_3 (blue, 0.09 g ZnO and 0.09 g ZnO–S-1_3) and an analogue of commercial K–CrO_{*x*}/Al₂O₃ (grey, 0.302 g). Reaction conditions: 550 °C, (0): C₃H₈:H₂:N₂ = 4:2:4, 10 or 6 ml min⁻¹, (I): C₃H₈:H₂:N₂ = 4:2:4, 6 ml min⁻¹, (II) C₃H₈:N₂ = 4:6, 6 ml min⁻¹, (III) C₃H₈:H₂:N₂ = 4:4:2, 6 ml min⁻¹, and (IV) C₃H₈:N₂ = 7:3, 6 ml min⁻¹. **e**, A schematic of catalytic tests for **f**. **f**, The X(C₃H₈), S(C₃H₆), S(cracking products), and S(coke) as well as carbon balance in 2 h propane on stream over ZnO–S-1_3 tested at 550 °C or 600 °C using C₃H₈:N₂ = 2:3 with WHSV_(C3H8) of 7.9 or 15.8 h⁻¹. All carbon balance values are above 95%.

[Source data](#)

[Extended Data Fig. 8 ZnO_{*x*} species formation over different metal oxides.](#)

a, Concentration profiles of H₂ and H₂O detected by an on-line mass spectrometer upon temperature-programmed heating of bare supports or physically mixed metallic Zn⁰ and a certain support in Ar. **b**, In situ DRIFTS spectra of bare supports or a mixture of ZnO with a certain support. Reaction conditions: 550 °C, 50vol%H₂ in Ar.

[Source data](#)

Extended Data Table 1 Synthesis conditions and physicochemical properties of differently prepared S-1 supports

Extended Data Table 2 Fitting results

Extended Data Table 3 Comparison of Zn-containing catalysts

Supplementary information

Peer Review File

Source data

Source Data Fig. 1

Source Data Fig. 3

Source Data Extended Data Fig. 1

Source Data Extended Data Fig. 2

Source Data Extended Data Fig. 3

Source Data Extended Data Fig. 4

Source Data Extended Data Fig. 7

Source Data Extended Data Fig. 8

Rights and permissions

Open Access This article is licensed under a Creative Commons Attribution 4.0 International License, which permits use, sharing, adaptation, distribution and reproduction in any medium or format, as long as you give appropriate credit to the original author(s) and the source, provide a link to the Creative Commons license, and indicate if changes were made. The images or other third party material in this article are included in the article's Creative Commons license, unless indicated otherwise in a credit line to the material. If material is not included in the article's Creative Commons license and your intended use is not permitted by statutory regulation or exceeds the permitted use, you will need to obtain permission directly from the copyright holder. To view a copy of this license, visit <http://creativecommons.org/licenses/by/4.0/>.

Reprints and Permissions

About this article

Cite this article

Zhao, D., Tian, X., Doronkin, D.E. *et al.* In situ formation of ZnO_x species for efficient propane dehydrogenation. *Nature* **599**, 234–238 (2021).
<https://doi.org/10.1038/s41586-021-03923-3>

- Received: 06 May 2020
- Accepted: 18 August 2021
- Published: 10 November 2021
- Issue Date: 11 November 2021
- DOI: <https://doi.org/10.1038/s41586-021-03923-3>

Share this article

Anyone you share the following link with will be able to read this content:

[Get shareable link](#)

Sorry, a shareable link is not currently available for this article.

[Copy to clipboard](#)

Provided by the Springer Nature SharedIt content-sharing initiative

This article was downloaded by **calibre** from <https://www.nature.com/articles/s41586-021-03923-3>

| [Section menu](#) | [Main menu](#) |

- Article
- [Published: 10 November 2021](#)

Globally resolved surface temperatures since the Last Glacial Maximum

- [Matthew B. Osman](#) ORCID: [orcid.org/0000-0002-5636-698X¹](https://orcid.org/0000-0002-5636-698X),
- [Jessica E. Tierney](#) ORCID: [orcid.org/0000-0002-9080-9289¹](https://orcid.org/0000-0002-9080-9289),
- [Jiang Zhu](#) ORCID: [orcid.org/0000-0002-0908-5130²](https://orcid.org/0000-0002-0908-5130),
- [Robert Tardif³](#),
- [Gregory J. Hakim³](#),
- [Jonathan King¹](#) &
- [Christopher J. Poulsen](#) ORCID: [orcid.org/0000-0001-5104-4271⁴](https://orcid.org/0000-0001-5104-4271)

[Nature](#) volume 599, pages 239–244 (2021)

- 1318 Accesses
- 784 Altmetric
- [Metrics details](#)

Subjects

- [Climate and Earth system modelling](#)
- [Palaeoceanography](#)
- [Palaeoclimate](#)

Abstract

Climate changes across the past 24,000 years provide key insights into Earth system responses to external forcing. Climate model simulations^{1,2} and proxy data^{3,4,5,6,7,8} have independently allowed for study of this crucial interval; however, they have at times yielded disparate conclusions. Here, we leverage both types of information using paleoclimate data assimilation^{9,10} to produce the first proxy-constrained, full-field reanalysis of surface temperature change spanning the Last Glacial Maximum to present at 200-year resolution. We demonstrate that temperature variability across the past 24 thousand years was linked to two primary climatic mechanisms: radiative forcing from ice sheets and greenhouse gases; and a superposition of changes in the ocean overturning circulation and seasonal insolation. In contrast with previous proxy-based reconstructions^{6,7} our results show that global mean temperature has slightly but steadily warmed, by $\sim 0.5^{\circ}\text{C}$, since the early Holocene (around 9 thousand years ago). When compared with recent temperature changes¹¹, our reanalysis indicates that both the rate and magnitude of modern warming are unusual relative to the changes of the past 24 thousand years.

Access options

Subscribe to Journal

Get full journal access for 1 year

\$199.00

only \$3.90 per issue

[Subscribe](#)

All prices are NET prices.

VAT will be added later in the checkout.

Tax calculation will be finalised during checkout.

Rent or Buy article

Get time limited or full article access on ReadCube.

from \$8.99

[Rent or Buy](#)

All prices are NET prices.

Additional access options:

- [Log in](#)
- [Access through your institution](#)
- [Learn about institutional subscriptions](#)

Fig. 1: Locations and temporal coverage of the SST proxies.

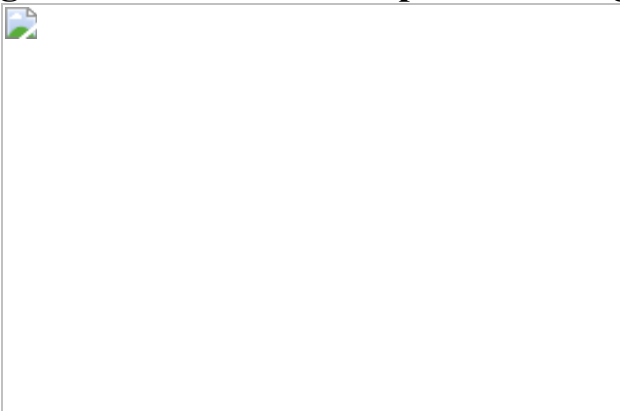


Fig. 2: Global mean surface temperature change over the past 24 kyr.

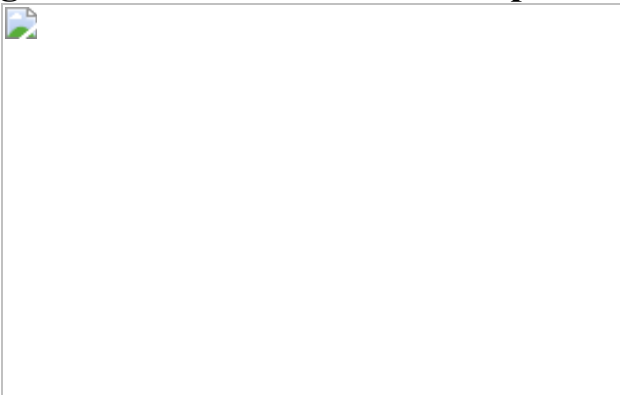


Fig. 3: Leading modes of LGM-to-present surface temperature variability.

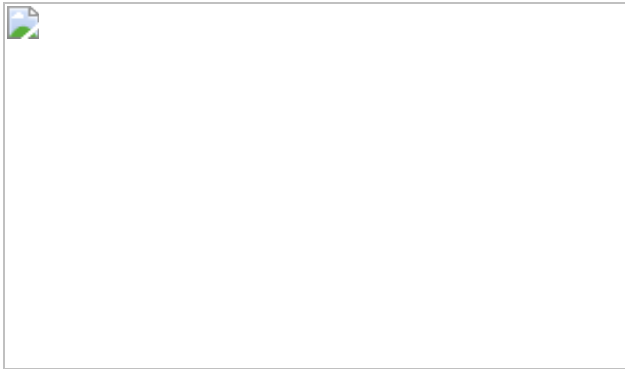


Fig. 4: Comparison of LGM-to-present surface temperature reconstructions.

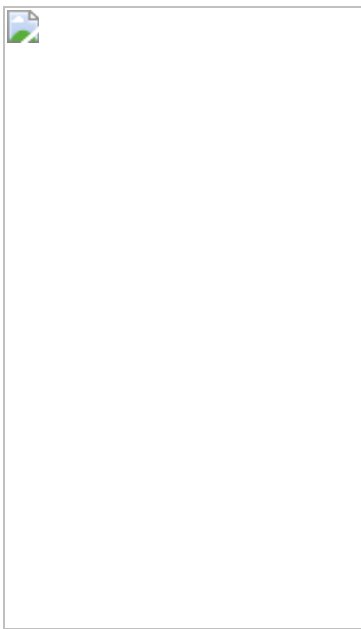
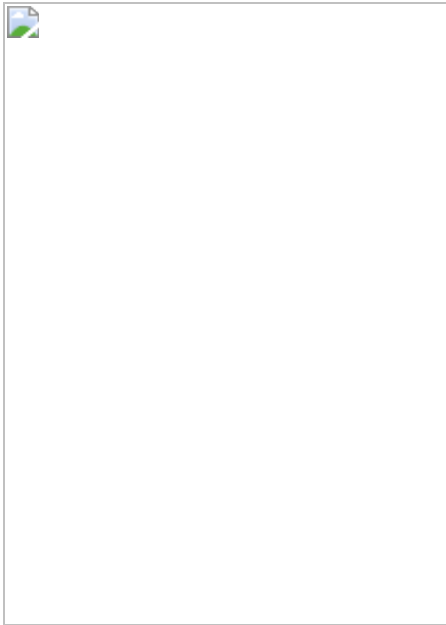


Fig. 5: Contextualizing rates of modern warming.



Data availability

All LGMR and associated proxy data are publicly available via the National Oceanic and Atmospheric Administration (NOAA) Paleoclimatology Data Archive (<https://www.ncdc.noaa.gov/paleo/study/33112>). Source data are provided with this paper.

Code availability

The MATLAB code used for the reconstruction (DASH) are publicly available (<https://github.com/JonKing93/DASH>), as are all accompanying Bayesian proxy forward models (BAYSPAR, BAYSPLINE, BAYFOX, and BAYMAG) used in this study (<https://github.com/jesstierney>). The iCESM1.2 model code is available at <https://github.com/NCAR/iCESM1.2>.

References

1. 1.

Liu, Z. et al. Transient simulation of last deglaciation with a new mechanism for Bølling-Allerød warming. *Science* **325**, 310–314

(2009).

2. 2.

Liu, Z. et al. The Holocene temperature conundrum. *Proc. Natl Acad. Sci. USA* **111**, E3501–E3505 (2014).

3. 3.

Shakun, J. D. et al. Global warming preceded by increasing carbon dioxide concentrations during the last deglaciation. *Nature* **484**, 49–54 (2012).

4. 4.

Snyder, C. W. Evolution of global temperature over the past two million years. *Nature* **538**, 226–228 (2016).

5. 5.

Bereiter, B., Shackleton, S., Baggenstos, D., Kawamura, K. & Severinghaus, J. Mean global ocean temperatures during the last glacial transition. *Nature* **553**, 39–44 (2018).

6. 6.

Marcott, S. A., Shakun, J. D., Clark, P. U. & Mix, A. C. A reconstruction of regional and global temperature for the past 11,300 years. *Science* **339**, 1198–1201 (2013).

7. 7.

Kaufman, D. et al. Holocene global mean surface temperature, a multi-method reconstruction approach. *Sci. Data* **7**, 201 (2020).

8. 8.

Bova, S., Rosenthal, Y., Liu, Z., Godad, S. P. & Yan, M. Seasonal origin of the thermal maxim at the Holocene and the last interglacial.

Nature **589**, 548–553 (2021).

9. 9.

Hakim, G. J. et al. The last millennium climate reanalysis project: framework and first results. *J. Geophys. Res. Atmos.* **121**, 6745–6764 (2016).

10. 10.

Tierney, J. E. et al. Glacial cooling and climate sensitivity revisited. *Nature* **584**, 569–573 (2020).

11. 11.

Morice, C. P. et al. An updated assessment of near-surface temperature change from 1850: the HadCRUT5 dataset. *J. Geophys. Res. Atmos.* **126**, e2019JD032361 (2020).

12. 12.

Marsicek, J., Shuman, B. N., Bartlein, P. J., Shafer, S. L. & Brewer, S. Reconciling divergent trends and millennial variations in Holocene temperatures. *Nature* **554**, 92–96 (2018).

13. 13.

Baggenstos, D. et al. Earth’s radiative imbalance from the Last Glacial Maximum to the present. *Proc. Natl Acad. Sci. USA* **116**, 14881–14886 (2019).

14. 14.

Kageyama, M. et al. The PMIP4-CMIP6 Last Glacial Maximum experiments: preliminary results and comparison with the PMIP3-CMIP5 simulations. *Clim. Past* **17**, 1065–1089 (2021).

15. 15.

Brierley, C. M. et al. Large-scale features and evaluation of the PMIP4-CMIP6 mid Holocene simulations. *Clim. Past* **16**, 1847–1872 (2020).

16. 16.

Park, H.-S., Kim, S.-J., Stewart, A. L., Son, S.-W. & Seo, K.-H. Mid-Holocene Northern Hemisphere warming driven by Arctic amplification. *Sci. Adv.* **5**, eaax8203 (2019).

17. 17.

Tardif, R. et al. Last Millennium Reanalysis with an expanded proxy database and seasonal proxy modeling. *Clim. Past* **15**, 1251–1273 (2019).

18. 18.

Tierney, J. E. & Tingley, M. P. A Bayesian, spatially-varying calibration model for the TEX₈₆ proxy. *Geochim. Cosmochim. Acta* **127**, 83–106 (2014).

19. 19.

Tierney, J. E. & Tingley, M. P. BAYSPLINE: a new calibration for the alkenone paleothermometer. *Paleoceanogr. Paleoclimatol.* **33**, 281–301 (2018).

20. 20.

Malevich, S. B., Vetter, L. & Tierney, J. E. Global core top calibration of δ¹⁸O in planktic foraminifera to sea surface temperature. *Paleoceanogr. Paleoclimatol.* **34**, 1292–1315 (2019).

21. 21.

Tierney, J. E., Malevich, S. B., Gray, W., Vetter, L. & Thirumalai, K. Bayesian calibration of the Mg/Ca paleothermometer in planktic

foraminifera. *Paleoceanogr. Paleoclimatol.* **34**, 2005–2030 (2019).

22. 22.

Brady, E. et al. The connected isotopic water cycle in the community Earth system model version 1. *J. Adv. Model. Earth Sys.* **11**, 2547–2566 (2019).

23. 23.

Amrhein, D. E., Hakim, G. J. & Parsons, L. A. Quantifying structural uncertainty in paleoclimate data assimilation with an application to the last millennium. *Geophys. Res. Lett.* **47**, e2020GL090485 (2020).

24. 24.

Köhler, P., Nehrbass-Ahles, C., Schmitt, J., Stocker, T. F. & Fischer, H. A 156 kyr smoothed history of the atmospheric greenhouse gases CO₂, CH₄, and N₂O and their radiative forcing. *Earth Syst. Sci. Data* **9**, 363–387 (2017).

25. 25.

Braconnot, P. & Kageyama, M. Shortwave forcing and feedbacks in Last Glacial Maximum and Mid-Holocene PMIP3 simulations. *Philos. Trans. R. Soc. A* **373**, 20140424 (2015).

26. 26.

Berger, A. Long-term variations of daily insolation and quaternary climatic changes. *J. Atmos. Sci.* **35**, 2362–2367 (1978).

27. 27.

Huybers, P. & Denton, G. Antarctic temperature at orbital timescales controlled by local summer duration. *Nat. Geosci.* **1**, 787–792 (2008).

28. 28.

Imbrie, J. et al. On the structure and origin of major glaciation cycles 1. Linear responses to Milankovitch forcing. *Paleoceanography* **7**, 701–738 (1992).

29. 29.

McManus, J. F., Francois, R., Gherardi, J.-M., Keigwin, L. D. & Brown-Leger, S. Collapse and rapid resumption of Atlantic meridional circulation linked to deglacial climate changes. *Nature* **428**, 834–837 (2004).

30. 30.

Böhm, E. et al. Strong and deep Atlantic meridional overturning circulation during the last glacial cycle. *Nature* **517**, 73–76 (2015).

31. 31.

Lippold, J. et al. Constraining the variability of the Atlantic meridional overturning circulation during the Holocene. *Geophys. Res. Lett.* **46**, 11338–11346 (2019).

32. 32.

Shakun, J. D. & Carlson, A. E. A global perspective on Last Glacial Maximum to Holocene climate change. *Quat. Sci. Rev.* **29**, 1801–1816 (2010).

33. 33.

Clark, P. U. et al. Global climate evolution during the last deglaciation. *Proc. Natl Acad. Sci. USA* **109**, E1134–E1142 (2012).

34. 34.

Pedro, J. B. et al. Beyond the bipolar seesaw: toward a process understanding of interhemispheric coupling. *Quat. Sci. Rev.* **192**, 27–46 (2018).

35. 35.

He, F. et al. Northern Hemisphere forcing of Southern Hemisphere climate during the last deglaciation. *Nature* **494**, 81–85 (2013).

36. 36.

Ritz, S. P., Stocker, T. F., Grimalt, J. O., Menviel, L. & Timmermann, A. Estimated strength of the Atlantic overturning circulation during the last deglaciation. *Nat. Geosci.* **6**, 208–212 (2013).

37. 37.

Praetorius, S. K. et al. The role of Northeast Pacific meltwater events in deglacial climate change. *Sci. Adv.* **6**, eaay2915 (2020).

38. 38.

Gray, W. R. et al. Wind-driven evolution of the North Pacific subpolar gyre over the last deglaciation. *Geophys. Res. Lett.* **47**, e2019GL086328 (2020).

39. 39.

Reimer, P. J. et al. IntCal13 and Marine13 radiocarbon age calibration curves 0–50,000 years cal BP. *Radiocarbon* **55**, 1869–1887 (2013).

40. 40.

Blaauw, M. & Christen, J. A. Flexible paleoclimate age-depth models using an autoregressive gamma process. *Bayesian Anal.* **6**, 457–474 (2011).

41. 41.

Locarnini, R. A. et al. *World Ocean Atlas 2013. Volume 1, Temperature* (NOAA, 2013).

42. 42.

Wang, K. J. et al. Group 2i Isochrysidales produce characteristic alkenones reflecting sea ice distribution. *Nat. Commun.* **12**, 15 (2021).

43. 43.

Sachs, J. P. Cooling of Northwest Atlantic slope waters during the Holocene. *Geophys. Res. Lett.* **34**, L03609 (2007).

44. 44.

Tierney, J. E., Haywood, A. M., Feng, R., Bhattacharya, T. & Otto-Btiesner, B. L. Pliocene warmth consistent with greenhouse gas forcing. *Geophys. Res. Lett.* **46**, 9136–9144 (2019).

45. 45.

Rayner, N. A. et al. Global analyses of sea surface temperature, sea ice, and night marine air temperature since the late nineteenth century. *J. Geophys. Res.* **108**, 4407 (2003).

46. 46.

Gray, W. R. & Evans, D. Nonthermal influences on Mg/Ca in planktonic foraminifera: a review of culture studies and application to the Last Glacial Maximum. *Paleoceanogr. Paleoclimatol.* **34**, 306–315 (2019).

47. 47.

Lambeck, K., Rouby, H., Purcell, A., Sun, Y. & Sambridge, M. Sea level and global ice volumes from the Last Glacial Maximum to the Holocene. *Proc. Natl Acad. Sci. USA* **111**, 15296–15303 (2014).

48. 48.

Monnin, E. et al. Atmospheric CO₂ concentrations over the Last Glacial Termination. *Science* **291**, 112–114 (2001).

49. 49.

MacFarling Meure, C. et al. Law Dome CO₂, CH₄ and N₂O ice core records extended to 2000 years BP. *Geophys. Res. Lett.* **33**, L14810 (2006).

50. 50.

Rubino, M. et al. A revised 1000-year atmospheric ¹³C-CO₂ record from Law Dome and South Pole, Antarctica. *J. Geophys. Res. Atmos.* **118**, 8482–8499 (2013).

51. 51.

Marcott, S. A. et al. Centennial-scale changes in the global carbon cycle during the last deglaciation. *Nature* **514**, 616–619 (2014).

52. 52.

Ahn, J. & Brook, E. J. Siple Dome ice reveals two modes of millennial CO₂ change during the last ice age. *Nat. Commun.* **5**, 3723 (2014).

53. 53.

Bereiter, B. et al. Revision of the EPICA Dome C CO₂ record from 800 to 600 kyr before present. *Geophys. Res. Lett.* **42**, 542–549 (2015).

54. 54.

Olsen, A. et al. The Global Ocean Data Analysis Project version 2 (GLODAPv2) – an internally consistent data product for the world ocean. *Earth Syst. Sci. Data* **8**, 297–323 (2016).

55. 55.

Lisiecki, L. E. & Raymo, M. E. A Pliocene-Pleistocene stack of 57 globally distributed benthic δ¹⁸O records. *Paleoceanography* **20**, PA1003 (2005).

56. 56.

Schrag, D. P., Hampt, G. & Murray, D. W. Pore fluid constraints on the temperature and oxygen isotopic composition of the glacial ocean. *Science* **272**, 1930–1932 (1996).

57. 57.

LeGrande, A. N. & Schmidt, G. A. Global gridded data set of the oxygen isotopic composition in seawater. *Geophys. Res. Lett.* **33**, L12604 (2006).

58. 58.

Zhu, J., Poulsen, C. J. & Tierney, J. E. Simulation of Eocene extreme warmth and high climate sensitivity through cloud feedbacks. *Sci. Adv.* **5**, eaax1874 (2019).

59. 59.

Hurrell, J. W. et al. The community Earth system model: a framework for collaborative research. *Bull. Am. Meteorol. Soc.* **94**, 1339–1360 (2013).

60. 60.

Meehl, G. A. et al. Effects of model resolution, physics, and coupling on Southern Hemisphere storm tracks in CESM1.3. *Geophys. Res. Lett.* **46**, 12408–12416 (2019).

61. 61.

Zhu, J. et al. Reduced ENSO variability at the LGM revealed by an isotope-enabled Earth system model. *Geophys. Res. Lett.* **44**, 6984–6992 (2017).

62. 62.

Stevenson, S. et al. Volcanic eruption signatures in the isotope-enabled last millennium ensemble. *Paleoceanogr. Paleoclimatol.* **34**, 1534–1552 (2019).

63. 63.

Lüthi, D. et al. High-resolution carbon dioxide concentration record 650,000–800,000 years before present. *Nature* **453**, 379–382 (2008).

64. 64.

Louergue, L. et al. Orbital and millennial-scale features of atmospheric CH₄ over the past 800,000 years. *Nature* **453**, 383–386 (2008).

65. 65.

Schilt, A. et al. Atmospheric nitrous oxide during the last 140,000 years. *Earth Planet. Sci. Lett.* **300**, 33–43 (2010).

66. 66.

Peltier, W. R., Argus, D. F. & Drummond, R. Space geodesy constrains ice age terminal deglaciation: The global ICE-6G_C (VM5a) model. *J. Geophys. Res. Solid Earth* **120**, 450–487 (2015).

67. 67.

DiNezio, P. N. et al. Glacial changes in tropical climate amplified by the Indian Ocean. *Sci. Adv.* **4**, eaat9658 (2018).

68. 68.

Duplessy, J. C., Labeyrie, L. & Waelbroeck, C. Constraints on the ocean oxygen isotopic enrichment between the Last Glacial Maximum and the Holocene: Paleoceanographic implications. *Quat. Sci. Rev.* **21**, 315–330 (2002).

69. 69.

Kageyama, M. et al. The PMIP4 contribution to CMIP6–part 4: scientific objectives and experimental design of the PMIP4-CMIP6

Last Glacial Maximum experiments and PMIP4 sensitivity experiments. *Geosci. Model Dev.* **10**, 4035–4055 (2017).

70. 70.

Otto-Bliesner, B. L. et al. The PMIP4 contribution to CMIP6—part 2: two interglacials, scientific objective and experimental design for Holocene and Last Interglacial simulations. *Geosci. Model Dev.* **10**, 3979–4003 (2017).

71. 71.

Lawrence, D. M. et al. Parameterization improvements and functional and structural advances in Version 4 of the Community Land Model. *J. Adv. Model. Earth Sys.* **3**, M03001 (2011).

72. 72.

Bartlein, P. J. & Shafer, S. L. Paleo calendar-effect adjustments in time-slice and transient climatemodel simulations (PaleoCalAdjust v1.0): impact and strategies for data analysis. *Geosci. Model Dev.* **12**, 3889–3913 (2019).

73. 73.

Whitaker, J. S. & Hamill, T. M. Ensemble data assimilation without perturbed observations. *Mon. Weather Rev.* **130**, 1913–1924 (2002).

74. 74.

Hamill, T. M. Interpretation of rank histograms for verifying ensemble forecasts. *Mon. Weather Rev.* **129**, 550–560 (2001).

75. 75.

Jones, T. R. et al. Water isotope diffusion in the WAIS Divide ice core during the Holocene and last glacial. *J. Geophys. Res. Earth Surface* **122**, 290–309 (2017).

76. 76.

Sokratov, S. A. & Golubev, V. N. Snow isotopic content change by sublimation. *J. Glaciol.* **55**, 823–828 (2009).

77. 77.

Comas-Bru, L. et al. Evaluating model outputs using integrated global speleothem records of climate change since the last glacial. *Clim. Past* **15**, 1557–1579 (2019).

78. 78.

Atsawawaranunt, K. et al. The SISAL database: a global resource to document oxygen and carbon isotope records from speleothems. *Earth Syst. Sci. Data* **10**, 1687–1713 (2018).

79. 79.

Blunier, T. & Brook, E. J. Timing of millennial-scale climate change in Antarctica and Greenland during the Last Glacial Period. *Science* **291**, 109–112 (2001).

80. 80.

Stenni, B. et al. Expression of the bipolar see-saw in Antarctic climate records during the last deglaciation. *Nat. Geosci.* **4**, 46–49 (2011).

81. 81.

Watanabe, O. et al. Homogeneous climate variability across East Antarctica over the past three glacial cycles. *Nature* **422**, 509–512 (2003).

82. 82.

Brook, E. J. et al. Timing of millennial-scale climate change at Siple Dome, West Antarctica, during the last glacial period. *Quat. Sci. Rev.* **24**, 1333–1343 (2005).

83. 83.

Stenni, B. et al. The deuterium excess records of EPICA Dome C and Dronning Maud Land ice cores (East Antarctica). *Quat. Sci. Rev.* **29**, 146–159 (2010).

84. 84.

Steig, E. J. et al. Synchronous climate changes in Antarctica and the North Atlantic. *Science* **282**, 92–95 (1998).

85. 85.

Petit, J. R. et al. Climate and atmospheric history of the past 420,000 years from the Vostok ice core, Antarctica. *Nature* **399**, 429–436 (1999).

86. 86.

Markle, B. R. et al. Global atmospheric teleconnections during Dansgaard–Oeschger events. *Nat. Geosci.* **10**, 36–40 (2017).

87. 87.

Vinther, B. M. et al. Synchronizing ice cores from the Renland and Agassiz ice caps to the Greenland Ice Core Chronology. *J. Geophys. Res. Atmos.* **113**, D08115 (2008).

88. 88.

Stuiver, M. & Grootes, P. M. GISP2 oxygen isotope ratios. *Quat. Res.* **53**, 277–284 (2000).

89. 89.

Johnsen, S. J. et al. The $\delta^{18}\text{O}$ record along the Greenland Ice Core Project deep ice core and the problem of possible Eemian climatic instability. *J. Geophys. Res. Oceans* **102**, 26397–26410 (1997).

90. 90.

Andersen, K. K. et al. High-resolution record of Northern Hemisphere climate extending into the last interglacial period. *Nature* **431**, 147–151 (2004).

91. 91.

Holmgren, K. et al. Persistent millennial-scale climatic variability over the past 25,000 years in Southern Africa. *Quat. Sci. Rev.* **22**, 2311–2326 (2003).

92. 92.

Novello, V. F. et al. A high-resolution history of the South American Monsoon from Last Glacial Maximum to the Holocene. *Sci. Rep.* **7**, 44267 (2017).

93. 93.

Cheng, H. et al. The climate variability in northern Levant over the past 20,000 years. *Geophys. Res. Lett.* **42**, 8641–8650 (2015).

94. 94.

Dutt, S. et al. Abrupt changes in Indian summer monsoon strength during 33,800 to 5500 years B.P. *Geophys. Res. Lett.* **42**, 5526–5532 (2015).

95. 95.

Ayliffe, L. K. et al. Rapid interhemispheric climate links via the Australasian monsoon during the last deglaciation. *Nat. Commun.* **4**, 2908 (2013).

96. 96.

Partin, J. W., Cobb, K. M., Adkins, J. F., Clark, B. & Fernandez, D. P. Millennial-scale trends in west Pacific warm pool hydrology since the

Last Glacial Maximum. *Nature* **449**, 452–455 (2007).

97. 97.

Cai, Y. et al. Variability of stalagmite-inferred Indian monsoon precipitation over the past 252,000 y. *Proc. Natl Acad. Sci. USA* **112**, 2954–2959 (2015).

98. 98.

Fleitmann, D. et al. Timing and climatic impact of Greenland interstadials recorded in stalagmites from northern Turkey. *Geophys. Res. Lett.* **36**, L19707 (2009).

99. 99.

Cruz, F. W. et al. Insolation-driven changes in atmospheric circulation over the past 116,000 years in subtropical Brazil. *Nature* **434**, 63–66 (2005).

100. 100.

Hellstrom, J., McCulloch, M. & Stone, J. A detailed 31,000-year record of climate and vegetation change, from the isotope geochemistry of two New Zealand speleothems. *Quat. Res.* **50**, 167–178 (1998).

101. 101.

Grant, K. M. et al. Rapid coupling between ice volume and polar temperature over the past 150,000 years. *Nature* **491**, 744–747 (2012).

102. 102.

Cheng, H. et al. Climate change patterns in Amazonia and biodiversity. *Nat. Commun.* **4**, 1411 (2013).

Acknowledgements

We thank B. Malevich for early discussions and explorations on LGM-to-present data assimilation, and M. Fox and N. Rapp for help in compiling the proxy data. We thank P. DiNezio for providing initial and boundary condition files for the CESM simulations, and B. Markle for assistance in compiling and sharing the ice core water isotope data. This study was supported by National Science Foundation (NSF) grant numbers AGS-1602301 and AGS-1602223, and Heising-Simons Foundation grant numbers 2016-012, 2016-014 and 2016-015. The CESM project is supported primarily by the NSF. This material is based on work supported by the National Center for Atmospheric Research, which is a major facility sponsored by the NSF under Cooperative Agreement No. 1852977. Computing and data storage resources, including the Cheyenne supercomputer (<https://doi.org/10.5065/D6RX99HX>), were provided by the Computational and Information Systems Laboratory (CISL) at NCAR.

Author information

Affiliations

1. Department of Geosciences, University of Arizona, Tucson, AZ, USA

Matthew B. Osman, Jessica E. Tierney & Jonathan King

2. Climate and Global Dynamics Laboratory, National Center for Atmospheric Research, Boulder, CO, USA

Jiang Zhu

3. Department of Atmospheric Sciences, University of Washington, Seattle, WA, USA

Robert Tardif & Gregory J. Hakim

4. Department of Earth and Environmental Sciences, University of Michigan, Ann Arbor, MI, USA

Christopher J. Poulsen

Contributions

M.B.O. conducted the data assimilation, led the analysis and interpretation of the results, and designed the figures. M.B.O. and J.E.T. led the writing of this paper. J.E.T. led the proxy data compilation. J.K. wrote the DASH code, based on methods and input by R.T. and G.J.H. J.Z. and C.J.P. planned and conducted the iCESM simulations. All authors contributed to the design of the study and the writing of this manuscript.

Corresponding author

Correspondence to [Matthew B. Osman](#).

Ethics declarations

Competing interests

The authors declare no competing interests.

Additional information

Peer review information *Nature* thanks William Gray and the other, anonymous, reviewer(s) for their contribution to the peer review of this work. Peer reviewer reports are available.

Publisher's note Springer Nature remains neutral with regard to jurisdictional claims in published maps and institutional affiliations.

Extended data figures and tables

[Extended Data Fig. 1 Time resolution and temporal coverage of the SST proxy data compilation.](#)

a, Histogram of record resolution (denoting the median sample resolution for each record), computed for each proxy type. **b**, Histogram of record

length for each proxy type.

Extended Data Fig. 2 Statistical validation of randomly withheld marine geochemical proxies.

a, From left: observed versus forward-modelled $\delta^{18}\text{O}_c$ mean values for each site using the posterior data assimilation estimates. Shown at right are the associated median $R^2_{\text{validation}}$ scores (each based on $n = \sim 100$ LGMR ensemble members), computed on a per-site basis (see [Methods](#) section “Internal and external validation testing”). **b–d**, As in **a**, but for $\Delta\delta^{18}\text{O}_{\text{p}}(37\text{K})$ (**b**), Mg/Ca (**c**) and TEX₈₆ (**d**), respectively.

Extended Data Fig. 3 Validation using independent $\delta^{18}\text{O}_{\text{p}}$ ice core and speleothem records.

a, 3 ka–preindustrial (PI; 0 ka) posterior $\Delta\delta^{18}\text{O}_{\text{p}}$ field; overlying markers show the observed 3 ka–PI $\Delta\delta^{18}\text{O}_{\text{p}}$ values from speleothems and ice cores. Only records spanning at least 18 of the past 24 kyr are shown. ΔR^2 and ΔRMSEP values denote the change in observed versus posterior assimilated $\Delta\delta^{18}\text{O}_{\text{p}}$ values relative to the prior (that is, iCESM) estimated values. **b–h**, As in **a**, but for values differenced at 6, 9, 12, 14, 16, 18 and 21 ka versus the PI, respectively. **i**, All observed $\Delta\delta^{18}\text{O}_{\text{p}}$ versus model prior values; dashed line indicates the 1:1 relationship. **j**, All observed $\Delta\delta^{18}\text{O}_{\text{p}}$ versus posterior values, which show a strong improvement in ΔR^2 and ΔRMSEP over the prior. Note that each scatter point shown in panels **i**, **j** corresponds to an external validation site shown in panels **a–h**.

Extended Data Fig. 4 Time-comparison of posterior LGMR $\delta^{18}\text{O}_{\text{p}}$ with selected $\delta^{18}\text{O}_{\text{p}}$ ice core and speleothem records.

Uncertainty ranges denote the $\pm 1\sigma$ level (dark) and 95% confidence range (light) from the LGMR ensemble. Also shown for comparison are the full

range (shaded grey) and median iCESM time slice prior values (50-year means) for each site. See also Extended Data Table 2.

Extended Data Fig. 5 Influences on global surface temperature evolution during the past 24 kyr.

a–c, Spatial LGM-to-present correlations between surface air temperature (SAT) and combined greenhouse gas²⁴ and global albedo radiative forcing¹³ (**a**); summer length at 65°S;²⁷ (**b**); and the $-1 \times ^{231}\text{Pa}/^{230}\text{Th}$ AMOC proxy index from Bermuda Rise^{29,30,31} (**c**; shown such that SAT correlations are positive with AMOC strength).

Extended Data Fig. 6 Proxy-specific GMST reconstructions and comparison of Holocene GMST trends.

a, $\delta^{18}\text{O}_c$, (U_{37}^K) , and Mg/Ca-derived GMST reconstructions, derived using both the proxy-only (PO) and data assimilation (DA) approaches. In **a**, the shaded regions show the $\pm 1\sigma$ range across $n = 50$ ensemble members for the DA-based GMST estimates, and $n = 10,000$ realizations for the PO-based GMST estimates (note uncertainty ranges are not shown for the dotted-dashed curves). **b**, Sensitivity of the Holocene GMST evolution to the removal of proxies situated in contiguous 15° latitudinal bands, both for the PO and DA approaches. **c**, Sensitivity of the DA-based Holocene GMST evolution to proxy seasonality (computed by fixing foraminifera growth seasonality to either preindustrial (PI) or LGM monthly SSTs for Mg/Ca and $\delta^{18}\text{O}_c$, or by removing records with seasonal alkenone production for (U_{37}^K)), and to the ‘pooled’ foraminifera species SST calibrations of refs. ^{20,21} (see [Supplementary Information](#)). All ΔGMST time series denote deviations relative to the past 2 kyr.

Extended Data Fig. 7 Hemispheric variability during the past 24 kyr.

Ensemble distribution ($n = 500$) of LGMR-estimated Northern Hemisphere (NH; red) and Southern Hemisphere (SH; blue) mean hemispheric temperatures during the past 24 kyr. Shown at top is the surface temperature spatial difference for the Bølling–Allerød (BA) and Younger Dryas (YD) intervals. Range of hemispheric last deglacial and interglacial onset timings are shown as histograms at bottom. The LGMR is plotted alongside reconstructed decadal hemispheric temperatures from the last millennium reanalysis v2.1^{[17](#)} and HadCRUT5 observational product^{[11](#)}.

Extended Data Table 1 Information on the iCESM simulations used for generating model priors

Extended Data Table 2 Geographical and site identification

information for ice core and speleothem $\delta^{18}\text{O}_\text{p}$ records used for LGMR external validation

Extended Data Table 3 External validation statistics associated with different choices of covariance localization and the 1σ ‘length-scale’ range of the evolving prior sampling

Supplementary information

Supplementary Information

This file contains Supplementary Information sections 1–5.

Peer Review File

Source data

Source Data Fig. 2

Source Data Fig. 4

Rights and permissions

Reprints and Permissions

About this article

Cite this article

Osman, M.B., Tierney, J.E., Zhu, J. *et al.* Globally resolved surface temperatures since the Last Glacial Maximum. *Nature* **599**, 239–244 (2021). <https://doi.org/10.1038/s41586-021-03984-4>

- Received: 26 March 2021
- Accepted: 01 September 2021
- Published: 10 November 2021
- Issue Date: 11 November 2021
- DOI: <https://doi.org/10.1038/s41586-021-03984-4>

Share this article

Anyone you share the following link with will be able to read this content:

[Get shareable link](#)

Sorry, a shareable link is not currently available for this article.

[Copy to clipboard](#)

Provided by the Springer Nature SharedIt content-sharing initiative

[Global temperature changes mapped across the past 24,000 years](#)

- Shaun A. Marcott
- Jeremy D. Shakun

News & Views 10 Nov 2021

This article was downloaded by **calibre** from <https://www.nature.com/articles/s41586-021-03984-4>

| [Section menu](#) | [Main menu](#) |

- Article
- [Published: 10 November 2021](#)

Dynamic slab segmentation due to brittle–ductile damage in the outer rise

- [T. V. Gerya](#) ORCID: orcid.org/0000-0002-1062-2722¹,
- [D. Bercovici](#)² &
- [T. W. Becker](#) ORCID: orcid.org/0000-0002-5656-4564^{3,4,5}

Nature volume 599, pages 245–250 (2021)

- 132 Accesses
- 70 Altmetric
- [Metrics details](#)

Subjects

- [Geodynamics](#)
- [Geophysics](#)
- [Tectonics](#)

Abstract

Subduction is the major plate driving force, and the strength of the subducting plate controls many aspects of the thermochemical evolution of Earth. Each subducting plate experiences intense normal faulting^{1,2,3,4,5,6,7,8,9} during bending that accommodates the transition from

horizontal to downwards motion at the outer rise at trenches. Here we investigate the consequences of this bending-induced plate damage using numerical subduction models in which both brittle and ductile deformation, including grain damage, are tracked and coupled self-consistently. Pervasive slab weakening and pronounced segmentation can occur at the outer-rise region owing to the strong feedback between brittle and ductile damage localization. This slab-damage phenomenon explains the subduction dichotomy of strong plates and weak slabs¹⁰, the development of large-offset normal faults^{6,7} near trenches, the occurrence of segmented seismic velocity anomalies¹¹ and distinct interfaces imaged within subducted slabs^{12,13}, and the appearance of deep, localized intraplate areas of reduced effective viscosity¹⁴ observed at trenches. Furthermore, brittle-viscously damaged slabs show a tendency for detachment at elevated mantle temperatures. Given Earth's planetary cooling history¹⁵, this implies that intermittent subduction with frequent slab break-off episodes¹⁶ may have been characteristic for Earth until more recent times than previously suggested¹⁷.

Access options

Subscribe to Journal

Get full journal access for 1 year

\$199.00

only \$3.90 per issue

[Subscribe](#)

All prices are NET prices.

VAT will be added later in the checkout.

Tax calculation will be finalised during checkout.

Rent or Buy article

Get time limited or full article access on ReadCube.

from \$8.99

[Rent or Buy](#)

All prices are NET prices.

Additional access options:

- [Log in](#)
- [Access through your institution](#)
- [Learn about institutional subscriptions](#)

Fig. 1: Dynamics of subduction and slab segmentation for a 40-million-year-old oceanic plate.

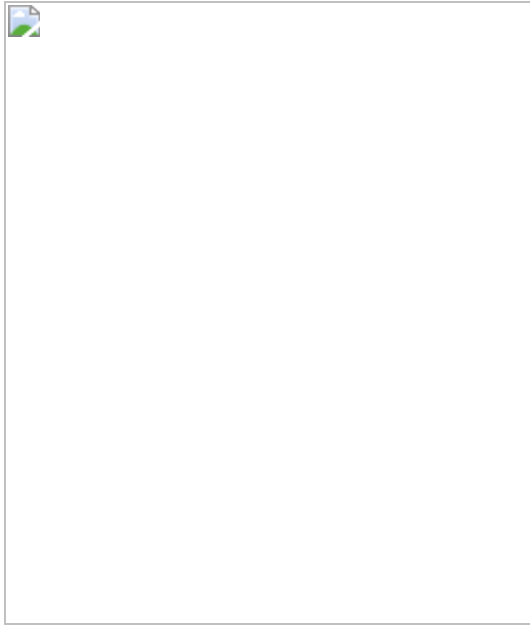


Fig. 2: Development of large-offset normal faults in the reference model and at the Japan Trench.

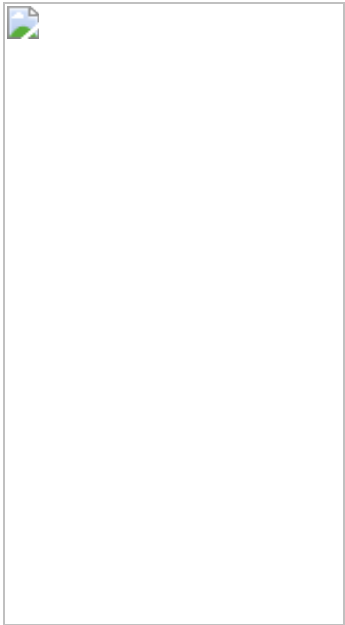


Fig. 3: Development of moderate-offset (throw ≤ 250 m) normal faults in the reference model and at the southeast portion of the Middle American Trench.

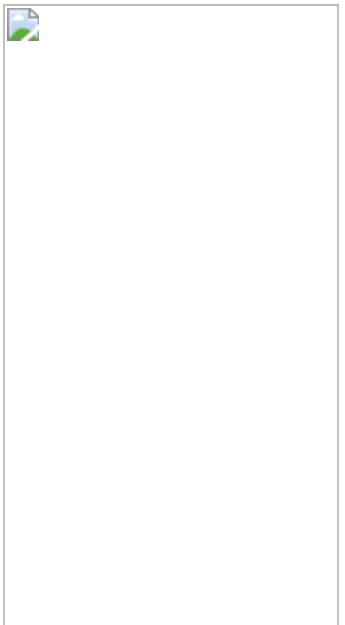
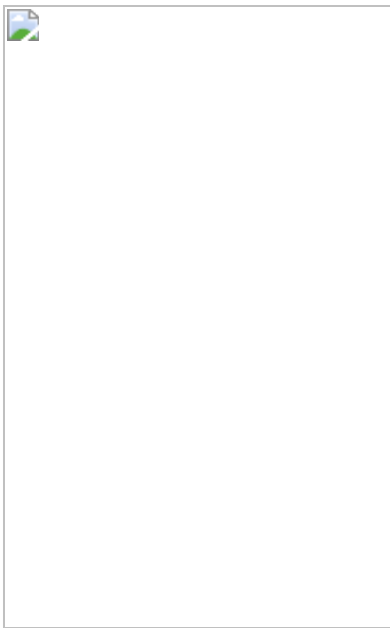


Fig. 4: Comparison of slab-segment width measured in the reference model and within the Japan slab.



Fig. 5: Comparison of modelled grain-size distribution in the reference model with seismic discontinuities in the Japan slab.



Data availability

All input files used in the numerical modelling are available at <https://doi.org/10.17605/OSF.IO/bnvth>. [Source data](#) are provided with this paper.

Code availability

The C and Matlab codes used for numerical experiments and visualization are available at <https://doi.org/10.17605/OSF.IO/bnvth>.

References

1. 1.

Ranero, C. R., Phipps Morgan, J. & Reichert, C. Bending-related faulting and mantle serpentinization at the Middle America Trench. *Nature* **425**, 367–373 (2003).

2. 2.

Ranero, C. R. & Sallarès, V. Geophysical evidence for hydration of the crust and mantle of the Nazca Plate during bending at the North Chile Trench. *Geology* **32**, 549–552 (2004).

3. 3.

Grevemeyer, I., Ranero, C. R., Flueh, E. R., Kläschen, D. & Bialas, J. Passive and active seismological study of bending-related faulting and mantle serpentinization at the Middle America Trench. *Earth Planet. Sci. Lett.* **258**, 528–542 (2007).

4. 4.

Faccenda, M., Gerya, T. V. & Burlini, L. Deep slab hydration induced by bending related variations in tectonic pressure. *Nat. Geosci.* **2**, 790–793 (2009).

5. 5.

Van Avendonk, H. J. A., Holbrook, W. S., Lizarralde, D. & Denyer, P. Structure and serpentinization of the subducting Cocos Plate offshore

Nicaragua and Costa Rica. *Geochem. Geophys. Geosyst.* **12**, Q06009 (2011).

6. 6.

Nakamura, Y., Kodaira, S., Miura, S., Regalla, C., Takahashi, N. High-resolution seismic imaging in the Japan Trench axis area off Miyagi, northeastern Japan. *Geophys. Res. Lett.* **40**, 1713–1718 (2013).

7. 7.

Boston, B., Moore, G. F., Nakamura, Y. & Kodaira, S. Outer-rise normal fault development and influence on near-trench décollement propagation along the Japan Trench, off Tohoku. *Earth Planets Space* **66**, 135 (2014).

8. 8.

Shillington, D. J. et al. Link between plate fabric, hydration and subduction zone seismicity in Alaska. *Nat. Geosci.* **8**, 961–964 (2015).

9. 9.

Korenaga, J. On the extent of mantle hydration caused by plate bending. *Earth Plant. Sci. Lett.* **457**, 1–9 (2017).

10. 10.

Petersen, R. I., Stegman, D. R. & Tackley, P. J. The subduction dichotomy of strong plates and weak slabs. *Solid Earth*. <https://doi.org/10.5194/se-2016-56> (2016).

11. 11.

Tao, K., Grand, S. P. & Niu, F. Seismic structure of the upper mantle beneath eastern Asia from full waveform seismic tomography. *Geochem. Geophys. Geosyst.* **19**, 2732–2763 (2018).

12. 12.

Kawakatsu, H. et al. Seismic evidence for sharp lithosphere–asthenosphere boundaries of oceanic plates. *Science* **324**, 499–502 (2009).

13. 13.

Wang, X. et al. Distinct slab interfaces imaged within the mantle transition zone. *Nat. Geosci.* **13**, 822–827 (2020).

14. 14.

Freed, A. M. et al. Resolving depth-dependent subduction zone viscosity and afterslip from postseismic displacements following the 2011 Tohoku-oki, Japan earthquake. *Earth Planet. Sci. Lett.* **459**, 279–290 (2017).

15. 15.

Herzberg, C. et al. Thermal history of the Earth and its petrological expression. *Earth Planet. Sci. Lett.* **292**, 79–88 (2010).

16. 16.

van Hunen, J. & van den Berg, A. Plate tectonics on the early Earth: limitations imposed by strength and buoyancy of subducted lithosphere. *Lithos* **103**, 217–235 (2008).

17. 17.

Sizova, E., Gerya, T., Brown, M. & Perchuk, L. L. Subduction styles in the Precambrian: insight from numerical experiments. *Lithos* **116**, 209–229 (2010).

18. 18.

Zhong, S. & Davies, G. F. Effects of plate and slab viscosities on the geoid. *Earth Plant. Sci. Lett.* **170**, 487–496 (1999).

19. 19.

Billen, M. I. & Gurnis, M. Constraints on subducting plate strength within the Kermadec Trench. *J. Geophys. Res.* **110**, B05407 (2005).

20. 20.

van Summeren, J., Conrad, C. P. & Lithgow-Bertelloni, C. The importance of slab pull and a global asthenosphere to plate motions. *Geochem. Geophys. Geosyst.* **13**, Q0AK03 (2012).

21. 21.

Garel, F. et al. Interaction of subducted slabs with the mantle transition-zone: a regime diagram from 2-D thermo-mechanical models with a mobile trench and an overriding plate. *Geochem. Geophys. Geosyst.* **15**, 1739–1765 (2014).

22. 22.

Tao, W. C. & O'Connell, R. J. Deformation of a weak subducted slab and variation of seismicity with depth. *Nature* **361**, 626–628 (1993).

23. 23.

Wu, B., Conrad, C. P., Heuret, A., Lithgow-Bertelloni, C. & Lallemand, S. Reconciling strong slab pull and weak plate bending: the plate motion constraint on the strength of mantle slabs. *Earth Planet. Sci. Lett.* **272**, 412–421 (2008).

24. 24.

Gerya, T. V., Connolly, J. A. D. & Yuen, D. A. Why is terrestrial subduction one-sided? *Geology* **36**, 43–46 (2008).

25. 25.

Čížková, H., van Hunen, J., van den Berg, A. P. & Vlaar, N. J. The influence of rheological weakening and yield stress on the interaction of slabs with the 670-km discontinuity. *Earth Planet. Sci. Lett.* **199**, 447–457 (2002).

26. 26.

Ribe, N. M. Bending mechanics and mode selection in free subduction: a thin-sheet analysis. *Geophys. J. Int.* **180**, 559–576 (2010).

27. 27.

Ghosh, A., Becker, T. W. & Zhong, S. J. Effects of lateral viscosity variations on the geoid. *Geophys. Res. Lett.* **37**, L01301 (2010).

28. 28.

Ranalli, G. *Rheology of the Earth* (Chapman and Hall, 1995).

29. 29.

Funiciello, F. et al. Trench migration, net rotation and slab–mantle coupling. *Earth Planet. Sci. Lett.* **271**, 233–240.

30. 30.

Liu, L. & Stegman, D. R. Segmentation of the Farallon slab. *Earth Planet. Sci. Lett.* **311**, 1–10 (2011).

31. 31.

Craig, T. J., Copley, A. & Jackson, J. A reassessment of outer-rise seismicity and its implications for the mechanics of oceanic lithosphere. *Geophys. J. Int.* **197**, 63–89 (2014).

32. 32.

Bercovici, D., Ricard, Y. Mechanisms for the generation of plate tectonics by two- phase grain-damage and pinning. *Phys. Earth Planet. Inter.* **202–203**, 27–55 (2012).

33. 33.

Mulyukova, E. & Bercovici, D. Formation of lithospheric shear zones: effect of temperature on two-phase grain damage. *Phys. Earth Planet. Inter.* **270**, 195–212 (2017).

34. 34.

Mulyukova, E. & Bercovici, D. Collapse of passive margins by lithospheric damage and plunging grain size. *Earth. Planet. Sci. Lett.* **484**, 341–352 (2018).

35. 35.

Mulyukova, E. & Bercovici, D. The generation of plate tectonics from grains to global scales: a brief review. *Tectonics* **38**, 4058–4076 (2019).

36. 36.

Bercovici, D. & Mulyukova, E. Evolution and demise of passive margins through grain mixing and damage. *Proc. Natl Acad. Sci. USA* **118**, e2011247118 (2021).

37. 37.

Gurnis, M., Hall, C. & Lavier, L., Evolving force balance during incipient subduction. *Geochem. Geophys. Geosyst.* **5**, Q07001 (2004).

38. 38.

Masson, D. G. Fault patterns at outer trench walls. *Mar. Geophys. Res.* **13**, 209–225 (1991).

39. 39.

Ranero, C. R., Villasenor, A., Morgan, J. P. & Weinrebe, W. Relationship between bend-faulting at trenches and intermediate-depth seismicity. *Geochem. Geophys. Geosyst.* **6**, Q12002 (2005).

40. 40.

Lavier, L. L., Buck, W. R. & Poliakov, A. N. B. Factors controlling normal fault offset in an ideal brittle layer. *J. Geophys. Res.* **105**, 23431–23442 (2000).

41. 41.

Choi, E., Lavier, L. & Gurnis, M. Thermomechanics of mid-ocean ridge segmentation. *Phys. Earth Planet. Inter.* **171**, 374–386 (2008).

42. 42.

Whitney, D. L., Teyssier, C., Rey, P. & Buck, W. R. Continental and oceanic core complexes. *Geol. Soc. Am. Bull.* **125**, 273–298 (2013).

43. 43.

Hirauchi, K., Fukushima, K., Kido, M., Muto, J. & Okamoto, A. Reaction-induced rheological weakening enables oceanic plate subduction. *Nat. Commun.* **7**, 12550 (2016).

44. 44.

Duretz, T. et al. The importance of structural softening for the evolution and architecture of passive margins. *Sci. Rep.* **6**, 38704 (2016).

45. 45.

John, T. et al. Generation of intermediate-depth earthquakes by self-localizing thermal runaway. *Nat. Geosci.* **2**, 137–140 (2009).

46. 46.

Pozzi, G. et al. Coseismic ultramylonites: an investigation of nanoscale viscous flow and fault weakening during seismic slip. *Earth Planet. Sci. Lett.* **516**, 164–175 (2019).

47. 47.

Verberne, B. A. et al. Microscale cavitation as a mechanism for nucleating earthquakes at the base of the seismogenic zone. *Nat. Commun.* **8**, 1645 (2017).

48. 48.

Craig, T. J., Copley, A. & Middleton, T. A. Constraining fault friction in oceanic lithosphere using the dip angles. *Earth Planet. Sci. Lett.* **392**, 94–99 (2014).

49. 49.

Brace, W. F. & Kohlstedt, D. T. Limits on lithospheric stress imposed by laboratory experiments. *J. Geophys. Res.* **85**, 6248–6252 (1980).

50. 50.

Boston, B., Moore, G. F., Nakamura, Y. & Kodaira, S. Forearc slope deformation above the Japan Trench megathrust: implications for subduction erosion. *Earth Planet. Sci. Lett.* **462**, 26–34 (2017).

51. 51.

Boneh, Y. et al. Intermediate-depth earthquakes controlled by incoming plate hydration along bending-related faults. *Geophys. Res. Lett.* **46**, 3688–3697 (2019).

52. 52.

Naliboff, J. B., Billen, M. I., Gerya, T. & Saunders, J. Dynamics of outer rise faulting in oceanic–continental subduction systems. *Geochem. Geophys. Geosyst.* **14**, 2310–2327 (2013).

53. 53.

Faul, U. H. & Jackson, I. The seismological signature of temperature and grain size variations in the upper mantle. *Earth Planet. Sci. Lett.* **234**, 119–134 (2005).

54. 54.

Honda, S. Strength of slab inferred from the seismic tomography and geologic history around the Japanese Islands. *Geochem. Geophys. Geosyst.* **15**, 1333–1347 (2014).

55. 55.

Turner, A. J., Katz, R. F. & Behn, M. D. Grain-size dynamics beneath mid-ocean ridges: Implications for permeability and melt extraction. *Geochem. Geophys. Geosyst.* **16**, 925–946 (2015).

56. 56.

Gerya, T. V. & Yuen, D. A., Characteristics-based marker-in-cell method with conservative finite-differences schemes for modeling geological flows with strongly variable transport properties. *Phys. Earth Planet. Inter.* **140**, 293–318 (2003).

57. 57.

Gerya T. V. *Introduction to Numerical Geodynamic Modelling* 2nd edn (Cambridge Univ. Press, 2019).

58. 58.

Karato, S. & Wu, P. Rheology of the upper mantle: a synthesis. *Science* **260**, 771–778 (1993).

59. 59.

Hofmeister, A. M. Mantle values of thermal conductivity and the geotherm from phonon lifetimes. *Science* **283**, 1699–1706 (1999).

60. 60.

Turcotte, D. L. & Schubert, G. *Geodynamics* (Cambridge Univ. Press, 2002).

61. 61.

Clauser, C. & Huenges, E. in *Rock Physics and Phase Relations* AGU Reference Shelf 3 (ed. Ahrens, T. J.) 105–126 (American Geophysical Union, 1995).

62. 62.

Hirth, G. & Kohlstedt, D. in *Subduction Factor Monograph Vol. 138* (ed. Eiler, J.) 83–105 (American Geophysical Union, 2003).

63. 63.

Hilairet, N. B. et al. High-pressure creep of serpentine, interseismic deformation, and initiation of subduction. *Science* **318**, 1910–1913 (2007).

64. 64.

Schmeling, H. et al. A benchmark comparison of spontaneous subduction models: Towards a free surface. *Phys. Earth Planet. Inter.* **171**, 198–223 (2008).

65. 65.

Gerya, T. V. & Yuen, D. A. Rayleigh–Taylor instabilities from hydration and melting propel “cold plumes” at subduction zones. *Earth Planet. Sci. Lett.* **212**, 47–62 (2003).

66. 66.

Baitsch-Ghirardello, B., Gerya, T. V. & Burg, J.-P. Geodynamic regimes of intra-oceanic subduction: implications forearc extension vs. shortening processes. *Gondwana Res.* **25**, 546–560 (2014).

67. 67.

Katsura, T. & Ito, E. The system Mg_2SiO_4 – Fe_2SiO_4 at high pressures and temperatures: precise determination of stabilities of olivine,

modified spinel, and spinel. *J. Geophys. Res.* **94**, 663–670 (1989).

68. 68.

Ito, E. et al. Negative pressure–temperature slopes for reactions forming MgSiO_3 perovskite from calorimetry. *Science* **2J9**, 1275–1278 (1990).

69. 69.

Ito, K. & Kennedy, G. C. in *The Structure and Physical Properties of the Earth's Crust* Geophysical Monograph Series 14 (ed. Heacock, J. G.) 303–314 (American Geophysical Union, 1971).

70. 70.

Bercovici, D. & Ricard, Y. Generation of plate tectonics with two-phase grain-damage and pinning: source–sink model and toroidal flow. *Earth Planet. Sci. Lett.* **365**, 275–288 (2013).

71. 71.

Bercovici, D. & Ricard, Y. Plate tectonics, damage and inheritance. *Nature* **508**, 513–516 (2014).

72. 72.

Bercovici, D., Schubert, G. & Ricard, Y. Abrupt tectonics and rapid slab detachment with grain damage. *Proc. Natl Acad. Sci. USA* **112**, 1287–1291 (2015).

73. 73.

Rozel, A., Ricard, Y. & Bercovici, D. A thermodynamically self-consistent damage equation for grain size evolution during dynamic recrystallization. *Geophys. J. Int.* **184**, 719–728 (2011).

74. 74.

Hayes, P. et al. Slab2, a comprehensive subduction zone geometry model. *Science* **362**, 58–61 (2018).

75. 75.

Bird, P. An updated digital model of plate boundaries. *Geochim. Geophys. Geosyst.* **4**, 1027 (2003).

Acknowledgements

This work was supported by SNF projects 200021_182069 and 200021_192296 and ETH+ project BECCY (to T.V.G.) and NSF EAR-1853856 (to T.W.B.) and NSF EAR-1853184 (to D.B.). The simulations were performed on the ETH-Zurich Euler and Leonhard clusters.

Author information

Affiliations

1. Department of Earth Sciences, Swiss Federal Institute of Technology Zurich, Zurich, Switzerland

T. V. Gerya

2. Department of Earth and Planetary Sciences, Yale University, New Haven, CT, USA

D. Bercovici

3. Institute for Geophysics, Jackson School of Geosciences, The University of Texas at Austin, Austin, TX, USA

T. W. Becker

4. Department of Geological Sciences, Jackson School of Geosciences, The University of Texas at Austin, Austin, TX, USA

T. W. Becker

5. Oden Institute for Computational Engineering & Sciences, The University of Texas at Austin, Austin, TX, USA

T. W. Becker

Contributions

T.V.G. programmed the numerical code, designed the study and conducted the numerical experiments; D.B. formulated the grain size evolution algorithm and programmed the numerical code; and T.W.B. compiled and annotated Extended Data Figs. [7](#), [8](#) and provided related text. All authors discussed the results, problems and methods, and contributed to interpretation of the data and writing the paper.

Corresponding author

Correspondence to [T. V. Gerya](#).

Ethics declarations

Competing interests

The authors declare no competing interests.

Additional information

Peer review information *Nature* thanks the anonymous reviewers for their contribution to the peer review of this work. Peer reviewer reports are available.

Publisher's note Springer Nature remains neutral with regard to jurisdictional claims in published maps and institutional affiliations.

Extended data figures and tables

Extended Data Fig. 1 Initial conditions for two types of subduction model explored in this study.

a, Model setup with free subducting plate detached from the right model boundary; subducting plate age changes to 1,000 yr linearly with the distance within 500 km at the right model boundary. **b**, Model setup with subducting plate attached to the right model boundary; subducting plate age does not change toward the boundary. White lines with numbers are isotherms in °C.

Extended Data Fig. 2 Influence of faults weakening and grain size evolution on subduction dynamics.

The distribution of the effective viscosity (left column, panels **a–d**) and grain size in the mantle (right column, panels **e–h**). **a, e**, Model with both faults weakening and grain size evolution (model xbeqc, Extended Data Table 2). **b, f**, Model with faults weakening but without grain size evolution (model xbeqca, Extended Data Table 2). **c, g**, Model with grain size evolution but without faults weakening ($\mu_0 = \mu_1 = 0.6$ for the lower oceanic crust and lithosphere–asthenosphere mantle, model xbeqcb, Extended Data Table 2). **d, h**, Model with neither fault weakening nor grain size evolution ($\mu_0 = \mu_1 = 0.6$ for the lower oceanic crust and lithosphere–asthenosphere mantle, model xbeqcc, Extended Data Table 2). Mantle temperature is taken 100 K higher than present day values. Other parameters are the same as in the reference model (Fig. 1). Solid black lines indicate position of 1225 °C isotherm.

Extended Data Fig. 3 Influence of model parameters on subduction dynamics in models with standard grain size evolution.

The distribution of the effective viscosity (left column, panels **a–d**) and grain size in the mantle (right column, panels **e–h**). **a, e**, Failed subduction initiation in the model with 40 Ma subducting plate but without faults weakening ($\mu_0 = \mu_1 = 0.6$ for the lower oceanic crust and lithosphere–

asthenosphere mantle, $h_{\max} = 6$ mm for the grain size color code, model xbeqab, Extended Data Table 2). **b, f**, No slab segmentation in the model with 40 Myr old slab but with 2.5 times slower rate of faults weakening with strain ($h_{\max} = 10$ mm, model xbes, Extended Data Table 2). **c, g**, Reference slab segmentation model with 40 Myr subducting plate and standard faults weakening ($h_{\max} = 6$ mm, model xbeq, Fig. 1, Extended Data Table 2). **d, h**, Wider slab segments in the model with 100 Myr old slab and standard fault weakening ($h_{\max} = 10$ mm, model xber, Extended Data Table 2). Mantle temperature is taken at present day values. Other parameters are the same as in the reference model (Fig. 1). Solid black lines indicate position of 1225 °C isotherm.

[Extended Data Fig. 4 Influence of grain size evolution and faults weakening on subduction dynamics.](#)

The distribution of the effective viscosity (left column, panels **a–d**) and grain size in the mantle (right column, panels **e–h**). **a, e**, Model with both fault weakening and grain size evolution (40 Myr old slab, model xbeqd, Extended Data Table 2). **b, f**, Model with fault weakening but without grain size evolution (40 Myr old slab, model xbeqda, Extended Data Table 2). **c, g**, Model with both fault weakening and grain size evolution (100 Myr old slab, model xbeqq, Extended Data Table 2). **d, h**, Model with grain size evolution but without fault weakening (100 Myr old slab, model xbeqs, Extended Data Table 2). Mantle potential temperature in **a, b, e, f** is 150 K higher than present day values. Other parameters are the same as in the reference model (Fig. 1). Solid black lines indicate position of 1225 °C isotherm.

[Extended Data Fig. 5 Influence of pre-existing faults in the subducting plate on slab segmentation and subduction dynamics.](#)

a, e, Model with 20 km spaced faults dipping toward the trench (model xbeql, Extended Data Table 2). **b, f**, Model with 10 km spaced faults dipping toward the trench (model xbeqm, Extended Data Table 2). **c, g**, Model with 5 km spaced faults dipping toward the trench (model xbeqn,

Extended Data Table 2). **d, h**, Model with 10 km spaced faults dipping outward the trench (model xbeqo, Extended Data Table 2). Pre-existing faults are prescribed as 1 km wide and 14 km deep zones of weak basaltic crust and serpentinized mantle within stronger gabbroic crust and lithospheric mantle, respectively (Extended Data Table 1). Initial fault dip is 63°.

Extended Data Fig. 6 Gradual development of large-offset normal faults in the reference model (Fig. 1).

a–d, Distribution of the plastic strain γ (regions with $\gamma > 0.02$ are shown) and mantle grain size in the lithosphere. Solid white line indicates position of the reference surface along which fault throws are evaluated (Methods). **e–h**, Fault throw distribution for respective time steps shown in **a–d**. Only faults with throw >20 m are considered.

[Source data](#)

Extended Data Fig. 7 Positions of five along-dip seismic tomography profiles (blue solid lines with circles) for the Japan slab analysed in Fig. 4c, d and Extended Data Fig. 8.

Colour code corresponds to slab upper surface based on seismicity depths from SLAB2.0 model⁷⁴. Solid blue lines show positions of plate boundaries⁷⁵.

Extended Data Fig. 8 Tomographic images for five analyzed (Fig. 4d, Methods) seismic tomography profiles of the Japan slab (Extended Data Fig. 7).

The distribution of v_p (left column, panels **a–e**) and v_s (right column, panels **f–j**) seismic velocity anomaly is based on the tomography model of Tao et al.¹³. Positions of segment boundaries (red triangles) defined along the middle-slab line (red solid lines) are inferred on the basis of visual inspection (Methods).

Extended Data Table 1 Physical properties of rocks^{58,59,60,61,62,63} used in numerical experiments

Extended Data Table 2 Conditions and results of numerical experiments

Supplementary information

Peer Review File

Source data

Source Data Fig. 2

Source Data Fig. 3

Source Data Fig. 4

Source Data Extended Data Fig. 6

Rights and permissions

Reprints and Permissions

About this article

Cite this article

Gerya, T.V., Bercovici, D. & Becker, T.W. Dynamic slab segmentation due to brittle–ductile damage in the outer rise. *Nature* **599**, 245–250 (2021). <https://doi.org/10.1038/s41586-021-03937-x>

- Received: 30 September 2020
- Accepted: 20 August 2021

- Published: 10 November 2021
- Issue Date: 11 November 2021
- DOI: <https://doi.org/10.1038/s41586-021-03937-x>

Share this article

Anyone you share the following link with will be able to read this content:

[Get shareable link](#)

Sorry, a shareable link is not currently available for this article.

[Copy to clipboard](#)

Provided by the Springer Nature SharedIt content-sharing initiative

This article was downloaded by **calibre** from <https://www.nature.com/articles/s41586-021-03937-x>

| [Section menu](#) | [Main menu](#) |

- Article
- Open Access
- [Published: 27 October 2021](#)

Fossil evidence unveils an early Cambrian origin for Bryozoa

- [Zhiliang Zhang](#) [ORCID: orcid.org/0000-0003-2296-5973^{1,2}](#),
- [Zhifei Zhang](#) [ORCID: orcid.org/0000-0003-0325-5116¹](#),
- [Junye Ma³](#),
- [Paul D. Taylor](#) [ORCID: orcid.org/0000-0002-3127-080X⁴](#),
- [Luke C. Strotz](#) [ORCID: orcid.org/0000-0002-8818-1832¹](#),
- [Sarah M. Jacquet](#) [ORCID: orcid.org/0000-0001-6673-4929⁵](#),
- [Christian B. Skovsted](#) [ORCID: orcid.org/0000-0001-7366-7680⁶](#),
- [Feiyang Chen](#) [ORCID: orcid.org/0000-0001-8994-4187^{1,2,7}](#),
- [Jian Han](#) [ORCID: orcid.org/0000-0002-2134-4078¹](#) &
- [Glenn A. Brock](#) [ORCID: orcid.org/0000-0002-2277-7350^{1,2}](#)

Nature volume 599, pages 251–255 (2021)

- 8470 Accesses
- 1 Citations
- 180 Altmetric
- [Metrics details](#)

Subjects

- [Palaeontology](#)
- [Taxonomy](#)

Abstract

Bryozoans (also known as ectoprocts or moss animals) are aquatic, dominantly sessile, filter-feeding lophophorates that construct an organic or calcareous modular colonial

(clonal) exoskeleton^{1,2,3}. The presence of six major orders of bryozoans with advanced polymorphisms in lower Ordovician rocks strongly suggests a Cambrian origin for the largest and most diverse lophophorate phylum^{2,4,5,6,7,8}. However, a lack of convincing bryozoan fossils from the Cambrian period has hampered resolution of the true origins and character assembly of the earliest members of the group. Here we interpret the millimetric, erect, bilaminate, secondarily phosphatized fossil *Protomelission gatehousei*⁹ from the early Cambrian of Australia and South China as a potential stem-group bryozoan. The monomorphic zooid capsules, modular construction, organic composition and simple linear budding growth geometry represent a mixture of organic Gymnolaemata and biomineralized Stenolaemata character traits, with phylogenetic analyses identifying *P. gatehousei* as a stem-group bryozoan. This aligns the origin of phylum Bryozoa with all other skeletonized phyla in Cambrian Age 3, pushing back its first occurrence by approximately 35 million years. It also reconciles the fossil record with molecular clock estimations of an early Cambrian origination and subsequent Ordovician radiation of Bryozoa following the acquisition of a carbonate skeleton^{10,11,12,13}.

[Download PDF](#)

Main

The Cambrian fossil record chronicles in exceptional detail the emergence of major bilaterian clades and continues to provide chronological constraints on the evolutionary diversification of disparate metazoans from a common ancestor^{12,13,14,15}. Nearly all animal phyla, including soft-bodied Deuterostoma¹⁴, Entoprocta¹⁶, Phoronida¹⁷ and Priapulida¹², made their first appearance during the Cambrian evolutionary radiation^{12,13,18}. A key exception is the ‘missing’ colonial lophotrochozoan phylum Bryozoa, in which six of the eight recognized orders belonging to the classes Stenolaemata and Gymnolaemata appear abruptly with considerable diversity during the early Ordovician period^{6,7,19,20}. Furthermore, there is a major time gap (approximately 44 million years) between the first fossil record of unequivocal bryozoans in the earliest Ordovician (Tremadocian)^{4,7} and the deeper origination in the early Cambrian (Terreneuvian) estimated using modern molecular clock analyses^{10,11,12,21}.

Bryozoa is the most speciose of the lophophorate phyla firmly nested within Lophotrochozoa, characterized by iterated units (zooids) demonstrating hierarchical levels of modularity, and (apart from one genus) is the only exclusively colonial group of metazoans^{1,22,23,24}. The key innovation of modularity initiated a novel pattern of colonial growth that led directly to a burst of morphological diversification and subsequent ecosystem proliferation, especially during the Great Ordovician

Biodiversification Event^{1,18,25,26}. Increased fossil sampling has gradually pushed back the oldest occurrence of bryozoans^{19,20}, most recently into the early Tremadocian⁴, while the bryozoan affinity of the late Cambrian (Furongian) genus *Pywackia* remains highly debated^{2,4,7,18}. Hence, a Cambrian origin for Bryozoa is not completely unpredicted and many authors have suggested a non-mineralized organic colony might explain the lack of a Cambrian record for the group^{3,4,5,6,7,19,20}.

Here we describe rare but exquisitely preserved specimens of a millimetric modular fossil, *Protomelission gatehousei*⁹ from the early Cambrian of Australia and South China (Extended Data Fig. 1). Scanning electron microscopy (Figs. 1, 2, Extended Data Figs. 2, 3) and X-ray tomographic microscopy (Fig. 3, Extended Data Fig. 4) images reveal a combination of character traits that suggest a stem-group bryozoan affinity for *P. gatehousei* but distinguish the taxon from all extant and extinct clades. The interpretation of this secondarily phosphatized fossil from lower Cambrian rocks of South China and South Australia as a putative bryozoan indicates that modular bryozoans evolved synchronously with most other stem-group metazoans during the Cambrian evolutionary radiation¹².

Fig. 1: *Protomelission gatehousei* from the Cambrian Wirrealpa Limestone, South Australia.

 **figure1**

a–g, Holotype, SADME 10470. **a**, Front side of the colony originally published in ref. [2](#), noting the seven series of zooids. Top box corners indicate the area shown in **f**; bottom box corners show the broken-off part in **c**. **b**, The top broken part of **a**. **c**, The lower broken part of **a**. **d**, Oblique lateral view of the bilaminar colony. **e**, Enlarged view of **d**, showing the staggered budding pattern and the curved basal walls of the two back-to-back layers (arrows and tailed arrows) in the bifoliate colony. **f**, Quincuncial arrangement of sub-hexagonal zooids with broken frontal walls, originally published in ref. [2](#). **g**, Lateral view of uncovered zooids; note the minute spoon-shaped structure (arrow) at the proximal end of basal wall extending backwards underneath the distal part of the parent zooid. **h, i**, SADME 10470-2. **h**, Lateral view of a broken colony, showing the largely broken frontal walls (tailed arrows) and basal walls of opposite layer (arrows). **i**, Enlarged view of three adjacent zooids. Note the

dome shape of the distal part of frontal wall (tailed arrows), and almost circular orifice of zooid. B, basal wall; F, frontal wall.

Fig. 2: *Protomelission gatehousei* from the Cambrian Xihaoping Member, Dengying Formation, South China, ELI XYB 4 AN02.

 figure2



a, Front side of the colony, noting the five series of zooids, box corners indicate the area shown in **d**. **b**, Oblique lateral view of the bifoliate colony, showing zooids in the back-to-back layers and the median mesotheca (arrow). **c**, Oblique basal view showing holdfast base and zooids of the opposite layer, box corners indicate the area shown in **f**. **d**, Quincuncial arrangement of hexagonal zooids; note spaces between adjacent zooids (arrows), frontal walls (tailed arrows) and basal walls. **e**, Lateral view showing the staggered pattern of zooids (arrows) in both layers, and a frontal wall on the margin (tailed arrow). **f**, Hexagonal zooids, showing the bases of the frontal walls (arrows). **g**, Enlargement of the fine wrinkles on the frontal walls, and granular phosphatized basal wall (arrow). B, basal wall.

Fig. 3: X-ray tomographic microscopy images of *P. gatehousei*.

 **figure3**

a, ELI XYB 4 AN02, longitudinal section. Frontal wall (tailed arrow) and basal wall (arrow) are indicated. **b–g**, SADME 10470. **b, c**, Tangential section. **b**, Five series of zooids and related four lines of frontal walls (tailed arrows). The space between adjacent zooids marked by arrows. **c**, Mesotheca/median lamina connected with above

basal walls, box corners indicate the area shown in **h**. **d**, **e**, Transverse section. **d**, Zooids on both layers along with median mesotheca, noting new budding zooid (tailed arrow) and daughter basal wall overlapping parent frontal wall (arrow). **e**, Possible zooidal connection through the space of the median mesotheca (arrow), box corners indicate area shown in **i**. **f**, **g**, Longitudinal section, showing bilaminate pattern of zooids on the two back-to-back layers. **f**, Staggered pattern of zooids in both layers. The curved basal wall is indicated with arrows. **g**, Probable connections between adjacent zooids from back-to-back layers through space of median mesotheca, indicated by tailed arrows. **h**, Two pairs of zooids, magnified, showing spoon-shaped structures of parent and daughter zooids indicated by tailed arrows. **i**, Close-up of zooidal connection. Blue, frontal wall; green, mesotheca with secondary phosphatic cement in yellow; red, basal wall. H, holdfast; M, mesotheca; Z, zooid.

Results

The finely phosphatized millimetric colony of *P. gatehousei* is bifoliate, compressed, lacks bifurcation, tapers apically and has an elliptical holdfast at the base (Figs. [1a–c](#), [2a–c](#), [3a](#)), suggesting an erect, self-supported colony anchored to the substrate (Extended Data Fig. [2a, b](#)). Colonies range from 1.8–2.2 mm in height, 0.1–0.2 mm in thickness and 1.0–1.5 mm in width, which is very similar to the width of Ordovician erect bifoliate cryptostomes^{[27](#)} (2.1 mm). The erect colony is composed of two layers of zooids (Figs. [1d–e](#), [2b](#), Extended Data Figs. [2c](#), [3c](#)) arranged in simple linear series as back-to-back laminae^{[23,27](#)} (Fig. [3a, d–g](#), Extended Data Fig. [4](#), Supplementary Videos [1–6](#)).

The zooids are sub-hexagonal in outline and flat box-shaped (Figs. [1f](#), [h](#), [2d](#), Extended Data Fig. [3a–c](#)). They are uniform in size, with an average width of 174 µm and length of 220 µm (Extended Data Table [1](#)). There are up to 100 zooids in total in the bilaminate colony (Fig. [1a](#)). Polymorphic differentiation of the zooids is absent, and there are no diaphragm-like structures in the zooids^{[7](#)} (Figs. [1–3](#), Extended Data Figs. [2–4](#)). Zooids are inclined at about 25° to the median lamina (mesotheca) (Fig. [3f](#), Extended Data Fig. [4a](#)) and form a quincuncial pattern on the surface of the colonies (Figs. [1f](#), [2d](#), [f](#), [3b](#), Extended Data Fig. [3f](#)), with 8–11 zooids within 2 mm longitudinally, and 7, 5 or 3 primary-order modular units of zooids arranged symmetrically on either side of the main median longitudinal axis (series-3) of the colony (Figs. [1a](#), [2a](#), [3b](#)). The inflated frontal wall is thin and convex, imperforate, apically forming part of a hemispherical dome with a circular to ovoid opening in the best-preserved specimens (Fig. [1h, i](#), Extended Data Fig. [3a, b, f](#)). Fine wrinkle structures developed on the frontal wall (Figs. [2g](#), Extended Data Fig. [2d, h](#)) suggest an originally organic composition with labile and ductile properties, probably secreted by an underlying epithelium^{[2](#)} and replicated during early diagenetic phosphatization (Extended Data Figs. [2i, j](#), [3h, j, k](#), [5c–k](#)). The ultrastructure of the basal and frontal

walls consists of diagenetic irregular apatite (Fig. 2g, Extended Data Figs. 2i, 3k), reflecting the secondary phosphatization of the original organic zooid body wall (Extended Data Fig. 5c–k). Spherulitic microstructures (Extended Data Figs. 2j, 3j) are also present and may be associated with microbially mediated phosphate replacement or diagenetic processes²⁸.

The developmental sequence of zooidal budding consists of five or seven alternating, back-to-back linear (longitudinal) series resulting in a palmate multiserial bilaminar colony (Figs. 3a–g, 4a). New zooids were budded at the distal tip of the colony, from pre-existing parents in an upward tapering growth vector (Figs. 1e, 3f, g, 4b, c). During clonal growth, the newly formed basal wall sequentially grew into contact with the walls of three adjacent zooids, entirely partitioning the original body (Fig. 3b, d, f, Extended Data Fig. 4a, f), demonstrating a zooidal budding process^{1,29} (Fig. 4c, d, Extended Data Fig. 4a). As the colony grew apically, longitudinal module series of zooids on either side (series-02 and series-04) of the main median series-3 axis stopped budding to provide accommodation space for adjacent linear series of zooids to grow (Figs. 1a, 4b, d). As a consequence, the whole colony achieved a distally tapering morphology (Figs. 1a, 2a, 4a, b, Extended Data Fig. 5a, b). The exhalant currents of filtered water would probably have been vented out from the sharp colony edges by analogy with living bryozoans with palmate branches¹. Compared with central series zooids, the marginal series (series-1 and series-5) demonstrate a relatively slow growth of zooids, which probably resulted from high-level control on the relative growth rates across different parts of the colony^{1,29} (Figs. 1b, 4a, Extended Data Fig. 6a).

Fig. 4: Reconstruction and growth pattern of *P. gatehousei*, and its inferred phylogenetic relationships.

 **figure4**

a, Front surface view, artwork created by X. Liu. **b**, Seven series of zooids, two of which terminate distally, resulting in five series; dashed line indicates the plane of sectioning in figure d. **c**, Budding process of two layers along the median mesotheca in longitudinal section. **d**, Distal zooidal bud formation²⁹ in six adjacent linear series,

with termination of series-02. e, Fifty-percent-majority rule consensus phylogenetic tree inferred using morphological characters and Bayesian analysis based on a matrix of 21 taxa and 52 characters (see Methods and Supplementary Data 3, 4 for source data and additional information). Node values are Bayesian posterior probability support values. Coloured areas indicate the three taxonomic classes that comprise the Bryozoa, along with *P. gatehousei* and outgroups. Purple, outgroups; yellow, *Protomelission*; blue, Phylactolaemata; red, Gymnolaemata; green, Stenolaemata.

Discussion

Protomelission gatehousei meets almost all recognition criteria expected in fossil bryozoans² (Extended Data Fig. 6b, Extended Data Table 2). The general morphology, zooid arrangement, budding direction and pattern are comparable to members of the Stenolaemata, which have been suggested to have been derived from a soft-bodied ctenostome-grade ancestor during the Cambrian^{2,5,19,30}. With an originally unmineralized body-plan, phosphatized preservation and box-shaped zooids, and in keeping with its basal phylogenetic position (Fig. 4e), *P. gatehousei* shares traits with taxa from a number of classes within Bryozoa, including the soft-bodied Gymnolaemata (Ctenostomata)^{19,20,30}. On the basis of phylogenetic analyses, we conclude that *P. gatehousei* potentially represents a stem-group bryozoan (Fig. 4e, Extended Data Fig. 8, Supplementary Data 3, 4). Notably, the erect bilaminite body-plan of *P. gatehousei* provides the earliest example of a colony form that has been repeatedly modified with adaptive branching structure in younger Palaeozoic bryozoans^{2,7,19,22,23,27} (Extended Data Fig. 7). Although the last common ancestor of total-group Bryozoa remains enigmatic, the organic nature and basal phylogenetic position of *Protomelission* support the interpretation that crown-group Bryozoa most probably evolved from a colonial (rather than solitary) ancestor^{23,24,25} with skeletal biomineralization independently evolving at least twice across two major bryozoan clades in post-Cambrian times; the Stenolaemata during the Early Ordovician and the Gymnolaemata (Cheilostomata) in the Jurassic period^{2,5,6,19} (Fig. 4e).

The discovery of a stem bryozoan in the Cambrian narrows the origination gap that previously existed between the known fossil record and independent molecular clock estimates^{11,12,21}. Our results push back the fossil record of the Bryozoa by approximately 35 million years and show that the colonial body-plan of Bryozoa can be traced back to the early Cambrian (Age 3), coincident with other major metazoan phyla belonging to the deuterostomes¹⁴, lophotrochozoans^{16,17,21} and ecdysozoans^{12,25}. The miniaturized body-plan, much thinner, unmineralized cuticles (compared to arthropods and ‘worms’) and hard substrate habitat of early bryozoans such as *P. gatehousei* explain the poor fossil record and cryptic history of bryozoan stem taxa in the Cambrian^{11,14,28}. However, the rapid diversification of the

Bryozoa^{6,7,30} during the Ordovician probably coincides with calcite seas⁵, increasing hardground development and more robust biomineralization, leading to increased bryozoan colony size (centimetre to decimetre scale) and enhancing fossilization potential^{4,5,8,11,20}. Thus, the recognized sequence of appearance for bryozoan taxa over geological time probably does not fully convey the real evolutionary history and may not provide a comprehensive understanding of bryozoan phylogeny^{2,7}.

The early Cambrian is recognized as an important phosphatization window for microfossil preservation^{11,28} and the phosphatized stem bryozoan reported here reveals a previously hidden history for Bryozoa that provides a new framework for understanding the origin and phylogeny of the phylum^{2,7}. The honeycomb-like network of zooids in *P. gatehousei* demonstrates that hierarchical architecture and complexity^{24,29} of colonial life was also an important evolutionary innovation during the Cambrian radiation of animal life.

Methods

Terminology

We follow the morphological terminology used in previous studies of fossil and extant bryozoans^{1,2,4,19,20}.

Material

Secondarily phosphatized specimens were recovered through standard acetic leaching of fossiliferous limestone samples, along with abundant benthic filter-feeding brachiopods³¹. Fossils were manually picked from acid residues using a binocular stereo microscope. Five incomplete specimens (Sample SADME 10470, 10470-1–10470-4) were collected from nodular, sandy limestones of the lower Wirrealpa Limestone (Cambrian Stage 4) at the Ten Mile Creek section, Bunkers Graben, South Australia⁹. One complete specimen of *P. gatehousei* (Sample ELI XYB 4 AN04) was collected from grey fossiliferous limestones in the Xihaojing Member of the Dengying Formation (Cambrian Stage 3), at the Xiaoyangba section, Hanzhong, South China. The geological and geographic setting has been previously described in detail³¹.

Scanning electron microscopy

Identified specimens were selected for the study using a Zeiss Supra 35 VP field emission at Uppsala University, Fei Quanta 450-FEGSEM at Northwest University and JEOL JSM 7100F-FESEM at Macquarie University. Coated specimens were

further analysed with Backscattered electron imaging (BSE) in Quanta FEG 450 and JEOL JSM 7100F, with attached Energy Dispersive X-ray spectrometry (EDS) system, with 20.0 kV, 60 Pa and WD 11.4 mm at Northwest University and Macquarie University.

X-ray tomographic microscopy

Two specimens were scanned using an Xradia MicroXCT-400 system (Carl Zeiss XRM) with the source operating at 80 kV, 125 µA over 180° sample rotation (−92° to 92°) at The University of Sydney. Geometric and optical magnification settings were chosen to collect projections with *xy*-pixel dimensions of 2.0334 µm (Samples SADME 10470 and ELI XYB 4 AN02). The projections were reconstructed using XMReconstructor Version 7.0.2817 (Carl Zeiss XRM) to produce a series of 16-bit TIFF images with a slice spacing equivalent to the pixel *xy* dimensions (isotropic voxels) and voxel size of 2.03 µm. The X-ray tomographic microscopy (µCT) images were visualized and segmented via thresholding using ORS Dragonfly 324 version 2020.2 (software available at <http://www.theobjects.com/dragonfly>). Before feature extraction, images were applied with a normalization filter, unsharp mask and mean shift filter using the image processing function of Dragonfly. Morphological features of interest were coloured separately to assist in distinguishing them from one another. Three-dimensional videos are provided in Supplementary Videos 1–6.

Measurements

Measurements of the length, width and angle of different parts of *P. gatehousei* were performed on µCT and SEM images by TpsDig2 v. 2.16. Scatter plots of different specimens, analysed by PAST v. 3, showing morphological variations, were also constructed. Raw data are provided in Supplementary Data 1, 2. Abbreviations used in the figures: B, basal wall; F, frontal wall; H, holdfast; M, mesotheca/median lamina; Z, zooid.

Phylogenetic analysis

Fifty-two characters were coded for *Protomelission*, 18 bryozoan genera and 2 outgroup taxa (a total of 21 taxa). The phylogenetic data matrix was built in Microsoft Excel 2016. The 18 bryozoan genera are exemplars of the eight major bryozoan orders, and the fossil genera chosen all occur in the Ordovician (except for *Fenestrapora*, which is Devonian). The two outgroup taxa (*Eoobolus* and *Phoronis*) correspond to the two major non-bryozoan clades within the Lophophorata. Character codings were based on previously published data (Supplementary Data 3). All character codings are provided in Nexus format, along with a full list of the characters used, in Supplementary Data 3, 4.

Phylogenetic trees were inferred using both maximum parsimony and Bayesian methods. Parsimony analysis was performed using PAUP* (v. 4.0a169)³². A non-parametric bootstrap search based on 1,000 replicates was conducted using a heuristic search algorithm, with starting trees built using stepwise addition and branch swapping undertaken using tree bisection and reconnection (TBR). Results of this bootstrap analysis were summarized as a 50% majority rule consensus tree (Extended Data Fig. 8). Bayesian analyses were run using MrBayes (v.3.2.7)³³ and the Mkv model³⁴, with gamma-distributed rate variation and variable coding. The analysis used a sampling frequency of 1,000, two concurrent runs, four Metropolis-coupled chains, and was run for 10 million generations. A 25% relative burn-in was implemented for all summary statistics. The resulting phylogenetic tree is presented in Fig. 4e.

Reporting summary

Further information on research design is available in the [Nature Research Reporting Summary](#) linked to this paper.

Data availability

All data analysed in this study, including the phylogenetic datasets, are available in the Article, Extended Data Figs. 1–8, Extended Data Tables 1, 2 or [Supplementary Information](#). Raw datasets are provided in the Dryad Digital Repository (<https://doi.org/10.5061/dryad.rn8pk0pbd>). CT scans and parameters used for scanning of specimens in this publication can be accessed in the MorphoSource Repository (<https://doi.org/10.17602/M2/M379121> and <https://doi.org/10.17602/M2/M379116>) and the affiliated project (<https://www.morphosource.org/projects/000378949?locale=en>).

References

1. 1.
McKinney, F. K. & Jackson, J. B. C. *Bryozoan Evolution* (Univ. Chicago Press, 1989).
2. 2.
Taylor, P. D. & Waeschenbach, A. Phylogeny and diversification of bryozoans. *Palaeontology* **58**, 585–599 (2015).
3. 3.

Schwaha, T. F., Ostrovsky, A. N. & Wanninger, A. Key novelties in the evolution of the aquatic colonial phylum Bryozoa: evidence from soft body morphology. *Biol. Rev.* **95**, 696–729 (2020).

4. 4.

Ma, J., Taylor, P. D., Xia, F. & Zhan, R. The oldest known bryozoan: *Prophyllodictya* (Cryptostomata) from the lower Tremadocian (Lower Ordovician) of Liujiachang, south-western Hubei, central China. *Palaeontology* **58**, 925–934 (2015).

5. 5.

Taylor, P. D., Lombardi, C. & Cocito, S. Biomineralization in bryozoans: present, past and future: bryozoan biomineralization. *Biol. Rev.* **90**, 1118–1150 (2015).

6. 6.

Ernst, A. Diversity dynamics of Ordovician Bryozoa. *Lethaia* **51**, 198–206 (2018).

7. 7.

Hageman, S. J. & Ernst, A. The last phylum: Occupation of Bryozoa morphospace (colony growth habits) during the early phase of the Great Ordovician Biodiversification Event. *Palaeogeogr. Palaeoclimatol. Palaeoecol.* **534**, 109270 (2019).

8. 8.

Ernst, A., Bogolepova, O. K., Hubmann, B., Golubkova, E. Y. U. & Gubanov, A. P. *Dianulites* (Trepustomata, Bryozoa) from the Early Ordovician of Severnaya Zemlya, Arctic Russia. *Geol. Mag.* **151**, 328–338 (2014).

9. 9.

Brock, G. A. & Cooper, B. J. Shelly fossils from the early Cambrian (Toyonian) Wirrealpa, Aroona Creek, and Ramsay Limestones of South Australia. *J. Paleontol.* **67**, 758–787 (1993).

10. 10.

Erwin, D. H. et al. The Cambrian conundrum: early divergence and later ecological success in the early history of animals. *Science* **334**, 1091–1097

(2011).

11. 11.

Wray, G. A. Molecular clocks and the early evolution of metazoan nervous systems. *Philos. Trans. R.* **370**, 20150046–20150046 (2015).

12. 12.

Erwin, D. H. The origin of animal body plans: a view from fossil evidence and the regulatory genome. *Development* **147**, dev182899 (2020).

13. 13.

Zhang, X. & Shu, D. Current understanding on the Cambrian Explosion: questions and answers. *PalZ* <https://doi.org/10.1007/s12542-021-00568-5> (2021).

14. 14.

Han, J., Morris, S. C., Ou, Q., Shu, D. & Huang, H. Meiofaunal deuterostomes from the basal Cambrian of Shaanxi (China). *Nature* **542**, 228–231 (2017).

15. 15.

Wood, R. et al. Integrated records of environmental change and evolution challenge the Cambrian Explosion. *Nat. Ecol. Evol.* **3**, 528–538 (2019).

16. 16.

Zhang, Z. et al. A sclerite-bearing stem group entoproct from the early Cambrian and its implications. *Sci. Rep.* **3**, 1066 (2013).

17. 17.

Hou, X. et al. *The Cambrian fossils of Chengjiang, China: The Flowering of Early Animal Life* (John Wiley & Sons, 2017).

18. 18.

Landing, E. et al. Early evolution of colonial animals (Ediacaran Evolutionary Radiation–Cambrian Evolutionary Radiation–Great Ordovician Biodiversification Interval). *Earth Sci. Rev.* **178**, 105–135 (2018).

19. 19.

Ernst, A. in *Fossil Record and Evolution of Bryozoa* (eds Helmcke, J.-G., Starck, D. & Wermuth, H.) 11–56 (De Gruyter, 2020).

20. 20.

Taylor, P. D. *Bryozoan Paleobiology* (John Wiley & Sons, 2020).

21. 21.

Budd, G. E. & Jackson, I. S. C. Ecological innovations in the Cambrian and the origins of the crown group phyla. *Philos. Trans. R. Soc. B* **371**, 20150287 (2016).

22. 22.

Mackie, G. O. From aggregates to integrates: physiological aspects of modularity in colonial animals. *Philos. Trans. R. Soc. B* **313**, 175–196 (1986).

23. 23.

Hughes, R. N. Lessons in modularity: the evolutionary ecology of colonial invertebrates. *Sci. Mar.* **69**, 169–179 (2005).

24. 24.

Lidgard, S., Carter, M. C., Dick, M. H., Gordon, D. P. & Ostrovsky, A. N. Division of labor and recurrent evolution of polymorphisms in a group of colonial animals. *Evol. Ecol.* **26**, 233–257 (2012).

25. 25.

Carroll, S. B. Chance and necessity: the evolution of morphological complexity and diversity. *Nature* **409**, 1102–1109 (2001).

26. 26.

Lombardi, C., Cocito, S., Gambi, M. C. & Taylor, P. D. Morphological plasticity in a calcifying modular organism: evidence from an in situ transplant experiment in a natural CO₂ vent system. *R. Soc. Open Sci.* **2**, 140413 (2015).

27. 27.

McKinney, F. K. Historical record of erect bryozoan growth forms. *Proc. R. Soc. Lond. B* **228**, 133–149 (1986).

28. 28.
- Schiffbauer, J. D., Wallace, A. F., Broce, J. & Xiao, S. Exceptional fossil conservation through phosphatization. *Paleontol. Soc. Pap.* **20**, 59–82 (2014).
29. 29.
- Lidgard, S. Zooid and colony growth in encrusting cheilostome bryozoans. *Palaeontology* **28**, 255–291 (1985).
30. 30.
- Todd, J. A. The central role of ctenostomes in bryozoan phylogeny. In *Proc. 11th Int. Bryozool. Assoc. Conf.* 104, 104–135 (2000).
31. 31.
- Zhang, Z. L. et al. The oldest Cambrian trilobite—brachiopod association in South China. *Gondwana Res.* **89**, 147–167 (2021).
32. 32.
- Swofford, D. L. *Phylogenetic Analysis Using Parsimony (*and Other Methods)* (Sinauer Associates, 2003).
33. 33.
- Ronquist, F. & Huelsenbeck, J. P. MrBayes 3: Bayesian phylogenetic inference under mixed models. *Bioinformatics* **19**, 1572–1574 (2003).
34. 34.
- Lewis, P. O. A likelihood approach to estimating phylogeny from discrete morphological character data. *Syst. Biol.* **50**, 913–925 (2001).
35. 35.
- Torsvik, T. H. & Cocks, L. R. M. New global palaeogeographical reconstructions for the Early Palaeozoic and their generation. *Geological Society, London, Memoirs* **38**, 5–24 (2013).
36. 36.

Betts, M. J. et al. Early Cambrian chronostratigraphy and geochronology of South Australia. *Earth Sci. Rev.* **185**, 498–543 (2018).

37. 37.

Taylor, P. D. & Jenkins, H. L. Evolution of larval size in cyclostome bryozoans. *Hist. Biol.* **30**, 535–545 (2018).

38. 38.

Xia, F. S., Zhang, S. G. & Wang, Z. Z. The oldest bryozoans: new evidence from the Late Tremadocian (Early Ordovician) of east Yangtze gorges in China. *J. Paleontol.* **81**, 1308–1326 (2007).

39. 39.

Koromyslova, A. V., Martha, S. O. & Pakhnevich, A. V. The internal morphology of *Acoscinoplaera* Voigt, 1956 (Ciliostomata, Bryozoa) from the Campanian–Maastrichtian of Central and Eastern Europe. *PalZ* **92**, 241–266 (2018).

40. 40.

Pushkin, V. I. & Popov, L. E. Early Ordovician bryozoans from north-western Russia. *Palaeontology* **42**, 171–189 (1999).

41. 41.

Porter, J. S. Morphological and genetic characteristics of erect subtidal species of *Alcyonidium* (Ctenostomata: Bryozoa). *J. Mar. Biol. Assoc. UK* **84**, 243–252 (2004).

Acknowledgements

This study was supported by a Macquarie University Research Fellowship (2019 MQRF), National Natural Science Foundation of China (41720104002, 41621003, 41890844 and 41772010), Strategic Priority Research Program of Chinese Academy of Sciences (XDB26000000), Ministry of Science and 111 project of Ministry of Education of China (D17013), Thousand Talents Program and 1000 Talent Shaanxi Province Fellowship. We thank Cambridge University Press for permission to illustrate *P. gatehousei* in Fig. 1a, f, reproduced from ref. [9](#), with permission from Cambridge University Press. The palaeogeographic map in Extended Data Fig. 1 is reproduced from ref. [35](#) with permission from Geological Society Publishing House and Extended Data Fig. 1b is reproduced from ref. [31](#) with permission from Elsevier

Science & Technology Journals. We thank L. E. Holmer and M. Streng at Uppsala University, Y. L. Pang at Northwest University, and S. Lindsay and C. Shen at the Microscopy Unit of Macquarie University for assistance with SEM imaging, M. Foley at University of Sydney for technical assistance with μ CT imaging, X. Liu for reconstruction, Q. C. Feng for sample preparation, and J. Alroy, C. Simpson and M. Steinthorsdottir for discussion.

Author information

Affiliations

1. State Key Laboratory of Continental Dynamics, Shaanxi Key Laboratory of Early Life & Environments and Department of Geology, Northwest University, Xi'an, China

Zhiliang Zhang, Zhifei Zhang, Luke C. Strotz, Feiyang Chen, Jian Han & Glenn A. Brock

2. Department of Biological Sciences, Macquarie University, Sydney, New South Wales, Australia

Zhiliang Zhang, Feiyang Chen & Glenn A. Brock

3. State Key Laboratory of Palaeobiology and Stratigraphy, Nanjing Institute of Geology and Palaeontology, CAS, Nanjing, China

Junye Ma

4. Department of Earth Sciences, Natural History Museum, London, UK

Paul D. Taylor

5. Department of Geological Sciences, University of Missouri, Columbia, MO, USA

Sarah M. Jacquet

6. Department of Palaeobiology, Swedish Museum of Natural History, Stockholm, Sweden

Christian B. Skovsted

7. School of Resources and Geosciences, China University of Mining and Technology, Xuzhou, China

Feiyang Chen

Contributions

Zhiliang Zhang, Zhifei Zhang and G.A.B. conceived the research. G.A.B. and Zhifei Zhang led fieldwork in Australia and China, respectively. Zhiliang Zhang prepared all specimens, photographs and figures. J.M, P.D.T., L.C.S. and Zhiliang Zhang undertook phylogenetic analyses. S.M.J. performed visualization with μ CT data. Zhiliang Zhang and G.A.B. wrote early drafts of the paper with input from all other authors. All authors discussed the results and approved the final manuscript.

Corresponding authors

Correspondence to [Zhiliang Zhang](#), [Zhifei Zhang](#) or [Luke C. Strotz](#).

Ethics declarations

Competing interests

The authors declare no competing interests.

Additional information

Peer review information *Nature* thanks Andrej Ernst, Juan López-Gappa and Mark Wilson for their contribution to the peer review of this work. Peer reviewer reports are available.

Publisher's note Springer Nature remains neutral with regard to jurisdictional claims in published maps and institutional affiliations.

Extended data figures and tables

[Extended Data Fig. 1 Geographic map of fossil localities and palaeogeographic distribution of Australia \(AU\) and South China \(SC\) platforms during the early Cambrian](#)[35](#).

a, Locality of the Ten Mile Creek section, Arrowie Basin, South Australia (SA), showing Cambrian outcrop^{9,36}. **b**, Locality map of the Xiaoyangba section, Hanzhong, South China³¹.

Extended Data Fig. 2 *Protomelission gatehousei* from the early Cambrian Xihaojing Member of Dengying Formation, South China, ELI XYB 4 AN02.

a, Oblique lateral view of the colony; note five series of zooids. **b**, Oblique basal view showing the elliptical holdfast. **c**, Oblique view of the opposite colony surface. **d**, BSE imaging demonstrates distinct wrinkles along the zooid edges. **e**, BSE imaging, arrows demonstrate the space between adjacent zooids, box corners indicate the spherulitic microstructures shown in figure j. **f**, Close-up of holdfast with tailed arrows showing attached small grains. **g**, Enlargement of weakly phosphatized colony apex; note basal walls of three adjacent zooids indicated by tailed arrows and median mesotheca by an arrow. **h**, Detail of wrinkles of frontal wall. **i**, Enlarged diagenetic apatite of figure h. **j**, Enlargement of spherulitic microstructures between adjacent zooids.

Extended Data Fig. 3 *Protomelission gatehousei* from the early Cambrian Wirrealpa Limestone, South Australia.

a–c and **j–k**, SADME 10470-2. **a**, Front side of a broken colony, highlighting five series of zooids, upper box corners indicate the area shown in figure c, lower box corners show the microstructures in figure j. **b**, Oblique lateral view, with relatively well preserved frontal walls and circular orifice of zooids. **c**, Lateral view showing the staggered pattern of zooids in both layers of bifoliate colony; note basal walls and largely broken frontal wall (tailed arrow), and basal walls from opposite layer (arrows). **d**, SADME 10470-3, back view of one colonial layer with the exfoliated opposite layer, showing three broken zooids from the opposite layer (arrows) and space between adjacent zooids (tailed arrows). **e–i**, Holotype, SADME 10470. **e**, Oblique lateral view with arrows showing the median mesotheca between two layers. **f**, Quincuncial arrangement of box-shaped zooids, showing dome shaped frontal wall (arrow). **g**, Detail of spoon-shaped structure at the zooid proximal end, indicated by a tailed arrow. **h**, Recrystallized granules and fibres of frontal wall. **i**, Lateral view showing one frontal wall (arrow) and two basal walls of the same layers, and the phosphatized median mesotheca (tailed arrow). **j**, Spherulitic microstructures of frontal wall. **k**, Enlarged diagenetic apatite of basal wall. B, basal wall.

Extended Data Fig. 4 μCT images of *Protomelission gatehousei* from the early Cambrian of South Australia and South China.

a–f, SADME 10470. **a**, Longitudinal section, showing bifoliate pattern of zooids on the back-to-back layers; note the space between the frontal wall of parent and daughter zooids by arrows. **b–c**, Tangential section. **b**, Median mesotheca and curved basal walls by tailed arrows. **c**, Frontal walls of Series-3, demonstrating the concave centre of the back/opposite layer. **d**, Longitudinal section shows detail of probable colonial connection between adjacent zooids from back-to-back layers (tailed arrows) through space of median mesotheca. **e–f**, Transverse section showing zooids on bilaminar layers along mesotheca. **e**, New budding zooids indicated by arrows, and daughter basal wall overlapping parent frontal wall indicated by a tailed arrow. **f**, Basal walls of new budding zooids indicated by arrows. **g**, ELI XYB 4 AN02, transverse section showing zooids on both layers and median mesotheca of the colony. Blue, frontal wall; Green, mesotheca with secondary phosphatic cement in yellow; Red, basal wall. M, mesotheca; Z, zooid.

Extended Data Fig. 5 Relationship between colony growth and colony surface area, and elemental mapping of the zooids of *Protomelission gatehousei*.

a, Plots of increasing colony surface area and colony generations (1–8). **b**, Plots of total colony surface area and colony height, indicating a uniform increase of the colonial surface area during development. **c–k**, EDS elemental mapping, SADME 10470. **c**, SEM image. **d**, Elemental map of C. **e**, Elemental map of O. **f**, Elemental map of Al. **g**, Elemental map of Si. **h**, Elemental map of P. **i**, Elemental map of S. **j**, Elemental map of Ca. **k**, Elemental map of P, Ca and Si concentrations, noting the clastic particles adhered to the space between adjacent zooids.

Extended Data Fig. 6 Plots of zooid size of *Protomelission gatehousei*.

Each pair of width (greatest width perpendicular to the proximal-distal axis of the zooid) and length (proximal-distal axis of the zooid) values correspond to a single zooid. **a**, Boxplots of zooid width for five adjacent series (different colours) from two *P. gatehousei* colonies from South Australia and South China, with the mean value for each series indicated by the \times . The colour of each series matches the colours used in Fig. 4d. Values for boxplots are provided in Supplementary Data 1. N = 49 biologically independent measurements of zooid size. **b**, Zooid length and width of different bryozoan taxa (different colours) from the literature with the geological age of each taxon indicated in the key. Raw data for scatter plots are provided in Supplementary Data 2. N = 172 biologically independent measurements of zooid size (86 zooids). Note that for Ordovician taxa, the size range is comparable to *Protomelission*. Red = *Protomelission gatehousei* (circle, SADME 10470; solid circle, ELI XYB 4 AN02); Yellow = Cyclostomata; Green = Trepustomata; Blue = Cryptostomata; Purple =

Cheilostomata; Pink = Ctenostomata^{4,5,26,37,38,39,40,41}. C, Cambrian, O: Ordovician; J, Jurassic; K, Cretaceous, R: Recent.

Extended Data Fig. 7 Erect bifoliate bryozoan *Stictopora* sp. from the Late Ordovician Bowen Park Group, New South Wales, Australia.

a–d, Bowen-DQ-01. **a**, Front side of the colony, noting the five series of zooids and arc-shaped holdfast. **b**, Oblique basal view. **c**, Lateral view showing zooids on both layers by arrows, and arc-shaped holdfast. **d**, Enlarged holdfast, note the relatively smooth surface as an adaptation to a hard substrate. **e–f**, Bowen-DQ-02. **e**, Front side of a larger colony showing five series of zooids and new budding series at the apex indicated by tailed arrows. Box corners indicate the area in figure f. **f**, Enlargement of five series of zooids.

Extended Data Fig. 8 Phylogenetic tree inferred using parsimony based on a matrix of 21 taxa and 52 characters.

Fifty-percent majority rule bootstrap consensus tree generated using a heuristic search algorithm by PAUP*. Node values are bootstrap probabilities. Coloured areas indicate the three taxonomic classes that comprise the Bryozoa, along with the position of *P. gatehousei* and outgroups (see Supplementary Data 3-4 for details). Purple = outgroups; Yellow = *Protomelission*; Blue = Phylactolaemata; Red = Gymnolaemata; Green = Stenolaemata.

Extended Data Table 1 Width and length of five adjacent series of zooids of *Protomelission gatehousei*

Extended Data Table 2 Character traits expected in ancestral Cambrian bryozoans²

Supplementary information

Supplementary Information

This file contains Supplementary Data 1–4. (1) Derived values for box plots of *Protomelission gatehousei* zooid width provided in Extended Fig. 6a. (2) Raw data of zooid width and length of 13 bryozoan taxa in Extended Fig. 6b. (3) Character trait dataset and morphological states for bryozoans. (4) Character taxon matrix in NEXUS format.

Reporting Summary

Peer Review File

Supplementary Video 1

3D video of *P. gatehousei* SADME 10470 (full). This 59-second-3D video reveals the morphology of the external zooid arrangement, along with the transverse, tangential and longitudinal virtual dissection of the internal morphology of the colony of *P. gatehousei* (Specimen: SADME 10470). False colours are used to differentiate important character traits. Blue, frontal wall; Green, mesotheca with secondary phosphatic cement in yellow; Red, basal wall.

Supplementary Video 2

3D video of *P. gatehousei* SADME 10470 (longitudinal section). This 13-second-3D video reveals the longitudinal virtual dissection of the internal morphology of the colony of *P. gatehousei* (Specimen: SADME 10470). False colours are used to differentiate important character traits. Blue, frontal wall; Green, mesotheca with secondary phosphatic cement in yellow; Red, basal wall.

Supplementary Video 3

3D video of *P. gatehousei* SADME 10470 (tangential section). This 6-second-3D video reveals the tangential virtual dissection of the internal morphology of the colony of *P. gatehousei* (Specimen: SADME 10470). False colours are used to differentiate important character traits. Blue, frontal wall; Green, mesotheca with secondary phosphatic cement in yellow; Red, basal wall.

Supplementary Video 4

3D video of *P. gatehousei* SADME 10470 (transverse section). This 24-second-3D video reveals the transverse virtual dissection of the internal morphology of the colony of *P. gatehousei* (Specimen: SADME 10470). False colours are used to differentiate important character traits. Blue, frontal wall; Green, mesotheca with secondary phosphatic cement in yellow; Red, basal wall.

Supplementary Video 5

3D video of *P. gatehousei* SADME 10470. This 25-second-3D video reveals the external zooid arrangement and morphology of the colony of *P. gatehousei* (Specimen: SADME 10470).

Supplementary Video 6

3D video of *P. gatehousei* EIL XYB 4 AN02. This 22-second-3D video reveals the external zooid arrangement and morphology of the colony of *P. gatehousei* (Specimen: ELI XYB 4 AN02).

Rights and permissions

Open Access This article is licensed under a Creative Commons Attribution 4.0 International License, which permits use, sharing, adaptation, distribution and reproduction in any medium or format, as long as you give appropriate credit to the original author(s) and the source, provide a link to the Creative Commons license, and indicate if changes were made. The images or other third party material in this article are included in the article's Creative Commons license, unless indicated otherwise in a credit line to the material. If material is not included in the article's Creative Commons license and your intended use is not permitted by statutory regulation or exceeds the permitted use, you will need to obtain permission directly from the copyright holder. To view a copy of this license, visit <http://creativecommons.org/licenses/by/4.0/>.

Reprints and Permissions

About this article

Cite this article

Zhang, Z., Zhang, Z., Ma, J. *et al.* Fossil evidence unveils an early Cambrian origin for Bryozoa. *Nature* **599**, 251–255 (2021). <https://doi.org/10.1038/s41586-021-04033-w>

- Received: 03 August 2021
- Accepted: 16 September 2021
- Published: 27 October 2021
- Issue Date: 11 November 2021
- DOI: <https://doi.org/10.1038/s41586-021-04033-w>

Share this article

Anyone you share the following link with will be able to read this content:

[Get shareable link](#)

Sorry, a shareable link is not currently available for this article.

[Copy to clipboard](#)

Provided by the Springer Nature SharedIt content-sharing initiative

Further reading

- [**Bryozoan fossils found at last in deposits from the Cambrian period**](#)

- Andrej Ernst
- & Mark A. Wilson

Nature (2021)

[**Bryozoan fossils found at last in deposits from the Cambrian period**](#)

- Andrej Ernst
- Mark A. Wilson

News & Views 27 Oct 2021

This article was downloaded by **calibre** from <https://www.nature.com/articles/s41586-021-04033-w>

| [Section menu](#) | [Main menu](#) |

- Article
- Open Access
- [Published: 27 October 2021](#)

The genomic origins of the Bronze Age Tarim Basin mummies

- [Fan Zhang](#) ORCID: orcid.org/0000-0001-9259-2223¹ nal,
- [Chao Ning](#) ORCID: orcid.org/0000-0002-8848-3961² nal,
- [Ashley Scott](#) ORCID: orcid.org/0000-0001-8892-1557² nal,
- [Qiaomei Fu](#) ORCID: orcid.org/0000-0002-7141-0002³,
- [Rasmus Bjørn](#)²,
- [Wenying Li](#)⁴,
- [Dong Wei](#)⁵,
- [Wenjun Wang](#)³,
- [Linyuan Fan](#)¹,
- [Idilisi Abuduresule](#)⁴,
- [Xingjun Hu](#)⁴,
- [Qiurong Ruan](#)⁴,
- [Alipujiang Niyazi](#)⁴,
- [Guanghui Dong](#) ORCID: orcid.org/0000-0001-8005-759X⁶,
- [Peng Cao](#)³,
- [Feng Liu](#)³,
- [Qingyan Dai](#)³,
- [Xiaotian Feng](#)³,
- [Ruowei Yang](#)³,
- [Zihua Tang](#)⁷,
- [Pengcheng Ma](#) ORCID: orcid.org/0000-0003-3446-9125¹,
- [Chunxiang Li](#)¹,
- [Shizhu Gao](#)⁸,
- [Yang Xu](#)¹,
- [Sihao Wu](#)¹,
- [Shaoqing Wen](#)⁹,
- [Hong Zhu](#)⁵,
- [Hui Zhou](#)¹,

- [Martine Robbeets](#) ORCID: [orcid.org/0000-0002-2860-0230²](https://orcid.org/0000-0002-2860-0230),
- [Vikas Kumar³](#),
- [Johannes Krause](#) ORCID: [orcid.org/0000-0001-9144-3920^{2,10}](https://orcid.org/0000-0001-9144-3920),
- [Christina Warinner](#) ORCID: [orcid.org/0000-0002-4528-5877^{2,11}](https://orcid.org/0000-0002-4528-5877),
- [Choongwon Jeong](#) ORCID: [orcid.org/0000-0003-3049-2352¹²](https://orcid.org/0000-0003-3049-2352) &
- [Yinqiu Cui](#) ORCID: [orcid.org/0000-0003-3702-5773^{1,13,14}](https://orcid.org/0000-0003-3702-5773)

[Nature](#) volume 599, pages 256–261 (2021)

- 64k Accesses
- 2 Citations
- 851 Altmetric
- [Metrics details](#)

Subjects

- [Archaeology](#)
- [Evolutionary genetics](#)
- [Population genetics](#)

Abstract

The identity of the earliest inhabitants of Xinjiang, in the heart of Inner Asia, and the languages that they spoke have long been debated and remain contentious¹. Here we present genomic data from 5 individuals dating to around 3000–2800 bc from the Dzungarian Basin and 13 individuals dating to around 2100–1700 bc from the Tarim Basin, representing the earliest yet discovered human remains from North and South Xinjiang, respectively. We find that the Early Bronze Age Dzungarian individuals exhibit a predominantly Afanasievo ancestry with an additional local contribution, and the Early–Middle Bronze Age Tarim individuals contain only a local ancestry. The Tarim individuals from the site of Xiaohe further exhibit strong evidence of milk proteins in their dental calculus, indicating a reliance on dairy pastoralism at the site since its founding. Our results do not support previous hypotheses for the origin of the Tarim mummies, who were argued to be Proto-Tocharian-speaking pastoralists descended from the Afanasievo^{1,2} or to have originated among the Bactria–Margiana Archaeological Complex³ or Inner Asian Mountain Corridor cultures⁴. Instead, although Tocharian may have been plausibly introduced to the Dzungarian Basin by Afanasievo migrants during the Early Bronze Age, we find that the earliest Tarim

Basin cultures appear to have arisen from a genetically isolated local population that adopted neighbouring pastoralist and agriculturalist practices, which allowed them to settle and thrive along the shifting riverine oases of the Taklamakan Desert.

[Download PDF](#)

Main

As part of the Silk Road and located at the geographic confluence of Eastern and Western cultures, the Xinjiang Uyghur Autonomous Region (henceforth Xinjiang) has long served as a major crossroads for trans-Eurasian exchanges of people, cultures, agriculture and languages^{1,5,6,7,8,9}. Bisected by the Tianshan mountains, Xinjiang can be divided into two subregions referred to as North Xinjiang, which contains the Dzungarian Basin, and South Xinjiang, which contains the Tarim Basin (Fig. 1). The Dzungarian Basin in the north consists of the Gurbantünggüt Desert, which is surrounded by a vast expanse of grasslands traditionally inhabited by mobile pastoralists. The southern part of Xinjiang consists of the Tarim Basin, a dry inland sea that now forms the Taklamakan Desert. Although mostly uninhabitable, the Tarim Basin also contains small oases and riverine corridors, fed by runoff from thawing glacier ice and snow from the surrounding high mountains^{4,10,11}.

Fig. 1: Overview of the Xinjiang Bronze Age archaeological sites analysed in this study.

 **figure1**

a, Overview of key Eurasian geographic regions, features and archaeological sites discussed in the text; new sites analysed in this study are shown in grey. **b**, Enhanced view of Xinjiang and the six new sites analysed in this study. **c**, Timeline of the sites in **a**. The timeline is organized by region, and the median date for each studied group is shown. The base maps in **a** and **b** were obtained from the Natural Earth public domain map dataset (<https://www.naturalearthdata.com/downloads/10m-raster-data/10m-cross-blend-hypso/>). In the group labels, the suffixes represent the archaeological time periods of each group: N, Neolithic; EN, MN and LN, Early, Middle and Late Neolithic, respectively; EN, Eneolithic for Geoksyur, Parkhai and Sarazm; CA, Chalcolithic Age; BA, Bronze Age; MBA, Middle Bronze Age; EIA, Early Iron Age. MA-1, Mal'ta; EHG, Eastern European hunter-gatherers.

Within and around the Dzungarian Basin, pastoralist Early Bronze Age (EBA) Afanasievo (3000–2600 bc) and Chemurchek (or Qiemu'erqieke) (2500–1700 bc)¹² sites have been plausibly linked to the Afanasievo herders of the Altai–Sayan region in southern Siberia (3150–2750 bc), who in turn have close genetic ties with the Yamnaya (3500–2500 bc) of the Pontic–Caspian steppe located 3,000 km to the west^{13,14,15}. Linguists have hypothesized that the Afanasievo dispersal brought the now extinct Tocharian branch of the Indo-European language family eastwards, separating it from other Indo-European languages by the third or fourth millennium bc (ref. ¹⁴). However, although Afanasievo-related ancestry has been confirmed among Iron Age Dzungarian populations (around 200–400 bc)⁷, and Tocharian is recorded in

Buddhist texts from the Tarim Basin dating to ad 500–1000 (ref. [13](#)), little is known about earlier Xinjiang populations and their possible genetic relationships with the Afanasievo or other groups.

Since the late 1990s, the discovery of hundreds of naturally mummified human remains dating to around 2000 bc to ad 200 in the Tarim Basin has attracted international attention due to their so-called Western physical appearance, their felted and woven woollen clothing, and their agropastoral economy that included cattle, sheep/goats, wheat, barley, millet and even kefir cheese^{[16,17,18,19](#)}. Such mummies have now been found throughout the Tarim Basin, among which the earliest are those found in the lowest layers of the cemeteries at Gumugou (2135–1939 bc), Xiaohe (1884–1736 bc) and Beifang (1785–1664 bc) (Fig. [1](#), Extended Data Fig. [1](#) and Extended Data Table [1](#)). These and related Bronze Age sites are grouped within the Xiaohe archaeological horizon on the basis of their shared material culture^{[13,16,20](#)}.

Multiple contrasting hypotheses have been suggested by scholars to explain the origins and Western elements of the Xiaohe horizon, including the Yamnaya/Afanasievo steppe hypothesis^{[16](#)}, the Bactrian oasis hypothesis^{[21](#)} and the Inner Asian Mountain Corridor (IAMC) island biogeography hypothesis^{[4](#)}. The Yamnaya/Afanasievo steppe hypothesis posits that the Afanasievo-related EBA populations in the Altai–Sayan mountains spread via the Dzungarian Basin into the Tarim Basin and subsequently founded the agropastoralist communities making up the Xiaohe horizon around 2000 bc (refs. [16,22,23](#)). By contrast, the Bactrian oasis hypothesis posits that the Tarim Basin was initially colonized by migrating farmers of the Bactria–Margiana Archaeological Complex (BMAC) (around 2300–1800 bc) from the desert oases of Afghanistan, Turkmenistan and Uzbekistan via the mountains of Central Asia. Support for this hypothesis is largely based on similarities in the agricultural and irrigation systems between the two regions that reflect adaptations to a desert environment, as well as evidence for the ritual use of *Ephedra* at both locations^{[3,21](#)}. The IAMC island biogeography hypothesis similarly posits a mountain Central Asian origin for the Xiaohe founder population, but one linked to the transhumance of agropastoralists in the IAMC to the west and north of the Tarim Basin^{[4,24,25](#)}. In contrast to these three migration models, the greater IAMC, which spans the Hindu Kush to Altai mountains, may have alternatively functioned as a geographic arena through which cultural ideas, rather than populations, primarily moved^{[25](#)}.

Recent archaeogenomic research has shown that Bronze Age Afanasievo of southern Siberia and IAMC/BMAC populations of Central Asia have distinguishable genetic profiles^{[15,26](#)}, and that these profiles are likewise also distinct from those of pre-agropastoralist hunter-gatherer populations in Inner Asia^{[2,5,7,27,28,29,30](#)}. As such, an archaeogenomic investigation of Bronze Age Xinjiang populations presents a powerful approach for reconstructing the population histories of the Dzungarian and

Tarim basins and the origins of the Bronze Age Xiaohe horizon. Examining the skeletal material of 33 Bronze Age individuals from sites in the Dzungarian (Nileke, Ayituan and Songshugou) and Tarim (Xiaohe, Gumugou and Beifang) basins, we successfully retrieved ancient genome sequences from 5 EBA Dzungarian individuals (3000–2800 bc) culturally assigned as Afanasievo, and genome-wide data from 13 Early–Middle Bronze Age (EMBA) Tarim individuals (2100–1700 bc) belonging to the Xiaohe horizon (Extended Data Table 1 and Supplementary Data 1A). We additionally report dental calculus proteomes of seven individuals from basal layers at the site of Xiaohe in the Tarim Basin (Extended Data Table 2). To the best of our knowledge, these individuals represent the earliest human remains excavated to date in the region.

Genetic diversity of the Bronze Age Xinjiang

We obtained genome-wide data for 18 of 33 attempted individuals by either whole-genome sequencing or DNA enrichment for a panel of about 1.2 million single-nucleotide polymorphisms (1,240k panel SNPs) (Supplementary Data 1A). Overall, endogenous DNA was well preserved with minimal levels of contamination (Extended Data Table 1 and Supplementary Data 1A). To explore the genetic profiles of ancient Xinjiang populations, we first calculated the principal components of present-day Eurasian and Native American populations onto which we projected those of ancient individuals. Ancient Xinjiang individuals form several distinct clusters distributed along principal component 1 (PC1) (Fig. 2), the main principal component that separates eastern and western Eurasian populations. EBA Dzungarian individuals from the sites of Ayituan and Songshugou near the Altai Mountains (Dzungaria_EBA1) fall close to EBA Afanasievo steppe herders from the Altai–Sayan mountains to the north. Genetic clustering with ADMIXTURE further supports this observation (Extended Data Fig. 3). The contemporaneous individuals from the Nileke site near the Tianshan mountains (Dzungaria_EBA2) are slightly shifted along PC1 towards the later Tarim individuals. In contrast to the EBA Dzungarian individuals, the EMBA individuals from the eastern Tarim sites of Xiaohe and Gumugou (Tarim_EMBA1) form a tight cluster close to pre-Bronze Age central steppe and Siberian individuals who share a high level of ancient North Eurasian (ANE) ancestry (for example, Botai_CA). A contemporaneous individual from the Beifang site (Tarim_EMBA2) in the southern Tarim Basin is slightly displaced from the Tarim_EMBA1 towards EBA individuals from the Baikal region.

Fig. 2: Genetic structure of ancient and present-day populations included in this study.



Principal component analysis of ancient individuals projected onto Eurasian and Native American populations; the inset displays ancient individuals projected onto only Eurasian populations.

Afanasievo genetic legacy in Dzungaria

Outgroup f_3 statistics supports a tight genetic link between the Dzungarian and Tarim groups (Extended Data Fig. 2A). Nevertheless, both of the Dzungarian groups are significantly different from the Tarim groups, showing excess affinity with various western Eurasian populations and sharing fewer alleles with ANE-related groups (Extended Data Fig. 2b,c). To understand this mixed genetic profile, we used qpAdm to explore admixture models of the Dzungarian groups with Tarim_EMBA1 or a terminal Pleistocene individual (AG3) from the Siberian site of Afontova Gora³¹, as a source (Supplementary Data 1D). AG3 is a distal representative of the ANE ancestry and shows a high affinity with Tarim_EMBA1. Although the Tarim_EMBA1 individuals lived a millennium later than the Dzungarian groups, they are more genetically distant from the Afanasievo than the Dzungarian groups, suggesting that they have a higher proportion of local autochthonous ancestry. Here we define autochthonous to signify a genetic profile that has been present in a region for millennia, rather than being associated with more recently arrived groups.

We find that Dzungaria_EBA1 and Dzungaria_EBA2 are both best described by three-way admixture models (Fig. 3c, Extended Data Table 3 and Supplementary Data 1D) in which they derive a majority ancestry from Afanasievo (about 70% in Dzungaria_EBA1 and about 50% in Dzungaria_EBA2), with the remaining ancestry best modelled as a mixture of AG3/Tarim_EMBA1 (19–36%) and Baikal_EBA (9–21%). When we use Eneolithic and Bronze Age populations from the IAMC as a source, models fail when Afanasievo is not included as a source, and no contribution is allocated to the IAMC groups when Afanasievo is included (Supplementary Data 1D). Thus, Afanasievo ancestry, without IAMC contributions, is sufficient to explain the western Eurasian component of the Dzungarian individuals. We also find that the Chemurchev, an EBA pastoralist culture that succeeds the Afanasievo in both the Dzungarian Basin and Altai Mountains, derive approximately two-thirds of their ancestry from Dzungaria_EBA1 with the remainder from Tarim_EMBA1 and IAMC/BMAC-related sources (Fig. 3, Extended Data Table 3, Supplementary Data 1F and Supplementary Text 5). This helps to explain both the IAMC/BMAC-related ancestry previously noted in Chemurchev individuals³⁰ and their reported cultural and genetic affiliations to Afanasievo groups³². Taken together, these results indicate that the early dispersal of the Afanasievo herders into Dzungaria was accompanied by a substantial level of genetic mixing with local autochthonous populations, a pattern distinct from that of the initial formation of the Afanasievo culture in southern Siberia.

Fig. 3: Genetic ancestry and admixture dating of ancient populations from Xinjiang and its vicinity.

 **figure3**

a, qpAdm-based estimates of the ancestry proportion of Dzungaria_EBA and Tarim_EMBA from three ancestry sources (AG3, Afanasievo and Baikal_EBA) (Supplementary Data [1D, E](#)). Unlike Dzungaria_EBA individuals, Tarim_EMBA individuals are adequately modelled without EBA Eurasian steppe pastoralist (for example, Afanasievo) ancestry. **b**, Genetic admixture dates for key Bronze Age populations in Inner Asia, including Dzungaria_EBA1 ($n = 3$), Chemurchek ($n = 3$), Kumsay_EBA ($n = 4$), Mereke_MBA ($n = 2$), Dali_EBA ($n = 1$) and Tarim_EMBA1 ($n = 12$). The blue shade represents the radiocarbon dating range of the Yamnaya and Afanasievo individuals. The orange circles and the associated vertical bars represent the averages and standard deviations of median radiocarbon dates, respectively. The circles above each orange circle represent the estimated admixture dates with a generation time of 29 years, and the vertical bars represent the sum of standard errors of the admixture date and the radiocarbon date estimate. **c**, Representative qpAdm-based admixture models of ancient Eurasian groups (Supplementary Data [1D-I](#)). For Dzungaria_EBA1 and Geoksyur_EN, we show their three-way admixture models including Tarim_EMBA1 as a source. For later populations in Xinjiang, IAMC and nearby regions, we used them as sources, and allocated a colour to each of them (blue for Dzungaria_EBA1; magenta for Geoksyur_EN). The base map in **c** was obtained from the Natural Earth public domain map dataset (<https://www.naturalearthdata.com/downloads/10m-raster-data/10m-gray-earth/>).

Genetic isolation of the Tarim group

The Tarim_EMBA1 and Tarim_EMBA2 groups, although geographically separated by over 600 km of desert, form a homogeneous population that had undergone a substantial population bottleneck, as suggested by their high genetic affinity without close kinship, as well as by the limited diversity in their uniparental haplogroups (Figs. 1 and 2, Extended Data Fig. 4, Extended Data Table 1, Supplementary Data 1B and Supplementary Text 4). Using qpAdm, we modelled the Tarim Basin individuals as a mixture of two ancient autochthonous Asian genetic groups: the ANE, represented by an Upper Palaeolithic individual from the Afontova Gora site in the upper Yenisei River region of Siberia (AG3) (about 72%), and ancient Northeast Asians, represented by Baikal_EBA (about 28%) (Supplementary Data 1E and Fig. 3a). Tarim_EMBA2 from Beifang can also be modelled as a mixture of Tarim_EMBA1 (about 89%) and Baikal_EBA (about 11%). For both Tarim groups, admixture models unanimously fail when using the Afanasievo or IAMC/BMAC groups as a western Eurasian source (Supplementary Data 1E), thus rejecting a western Eurasian genetic contribution from nearby groups with herding and/or farming economies. We estimate a deep formation date for the Tarim_EMBA1 genetic profile, consistent with an absence of western Eurasian EBA admixture, placing the origin of this gene pool at 183 generations before the sampled Tarim Basin individuals, or $9,157 \pm 986$ years ago when assuming an average generation time of 29 years (Fig. 3b). Considering these findings together, the genetic profile of the Tarim Basin individuals indicates that the earliest individuals of the Xiaohe horizon belong to an ancient and isolated autochthonous Asian gene pool. This autochthonous ANE-related gene pool is likely to have formed the genetic substratum of the pre-pastoralist ANE-related populations of Central Asia and southern Siberia (Fig. 3c, Extended Data Fig. 2 and Supplementary Text 5).

Pastoralism in the Tarim Basin

Although the harsh environment of the Tarim Basin may have served as a strong barrier to gene flow into the region, it was not a barrier to the flow of ideas or technologies, as foreign innovations, such as dairy pastoralism and wheat and millet agriculture, came to form the basis of the Bronze Age Tarim economies. Woollen fabrics, horns and bones of cattle, sheep and goats, livestock manure, and milk and kefir-like dairy products have been recovered from the upper layers of the Xiaohe and Gumugou cemeteries^{33,34,35,36}, as have wheat and millet seeds and bundles of *Ephedra* twigs^{34,37,38}. Famously, many of the mummies dating to 1650–1450 bc were even buried with lumps of cheese³⁵. However, until now it has not been clear whether this pastoralist lifestyle also characterized the earliest layers at Xiaohe.

To better understand the dietary economy of the earliest archaeological periods, we analysed the dental calculus proteomes of seven individuals at the site of Xiaohe dating to around 2000–1700 bc. All seven individuals were strongly positive for ruminant-milk-specific proteins (Extended Data Table 2), including β -lactoglobulin, α -

S1-casein and α -lactalbumin (Extended Data Fig. 5), and peptide recovery was sufficient to provide taxonomically diagnostic matches to cattle (*Bos*), sheep (*Ovis*) and goat (*Capra*) milk (Extended Data Fig. 5, Extended Data Table 2 and Supplementary Data 3). These results confirm that dairy products were consumed by individuals of autochthonous ancestry (Tarim_EMBA1) buried in the lowest levels of the Xiaohe cemetery (Extended Data Table 2). Importantly, however, and in contrast to previous hypotheses³⁶, none of the Tarim individuals was genetically lactase persistent (Supplementary Data 1J). Rather, the Tarim mummies contribute to a growing body of evidence that prehistoric dairy pastoralism in Inner and East Asia spread independently of lactase persistence genotypes^{28,30}.

Discussion

Although human activities in Xinjiang can be traced back to around 40,000 years ago^{24,39}, the earliest evidence for sustained human habitation in the Tarim Basin dates only to the late third to early second millennium bc. There, at the sites of Xiaohe, Gumugou and Beifang, well-preserved mummified human remains buried within wooden coffins and associated with rich organic grave good assemblages represent the earliest known archaeological cultures of the region. Since their initial discovery in the early twentieth century and subsequent large-scale excavations beginning in the 1990s (ref. 16), the Tarim mummies have been at the centre of debates with regard to their origins, their relationship to other Bronze Age steppe (Afanasievo), oasis (BMAC) and mountain (IAMC and Chemurchek) groups, and their potential connection to the spread of Indo-European languages into this region^{3,4,40}.

The palaeogenomic and proteomic data we present here suggest a very different and more complex population history than previously proposed. Although the IAMC may have been a vector for transmitting cultural and economic factors into the Tarim Basin, the known sites from the IAMC do not provide a direct source of ancestry for the Xiaohe populations. Instead, the Tarim mummies belong to an isolated gene pool whose Asian origins can be traced to the early Holocene epoch. This gene pool is likely to have once had a much wider geographic distribution, and it left a substantial genetic footprint in the EMBA populations of the Dzungarian Basin, IAMC and southern Siberia. The Tarim mummies' so-called Western physical features are probably due to their connection to the Pleistocene ANE gene pool, and their extreme genetic isolation differs from the EBA Dzungarian, IAMC and Chemurchek populations, who experienced substantial genetic interactions with the nearby populations mirroring their cultural links, pointing towards a role of extreme environments as a barrier to human migration.

In contrast to their marked genetic isolation, however, the populations of the Xiaohe horizon were culturally cosmopolitan, incorporating diverse economic elements and

technologies with far-flung origins. They made cheese from ruminant milk using a kefir-like fermentation³⁷, perhaps learned from descendants of the Afanasievo, and they cultivated wheat, barley and millet^{37,41}, crops that were originally domesticated in the Near East and northern China and which were introduced into Xinjiang no earlier than 3500 bc (refs. ^{8,42}), probably via their IAMC neighbours²⁴. They buried their dead with *Ephedra* twigs in a style reminiscent of the BMAC oasis cultures of Central Asia, and they also developed distinctive cultural elements not found among other cultures in Xinjiang or elsewhere, such as boat-shaped wooden coffins covered with cattle hides and marked by timber poles or oars, as well as an apparent preference for woven baskets over pottery^{43,44}. Considering these findings together, it appears that the tightknit population that founded the Xiaohe horizon were well aware of different technologies and cultures outside the Tarim Basin and that they developed their unique culture in response to the extreme challenges of the Taklamakan Desert and its lush and fertile riverine oases⁴.

This study illuminates in detail the origins of the Bronze Age human populations in the Dzungarian and Tarim basins of Xinjiang. Notably, our results support no hypothesis involving substantial human migration from steppe or mountain agropastoralists for the origin of the Bronze Age Tarim mummies, but rather we find that the Tarim mummies represent a culturally cosmopolitan but genetically isolated autochthonous population. This finding is consistent with earlier arguments that the IAMC served as a geographic corridor and vector for regional cultural interaction that connected disparate populations from the fourth to the second millennium bc (refs. ^{24,25}). While the arrival and admixture of Afanasievo populations in the Dzungarian Basin of northern Xinjiang around 3000 bc may have plausibly introduced Indo-European languages to the region, the material culture and genetic profile of the Tarim mummies from around 2100 bc onwards call into question simplistic assumptions about the link between genetics, culture and language and leave unanswered the question of whether the Bronze Age Tarim populations spoke a form of proto-Tocharian. Future archaeological and palaeogenomic research on subsequent Tarim Basin populations—and most importantly, studies of the sites and periods where first millennium ad Tocharian texts have been recovered—are necessary to understand the later population history of the Tarim Basin. Finally, the palaeogenomic characterization of the Tarim mummies has unexpectedly revealed one of the few known Holocene-era genetic descendant populations of the once widespread Pleistocene ANE ancestry profile. The Tarim mummy genomes thus provide a critical reference point for genetically modelling Holocene-era populations and reconstructing the population history of Asia.

Methods

Sample provenance

The archaeological human remains studied in this manuscript were excavated by the Xinjiang Institute of Cultural Relics and Archaeology from 1979 to 2017. Scientific investigation of these remains was approved by the Xinjiang Cultural Relics and Archaeology Institute, which holds the custodianship of the studied remains, based on the written agreements.

Radiocarbon dating

Of the 18 individuals reported in this study, 10 were directly dated using accelerator mass spectrometry (AMS) at Beta Analytic, Miami, USA, and/or at Lanzhou University, China. To confirm the reliability of our AMS dating results, 4 out of the 10 individuals were AMS-dated at both Beta Analytic and Lanzhou University. Consistent dates were obtained in all cases (Supplementary Data 1C). The calibration of the dated samples was performed on the basis of the IntCal20 database⁴⁵ and using the OxCal v.4.4 program⁴⁶. All of the samples were dated to time periods consistent with those estimated from archaeological stratigraphic layers and excavated grave goods.

DNA laboratory procedures

Ancient DNA work was conducted in dedicated cleanroom laboratory facilities at the ancient DNA laboratories of Jilin University in Changchun and the Institute of Vertebrate Paleontology and Paleoanthropology in Beijing (Extended Data Table 1 and Supplementary Data 1A). For the 33 individuals initially screened in this study, approximately 50 mg of dentine or bone powder was obtained per individual from either teeth or bones. DNA was extracted following established protocols⁴⁷ with slight modifications (<https://doi.org/10.17504/protocols.io.baksicwe>). A subset of DNA extracts ($n = 16$) was subjected to a partial uracil-specific excision reagent repair following the methods described in ref. ⁴⁸ (Extended Data Table 1 and Supplementary Data 1A). All 33 DNA extracts were built into double-stranded dual-index Illumina libraries. Libraries that were prepared in Jilin ($n = 26$) were directly shotgun sequenced on an Illumina HiSeq X10 or HiSeq 4000 instrument using 2×150 -base-pair (bp) chemistry, and those with endogenous human DNA higher than 10% ($n = 12$) were sent for deeper sequencing. One of the 12 individuals (XHBM1) was later excluded from this study owing to high modern human DNA contamination (Supplementary Data 1A). For libraries prepared at the Institute of Vertebrate Paleontology and Paleoanthropology, samples with 0.1% or more human DNA from the initial screening ($n = 7$) were further enriched for approximately 1.2 million nuclear SNPs and then deeper sequenced on an Illumina HiSeq 4000 instrument using 2×150 -bp chemistry.

Together, a total of 18 individuals yielded sufficient high-quality ancient genomic data for downstream analyses (Extended Data Table 1).

DNA sequence data processing

Raw read data were processed with EAGER v.1.92.55 (ref. 49), a pipeline specially designed for processing ancient DNA sequence data. Specifically, raw reads were trimmed for Illumina adaptor sequences, and overlapping pairs were collapsed into single reads using AdapterRemoval 2.2.0 (ref. 50). Merged reads were mapped to the human reference genome (hs37d5; GRCh37 with decoy sequences) using the aln/samse programs in BWA v.0.7.12 (ref. 51). PCR duplicates were removed using DeDup v.0.12.2 (ref. 49). To minimize the effect of postmortem DNA damage on genotyping, we trimmed BAM files generated from samples treated ($n = 11$) or not ($n = 7$) with uracil DNA glycosylase (UDG) by soft-masking up to 10 bp on both ends of each read using the trimbam function on bamUtils v.1.0.13 (ref. 52) on the basis of the DNA misincorporation pattern per library tabulated using mapDamage v.2.0.9 (ref. 53). For each SNP in the 1,240k panel, a single base from a high-quality read (base and mapping quality score 30 or higher) was randomly sampled to represent a pseudo-diploid genotype using the pileupCaller v.1.4.0.5 downloaded from <https://github.com/stschiff/sequenceTools> under the random haploid calling mode (-randomHaploid). For the transition SNPs (C/T and G/A), trimmed BAM files were used. For the transversion SNPs, BAM files without trimming were used.

Ancient DNA authentication

We assessed the authenticity of our ancient DNA data as follows. First, we computed the proportion of C-to-T deamination errors at both the 5' and 3' ends of the sequencing reads, and found that all samples exhibited postmortem damage patterns characteristic of ancient DNA (Supplementary Data 1A). We then estimated mitochondrial DNA contamination for all individuals using the Schmutzi v.1.5.1 program⁵⁴. To do this, we mapped adapter-trimmed reads to a 500-bp-extended revised Cambridge Reference Sequence (rCRS) of the human mitochondrial genome ([NC_012920.1](#)) to preserve reads passing through the origin, and then wrapped up the alignment to the regular rCRS with the circularmapper v.1.1 (ref. 49). We successively ran the contDeam and schmutzi modules in the schmutzi program against the worldwide allele frequency database of 197 individuals to estimate the mitochondrial DNA contamination rate. Last, we estimated the nuclear contamination rate on men using ANGSD v.0.910 (ref. 55), on the basis of the principle that men have only a single copy of the X chromosome, and thus contamination will introduce extra mismatches among reads in SNP sites but not in the flanking monomorphic sites.

DNA reference datasets

We compared the genome sequences of our ancient individuals to two sets of worldwide genotype panels, one based on the Affymetrix Axiom Genome-wide Human Origins 1 array (HumanOrigins; 593,124 autosomal SNPs)^{56,57,58} and the other on the 1,240k dataset (1,233,013 autosomal SNPs including all of the HumanOrigins SNPs)⁵⁹. We augmented both datasets by adding the Simons Genome Diversity Panel⁶⁰ and published ancient genomes (Supplementary Data 2A).

Genetic relatedness analysis

We used pairwise mismatch rate (pmr)⁶¹ and lcMLkin v0.5.0 (ref. 62), to determine the genetic relatedness between ancient individuals. We calculated pmr for all pairs of ancient individuals in this study using the autosomal SNPs in the 1,240k panel and kept individual pairs with at least 8,000 SNPs covered by both to remove noisy estimates from low-coverage samples. We used lcMLkin to validate our observation in pmr analysis and to distinguish between parent–offspring and full sibling pairs.

Uniparental haplogroup assignment

We aligned the adapter-trimmed reads to the rCRS NC_012920.1, and then generated the mitochondrial consensus sequence of each ancient individual using Geneious software v.11.1.3 (ref. 63; <https://www.geneious.com/>). We assigned each consensus sequence into a specific haplogroup using HaploGrep2 (ref. 64). For the Y chromosome, we used lineage-informative SNPs from the International Society of Genetic Genealogy 2016 tree (<https://isogg.org/tree/2016/index16.html>). For these SNPs, we called each individual’s genotype using bcftools v.1.7 (ref. 51) mpileup and call modules, after removing reads with mapping quality score < 30 (-q 30) and bases with quality score < 30 (-Q 30). We subsequently removed all heterozygous genotype calls. Then we assigned each individual to a specific Y haplogroup by manually comparing the genotype calls with the International Society of Genetic Genealogy SNPs. Before variant calling, we filtered alignment data using the pysam library v.0.15.2 (<https://pysam.readthedocs.io/en/latest/>) to reduce false positive variants due to postmortem damage and modern human contamination. We kept an observed base only if it was from a read shorter than 100 bp and the base was more than 10 bp away from the read ends. For transition SNPs, we further removed aligned bases if they were from a read with no postmortem damage pattern (that is, no C-to-T or G-to-A substitution). We determined each individual’s Y haplogroup primarily on the basis of the transversion SNPs and additionally considered transitions if transversions were insufficient.

Population genetic analysis

We performed principal component analysis as implemented in smartpca v.16000 (ref. [65](#)) using a set of 2,077 present-day Eurasian individuals from the HumanOrigins dataset (Supplementary Data [2B](#)) with the options ‘lsqproject: YES’ and ‘shrinkmode: YES’. The unsupervised admixture analysis was performed with ADMIXTURE v.1.3.0 (ref. [66](#)). For ADMIXTURE, we removed genetic markers with minor allele frequency lower than 1% and pruned for linkage disequilibrium using the -indep-pairwise 200 25 0.2 option in PLINK v.1.90 (ref. [67](#)). We used outgroup f_3 statistics^{[68](#)} to obtain a measurement of genetic relationship of the target population to a set of the Eurasian populations since their divergence from an African outgroup. We calculated f_4 statistics with the ‘f4mode: YES’ function in the ADMIXTOOLS package^{[58](#)}. f_3 and f_4 statistics were calculated using qp3Pop v.435 and qpDstat v.755 in the ADMIXTOOLS package.

Runs of homozygosity

We characterized whether the Bronze Age Xinjiang individuals descended from genetically related parents by estimating the runs of homozygosity (ROH). ROH refers to segments of the genome where the two chromosomes in an individual are identical to each other owing to recent common ancestry. Therefore, the presence of long ROH segments strongly suggests that an individual’s parents are related. We applied the hapROH method^{[69](#)} using the Python library hapROH v.0.3a4 with default parameters. The method was developed to identify ROH from low-coverage genotype data typical of ancient DNA and is still robust enough to identify ROH for individuals with a coverage down to 0.5× (ref. [69](#)). We reported the total sum of ROH longer than 4, 8, 12 and 20 cM, and visualized the results using DataGraph v.4.5.1.

Genetic admixture modelling with qpAdm

We modelled our ancient Xinjiang populations using the qpWave/qpAdm programs (qpWave v.410 (ref. [70](#)) and qpAdm v.810 (ref. [57](#))). We used the following eight populations in the 1,240k dataset as the base set of outgroups (base) unless explicitly stated otherwise: Mbuti ($n = 5$), Natufian ($n = 6$), Onge ($n = 2$), Iran_N ($n = 5$), Villabruna ($n = 1$), Mixe ($n = 3$), Ami ($n = 2$), Anatolia_N ($n = 23$). This set includes an African outgroup (Mbuti), early Holocene Levantine hunter-gatherers (Natufian), Andamanese islanders (Onge), early Neolithic Iranians from the Tepe Ganj Dareh site (Iran_N), late Pleistocene Western European hunter-gatherers (Villabruna), Central Native Americans (Mixe), an indigenous group native to Taiwan (Ami) and Neolithic farmers from Anatolia (Anatolia_N). To compare competing models, we also took a

‘rotating’ approach, where we reciprocally added a source from a model to outgroups for a competing model. We specified which outgroups are used for all qpAdm models.

Admixture dating with DATES

We used DATES v.753 (ref. [26](#)) for the dating of admixture events of the ancient populations with the pseudo-haploid genotype data under the simplified assumption that gene flow occurred as a single event, and assuming a generation time of 29 years (ref. [58](#)). The DATES software measures the decay of ancestry covariance to infer the admixture time and estimates jackknife standard errors. In the parameter file for running DATES, we used the options binsize: 0.001, maxdis: 0.5, runmode: 1, qbin: 10 and lovalfit: 0.45 in every run on the pseudo-haploid genotype data. For each target population, we chose a pair of reference populations that we identified as good sources in the qpAdm analysis. In cases in which the qpAdm source had limited sample size or SNP coverage, we chose an alternative that had a similar genetic profile to the qpAdm source but with better data quality to enhance the statistical power of the DATES analysis (Supplementary Data [1D-G](#)). For Dzungaria_EBA1 and Chemurchek, we used the Afanasievo ($n = 20$) and Baikal_EBA ($n = 9$) as the references. For Kumsay_EBA and Mereke_MBA, we used the Afanasievo ($n = 20$) and Baikal_EN ($n = 15$). For Dali_EBA, we used Tarim_EMBA1 ($n = 12$) and Baikal_EBA ($n = 9$). For Tarim_EMBA1, we used West_Siberia_N ($n = 3$) and DevilsCave_N ($n = 4$).

Protein extraction, digestion and liquid chromatography with tandem mass spectrometry

Total protein extractions were performed on dental calculus obtained from seven Xiaohe individuals excavated from layers 4 and 5 (Extended Data Table [2](#)). Only individuals with calculus deposits >5 mg were analysed, and 5–10 mg of dental calculus was processed for each sample. Samples were extracted and digested using a filter-aided sample preparation, following decalcification in 0.5 M EDTA (ref. [71](#)). Extracted peptides were analysed by liquid chromatography with tandem mass spectrometry (MS/MS) using a Q-Exactive mass spectrometer (Thermo Scientific) coupled to an ACQUITY UPLC M-Class system (Waters AG) according to previously described protocols^{[28](#)}. Potential contamination and sample carryover were monitored through the use of extraction blanks as well as injection blanks between each sample.

Protein database searching

Tandem mass spectra were converted to Mascot generic files by MSConvert version 3.0.11781 using the 100 most intense MS/MS peaks. All MS/MS samples were analysed using Mascot (Matrix Science; v.2.6.0). Mascot was set up to search the

SwissProt Release 2019_08 database (560,823 entries) assuming the digestion enzyme trypsin. Mascot was searched with a fragment ion mass tolerance of 0.050 Da and a parent ion tolerance of 10.0 ppm. Carbamidomethylation of cysteine was specified in Mascot as a fixed modification. Deamidation of asparagine and glutamine and oxidation of methionine and proline were specified in Mascot as variable modifications. A subset of samples were analysed in duplicate (Supplementary Data 3), and the results were combined using multidimensional protein identification technology (MudPIT) before analysis.

Criteria for protein identification

MS/MS-based protein and peptide identifications were validated using Scaffold (version Scaffold_4.9.0, Proteome Software). Peptide identifications were accepted if they could be established at greater than 86.0% probability to achieve a false discovery rate (FDR) less than 1.0% by the Peptide Prophet algorithm⁷¹ with Scaffold delta-mass correction. Protein identifications were accepted if they could be established at an FDR of less than 5.0% and contained at least two unique peptides. Final protein and peptide FDRs were 1.8% and 0.99%, respectively. Protein probabilities were assigned by the Protein Prophet algorithm⁷². After establishing the presence of the milk proteins β -lactoglobulin and α -S1-casein using these criteria, we expanded our analysis to accept further milk proteins identified on the basis of single peptides for high-scoring PSMs (>60), which resulted in the additional identification of α -lactalbumin. Proteins that contained similar peptides that could not be differentiated on the basis of MS/MS analysis alone were grouped to satisfy the principles of parsimony. All samples yielded proteomes typical of a dental calculus oral microbiome, and damage-associated modifications (N and Q deamidation) characteristic of ancient proteins were observed (Supplementary Data 3).

Reporting summary

Further information on research design is available in the [Nature Research Reporting Summary](#) linked to this paper.

Data availability

The DNA sequences reported in this paper have been deposited in the European Nucleotide Archive under the accession number [PRJEB46875](#). Haplod genotype data of ancient individuals in this study on the 1,240k panel are available in the EIGENSTRAT format at <https://edmond.mpdl.mpg.de/imeji/collection/OMm2fpu0jR3jSqnY>. The protein spectra have been deposited in the ProteomeXchange Consortium via the PRIDE

partner repository under the accession number [PDX027706](#). The publicly available database SwissProt release 2019_08 is accessible through the UniProt Knowledge Base (<https://www.uniprot.org>). The basemaps used in Figs. 1, 3 are in the public domain and accessible through the Natural Earth website (<https://www.naturalearthdata.com/downloads/10m-raster-data/>).

Code availability

All of the analyses performed in this study are based on publicly available software programs. Specific version information and non-default arguments are described in the Methods.

References

1. 1. Peyrot, M. in *Aspects of Globalisation: Mobility, Exchange and the Development of Multi-Cultural States* 12–17 (2017).
2. 2. Damgaard, P. et al. 137 ancient human genomes from across the Eurasian steppes. *Nature* **557**, 369–374 (2018).
3. 3. Hemphill, B. E. & Mallory, J. P. Horse-mounted invaders from the Russo-Kazakh steppe or agricultural colonists from western Central Asia? A craniometric investigation of the Bronze Age settlement of Xinjiang. *Am. J. Phys. Anthropol.* **124**, 199–222 (2004).
4. 4. Betts, A., Jia, P. & Abduresule, I. A new hypothesis for early Bronze Age cultural diversity in Xinjiang, China. *Archaeol. Res. Asia* **17**, 204–213 (2019).
5. 5. Li, C. et al. Evidence that a West-East admixed population lived in the Tarim Basin as early as the early Bronze Age. *BMC Biol.* **8**, 15 (2010).
6. 6.

Li, C. et al. Analysis of ancient human mitochondrial DNA from the Xiaohe cemetery: insights into prehistoric population movements in the Tarim Basin, China. *BMC Genet.* **16**, 78 (2015).

7. 7.

Ning, C. et al. Ancient genomes reveal Yamnaya-related ancestry and a potential source of Indo-European speakers in Iron Age Tianshan. *Curr. Biol.* **29**, 2526–2532 (2019).

8. 8.

Zhou, X. et al. 5,200-year-old cereal grains from the eastern Altai Mountains redate the trans-Eurasian crop exchange. *Nat. Plants* **6**, 78–87 (2020).

9. 9.

Wang, T. et al. Tianshanbeilu and the isotopic millet road: reviewing the late Neolithic/Bronze Age radiation of human millet consumption from north China to Europe. *Natl Sci. Rev.* **6**, 1024–1039 (2019).

10. 10.

Zhang, Y. et al. Holocene environmental changes around Xiaohe Cemetery and its effects on human occupation, Xinjiang, China. *J. Geogr. Sci.* **27**, 752–768 (2017).

11. 11.

Hong, Z., Jian-Wei, W., Qiu-Hong, Z. & Yun-Jiang, Y. A preliminary study of oasis evolution in the Tarim Basin, Xinjiang, China. *J. Arid Environ.* **55**, 545–553 (2003).

12. 12.

Jia, P. & Betts, A. A re-analysis of the Qiemu'erqieke (Shamirshak) cemeteries, Xinjiang, China. *J. Indo-Eur. Stud.* **38**, 275–317 (2010).

13. 13.

Peyrot, M. The deviant typological profile of the Tocharian branch of Indo-European may be due to Uralic substrate influence. *Indo-Eur. Linguist.* **7**, 72–121 (2019).

14. 14.

Bouckaert, R. et al. Mapping the origins and expansion of the Indo-European language family. *Science* **337**, 957–960 (2012).

15. 15.

Allentoft, M. E. et al. Population genomics of Bronze Age Eurasia. *Nature* **522**, 167–172 (2015).

16. 16.

Mallory, J. P. & Mair, V. H. *The Tarim Mummies: Ancient China and the Mystery of the Earliest Peoples from the West* (Thames & Hudson, 2000).

17. 17.

Barber, E. W. *Mummies of Urumchi* (W. W. Norton & Co., 1999).

18. 18.

Mair, V. H. Prehistoric Caucasoid corpses of the Tarim Basin. *J. Indo-Euro. Stud.* **23**, 281–307 (1995).

19. 19.

Mair, V. H. in *The Bronze Age and Early Iron Age Peoples of Eastern Central Asia* Vol. 2 835–855 (Institute for the Study of Man and the University of Pennsylvania Museum, 1998).

20. 20.

Mallory, J. P. *The Problem of Tocharian Origins: an Archaeological Perspective* (Univ. Pennsylvania Press, 2015).

21. 21.

Chen, K. & Hiebert, F. T. The late prehistory of Xinjiang in relation to its neighbors. *J. World Prehist.* **9**, 243–300 (1995).

22. 22.

Han, K. Craniometric study on the ancient individuals from the Gumugou site, Xinjiang (in Chinese). *Kaogu Xuebao* 361–384 (1986).

23. 23.
Kuzmina, E. E. in *Archeology, Migration and Nomadism, Linguistics* Vol. 1 63–93 (Univ. Pennsylvania Museum Publications, 1998).
24. 24.
Li, Y. Agriculture and palaeoeconomy in prehistoric Xinjiang, China (3000–200 BC). *Veg. Hist. Archaeobot.* **30**, 287–303 (2021).
25. 25.
Frachetti, M. D. Multiregional emergence of mobile pastoralism and nonuniform institutional complexity across Eurasia. *Curr. Anthropol.* **53**, 2–38 (2012).
26. 26.
Narasimhan, V. M. et al. The formation of human populations in South and Central Asia. *Science* **365**, eaat7487 (2019).
27. 27.
Feng, Q. et al. Genetic history of Xinjiang’s Uyghurs suggests Bronze Age multiple-way contacts in Eurasia. *Mol. Biol. Evol.* **34**, 2572–2582 (2017).
28. 28.
Jeong, C. et al. Bronze Age population dynamics and the rise of dairy pastoralism on the eastern Eurasian steppe. *Proc. Natl Acad. Sci. USA* **115**, E11248–E11255.
29. 29.
Yu, H. et al. Paleolithic to Bronze Age Siberians reveal connections with first Americans and across Eurasia. *Cell* **181**, 1232–1245 (2020).
30. 30.
Jeong, C. et al. A dynamic 6,000-year genetic history of Eurasia’s Eastern Steppe. *Cell* **183**, 890–904 (2020).
31. 31.
Fu, Q. et al. The genetic history of Ice Age Europe. *Nature* **534**, 200–205 (2016).
32. 32.

Wang, C.-C. et al. Genomic insights into the formation of human populations in East Asia. *Nature* **591**, 413–419 (2021).

33. 33.

Li, J.-F. et al. Buried in sands: environmental analysis at the archaeological site of Xiaohe Cemetery, Xinjiang, China. *PLoS ONE* **8**, e68957 (2013).

34. 34.

Qiu, Z. et al. Paleo-environment and paleo-diet inferred from Early Bronze Age cow dung at Xiaohe Cemetery, Xinjiang, NW China. *Quat. Int.* **349**, 167–177 (2014).

35. 35.

Yang, Y. et al. Proteomics evidence for kefir dairy in Early Bronze Age China. *J. Archaeol. Sci.* **45**, 178–186 (2014).

36. 36.

Xie, M. et al. Identification of a dairy product in the grass woven basket from Gumugou Cemetery (3800 BP, northwestern China). *Quat. Int.* **426**, 158–165 (2016).

37. 37.

Yang, R. et al. Investigation of cereal remains at the Xiaohe Cemetery in Xinjiang, China. *J. Archaeol. Sci.* **49**, 42–47 (2014).

38. 38.

Zhang, G. et al. Ancient plant use and palaeoenvironmental analysis at the Gumugou Cemetery, Xinjiang, China: implication from desiccated plant remains. *Archaeol. Anthropol. Sci.* **9**, 145–152 (2017).

39. 39.

Yu, J. & He, J. Significant discoveries from the excavation of Jimunai Tongtiandong site (in Chinese). *Wenwubao* **8** (2017).

40. 40.

Holland, C. et al. New genetic evidence of affinities and discontinuities between Bronze Age Siberian populations. *Am. J. Phys. Anthropol.* **167**, 97–107 (2018).

41. 41.

Li, C. et al. Ancient DNA analysis of desiccated wheat grains excavated from a Bronze Age cemetery in Xinjiang. *J. Archaeol. Sci.* **38**, 115–119 (2011).

42. 42.

Stevens, C. J. & Fuller, D. Q. The spread of agriculture in eastern Asia: archaeological bases for hypothetical farmer/language dispersals. *Lang. Dyn. Change* **7**, 152–186 (2017).

43. 43.

Abuduresule, I. Archaeological report of Xiaohe cemetery of 2003 (in Chinese). *Wenwu* 4–42 (2007).

44. 44.

Abuduresule, Y., Li, W. & Hu, X. in *The Cultures of Ancient Xinjiang, Western China: Crossroads of the Silk Roads* 19–51 (Archaeopress, 2019).

45. 45.

Reimer, P. J. et al. The IntCal20 Northern Hemisphere radiocarbon age calibration curve (0–55 cal kBP). *Radiocarbon* **62**, 725–757 (2020).

46. 46.

Ramsey, C. B. Methods for summarizing radiocarbon datasets. *Radiocarbon* **59**, 1809–1833 (2017).

47. 47.

Dabney, J. et al. Complete mitochondrial genome sequence of a Middle Pleistocene cave bear reconstructed from ultrashort DNA fragments. *Proc. Natl Acad. Sci. USA* **110**, 15758–15763 (2013).

48. 48.

Rohland, N., Harney, E., Mallick, S., Nordenfelt, S. & Reich, D. Partial uracil–DNA–glycosylase treatment for screening of ancient DNA. *Philos. Trans. R. Soc.*

B **370**, (2015).

49. 49.

Peltzer, A. et al. EAGER: efficient ancient genome reconstruction. *Genome Biol.* **17**, 60 (2016).

50. 50.

Schubert, M., Lindgreen, S. & Orlando, L. AdapterRemoval v2: rapid adapter trimming, identification, and read merging. *BMC Res. Notes* **9**, (2016).

51. 51.

Li, H. & Durbin, R. Fast and accurate short read alignment with Burrows–Wheeler transform. *Bioinformatics* **25**, 1754–1760 (2009).

52. 52.

Jun, G., Wing, M. K., Abecasis, G. R. & Kang, H. M. An efficient and scalable analysis framework for variant extraction and refinement from population-scale DNA sequence data. *Genome Res.* **25**, 918–925 (2015).

53. 53.

Jónsson, H., Ginolhac, A., Schubert, M., Johnson, P. L. F. & Orlando, L. mapDamage2.0: fast approximate Bayesian estimates of ancient DNA damage parameters. *Bioinformatics* **29**, 1682–1684 (2013).

54. 54.

Renaud, G., Slon, V., Duggan, A. T. & Kelso, J. Schmutzi: estimation of contamination and endogenous mitochondrial consensus calling for ancient DNA. *Genome Biol.* **16**, 224 (2015).

55. 55.

Korneliussen, T. S., Albrechtsen, A. & Nielsen, R. ANGSD: Analysis of Next Generation Sequencing Data. *BMC Bioinformatics* **15**, 356 (2014).

56. 56.

Jeong, C. et al. The genetic history of admixture across inner Eurasia. *Nat. Ecol. Evol.* **3**, 966–976 (2019).

57. Lazaridis, I. et al. Genomic insights into the origin of farming in the ancient Near East. *Nature* **536**, 419–424 (2016).
58. Patterson, N. et al. Ancient admixture in human history. *Genetics* **192**, 1065–1093 (2012).
59. Fu, Q. et al. An early modern human from Romania with a recent Neanderthal ancestor. *Nature* **524**, 216–219 (2015).
60. Mallick, S. et al. The Simons Genome Diversity Project: 300 genomes from 142 diverse populations. *Nature* **538**, 201–206 (2016).
61. Kennett, D. J. et al. Archaeogenomic evidence reveals prehistoric matrilineal dynasty. *Nat. Commun.* **8**, 14115 (2017).
62. Lipatov, M., Sanjeev, K., Patro, R. & Veeramah, K. R. Maximum likelihood estimation of biological relatedness from low coverage sequencing data. Preprint at <https://doi.org/10.1101/023374> (2015).
63. Kearse, M. et al. Geneious Basic: an integrated and extendable desktop software platform for the organization and analysis of sequence data. *Bioinformatics* **28**, 1647–1649 (2012).
64. Weissensteiner, H. et al. HaploGrep 2: mitochondrial haplogroup classification in the era of high-throughput sequencing. *Nucleic Acids Res.* **44**, W58–W63 (2016).
- 65.

Patterson, N., Price, A. L. & Reich, D. Population structure and eigenanalysis. *PLoS Genet.* **2**, e190 (2006).

66. 66.

Alexander, D. H., Novembre, J. & Lange, K. Fast model-based estimation of ancestry in unrelated individuals. *Genome Res.* **19**, 1655–1664 (2009).

67. 67.

Chang, C. C. et al. Second-generation PLINK: rising to the challenge of larger and richer datasets. *Gigascience* **4**, (2015).

68. 68.

Raghavan, M. et al. Upper Palaeolithic Siberian genome reveals dual ancestry of Native Americans. *Nature* **505**, 87–91 (2014).

69. 69.

Ringbauer, H., Novembre, J. & Steinrücken, M. Detecting runs of homozygosity from low-coverage ancient DNA. Preprint at <https://doi.org/10.1101/2020.05.31.126912> (2020).

70. 70.

Reich, D. et al. Reconstructing Native American population history. *Nature* **488**, 370–374 (2012).

71. 71.

Keller, A., Nesvizhskii, A. I., Kolker, E. & Aebersold, R. Empirical statistical model to estimate the accuracy of peptide identifications made by MS/MS and database search. *Anal. Chem.* **74**, 5383–5392 (2002).

72. 72.

Nesvizhskii, A. I., Keller, A., Kolker, E. & Aebersold, R. A statistical model for identifying proteins by tandem mass spectrometry. *Anal. Chem.* **75**, 4646–4658 (2003).

Acknowledgements

We thank Xinjiang Institute of Cultural Relics and Archaeology and Renmin University of China for providing such valuable samples for study; Lanzhou University for providing the AMS dating results; K. Wang, H. Yu and G. A. Gnechi-Ruscone for helpful comments on the genetic landscapes of the Eurasian steppe; T. Hermes and R. Flad for helpful comments on the broader archaeological context of the region. This work was supported by the National Key R&D Program of China (grant numbers 2016YFE0203700 and 2018YFA0606402), the National Natural Science Foundation of China (grant number 42072018, 41925009), the Fundamental Research Funds for the Central Universities, the European Research Council under the European Union's Horizon 2020 research and innovation programme (grant agreement numbers 804884-DAIRYCULTURES and 646612-Eurasia3angle), the Humanities and Social Sciences Key Research Base of the Ministry of Education (16JJD780005), the National Research Foundation of Korea grant funded by the Korean Government (MSIT; 2020R1C1C1003879) and the Max Planck Society.

Funding

Open access funding provided by Max Planck Society.

Author information

Author notes

1. These authors contributed equally: Fan Zhang, Chao Ning, Ashley Scott

Affiliations

1. School of Life Sciences, Jilin University, Changchun, China

Fan Zhang, Linyuan Fan, Pengcheng Ma, Chunxiang Li, Yang Xu, Sihao Wu, Hui Zhou & Yinqui Cui

2. Max Planck Institute for the Science of Human History, Jena, Germany

Chao Ning, Ashley Scott, Rasmus Bjørn, Martine Robbeets, Johannes Krause & Christina Warinner

3. Key Laboratory of Vertebrate Evolution and Human Origins, Institute of Vertebrate Paleontology and Paleoanthropology, Center for Excellence in Life and Paleoenvironment, Chinese Academy of Sciences, Beijing, China

Qiaomei Fu, Wenjun Wang, Peng Cao, Feng Liu, Qingyan Dai, Xiaotian Feng, Ruowei Yang & Vikas Kumar

4. Xinjiang Institute of Cultural Relics and Archaeology, Ürümqi, China

Wenying Li, Idilisi Abuduresule, Xingjun Hu, Qiurong Ruan & Alipujiang Niyazi

5. School of Archaeology, Jilin University, Changchun, China

Dong Wei & Hong Zhu

6. MOE Key Laboratory of Western China's Environmental Systems, College of Earth & Environmental Sciences, Lanzhou University, Lanzhou, China

Guanghui Dong

7. Key Laboratory of Cenozoic Geology and Environment, Institute of Geology and Geophysics, Chinese Academy of Sciences, Beijing, China

Zihua Tang

8. College of Pharmacia Sciences, Jilin University, Changchun, China

Shizhu Gao

9. Institute of Archaeological Science, Fudan University, Shanghai, China

Shaoqing Wen

10. Max Planck Institute for Evolutionary Anthropology, Leipzig, Germany

Johannes Krause

11. Department of Anthropology, Harvard University, Cambridge, MA, USA

Christina Warinner

12. School of Biological Sciences, Seoul National University, Seoul, Republic of Korea

Choongwon Jeong

13. Key Laboratory for Evolution of Past Life and Environment in Northeast Asia, Ministry of Education, Jilin University, Changchun, China

Yinqiu Cui

14. Research Center for Chinese Frontier Archaeology of Jilin University, Jilin University, Changchun, China

Yinqiu Cui

Contributions

Y.C., C.J., C.W., C.N. and J.K. conceived and supervised the study. F.Z., A.S, L.F., P.C., R.Y., F.L. and Q.D. performed the laboratory work. Q.F., D.W., W.L., X.H., Q.R., I.A., C.L., S.G., Y.X., S. Wu, S. Wen, H. Zhu, H. Zhou and A.N. provided archaeological materials and associated information. R.B. and M.R. provided the linguistic background and G.D. and Z.T. assisted with the AMS dating. C.N., F.Z., A.S., C.W., C.J., Q.F., P.M., X.F., W.W. and V.K. analysed data. C.N., C.W., C.J., Y.C., F.Z. and A.S. wrote the manuscript with input from all coauthors.

Corresponding authors

Correspondence to [Chao Ning](#), [Johannes Krause](#), [Christina Warinner](#), [Choongwon Jeong](#) or [Yinqiu Cui](#).

Ethics declarations

Competing interests

The authors declare no competing interests.

Additional information

Peer review information *Nature* thanks Paula Dupuy, Michael Frachetti and the other, anonymous, reviewer(s) for their contribution to the peer review of this work. Peer reviewer reports are available.

Publisher's note Springer Nature remains neutral with regard to jurisdictional claims in published maps and institutional affiliations.

Extended data figures and tables

[**Extended Data Fig. 1 Burial goods excavated from the Xiaohe cemetery.**](#)

A, a wooden sculpture excavated from the upper layer of a double-layer mud coffin of XHM75. **B**, an oar-plank placed in front of a male burial. **C**, a wooden pole placed in front of a female burial. **D**, Burial XHM66 from layer 4 of the Xiaohe cemetery illustrating typical features of early burials, including boat-shaped coffins and mummified remains dressed in woollen garments. This burial style is common at Bronze Age cemeteries throughout the Tarim Basin, including Beifang and Gumugou. **E**, Side view of the Xiaohe cemetery showing wooden grave markers and fencing.

Extended Data Fig. 2 F-statistics for the ancient Xinjiang and the Eurasian steppe populations.

A, we show top 5 outgroup f_3 -statistics of the form $f_3(\text{Target}, X; \text{Mbuti})$ for the 361 world-wide populations as contrast populations X, and 8 populations from this study and the Eurasian Steppe as target: Dzungaria_EBA1, Dzungaria_EBA2, Chemurchek, Dzungaria_EIA, Okunevo_EMBA, Kazakhstan_EMBA, Botai_CA, West_Siberia_N, horizontal bars represent ± 1 standard error measure (s.e.m.) calculated by 5 cM block jackknifing. **B**, f_4 -statistics of the form $f_4(\text{Mbuti}, X; \text{Dzungaria_EBA1}, \text{Tarim_EMBA1})$, horizontal bars represent ± 3 (thin) and ± 1 (thick) s.e.m. calculated by 5 cM block jackknifing, and **C**, f_4 -statistics of the form $f_4(\text{Mbuti}, X; \text{Dzungaria_EBA2}, \text{Tarim_EMBA1})$, where X is 361 world-wide populations. We show the top and the bottom 15 f_4 statistics. Horizontal bars represent the point estimate ± 3 (thin) and ± 1 (thick) s.e.m., respectively, as estimated using 5 cM block jackknifing. F_4 statistics deviating three s.e.m. or more from zero are marked in red.

Extended Data Fig. 3 Unsupervised ADMIXTURE plot for the Bronze Age Xinjiang individuals.

We plot ancestry component estimates for K = 8 using ‘AncestryPainter’ (<https://www.picb.ac.cn/PGG/resource.php>). Dzungaria_EBA individuals show an ancestry pattern close to Afanasievo and Yamnaya, while Tarim_EMBA individuals show a pattern similar to AG3, West_Siberia_N and Botai_CA from the Eurasia steppe.

Extended Data Fig. 4 Reduced genetic diversity of the Tarim_EMBA individuals.

A, a comparison of individual outgroup f_3 -statistics for the ancient Xinjiang populations and their neighboring populations from Inner Asia, including Tarim_EMBA1 (n = 12), Tarim_EMBA2 (n = 1), ANE (n = 3), Dzungaria_EBA1 (n = 3), Dzungaria_EBA2 (n = 2), West_Siberia_N (n = 3) and Botai_CA (n = 3), which Tarim Basin individuals show the highest affinity to each other. In each boxplot, the

box marks the 25th and 75th quartiles of the distribution, respectively, and the horizontal line within the box marks the median. The whisker delineates the maximum and the minimum. **B**, the cumulative distribution of ROH tracts shows that Tarim_EMBA individuals did not descend from close related parents. **C**, pairwise mismatch rate (pmr) between individuals in the ancient populations of Xinjiang and its neighboring regions, including all pairs of individuals within the Afanasievo (n = 27), ANE (n = 3), Baikal_EBA (n = 9), Baikal_EN (n = 15), Botai_CA (n = 3), Dzungaria_EBA (n = 5), Dzungaria_EIA (n = 10), Sintashta_MLBA (n = 51), Tarim_EMBA (n = 13), West_Siberia_N (n = 3), as well as present-day isolated populations such as Papuan and Karitiana. Tarim_EMBA individuals uniformly show a much reduced pmr value that is equivalent to the first-degree relatives in Afanasievo or Sintashta_MLBA. The red dotted lines mark the expected pmr value for the given coefficient of relationship (r), ranging from 0 (unrelated) and 1/4 (second degree relatives) to 1/2 (first degree relatives), based on the mean value of pmr among these populations, respectively. In each box plot, the box represents the interquartile range (the 25th and 75th quartiles), and the horizon line within the box represents the median. Black-filled and open circles represent outliers (1.5 times beyond the IQR) and extreme outliers (3 times beyond the IQR), respectively. The whisker delineates the smallest and the largest non-outlier observations. **D**, Y chromosome phylogeny of the Bronze Age Xinjiang male individuals. Xiaohe male individuals fall into a branch distinct from western Bronze Age steppe pastoralists, such as Afanasievo and Yamnaya. One individual from Beifang falls in a position that is more basal than Xiaohe, but its phylogenetic position cannot be fixed due to low coverage, and its proximate position(s) are instead indicated with an asterisk.

[Extended Data Fig. 5 Proteomic evidence for dairy consumption in Xiaohe dental calculus, ca. 2000-1800 BCE.](#)

A, B- and Y-ion series for the frequently observed β -lactoglobulin peptide TPEVD(D/N/K)EALEK, which contains a taxon-specific polymorphic residue: D, Bovinae; N, *Ovis*; K, *Capra*. See SI Appendix. **B**, Taxonomically assigned β -lactoglobulin (black), α -S1-casein (dark grey), and α -lactalbumin peptide spectral matches (PSMs) presented as scaled pie charts on a cladogram of dairy livestock. Bracketed numbers represent the number of PSMs (excluding duplicates) assigned to each node. †Included on the Bovidae node are: 13 PSMs assigned to Bovidae; 21 PSMs assigned to Bovidae but excluding *Capra*.

Extended Data Table 1 A summary of the Bronze Age Xinjiang individuals reported in this study

Extended Data Table 2 Dietary proteins identified in the dental calculus of individuals analyzed from the Tarim Basin Xiaohe cemetery

Extended Data Table 3 Robustness of key qpAdm admixture models

Supplementary information

Supplementary Information

This PDF file includes five sections of Supplementary text. (1) Environmental setting of Xinjiang; (2) Archaeological sites and context; (3) Linguistic background of the population history in Xinjiang; (4) Detailed description of genetic isolation of the Tarim group; and (5) Tarim mummies and the pre-pastoralist Central Asian genetic substratum.

Reporting Summary

Peer Review File

Supplementary Data 1

Sample information, qpAdm modelling results and phenotypic traits of the studied individuals.

Supplementary Data 2

Ancient and modern populations analysed in this study.

Supplementary Data 3

Dairy peptides identified within the Xiaohe dental calculus samples.

Rights and permissions

Open Access This article is licensed under a Creative Commons Attribution 4.0 International License, which permits use, sharing, adaptation, distribution and reproduction in any medium or format, as long as you give appropriate credit to the original author(s) and the source, provide a link to the Creative Commons license, and indicate if changes were made. The images or other third party material in this article are included in the article's Creative Commons license, unless indicated otherwise in a credit line to the material. If material is not included in the article's Creative Commons license and your intended use is not permitted by statutory regulation or exceeds the permitted use, you will need to obtain permission directly from the copyright holder. To view a copy of this license, visit <http://creativecommons.org/licenses/by/4.0/>.

Reprints and Permissions

About this article

Cite this article

Zhang, F., Ning, C., Scott, A. *et al.* The genomic origins of the Bronze Age Tarim Basin mummies. *Nature* **599**, 256–261 (2021). <https://doi.org/10.1038/s41586-021-04052-7>

- Received: 19 November 2020
- Accepted: 23 September 2021
- Published: 27 October 2021
- Issue Date: 11 November 2021
- DOI: <https://doi.org/10.1038/s41586-021-04052-7>

Share this article

Anyone you share the following link with will be able to read this content:

[Get shareable link](#)

Sorry, a shareable link is not currently available for this article.

[Copy to clipboard](#)

Provided by the Springer Nature SharedIt content-sharing initiative

Further reading

- [**DNA reveals surprise ancestry of mysterious Chinese mummies**](#)
 - Smriti Mallapaty

Nature (2021)
- [**The unexpected ancestry of Inner Asian mummies**](#)
 - Paula N. Doumani Dupuy

Nature (2021)

Genomics unwraps mystery of the Tarim mummies

- Nick Petrić Howe
- Shamini Bundell

Nature Podcast 27 Oct 2021

The unexpected ancestry of Inner Asian mummies

- Paula N. Doumani Dupuy

News & Views 27 Oct 2021

Podcast special: onboard the climate train to COP26

- Benjamin Thompson

Nature Podcast 03 Nov 2021

This article was downloaded by **calibre** from <https://www.nature.com/articles/s41586-021-04052-7>

| [Section menu](#) | [Main menu](#) |

- Article
- [Published: 13 October 2021](#)

Neural control of affiliative touch in prosocial interaction

- [Ye Emily Wu](#) ORCID: [orcid.org/0000-0001-8052-1073^{1,2}](https://orcid.org/0000-0001-8052-1073) na1,
- [James Dang](#)^{1,2} na1,
- [Lyle Kingsbury](#)^{1,2},
- [Mingmin Zhang](#)^{1,2},
- [Fangmiao Sun](#)^{1,2},
- [Rongfeng K. Hu](#)^{1,2} &
- [Weizhe Hong](#) ORCID: [orcid.org/0000-0003-1523-8575^{1,2}](https://orcid.org/0000-0003-1523-8575)

[Nature](#) volume **599**, pages 262–267 (2021)

- 7916 Accesses
- 1 Citations
- 180 Altmetric
- [Metrics details](#)

Subjects

- [Neural circuits](#)
- [Social behaviour](#)

Abstract

The ability to help and care for others fosters social cohesiveness and is vital to the physical and emotional well-being of social species, including humans^{1,2,3}. Affiliative social touch, such as allogrooming (grooming behaviour directed towards another individual), is a major type of prosocial behaviour that provides comfort to others^{1,2,3,4,5,6}. Affiliative touch serves to establish and strengthen social bonds between animals and can help to console distressed conspecifics. However, the neural circuits that promote prosocial affiliative touch have remained unclear. Here we show that mice exhibit affiliative allogrooming behaviour towards distressed partners, providing a consoling effect. The increase in allogrooming occurs in response to different types of stressors and can be elicited by olfactory cues from distressed individuals. Using microendoscopic calcium imaging, we find that neural activity in the medial amygdala (MeA) responds differentially to naive and distressed conspecifics and encodes allogrooming behaviour. Through intersectional functional manipulations, we establish a direct causal role of the MeA in controlling affiliative allogrooming and identify a select, tachykinin-expressing subpopulation of MeA GABAergic (γ -aminobutyric-acid-expressing) neurons that promote this behaviour through their projections to the medial preoptic area. Together, our study demonstrates that mice display prosocial comforting behaviour and reveals a neural circuit mechanism that underlies the encoding and control of affiliative touch during prosocial interactions.

Access options

Subscribe to Journal

Get full journal access for 1 year

\$199.00

only \$3.90 per issue

[Subscribe](#)

All prices are NET prices.

VAT will be added later in the checkout.

Tax calculation will be finalised during checkout.

Rent or Buy article

Get time limited or full article access on ReadCube.

from \$8.99

[Rent or Buy](#)

All prices are NET prices.

Additional access options:

- [Log in](#)
- [Access through your institution](#)
- [Learn about institutional subscriptions](#)

Fig. 1: Mice display prosocial comforting behaviour.

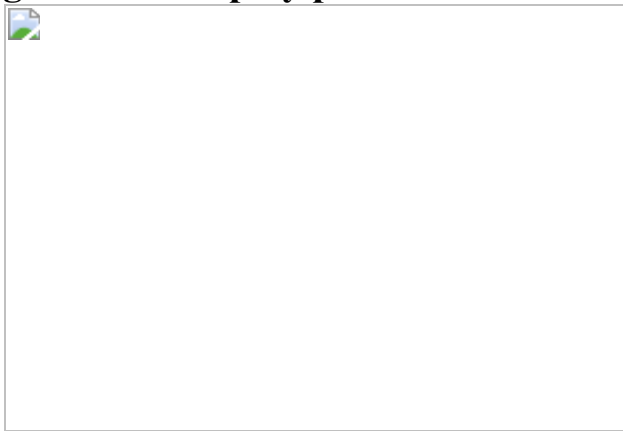


Fig. 2: MeA neural dynamics during prosocial interaction.

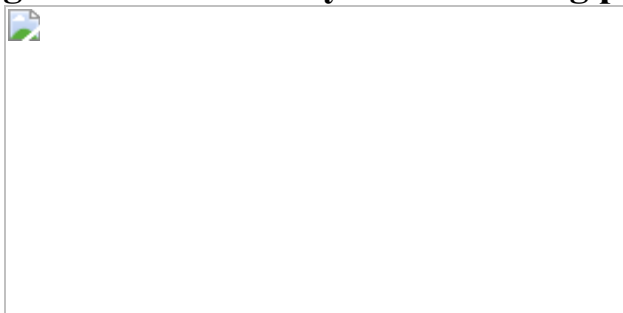


Fig. 3: MeA^{Tac1} neurons underlie allogrooming.

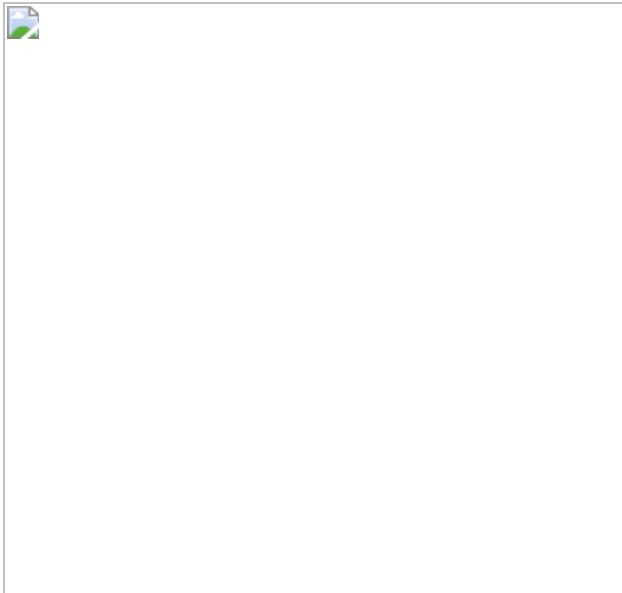


Fig. 4: MPOA-projecting MeA^{Tac1 \cap Vgat} neurons drive allogrooming.



Data availability

Additional data relating to the paper are available from the corresponding author on reasonable request. [Source data](#) are provided with this paper.

Code availability

Code for the behavioural analysis (<https://github.com/pdollar/toolbox>), animal pose tracking (<https://github.com/murthylab/sleep/releases/tag/v1.0.9>), microendoscopic imaging data analysis (<https://github.com/etterguillaume/MiniscopeAnalysis>, https://github.com/zhoupc/CNMF_E and <https://github.com/flatironinstitute/NoRMCorre>) is available at GitHub. The pretrained Google Inception v3 network is available online (<https://download.tensorflow.org/models/image/imagenet/inception-2015-12-05.tgz>). Additional code relating to the paper is available from the corresponding author on reasonable request.

References

1. 1.
de Waal, F. B. M. & Preston, S. D. Mammalian empathy: behavioural manifestations and neural basis. *Nat. Rev. Neurosci.* **18**, 498–509 (2017).
2. 2.
Dunfield, K. A. A construct divided: prosocial behavior as helping, sharing, and comforting subtypes. *Front. Psychol* **5**, 958 (2014).
3. 3.
Rault, J.-L. Be kind to others: prosocial behaviours and their implications for animal welfare. *Appl. Anim. Behav. Sci.* **210**, 113–123 (2019).
4. 4.
Morrison, I. Keep calm and cuddle on: social touch as a stress buffer. *Adapt. Hum. Behav. Physiol.* **2**, 344–362 (2016).
5. 5.

Spruijt, B. M., Hooff, J. A. V. & Gispen, W. H. Ethology and neurobiology of grooming behavior. *Physiol. Rev.* **72**, 825–852 (1992).

6. 6.

Jablonski, N. G. Social and affective touch in primates and its role in the evolution of social cohesion. *Neuroscience* **464**, 117–125 (2020).

7. 7.

Burkett, J. P. et al. Oxytocin-dependent consolation behavior in rodents. *Science* **351**, 375–378 (2016).

8. 8.

Li, L.-F. et al. Involvement of oxytocin and GABA in consolation behavior elicited by socially defeated individuals in mandarin voles. *Psychoneuroendocrinology* **103**, 14–24 (2019).

9. 9.

Sterley, T.-L. & Bains, J. S. Social communication of affective states. *Curr. Opin. Neurobiol.* **68**, 44–51 (2021).

10. 10.

Paradiso, E., Gazzola, V. & Keysers, C. Neural mechanisms necessary for empathy-related phenomena across species. *Curr. Opin. Neurobiol.* **68**, 107–115 (2021).

11. 11.

Kwon, J.-T. et al. An amygdala circuit that suppresses social engagement. *Nature* **593**, 114–118 (2021).

12. 12.

Chen, P. & Hong, W. Neural circuit mechanisms of social behavior. *Neuron* **98**, 16–30 (2018).

13. 13.

Raam, T. & Hong, W. Organization of neural circuits underlying social behavior: a consideration of the medial amygdala. *Curr. Opin. Neurobiol.* **68**, 124–136 (2021).

14. 14.

Unger, E. K. et al. Medial amygdalar aromatase neurons regulate aggression in both sexes. *Cell Rep.* **10**, 453–462 (2015).

15. 15.

Li, Y. et al. Neuronal representation of social information in the medial amygdala of awake behaving mice. *Cell* **171**, 1176–1190 (2017).

16. 16.

Twining, R. C., Vantrease, J. E., Love, S., Padival, M. & Rosenkranz, J. A. An intra-amygdala circuit specifically regulates social fear learning. *Nat. Neurosci.* **20**, 459–469 (2017).

17. 17.

Hong, W., Kim, D.-W. & Anderson, D. J. Antagonistic control of social versus repetitive self-grooming behaviors by separable amygdala neuronal subsets. *Cell* **158**, 1348–1361 (2014).

18. 18.

Chen, P. B. et al. Sexually dimorphic control of parenting behavior by the medial amygdala. *Cell* **176**, 1206–1221 (2019).

19. 19.

Allsop, S. A. et al. Corticoamygdala transfer of socially derived information gates observational learning. *Cell* **173**, 1329–1342 (2018).

20. 20.

Jeon, D. et al. Observational fear learning involves affective pain system and $\text{Ca}_v1.2$ Ca^{2+} channels in ACC. *Nat. Neurosci.* **13**, 482–488 (2010).

21. 21.

Sterley, T.-L. et al. Social transmission and buffering of synaptic changes after stress. *Nat. Neurosci.* **21**, 393–403 (2018).

22. 22.

Gangopadhyay, P., Chawla, M., Monte, O. D. & Chang, S. W. C. Prefrontal–amygdala circuits in social decision-making. *Nat. Neurosci.* **24**, 5–18 (2021).

23. 23.

Canteras, N. S., Simerly, R. B. & Swanson, L. W. Organization of projections from the medial nucleus of the amygdala: a PHAL study in the rat. *J. Comp. Neurol.* **360**, 213–245 (1995).

24. 24.

Cádiz-Moretti, B., Otero-García, M., Martínez-García, F. & Lanuza, E. Afferent projections to the different medial amygdala subdivisions: a retrograde tracing study in the mouse. *Brain Struct. Funct.* **221**, 1033–1065 (2016).

25. 25.

Mahn, M. et al. High-efficiency optogenetic silencing with soma-targeted anion-conducting channelrhodopsins. *Nat. Commun.* **9**, 4125 (2018).

26. 26.

Fenno, L. E. et al. Targeting cells with single vectors using multiple-feature Boolean logic. *Nat. Methods* **11**, 763–772 (2014).

27. 27.

Chen, T.-W. et al. Ultrasensitive fluorescent proteins for imaging neuronal activity. *Nature* **499**, 295–300 (2013).

28. 28.

Dana, H. et al. High-performance calcium sensors for imaging activity in neuronal populations and microcompartments. *Nat. Methods* **16**, 649–657 (2019).

29. 29.

Lim, B. K., Huang, K. W., Grueter, B. A., Rothwell, P. E. & Malenka, R. C. Anhedonia requires MC4R-mediated synaptic adaptations in nucleus accumbens. *Nature* **487**, 183–189 (2012).

30. 30.

Ghosh, K. K. et al. Miniaturized integration of a fluorescence microscope. *Nat. Methods* **8**, 871–878 (2011).

31. 31.

Kingsbury, L. et al. Correlated neural activity and encoding of behavior across brains of socially interacting animals. *Cell* **178**, 429–446 (2019).

32. 32.

Pnevmatikakis, E. A. & Giovannucci, A. NoRMCorre: an online algorithm for piecewise rigid motion correction of calcium imaging data. *J. Neurosci. Methods* **291**, 83–94 (2017).

33. 33.

Zhou, P. et al. Efficient and accurate extraction of in vivo calcium signals from microendoscopic video data. *Elife* **7**, e28728 (2018).

34. 34.

Kingsbury, L. et al. Cortical representations of conspecific sex shape social behavior. *Neuron* **107**, 941–953 (2020).

35. 35.

Hong, W. et al. Automated measurement of mouse social behaviors using depth sensing, video tracking, and machine learning. *Proc. Natl Acad. Sci. USA* **112**, E5351–E5360 (2015).

36. 36.

Wiltschko, A. B. et al. Mapping sub-second structure in mouse behavior. *Neuron* **88**, 1121–1135 (2015).

37. 37.

Kabra, M., Robie, A. A., Rivera-Alba, M., Branson, S. & Branson, K. JAABA: interactive machine learning for automatic annotation of animal behavior. *Nat. Methods* **10**, 64–67 (2013).

38. 38.

Jhuang, H. et al. Automated home-cage behavioural phenotyping of mice. *Nat. Commun.* **1**, 68 (2010).

39. 39.

Nilsson, S. R. et al. Simple Behavioral Analysis (SimBA)—an open source toolkit for computer classification of complex social behaviors in experimental animals. Preprint at *bioRxiv* <https://doi.org/10.1101/2020.04.19.049452> (2020).

40. 40.

LeCun, Y., Bengio, Y. & Hinton, G. Deep learning. *Nature* **521**, 436–444 (2015).

41. 41.

Szegedy, C., Vanhoucke, V., Ioffe, S., Shlens, J. & Wojna, Z. Rethinking the inception architecture for computer vision. Preprint at <https://arxiv.org/abs/1512.00567v3> (2015).

42. 42.

Pereira, T. D. et al. SLEAP: multi-animal pose tracking. Preprint at *bioRxiv* <https://doi.org/10.1101/2020.08.31.276246> (2020).

43. 43.

Hochreiter, S. & Schmidhuber, J. Long short-term memory. *Neural Comput.* **9**, 1735–1780 (1997).

44. 44.

Lipton, Z. C., Berkowitz, J. & Elkan, C. A critical review of recurrent neural networks for sequence learning. Preprint at <https://arxiv.org/abs/1506.00019> (2015).

45. 45.

Wu, Y. E., Pan, L., Zuo, Y., Li, X. & Hong, W. Detecting activated cell populations using single-cell RNA-seq. *Neuron* **96**, 313–329 (2017).

46. 46.

Harris, J. A. et al. Anatomical characterization of Cre driver mice for neural circuit mapping and manipulation. *Front. Neural Circuits* **8**, 76 (2014).

47. 47.

Taniguchi, H. et al. A resource of Cre driver lines for genetic targeting of GABAergic neurons in cerebral cortex. *Neuron* **71**, 995–1013 (2011).

48. 48.

Daigle, T. L. et al. A suite of transgenic driver and reporter mouse lines with enhanced brain-cell-type targeting and functionality. *Cell* **174**, 465–480 (2018).

49. 49.

Hu, R. K. et al. An amygdala-to-hypothalamus circuit for social reward. *Nat. Neurosci.* **24**, 831–842 (2021).

50. 50.

Stuber, G. D. et al. Excitatory transmission from the amygdala to nucleus accumbens facilitates reward seeking. *Nature* **475**, 377–380 (2011).

51. 51.

Bankhead, P. et al. QuPath: open source software for digital pathology image analysis. *Sci. Rep.* **7**, 16878 (2017).

52. 52.

Fenno, L. E. et al. Comprehensive dual- and triple-feature intersectional single-vector delivery of diverse functional payloads to cells of behaving mammals. *Neuron* **107**, 836–853 (2020).

Acknowledgements

We thank V. Wan and P. B. Chen for technical assistance and contributions to the project; D. Aharoni, P. Golshani and P. Zhao for assistance in setting up the miniscope (v4) imaging system; D. J. Anderson for comments and feedback on the project; and members of the Hong laboratory for valuable comments. Illustrations of mice and mouse brain schematics in Figs. [1a](#), u–x, [2a](#), [3a](#), e, k and [4d](#), [h](#), [l](#), [p](#) and Extended Data Figs. [7b](#), [8c](#), h, [9a](#) and [10b](#) were created using BioRender.com. This work was supported in part by NIH grants (R01 NS113124 and U01 NS122124), a Searle Scholars Award,

a Packard Fellowship in Science and Engineering, a Keck Foundation Junior Faculty Award, a McKnight Scholar Award, a Vallee Scholar Award, a Mallinckrodt Scholar Award, a NARSAD Young Investigator grant, a Klingenstein-Simons Fellowship Award and a Brain Research Foundation grant (to W.H.) and NIH training grant (T32 NS048004, to J.D.).

Author information

Author notes

1. These authors contributed equally: Ye Emily Wu and James Dang

Affiliations

1. Department of Biological Chemistry, David Geffen School of Medicine, University of California, Los Angeles, CA, USA

Ye Emily Wu, James Dang, Lyle Kingsbury, Mingmin Zhang, Fangmiao Sun, Rongfeng K. Hu & Weizhe Hong

2. Department of Neurobiology, David Geffen School of Medicine, University of California, Los Angeles, CA, USA

Ye Emily Wu, James Dang, Lyle Kingsbury, Mingmin Zhang, Fangmiao Sun, Rongfeng K. Hu & Weizhe Hong

Contributions

Y.E.W. and W.H. designed the study. Y.E.W., J.D., M.Z., F.S. and R.K.H. performed experiments. Y.E.W., W.H., L.K., J.D., M.Z. and F.S. analysed data. Y.E.W. and W.H. wrote the manuscript with inputs from J.D. and L.K. W.H. supervised the entire study.

Corresponding authors

Correspondence to [Ye Emily Wu](#) or [Weizhe Hong](#).

Ethics declarations

Competing interests

The authors declare no competing interests.

Additional information

Peer review information *Nature* thanks Steve Chang and the other, anonymous, reviewer(s) for their contribution to the peer review of this work.

Publisher's note Springer Nature remains neutral with regard to jurisdictional claims in published maps and institutional affiliations.

Extended data figures and tables

[Extended Data Fig. 1 Characterization of prosocial allogrooming in female mice.](#)

a, Example raster plots showing allogrooming and self-grooming behaviours exhibited by female subjects when they interact with unstressed (separation only, control) or stressed (foot-shocked) female partners. Each row represents an individual animal. **b**, Time-course of cumulative duration of allogrooming exhibited by subjects and partners after partners experience foot-shocks. Mean \pm s.e.m. **c**, **d**, Total duration (**c**) and onset latency (**d**) of allogrooming exhibited by subjects toward unstressed (control) or foot-shocked partners during 13 min of interaction. While females exhibit elevated allogrooming toward stressed partners similar to males, the total duration of allogrooming toward stressed partners is shorter in females compared to males (Fig. [1d](#), Supplementary Note [1](#)). **e**, **f**, Total number of allogrooming bouts (**e**) and average per-bout duration of allogrooming (**f**) in individual subjects interacting with unstressed (control) or foot-shocked partners. **g**, Total duration of self-grooming exhibited by subjects during interaction with unstressed (control) or foot-shocked partners. **h**, **i**, Total

duration of allogrooming (**h**) and total number of social approaches (**i**) toward subjects exhibited by partners after separation only or foot-shocks. Boxplots: median with quartiles, $1.5 \times \text{IQR}$ and outliers. **b-i**, $n = 10$ pairs of female mice. Two-sided Wilcoxon signed-rank test. $**P < 0.01$, $*P < 0.05$. ns, not significant. For details of statistical analyses, see Supplementary Table 1

[Source data.](#)

Extended Data Fig. 2 Behavioral analysis using convolutional and recurrent neural networks.

a, Schematic of behavior classification using recurrent neural network (RNN) based on CNN-derived spatial features, tracking-based features, and/or head orientation-based features. **b–e**, Performance of binary classifiers trained to discriminate between different pairs of behaviors using the CNN + RNN framework. **f**, Comparison of performance of four-way multi-class classifiers trained to discriminate between allogrooming, sniffing, self-grooming, or other behaviors. Different classifiers used CNN-derived spatial features, tracking-based features, head orientation-based features, or all three types of features to train the recurrent neural network. Data for the “CNN features” and shuffled control groups are the same as those in Fig. 1q and are presented here for comparison. **g**, PC projections of population vectors associated with different types of behavior bouts from one example microendoscopic imaging session. PCA is first performed using population activity during manually annotated behavior bouts (dots). Population activity during behavior bouts predicted using the CNN-RNN method (circles) was then projected onto this PC space. **h**, Mean pairwise Euclidean distances (in a space defined by PCs 1-4) between different pairs of behavior events that were either human annotated (“h.a.”) or predicted using the CNN-RNN method during each independent imaging session. Boxplots: median with quartiles, $1.5 \times \text{IQR}$ and outliers. **b–f**, $n = 9$ different partitions of training/validation/test datasets in each group. **h**, $n = 7$ independent imaging sessions in 6 subject mice. **b–e**, Two-sided Wilcoxon signed-rank test. **f**, One-way ANOVA followed by Bonferroni’s multiple comparisons test. **h**, Friedman test followed by post hoc Dunn’s multiple

comparisons test. *** $P < 0.001$, ** $P < 0.01$, * $P < 0.05$. ns, not significant. For details of statistical analyses, see Supplementary Table 1

[Source data](#).

Extended Data Fig. 3 MeA neuronal responses during prosocial interaction.

a, b, Example calcium traces from individual allogrooming-suppressed (**a**) and sniffing-suppressed (**b**) neurons during allogrooming or sniffing toward stressed conspecifics. **c, d,** Heatmaps showing average responses of example neurons with decreased activity during allogrooming (**c**) or sniffing (**d**). **e,** Cumulative distributions of pairwise distances between neurons of the same response type (allogrooming-responsive or sniffing-responsive) and distribution based on shuffled data in which the response type is randomly permuted (100 rounds of shuffling). **f,** Example calcium traces from single neurons that show increased activity during self-grooming but not allogrooming or sniffing. **g,** Heatmaps showing average responses of example self-grooming-responsive cells (with either increased or decreased activity) centered around self-grooming onset. **h,** Fraction of cells activated during both self-grooming and allogrooming or during both self-grooming and sniffing. **i,** Example image showing retrograde labelling of neurons in the accessory olfactory bulb (AOB) by injecting a retrograde AAV-EGFP virus in the MeA. Scale bar, 200 μm . **c, d, g,** Time 0 indicates behavior onset. **e,** $n = 338$, 1560, and 189800 pairwise distances for allogrooming-encoding cells, sniffing-encoding cells, and cells with shuffled identity, respectively. Kolmogorov-Smirnov test. **h,** Hypergeometric test. ns, not significant. For details of statistical analyses, see Supplementary Table 1

[Source data](#).

Extended Data Fig. 4 MeA population activity encodes allogrooming and other behaviors during prosocial interaction.

a, Projection of MeA population activity onto the first principal component (PC) overlaid with annotation of social interaction (including allogrooming

and sniffing) in an example animal. **b**, Trial-averaged PC1 activity centered around onset of social interaction across all bouts from all sessions. **c**, Quantification of area under ROC curve (auROC) characterizing the relationship between PC1 activity and social interaction. **d**, Pairwise comparisons of the average within- and between-behavior class Euclidean distances (measured on the first 2 PCs within each session) for allogrooming vs. sniffing, allogrooming vs. self-grooming, and sniffing vs. self-grooming. **e**, Performance of three-way multi-class SVM decoders trained to predict allogrooming, sniffing, or self-grooming behavior. **f–h**, Fraction of time that subjects show different types of behaviors (allogrooming, sniffing, or self-grooming) during the 3 s prior to the onsets of allogrooming (**f**), sniffing (**g**), and self-grooming events (**h**). **i**, Time-course of behavior decoder performance in discriminating between allogrooming and sniffing centered around onset of behavior. Shuffle control decoders are constructed using time-permuted calcium traces. Note that although a fraction of allogrooming events were preceded by sniffing events (**f**), the performance of the decoder remains at chance level prior to the onset of behavior (**i**), suggesting that neural activity during preceding sniffing events is not sufficient to decode allogrooming vs. sniffing. **j**, ROC curve quantifying performance of a binary decoder to predict whether an allogrooming bout is short (≤ 5 s) or long (> 5 s) using population activity centered around onset of allogrooming. **k**, Decoder performance in (**j**) compared with a null distribution constructed using time-permuted calcium traces. Whiskers indicate the 2.5th and 97.5th percentiles of null distribution. Blue line: auROC from real data. **l–n**, Fraction of time that subjects show allogrooming (**l**), sniffing (**m**), or self-grooming (**n**) during the 3 s prior to the onsets of long or short allogrooming events. Mean \pm s.e.m. The ability to predict allogrooming bout duration using population activity is unlikely to be attributable to differences in behaviors preceding allogrooming as there is no difference in the distribution of different behaviors prior to allogrooming onset between the long and short bouts. **b**, **i**, Time 0 indicates behavior onset. **b**, **f–i**, **l–n**, mean \pm s.e.m. Boxplots: median with quartiles, $1.5 \times$ IQR and outliers. **b**, $n = 7$ independent imaging sessions (from 6 subject mice). **c**, $n = 7$ independent imaging sessions (from 6 subject mice) and 70 rounds of shuffling (10 rounds for each imaging session) for control group. Two-sided Wilcoxon rank-sum test. **d**, **e**, $n = 7$ independent imaging sessions (from 6 subject animals). Two-sided Wilcoxon signed-rank test. **f–**

h, $n = 51, 292, 223$ allogrooming (**f**), sniffing (**g**), and self-grooming (**h**) bouts, respectively (in 7 independent imaging sessions in 6 subject animals). **k**, permutation test (1000 rounds of permutation). **l–n**, $n = 51$ short and 38 long allogrooming bouts (from 7 independent imaging sessions in 6 subject animals). Two-sided Wilcoxon rank-sum test. *** $P < 0.001$, ** $P < 0.01$, * $P < 0.05$. ns, not significant. For details of statistical analyses, see Supplementary Table 1

[Source data](#).

[Extended Data Fig. 5 Activation of MeA Tac1 neurons promotes allogrooming and self-grooming in males and females.](#)

a–f, i–n, Probability of allogrooming (**a–c, i–k**) and self-grooming (**d–f, l–n**) (fraction of trials showing a particular behavior at different time points) with respect to stimulation onset during optogenetic activation in male (**a–f**) and female (**i–n**) Tac1-Cre (**a, d, i, l**), Sst-Cre (**b, e, j, m**), and Cck-Cre (**c, f, k, n**) animals injected with ChR2 in the MeA. Blue areas: duration of light illumination; time 0: stimulation onset. **g, h, o, p**, Duration of allogrooming (**g, o**) and self-grooming (**h, p**) during photostimulations in male (**g, h**) and female (**o, p**) Tac1-Cre, Sst-Cre, and Cck-Cre animals injected with ChR2 in the MeA. **q**, Average trace showing Ca^{2+} signal changes during allogrooming toward stressed partners in Sst-Cre subjects expressing GCaMP. Mean \pm s.e.m. Time 0: allogrooming onset. **r**, Comparison of Ca^{2+} signal changes between Sst^+ and $\text{Tac1}^+/\text{Vgat}^+$ neurons during allogrooming using mean $\Delta F/F$ after behavior onset. Boxplots: median with quartiles, 1.5 \times IQR and outliers. **a–p**, Tac1-Cre, $n = 35$ trials in 2 males and 17 trials 2 females for both allogrooming and self-grooming. Sst-Cre, $n = 25$ trials in 2 males and 36 trials in 2 females for both allogrooming and self-grooming. Cck-Cre, $n = 24$ trials in 2 males and 22 trials in 2 females for both allogrooming and self-grooming. Kruskal-Wallis test followed by post hoc Dunn's multiple comparisons test. **r**, $n = 40$ bouts in 7 GCaMP animals for Sst^+ neurons. $n = 19$ bouts in 6 GCaMP animals for $\text{Tac1}^+/\text{Vgat}^+$ neurons. Data for $\text{Tac1}^+/\text{Vgat}^+$ neurons are the same as those in Fig. 4k and are presented here for comparison. Two-sided Wilcoxon rank-sum test. *** $P <$

0.001. ** $P < 0.01$. For details of statistical analyses, see Supplementary Table 1

[Source data](#).

Extended Data Fig. 6 Activation of MeA $\text{Tac1} \cap \text{Vgat}$ neurons promotes affiliative allogrooming in males and females.

a, d, Probability of allogrooming toward stressed partners (fraction of trials showing allogrooming at different time points) with respect to stimulation onset in male (**a**) and female (**d**) ChR2 animals. **b, c, e, f**, Boxplots of duration (**b, e**) and onset latency (**c, f**) of allogrooming during photostimulations in male (**b, c**) and female (**e, f**) eYFP control and ChR2 animals. **g**, No significant difference in the duration of sniffing during photostimulations between eYFP control and ChR2 animals. Blue areas: duration of light illumination; time 0: stimulation onset. eYFP control males, $n = 22$ trials in 2 mice. ChR2 males, $n = 58$ trials in 4 mice. eYFP control females, $n = 55$ trials in 4 mice. ChR2 females, $n = 115$ trials in 4 mice. In **g**, trials from males and females are combined. Boxplots: median with quartiles, $1.5 \times \text{IQR}$ and outliers. Two-sided Wilcoxon rank-sum test. *** $P < 0.001$. ns, not significant. For details of statistical analyses, see Supplementary Table 1

[Source data](#).

Extended Data Fig. 7 Activation of MeA $\text{Tac1}^+/\text{Vgat}^-$ neurons promotes self-grooming but not allogrooming.

a, b, Schematic of an intersectional approach for expression of ChR2 in $\text{Tac1}^+/\text{Vgat}^-$ neurons in the MeA using a Cre-on and Flp-off AAV virus. **c**, Example images showing that the majority of eYFP $^+$ cells are glutamatergic (Vglut2^+ , $64.0 \pm 1.8\%$, mean \pm s.e.m.) and Tac1^+ ($91.8 \pm 0.5\%$, mean \pm s.e.m.) in $\text{Tac1}^{cre/+}/\text{Vgat}^{flp/+}$ animals injected with the Con/Foff-eYFP virus ($n = 3$ hemispheres independently injected with the virus from 2 mice (5-7 sections per hemisphere). Scale bar, 25 μm . **d, e**, Probability of self-grooming (**d**) and allogrooming (**e**) toward stressed partners (fraction of

trials showing a particular behavior at different time points) with respect to stimulation onset in ChR2 animals. Blue areas: duration of light illumination; time 0: stimulation onset. **f**, Duration of self-grooming and allogrooming toward stressed partners during photostimulations. Boxplots: median with quartiles, $1.5 \times \text{IQR}$ and outliers. **d–f**, $n = 39$ trials in 4 mice (18 trials in 2 females and 21 trials in 2 males) for both self-grooming and allogrooming. The Cre-on/Flp-off virus used in the current study has been reported to lead to residual expression in a minor fraction of $\text{Cre}^+/\text{Flp}^+$ cells, possibly due to insufficiency of Flp relative to Cre (refs. [26](#), [52](#)). Nonetheless, we found that when using this virus, the majority of eYFP⁺ cells ($64.0 \pm 1.8\%$, mean \pm s.e.m.) were Vglut2⁺. Of note, the observation that the Cre-on/Flp-off animals did not show induction of allogrooming behavior suggests that activation of the small fraction of Tac1⁺/Vgat⁺ neurons in these animals (concurrent with activation of Tac1⁺/Vgat⁻ neurons) was not sufficient to drive allogrooming behavior. On the other hand, the observation that activation of Tac1⁺/Vgat⁺ neurons in animals injected with the Cre-on/Flp-on virus did not trigger self-grooming behavior suggests that the residual Tac1⁺/Vgat⁺ neurons labelled with the Cre-on/Flp-off virus are not responsible for the induction of self-grooming

[Source data](#)

[Extended Data Fig. 8 MPOA-projecting MeA^{Tac1 \$\cap\$ Vgat} neurons drive affiliative allogrooming in males and females.](#)

a, b, Example images showing axonal terminals of MeA^{Tac1 \cap Vgat} neurons in the MPOA in male (**a**) and female (**b**) animals, revealed by immunostaining for eYFP in $\text{Tac1}^{\text{cre}+/+}/\text{Vgat}^{\text{flp}+/+}$ animals injected with Con/Fon-ChR2-eYFP. Scale bar, 200 μm . **(c, h)** Schematics of viral injection and fibre implantation strategies for soma stimulation of retrogradely labelled, MPOA-projecting MeA^{Tac1 \cap Vgat} neurons (**c**) or stimulation of the axonal projection of MeA^{Tac1 \cap Vgat} neurons in the MPOA (**h**). **d–g**, Duration (**d, f**) and onset latency (**e, g**) of allogrooming during photostimulations in eYFP control and ChR2 males (**d, e**) and females (**f, g**) with soma stimulation of MPOA-projecting MeA^{Tac1 \cap Vgat} neurons. **i–l**, Duration (**i, k**) and onset

latency (**j**, **l**) of allogrooming during photostimulations in eYFP control and ChR2 males (**i**, **j**) and females (**k**, **l**) with stimulation of the MPOA projection of MeA^{Tac1 \cap Vgat} neurons. **m–o**, Probability of allogrooming toward stressed partners (fraction of trials showing allogrooming at different time points) with respect to stimulation onset (**m**, **n**) and allogrooming duration (**o**) during photostimulations of the MPOA projection of MeA^{Tac1 \cap Vgat} neurons without or with infusion of lidocaine in the MeA. Blue areas: duration of light illumination; time 0: stimulation onset. **p**, Example image showing axonal projections of MeA^{Tac1 \cap Vgat} neurons in the PMv. Scale bar, 200 μ m. **q**, Duration of allogrooming during photostimulation of the MPOA or PMv projection of MeA^{Tac1 \cap Vgat} neurons. Data for MPOA projection stimulation are the same as those in Fig. 4r and are presented here for comparison. Boxplots: median with quartiles, $1.5 \times$ IQR and outliers. **d–g**, **i–l**, eYFP control, MeA soma stimulation, $n = 52$ trials in 4 females and 29 trials in 2 males. ChR2, MeA soma stimulation, $n = 68$ trials in 4 females and 59 trials in 2 males. eYFP control, MPOA projection stimulation, $n = 45$ trials in 4 females and 22 trials in 2 males. ChR2, MPOA projection stimulation, $n = 40$ trials in 3 females and 53 trials in 3 males. **m–o**, $n = 36$ trials in 4 mice (24 trials from 3 females and 12 trials from 1 male) for the “no lidocaine” group. $n = 58$ trials in 4 mice (39 trials from 3 females and 19 trials from 1 male) for the “lidocaine” group. **q**, $n = 93$ trials in 6 mice (40 trials in 3 females and 53 trials in 3 males) for MPOA stimulation, $n = 118$ trials in 4 mice (65 trials in 2 females and 53 trials in 2 males) for PMv stimulation. Two-sided Wilcoxon rank-sum test. *** $P < 0.001$. ns, not significant. For details of statistical analyses, see Supplementary Table 1

[Source data](#).

Extended Data Fig. 9 Activation of MeA^{Vgat} neurons can promote allogrooming during prosocial interaction.

a, Schematic of ChR2 activation in MeA^{Vgat} neurons. **b**, **c**, Duration of allogrooming (**b**) and sniffing (**c**) toward stressed partners during low-intensity photostimulations in ChR2 and eYFP control animals. The increase in sniffing (~1.5 s) appears to be substantially smaller than that in

allogrooming (~5 s), suggesting that increased allogrooming is the predominant behavioral effect. **d**, Duration of triggered allogrooming when subject animals are in the vicinity of and attending to the partners (“optimal” condition) compared to all stimulations. Boxplots: median with quartiles, $1.5 \times \text{IQR}$ and outliers. **b**, eYFP control, $n = 119$ trials in 11 mice (74 trials in 6 females and 45 trials in 5 males); ChR2, $n = 141$ trials in 12 mice (88 trials in 7 females and 53 trials in 5 males). **c**, eYFP control, $n = 119$ trials in 11 mice (74 trials in 6 females and 45 trials in 5 males); ChR2, $n = 142$ trials in 12 mice (89 trials in 7 females and 53 trials in 5 males). **d**, All condition, $n = 78$ trials in 5 male mice; optimal condition (subject within half a body-length and facing the partner), $n = 53$ trials in 5 male mice. **b–d**, Two-sided Wilcoxon rank-sum test. *** $P < 0.001$, ** $P < 0.01$. For details of statistical analyses, see Supplementary Table 1

[Source data](#).

Extended Data Fig. 10 Activation of MeA Tac1[−]/Vgat⁺ neurons promotes aggression.

a–b, Schematic of an intersectional approach for specific expression of ChR2 in Tac1[−]/Vgat⁺ neurons in the MeA using a Cre-off and Flp-on AAV. **c**, Example images showing that eYFP⁺ cells are predominantly Vgat⁺ ($99.3 \pm 1.4\%$, mean \pm s.e.m.) and Tac1[−] ($90.1 \pm 1.9\%$, mean \pm s.e.m.) in *Tac1^{cre/+}/Vgat^{flp/+}* animals injected with the Coff/Fon-eYFP AAV ($n = 4$ hemispheres independently injected with the virus from 2 mice (4–5 sections per hemisphere). Scale bar, 25 μm . **d**, **e**, Probability of aggression (**d**) and allogrooming (**e**) toward stressed partners (fraction of trials showing a particular behavior at different time points) with respect to stimulation onset in ChR2 animals. Blue areas: duration of light illumination; time 0: stimulation onset. **f**, Duration of aggression and allogrooming toward stressed partners during photostimulations. Boxplots: median with quartiles, $1.5 \times \text{IQR}$ and outliers. **d–f**, $n = 83$ and 80 trials in 4 male mice for aggression and allogrooming, respectively

[Source data](#).

Supplementary information

Supplementary Information

Supplementary Table 1, Supplementary Notes 1–8 and Supplementary References.

Reporting Summary

Supplementary Video 1 Affiliative allogrooming in mice

Naive mice display increased affiliative allogrooming towards stressed partners.

Supplementary Video 2 Microendoscopic imaging during prosocial interaction

Raw calcium fluorescence video (left) from microendoscopic imaging and extracted ROIs (right) showing single-neuron activity changes in the MeA during interaction with stressed conspecifics.

Supplementary Video 3 ChR2 activation of MeA Tac1⁺Vgat⁺ neurons triggers allogrooming

Optogenetic activation of MeA Tac1⁺Vgat⁺ neurons using ChR2 elicits allogrooming towards stressed partners in a time-locked manner.

Supplementary Video 4 ChR2 activation of the MPOA projection of MeA Tac1⁺Vgat⁺ neurons triggers allogrooming

Optogenetic activation of the MPOA projection of MeA Tac1⁺Vgat⁺ neurons using ChR2 elicits allogrooming towards stressed partners in a time-locked manner.

Source data

[**Source Data Fig. 1**](#)

[**Source Data Fig. 2**](#)

[**Source Data Fig. 3**](#)

[**Source Data Fig. 4**](#)

[**Source Data Extended Data Fig. 1**](#)

[**Source Data Extended Data Fig. 2**](#)

[**Source Data Extended Data Fig. 3**](#)

[**Source Data Extended Data Fig. 4**](#)

[**Source Data Extended Data Fig. 5**](#)

[**Source Data Extended Data Fig. 6**](#)

[**Source Data Extended Data Fig. 7**](#)

[**Source Data Extended Data Fig. 8**](#)

[**Source Data Extended Data Fig. 9**](#)

[**Source Data Extended Data Fig. 10**](#)

Rights and permissions

[**Reprints and Permissions**](#)

About this article

Cite this article

Wu, Y.E., Dang, J., Kingsbury, L. *et al.* Neural control of affiliative touch in prosocial interaction. *Nature* **599**, 262–267 (2021).
<https://doi.org/10.1038/s41586-021-03962-w>

- Received: 21 January 2021
- Accepted: 26 August 2021
- Published: 13 October 2021
- Issue Date: 11 November 2021
- DOI: <https://doi.org/10.1038/s41586-021-03962-w>

Share this article

Anyone you share the following link with will be able to read this content:

[Get shareable link](#)

Sorry, a shareable link is not currently available for this article.

[Copy to clipboard](#)

Provided by the Springer Nature SharedIt content-sharing initiative

This article was downloaded by **calibre** from <https://www.nature.com/articles/s41586-021-03962-w>

- Article
- [Published: 27 October 2021](#)

Human neural tube morphogenesis in vitro by geometric constraints

- [Eyal Karzbrun](#) [ORCID: orcid.org/0000-0001-8724-7855^{1,2}](#) na1,
- [Aimal H. Khankhel](#)³ na1,
- [Heitor C. Megale](#)¹,
- [Stella M. K. Glassauer](#) [ORCID: orcid.org/0000-0002-0171-094X^{4,5}](#),
- [Yofiel Wyle](#)⁴,
- [George Britton](#)⁶,
- [Aryeh Warmflash](#) [ORCID: orcid.org/0000-0002-5679-2268^{7,8}](#),
- [Kenneth S. Kosik](#) [ORCID: orcid.org/0000-0003-3224-5179^{4,5}](#),
- [Eric D. Siggia](#)⁹,
- [Boris I. Shraiman](#)^{1,2} &
- [Sebastian J. Streichan](#) [ORCID: orcid.org/0000-0002-6105-9087^{1,3}](#)

[Nature](#) volume **599**, pages 268–272 (2021)

- 4734 Accesses
- 67 Altmetric
- [Metrics details](#)

Subjects

- [Development of the nervous system](#)
- [Morphogenesis](#)
- [Tissue engineering](#)

Abstract

Understanding human organ formation is a scientific challenge with far-reaching medical implications^{1,2}. Three-dimensional stem-cell cultures have provided insights into human cell differentiation^{3,4}. However, current approaches use scaffold-free stem-cell aggregates, which develop non-reproducible tissue shapes and variable cell-fate patterns. This limits their capacity to recapitulate organ formation. Here we present a chip-based culture system that enables self-organization of micropatterned stem cells into precise three-dimensional cell-fate patterns and organ shapes. We use this system to recreate neural tube folding from human stem cells in a dish. Upon neural induction^{5,6}, neural ectoderm folds into a millimetre-long neural tube covered with non-neural ectoderm. Folding occurs at 90% fidelity, and anatomically resembles the developing human neural tube. We find that neural and non-neural ectoderm are necessary and sufficient for folding morphogenesis. We identify two mechanisms drive folding: (1) apical contraction of neural ectoderm, and (2) basal adhesion mediated via extracellular matrix synthesis by non-neural ectoderm. Targeting these two mechanisms using drugs leads to morphological defects similar to neural tube defects. Finally, we show that neural tissue width determines neural tube shape, suggesting that morphology along the anterior–posterior axis depends on neural ectoderm geometry in addition to molecular gradients⁷. Our approach provides a new route to the study of human organ morphogenesis in health and disease.

Access options

Subscribe to Journal

Get full journal access for 1 year

\$199.00

only \$3.90 per issue

[Subscribe](#)

All prices are NET prices.
VAT will be added later in the checkout.
Tax calculation will be finalised during checkout.

Rent or Buy article

Get time limited or full article access on ReadCube.

from \$8.99

[Rent or Buy](#)

All prices are NET prices.

Additional access options:

- [Log in](#)
- [Access through your institution](#)
- [Learn about institutional subscriptions](#)

Fig. 1: A reproducible human stem-cell model of neural-tube morphogenesis.

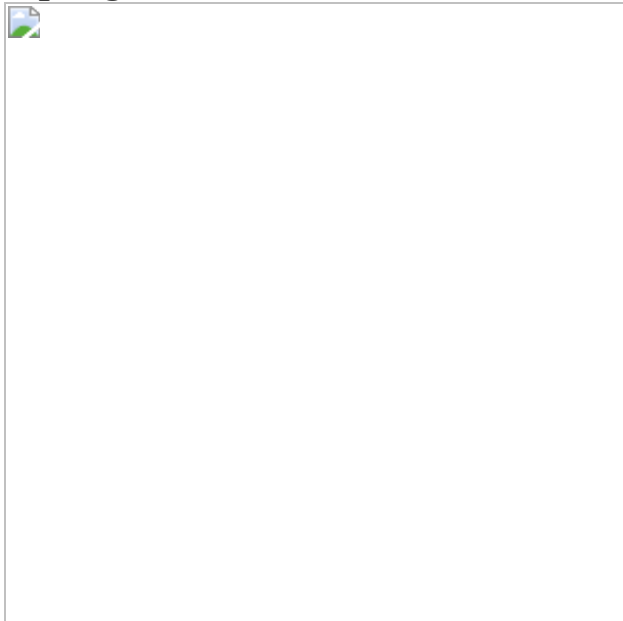


Fig. 2: Formation of a neural and non-neural ectoderm bilayer.

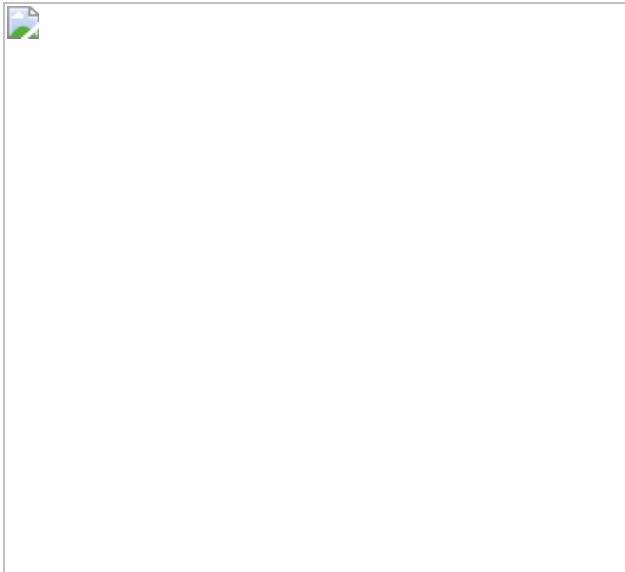


Fig. 3: Towards modelling neural tube defects.

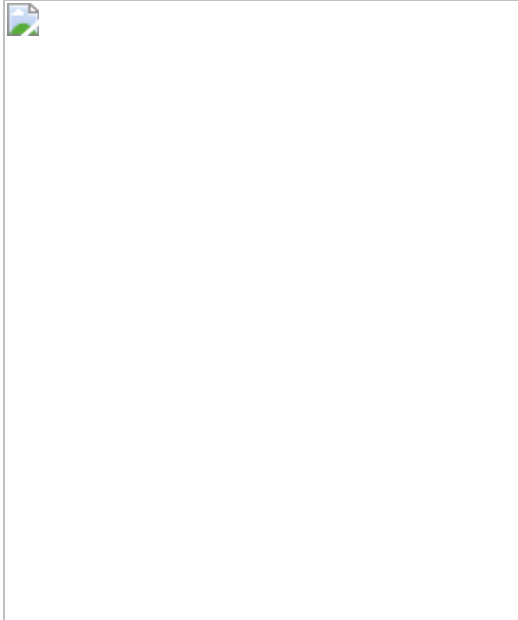
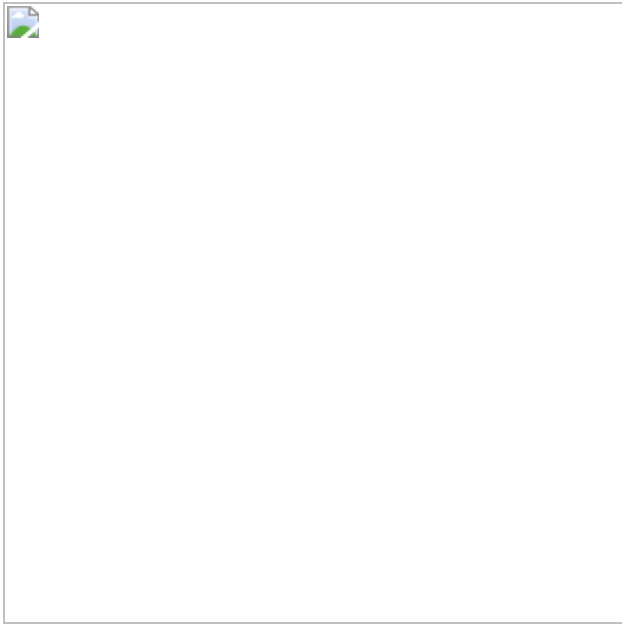


Fig. 4: Neural plate size determines neural tube shape.



Data availability

Source data are provided with this paper. scRNA-seq data have been deposited and are publicly available in the NCBI Gene Expression Omnibus (GEO; <http://www.ncbi.nlm.nih.gov/geo>) under accession [GSE173492](#). [Source data](#) are provided with this paper.

Code availability

The Matlab code for the simulation used in this manuscript is deposited in GitHub (<https://github.com/heitormegale/Neural-fold-simulation>).

References

1. 1.

Wallingford, J. B., Niswander, L. A., Shaw, G. M. & Finnell, R. H. The continuing challenge of understanding, preventing, and treating neural tube defects. *Science* **339**, 1222002 (2013).

2. 2.

Lee, S. & Gleeson, J. G. Closing in on mechanisms of open neural tube defects. *Trends Neurosci.* **43**, 519–532 (2020).

3. 3.

Kim, J., Koo, B.-K. & Knoblich, J. A. Human organoids: model systems for human biology and medicine. *Nat. Rev. Mol. Cell Biol.* **21**, 571–584 (2020).

4. 4.

Quadrato, G. & Arlotta, P. Present and future of modeling human brain development in 3D organoids. *Curr. Opin. Cell Biol.* **49**, 47–52 (2017).

5. 5.

Haremake, T. et al. Self-organizing neuruloids model developmental aspects of Huntington's disease in the ectodermal compartment. *Nat. Biotechnol.* **37**, 1198–1208 (2019).

6. 6.

Britton, G., Heemskerk, I., Hodge, R., Qutub, A. A. & Warmflash, A. A novel self-organizing embryonic stem cell system reveals signaling logic underlying the patterning of human ectoderm. *Development* **146**, dev179093 (2019).

7. 7.

Ybot-Gonzalez, P., Cogram, P., Gerrelli, D. & Copp, A. J. Sonic hedgehog and the molecular regulation of mouse neural tube closure. *Development* **129**, 2507–2517 (2002).

8. 8.

Nikolopoulou, E., Galea, G. L., Rolo, A., Greene, N. D. E. & Copp, A. J. Neural tube closure: cellular, molecular and biomechanical mechanisms. *Development* **144**, 552–566 (2017).

9. 9.

Nikolaev, M. et al. Homeostatic mini-intestines through scaffold-guided organoid morphogenesis. *Nature* **585**, 574–578 (2020).

10. 10.

Xue, X. et al. Mechanics-guided embryonic patterning of neuroectoderm tissue from human pluripotent stem cells. *Nat. Mater.* **17**, 633–641 (2018).

11. 11.

Zheng, Y. et al. Dorsal-ventral patterned neural cyst from human pluripotent stem cells in a neurogenic niche. *Sci. Adv.* **5**, eaax5933 (2019).

12. 12.

Sahni, G. et al. A micropatterned human-specific neuroepithelial tissue for modeling gene and drug-induced neurodevelopmental defects. *Adv. Sci.* **8**, 2001100 (2021).

13. 13.

Developmental Stages in Human Embryos (eds O'Rahilly, R. & Müller, F.) (Carnegie Institute of Washington, 1987).

14. 14.

Ray, H. J. & Niswander, L. A. Dynamic behaviors of the non-neural ectoderm during mammalian cranial neural tube closure. *Dev. Biol.* **416**, 279–285 (2016).

15. 15.

Rolo, A. et al. Regulation of cell protrusions by small GTPases during fusion of the neural folds. *eLife* **5**, e13273 (2016).

16. 16.

Martins-Green, M. Origin of the dorsal surface of the neural tube by progressive delamination of epidermal ectoderm and neuroepithelium: implications for neurulation and neural tube defects. *Development* **103**, 687–706 (1988).

17. 17.

Molè, M. A. et al. Integrin-mediated focal anchorage drives epithelial zippering during mouse neural tube closure. *Dev. Cell* **52**, 321–334.e6 (2020).

18. 18.

Ji, Y. et al. Single cell transcriptomics and developmental trajectories of murine cranial neural crest cell fate determination and cell cycle progression. Preprint at <https://doi.org/10.1101/2021.05.10.443503> (2021).

19. 19.

Vega, F. M., Fruhwirth, G., Ng, T. & Ridley, A. J. RhoA and RhoC have distinct roles in migration and invasion by acting through different targets. *J. Cell Biol.* **193**, 655–665 (2011).

20. 20.

Baldassarre, M. et al. Filamins regulate cell spreading and initiation of cell migration. *PLoS ONE* **4**, e7830 (2009).

21. 21.

Grande-García, A. et al. Caveolin-1 regulates cell polarization and directional migration through Src kinase and Rho GTPases. *J. Cell Biol.* **177**, 683–694 (2007).

22. 22.

de Almeida, P. G., Pinheiro, G. G., Nunes, A. M., Gonçalves, A. B. & Thorsteinsdóttir, S. Fibronectin assembly during early embryo development: A versatile communication system between cells and tissues. *Dev. Dyn.* **245**, 520–535 (2016).

23. 23.

Haigo, S. L., Hildebrand, J. D., Harland, R. M. & Wallingford, J. B. Shroom induces apical constriction and is required for hinge point formation during neural tube closure. *Curr. Biol.* **13**, 2125–2137 (2003).

24. 24.

Chen, Z., Kuang, L., Finnell, R. H. & Wang, H. Genetic and functional analysis of SHROOM1–4 in a Chinese neural tube defect cohort. *Hum. Genet.* **137**, 195–202 (2018).

25. 25.

Butler, M. B. et al. Rho kinase-dependent apical constriction counteracts M-phase apical expansion to enable mouse neural tube closure. *J. Cell Sci.* **132**, jcs230300 (2019).

26. 26.

Schoenwolf, G. C. & Smith, J. L. Mechanisms of neurulation: traditional viewpoint and recent advances. *Development* **109**, 243–270 (1990).

27. 27.

Hernandez, I. et al. A farnesyltransferase inhibitor activates lysosomes and reduces tau pathology in mice with tauopathy. *Sci. Transl. Med.* **11**, eaat3005 (2019).

28. 28.

Karzbrun, E., Khankhel, A. & Streichan, S. J. Recapitulating neural tube morphogenesis with human pluripotent stem cells. *Protoc. Exch.* <https://doi.org/10.21203/rs.3.pex-1606/v1> (2021).

29. 29.

Li, L. et al. Ectodermal progenitors derived from epiblast stem cells by inhibition of Nodal signaling. *J. Mol. Cell. Biol.* **7**, 455–465 (2015).

30. 30.

Wilson, P. A., Lagna, G., Suzuki, A. & Hemmati-Brivanlou, A. Concentration-dependent patterning of the *Xenopus* ectoderm by BMP4 and its signal transducer Smad1. *Development* **124**, 3177–3184 (1997).

31. 31.

Boel, N. M.-E., Hunter, M. C. & Edkins, A. L. LRP1 is required for novobiocin-mediated fibronectin turnover. *Sci. Rep.* **8**, 11438 (2018).

32. 32.

Robert, E. & Guibaud, P. Maternal valproic acid and congenital neural tube defects. *Lancet* **320**, 937 (1982).

33. 33.

Hughes, A., Greene, N. D. E., Copp, A. J. & Galea, G. L. Valproic acid disrupts the biomechanics of late spinal neural tube closure in mouse embryos. *Mech. Dev.* **149**, 20–26 (2018).

34. 34.

Hamburger, V. & Hamilton, H. L. A series of normal stages in the development of the chick embryo. *Dev. Dyn.* **195**, 231–272 (1992).

35. 35.

Theiler, K. *The House Mouse: Atlas of Embryonic Development* (Springer Science & Business Media, 1989).

36. 36.

Butler, A., Hoffman, P., Smibert, P., Papalexi, E. & Satija, R. Integrating single-cell transcriptomic data across different conditions, technologies, and species. *Nat. Biotechnol.* **36**, 411–420 (2018).

37. 37.

Stuart, T. et al. Comprehensive integration of single-cell data. *Cell* **177**, 1888–1902.e21 (2019).

38. 38.

McGinnis, C. S., Murrow, L. M. & Gartner, Z. J. DoubletFinder: doublet detection in single-cell RNA sequencing data using artificial nearest neighbors. *Cell Syst.* **8**, 329–337.e4 (2019).

39. 39.

Hafemeister, C. & Satija, R. Normalization and variance stabilization of single-cell RNA-seq data using regularized negative binomial regression. *Genome Biol.* **20**, 296 (2019).

40. 40.

Zhou, Y. et al. Metascape provides a biologist-oriented resource for the analysis of systems-level datasets. *Nat. Commun.* **10**, 1523 (2019).

41. 41.

Tirosh, I. et al. Dissecting the multicellular ecosystem of metastatic melanoma by single-cell RNA-seq. *Science* **352**, 189–196 (2016)

Acknowledgements

S.J.S. acknowledges NIH grant R21 HD099598-0. E.K. acknowledges the Human Frontier Science Program for the long-term postdoctoral fellowship (LT000629/2018-L). A.H.K. acknowledges support of the National Science Foundation Graduate Research Fellowship Program (grant no. 1650114). E.D.S. acknowledges NSF grant 2013131. A.W. acknowledges Welch Foundation grant no C-2021. S.M.K.G. was recipient of an Early Postdoc Mobility grant and a Postdoc Mobility grant from the Swiss National Science Foundation (P2ZHP3_174753 and P400PB_186800). B.I.S. acknowledges NSF Physics grant 1707973. K.S.K. acknowledges support from Dr Miriam and Sheldon G. Adelson Medical Research Foundation. We thank Y. Huang and the Gladstone institute for sharing CTR2 hiPS cell line, and Brivanlou laboratory and the Rockefeller University for sharing RUES2 embryonic and reporter lines. We thank UCLA Technology Center for Genomics and Bioinformatics for sequencing of 10X libraries. We thank the Streichan and Kosik laboratory members, as well as the UCSB Stem Cell Center and associate director C. Arnold for fruitful discussions and advice. Finally, we thank A. M. Tayar for valuable comments on the manuscript.

Author information

Author notes

1. These authors contributed equally: Eyal Karzbrun, Aimal H. Khankhel

Affiliations

1. Department of Physics, University of California Santa Barbara, Santa Barbara, CA, USA

Eyal Karzbrun, Heitor C. Megale, Boris I. Shraiman & Sebastian J. Streichan

2. Kavli Institute for Theoretical Physics, Santa Barbara, CA, USA

Eyal Karzbrun & Boris I. Shraiman

3. Biomolecular Science and Engineering, University of California Santa Barbara, Santa Barbara, CA, USA

Aimal H. Khankhel & Sebastian J. Streichan

4. Department of Molecular, Cellular, Developmental Biology, University of California Santa Barbara, Santa Barbara, CA, USA

Stella M. K. Glasauer, Yofiel Wyle & Kenneth S. Kosik

5. Neuroscience Research Institute, University of California Santa Barbara, Santa Barbara, CA, USA

Stella M. K. Glasauer & Kenneth S. Kosik

6. Systems Synthetic and Physical Biology Program, Rice University Houston, Houston, TX, USA

George Britton

7. Department of Biosciences, Rice University Houston, Houston, TX, USA

Aryeh Warmflash

8. Department of Bioengineering, Rice University Houston, Houston, TX, USA

Aryeh Warmflash

9. Center for Studies in Physics and Biology, The Rockefeller University, New York, NY, USA

Eric D. Siggia

Contributions

E.K. and S.J.S. designed research. E.K., A.H.K., S.M.K.G., Y.W. and G.B. performed experiments. E.K., A.H.K. and H.C.M., analysed the data. A.W.

and E.D.S. provided valuable information on data interpretation. E.K., H.C.M. and B.I.S. developed and analysed the physical model. S.M.K.G. and K.S.K. performed single-cell sequencing experiment and analysis. E.K., A.H.K. and S.J.S. wrote the manuscript. S.J.S. supervised the project.

Corresponding authors

Correspondence to [Eyal Karzbrun](#) or [Sebastian J. Streichan](#).

Ethics declarations

Competing interests

The authors declare no competing interests.

Additional information

Peer review information *Nature* thanks Gioele La Manno, Matthias Lutolf and the other, anonymous, reviewer(s) for their contribution to the peer review of this work.

Publisher's note Springer Nature remains neutral with regard to jurisdictional claims in published maps and institutional affiliations.

Extended data figures and tables

[Extended Data Fig. 1 hPS cell-derived neural tube protocol.](#)

(a) Scheme showing stem-cell derived neural tube protocol. (b) Scheme showing shape-controlled ECM pattern deposited on glass surface. (c) Seeding of hPS cells onto micropatterns results in two-dimensional cultures which are restricted to the micropattern geometry. ZO1-GFP indicates tight epithelia. (d) Adding 4% Matrigel to the media results in three-dimensional stem-cell cultures containing a single large lumen. (e) The hPS cell lumen forms a tight biochemical niche. hPS cell reporter line endogenously

expressed tight junction protein ZO1 tagged with GFP (AICS-0023) is used. The 3D culture is exposed to 10kda dextran tagged with Texas Red fluorophore. Horizontal sections show that tight junctions are localized to the inner surface facing the lumen (green). Dextran is visible outside the tissue, but the lumen is devoid of dextran (red). (f) The fluorescence of dextran is quantified inside and outside the lumen, showing a 10-60 fold decrease in the lumen dextran concentration. Data are presented as mean values +/- SD. (N = 9). (g) Plot of the relative fraction of closed lumens as a function of Matrigel concentration, after 24hrs incubation. Data are presented as mean values +/- SD. Total N = 88 samples. (h) Scheme showing micropatterned hPS cell before and after exposure to Matrigel. (i) Vertical and (j) horizontal sections of pluripotent markers NANOG, OCT4 and SOX2, as well as epithelial marker ZO1. Images taken before and after lumen formation. (k) Horizontal section of an array of 2D (left) and 3D (right) stem-cell cultures immunostained with OCT4. (l) Lumen formation success rate as a function of micropattern size. Total N = 510 samples. (m) Segmentation of single nuclei is used to count the number of cells in each sample. Each nucleus is labeled with a different color. (n) Total cell number in each sample (green curve) scales linearly with pattern area while cell density (black curve) remains constant. Data are presented as mean values +/- SD. Total N = 194 samples. Scale bars are 50 μ m (d,e,i,j), and 500 μ m (k).

[Source data](#)

Extended Data Fig. 2 In vitro morphogenesis Road Map.

(a) Schematic representation of in vitro morphogenesis in four differentiation protocols. Observed cell markers are indicated. (i) Exposure to BMP, without neural induction, results in an amnion-like tissue containing cells from three germ layers without formation of a neural fold. (ii) Neural tube morphogenesis is observed when neural induction is followed by exposure to BMP4. (iii) Homogenous expression of forebrain markers is observed under exposure to neural induction without BMP. (iv) Dorsoventral axis formation is observed in response to SHH activation (SAG) and WNT downregulation (IWP2). (b) Experimental timeline for the four protocols. Neural induction media includes N2 supplement and TGF- β

inhibitor SB-431542 (SB). (c-f) Vertical sections of immunostained samples from the four differentiation protocols. (g) Horizontal section close to the glass surface and (h) an array of 20 samples. FOXA2+ cells always appear at the midline. Scale bar is 50 μ m (c,f-h), 50 μ m (d,e).

Extended Data Fig. 3 Folding morphogenesis is reproducible.

(a) Horizontal sections of 16 circular cultures from a single array exhibit stereotypic fate-patterning and morphology. (b) Bar plot showing success rate of neural tissue folding morphogenesis, in 13 experiments, with total N = 100 samples. Data are presented as mean values +/- SD. (c) Neural opening area as a function of time. Data are presented as mean values +/- SD. N = 3. (d) Neural closure period in the stem-cell system compared to chick, mouse, and human. (e) Images of six samples at 96hrs showing closed neural tissue (red, N-Cadherin) covered by non-neural ectoderm (cyan, E-cadherin). Samples were generated on rectangle shaped micropatterns. Scale bar is 500 μ m (a), 50 μ m in (c,e).

[Source data](#)

Extended Data Fig. 4 Folding morphogenesis is not observed in 2D micropatterned cultures.

(a) Induction of neural pattern formation in 3D stem-cell cultures with a lumen triggers folding morphogenesis. In contrast triggering pattern formation in 2D micropatterned cultures does not trigger folding morphogenesis. Vertical sections of a 3D immunostained sample (top) and 2D immunostained sample (bottom). Imaged 72hrs after BMP. (b) Vertical section at 36hrs post BMP, and before folding. The neural tissue thickness and width are indicated. (c) Quantification of neural tissue thickness and width as a function of micropattern size analyzed 36hrs after BMP exposure. Data are presented as mean values +/- SD, Total N = 23. (d) Vertical section of immunostained samples during neural fold morphogenesis. Arrows indicate hinge points. (e) Distance between hinge points as a function of time after BMP exposure. Data are presented as mean values +/- SD, N = 3. Scale bars are 50 μ m.

Source data

Extended Data Fig. 5 Neural hinge points and apical surface characterization.

(a) Vertical sections of a hinge points showing changes in nuclei orientation across the hinge. (b) Neural crest membrane marker P75 appears in a layer of cells in between the neural tissue and surface ectoderm (ECAD). (c) Immunostaining of shroom3 and (d) F-actin at the neural apical surface. (e) Image projection of apical marker PKC ζ and primary cilia marker ARL13B. (f) Sparse labeling of cells with CAAX-GFP. Labeled cells arise from a single clone indicating motility of cells following proliferation. (g) Live-cell imaging showing active filopodia (arrows) of neural cells as they change their position and shape over time. The continuous spectrum of colors indicates distance from glass (red 0 μ m -green - blue 35 μ m). Scale bars are 25 μ m (a,f) 10 μ m (b-e,g).

Extended Data Fig. 6 Live imaging of neural crest cells.

Time-lapse images showing motion of neural crest cells (SOX10-GFP). (a) Scheme indicating region in which live imaging was performed. (b) Low magnification image showing neural crest cells are organized in a stream. (c) Neural crest cell motion along the stream. A single cell is tracked and artificially colored in red. Scale bar 25 μ m.

Extended Data Fig. 7 Extracellular localization and expression during neural folding.

(a) Scheme showing ECM composition in three interfaces: surface-ectoderm/glass, surface-ectoderm/ neural-ectoderm and neural-ectoderm/glass. (b) Collagen and fibronectin fluorescence intensity compared at the three interfaces. Data are presented as mean values +/- SD. N = 3 independent samples (c) Vertical sections show fibronectin. (d) Horizontal sections near the glass interface show collagen V and fibronectin. Dashed line indicates border between neural and non-neural ectoderm. (e) UMAP projection and (f) violin plots of ECM genes and

ECM modulators are localized to the surface ectoderm clusters. Average expression was 1-2 orders of magnitude higher in surface ectoderm vs neural ectoderm. (g) Vertical sections showing immunostaining of fibronectin matrix in control sample, ROCK inhibition (Y-27632, 10 μ M), and Novobiocin (100 μ M). (h) Fluorescence intensities of immunostained fibronectin were measured at the neural/surface-ectoderm interface and at the neural/glass interface in all three experimental conditions.

Immunostaining and imaging conditions were identical for all conditions. Fluorescence values were measured by averaging the raw fluorescence intensities in a region of interest in the image. The number of independent samples N is indicated within the plot. (i) Cell velocity of non-neural ectoderm cells measured by live-imaging of H2B-RFP cell line. No significant difference is observed in ROCK inhibited samples. N = 6. Data are presented as mean values +/- SD (b,h,i). Scale bars are 25 microns. Two-sided t-test was applied (b,h).

[Source data](#)

Extended Data Fig. 8 Single cell expression of key cell type markers.

(a) UMAP plots of single cell gene expression color coded by cluster identity (top) and experimental time point (bottom). Four main cell clusters are observed. (b) Temporal evolution of gene expression in the neural crest population indicate a transition from neural plate border/neural crest specification to migration and divarication. (c) Inferred cell-cycle populations for three clusters: neural ectoderm (NE), surface ectoderm (SE), and neural crest (NC). SE exhibits increase in G1 over time, and NC exhibits a decrease in G1. (d) Expression of key cell type markers from the four main clusters. (e) Sub-clustering of NE and SE. Neural cells sub-cluster mainly by experimental time and cell-cycle phase, which correspond to UMAP 1 and 2. In contrast, surface ectoderm cells sub-clusters do not cluster by cell-cycle or experimental time, suggesting additional differences in cell identity. (f) Scheme showing cellular process in each cluster. Titles are enriched GO pathways, and example genes appearing within each pathway.

Extended Data Fig. 9 Folding morphogenesis occurs in the absence of mesendoderm tissue.

(a) Experimental timeline to examine effect of neural induction on cell fate and folding morphogenesis. (b-d) Vertical (left) and horizontal (middle, right) sections showing that neural fates (NCAD) are upregulated with longer neural induction, whereas mesendoderm fates (Brachyury) are downregulated. (e,f) A small number of Brachyury+ cells (<10) is present in the protocol used to for neural tube morphogenesis. Total number of cells in the tissue is ~5000 cells. Scale bar is 50 μ m. Dome present in all cases.

Extended Data Fig. 10 Computational model of neural folding recapitulates in vitro morphology.

(a) Vertex model scheme. Vertices are connected by Hookean springs of length $\|\vec{r}_i\|$. $\{\vec{r}_i\}^a$ and $\{\vec{r}_i\}^b$ are the apical and basal vertices (x and z) of cell i . Neural cells have additional myosin dependent positive apical line tension, and there is a negative line tension between neural and non-neural basal surfaces (see [Supplementary Notes](#) details). (b) Time sequence of simulation showing initial cell pattern (neural tissue in red, non-neural in blue), followed by neural bending, folding and hinge formation, and closure. Each time unit corresponds to 1000 steps in the simulation. Apical lines in the neural domain strongly contract due to myosin, but never reach zero values. (c) Energy of the tissue reduces over time and reaches a minimum. (d) Interface radius and (e) Number of cells on the interface as a function of time. Both reach a steady-state value. (f) Phase diagram of the dimensionless parameters interface energy (ϵ), neural contractility (α). Each point represents a simulation that reached a steady state. Color code represents the final configuration of the simulations: neural fold closed (red), formation of neural/non-neural interface without closure (blue), and no interface formation (black). Shaded colors were drawn by hand to highlight regime boundaries. (g) Final configuration images (steady state shapes) from the simulation in different regions i) high neural apical contractility and high interface energy leads to a closed fold; ii) Low neural apical contractility and high interface energy

leads to the formation of the interface but an open fold; iii) High neural apical contractility and low interface energy leads to a flat tissue. (h) The interface radius of curvature as a function of neural apical contractility. (i) The number of cells in an interface as a function of interface energy. (j) Bar plots showing the neural apical curvature, neural apical area, and interface size for the three conditions whose final configuration are shown in g. (k) Three simulations with a 40 non-neural cells, and a varying number of neural cells $N = 10, 30, 40$. Left: images of the simulation at time zero. Right: Images of the simulation at the hinge formation stage. Images were taken at this stage for consistency with experimental data (Fig. 4d, 72hrs). We observe the formation of a single hinge point for $N = 10$, and two lateral hinges for $N = 30, 40$.

[Source data](#)

Supplementary information

[Supplementary Information](#)

This file contains a Supplementary Note on the physical model of neural folding.

[Reporting Summary](#)

[Supplementary Table 1](#)

This table contains top differentially expressed genes for cell clusters identified by scRNA-seq.

[Supplementary Table 2](#)

This table contains GO Analysis for cell clusters identified by scRNA-seq.

[Supplementary Table 3](#)

This table contains a list of media and reagents used in this work.

Supplementary Table 4

This table contains a list of primary and secondary antibodies used in this work.

Supplementary Video 1

Interkinetic nuclear migration. Live-cell imaging of interkinetic nuclear migrations. Time-lapse microscopy video using a 40 \times objective in the region of the neural fold from 72–94 h post BMP using a live reporter cell line (RUES2, H2B-RFP).

Supplementary Video 2

Neural progenitors. Live-cell imaging of CAAX-RFP reporter line mixed into a background non-fluorescent cell line. Color indicates distance from glass (red 0 μ m–blue 35 μ m). 72 h post-BMP. Elongated neural progenitor cells are observed exhibiting motion and filopodia. Frame rate: one frame every 30 min.

Supplementary Video 3

Primary cilia. 63 \times image slices of a fixed stem cell-derived neural tube at 120 h post-BMP. Apical marker PKC ζ (red), and primary cilia marker ARL13B (yellow) are shown at the apical surface of neural tissue region.

Supplementary Video 4

Surface ectoderm cell migration. Live-cell imaging of H2B-RFP reporter line showing directional migration of non-neural cells in parallel to the culture long axis. Frame rate: one frame every 25 min.

Supplementary Video 5

Neural crest cells 3D. Three-dimensional view of a fixed stem cell-derived neural tube at 96 h post-BMP. Neural crest (SOX10) and non-neural

ectoderm (ECAD) cells shown.

Supplementary Video 6

Neural crest migration. Live-cell imaging of SOX10-GFP reporter cell line showing a neural crest cell migrating and proliferating. Frame rate: one frame every 10 min.

Supplementary Video 7

Live-cell imaging of H2B-RFP reporter line demonstrating cell motility in control sample 72 h post-BMP. Frame rate: one frame every 5 min.

Supplementary Video 8

Live-cell imaging of H2B-RFP reporter line demonstrating cell motility in ROCK-inhibited sample. 72 h post-BMP. Frame rate: one frame every 5 min.

Source data

Source Data Fig. 1

Source Data Fig. 3

Source Data Fig. 4

Source Data Extended Data Fig. 1

Source Data Extended Data Fig. 3

Source Data Extended Data Fig. 4

Source Data Extended Data Fig. 7

Source Data Extended Data Fig. 10

Rights and permissions

Reprints and Permissions

About this article

Cite this article

Karzbrun, E., Khankhel, A.H., Megale, H.C. *et al.* Human neural tube morphogenesis in vitro by geometric constraints. *Nature* **599**, 268–272 (2021). <https://doi.org/10.1038/s41586-021-04026-9>

- Received: 23 November 2020
- Accepted: 13 September 2021
- Published: 27 October 2021
- Issue Date: 11 November 2021
- DOI: <https://doi.org/10.1038/s41586-021-04026-9>

Share this article

Anyone you share the following link with will be able to read this content:

[Get shareable link](#)

Sorry, a shareable link is not currently available for this article.

[Copy to clipboard](#)

Provided by the Springer Nature SharedIt content-sharing initiative

This article was downloaded by **calibre** from <https://www.nature.com/articles/s41586-021-04026-9>

| [Section menu](#) | [Main menu](#) |

- Article
- [Published: 27 October 2021](#)

Cell surface and intracellular auxin signalling for H⁺ fluxes in root growth

- [Lanxin Li¹](#) na1,
- [Inge Verstraeten](#) [ORCID: orcid.org/0000-0001-7241-2328](#)¹ na1,
- [Mark Roosjen²](#),
- [Koji Takahashi](#) [ORCID: orcid.org/0000-0001-5438-7624](#)^{3,4},
- [Lesia Rodriguez¹](#),
- [Jack Merrin¹](#),
- [Jian Chen^{5,6}](#),
- [Lana Shabala⁷](#),
- [Wouter Smet^{5,6}](#),
- [Hong Ren⁸](#),
- [Steffen Vanneste](#) [ORCID: orcid.org/0000-0002-9948-9672](#)^{5,9,10},
- [Sergey Shabala^{7,11}](#),
- [Bert De Rybel^{5,6}](#),
- [Dolf Weijers](#) [ORCID: orcid.org/0000-0003-4378-141X](#)²,
- [Toshinori Kinoshita](#) [ORCID: orcid.org/0000-0001-7621-1259](#)^{3,4},
- [William M. Gray](#) [ORCID: orcid.org/0000-0002-1320-290X](#)⁸ &
- [Jiří Friml](#) [ORCID: orcid.org/0000-0002-8302-7596](#)¹

Nature volume **599**, pages 273–277 (2021)

- 5693 Accesses
- 1 Citations

- 58 Altmetric
- [Metrics details](#)

Subjects

- [Auxin](#)
- [Plant physiology](#)

Abstract

Growth regulation tailors development in plants to their environment. A prominent example of this is the response to gravity, in which shoots bend up and roots bend down¹. This paradox is based on opposite effects of the phytohormone auxin, which promotes cell expansion in shoots while inhibiting it in roots via a yet unknown cellular mechanism². Here, by combining microfluidics, live imaging, genetic engineering and phosphoproteomics in *Arabidopsis thaliana*, we advance understanding of how auxin inhibits root growth. We show that auxin activates two distinct, antagonistically acting signalling pathways that converge on rapid regulation of apoplastic pH, a causative determinant of growth. Cell surface-based TRANSMEMBRANE KINASE1 (TMK1) interacts with and mediates phosphorylation and activation of plasma membrane H⁺-ATPases for apoplast acidification, while intracellular canonical auxin signalling promotes net cellular H⁺ influx, causing apoplast alkalinization. Simultaneous activation of these two counteracting mechanisms poises roots for rapid, fine-tuned growth modulation in navigating complex soil environments.

Access options

Subscribe to Journal

Get full journal access for 1 year

\$199.00

only \$3.90 per issue

[Subscribe](#)

All prices are NET prices.

VAT will be added later in the checkout.

Tax calculation will be finalised during checkout.

Rent or Buy article

Get time limited or full article access on ReadCube.

from \$8.99

[Rent or Buy](#)

All prices are NET prices.

Additional access options:

- [Log in](#)
- [Access through your institution](#)
- [Learn about institutional subscriptions](#)

Fig. 1: Auxin rapidly inhibits root growth by apoplast alkalinization.

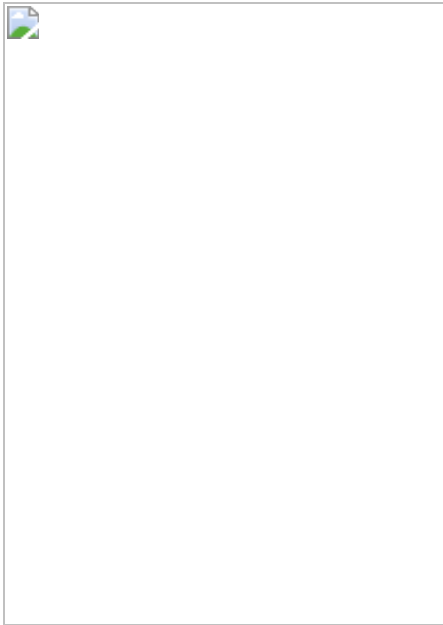


Fig. 2: Auxin-triggered H^+ -ATPase activation counteracts auxin-triggered apoplast alkalinization.

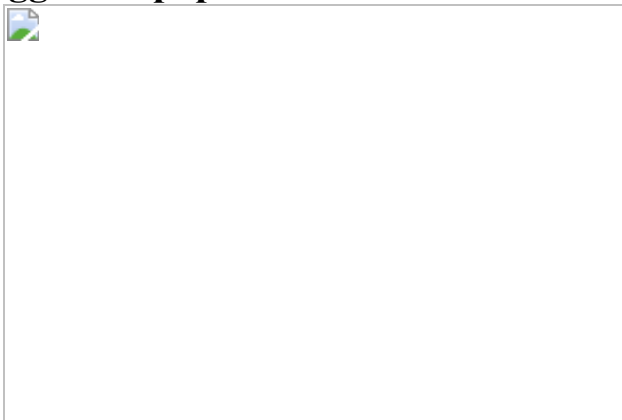


Fig. 3: TMK1 directly mediates auxin-induced H^+ -ATPase activation.

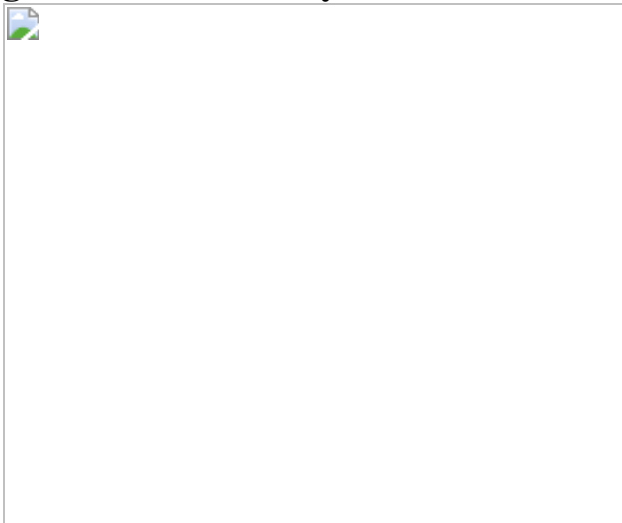
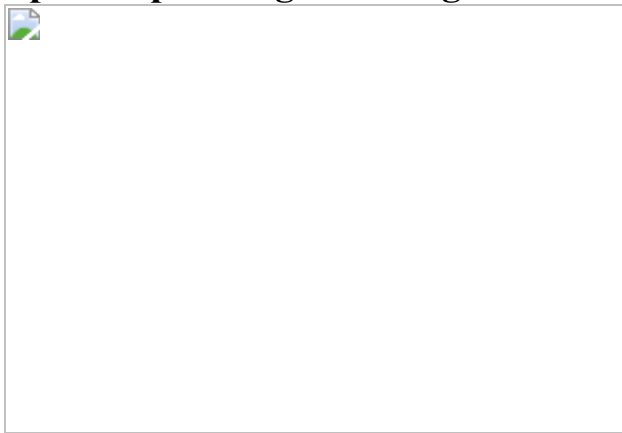


Fig. 4: Antagonistic TIR1/AFB and TMK1 signalling converge on apoplastic pH for growth regulation.



Data availability

The data and full blots are available within the paper and its [Supplementary Information](#). [Source data](#) are provided with this paper.

Code availability

All codes used in the manuscript are provided in the [Supplementary Information](#).

References

1. 1.

Estelle, M. Plant tropisms: the ins and outs of auxin. *Curr. Biol.* **6**, 1589–1591 (1996).

2. 2.

Gallei, M., Luschnig, C. & Friml, J. Auxin signalling in growth: Schrödinger's cat out of the bag. *Curr. Opin. Plant Biol.* **53**, 43–49 (2020).

3. 3.

Spartz, A. K. et al. SAUR inhibition of PP2C-D phosphatases activates plasma membrane H⁺-ATPases to promote cell expansion in *Arabidopsis*. *Plant Cell* **26**, 2129–2142 (2014).

4. 4.

Fendrych, M., Leung, J. & Friml, J. TIR1/AFB–Aux/IAA auxin perception mediates rapid cell wall acidification and growth of *Arabidopsis* hypocotyls. *eLife* **5**, e19048 (2016).

5. 5.

Du, M., Spalding, E. P. & Gray, W. M. Rapid auxin-mediated cell expansion. *Annu. Rev. Plant Biol.* **71**, 379–402 (2020).

6. 6.

Fendrych, M. et al. Rapid and reversible root growth inhibition by TIR1 auxin signalling. *Nat. Plants* **4**, 453–459 (2018).

7. 7.

Dai, N., Wang, W., Patterson, S. E. & Bleecker, A. B. The TMK subfamily of receptor-like kinases in *Arabidopsis* display an essential role in growth and a reduced sensitivity to auxin. *PLoS ONE* **8**, e60990 (2013).

8. 8.

Cao, M. et al. TMK1-mediated auxin signalling regulates differential growth of the apical hook. *Nature* **568**, 240–243 (2019).

9. 9.

Chen, X. et al. Inhibition of cell expansion by rapid ABP1-mediated auxin effect on microtubules. *Nature* **516**, 90–93 (2014).

10. 10.

Adamowski, M., Li, L. & Friml, J. Reorientation of cortical microtubule arrays in the hypocotyl of *Arabidopsis thaliana* is induced by the cell growth process and independent of auxin signaling. *Int. J. Mol. Sci.* **20**, 3337 (2019).

11. 11.

Scheuring, D. et al. Actin-dependent vacuolar occupancy of the cell determines auxin-induced growth repression. *Proc. Natl Acad. Sci. USA* **113**, 452–457 (2016).

12. 12.

Barbez, E., Dünser, K., Gaidora, A., Lendl, T. & Busch, W. Auxin steers root cell expansion via apoplastic pH regulation in *Arabidopsis thaliana*. *Proc. Natl Acad. Sci. USA* **114**, E4884–E4893 (2017).

13. 13.

Monshausen, G. B., Miller, N. D., Murphy, A. S. & Gilroy, S. Dynamics of auxin-dependent Ca^{2+} and pH signaling in root growth revealed by integrating high-resolution imaging with automated computer vision-based analysis. *Plant J.* **65**, 309–318 (2011).

14. 14.

Shih, H.-W., DePew, C. L., Miller, N. D. & Monshausen, G. B. The cyclic nucleotide-gated channel CNGC14 regulates root gravitropism in *Arabidopsis thaliana*. *Curr. Biol.* **25**, 3119–3125 (2015).

15. 15.

Von Wangenheim, D. et al. Live tracking of moving samples in confocal microscopy for vertically grown roots. *eLife* **6**, e26792 (2017).

16. 16.

Martinière, A. et al. Uncovering pH at both sides of the root plasma membrane interface using noninvasive imaging. *Proc. Natl Acad. Sci. USA* **115**, 6488–6493 (2018).

17. 17.

Dindas, J. et al. AUX1-mediated root hair auxin influx governs SCF^{TIR1/AFB}-type Ca²⁺ signaling. *Nat. Commun.* **9**, 1174 (2018).

18. 18.

Han, H. et al. Rapid auxin-mediated phosphorylation of myosin regulates trafficking and polarity in *Arabidopsis*. Preprint at *bioRxiv* <https://doi.org/10.1101/2021.04.13.439603> (2021).

19. 19.

Haruta, M., Gray, W. M. & Sussman, M. R. Regulation of the plasma membrane proton pump (H⁺-ATPase) by phosphorylation. *Curr. Opin. Plant Biol.* **28**, 68–75 (2015).

20. 20.

Takahashi, K., Hayashi, K.-i. & Kinoshita, T. Auxin activates the plasma membrane H⁺-ATPase by phosphorylation during hypocotyl elongation in *Arabidopsis*. *Plant Physiol.* **159**, 632–641 (2012).

21. 21.

Yang, Z. et al. TMK-based cell surface auxin signaling activates cell wall acidification in *Arabidopsis*. *Nature* <https://doi.org/10.1038/s41586-021-03976-4> (2021).

22. 22.

Zhang, Y., Xiao, G., Wang, X., Zhang, X. & Friml, J. Evolution of fast root gravitropism in seed plants. *Nat. Commun.* **10**, 3480 (2019).

23. 23.

Kinoshita, T. & Shimazaki, K. Analysis of the phosphorylation level in guard-cell plasma membrane H⁺-ATPase in response to fusicoccin. *Plant Cell Physiol.* **42**, 424–432 (2001).

24. 24.

Yang, Y., Hammes, U. Z., Taylor, C. G., Schachtman, D. P. & Nielsen, E. High-affinity auxin transport by the AUX1 influx carrier protein. *Curr. Biol.* **16**, 1123–1127 (2006).

25. 25.

Serre, N. B. et al. AFB1 controls rapid auxin signalling through membrane depolarization in *Arabidopsis thaliana* root. *Nat. Plants.* **7**, 1229–1238 (2021).

26. 26.

Prigge, M. J. et al. Genetic analysis of the *Arabidopsis* TIR1/AFB auxin receptors reveals both overlapping and specialized functions. *eLife* **9**, e54740 (2020).

27. 27.

Hayashi, K. et al. Rational design of an auxin antagonist of the SCF^{TIR1} auxin receptor complex. *ACS Chem. Biol.* **7**, 590–598 (2012).

28. 28.

Uchida, N. et al. Chemical hijacking of auxin signaling with an engineered auxin–TIR1 pair. *Nat. Chem. Biol.* **14**, 299–305 (2018).

29. 29.

Haruta, M., Sabat, G., Stecker, K., Minkoff, B. B. & Sussman, M. R. A peptide hormone and its receptor protein kinase regulate plant cell expansion. *Science* **343**, 408–411 (2014).

30. 30.

Komaki, S. et al. Nuclear-localized subtype of end-binding 1 protein regulates spindle organization in *Arabidopsis*. *J. Cell Sci.* **123**, 451–459 (2010).

31. 31.

Marc, J. et al. A *GFP-MAP4* reporter gene for visualizing cortical microtubule rearrangements in living epidermal cells. *Plant Cell* **10**, 1927–1939 (1998).

32. 32.

Robert, S. et al. Endosidin1 defines a compartment involved in endocytosis of the brassinosteroid receptor BRI1 and the auxin transporters PIN2 and AUX1. *Proc. Natl Acad. Sci. USA* **105**, 8464–8469 (2008).

33. 33.

Moreno-Risueno, M. A. et al. Oscillating gene expression determines competence for periodic *Arabidopsis* root branching. *Science* **329**, 1306–1311 (2010).

34. 34.

Toyota, M. et al. Glutamate triggers long-distance, calcium-based plant defense signaling. *Science* **361**, 1112–1115 (2018).

35. 35.

Parry, G. et al. Complex regulation of the TIR1/AFB family of auxin receptors. *Proc. Natl Acad. Sci. USA* **106**, 22540–22545 (2009).

36. 36.

Dharmasiri, N. et al. Plant development is regulated by a family of auxin receptor F box proteins. *Dev. Cell* **9**, 109–119 (2005).

37. 37.

Swarup, R. et al. Structure–function analysis of the presumptive *Arabidopsis* auxin permease AUX1. *Plant Cell* **16**, 3069–3083 (2004).

38. 38.

Wang, R. et al. HSP90 regulates temperature-dependent seedling growth in *Arabidopsis* by stabilizing the auxin co-receptor F-box protein TIR1. *Nat. Commun.* **7**, 10269 (2016).

39. 39.

Rast-Somssich, M. I. et al. The *Arabidopsis JAGGED LATERAL ORGANS (JLO)* gene sensitizes plants to auxin. *J. Exp. Bot.* **68**, 2741–2755 (2017).

40. 40.

Haruta, M. et al. Molecular characterization of mutant *Arabidopsis* plants with reduced plasma membrane proton pump activity. *J. Biol. Chem.* **285**, 17918–17929 (2010).

41. 41.

Yamauchi, S. et al. The plasma membrane H⁺-ATPase AHA1 plays a major role in stomatal opening in response to blue light. *Plant Physiol.* **171**, 2731–2743 (2016).

42. 42.

Carbonell, A. et al. New generation of artificial microRNA and synthetic *trans*-acting small interfering RNA vectors for efficient gene silencing in *Arabidopsis*. *Plant Physiol.* **165**, 15–29 (2014).

43. 43.

Karimi, M., Bleys, A., Vanderhaeghen, R. & Hilson, P. Building blocks for plant gene assembly. *Plant Physiol.* **145**, 1183–1191 (2007).

44. 44.

Marquès-Bueno, M. M. et al. A versatile multisite Gateway-compatible promoter and transgenic line collection for cell type-specific functional genomics in *Arabidopsis*. *Plant J.* **85**, 320–333 (2016).

45. 45.

Fuglsang, A. T. et al. Receptor kinase-mediated control of primary active proton pumping at the plasma membrane. *Plant J.* **80**, 951–964 (2014).

46. 46.

Wang, Q. et al. A phosphorylation-based switch controls TAA1-mediated auxin biosynthesis in plants. *Nat. Commun.* **11**, 679 (2020).

47. 47.

Lee, J. et al. Type III secretion and effectors shape the survival and growth pattern of *Pseudomonas syringae* on leaf surfaces. *Plant Physiol.* **158**, 1803–1818 (2012).

48. 48.

Robert, S. et al. ABP1 mediates auxin inhibition of clathrin-dependent endocytosis in *Arabidopsis*. *Cell* **143**, 111–121 (2010).

49. 49.

Li, L., Krens, S. G., Fendrych, M. & Friml, J. Real-time analysis of auxin response, cell wall pH and elongation in *Arabidopsis thaliana* hypocotyls. *Bio. Protoc.* **8**, e2685 (2018).

50. 50.

Gelová, Z. et al. Developmental roles of auxin binding protein 1 in *Arabidopsis thaliana*. *Plant Sci.* **303**, 110750 (2021).

51. 51.

Boudaoud, A. et al. FibrilTool, an ImageJ plug-in to quantify fibrillar structures in raw microscopy images. *Nat. Protoc.* **9**, 457–463 (2014).

52. 52.

Narasimhan, M. et al. Systematic analysis of specific and nonspecific auxin effects on endocytosis and trafficking. *Plant Physiol.* **186**, 1122–1142 (2021).

53. 53.

Shabala, S. N., Newman, I. A. & Morris, J. Oscillations in H⁺ and Ca²⁺ ion fluxes around the elongation region of corn roots and effects of external pH. *Plant Physiol.* **113**, 111–118 (1997).

54. 54.

De Rybel, B. et al. A bHLH complex controls embryonic vascular tissue establishment and indeterminate growth in *Arabidopsis*. *Dev. Cell* **24**, 426–437 (2013).

55. 55.

Wendrich, J. R., Boeren, S., Möller, B. K., Weijers, D. & De Rybel, B. in *Plant Hormones*. 147–158 (Springer, 2017).

56. 56.

Nikonorova, N. et al. Early mannitol-triggered changes in the *Arabidopsis* leaf (phospho)proteome reveal growth regulators. *J. Exp. Bot.* **69**, 4591–4607 (2018).

57. 57.

Hayashi, Y. et al. Biochemical characterization of in vitro phosphorylation and dephosphorylation of the plasma membrane H⁺-ATPase. *Plant Cell Physiol.* **51**, 1186–1196 (2010).

58. 58.

Inoue, S., Takahashi, K., Okumura-Noda, H. & Kinoshita, T. Auxin influx carrier AUX1 confers acid resistance for *Arabidopsis* root elongation through the regulation of plasma membrane H⁺-ATPase. *Plant Cell Physiol.* **57**, 2194–2201 (2016).

59. 59.

Walter, M. et al. Visualization of protein interactions in living plant cells using bimolecular fluorescence complementation. *Plant J.* **40**, 428–438 (2004).

60. 60.

Leuzinger, K. et al. Efficient agroinfiltration of plants for high-level transient expression of recombinant proteins. *J. Vis. Exp.* **77**, <https://doi.org/10.3791/50521> (2013).

61. 61.

Ren, H., Park, M. Y., Spartz, A. K., Wong, J. H. & Gray, W. M. A subset of plasma membrane-localized PP2C.D phosphatases negatively regulate SAUR-mediated cell expansion in *Arabidopsis*. *PLoS Genet.* **14**, e1007455 (2018).

62. 62.

Wong, J. H., Spartz, A. K., Park, M. Y., Du, M. & Gray, W. M. Mutation of a conserved motif of PP2C.D phosphatases confers SAUR immunity and constitutive activity. *Plant Physiol.* **181**, 353–366 (2019).

63. 63.

Czechowski, T., Stitt, M., Altmann, T., Udvardi, M. K. & Scheible, W.-R. Genome-wide identification and testing of superior reference genes for transcript normalization in *Arabidopsis*. *Plant Physiol.* **139**, 5–17 (2005).

64. 64.

Dumont, J. N. Oogenesis in *Xenopus laevis* (Daudin). I. Stages of oocyte development in laboratory maintained animals. *J. Morphol.* **136**, 153–179 (1972).

Acknowledgements

We thank N. Gnyliukh and L. Hörmayer for technical assistance and N. Paris for sharing *PM-Cyto* seeds. We gratefully acknowledge the Life Science, Machine Shop and Bioimaging Facilities of IST Austria. This project has received funding from the European Research Council Advanced Grant (ETAP-742985) and the Austrian Science Fund (FWF) under I 3630-B25 to J.F., the National Institutes of Health (GM067203) to W.M.G., the Netherlands Organization for Scientific Research (NWO; VIDI-864.13.001), Research Foundation-Flanders (FWO; Odysseus II G0D0515N) and a European Research Council Starting Grant (TORPEDO-714055) to W.S. and B.D.R., the VICI grant (865.14.001) from the Netherlands Organization for Scientific Research to M.R. and D.W., the Australian Research Council and China National Distinguished Expert Project (WQ20174400441) to S.S., the MEXT/JSPS KAKENHI to K.T. (20K06685) and T.K. (20H05687 and 20H05910), the European Union’s Horizon 2020 research and innovation programme under Marie Skłodowska-Curie grant agreement no. 665385 and the DOC Fellowship of the Austrian Academy of Sciences to L.L., and the China Scholarship Council to J.C.

Author information

Author notes

1. These authors contributed equally: Lanxin Li and Inge Verstraeten

Affiliations

1. Institute of Science and Technology (IST) Austria, Klosterneuburg, Austria

Lanxin Li, Inge Verstraeten, Lesia Rodriguez, Jack Merrin & Jiří Friml

2. Laboratory of Biochemistry, Department of Agrotechnology and Food Sciences, Wageningen University, Wageningen, the Netherlands

Mark Roosjen & Dolf Weijers

3. Institute of Transformative Bio-Molecules, Division of Biological Science, Nagoya University Chikusa, Nagoya, Japan

Koji Takahashi & Toshinori Kinoshita

4. Graduate School of Science, Nagoya University Chikusa, Nagoya, Japan

Koji Takahashi & Toshinori Kinoshita

5. Department of Plant Biotechnology and Bioinformatics, Ghent University, Ghent, Belgium

Jian Chen, Wouter Smet, Steffen Vanneste & Bert De Rybel

6. VIB Center for Plant Systems Biology, Ghent, Belgium

Jian Chen, Wouter Smet & Bert De Rybel

7. Tasmanian Institute of Agriculture, College of Science and Engineering, University of Tasmania, Hobart, Tasmania, Australia

Lana Shabala & Sergey Shabala

8. Department of Plant & Microbial Biology, University of Minnesota, St. Paul, MN, USA

Hong Ren & William M. Gray

9. Laboratory of Plant Growth Analysis, Ghent University Global Campus, Incheon, Republic of Korea

Steffen Vanneste

10. Department of Plants and Crops, HortiCell, Ghent University, Ghent, Belgium

Steffen Vanneste

11. International Research Centre for Environmental Membrane Biology, Foshan University, Foshan, China

Sergey Shabala

Contributions

L.L., I.V. and J.F. conceived and designed the experiments. L.L. and I.V. carried out most of the experiments and analysis. M.R. and D.W. performed the phosphoproteomics analysis and TIR1/AFB1 IP–MS/MS. I.V., W.S. and B.D.R. performed TMK1 IP–MS/MS experiments and statistical analysis. MS/MS analysis was performed by the VIB Proteomics Core. L.S. and S.S. performed MIFE experiments. K.T. and T.K. performed the ATP hydrolysis assays. J.C. and S.V. created and shared the *AtTAS1c-AHA* lines. L.R. and L.L. created transgenic lines and crosses. H.R. and W.M.G. conducted [γ -³²P]ATP kinase assays and leaf wilting phenotype analysis, shared plasmids and seed materials, and contributed to discussion of the results. J.M. and L.L. modified the microfluidic chip. L.L., I.V. and J.F. wrote the manuscript.

Corresponding author

Correspondence to [Jiří Friml](#).

Ethics declarations

Competing interests

The authors declare no competing interests.

Additional information

Peer review information *Nature* thanks Malcolm Bennett, Anthony Bishopp and the other, anonymous, reviewer(s) for their contribution to the peer review of this work. Peer reviewer reports are available.

Publisher's note Springer Nature remains neutral with regard to jurisdictional claims in published maps and institutional affiliations.

Extended data figures and tables

[Extended Data Fig. 1 Investigation of CMT and vacuolar morphology in auxin-induced rapid root growth inhibition.](#)

a, Scheme of the modified vRootchip, with added valve 6 and adjusted valve routes. **b, c**, Dynamic cortical microtubule (CMT) transversal to longitudinal reorientation in response to 100nM IAA treatment. CMT were imaged at 6.25s intervals in elongating root epidermal cells in the *pEB1b::EB1b-GFP* marker line in vRootchip. Max Z-projection of 10 subsequent time frames was analysed using the FibrilTool. Average orientation of CMT is represented by the slope of the red line and the length of the line represents its anisotropy (**b**). (**c**) Quantification of CMT reorientation as in **b**. CMT reorientation at every time point is calculated as the difference in angle of that time point minus the initial time point angle divided by the difference in the angles of the initial time point and end time point (42min). Mean of 5 elongating cells \pm s.d. (**c**). **d–f**, Analysis of CMT reorientation in elongating root epidermal cells (**d, e**) and root growth (**f**) of *p35S::MAP4-GFP* in response to 10nM IAA, 10 μ M taxol and IAA+taxol co-treatment. CMT orientation was analysed with the Bioline script. Green-colored CMTs mark transversal oriented CMT (angle between -45° and $+45^\circ$), while red-colored CMTs indicate longitudinal orientation (angle between $+45^\circ$ and 135°). Scale bar=15 μ m (**d**). Percentage of longitudinal CMT. $n > 11$ roots, One-way ANOVA (**e**). Growth on respective treatments after 2h. $n > 10$ roots. Box plots depicts minimum to maximum, mean \pm s.d.

One-way ANOVA without modifications for multiple comparison (**f**).

* $P \leq 0.05$, **** $P \leq 0.0001$. **g**, Vacuolar morphology tracked using *pSYP22::SYP22-YFP* (green signal) in elongating cells before and after 30min of 100nM IAA. Scale bar=15 μ m. Magenta signal represents propidium-iodide stained cell walls.

[Source data](#)

[Extended Data Fig. 2 Apoplastic pH in auxin-induced rapid root growth inhibition.](#)

a, Apoplastic pH dynamics measured across the whole EZ (p1-p8) in vRootchip. The TL and blue-yellow scale image are from the same sample shown in Fig. [1a](#). Scale bar=30 μ m. The upper charts depict apoplastic pH in the indicated cells in response to 5nM IAA, and the lower charts represent the pH in response to washout. The right two charts show the speed at which each cell reaches its maximum pH change calculated as the difference between pH at a given time point and pre-stimulus pH, divided by the final pH change. **b**, Dynamics of root surface pH and medium pH in vRootchip. The left graph shows the elongation zone of the root. ROIs p1-p5 were chosen vertically along the root, 30 μ m away from the root surface indicated by the vertical white dotted line, while ROIs p6-p9 were distanced horizontally away from the root. The pH at the surface of the root (p1-p5) increased after IAA and recovered within 30s after washout. In contrast, the pH away from the root surface did not change significantly (p6-p9). **c**, H⁺-net influx measured by a non-invasive microelectrode before and after 10nM IAA treatment in the elongating zone of WT roots. Mean of 9 roots+s.e.m. **d**, **e**, Changes in medium pH (**d**) and apoplastic pH (**e**) after different medium pH exchanges in vRootchip. Sequentially used media: basal medium at pH 5.8, auxin-containing medium at pH 5.8, more acidic medium of pH 5.6, followed by pH 5.4 and again basal medium at pH 5.8. **f**, Quantification of root growth in response to gradual addition of KOH in the medium in the vRootchip. The greener the shade, the more KOH was added and followed by washout with initial pH 5.8 medium

[Source data](#)

Extended Data Fig. 3 H⁺-ATPase activation counteracts auxin-mediated apoplast alkalinization and growth inhibition.

a, b, Apoplastic pH of WT elongating root cells pre-treated (yellow) with 1 μ M cycloheximide (CHX) for 3min (**a**), or 50 μ M cordycepin (CORD) for 32min (**b**) followed by addition of 5nM IAA (pink). Mean of 3 (**a**) or 4 (**b**) roots+s.d. **c**, 10nM IAA induced Thr⁹⁴⁷ phosphorylation in roots using AHA2 and pThr947 specific antibodies. Band intensities of the different lanes were quantified by the Gel Analysis function in ImageJ. **d**, Measurement of *DR5::LUC* luminescence intensity in the root tip after 10 μ M FC, 10nM IAA and IAA+FC co-treatment. $n>3$ roots. IAA and IAA+FC are significantly different from the mock ($P\leq0.0001$). No significant difference between IAA and IAA+FC (ns, $P>0.05$). Two-way ANOVA. **e–k**, FC and IAA counteract each other. In vRootchip, addition of IAA still increased apoplastic pH (**e**) and inhibited root growth (**f**) in presence of FC, while addition of FC decreased apoplastic pH (**j**) and promoted root growth (**k**) in presence of IAA. Upon simultaneous addition of 10 μ M FC and 10nM IAA, both apoplastic pH (Fig **2d**) and root growth (**g**) were less affected than by IAA alone. Shaded area represents the duration of the treatments. Mean of 4 roots+s.d. *** $P\leq0.0001$ between IAA and IAA+FC from 0–31min (**g**), Two-way ANOVA. **(h-i)** Steady-state 1h root growth after FC, IAA and co-treatment was obtained by scanner. 1 μ M FC and 10nM IAA were used in (**h**) while 10 μ M FC and 2nM IAA were used in (**i**). $n>9$ roots. Box plot depicts minimum to maximum, mean \pm s.d. ns $P>0.05$, * $P\leq0.05$, ** $P\leq0.01$, *** $P\leq0.0001$, One-way ANOVA (**h, i**). **l**, Dose-response of auxin-induced root growth inhibition of *aha* single mutants. $n>22$ roots. Relative GR is ratio between auxin-affected growth and mock for the same genotype. ns $P>0.05$, ** $P\leq0.01$, *** $P\leq0.001$, Welch ANOVA. **m**, Quantitative Real-time PCR on the *AHA1,2,7,11* expression in root tips of *AtTAS1c-AHA#2* and #4. The expression level was normalized to *EF1 α* as housekeeping gene. Mean of 6 biological replicates in 3 technical replicates+s.d. Box plot depicts minimum to maximum, mean \pm s.d. ns $P>0.05$, * $P\leq0.05$, ** $P\leq0.01$, *** $P\leq0.001$, One-way ANOVA. **n**, Dose-response of auxin-induced root growth inhibition of *AtTAS1c-AHA* lines and *ost2-3D* mutants reveals hypersensitivity and resistance respectively to IAA in comparison to WT

($n > 15$ roots). Relative GR is calculated as mentioned in (1). ns $P > 0.05$, * $P \leq 0.05$, ** $P \leq 0.01$, *** $P \leq 0.001$, **** $P \leq 0.0001$, Welch ANOVA

[Source data](#).

Extended Data Fig. 4 TMK1 interacts with PM H⁺-ATPase.

a, TMK1 expression pattern in the elongation zone (EZ), meristematic and transition zone (MZ-TZ) in the primary root shown by *pTMK1::TMK1-GFP*. Scale bar=60 μm . **b, c**, IP-MS/MS on *pTIR1::TIR1-VENUS* in *tir1-1* (**b**) and *pAFB1::AFB1-VENUS* in *afb1-3* (**c**) under mock condition compared to 1h 50 μM MG132 pre-treatment and 2min 100nM IAA treatment. Proteins surpassing the threshold FDR of 0.05 are marked. Green depicts the respective bait protein and red depicts known members of the SCF E3 ubiquitin ligase complex. Pulldowns were performed in triplicate, LFQ analysis. **d**, IP-MS/MS on *pTMK1::TMK1-GFP*. Peptides corresponding to AHA1/2 are shown in red. p-values are calculated based on three biological replicates using two-sided t-tests. **e**, Co-IP of *pAHA2::AHA2-GFP* roots, followed by Western blot detection of TMK1 and Thr⁹⁴⁷-phosphorylated AHA2 after 100nM IAA for 30min. Auxin did not affect interaction, but induced AHA2-phosphorylation. Input of *pAHA2::AHA2-GFP* roots was the control. **f**, Bimolecular Fluorescent Complementation (BiFC) in *Nicotiana benthamiana* leaves transiently transformed with the reciprocal controls for Fig. 3b: *YFP^N-TMK1*, *AHA2-YFP^C* or both. Scale bar=10 μm . **g**, Demonstration of specific interaction between *YFP^N-TMK1^{K616R}* and *AHA2-YFP^C* as no complementation was observed in the leaves expressing *YFP^N-TMK1^{K616R}* and *AUX1-YFP^C* or leaves expressing *YFP^N-AHA2* and *AUX1-YFP^C*. Scale bar=100 μm

[Source data](#).

Extended Data Fig. 5 TMK1 directly phosphorylates PM H⁺-ATPases.

a, Wilting *N. benthamiana* leaves that transiently express *TMK1^{WT}* and ATP-site mutated forms *TMK1^{K616E}* or *K616R*. **b**, Western blot analysis of the

AHA2 levels and the Thr947 phosphorylation in roots of *DEX::TMK1^{WT}* or *K616R-HA* treated +/- DEX (30μM for 24h) and +/- IAA (100nM for 1h). **c**, Ponceau-stained SDS-PAGE gel as loading control for *in vitro* kinase assay with [γ -³²P]-ATP, substrate C-terminal AHA2 (AHA2-C) and the intracellular kinase domain of TMK1^{WT} or kinase dead TMK1^{K616E}. **d, e**, Western blot detection of AHA2 levels and Thr947 phosphorylation in *tmk1,3* roots (**d**) or *tmk1,4* roots (**e**) treated with 100nM IAA for 1h. WT control for (**d**) is shown in Fig. 3e.

Extended Data Fig. 6 Cytosolic TIR1/AFB mediates rapid apoplast alkalinization and root growth inhibition.

a, b, Apoplastic alkalinization (**a**) and root growth inhibition (**b**) in response to IAA measured in *aux1-100* mutant compared to WT roots in vRootchip. Mean of 3 roots+s.d. *** $P \leq 0.0001$, Two-way ANOVA. **c, d**, Apoplastic alkalinization (**c**) and root growth inhibition (**d**) in response to 2,4-D in *aux1-100* mutant compared to WT roots. Steady state pH measured 30min after 100nM 2,4-D treatment. Mean of >6 roots+s.d., One-way ANOVA (**c**). (**d**) Growth obtained in 2h was captured by scanner. Mean of >4 roots+s.d., One-way ANOVA. ns $P > 0.05$, ** $P \leq 0.01$, *** $P \leq 0.001$. **e**, Root growth of *tir triple* mutants compared to WT in response to 5nM IAA in the vRootchip. Mean of 3, 2 roots+s.d. *** $P \leq 0.0001$, two-way ANOVA. **f, g**, Apoplastic pH (**f**) and root growth (**g**) after 10μM PEO-IAA and 5nM IAA. The steady state pH was measured 30min after treatments, while the root growth obtained in 1h was recorded by scanning. Mean of >7 roots+s.d.. ns $P > 0.05$, ** $P \leq 0.01$, *** $P \leq 0.0001$, One-way ANOVA. **h, i**, Dose-response of auxin-induced root growth inhibition of *tir1-1*, *tir1-10* and *afb1-3* mutants reveals slight resistance to 5nM IAA in comparison to WT ($n > 6$ roots). Relative GR is calculated as the ratio of GR at 1h (**h**) or 6h (**i**) after IAA treatments relative to mock-treated GR of the same genotype. Mean+s.d. * $P \leq 0.05$, *** $P \leq 0.001$, One-way ANOVA. **j, k**, Apoplastic pH (**j**) and root growth (**k**) analysis comparing *tir1-10* null mutant and *afb1-3* mutants in response to IAA in vRootchip. Shaded area represents the duration of the treatment. Mean of 4 roots for each treatment+s.d. $P \leq 0.0001$ (**j**) and $P \leq 0.05$ (**k**), Two-way ANOVA. **l**, Steady-state root growth over 6h in *tmk1*-related mutants. $n = 6$ roots for *tmk1,4*; $n > 26$ for others. Mean+s.d.

Box plot depicts minimum to maximum, mean \pm s.d. **** $P\leq 0.0001$, One-way ANOVA. **m**, Dose-response of auxin-induced root growth inhibition of *pUBQ10::TMK1-3HA* compared to WT and *tmk1-1*. Relative GR is the ratio between auxin-affected growth to the mock growth in the same genotype. Mean of > 7 roots \pm s.d.. ns $P>0.05$, * $P\leq 0.05$, Welch ANOVA. **n**, **o**, Raw data for Fig. [4d](#), [e](#), respectively. $n>16$ roots. Box plot depicts minimum to maximum, mean \pm s.d. ns $P>0.05$, ** $P\leq 0.01$, **** $P\leq 0.0001$, One-way ANOVA

[Source data](#).

[Extended Data Fig. 7 PM potential and AUX1 involvement in auxin-induced apoplast alkalinization.](#)

Since auxin causes simultaneously membrane depolarization²⁵ and apoplast alkalinization, both of which are interdependent and required for growth, we addressed which of them mediates the auxin effect on root inhibition. By manipulating the external pH, we found that pH and growth were correlated (Fig. [1d-g](#)) while membrane potential (MP) was uncoupled (**a**, **b**). Additionally, we observed that K⁺ efflux (**c**) compensates auxin-induced H⁺ and Ca²⁺ influx (Extended Data Fig. [2c](#), Extended Data Fig. [8a](#)), suggesting that auxin-induced MP change is the result of complex ion fluxes, while H⁺ influx and resulting apoplastic pH change for growth regulation is just a subset of those. **a**, **b**, Membrane potential recorded by invasive micro-electrode in root elongating cells with IAA treatment (magenta). 4 roots \pm s.e.m. (**a**). Membrane potential measured in root elongating cells after 40min incubation in different pH medium. $n>5$ roots \pm s.e.m. * $P\leq 0.05$, One-way ANOVA (**b**). Alkaline medium, which alkalinized the apoplast and inhibited root growth (Fig. [1d](#), [e](#)) mimicking the auxin effect, did not result in membrane depolarization. Acidic medium, which acidified the apoplast and promoted root growth (Fig. [1f](#), [g](#)) depolarized membrane. MP is thus uncoupled from growth and apoplastic pH. **c**, PM net K⁺ efflux measured by a non-invasive microelectrode before and after 10nM IAA treatment in the elongating zone of WT roots. 16 roots \pm s.e.m. **d**, Scheme showing AUX1/LAX-mediated IAA⁻/2H⁺ symport and mechanistically elusive H⁺ influx. IAA⁻/2H⁺ symport by AUX1 auxin

influx carrier was proposed¹⁷ a possible mechanism of auxin-induced H⁺ influx and apoplast alkalinization. Comparison of H⁺ influx rates in root hair cells¹⁷, or elongating root epidermal cells (Extended Data Fig. 2c) and conservative estimates of AUX1-mediated ³H-IAA transport in Xenopus oocytes^{24,64} argue against this. Below we show that calculations based on data of Xenopus oocytes, primary root and root hairs suggest that AUX1-mediated H⁺ symport is not sufficient to account for the auxin-induced H⁺ fluxes: (1) ³H-IAA transport in the AUX1 overexpressing Xenopus oocytes after 100nM ³H-IAA²⁴ is ca. $2.6 \times 10^{-14} \text{ mol min}^{-1}$. The min. diameter of the Xenopus oocyte at stage V/VI⁶⁴ is ca. 1.0mm, so the surface area is minimally $3.142 \times 10^{-6} \text{ m}^2$. The max. speed of IAA uptake across the membrane is calculated as: $2.6 \times 10^{-14} \text{ mol} / (60 \text{ s} \times 3.142 \times 10^{-6} \text{ m}^2) = 1.38 \times 10^{-10} \text{ mol m}^{-2} \text{ s}^{-1}$. Based on 2 H⁺ per IAA⁻, the max. speed of AUX1-symported H⁺ is $2.76 \times 10^{-10} \text{ mol m}^{-2} \text{ s}^{-1}$. (2) H⁺ uptake after 10nM IAA (ten times less than in Xenopus) in *Arabidopsis* root elongating cells: $1.7 \times 10^{-8} \text{ mol m}^{-2} \text{ s}^{-1}$ (Extended Data Fig. 2c). This is still 62 times more than the conservatively estimated max. speed in (1). (3) H⁺ uptake NAA in *Arabidopsis* root hairs¹⁷ is ca. $1.0 \times 10^{-7} \text{ mol m}^{-2} \text{ s}^{-1}$. This is 362 times more than the conservatively estimated max. speed in (1)

[Source data](#)

Extended Data Fig. 8 FER does not mediate auxin-induced rapid growth inhibition.

Root growth of *fer-4* compared to Col-0 in response to application and washout of 100nM IAA in vRootchip. Shaded area indicates IAA treatment. Mean of 5 roots for Col-0 and 3 for *fer-4*+s.d. ns, $P>0.05$, Two-way ANOVA.

[Source data](#)

Extended Data Fig. 9 TIR1-mediated Ca²⁺ signalling contributes to auxin-induced apoplast alkalinization.

Another rapid output of TIR1/AFB perception mechanism are cytosolic Ca²⁺ transients in root hairs¹⁷. Therefore, we evaluated Ca²⁺ transients in apoplast alkalinization and root growth inhibition. Using vRootchip, GCaMP3 Ca²⁺ marker³³, non-invasive microelectrodes and cvxIAA-ccvTIR1 system²⁸, we confirmed that auxin via TIR1/AFB triggered rapid Ca²⁺ influx correlates with root growth inhibition (**a-d**). We noted a distinct Ca²⁺ response measured by the microelectrode (**a-b**) and GCaMP3 (**c**). Namely, Ca²⁺ channels are activated at the plasma membrane resulting in net influx, while the GCaMP3 reported more complex responses possibly involving intracellular Ca²⁺ storage and release. Moreover, the use of cvxIAA-ccvTIR1 (**d**) provided additional proof that TIR1-mediated auxin perception activates Ca²⁺ signalling. Further, we verified that mutants in the Ca²⁺ permeable cation channel *Cyclic NUCLEOTIDE-GATED CHANNEL 14 (CNGC14)* have delayed auxin-induced apoplast alkalinization and root growth inhibition (**e**) similarly as reported¹⁴. Furthermore, depletion of external Ca²⁺ resulted in attenuated auxin-induced Ca²⁺ spike, delayed apoplast alkalinization and growth inhibition (**b, f, g**). Ca²⁺ addition resulted in rapid growth inhibition (**h, i**). These observations collectively suggest that TIR1/AFB-mediated Ca²⁺ signalling is part of the mechanism for auxin-induced rapid apoplast alkalinization and growth inhibition. **a**, PM net Ca²⁺ influx measured by a non-invasive microelectrode before and after 10nM IAA treatment in the elongating zone of WT roots. **9**
roots+s.e.m. **b**, Normalized fluorescence intensity of GCaMP3, cytosolic Ca²⁺ marker, in elongating cells responding to 5nM IAA treatment in vRootchip. The intensity was normalized to the initial intensity of the same root. Mean of 7 roots+s.d. Note the three peaks in cytosol compared to the single major peak outside of cells (**a**). **c, d**, Root growth (**c**) and fluorescence intensity in elongating cells (**d**) in GCaMP3 crossed into ccvTIR1 compared to control. Growth rate and intensity are normalized to the pre-stimulus value. Mean of 7 for ccvTIR1 and 2 for control+s.d.
****P≤0.0001, Two-way ANOVA. **e**, Root growth (upper graph) and apoplastic pH (lower graph) analysis in cngc14-2 and WT in response to IAA in vRootchip. Mean of 5 roots for WT and 3 for cngc14-2+s.d.
****P≤0.0001, Two-way ANOVA. **f, g**, Root growth (upper graph in **f**) and apoplastic pH (lower graph in **f**) in WT, as well as cytosolic Ca²⁺ analysis in GCaMP3 reporter marker line in vRootchip (**g**) with 140min pre-treatment

of Ca^{2+} free medium (grey) followed by 5nM IAA addition (magenta for growth, blue for pH in **f** and yellow for Ca^{2+} in **g**). Auxin induced significant less Ca^{2+} response in Ca^{2+} free medium, compared to normal medium in (**b**). The red dotted square marked the non-responsive delay after auxin. Mean of 5 (**f**) and 6 (**g**) roots+s.d. **h**, **i**, Root growth (**h**) and apoplastic pH (**i**) analysis in WT upon Ca^{2+} addition after 140min Ca^{2+} free medium in the presence of 5nM IAA in vRootchip. Mean of 5 roots+s.d.

[Source data](#)

Supplementary information

[Supplementary Information](#)

This file contains Supplementary Fig. 1 and Codes 1 and 2. Supplementary Fig. 1: This figure contains the raw and uncropped data for every figure in which we show western blot results. The blots are labelled according to the corresponding figure, and the cropped area is indicated. Supplementary Codes 1 and 2: For easier manipulation of the Arduino device controlling medium flow in the vRootchip, two in-house-designed scripts were generated. These scripts were first used to generate the data shown in this manuscript, and we make them publicly available here.

[Reporting Summary](#)

[Peer Review Information](#)

[Supplementary Table 1](#)

Phosphoproteomic data of rapid auxin effects in roots and phosphoproteomic analysis of H^+ -ATPases in *tmk1-1* mutants. Differentially regulated phosphopeptides (FDR ≤ 0.05) in H^+ -ATPases in IAA-treated versus mock-treated roots. IAA treatment was at 100 nM for 2 min. QHF and LTQXL analyses are presented in tabs 1 and 2, respectively. Tab 3 shows the differentially phosphorylated phosphosites of AHAs in the *tmk1-1* background compared with WT.

Supplementary Table 2

IP–MS analysis of *pTIR1::TIR1-VENUS* and *pAFB1::AFB1-VENUS*. Overview of the putative TIR1 and AFB1 interactors after MaxQuant and Perseus statistical analysis. Samples were *TIR1*- and *AFB1-VENUS* lines with mock treatment or 50 µM MG132 preincubation for 1 h and 100 nM IAA treatment for 2 min. Proteins passing the threshold of FDR 0.05 and specific fold change are included in the table. *P* values were calculated based on the three replicates using a two-sided *t*-test. Pulldowns were performed in triplicate. The respective bait proteins are highlighted in yellow.

Supplementary Table 3

IP–MS analysis of *pTMK1::TMK1-GFP*. Overview of the putative TMK1 interactors after MaxQuant and Perseus statistical analysis. The list is sorted based on the ratio of *pTMK1::TMK1-GFP* versus WT control. Proteins passing the threshold of FDR 0.05 and specific fold change are included in the table. *P* values were calculated based on the three replicates using a two-sided *t*-test. Yellow, bait; green, GFP; orange, selected proteins.

Supplementary Table 4

Primers used for cloning and quantitative PCR analysis

Source data

Source Data Fig. 1

Source Data Fig. 2

Source Data Fig. 3

Source Data Fig. 4

[**Source Data Extended Data Fig. 1**](#)

[**Source Data Extended Data Fig. 2**](#)

[**Source Data Extended Data Fig. 3**](#)

[**Source Data Extended Data Fig. 4**](#)

[**Source Data Extended Data Fig. 6**](#)

[**Source Data Extended Data Fig. 7**](#)

[**Source Data Extended Data Fig. 8**](#)

[**Source Data Extended Data Fig. 9**](#)

Rights and permissions

[Reprints and Permissions](#)

About this article

Cite this article

Li, L., Verstraeten, I., Roosjen, M. *et al.* Cell surface and intracellular auxin signalling for H⁺ fluxes in root growth. *Nature* **599**, 273–277 (2021).
<https://doi.org/10.1038/s41586-021-04037-6>

- Received: 04 February 2021
- Accepted: 17 September 2021
- Published: 27 October 2021
- Issue Date: 11 November 2021

- DOI: <https://doi.org/10.1038/s41586-021-04037-6>

Share this article

Anyone you share the following link with will be able to read this content:

[Get shareable link](#)

Sorry, a shareable link is not currently available for this article.

[Copy to clipboard](#)

Provided by the Springer Nature SharedIt content-sharing initiative

Further reading

- [**TMK-based cell-surface auxin signalling activates cell-wall acidification**](#)
 - Wenwei Lin
 - , Xiang Zhou
 - , Wenxin Tang
 - , Koji Takahashi
 - , Xue Pan
 - , Jiawei Dai
 - , Hong Ren
 - , Xiaoyue Zhu
 - , Songqin Pan
 - , Haiyan Zheng
 - , William M. Gray
 - , Tongda Xu
 - , Toshinori Kinoshita
 - & Zhenbiao Yang

Nature (2021)

This article was downloaded by **calibre** from <https://www.nature.com/articles/s41586-021-04037-6>

| [Section menu](#) | [Main menu](#) |

- Article
- Open Access
- [Published: 27 October 2021](#)

TMK-based cell-surface auxin signalling activates cell-wall acidification

- [Wenwei Lin^{1,2}](#),
- [Xiang Zhou](#) [ORCID: orcid.org/0000-0001-7848-367X^{1,2}](#),
- [Wenxin Tang¹](#),
- [Koji Takahashi](#) [ORCID: orcid.org/0000-0001-5438-7624^{3,4}](#),
- [Xue Pan](#) [ORCID: orcid.org/0000-0001-9415-8316²](#),
- [Jiawei Dai¹](#),
- [Hong Ren⁵](#),
- [Xiaoyue Zhu¹](#),
- [Songqin Pan²](#),
- [Haiyan Zheng](#) [ORCID: orcid.org/0000-0003-1955-1817⁶](#),
- [William M. Gray](#) [ORCID: orcid.org/0000-0002-1320-290X⁵](#),
- [Tongda Xu](#) [ORCID: orcid.org/0000-0003-3398-9217¹](#),
- [Toshinori Kinoshita](#) [ORCID: orcid.org/0000-0001-7621-1259^{3,4}](#) &
- [Zhenbiao Yang](#) [ORCID: orcid.org/0000-0001-7482-6540^{1,2}](#)

Nature volume 599, pages 278–282 (2021)

- 8071 Accesses
- 67 Altmetric
- [Metrics details](#)

Subjects

- [Auxin](#)
- [Cell growth](#)
- [Growth factor signalling](#)
- [SARS-CoV-2](#)

Abstract

The phytohormone auxin controls many processes in plants, at least in part through its regulation of cell expansion¹. The acid growth hypothesis has been proposed to explain auxin-stimulated cell expansion for five decades, but the mechanism that underlies auxin-induced cell-wall acidification is poorly characterized. Auxin induces the phosphorylation and activation of the plasma membrane H⁺-ATPase that pumps protons into the apoplast², yet how auxin activates its phosphorylation remains unclear. Here we show that the transmembrane kinase (TMK) auxin-signalling proteins interact with plasma membrane H⁺-ATPases, inducing their phosphorylation, and thereby promoting cell-wall acidification and hypocotyl cell elongation in *Arabidopsis*. Auxin induced interactions between TMKs and H⁺-ATPases in the plasma membrane within seconds, as well as TMK-dependent phosphorylation of the penultimate threonine residue on the H⁺-ATPases. Our genetic, biochemical and molecular evidence demonstrates that TMKs directly phosphorylate plasma membrane H⁺-ATPase and are required for auxin-induced H⁺-ATPase activation, apoplastic acidification and cell expansion. Thus, our findings reveal a crucial connection between auxin and plasma membrane H⁺-ATPase activation in regulating apoplastic pH changes and cell expansion through TMK-based cell surface auxin signalling.

[Download PDF](#)

Main

Embedded in a rigid cell wall, the plant cell must modify its wall to gain the adjustable elasticity to regulate cell expansion in space and time. Auxin induces rapid cell expansion by acidifying the cell-wall space (apoplast), leading to the activation of cell-wall-localized proteins for wall loosening^{3,4}, a growth mechanism that has been known as the acid growth theory for half of a century⁵. Auxin triggers the efflux of protons, resulting in apoplastic acidification by activating the plasma membrane (PM)-localized P-type H⁺-ATPase^{6,7}. In *Arabidopsis*, PM H⁺-ATPase is encoded by an autoinhibited H⁺-ATPase (AHA) gene family comprising 11 members⁸. Phosphorylation of the conserved penultimate Thr residue (Thr948 in AHA1, Thr947 in AHA2) has been proposed to release the autoinhibition of the ATPase pump activity by the cytoplasmic C-terminal region^{9,10,11,12,13,14,15}. Fendrych et al. previously demonstrated that auxin-induced apoplastic acidification and growth are mediated by TIR1/AFB–Aux/IAA nuclear auxin perception in hypocotyls¹⁶. Auxin induces the TIR1/AFB-dependent expression of SAUR proteins that act as inhibitors of PP2C.D phosphatases, which dephosphorylate the penultimate Thr residue¹⁷. Although this mechanism can sustain H⁺-ATPase activity by preventing the

dephosphorylation of the penultimate Thr residue, it cannot account for how the PM H⁺-ATPase is initially phosphorylated to become activated.

The PM-localized TMK-receptor-like kinases have a vital role in auxin signalling in regulating pavement cell morphogenesis, differential growth of the apical hook, lateral root formation and root thermomorphogenesis in *Arabidopsis*^{18,19,20,21,22,23}. Auxin rapidly promotes TMK-dependent activation of PM-associated ROP GTPases within seconds, providing a mechanism for rapid auxin responses on the cell surface in addition to TIR1/AFB-based intracellular auxin signalling^{20,24,25,26}. To identify new components in TMK-mediated auxin-signalling pathways, we performed immunoprecipitation coupled with mass spectrometry (IP–MS) to isolate potential interactors of TMK1 in *Arabidopsis*. In brief, GFP-Trap agarose beads were used to immunoprecipitate the TMK1–GFP protein complex from *pTMK1::TMK1-GFP* transgenic plants, which was further analysed using MS. The proteins that were identified only from the *pTMK1::TMK1-GFP* transgenic plants but not from the *pTMK1::GFP* control plants were considered to be candidates for TMK1-associated proteins (Supplementary Table 2). Among them, we were especially interested in the PM H⁺-ATPases (AHAs) (Extended Data Fig. 1a), as the previous study showed that auxin triggers the activation of the PM H⁺-ATPase, which promotes hypocotyl cell elongation²⁷. We further confirmed that GFP–AHA1 co-immunoprecipitated with TMK1 and TMK4 in the 35S::GFP-AHA1 transgenic plants as detected by immunoblotting using anti-TMK1 and anti-TMK4 antibodies, respectively (Fig. 1a and Extended Data Fig. 1b). Furthermore, TMK1–GFP co-immunoprecipitated with AHA(s) from *pTMK1::TMK1-GFP* transgenic plants as detected by immunoblot analysis using anti-AHA2-cat antibodies after anti-GFP-Trap antibody immunoprecipitation (Extended Data Fig. 1c). An in vitro pull-down assay showed that the kinase domain of TMK1 (TMK1^{KD}), when fused to maltose-binding protein (MBP), directly interacted with the AHA2 C-terminal domain fused to glutathione S-transferase (GST) (GST–AHA2-C) (Extended Data Fig. 1d), suggesting that the kinase domain of TMK1 directly binds to the C-terminal region of AHA2. We postulated that TMK1 interacts with AHAs in vivo as both proteins are predominantly localized at the PM^{20,28,29}. A co-immunoprecipitation (co-IP) assay showed that the in vivo association between Myc-tagged TMK1 and HA-tagged AHA1 was enhanced within 1 min after treatment with 1-naphthaleneacetic acid (NAA) (Fig. 1b,c), suggesting that auxin rapidly promotes TMK1–AHA interactions. To test whether auxin rapidly induces a direct interaction between TMK1 and AHA1, we developed a microfluidics device enabling the high-resolution time-course analysis of a rapid induction of the dynamic interaction in a single *Arabidopsis* protoplast using fluorescence resonance energy transfer (FRET) imaging (Fig. 1d). Protoplasts co-expressing TMK1–mCherry and AHA1–GFP were captured in triangle traps within the device, enabling imaging before and immediately after auxin treatment (Fig. 1d and Extended Data Fig. 1e). Intriguingly, the TMK1–mCherry/AHA1–GFP FRET efficiency increased within 10 s

after auxin treatment, indicating that auxin very rapidly promotes the direct interaction between TMK1–mCherry and AHA1–GFP (Fig. 1e,f). By contrast, no increase in FRET efficiency was detected when protoplasts co-expressing TMK1–mCherry and AHA1–GFP were mock-treated with control buffer (Fig. 1e,f). Together, these results show that auxin promotes a rapid and direct interaction between TMK1 and AHA1 on the PM.

Fig. 1: TMK1 interacts directly with AHAs.

 figure1

a, Co-IP analysis of TMK1 with GFP–AHA1. *35S::GFP* (control) and *35S::GFP-AHA1* plants were immunoprecipitated with anti-GFP antibodies and analysed by western blotting using anti-TMK1 antibodies. **b**, Auxin induced interactions between TMK1–Myc and AHA–HA in *Arabidopsis* protoplasts. AHA1–HA and TMK1–Myc constructs were transiently expressed in protoplasts, which were then treated with 1 μ M NAA for 1, 2 and 5 min before being used for co-IP analysis. **c**, Quantification of AHA1–HA proteins co-immunoprecipitated with TMK1–Myc as shown in **b**. Data are the mean values of two independent biological replicates. **d**, The microfluidics device that was designed to investigate the auxin-induced rapid TMK1–AHA1 interaction using FRET analysis. Right, a triangle trap (top) for trapping a protoplast (bottom). The blue arrows indicate the flow of cell suspension, and the red arrows indicate the flow of NAA or mock solutions. Scale bar, 50 μ m. **e**, FRET analysis of the rapid induction of the TMK1–AHA interaction. A representative heat map of sensitized

emission efficiencies for the TMK1–mCherry/AHA1–GFP FRET on the PM region (further details are provided in Extended Data Fig. 1d). The times before and after treatment are indicated (−25 s and +150 s). Scale bars, 10 μm. f, Quantitative time-course analyses of changes in the FRET efficiencies. NAA (100 nM) or mock buffer was applied at 25 s after imaging started. The error bars indicate the s.d. of 10 cells scored. Statistical analysis was performed using two-sided Student's *t*-tests ($P < 0.05$); the grey background indicates significant differences during the covered periods.

Source data.

The phosphorylation of the conserved penultimate threonine residue on the H⁺-ATPase proteins is a primary mechanism by which the H⁺-ATPase is activated in response to multiple signals, including phytohormones, sucrose, NaCl, blue light and the fungal toxin fusicoccin^{13,14,27,30,31,32}. We first examined the phosphorylation status of the penultimate threonine residue in the aerial parts of *Arabidopsis* seedlings using phosphoproteomics (with the roots removed when the seedlings were prepared for the assay). The phosphorylation levels of the penultimate Thr residue of AHA2, AHA3 and AHA7 were compromised in the *tmk1-1 tmk4-1* mutant compared with the wild type (Extended Data Fig. 2a–e), implying a general reduction of H⁺-ATPase activity in the mutant. TMK1 and TMK4 are functionally redundant in the regulation of the growth of *Arabidopsis* seedlings, as neither of the *tmk1* and *tmk4* single-knockout mutants exhibit a visible growth defect, whereas the *tmk1 tmk4* double mutants show severe growth retardation, especially in hypocotyl elongation²⁸ (also see below).

We next analysed the phosphorylation status of the penultimate Thr residue by immunoblotting using antibodies against phosphorylated Thr947 (pThr947), which recognize the unique phosphorylation of the penultimate Thr residue in all of the AHA isoforms²⁷. Fusicoccin promotes the binding of 14-3-3 to the phosphorylated C-terminal region of PM H⁺-ATPase, resulting in the activation of the pump. As shown previously¹⁴, fusicoccin increased the level of phosphorylation of the penultimate Thr residue in wild type Col-0 seedlings (Extended Data Fig. 2f,g). Similarly, treatments with auxin at micromolar or nanomolar levels increased its phosphorylation levels (Fig. 2a,b and Extended Data Fig. 2f,g). Compared with the untreated wild type, the level of phosphorylation of the penultimate Thr residue was reduced in the *tmk1-1 tmk4-1* mutant (Fig. 2a,b and Extended Data Fig. 2f,g). Importantly, auxin-induced phosphorylation of this residue was nearly abolished in the *tmk1-1 tmk4-1* mutant (Fig. 2a,b and Extended Data Fig. 2f,g). By contrast, fusicoccin treatment still increased the level of phosphorylation of the penultimate Thr residue in the *tmk1-1 tmk4-1* mutant (Extended Data Fig. 2f,g), suggesting that the *tmk1-1 tmk4-1* mutant was able to respond to other stimuli in regulating AHA phosphorylation at the penultimate Thr residue. Thus, TMK1 and TMK4 are required selectively for the auxin-induced increase in phosphorylation of the penultimate Thr residue.

Fig. 2: TMK1 and TMK4 are required for auxin-induced phosphorylation and activation of the PM H⁺-ATPase.

 figure2

a, Western blot detection of phosphorylated H⁺-ATPase in the aerial parts of wild-type and *tmk1-1 tmk4-1* (*tmk1/4*) mutant plants (top, anti-pThr947). AHA protein levels were determined using anti-H⁺-ATPase antibodies (bottom). Seedlings were treated with mock buffer or 10 µM IAA for 30 min. **b**, Quantification of the phosphorylation level of the H⁺-ATPase. Data are mean ± s.d. $n = 4$ independent experiments. **c**, TMK1^{KD} phosphorylated AHA1–GFP in vitro. TMK1 (TMK1^{KD}, WT) or the kinase-dead form (TMK1^{KDKm}) was incubated with protoplast-expressed AHA1–GFP, and its phosphorylation state was determined using anti-pThr947 (pThr947) antibodies. CBB, Coomassie Brilliant Blue. **d**, Quantification of the Thr948 phosphorylation level (determined using anti-pThr947 antibodies) of the AHA1–GFP. Data are mean ± s.d. $n = 3$ biological replicates. **e**, MS detection of AHA1-C16 phosphorylation by TMK1^{KD} in vitro. The graph shows the abundance of phosphorylated peptides at the indicated residues analysed by MS. Data are mean ± s.d. $n = 3$. Two biological replicates with three technical replicates each were performed. **f**, Auxin induction of H⁺-ATPase activity was abolished in *tmk1-1 tmk4-1*. The values shown are relative ATP hydrolytic activity of indicated samples to that of mock Col-0. The box bounds the interquartile

range divided by the median (central lines), and the Tukey-style whiskers extend to a maximum of 1.5× interquartile range from 25th and 75th percentiles. $n = 11$ (mock) and $n = 8$ (IAA). Statistical analysis was performed using two-way ANOVA (**b** and **f**) or one-way ANOVA (**d** and **e**); *** $P < 0.0001$.

Source data.

To assess whether TMKs directly phosphorylate AHA at this penultimate Thr residue, we next immunoprecipitated AHA1-GFP from *Arabidopsis* protoplasts that transiently expressed this fusion protein for an in vitro phosphorylation assay. Recombinant TMK1 kinase domain (TMK1^{KD}), but not the kinase-dead mutant (TMK1^{Km}), greatly increased the phosphorylation of AHA1-GFP at the Thr948 residue in vitro (Fig. 2c, d). We further determined whether TMK1 phosphorylates a synthetic peptide containing the 16 C-terminal amino acid residues from AHA1 (AHA1-C16) in an in vitro assay using the recombinant TMK1^{KD}. MS analysis showed that the penultimate Thr residue (Thr15 of the peptide, Thr948 of AHA1) of AHA1-C16 was highly phosphorylated by TMK1^{KD}, but not by TMK1^{Km} (Fig. 2e and Extended Data Fig. 2h). The second to the last Thr residue (T9T15, Thr9 and Thr15 in the AHA1-C16 peptide.) on AHA1-C16 was weakly phosphorylated by TMK1^{KD}. Neither TMK1^{KD} nor TMK1^{Km} phosphorylated a scrambled synthetic peptide (Fig. 2e). Thus, TMK1 specifically phosphorylates the penultimate Thr residue of AHA1. Together with auxin-induced rapid interaction between TMK1 and AHA1 and the requirement of TMK1 and TMK4 for auxin-induced AHA phosphorylation in vivo, these results strongly indicate a role for auxin-activated TMK1 in directly phosphorylating AHA1.

We next investigated whether TMK1 and TMK4 are required for the activation of PM H⁺-ATPase by auxin. The activation of PM H⁺-ATPase couples with the ATP hydrolysis¹⁴. As shown previously²⁷, auxin treatment for 30 min increased ATP hydrolysis in the aerial parts of wild-type *Arabidopsis* seedlings by 50% (Fig. 2f). Neither *tmk1-1* nor *tmk4-1* mutations significantly affected the basal level of ATP hydrolysis or auxin-induced changes in ATP hydrolysis (Extended Data Fig. 2i). However, the basal level of ATP hydrolysis was significantly reduced in the *tmk1-1 tmk4-1* mutant (Fig. 2f), consistent with the reduced level of phosphorylation of the penultimate Thr residue (Fig. 2a, b). Importantly, auxin-induced enhancement of ATP hydrolysis was abolished in this double mutant (Fig. 2f), indicating that TMK1 and TMK4 are essential for auxin-induced H⁺-ATPase activation. In agreement with the compromised H⁺-ATPase activity, compared with the wild type, the *tmk1-1 tmk4-1* mutant was more tolerant to lithium (Extended Data Fig. 2j, k), a toxic alkali cation, the uptake of which is coupled with the activation of H⁺-ATPase and PM hyperpolarization. In particular, the aerial part of wild-type seedlings became chlorotic, whereas the aerial part of the *tmk1-1 tmk4-1* seedlings remained green after growth on lithium. This is in contrast to SAUR19-OX lines, which display increased

H^+ -ATPase activity and therefore exhibit much higher sensitivity to lithium¹⁷. These findings together demonstrate that TMK1 and TMK4 are required for auxin-induced PM H^+ -ATPase activation.

To assess the consequences of the reduced PM H^+ -ATPase activation in *tmk1-1 tmk4-1* plants, we introduced membrane-impermeable 8-hydroxypyrene-1,3,6-trisulfonic acid trisodium salt (HPTS) as a ratiometric fluorescent pH indicator for assessing changes in the apoplastic pH at a cellular resolution in *Arabidopsis thaliana* hypocotyls⁴. Two different forms of HPTS (the protonated and deprotonated forms) were visualized in two independent channels with excitation wavelengths of 405 nm and 458 nm, respectively. The apoplastic pH correlates with the ratiometric values (signal intensity from the 458 nm channel divided by that from the 405 nm channel)^{4,33}. As a positive control for the HPTS-based pH indicator, we monitored the apoplastic pH in hypocotyls of the *ost2-2D* mutant harbouring the constitutively activated AHA1 (ref. 34). As shown previously⁴, the *ost2-2D* mutant exhibited lower 458/405 values compared with the wild type (Fig. 3a, b), confirming its enhanced apoplastic acidification. By contrast, significantly higher 458/405 values were observed in *tmk1-1 tmk4-1* hypocotyls, suggesting apoplastic alkalization in the mutant (Fig. 3a, b). Furthermore, the apoplastic pH of the *tmk1-1 tmk4-1* mutant was restored to the wild-type level when this mutant was complemented with wild-type TMK1 (Extended Data Fig. 3a, b), indicating that TMK1 is essential for the regulation of the apoplastic pH.

Fig. 3: TMK1 and TMK4 are required for apoplastic acidification and cell elongation in *Arabidopsis* hypocotyl.

figure3

a, b, Comparison (imaging (**a**) and quantification (**b**)) of the apoplastic pH in wild type (Col-0), *ost2-2D* and *tmk1-1 tmk4-1* plants. Changes in pH were visualized with ratiometric values of fluorescent HPTS. The mean 458/405 values of *ost2-2D* and the *tmk1-1 tmk4-1* mutant relative to the WT are shown on the y axis. $n = 300$ (6 hypocotyls, 50 cells for each). **c**, Epidermal cell lengths of hypocotyls. $n = 140$ (Col-0), $n = 64$ (*ost2-2D*) and $n = 134$ (*tmk1-1 tmk4-1*) cells. Statistical analysis was

performed using one-way ANOVA (**b** and **c**) (three independent assays); *** $P \leq 0.0001$. For **a**, scale bars, 100 μm .

Source data.

Importantly, hypocotyl cell length was correlated with the pH value of the mutant when compared with the wild type (Fig. 3c). In *tmk1-1 tmk4-1* mutants, the mean length of hypocotyl cells was significantly shorter than in the wild type²⁸ (Figs. 3a,c), and the hypocotyl cell lengths were largely restored when the mutant was complemented with wild-type TMK1 (Extended Data Fig. 3c). By contrast, increased apoplastic acidification is linked to an increase in cell length and hypocotyl length in *ost2-2D* plants (Fig. 3a,c and Extended Data Fig. 3d,e).

Auxin promotes apoplastic acidification in hypocotyls through the activation of PM H⁺-ATPase, contributing to auxin-induced cell elongation^{16,27}. We found that the auxin-induced acidification in the apoplast was abolished in *tmk1-1 tmk4-1* plants (Fig. 4a,b), suggesting an essential role of TMK1 and TMK4 in auxin-triggered PM H⁺-ATPase activation. Moreover, exogenous NAA promoted the rapid elongation of auxin-depleted hypocotyl segments (Fig. 4c) and the elongation of whole hypocotyls (Fig. 4d) from wild-type seedlings, but not from the *tmk1-1 tmk4-1* seedlings. The *tmk1-1 tmk4-1* mutant complemented with TMK1 exhibited a normal response to auxin in promoting hypocotyl segment elongation (Fig. 4c). The severe defect in *tmk1-1 tmk4-1* hypocotyl elongation was partially rescued when *tmk1-1 tmk4-1* seedlings were grown on medium with a lower pH (pH 5.0 and pH 4.3) compared with standard medium (pH 5.7) (Extended Data Fig. 4a,b). Moreover, *ost2-2D*, which caused activation of the PM H⁺-ATPase, partially rescued the hypocotyl elongation defect of *tmk1-1 tmk4-1* mutants (Extended Data Fig. 4c,d). TMK1 and TMK4 probably activate other downstream pathways to regulate hypocotyl elongation in addition to the PM H⁺-ATPase activation, such as ROP GTPase signalling to the organization of the cytoskeleton^{20,35}. Such additional downstream pathways may explain the incomplete rescue of the hypocotyl elongation defect in *tmk1-1 tmk4-1* plants by *ost2-2D*. Together, our results indicate that TMK1 and TMK4 are required for apoplastic acidification through auxin-triggered activation of PM H⁺-ATPase, contributing to auxin regulation of hypocotyl cell elongation.

Fig. 4: TMK1 and TMK4 are required for auxin-induced apoplastic acidification and hypocotyl elongation.

 **figure4**

a, The effect of auxin (100 nM NAA for 15 min) on the apoplastic pH changes visualized by HPTS staining. **b**, Quantitative analysis of a. $n = 350$ (7 hypocotyls, 50 cells for each). **c**, Auxin-induced rapid elongation hypocotyl segments from wild-type, *tmk1-1 tmk4-1* (*tmk1/4*) and *tmk1-1 tmk4-1 TMK1* (*tmk1/4/TMK1*) plants. The relative length when comparing the hypocotyl segments at 30 min to that at 0 min is represented on the y axis. The results were analysed using two-way ANOVA. $n = 20$ hypocotyl sections per line. **d**, Auxin-induced hypocotyl elongation in seedlings. $n = 16$ (Col-0) and $n = 10$ (*tmk1-1 tmk4-1*) (three independent assays). Statistical analysis was performed by two-way ANOVA (b–d). ** $P \leq 0.01$, *** $P \leq 0.0001$; NS, not significant. For a, scale bars, 100 μ m.

[Source data](#).

In this Article, we show that TMK1 directly interacts with PM H⁺-ATPases on the PM, and this interaction was induced rapidly (within 10 s) by auxin treatment (Fig. 1e, f), well preceding an auxin-induced increase in cell elongation¹⁶. Thus, the auxin-induced TMK–AHA association can be considered to be the very early response for auxin signal transduction. Our results suggest that, once interacting with AHAs after auxin stimulation, TMK1 directly phosphorylates AHA1 at the penultimate Thr residue (Fig. 2 and Extended Data Fig. 2). An accompanying paper by Li et al. shows that this auxin-induced phosphorylation of AHA's penultimate Thr residue occurred in root tissues within 2 min after auxin treatment³⁶, nearly as rapid as the auxin-induced

interaction between TMK1 and AHA1 (Fig. 1b, f). TMKs therefore regulate AHA activation by affecting the phosphorylation status of the penultimate Thr residue. As a consequence, auxin induced apoplastic acidification in a TMK1/TMK4-dependent manner in hypocotyl cells (Figs. 3a, b and 4a, b). Moreover, reducing the apoplast pH either genetically by *ost2-2D* or growing seedlings in an acidic environment partially restored the hypocotyl elongation defect of *tmk1-1 tmk4-1* plants (Extended Data Fig. 4a–d). These data suggest that, after activation by auxin, the cell-surface auxin-signalling components TMKs act as protein kinases to directly and rapidly initiate the phosphorylation and activation of PM H⁺-ATPase, although our findings do not exclude the possibility that the TMK-mediated AHA phosphorylation may also respond to other stimuli under certain conditions. By contrast, the nuclear auxin signalling inhibits ATPase dephosphorylation through the TIR1/AFB-SAUR-PP2C.D pathway^{17,37,38}. Thus, the current findings support the hypothesis that the cell-surface and intracellular auxin-signalling pathways, respectively, initiate and sustain PM H⁺-ATPase activation in cells in which auxin promotes cell expansion, such as in hypocotyls, and collectively explain the acid growth theory. In roots, TMK-dependent auxin signalling also promotes ATPase activation, but to counter the rapid alkalization (or membrane depolarization) activated by TIR1/AFBs^{36,39,40}. Importantly, these findings, together with the recent findings on the TMK-mediated noncanonical auxin signalling in regulating pavement cell morphogenesis^{18,41}, differential growth of the apical hook¹⁸, lateral root formation¹⁹, root gravitropic response⁴² and thermomorphogenesis²³, are emerging as a common theme that auxin regulates growth and developmental processes through the coordinate actions of intracellular and cell-surface auxin-signalling systems.

Methods

Plant materials and growth conditions

A. thaliana Columbia ecotype (Col-0) was used as the wild type in this study. *ost2-2D* seeds were obtained from J. Leung. The *tmk1-1 tmk4-1* mutant in the Col-0 background and *pTMK1-TMK1-GFP* transgenic lines (in the *tmk1-1 tmk4-1* mutant) were described previously^{18,19}. The *ost2-2D tmk1-1 tmk4-1* mutants were generated by genetic crosses and confirmed by genotyping. *Arabidopsis* plants were grown in soil (Sungro S16-281) in a growth room at 23 °C, 40% relative humidity and 75 μE m⁻² s⁻¹ light under a 12 h photoperiod for approximate 4 weeks before protoplast isolations. To grow *Arabidopsis* seedlings, the seeds were surface-sterilized with 50% bleach for 10 min (*tmk1-1 tmk4-1* seeds were sterilized with 75% (v/v) ethanol for 5 min), and washed three times with sterilized distilled H₂O, and then placed onto plates with 1/2 MS medium containing 0.5% sucrose and 0.8% agar at pH 5.7 in the dark with vertical growth. Then 2–3 d after germination, hypocotyls were used for cell characterization.

Plasmid construction and generation of transgenic plants

Full-length and truncated variants *TMK1*, *AHA1* and *AHA2* were amplified by PCR from Col-0 cDNA and cloned into a protoplast transient expression vector (HBT vectors obtained from L. Shan and P. He) or the plant binary vectors pGWB641 and pGWB644. Stable transgenic lines were generated using standard *Agrobacterium tumefaciens*-mediated transformation in the *tmk1-1 tmk4-1* mutant or Col-0 (ref. [43](#)). The full-length cDNAs of *TMK1* and *AHA1* were amplified by PCR, and then cloned into the pDONR221-P1P4 and pDONR221-P3P2 vectors using the BP recombination reaction (Invitrogen), respectively. pDONR221-P1P4-TMK1 was recombined with pDONR221-P3P2-AHA1 into pFRETgc-2in1-NC to generate pFRET-mEGFP-AHA1+TMK1-mCherry^{[44](#)}. pDONR221-P3P2-AHA1 was recombined with pENTRL1-pLac-LacZalpha-L4 (Invitrogen) into pFRETgc-2in1-NC to generate pFRET-mEGFP-AHA1. pDONR221-P1P4-TMK1 was recombined with pENTRL3-pLac-Tet-L2 (Invitrogen) into pFRETgc-2in1-CC to generate pFRET-MK1-mCherry. The *AHA2* C-terminal region was cloned into pDest-565, and expressed in *Escherichia coli* (Rosetta, BL21) (a list of the primers is provided in Supplementary Table [1](#)).

Determination of H⁺-ATPase phosphorylation levels

The immunoblot analysis was performed as described by Hayashi^{[45](#)} using specific antibodies against the catalytic domain of AHA2 and phosphorylated Thr947 in AHA2 (1:5,000 dilution)^{[45](#)}. These antibodies recognize not only AHA2 but also other H⁺-ATPase isoforms in *Arabidopsis*^{[46](#)}. In brief, the roots were removed from 1/2 MS-grown seedlings (aged 5 d), and the remaining aerial sections were incubated in a KPSC buffer (10 mM potassium phosphate, pH 6.0, 2% sucrose, 50 µm chloramphenicol) in the dark for 10 h. The buffer was then replaced every hour. The pretreated tissues were incubated in the presence of 100 nM IAA for 10 min or 10 µM IAA for 30 min in the dark. The aerial sections were collected and grounded with a plastic pestle, followed by solubilization in 40 µl of SDS buffer (3% (w/v) SDS, 30 mM Tris-HCl (pH 8.0), 10 mM EDTA, 10 mM NaF, 30% (w/v) sucrose, 0.012% (w/v) Coomassie Brilliant Blue and 15% (v/v) 2-mercaptoethanol), and the homogenates were centrifuged at room temperature (10,000g for 5 min). Next, 12 µl of the supernatant was loaded onto 10% (w/v) SDS-PAGE gels to assess the H⁺-ATPase or the phosphorylated penultimate Thr levels using the respective above-mentioned antibodies. Goat anti-rabbit IgG (1:10,000 dilution) conjugated to horseradish peroxidase (Santa Cruz, sc-2357) was used as a secondary antibody. The chemiluminescent signal was quantified using ImageJ (Fiji, Java 1.8.0_172) (Fig. [2a](#), Extended Data Fig. [2f](#) and Supplementary Fig. [1](#)).

HPTS staining and imaging

HPTS staining and imaging were performed as described by Barbez⁴ with modifications. In brief, two-day etiolated seedlings were transferred and incubated with 1 mM HPTS (from 100 mM water stock) with 0.01% Triton X-100 under vacuum (10–15 pa) 5 min. The seedlings were then incubated with HPTS for 60 min in the liquid growth medium. The seedlings were subsequently mounted in the same growth medium on a microscopy slide and covered with a coverslip. For auxin treatment, seedlings were incubated in 1/2 MS growth medium supplemented with 1 mM HPTS and NAA in the stated concentration for 15 min and subsequently mounted in the same growth medium on a microscopy slide and covered with a coverslip. Seedling imaging was performed using an inverted Zeiss 880 confocal microscope equipped with a highly sensitive GaAsP detector. Fluorescent signals for the protonated HPTS form (excitation, 405 nm; emission peak, 514 nm), as well as the deprotonated HPTS form (excitation, 458 nm; emission peak, 514 nm), were detected using a ×10 water-immersion objective.

IP–MS analyses

The *pTMK1::gTMK1-GFP/tmk1-1 tmk4-1* seedlings were grown on 1/2 MS medium for 10 d, and the entire seedlings were collected and ground in liquid nitrogen with a mortar and pestle. Total proteins were extracted using extraction buffer (50 mM Tris-HCl pH 7.4, 150 mM NaCl, 5 mM EDTA, 0.5% Triton X-100 with protease inhibitor and phosphatase inhibitor) on ice. The extracts were centrifuged at 13,000g for 30 min, and the supernatants were incubated with GFP-Trap agarose beads (GFP-Trap_A, gta-20, ChromoTek) at 4 °C for 2 h to immunoprecipitate TMK1–GFP proteins. The agarose beads were washed and resuspended with 50 mM Tris-Cl buffer (pH 7.8). One tenth of the beads was used for immunoblot analysis with anti-GFP antibodies. The remaining agarose beads were used for LC coupled with tandem MS (LC–MS/MS) analysis. MS analysis was carried out by Orbitrap Fusion mass spectrometry (Thermo Fisher Scientific).

Phosphoproteomics analyses

Col-0 and the *tmk1-1 tmk4-1* seedlings were cultured on 1/2 MS plate for 5 d, then the aerial parts of seedlings were transferred to 1/2 MS liquid medium and incubated in the KPSC buffer (10 mM potassium phosphate, pH 6.0, 2% sucrose and 50 µm chloramphenicol) in the dark overnight, and the buffer was replaced every 1 h for 12 h (ref. ⁴⁷). Seedlings were collected and flash-frozen in liquid nitrogen. A total of 1 g of frozen shoots (fresh weight) was ground with a liquid-nitrogen-precooled mortar and pestle, and then homogenized in 5 ml extraction buffer (50 mM Tris-HCl buffer (pH 8), 0.1 M KCl, 30% sucrose, 5 mM EDTA and 1 mM dithiothreitol (DTT) in Milli-Q water, 1× complete protease inhibitor mixture and the PhosSTOP phosphatase inhibitor mixture) in a Dounce Homogenizer. At least 50 strokes were performed. The

homogenate was filtered through four layers of miracloth and centrifuged at 5,000g at 4 °C for 10 min. Half of the supernatant was used to resuspend the pellet, and the mixture was centrifuged again at 5,000g 4 °C for 10 min. The two fractions of the supernatants were combined and mixed with 3, 1 and 4 volumes of methanol, chloroform and water, respectively. The mixtures were centrifuged at 5,000g for 10 min, and the aqueous phase was removed. After the addition of four volumes of methanol, the proteins were pelleted by centrifugation at 4,000g for 10 min. The pellets were washed with 80% acetone and resuspended in 6 M guanidinium hydrochloride in 50 mM triethylammonium bicarbonate buffer (pH 8). The proteins were used for tandem mass tag labelling according to the Kit protocol (Thermo Fisher Scientific, 90096) and quantification by MS.

Nano-LC–MS/MS was performed using the Dionex rapid-separation liquid chromatography system interfaced with a QExactive HF (Thermo Fisher Scientific). Samples were loaded onto an Acclaim PepMap 100 trap column (75 µm × 2 cm, Thermo Fisher Scientific) and washed with buffer A (0.1% trifluoroacetic acid) for 5 min with a flow rate of 5 µl min⁻¹. The trap was brought in line with the nano analytical column (nanoEase, MZ peptide BEH C18, 130 Å, 1.7 µm, 75 µm×20 cm, Waters) with a flow rate of 300 nl min⁻¹ with a multistep gradient (4– 15% buffer B (0.16% formic acid and 80% acetonitrile) in 20 min, then 15–25% B in 40 min, followed by 25–50% B in 30 min). MS data were acquired using a data-dependent acquisition procedure with a cyclic series of a full scan acquired with a resolution of 120,000 followed by MS/MS scans (33% collision energy in the HCD cell) with a resolution of 45,000 of the 20 most intense ions with a dynamic exclusion duration of 20 s.

All LC–MS data were analysed using Maxquant (v.1.6.2.6) with the Andromeda search engine. The type of LC–MS run was set to reporter ion MS2 with 10 plex tandem mass tags as isobaric labels. Reporter ion mass tolerance was set at 0.003 Da. LC–MS data were searched against TIAR10 with the addition of potential contaminants. Protease was set as trypsin/P, allowing two misscuts for total proteomic data and three misscuts for the phosphor-enriched sample (post-translational modification sample). Carbamidomethylation of cysteine was set as a fixed modification, N-terminal acetylation, oxidation at methionine as well as phosphorylation at serine, threonine and tyrosine were set as variable modifications. Proteins with a false-discovery rate of <1% were reported. For quantification, spectra were filtered by minimum reporter PIF set at 0.6.

The results were further analysed using Perseus (v.1.6.1.3). The protein group results were first filtered for reverse and contaminant hits and the reporter ion intensity values were further log₂-transformed and normalized to the column total. For group comparisons, statistical significance between groups was analysed using Student's *t*-

tests with equal variance on both sides, requiring two valid values in total, and the Q value was calculated using the permutation test. S0 (ref. [48](#))² was set to 1.

The phospho(STY)-site reporter ions were first normalized to proteome column total, and then filtered for reverse and contaminant hits, and the reporter ion intensity values were further log₂-transformed. Each phospho(STY) site was further normalized to protein abundance from proteome data if available. Only sites that have site localization confidence > 75% were included in the analysis. For group comparison, statistical significance between groups was analysed using Student's *t*-tests with equal variance on both sides, requiring two valid values in total, and the Q value was calculated using the permutation test. S0 was set to 1.

Co-IP assays with transgenic plants

Approximately 1 g of 35S::GFP and 35S::GFP-AHA1 plants (aged 4 weeks) was ground in liquid N₂ and further ground in 0.5 ml of ice-cold co-IP buffer (10 mM HEPES at pH 7.5, 100 mM NaCl, 1 mM EDTA, 10% glycerol, 0.1% Triton X-100 and protease inhibitor mixture from Roche). The homogenates were centrifuged at 12,470g at 4 °C for 10 min. The supernatant was incubated with anti-GFP-Trap antibodies (Chromotek, 3h9, 1:1,000 dilution) for 2 h with gentle shaking. The beads were collected and washed three times with washing buffer (10 mM HEPES (pH 7.5), 100 mM NaCl, 1 mM EDTA, 10% glycerol and 0.1% Triton X-100) and once with 50 mM Tris-HCl (pH 7.5), and analysed by western blotting using anti-TMK1 or anti-TMK4 antibodies ¹⁸. The total input proteins were determined using anti-GFP antibodies (Fig. [1a](#), Extended Data Fig. [1b](#) and Supplementary Fig. [1](#)).

Co-IP analysis of the TMK–AHA interaction induced by auxin treatment in *Arabidopsis* protoplasts

Wild-type Col-0 leaf protoplasts were prepared as described by Yoo et al.⁴⁹. Protoplasts (2×10^5) were co-transfected with 35S::AHA1-HA or 35S::TMK1-Myc plasmid DNA, which was prepared using the Invitrogen PureLink Plasmid Maxiprep Kit, and incubated at room temperature for 10 h. Transfected protoplasts were then collected in 2 ml Eppendorf tubes and centrifuged at 100g for 1 min. The supernatant was discarded, and the protoplasts were resuspended with 100 µl W5 solution (2 mM MES-KOH, pH 5.7, 5 mM KCl, 154 mM NaCl and 125 mM CaCl₂). The protoplasts were treated with 1 µM NAA for the indicated time periods, frozen in liquid N₂ immediately and stored in -80 °C. The samples were lysed with 0.5 ml of extraction buffer (10 mM HEPES (pH 7.5), 100 mM NaCl, 1 mM EDTA, 10% (v/v) glycerol, 0.5% Triton X-100 and protease inhibitor mixture from Roche). After vortexing vigorously for 30 s, the samples were centrifuged at 12,470g for 10 min at 4 °C. The

supernatant was incubated with anti-Myc antibodies (Sinobiological, 100029-MM08, 1:1,000 dilution) for 2 h, and then incubated with protein G agarose beads (Pierce, 20397) for another 2 h at 4 °C with gentle shaking. Beads were collected by centrifugation at 100g for 1 min at 4 °C followed by washing twice with extraction buffer. The beads were washed with 50 mM Tris-Cl buffer (pH 7.5), and the immunoprecipitated proteins were analysed by immunoblotting with anti-HA–HRP antibodies (Invitrogen, 26183, 1:2,000 dilution) (Fig. [1b](#) and Supplementary Fig. [1](#)).

In vitro pull-down assay

MBP- or GST-fusion proteins were expressed in *E. coli* and affinity-purified using standard protocols. In brief, 200 ml of isopropyl-β-d-thiogalactoside-induced cell culture pellet was lysed in 20 ml lysis buffer (containing 0.5% Triton X-100) by sonication on ice. Centrifuge lysates were cleared by centrifuging at 10,000g for 30 min at 4 °C. The supernatant was then incubated with 100 µl amylose resins or glutathione-Sepharose beads at 4 °C for 4 h with gentle rotation. The beads were then centrifuged and washed three times with lysis buffer. Proteins were eluted with GST (10 mM reduced glutathione in 50 mM Tris pH 8.0) or MBP (20 mM Tris-HCl, 200 mM NaCl, 1 mM EDTA, 1 mM DTT, 10 mM maltose, pH 7.4) buffer. The protein concentration was estimated using the NanoDrop ND-1000 spectrophotometer and confirmed using the Bio-Rad Quick Start Bradford Dye Reagent. GST- or GST-fusion proteins (10 µg; immobilized on glutathione-Sepharose beads) were incubated with 10 µg prewashed MBP or MBP fusion proteins at 4 °C in 150 µl of incubation buffer (10 mM HEPES (pH 7.5), 100 mM NaCl, 1 mM EDTA, 10% glycerol and 0.5% Triton X-100) for 1 h. The beads were collected and washed three times with washing buffer (20 mM HEPES (pH 7.5), 300 mM NaCl, 1 mM EDTA and 0.5% NP-40) and once with 50 mM Tris-HCl (pH 7.5). Proteins in the beads were analysed by immunoblotting with anti-GST (Santa Cruz, sc-138, 1:1,000 dilution) or anti-MBP (Invitrogen, PA1-989, 1:1,000 dilution) antibodies (Extended Data Fig. [1d](#) and Supplementary Fig. [1](#)).

Vanadate-sensitive ATPase activity measurement

ATP hydrolysis by PM H⁺-ATPase was measured in a vanadate-sensitive manner as previously described^{[27](#)}. In brief, the aerial parts of seedlings (Col-0, *tmk1-1*, *tmk4-1*, and *tmk1-1 tmk4-1*; aged 14 d) were incubated in KPSC buffer (10 mM potassium phosphate, pH 6.0, 2% sucrose, 50 µM chloramphenicol) in the dark for 10 h. The buffer was replaced every hour. The pretreated tissues were incubated in the presence of 10 µM IAA for 30 min in darkness. The tissues were homogenized with homogenization buffer (50 mM MOPS-KOH, pH 7.0, 100 mM KNO₃, 2 mM sodium molybdate, 0.1 mM NaF, 2 mM EGTA, 1 mM phenylmethylsulfonyl fluoride and 20 µM leupeptin) and the homogenates were centrifuged at 10,000g for 10 min; the

obtained supernatant was further ultracentrifuged at 45,000g for 60 min. The resultant pellet (the microsomal fraction) was resuspended in the homogenization buffer. The ATP hydrolytic activity of the microsomal fraction was measured in a vanadate-sensitive manner, and the inorganic phosphate released from ATP was measured²⁷.

In vitro phosphorylation

Protoplasts were isolated from plants expressing AHA1–GFP as described above. Agarose-immobilized (GFP-Trap beads, Chromotek, gta-100) AHA1–GFP proteins were incubated with 1 µg MBP–TMK1^{KD} or MBP–TMK1^{KDKm} recombinant proteins (expressed in *E. coli* and isolated by affinity purification) in phosphorylation buffer (5 mM HEPES, 10 mM MgCl₂, 10 mM MnCl₂, 1 mM DTT and 50 µM ATP)¹⁸ at room temperature (24 °C) for 1 h. After incubation, the reaction was stopped by adding 4× SDS loading buffer. Proteins in the beads were analysed by immunoblotting using anti-pT947, anti-AHA1-cat or anti-GFP (Chromotek, 3h9) antibodies (Fig. 2c and Supplementary Fig. 1).

For in vitro phosphorylation of synthetic peptides, 10 mg synthetic peptide AHA1-C16 (KLKGLDIDTAGHHYTV) or scrambled peptide (GDAHVVKITHLDKGLIT) was incubated with 1 µg MBP–TMK1^{KD} or MBP–TMK1^{KDKm} recombinant proteins in phosphorylation buffer for 1 h. The peptide mixtures were then analysed using MS.

Auxin-induced rapid hypocotyl segment elongation

For analysing auxin-induced elongation of hypocotyl segments, the auxin-depleted hypocotyl sections (2 mm) were transferred to growth medium (10 mM KCl, 1 mM MES-KOH, pH 5.7, 0.8% agar) with/without 10 µM NAA for 30 min. The hypocotyl sections were photographed and measured using Image J at 0 min and 30 min after treatments. For analysing auxin-induced hypocotyl elongation in seedlings, 1/2 MS-grown seedlings (aged 4 d) were transferred into 1/2 MS medium containing the indicated concentrations of NAA and incubated for additional 48 h under normal growth conditions. Hypocotyl lengths were measured using Image J after treatment.

Fabrication of the protoplast-capture microfluidics chip

The design parameters for the protoplast capture chip (Extended Data Fig. 1e) are as follows: each capture unit consists of three pillars. The average diameter of each pillar is 50 µm. The distance between the two entrance pillars is 52 µm. The shortest distance between the entrance pillar and the bottom pillar is 27 µm. The height of the capture chamber is 80 µm. Each chip contains an array of 1,866 capture units. A master mould was fabricated on a silicon wafer using the traditional photolithography

technique by Beijing Borui Yisheng Technology. In brief, SU-8 3050 was centrifuged at 1,600 r.p.m., soft-baked at 95 °C for 30 min and exposed at 260 mJ cm⁻². After exposure, the wafer was post-exposure baked at 95 °C for 5 min, developed for 3 min and air-dried with pressurized nitrogen.

The protoplast capture chip was fabricated with soft lithography using polydimethylsiloxane (PDMS) (Sylgard 184 Silicone Elastomer Kit, The DOW Chemical Company). In brief, PDMS prepolymer and curing agent were mixed at a 10:1 ratio, degassed in a vacuum chamber with negative pressure, poured onto the master mould and baked at 80 °C for 2 h. After curing, the PDMS slab was peeled off, hole-punched and, finally, plasma-oxidized to adhere to the cover glass.

Auxin treatment and FRET analysis of protoplasts captured in microfluidics chips

Arabidopsis (Col-0) protoplasts were isolated and transfected with 2in1 AHA1-GFP, TMK1-mCherry and AHA1-GFP/TMK1-mCherry vectors as described. Before the experiment, the protoplast capture chip was filled with a protoplast-suspending WI solution (4 mM pH 5.7 MES-KOH, 0.5 M mannitol and 20 mM KCl). After air bubbles were entirely removed from the chip, the protoplast suspension was injected slowly into the chip from inlet 1 (Fig. 1e). The time-lapse FRET images were acquired at 5 s per frame using the Zeiss LSM880 confocal laser scanning microscope (argon 488 30%, and argon 561 3%). NAA or mock solution was injected into the chip from inlet 2 (Fig. 1e) at 25 s after the live imaging started.

The FRET efficiency was analysed using FRET sensitized emission methods⁴⁶. In brief, the AHA1–GFP only, TMK1–mCherry only sample and the FRET samples were imaged using the same microscope settings (the donor and FRET channels were excited with 30% argon 488 nm, and the emissions were collected using 498–551 nm and 600–670 nm, respectively; the acceptor channel was excited with 3% argon 561 nm and the emissions were collected using 600–670 nm). To avoid interference by chlorophyll autofluorescence, protoplasts with concentrated chloroplasts at one side of the cell were processed for quantification. A segmented line was drawn along the PM region opposite to the site of chloroplasts to measure the mean signal intensity for each channel using Image-Pro Plus (<http://www.mediacy.com/imageproplus>) and LAS-X (Leica). The correction factors β , α , γ and δ were calculated with the donor- and acceptor-only reference samples, then the FRET efficiency was calculated using the equation below⁵⁰.

$$\frac{\text{E}_1(F)R(E)T(S)}{\text{E}_1(F)R(E)T(S)-d_o n} = \frac{\text{E}_1(F)R(E)T(S)}{\text{E}_1(F)R(E)T(S)-d_o n} \times \frac{r}{r} \times \beta - \frac{a_c c_c}{c_c e}$$

$$\{ \rm{p} \} \{ \rm{t} \} \{ \rm{o} \} \{ \rm{r} \} \times (\gamma - \alpha \times \beta) \{ \{ \rm{a} \} \\ \{ \rm{c} \} \{ \rm{c} \} \{ \rm{e} \} \} \{ \rm{p} \} \{ \rm{t} \} \{ \rm{o} \} \{ \rm{r} \} \times (1 - \beta \times \delta) \} \}$$

The mean FRET efficiency and s.d. from 10 cells of 100 nM NAA or mock treatment are presented in Fig. 1g. To generate the FRET efficiency heat-map image, the plasma membrane region in the side opposite to the chloroplasts was cropped as the region of interest to avoid autofluorescence (Extended Data Fig. 1d). The cropped images from the donor, FRET and acceptor channels were processed using the image calculator module of ImageJ with the $E_{(\text{FRET-SE})}$ equation shown above.

Reporting summary

Further information on research design is available in the [Nature Research Reporting Summary](#) linked to this paper.

Data availability

Data supporting the findings of this study are available within the paper and its [Supplementary Information](#). Mass spectrometry raw data are available at the MassIVE under accession number msv000087822. [Source data](#) are provided with this paper.

References

1. 1. Du, M., Spalding, E. P. & Gray, W. M. Rapid auxin-mediated cell expansion. *Annu. Rev. Plant Biol.* **71**, 379–402 (2020).
2. 2. Haruta, M., Gray, W. M. & Sussman, M. R. Regulation of the plasma membrane proton pump (H^+ -ATPase) by phosphorylation. *Curr. Opin. Plant Biol.* **28**, 68–75 (2015).
3. 3. McQueen-Mason, S., Durachko, D. M. & Cosgrove, D. J. Two endogenous proteins that induce cell wall extension in plants. *Plant Cell* **4**, 1425–1433 (1992).
4. 4.

Barbez, E., Dunser, K., Gaidora, A., Lendl, T. & Busch, W. Auxin steers root cell expansion via apoplastic pH regulation in *Arabidopsis thaliana*. *Proc. Natl Acad. Sci. USA* **114**, E4884–E4893 (2017).

5. 5.

Rayle, D. L. & Cleland, R. Enhancement of wall loosening and elongation by acid solutions. *Plant Physiol.* **46**, 250–253 (1970).

6. 6.

Moloney, M. M., Elliott, M. C. & Cleland, R. E. Acid growth effects in maize roots: evidence for a link between auxin-economy and proton extrusion in the control of root growth. *Planta* **152**, 285–291 (1981).

7. 7.

Hager, A. Role of the plasma membrane H⁺-ATPase in auxin-induced elongation growth: historical and new aspects. *J. Plant Res.* **116**, 483–505 (2003).

8. 8.

Haruta, M. et al. Molecular characterization of mutant *Arabidopsis* plants with reduced plasma membrane proton pump activity. *J. Biol. Chem.* **285**, 17918–17929 (2010).

9. 9.

Palmgren, M. G., Sommarin, M., Serrano, R. & Larsson, C. Identification of an autoinhibitory domain in the C-terminal region of the plant plasma membrane H⁺-ATPase. *J. Biol. Chem.* **266**, 20470–20475 (1991).

10. 10.

Ekberg, K., Palmgren, M. G., Veierskov, B. & Buch-Pedersen, M. J. A novel mechanism of P-type ATPase autoinhibition involving both termini of the protein. *J. Biol. Chem.* **285**, 7344–7350 (2010).

11. 11.

Jahn, T. et al. The 14-3-3 protein interacts directly with the C-terminal region of the plant plasma membrane H⁺-ATPase. *Plant Cell* **9**, 1805–1814 (1997).

12. 12.

Olsson, A., Svennelid, F., Ek, B., Sommarin, M. & Larsson, C. A phosphothreonine residue at the C-terminal end of the plasma membrane H⁺-ATPase is protected by fusicoccin-induced 14-3-3 binding. *Plant Physiol.* **118**, 551–555 (1998).

13. 13.

Fuglsang, A. T. et al. Binding of 14-3-3 protein to the plasma membrane H⁺-ATPase AHA2 involves the three C-terminal residues Tyr(946)-Thr-Val and requires phosphorylation of Thr(947). *J. Biol. Chem.* **274**, 36774–36780 (1999).

14. 14.

Svennelid, F. et al. Phosphorylation of Thr-948 at the C terminus of the plasma membrane H⁺-ATPase creates a binding site for the regulatory 14-3-3 protein. *Plant Cell* **11**, 2379–2391 (1999).

15. 15.

Maudoux, O. et al. A plant plasma membrane H⁺-ATPase expressed in yeast is activated by phosphorylation at its penultimate residue and binding of 14-3-3 regulatory proteins in the absence of fusicoccin. *J. Biol. Chem.* **275**, 17762–17770 (2000).

16. 16.

Fendrych, M., Leung, J. & Friml, J. TIR1/AFB-Aux/IAA auxin perception mediates rapid cell wall acidification and growth of *Arabidopsis* hypocotyls. *eLife* **5**, <https://doi.org/10.7554/eLife.19048> (2016).

17. 17.

Spartz, A. K. et al. SAUR inhibition of PP2C-D phosphatases activates plasma membrane H⁺-ATPases to promote cell expansion in *Arabidopsis*. *Plant Cell* **26**, 2129–2142 (2014).

18. 18.

Cao, M. et al. TMK1-mediated auxin signalling regulates differential growth of the apical hook. *Nature* **568**, 240–243 (2019).

19. 19.

Huang, R. et al. Noncanonical auxin signaling regulates cell division pattern during lateral root development. *Proc. Natl Acad. Sci. USA* **116**, 21285–21290 (2019).

20. 20.

Xu, T. et al. Cell surface ABP1-TMK auxin-sensing complex activates ROP GTPase signaling. *Science* **343**, 1025–1028 (2014).

21. 21.

Baral, A. et al. External mechanical cues reveal a katanin-independent mechanism behind auxin-mediated tissue bending in plants. *Dev. Cell* **56**, 67–80 (2021).

22. 22.

Wang, Q. et al. A phosphorylation-based switch controls TAA1-mediated auxin biosynthesis in plants. *Nat. Commun.* **11**, 679 (2020).

23. 23.

Gallochet, C. et al. HY5 and phytochrome activity modulate shoot-to-root coordination during thermomorphogenesis in *Arabidopsis*. *Development* **147**, <https://doi.org/10.1242/dev.192625> (2020).

24. 24.

Xu, T. et al. Cell surface- and rho GTPase-based auxin signaling controls cellular interdigititation in *Arabidopsis*. *Cell* **143**, 99–110 (2010).

25. 25.

Leyser, O. Auxin signaling. *Plant Physiol.* **176**, 465–479 (2018).

26. 26.

Mockaitis, K. & Estelle, M. Auxin receptors and plant development: A new signaling paradigm. *Annu. Rev. Cell Dev. Bio.* **24**, 55–80 (2008).

27. 27.

Takahashi, K., Hayashi, K. & Kinoshita, T. Auxin activates the plasma membrane H⁺-ATPase by phosphorylation during hypocotyl elongation in *Arabidopsis*.

Plant Physiol. **159**, 632–641 (2012).

28. 28.

Dai, N., Wang, W., Patterson, S. E. & Bleecker, A. B. The TMK subfamily of receptor-like kinases in *Arabidopsis* display an essential role in growth and a reduced sensitivity to auxin. *PLoS ONE* **8**, e60990 (2013).

29. 29.

Falhof, J., Pedersen, J. T., Fuglsang, A. T. & Palmgren, M. Plasma membrane H⁺-ATPase regulation in the center of plant physiology. *Mol. Plant* **9**, 323–337 (2016).

30. 30.

Kinoshita, T. & Shimazaki, K. Blue light activates the plasma membrane H⁺-ATPase by phosphorylation of the C-terminus in stomatal guard cells. *EMBO J.* **18**, 5548–5558 (1999).

31. 31.

Kerkeb, L., Venema, K., Donaire, J. P. & Rodriguez-Rosales, M. P. Enhanced H⁺/ATP coupling ratio of H⁺-ATPase and increased 14-3-3 protein content in plasma membrane of tomato cells upon osmotic shock. *Physiol. Plant* **116**, 37–41 (2002).

32. 32.

Niittyla, T., Fuglsang, A. T., Palmgren, M. G., Frommer, W. B. & Schulze, W. X. Temporal analysis of sucrose-induced phosphorylation changes in plasma membrane proteins of *Arabidopsis*. *Mol. Cell. Proteomics* **6**, 1711–1726 (2007).

33. 33.

Han, J. & Burgess, K. Fluorescent indicators for intracellular pH. *Chem. Rev.* **110**, 2709–2728 (2010).

34. 34.

Merlot, S. et al. Constitutive activation of a plasma membrane H⁺-ATPase prevents abscisic acid-mediated stomatal closure. *EMBO J.* **26**, 3216–3226 (2007).

35. 35.

Fu, Y., Xu, T., Zhu, L., Wen, M. & Yang, Z. A ROP GTPase signaling pathway controls cortical microtubule ordering and cell expansion in *Arabidopsis*. *Curr. Biol.* **19**, 1827–1832 (2009).

36. 36.

Li, L. et al. Cell surface and intracellular auxin signalling for H⁺ fluxes in root growth. <https://doi.org/10.1038/s41586-021-04037-6> *Nature* (2021).

37. 37.

Ren, H., Park, M. Y., Spartz, A. K., Wong, J. H. & Gray, W. M. A subset of plasma membrane-localized PP2C.D phosphatases negatively regulate SAUR-mediated cell expansion in *Arabidopsis*. *PLoS Genet.* **14**, e1007455 (2018).

38. 38.

Spartz, A. K. et al. The SAUR19 subfamily of SMALL AUXIN UP RNA genes promote cell expansion. *Plant J.* **70**, 978–990 (2012).

39. 39.

Fendrych, M. et al. Rapid and reversible root growth inhibition by TIR1 auxin signalling. *Nat. Plants* **4**, 453–459 (2018).

40. 40.

Prigge, M. J. et al. Genetic analysis of the *Arabidopsis* TIR1/AFB auxin receptors reveals both overlapping and specialized functions. *eLife* **9**, <https://doi.org/10.7554/eLife.54740> (2020).

41. 41.

Chen, J. & Yang, Z. Novel ABP1-TMK auxin sensing system controls ROP GTPase-mediated interdigitated cell expansion in *Arabidopsis*. *Small GTPases* **5**, <https://doi.org/10.4161/sgtp.29711> (2014).

42. 42.

Marques-Bueno, M. M. et al. Auxin-regulated reversible inhibition of TMK1 signaling by MAKR2 modulates the dynamics of root gravitropism. *Curr. Biol.* **31**, 228–237 (2021).

43. 43.

Clough, S. J. & Bent, A. F. Floral dip: a simplified method for *Agrobacterium*-mediated transformation of *Arabidopsis thaliana*. *Plant J.* **16**, 735–743 (1998).

44. 44.

Hecker, A. et al. Binary 2in1 vectors improve in planta (co)localization and dynamic protein interaction studies. *Plant Physiol.* **168**, 776–787 (2015).

45. 45.

Hayashi, M., Inoue, S., Takahashi, K. & Kinoshita, T. Immunohistochemical detection of blue light-induced phosphorylation of the plasma membrane H⁺-ATPase in stomatal guard cells. *Plant Cell Physiol.* **52**, 1238–1248 (2011).

46. 46.

Hayashi, Y. et al. Biochemical characterization of in vitro phosphorylation and dephosphorylation of the plasma membrane H⁺-ATPase. *Plant Cell Physiol.* **51**, 1186–1196 (2010).

47. 47.

Thakur, J. K., Tyagi, A. K. & Khurana, J. P. *OsIAA1*, an Aux/IAA cDNA from rice, and changes in its expression as influenced by auxin and light. *DNA Res.* **8**, 193–203 (2001).

48. 48.

Tusher, V. G., Tibshirani, R. & Chu, G. Significance analysis of microarrays applied to the ionizing radiation response. *Proc Natl. Acad. Sci. USA* **98**, 5116–5121 (2001).

49. 49.

Yoo, S. D., Cho, Y. H. & Sheen, J. *Arabidopsis* mesophyll protoplasts: a versatile cell system for transient gene expression analysis. *Nature Protoc.* **2**, 1565–1572 (2007).

50. 50.

van Rheenen, J., Langeslag, M. & Jalink, K. Correcting confocal acquisition to optimize imaging of fluorescence resonance energy transfer by sensitized

emission. *Biophys. J.* **86**, 2517–2529 (2004).

Acknowledgements

We thank the members of the Yang laboratory for discussion and comments on this work; J. Leung (Department of Institute Jean-Pierre Bourgin, INRA) for *ost2-2D* seeds; K. Iba (Kyushu University) for 35S::GFP-AHA1 seeds; C. Grefen (University of Tubingen) for FRET analyses 2in1 binary vectors; and L. Shan (University of Texas A&M) for protoplast transient expression vectors. This work was in part supported by an NIH grant (GM100130) to Z.Y.; K.T. (20K06685) and T.K. (20H05687 and 20H05910) were funded by MEXT/JSPS KAKENHI. W.M.G. was funded by NIH (GM067203). H.Z. was funded by NIH (S10OD016400).

Author information

Affiliations

1. FAFU-UCR Joint Center for Horticultural Biology and Metabolomics, Haixia Institute of Science and Technology, Fujian Agriculture and Forestry University, Fuzhou, China

Wenwei Lin, Xiang Zhou, Wenxin Tang, Jiawei Dai, Xiaoyue Zhu, Tongda Xu & Zhenbiao Yang

2. Institute of Integrative Genome Biology and Department of Botany and Plant Science, University of California, Riverside, CA, USA

Wenwei Lin, Xiang Zhou, Xue Pan, Songqin Pan & Zhenbiao Yang

3. Graduate School of Science, Nagoya University, Nagoya, Japan

Koji Takahashi & Toshinori Kinoshita

4. Institute of Transformative Bio-Molecules, Nagoya University, Nagoya, Japan

Koji Takahashi & Toshinori Kinoshita

5. Department of Plant and Microbial Biology, University of Minnesota, St Paul, MN, USA

Hong Ren & William M. Gray

6. Biological Mass Spectrometry Facility, Robert Wood Johnson Medical School and Rutgers, the State University of New Jersey, Piscataway, NJ, USA

Haiyan Zheng

Contributions

W.L. and Z.Y. conceived the project and designed the experiments. W.L. conducted most of the experiments, with contributions from X.Z., W.T., K.T., X.P., J.D., H.R. and W.M.G.; W.L., S.P. and H.Z. conducted and analysed all the MS analyses of this paper; X.Z., J.D., X.P. and X.Y.Z. designed and conducted the FRET analyses. K.T. and T.K. conducted and analysed the ATPase activities. W.L., Z.Y. and W.M.G. wrote the manuscript with input from all of the other authors.

Corresponding author

Correspondence to [Zhenbiao Yang](#).

Ethics declarations

Competing interests

The authors declare no competing interests.

Additional information

Peer review information *Nature* thanks Malcolm Bennett and the other, anonymous, reviewer(s) for their contribution to the peer review of this work. Peer reviewer reports are available.

Publisher's note Springer Nature remains neutral with regard to jurisdictional claims in published maps and institutional affiliations.

Extended data figures and tables

[Extended Data Fig. 1 TMK interacts with AHAs in planta and in vitro.](#)

a, Summary of LC-MS/MS analysis of AHAs associated with TMK1-GFP. The number of unique AHA peptides identified in the immunoprecipitates from *pTMK1::TMK1-GFP* transgenic seedlings is shown. IP-MS did not identify any AHA

peptides from control *pTMK1::GFP* seedlings. **b**, TMK4 associates with AHA1 in transgenic plants. The membrane proteins from 4-week-old *35S::GFP* only and *35S::GFP-AHA1* plants were immunoprecipitated with α -GFP-Trap antibody and analysed with Western blots using an α -TMK4 antibody (Top). The expression of GFP-AHA1 and GFP control in transgenic plants is shown (Bottom). **c**, TMK1 associates with AHA2 in transgenic plants. Membrane proteins from 4-wk-old *35S::GFP* and *pTMK1::TMK1-GFP/tmk1-1/4-1* transgenic plants were immunoprecipitated with α -GFP-Trap antibody and analysed with Western blots using an α -AHA2 antibody (Top). The expression of TMK1-GFP and GFP control in transgenic plants is shown (Bottom). **d**, TMK1's cytoplasmic kinase domain (KD) interacts with AHA2's C-terminal domain *in vitro*. *E. coli*-expressed maltose-binding protein (MBP)-TMK1KD or MBP proteins were incubated with glutathione bead-bound glutathione-S-transferase (GST)-AHA2-C or GST (Pull-down:GST), and the beads were collected and washed for Western blotting of immunoprecipitated proteins with α -MBP antibody (left). The input GST-AHA2-C, MBP-TMK1KD, MBP, and GST proteins were detected by Coomassie brilliant blue staining (CBB). **e**, Representative confocal images of *Arabidopsis* protoplasts expressing TMK1-mCherry (FRET acceptor) and AHA1-GFP (FRET donor) used for FRET analysis. Shown are images collected before (-25 sec) and after ($+150$ sec) auxin treatment for three channels: Donor (excitation: 488 nm, emission: 498-551 nm), FRET (excitation: 488 nm, emission: 600-670) and acceptor (excitation: 561 nm, emission: 600-670 nm). These images are used for FRET efficiency analysis shown in Fig. 1e. To avoid autofluorescence from chlorophylls, only the PM region (dotted lines) away from chloroplasts was selected for FRET analysis. Scale bar, 10 μm . 3 independent analyses were conducted with similar results.

Extended Data Fig. 2 TMK1 and TMK4 impact the phosphorylation status of AHAs and the function of the PM H⁺-ATPase pump.

a, The phosphorylation status of AHAs was changed in the *tmk1-1 tmk4-1* (*tmk1/4*) mutant. The aerial part of 5-days auxin-depleted seedlings was used to prepare membrane proteins for TMT (Tandem mass tag) labelling and mass spectrometry quantification as described in Method. Mass spectrometry analysis showed that the abundance of the peptides containing phosphorylated penultimate threonine from AHA2, AHA3, and AHA7 was significantly decreased in *tmk1-1 tmk4-1* (*tmk1/4*) mutant relative to wild type. Values are means; $n = 2$. **b**, Summary of phosphorylated peptides mass spectrometry information. The C-terminal peptides of AHA1, AHA2, AHA3, AHA7, and AHA11 containing phosphorylated penultimate threonine were identified from mass spectrometry analysis. **c-e**, High-resolution fragmentation spectra of AHA2 (**c**), AHA3(**d**), and AHA11(**e**) C-terminal peptides containing phosphorylated penultimate threonine are presented. **f**, The *tmk1-1 tmk4-1*(*tmk1/4*) mutant is insensitive to auxin inducing AHA phosphorylation but remains sensitive to

fusicoccin. The endogenous auxin-depleted aerial sections of seedlings were incubated with 100 nM IAA for 10 min or 10 µm fusicoccin (FC) for 5 min, respectively. The amounts of AHA proteins and the phosphorylation status of the penultimate Thr in the C terminus were determined by immunoblot analysis with anti-AHA (H^+ -ATPase) and anti-pThr-947 (pThr 947) antibodies, respectively. **g**, Quantification of the phosphorylation level of the H^+ -ATPase. Values are means \pm SD; n = 3 independent biological replicates, * P \leq 0.05; ns, no significant, results of two way ANOVA test. **h**, Fragmentation spectra of peptides containing phosphorylated penultimate threonine of AHA1-C16 synthetical peptide (pT948 of AHA1) (see Fig. 2e). **i**, Auxin induction of H^+ -ATPase activity in the aerial parts of wild type, the *tmk1-1*, and *tmk4-1* mutant. Aerial sections of 14-days old seedlings were treated with 10 µm IAA for 30 min and used for vanadate-sensitive ATP hydrolysis assay by determining the inorganic phosphate released from ATP as described previously²⁷. The values shown are relative ATP hydrolytic activity of indicated samples to that of control Col-0 without auxin treatment. Values are means \pm SD; n = 3. * P \leq 0.05; ns, not significant. The results were analysed by a two-way ANOVA test. **j**, Lithium tolerance in the *tmk1-1 tmk4-1* (*tmk1/4*) mutant. Wild type (Col-0) and *tmk1-1 tmk4-1* (*tmk1/4*) mutant seedlings were grown on 1/2 MS medium with or without 18 mM LiCl for 5 days. LiCl treatment caused severe seedling growth retardation and severe chlorosis of the aerial parts in Col-0, whereas the *tmk1-1 tmk4-1* (*tmk1/4*) mutant was tolerant to LiCl, especially in the aerial parts. **k**, The root length of the seedlings was measured by ImageJ. Values are means \pm SD, n = 8. The number above the columns indicates the percentage of root growth inhibition induced by LiCl.

[Source data](#).

Extended Data Fig. 3 TMK1 and TMK4 regulate apoplastic pH and hypocotyl elongation.

a, TMK1 (*pTMK1::TMK1-GFP*) restored the apoplastic pH changes in the *tmk1-1 tmk4-1* (*tmk1/4*) mutant. Comparison of the apoplastic pH in WT, the *tmk1-1 tmk4-1* mutant, and the *tmk1-1 tmk4-1/TMK1-GFP* (*tmk1/4/TMK1*) complemented line. Visualized by HPTS staining (**a**). Y-Axis: the mean 458/405 values of the *tmk1-1 tmk4-1* mutant and the *TMK1* complemented line relative to wild type (**b**). 3 independent assays were conducted with similar results. **c**, Epidermal cell lengths of hypocotyls from two days-old etiolated seedlings were measured using Image J. Hypocotyl epidermal cells in the 100-500 µM region after apical hook were measured. n = 41, 52, and 53 for Col-0, *tmk1/4* and *tmk1/4/TMK1*. The results were analysed by one Way ANOVA tests in b, c. *** P \leq 0.0001. **d** and **e**, The *tmk1-1 tmk4-1* mutant showed a defect in hypocotyl elongation (**c**). Hypocotyl lengths of 3 days-old etiolated seedlings were measured by Image J (**d**). n = 21, 11, and 14 for Col-0, *ost2-2D*, and

tmk1/4, respectively. The results were analysed by one-way ANOVA tests in b, c, e. Scale bar = 100 µM (a), or 1 cm (d). * * P ≤ 0.01, ** *** P ≤ 0.0001; ns, not significant

[Source data.](#)

Extended Data. Fig. 4 Acidic environments and activation of the PM H⁺-ATPase pump partially restored hypocotyl elongation defect in *tmk1-1 tmk4-1*.

a and b, Low pH in the medium was able to partially restore the *tmk1-1 tmk4-1* (*tmk1/4*) defect in hypocotyl elongation. Seedlings were grown on 1/2 MS medium with indicated pH (a), and hypocotyl lengths were measured by ImageJ (b). The box plot centre lines represent median; box limits indicate the 25th and 75th percentiles; and whisker extend 1.5xIQR from the 25th and 75th percentiles (n = 15 hypocotyls per line). c and d, *ost2-2D* mutation partially restored the hypocotyl elongation defect of *tmk1-1 tmk4-1* mutant. Seedlings were grown on a 1/2 MS medium for 4 days, and hypocotyl lengths were measured by ImageJ. The box plot centre lines represent median; box limits indicate the 25th and 75th percentiles; and whisker extend 1.5xIQR from the 25th and 75th percentiles (n = 36 for Col-0, n = 24 for *tmk1/4* and n = 21 for *ost2-2D/tmk1/4*). Results were analysed by one-way ANOVA tests in b, d. Scale bar = 10 mm. * * p ≤ 0.01, ** *** p ≤ 0.0001

[Source data.](#)

Supplementary information

Supplementary Information

Supplementary Tables 2–4 and Supplementary Figs. 1 and 2.

Reporting Summary

Peer Review File

Supplemental Table1

List of primers used in this study.

Supplemental Table2

List of TMK1-GFP candidate interactors found in IP-mass spectrometry.

Source data

[Source Data Fig. 1](#)

[Source Data Fig. 2](#)

[Source Data Fig. 3](#)

[Source Data Fig. 4](#)

[Source Data Extended Data Fig. 2](#)

[Source Data Extended Data Fig. 3](#)

[Source Data Extended Data Fig. 4](#)

Rights and permissions

Open Access This article is licensed under a Creative Commons Attribution 4.0 International License, which permits use, sharing, adaptation, distribution and reproduction in any medium or format, as long as you give appropriate credit to the original author(s) and the source, provide a link to the Creative Commons license, and indicate if changes were made. The images or other third party material in this article are included in the article's Creative Commons license, unless indicated otherwise in a credit line to the material. If material is not included in the article's Creative Commons license and your intended use is not permitted by statutory regulation or exceeds the permitted use, you will need to obtain permission directly from the copyright holder. To view a copy of this license, visit <http://creativecommons.org/licenses/by/4.0/>.

[Reprints and Permissions](#)

About this article

Cite this article

Lin, W., Zhou, X., Tang, W. *et al.* TMK-based cell-surface auxin signalling activates cell-wall acidification. *Nature* **599**, 278–282 (2021). <https://doi.org/10.1038/s41586-021-03976-4>

- Received: 03 February 2021
- Accepted: 31 August 2021
- Published: 27 October 2021
- Issue Date: 11 November 2021
- DOI: <https://doi.org/10.1038/s41586-021-03976-4>

Share this article

Anyone you share the following link with will be able to read this content:

[Get shareable link](#)

Sorry, a shareable link is not currently available for this article.

[Copy to clipboard](#)

Provided by the Springer Nature SharedIt content-sharing initiative

This article was downloaded by **calibre** from <https://www.nature.com/articles/s41586-021-03976-4>

| [Section menu](#) | [Main menu](#) |

- Article
- [Published: 13 September 2021](#)

Virus-induced senescence is a driver and therapeutic target in COVID-19

- [Soyoung Lee](#) ORCID: orcid.org/0000-0002-4614-2931^{1,2,3,nal},
- [Yong Yu](#)^{4,nal},
- [Jakob Trimpert](#) ORCID: orcid.org/0000-0003-1616-0810⁵,
- [Fahad Benthani](#) ORCID: orcid.org/0000-0002-3283-307X⁴,
- [Mario Mairhofer](#)⁴,
- [Paulina Richter-Pechanska](#)¹,
- [Emanuel Wyler](#) ORCID: orcid.org/0000-0002-9884-1806²,
- [Dimitri Belenki](#) ORCID: orcid.org/0000-0002-9004-9849^{1,2},
- [Sabine Kaltenbrunner](#)⁴,
- [Maria Pammer](#)⁴,
- [Lea Kausche](#)^{1,6},
- [Theresa C. Firsching](#) ORCID: orcid.org/0000-0003-1378-4951⁷,
- [Kristina Dietert](#)^{7,8},
- [Michael Schotsaert](#) ORCID: orcid.org/0000-0003-3156-3132^{9,10},
- [Carles Martínez-Romero](#) ORCID: orcid.org/0000-0001-8888-7715^{9,10},
- [Gagandeep Singh](#) ORCID: orcid.org/0000-0003-3260-2631^{9,10},
- [Séverine Kunz](#) ORCID: orcid.org/0000-0002-0131-3506²,
- [Daniela Niemeyer](#) ORCID: orcid.org/0000-0002-1897-6365¹¹,
- [Riad Ghanem](#)⁶,
- [Helmut J. F. Salzer](#)¹²,
- [Christian Paar](#)¹³,
- [Michael Mülleder](#)¹⁴,
- [Melissa Uccellini](#)^{9,10 nAff28},
- [Edward G. Michaelis](#)¹⁵,
- [Amjad Khan](#)¹⁶,
- [Andrea Lau](#)¹,
- [Martin Schönlein](#)^{1,17},
- [Anna Habringer](#)¹³,
- [Josef Tomasits](#)¹³,

- [Julia M. Adler](#)⁵,
- [Susanne Kimeswenger](#) ORCID: [orcid.org/0000-0002-0443-8558](#)⁴,
- [Achim D. Gruber](#) ORCID: [orcid.org/0000-0002-4502-0393](#)⁷,
- [Wolfram Hoetzenegger](#)^{4,18},
- [Herta Steinkellner](#)¹⁹,
- [Bettina Purfürst](#)²,
- [Reinhard Motz](#)²⁰,
- [Francesco Di Pierro](#)^{21,22},
- [Bernd Lamprecht](#) ORCID: [orcid.org/0000-0003-3365-3449](#)^{4,12},
- [Nikolaus Osterrieder](#)^{5,23},
- [Markus Landthaler](#) ORCID: [orcid.org/0000-0002-1075-8734](#)²,
- [Christian Drosten](#) ORCID: [orcid.org/0000-0001-7923-0519](#)¹¹,
- [Adolfo García-Sastre](#) ORCID: [orcid.org/0000-0002-6551-1827](#)^{9,10,24,25},
- [Rupert Langer](#)^{4,20},
- [Markus Ralser](#)^{14,26},
- [Roland Eils](#) ORCID: [orcid.org/0000-0002-0034-4036](#)²⁷,
- [Maurice Reimann](#)¹,
- [Dorothy N. Y. Fan](#)^{1,3} &
- [Clemens A. Schmitt](#) ORCID: [orcid.org/0000-0002-4731-2226](#)^{1,2,3,4,6}

Nature volume **599**, pages 283–289 (2021)

- 46k Accesses
- 4 Citations
- 588 Altmetric
- [Metrics details](#)

Subjects

- [Experimental models of disease](#)
- [Mechanisms of disease](#)
- [SARS-CoV-2](#)
- [Senescence](#)
- [Virus–host interactions](#)

Abstract

Derailed cytokine and immune cell networks account for the organ damage and the clinical severity of COVID-19 (refs. [1,2,3,4](#)). Here we show that SARS-CoV-2, like other viruses, evokes cellular senescence as a primary stress response in infected cells. Virus-induced senescence (VIS) is indistinguishable from other forms of cellular senescence and is accompanied by a senescence-associated secretory phenotype (SASP), which comprises pro-inflammatory cytokines, extracellular-matrix-active factors and pro-coagulatory mediators^{[5,6,7](#)}. Patients with COVID-19 displayed markers of senescence in their airway mucosa *in situ* and increased serum levels of SASP factors. In vitro assays demonstrated macrophage activation with SASP-reminiscent secretion, complement lysis and SASP-amplifying secondary senescence of endothelial cells, which mirrored hallmark features of COVID-19 such as macrophage and neutrophil infiltration, endothelial damage and widespread thrombosis in affected lung tissue^{[1,8,9](#)}. Moreover, supernatant from VIS cells, including SARS-CoV-2-induced senescence, induced neutrophil extracellular trap formation and activation of platelets and the clotting cascade. Senolytics such as navitoclax and a combination of dasatinib plus quercetin selectively eliminated VIS cells, mitigated COVID-19-reminiscent lung disease and reduced inflammation in SARS-CoV-2-infected hamsters and mice. Our findings mark VIS as a pathogenic trigger of COVID-19-related cytokine escalation and organ damage, and suggest that senolytic targeting of virus-infected cells is a treatment option against SARS-CoV-2 and perhaps other viral infections.

[Download PDF](#)

Main

The causative agent of the COVID-19 pandemic, the human pathogenic coronavirus SARS-CoV-2, causes upper respiratory infections and subsequently lung disease that may become further complicated by septic multiorgan failure and is associated with increased mortality^{[10,11](#)}. Escalating immune activation with massive cytokine release seems to drive severe COVID-19 disease^{[1,2,3](#)}, possibly more than the virus infection itself. Mechanisms of viral entry—primarily through the interaction of the SARS-CoV-2 spike (S) protein with the host cell receptor angiotensin-converting enzyme 2 (ACE2)—and consecutive steps of RNA replication, virus assembly and budding represent therapeutic targets^{[12,13](#)}. Anti-inflammatory drugs are clinically being used or currently being tested; however, they have led to mixed results^{[14,15](#)}. Therefore, more comprehensive and specific measures to control the cytokine storm are needed.

Viral entry reflects a major cellular insult and induces marked biological changes in infected host cells that potentially lead to cellular senescence as a virus-triggered state switch^{[16,17](#)}. This can have a disparate impact on virus propagation^{[18,19](#)}. Senescence is

also acutely stress-induced by activated oncogenes (termed oncogene-induced senescence (OIS)) or by DNA-damaging cancer therapy, and physiologically occurs in embryonic development, wound healing and ageing⁶. Little is known about systemic ramifications of cellular senescence as an antiviral host defence. We hypothesize here that cellular senescence and its SASP, which is largely composed of pro-inflammatory cytokines, matrix-degrading proteases and pro-coagulatory factors^{5,6,7}, underlie the cytokine storm, macrophage activation, the formation of neutrophil extracellular traps (NETs), endothelialitis and widespread pulmonary thrombosis frequently observed in patients with COVID-19 (refs. ^{1,8,9}).

Properties of VIS

We first tested signs of senescence in human diploid fibroblast (HDF) models exposed to high-titre retrovirus. At day 5 after infection, most of the cells presented with characteristics typical of senescence. The cells had flattened, enlarged morphology and were stained positive in the senescence-associated β -galactosidase (SA- β -gal) assay²⁰. They also exhibited 4',6-diamidino-2-phenylindole (DAPI)-dense chromatin reminiscent of senescence-associated heterochromatin foci (SAHF)²¹ and overexpressed p16^{INK4A}, which is an inhibitor of cyclin-dependent kinase 4 (CDK4) and CDK6, in the nucleus (Fig. ^{1a}, Extended Data Fig. ^{1a}). Gene set enrichment analysis (GSEA) of HDF RNA sequencing (RNA-seq) datasets showed that senescence- and SASP-related Gene Ontology terms were skewed towards the VIS state and overlapped with the OIS state of the same cells in Ras-induced senescence (Fig. ^{1b}). GSEA also retrieved host responses to viral infection in OIS, which further underlines the overarching role of a senescent stress response in this context (Extended Data Fig. ^{1b}). Specific analyses of VIS-associated expression changes by quantitative PCR with reverse transcription (RT-qPCR) showed transcriptional changes typical of senescence in VIS cells^{21,22} (Fig. ^{1c}, Extended Data Fig. ^{1c}). Notably, lower virus titres did not induce senescent cell cycle arrest, which is the goal in retrovirus- or lentivirus-assisted gene transfer experiments (Extended Data Fig. ^{1d}). Multiplex protein analysis showed that VIS cells secreted a plethora of SASP factors, many of which are bona fide NF- κ B targets^{23,24} (Fig. ^{1d}). Importantly, these responses depended on gene activities that are essential in senescence. For example, HDFs expressing the H3K9me3-active demethylase JMJD2C or engineered with a small hairpin RNA (shRNA) to stably knockdown *p53* (also known as *TP53*) to genetically disable OIS^{22,25}, and mouse embryo fibroblasts without intact *p53* alleles failed to enter VIS and lacked senescence-typical changes, as assessed using RT-qPCR and multiplex secretome analyses (Fig. ^{1e}, Extended Data Fig. ^{1e-g}). After viral infection, only VIS-capable cells showed activation of the cGAS-STING pathway (Extended Data Fig. ^{1h}), which is a cytoplasmic DNA sensor driving SASP-mediated interferon responses²⁶. Notably, blocking retroviral replication using the reverse transcriptase

inhibitor azidothymidine prevented VIS and blunted cGAS–STING pathway activation (Extended Data Fig. 1*i,j*). cGAS–STING-mediated phospho-activation of the interferon regulatory factor IRF3 (ref. 27), the NF- κ B transcription factor p65 (ref. 28) and other nuclear senescence markers, such as p21^{CIP1} and heterochromatin-associated H3K9me3, were strongly increased in VIS cells. Conversely, non-G1-phase-hyperphosphorylated retinoblastoma (Rb) protein was markedly decreased in these cells (Fig. 1*f*). Hence, viral infection induces a host cell response reminiscent of and genetically dependent on key features of other well-established types of cellular senescence and their associated secretome.

Fig. 1: Senescence is a universal host cell response to viral stress.

 [figure1](#)

a, SA- β -gal, SAHF formation by DAPI and p16^{INK4A} staining of IMR90 cells 5 days after retroviral infection or mock control. **b**, GSEA probing senescence-associated genes in WI38 HDFs in VIS and OIS. A positive normalized enrichment score (NES) indicates enrichment compared to proliferating counterparts. Presented NES are significant (false discovery rate (FDR) $q < 0.05$; see [Supplementary Information](#) for individual values). **c**, Relative expression levels of core senescence and SASP transcripts in cells as in **a** by RT–qPCR compared to mock control. **d**, Multiplex bead-based protein analysis in the supernatant of HDF IMR90 (as in **a**), WI38 and Tig3 cells. MIP-1 α is also known as CCL3; MIP-1 β is also known as CCL4. **e**, SA- β -gal staining of IMR90 cells expressing JMJD2C, *p53* shRNA (*shp53*) or control vector. **f**, Immunoblot analysis of nuclear senescence markers in samples as in **d** (α -tubulin was used as a loading control). **g**, Quantification of SA- β -gal positivity in human cell lines (RPE1, A549) infected with AAV, lentivirus, HCoV-NL63 or VSV. **h**, Quantification of SA- β -gal positivity in human cell lines and primary HNEpC cells infected with VSV- Δ G*-CoV-S, VSV- Δ G*-CoV-2-S or VSV- Δ G*/empty vector (VSV- Δ G*-emp). NIH3T3 cells were used as ACE2-negative, infection-resistant controls. **i**, SA- β -gal staining of stable hACE2-engineered primary nasal epithelial cells (HNEpC-hACE2) infected with SARS-CoV-2 and treated as indicated at 48 h after infection. GS, GS-441425; UT, untreated. **j**, Relative expression levels of the indicated transcripts by

RT-qPCR of cells as in **i**, **k**, GSEA of RNA-seq-based GEP from AECs infected with SARS-CoV-2 compared with uninfected controls ($n = 4$). Preselected senescence-associated terms with FDR $q \leq 0.01$ are shown (see [Supplementary Information](#) for individual values). Scale bars, 100 μm (**a**, **e**) or 5 μm (SAHF row in **a**). All quantifications in this figure refer to the mean \pm s.d. of $n = 3$ independent experiments (except **k**) with individual values as dots in bar plots or representative photomicrographs shown.

Notably, VIS became detectable in response to a broad spectrum of viruses, including lentivirus, adeno-associated virus (AAV), vesicular stomatitis virus (VSV) and the low-pathogenic human alphacoronavirus NL63 (HCoV-NL63) in human lung carcinoma cells and in non-malignant epithelial cells (Fig. [1g](#), Extended Data Fig. [2a](#); see Extended Data Fig. [2b-d](#) for human primary bronchial HBEpC and nasal HNEpC epithelial cells, and the relationship between multiplicity of infection (MOI) and SA- β -gal). To closely mimic SARS-CoV-2 infection, we exposed ACE2-expressing HNEpC cells to SARS-CoV spike-protein-pseudotyped VSV glycoprotein G-deletion mutants (VSV- Δ G*/CoV-S and VSV- Δ G*/CoV-2-S). These pseudotypes all induced senescence in the cells in a spike-protein-dependent manner, as ACE2-negative NIH3T3 cells^{[29](#)} did not show senescence (Fig. [1h](#), Extended Data Fig. [2e](#)). Retrovirus- and VSV-induced senescent cells exhibited increased levels of reactive oxygen species (ROS) and γ -H2AX DNA damage foci (Extended Data Fig. [2f](#)). Conversely, the ROS scavenger *N*-acetylcysteine reduced γ -H2AX foci and abrogated VIS. Similarly, GS-441524, the active metabolite of the viral RNA polymerase inhibitor remdesivir, reduced γ -H2AX foci and blunted cGAS-STING pathway activation in VSV-infected cells (Extended Data Fig. [2g,h](#)).

Importantly, HNEpC cells infected with the authentic SARS-CoV-2 virus also displayed SASP-positive senescence that was prevented by *p53*-shRNA-mediated inhibition of senescence or by GS-441524 treatment (Fig. [1i,j](#), Extended Data Fig. [2i,j](#)). Moreover, RNA-seq analysis of SARS-CoV-2-infected alveolar epithelial cells (AECs) and publicly available RNA-seq datasets of normal human bronchus epithelial (NHBE) cells and lung cancer cell lines^{[4](#)} demonstrated that they also show robust signs of senescence induction (Fig. [1k](#), Extended Data Fig. [2k](#)). Thus, virus infection in general and SARS-CoV-2 infection of respiratory epithelial cells in particular induce full-featured cellular senescence, which underscores our hypothesis that VIS might play a critical pathogenic part in COVID-19 lung disease.

Cellular senescence in patients with COVID-19

Next, we asked whether VIS would be a typical feature detectable in patients infected with SARS-CoV-2. We specifically analysed nasopharyngeal and lung tissue specimens from patients with a fatal course of PCR-proven COVID-19.

Immunohistochemical analysis (IHA) of the senescence markers lipofuscin, p16^{INK4A}, p21^{CIP1} and H3K9me3, and interleukin-8 (IL-8; encoded by *CXCL8*) as a representative SASP marker, showed robust reactivity in samples from infected individuals with or without remaining SARS-CoV-2 RNA *in situ* but not in individuals without COVID-19 (Fig. 2a, Extended Data Fig. 3a). Single-cell RNA-seq (scRNA-seq) analyses of upper airway mucosa samples provided further evidence of a senescence switch in patients with COVID-19 (ref. 30). The nasopharyngeal specimens showed increased transcript levels of p16^{INK4A} (encoded by *CDKN2A*) and multiple SASP factors not only in SARS-CoV-2-permissive ciliated respiratory epithelial cells but also in macrophages, which implies that paracrine senescence spread to SASP-attracted macrophages and to other less virus-susceptible p16^{INK4A}-elevated mucosal epithelial cell types (Fig. 2b). Gene expression profiling (GEP) of upper and lower airway specimens showed SASP-reminiscent cytokines in COVID-19 specimens induced at the transcript level (Fig. 2c). scRNA-seq data further showed that predominantly ciliated epithelial cells and macrophages scored positive for p16^{INK4A} transcripts (Extended Data Fig. 3b).

Fig. 2: Patients with COVID-19 exhibit features of VIS.

 figure2

a, IHA of senescence markers and BCL-w, and *in situ* hybridization of SARS-CoV-2 RNA in the respiratory mucosa of nasopharyngeal specimens from patients with COVID-19 ($n = 6$ for p16^{INK4A} and IL-8, otherwise $n = 5$) compared with individuals without COVID-19 (non-COVID-19; $n = 2$). Quantification of affected areas is presented as the mean percentage of positive cells \pm s.d. or the mean percentage of positive area \pm s.d. (lipofuscin only). **b**, scRNA-seq-based GEP of upper airway tissue from patients with COVID-19 ($n = 19$) and healthy donors ($n = 5$). Colour-coded average-scaled (z scores) expression levels of the respective transcripts and cell types are shown. nrMa, non-residential macrophage; rMA, residential macrophage. **c**, GEP of SASP-reminiscent cytokines in upper (nasopharynx) and lower airway (lung) tissue from autopsy samples from patients with COVID-19 compared with individuals without COVID-19 ($n = 3$ each) by oligonucleotide-based transcript hybridization. **d**, CD86 IHA of macrophages in lung specimens from patients with COVID-19 ($n = 13$)

compared with individuals without COVID-19 ($n = 6$). Mean number of positive non-epithelial cells in $0.1 \text{ mm}^2 \pm \text{s.d.}$, $P = 0.0005$. **e**, Multiplex bead-based protein analysis of serum samples from patients with COVID-19 ($n = 32$) and healthy donors ($n = 8$). **f**, Mass spectrometry-based proteomics analysis of serum from patients with COVID-19 ($n = 26$) and from healthy donors (serum $n = 3$ and plasma $n = 11$). Heatmaps in **e** and **f** present scaled (z scores) protein intensities. **g**, Three-dimensional plot showing serum levels of D-dimer (clotting activity), SERPINA3 (coagulation-related SASP factor) and IL-6 (pro-inflammatory SASP factor) correlated to clinical COVID-19 severity per World Health Organization grades (g3–g6). $n = 133$ patients. The size of the sphere is proportional to the population size. Scale bars, $50 \mu\text{m}$ (**a, d**).

Key components of severe COVID-19 are a cytokine storm and macrophage activation syndrome³. We reasoned that the SASP of senescent upper airway epithelial cells may attract and activate macrophages through paracrine senescence induction³¹. This then contributes to the escalation of macrophage activation syndrome, a condition in which macrophages subsequently infiltrate the lungs. Notably, lungs of patients with COVID-19 showed infiltration by pro-inflammatory CD86⁺ macrophages and an M1-macrophage polarization profile^{32,33} (Fig. 2d, Extended Data Fig. 3c). In serum samples taken from patients with COVID-19, SASP peptides such as IL-8, PAI-1 (also known as serpin E1), CCL2 (also known as MCP-1), MMP-1, MMP-9 and TIMP-1 were among the most strongly upregulated factors (Fig. 2e). Selective scanning for clotting-relevant factors by ultrahigh-throughput mass-spectrometry-based proteomics³⁴ also showed that these factors were induced to a large degree in COVID-19 serum probes (Fig. 2f). This result is in line with the transcriptional skewing of the Gene Ontology terms ‘coagulation’ and ‘complement’ in SARS-CoV-2-infected NHBE cells and in retrovirally senescent and even OIS or irradiation-senescent HDF cells⁷ (Extended Data Figs. 1b, 2k). Further underscoring the pro-thrombogenic propensity in patients with COVID-19, we detected elevated CD62⁺-marked platelet activation in their blood samples (Extended Data Fig. 3d). Accordingly, clinically more severe cases of COVID-19 exhibited a tight association of high SASP serum levels, clotting-relevant factors and activated coagulation³⁵ (Fig. 2g, Extended Data Fig. 3e, f). There was also a close correlation between senescence marker transcripts and microthrombosis in lungs affected by COVID-19 *in situ* (Extended Data Fig. 3g, h). Thus, the findings from samples of patients with COVID-19 revealed alterations consistent with VIS and its SASP in the upper airway epithelia. Moreover, the results suggest that SASP-mediated effects are critical contributors to the respective lung disease and associated pro-inflammatory, tissue-damaging and pro-thrombogenic features.

Linking COVID-19 features to VIS

Next, we mechanistically interrogated whether supernatant from VIS cells (SN_{VIS}) might induce COVID-19-typical functionalities in critical target cell types. Indeed, human THP-1 macrophages turned into a CD86^+ or CD13^+ M1-like state³² when incubated with SN_{VIS} , but not supernatant from non-infected proliferating cells ($\text{SN}_{\text{prol.}}$) or genetically senescence-incapable virus-infected HDFs (Fig. 3a, Extended Data Fig. 4a). The HDFs exhibited a strong SASP-reminiscent secretory profile, which is indicative of paracrine senescence, as only replication-incompetent viruses were used here (Fig. 3b, Extended Data Fig. 4b). Notably, transcripts reminiscent of SN_{VIS} -induced CD86^+ -associated THP1 were similarly detected in lungs of patients with COVID-19 (Fig. 3c). Indeed, SN_{VIS} exposure enforced paracrine, SA- β -gal-positive senescence in macrophages (Fig. 3d), which is all in line with their contribution as a VIS-triggered SASP-amplifying cellular messenger in COVID-19. Underscoring the critical role of an altered endothelium as a cytokine-releasing relay³⁶, SN_{VIS} also induced paracrine senescence in HUVEC human endothelial cells, which—in turn—launched a pro-inflammatory and pro-thrombogenic SASP (Fig. 3e, Extended Data Fig. 4c). Consistent with the microangiopathic thrombosis observed in severely affected lungs of patients with COVID-19, transfer of SN_{VIS} , but not $\text{SN}_{\text{prol.}}$ or supernatant from virus-infected senescence-incapable HDFs, prompted platelet activation³⁷ (Fig. 3f), accelerated clotting time (Fig. 3g) and provoked NET formation in vitro⁹ (Fig. 3h). Moreover, we observed enhanced formation of the C5b–C9 membrane attack complex and its ultimate cytotoxic action on HUVEC cells in response to SN_{VIS} -activated human serum (Fig. 3i, j). This result mirrored the strongly elevated complement-activating factors in samples from patients with COVID-19. In essence, the pathogenesis of COVID-19 lung disease appears to be closely linked to senescence-governed immune escalation and pro-thrombotic effects.

Fig. 3: The VIS-associated secretome drives key immune-thrombotic components of COVID-19.

 **figure3**

a, The percentage of CD86⁺ cells in the THP-1 macrophage population exposed to supernatant from retroviral VIS compared with proliferating (Prol.) HDF IMR90 (as in Fig. 1a) and WI38 (as in Extended Data Fig. 1a) (left). Same experiment but using the supernatant of senescence-incapable IMR90 cells after mock or virus infection, as in Fig. 1e (right). **b**, Multiplex bead-based protein analysis of the supernatant of THP-1 exposed to supernatant as in **a**. SN_{VIS} without THP-1 cells is shown on the right. **c**, GEP of M1-macrophage polarization-related transcripts by RNA-seq of THP-1 cells exposed to SN_{prol.} or SN_{VIS} and sorted for CD86 positivity ($n = 2$ each, left) and by oligonucleotide-based transcript hybridization of lung tissue from autopsy samples of patients with COVID-19 compared with individuals without COVID-19 ($n = 3$ each, right). **d**, SA-β-gal staining (top) and the CD86⁺ fraction (bottom) of THP-1 cells exposed to the supernatant of RPE1-infected VSV-ΔG* variants as indicated. **e**, SA-β-

gal staining (top) and transcript expression by RT–qPCR (bottom) of HUVEC endothelial cells incubated with the supernatant of IMR90 cells. **f**, Platelet activation measured by ADP release from healthy donor platelets incubated with the supernatant of IMR90 cells as in **a**. $n = 5$ donors. **g**, Clotting time in whole-blood samples ($n = 4$ healthy donors) mixed with the indicated supernatant volumes (WI38, as in **b**). INTEM captures intrinsic, platelet-dependent clotting, whereas EXTEM captures extrinsic, non-platelet-dependent clotting. **h**, NET formation after exposing neutrophils to supernatant from HDFs as in **b**. $n = 4$ healthy donors, two measurements each. MPO, myeloperoxidase. **i**, Quantification of the cytolytic complement complex C5b–C9 on HUVEC cells incubated with human serum and supernatant as indicated. ina, inactivated. **j**, Cytotoxicity assay of HUVEC cells as in **i**. All quantifications (mean \pm s.d. with individual values as dots) and representative photomicrographs are from $n = 3$ independent experiments unless otherwise noted. $*P < 0.05$ by unpaired two-tailed *t*-test (**a, f, h–j**), unpaired one-tailed *t*-test (**d**) or paired two-tailed *t*-test (**g**). Scale bars, 100 μ m.

Eliminating VIS cells using senolytic drugs

On the basis of these findings, we considered VIS cells as a central therapeutic target in SARS-CoV-2 infection, and the early elimination of these cells might mitigate the course of disease. Previously, we and others presented evidence that senolysis (that is, the selective depletion of senescent cells) by drugs such as baflomycin, ABT-263 (a BCL-2 family inhibitor; also known as navitoclax) or fisetin and quercetin (flavonoids that inhibit multiple kinases, with the latter typically in combination with the tyrosine kinase inhibitor dasatinib), reduced undesirable local and system-wide effects that persistent senescent cells might otherwise exert^{38,39,40,41,42}. We first profiled transcript and protein expression of anti-apoptotic BCL-2 family members in VIS cells and found that BCL-xL (encoded by *BCL2L1*), BCL-w (encoded by *BCL2L2*) and MCL-1 (encoded by *BCL2L3*) were induced (Fig. 4a, Extended Data Fig. 5a; see also Fig. 2a, Extended Data Fig. 3a,b for elevated *BCL2L1* and *BCL2L2* expression in patients with COVID-19). This result suggests that navitoclax can selectively kill VIS cells. We also found that the PI3K–AKT–p70S6K axis, p38MAPK and the tyrosine kinase SRC were deregulated in VIS; therefore these serve as potential targets, especially for fisetin and for the combination of quercetin plus dasatinib (D/Q), according to predicted protein–chemical interactions^{43,44,45} (Fig. 4a, Extended Data Fig. 5b). Indeed, navitoclax, fisetin and D/Q were selectively cytotoxic in retrovirus-driven and VSV-driven VIS cells, but not in equally infected senescence-incapable HDFs *in vitro* (Fig. 4b, Extended Data Fig. 5c–e). By contrast, the BCL-2-specific venetoclax (also known as ABT-199) did not have these effects in the VIS cells. After senolysis, the release of infectious virions is a potential concern; however, we did not find enhanced infectivity after lysis of VIS cells (Extended Data Fig. 5f,g).

Fig. 4: VIS cells are sensitive to senolytic targeting.

 figure4

a, Immunoblots of BCL-2 family members (left) and kinases (right) in HDF lysates as indicated (α -tubulin was used as a loading control). **b**, The relative viability of IMR90 cells, as in Fig. 1e, 48 h after treatment with senolytics as indicated or with solvent-only (dimethyl sulfoxide (DMSO)). **c**, Viability of HNEpC-hACE2 cells infected with SARS-CoV-2 or mock, and treated with senolytics as indicated for **c–f**. **d**, The relative change of the CD86⁺ fraction in the THP-1 cell population after receiving supernatant from HNEpC-hACE2 cells as in **c**. Of note, supernatant transfer experiments were carried out in the presence of SARS-CoV-2-neutralizing anti-spike antibodies, which prevented the transmission of infection (as evidenced by negative target cell SARS-CoV-2 PCR, data not shown). **e**, Quantification of SA- β -gal staining of HUVEC endothelial cells after receiving supernatant from HNEpC-hACE2 cells as in **d**. **f**, Quantification of C5b–C9 on HUVEC cells exposed to human serum with supernatant from HNEpC-hACE2 cells as in **d**. All bar plots in this figure show the mean \pm s.d. of $n = 3$ independent experiments with individual values as dots. * $P < 0.05$ by unpaired two-tailed *t*-test.

Importantly, infection by the authentic SARS-CoV-2 virus rendered HNEpC cells susceptible to navitoclax, fisetin and D/Q (Fig. 4c). Moreover, as seen above with other viruses, supernatant transfer from SARS-CoV-2-infected cells expanded CD86⁺ THP-1 macrophages and led to paracrine senescence or complement-mediated lysis of HUVEC cells. These effects were not observed when supernatants of epithelial cells pretreated with *p53* shRNA or GS-441524 or exposed to any of the three senolytic treatment options were used for transfer (Fig. 4d–f, Extended Data Fig. 5h; see Extended Data Fig. 5i–l for VIS, SASP and senolytic susceptibility in the context of the SARS-CoV-2 variants Alpha and Beta, which have mutations that affect the spike protein).

Senolytic targeting of COVID-19 *in vivo*

To determine the impact of senolytic treatment on the clinical severity of COVID-19-like lung disease, we first tested early intervention with navitoclax in the well-established Syrian golden hamster model of SARS-CoV-2-driven lung disease^{46,47}. After intranasal infection with SARS-CoV-2, animals developed COVID-19-like pneumonia within the first 3–5 days. scRNA-seq profiling of SARS-CoV-2-infected and mock-infected hamster lungs revealed upregulated p16^{INK4A}, core senescence and SASP factors, as well as *Src* transcript expression in alveolar epithelial cells,

macrophages and neutrophils due to primary virus infection or paracrine senescence induction during days 3–5 after infection (Extended Data Fig. [6a](#)). This analysis also demonstrated induction of *BCL2L2* transcripts in these cell types at day 5 after infection (Extended Data Fig. [6b](#)), which provides support for the use of navitoclax as a suitable senolytic. Animals on the navitoclax protocol exhibited moderate adverse effects (Extended Data Fig. [6c, d](#)). However, they had a marked reduction in the number of senescent cells and improvements in the histopathological features compared with the solvent-only-treated but SARS-CoV-2-infected cohort on day 7 after infection (Fig. [5a](#), Extended Data Fig. [6e–g](#), Extended Data Table [1](#)). We also detected much lower concentrations of key pro-inflammatory SASP factors in the serum of navitoclax-treated hamsters on day 7 after infection, values that were almost indistinguishable from uninfected controls (Extended Data Fig. [6h](#)).

Fig. 5: Senolytic targeting mitigates disease features of COVID-19 in animal models and patients.

 figure5

a, H3K9me3 IHA in nasopharyngeal (top) and lung (middle) specimens, and lipofuscin-based detection (bottom) of senescent cells in the lungs of golden hamsters infected with SARS-CoV-2 and treated with navitoclax or solvent-only ($n = 5$ animals each), or mock-infected and untreated ($n = 3$ animals) at day 7 after infection. **b**, H3K9me3 IHA and lipofuscin staining in nasopharyngeal sections of Roborovski dwarf hamsters infected with SARS-CoV-2 or mock at day 4 after infection and treatment as indicated. **c**, Lung tissue of dwarf hamsters as in **b** on day 4 after infection stained with haematoxylin and eosin. Uninfected healthy hamsters (mock) are shown for comparison ((xiv)–(xvii)). (i), (v) and (x) are overviews of lung sections. Signs of COVID-19-like pneumonia and haemorrhage are indicated: hyperplasia of the bronchial epithelium (double-headed arrows), haemorrhage (asterisks) and necrosis (black arrowheads) of alveolar epithelial cells with neutrophil infiltration (white arrowheads), and endothelialitis (black arrows). **d**, Quantification of the findings in **c**. * $P < 0.05$ by unpaired *t*-test (one-tailed). **e**, Multiplex bead-based protein analysis of dwarf hamster serum samples on day 4 after infection (as in **b–d**). $n = 5$ each (**b–d**; $n =$

4 each in e) for SARS-CoV-2-infected and treated (with solvent (Sol.) or navitoclax (Navito.) animals. $n = 2$ for healthy (mock) control. f, Constellation plots of patients with COVID-19 (ref. 52) before (day 0) and after 7 days of standard care (SC) only or quercetin plus SC. Variables (Extended Data Table 2) were simultaneously analysed by agglomerative hierarchical clustering to visualize similarity (distance) between patients and separation of the cohorts after treatment. Multi-dimensional analysis of individual patient data, with each red or green dot indicating a patient, the line length represents the distance between patients, and axes showing arbitrary units. $n = 21$ for each group. All quantifications are mean \pm s.d. Scale bars, 20 μm (c, middle two columns), 50 μm (a, b, c (right column)) or 1 mm (c, left column).

To evaluate the potential of senolytic intervention in model systems with a more severe COVID-19-like clinical course, we next considered the Roborovski dwarf hamster model⁴⁸. On day 4 after infection and treatment with navitoclax, D/Q or solvent-only, animals with senolytic intervention presented with a substantial reduction of H3K9me3- or lipofuscin-marked senescent cells in their respiratory epithelium and a profound reduction in lung disease features, especially in the D/Q-treated group (Fig. 5b-d). Both senolytic regimens also produced a reduction in SASP-reminiscent serum cytokines on day 4 after infection in this model, to levels close to healthy controls (Fig. 5e). Effects in the D/Q-treated group were particularly meaningful: 5 out of 5 animals survived, displayed no apparent signs of disease and no or only moderate weight loss (Extended Data Fig. 7a). By contrast, 4 out of 5 animals in the navitoclax-treated group and 3 out of 5 animals in the placebo-treated group had to be euthanized due to weight loss and clinical impairment by day 4 after infection. Last, we investigated the *K18-hACE2*-transgenic mouse model, in which SARS-CoV-2 infection causes severe and typically lethal disease^{49,50}. Mice were treated in a similar manner to the dwarf hamster model, with oral administrations of navitoclax, D/Q or fisetin, and scheduled for lung analysis on day 6 after infection. For the solvent-only-treated mice, 2 out of 5 died on or before day 6, whereas 1 out of 5 of the navitoclax-treated mice died and the weight of another fell underneath the accepted weight limit on day 6. By contrast, all the D/Q-treated and fisetin-treated mice were alive, had limited weight loss and presented without clinical symptoms on day 6 (Extended Data Fig. 7a, b). Although overall histopathological analyses did not show overt differences regarding COVID-19-like parameters (Extended Data Fig. 7c; see Extended Data Fig. 7d regarding virus loads in this model and the hamster models), markers of senescent cells were significantly lower in the lungs of senolytic-treated mice across all treatment regimens (Extended Data Fig. 7e).

Quercetin was recently tested as an oral formulation with sunflower lecithin against standard care in two randomized clinical trials (ClinicalTrials.gov identifiers [NCT04578158](#) and [NCT04861298](#)) for patients with confirmed SARS-CoV-2 infection and mild COVID-19-associated symptoms. In both trials, based on 152

patients⁵¹ and 42 patients⁵², senolytic intervention led to clinical improvement^{51,52}. Agglomerative hierarchical clustering of data from the second trial⁵² across numerous parameters separated the patient population—which was indistinguishable at baseline—into quercetin and standard care at day 7 (Fig. 5f, Extended Data Table 2). Moreover, collective analysis of all 194 patients concluded that the quercetin-treated group showed significant risk reductions regarding the needs of hospitalization and oxygen therapy compared to standard care, particularly in terms of length of hospitalization, referral to the intensive care unit and number of deaths (Extended Data Fig. 8a,b). Together, early senolytic intervention during SARS-CoV-2 infection significantly attenuates COVID-19-like lung disease and systemic inflammation.

Our investigation marks VIS as a central pathogenic principle and a valid therapeutic target for SARS-CoV-2 infection to prevent severe COVID-19 lung disease. The primary virus–host cell encounter induces a senescence response associated with massive pro-inflammatory cytokine secretion that complements virus spreading to the lower airway tract. Our data pinpoint macrophages as pivotal cellular messengers in this process. Attracted to and primed by upper airway VIS cells, macrophages undergo a secondary, SASP-amplifying senescent-state switch. Subsequently deployed in the lungs, they further induce senescence, particularly in endothelial cells. System-wide and locally active pro-coagulatory and complement-activating SASP factors contribute to hallmark histopathological features and the clinical severity of COVID-19. Hence, early senolytic intervention is an appealing strategy to interrupt such an escalating immune cascade at its beginnings. The effects of D/Q, fisetin and navitoclax treatment that we observed here are encouraging, but optimized dose scheduling to maximize their clinical potential and limit potential toxicities is needed. Owing to their good safety profiles, compounds such as the flavonoids quercetin and fisetin are particularly attractive candidates as VIS-targeting senolytics. As already demonstrated for quercetin^{51,52}, fisetin is currently being investigated in COVID-19 trials. Robbins and colleagues⁵³ recently reported enhanced SASP production of pre-existing senescent cells in old mice by pathogen-associated molecular pattern factors such as lipopolysaccharide or the SARS-CoV-2 spike protein. In turn, pharmacological removal of senescent cells by fisetin or D/Q in β-coronavirus-infected mice was clinically effective. This adds to the rationale of senolytic VIS cell elimination, as proposed here, for SARS-CoV-2-induced senescence. Moreover, it will be interesting to explore whether early senolytic intervention can mitigate chronic post-COVID-19 impairment, which is known as long COVID⁵⁴. Finally, we highlight that although effective vaccinations are available worldwide and will hopefully make COVID-19 history soon, our approach remains conceptually valid in the context of other viral epidemics or pandemics in the future.

Methods

Cell culture and virus production

Cell lines were maintained according to the guideline of the suppliers. The HDF cell lines IMR90, WI38 and Tig3 have been previously described²². The human cell lines A549 and HUVEC were purchased from the American Type Culture Collection (ATCC) and RPE1 (hTERT RPE1) was provided by A. Schiebel. Primary human nasal or bronchial epithelial cells (HNEpC and HBEPc) were purchased from PromoCell. HNEpC cells with exogenous ACE2 expression (HNEpC-hACE2) were generated by lentiviral infection (hACE2 lentivirus, BPS Bioscience). THP-1 cells were provided by A. Walter. Senescence-incapable cell lines were generated by transduction with lentiviruses encoding JMJD2C or *p53* shRNA as previously described^{22,55}.

All viruses used in this work are tagged with green fluorescent protein (GFP), with the exception of HCoV-NL63 and SARS-CoV-2, and infection efficiency was monitored by detecting fluorescence levels in infected cells. Retrovirus was produced by transfecting Phoenix packaging cells with a murine stem cell virus (MSCV) GFP plasmid⁵⁶. Lentivirus was produced by transfecting 293T cells with psPAX2, pMD2.G (Addgene, 12260 and 12259) and pCDH-CMV-MCS-EF1-GFP plasmids²². AAV was obtained from the Charité Viral Core Facility. Caco-2 cell-adapted wild-type HCoV-NL63 virus at a titre of 3×10^6 PFU ml⁻¹ was provided by the M.L. laboratory. VSV-GFP was a gift from W. Brune. VSV-ΔG* GFP (Kerafast) and plasmids encoding SARS-CoV spike (pKS SARS St19; provided by S. Fukushi), SARS-CoV-2 spike (Wuhan SARS-CoV-2 spike deltaCT28; provided by C. Ratswohl and K. de la Rosa), SARS-CoV-2 spike variants Alpha and Beta (pCDH-CMV-spike-B117-EF1-puro and pCDH-CMV-spike-B1351-EF1-puro synthesized by GENEWIZ) proteins were used to generate mutant pseudotypes. SARS-CoV-2 (hCoV-19/Germany/BY-ChVir-984/2020, sequence reference EPI_ISL_406862) for in vitro applications was propagated in Vero E6 cells (ATCC, CRL-1586) and genome-sequenced to exclude stocks with mutations from further experiments. Infection was monitored by PCR, to detect viral genomic RNA in the supernatant 48 or 72 h after infection, as previously described⁵⁷. Experiments were conducted under appropriate biosafety conditions with enhanced respiratory personal protection equipment in the BSL-3 facility at the Institute for Virology, Charité, Berlin. In-house generated virus stocks were concentrated ten times using virus concentration kits (TaKaRa Bio and Abcam). High-titre virus infection to induce VIS reflect MOI of 50 for replication-incompetent retrovirus and lentivirus, 10 for replication-incompetent AAV and VSV-ΔG*, 10 for replication-competent HCoV-NL63, 1 for replication-competent VSV, and 0.1 for replication-competent SARS-CoV-2. VIS features were assessed on day 5 (retrovirus and lentivirus), day 3 (HCoV-NL63, VSV-ΔG* and SARS-CoV-2) or day 2 (VSV) after infection.

Patients with COVID-19, individuals without COVID-19 and healthy donor material

Upper (nasopharyngeal) and lower airway (lung) tissue formalin-fixed paraffin-embedded (FFPE) samples were derived from deceased patients infected with SARS-CoV-2 and from archive material from patients who passed away without notable clinical signs of a respiratory infection before October 2019 (that is, individuals without COVID-19), blood samples of patients with SARS-CoV-2 and hospitalized patients in the course of their COVID-19 disease, or blood samples from healthy volunteers were used based on approval by the local ethics commission of the Johannes Kepler University (reference number 1070/2020). All patients with COVID-19 were PCR-proven as SARS-CoV-2-positive; however, SARS-CoV-2 RNA was detectable in 4 out of 5 cases of COVID-19 shown in Fig. [2a](#). All participants gave informed consent. In addition, we conducted re-analyses of additional patient and control materials that were previously obtained and published elsewhere [30,34,51,52](#).

Flow cytometry, immunoblotting, immunofluorescence and immunohistochemical analysis

Flow cytometry, immunoblotting (IB), immunofluorescence (IF) and IHA were performed as previously described [24,58](#). Surface antigen detection by flow cytometry was carried out using fluorescence-conjugated antibodies against human CD86-PE-Cy7 (BioLegend, 374209; 1:200), CD13-APC-Cy7 (BioLegend, 301709; 1:200) and CD62P-PE (BioLegend, 304905; 1:200). Antigen detection by IB was carried out using the following antibodies: BCL-2 (Cell Signaling Technology (CST), 15071; 1:1,000); BCL-xL (CST, 2764, 1:1,000); BCL-w (CST, 2724; 1:1,000); MCL-1 (CST, 39224; 1:1,000); phospho-p65-Ser536 (CST, 3033; 1:1,000); phospho-IRF3-Ser386 (CST, 37829; 1:1,000); phospho-Rb-Ser807/811 (CST, 8516; 1:1,000); p21^{CIP1} (Santa Cruz Biotechnology (SCBT), sc-6246; 1:200); p16^{INK4A} (SCBT, sc-1661; 1:200); H3K9me3 (Abcam, ab8898; 1:2,000); phospho-Akt (Thr308) (CST, 13038T; 1:2,000); phospho-p38 MAPK (Thr180/Tyr182) (CST, 4511T; 1:1,000); phospho-p70 S6 kinase (Thr389) (CST, 9234T; 1:1,000); phospho-SRC (Tyr416) (CST, 6943T; 1:1,000); and α -tubulin (Sigma, T5168; 1:2,000). Anti-mouse or anti-rabbit horseradish-peroxidase-conjugated antibodies were used as secondary antibodies (GE Healthcare, RPN4301 and NA931V, respectively). Antigen detection by IF was performed using the following antibodies: phospho-H2A.X (CST, 9718; 1:400); p16^{INK4A} (Abcam, ab211542; 1:250); C5b-C9 (SCBT, sc-58935; 1:250); anti-mouse-Cy3 secondary antibody (Thermo Fisher, A10521; 1:1,000); and anti-rabbit-594 secondary antibody (Thermo Fisher, A11012; 1:1,000). Antigen detection by IHA was performed using a HiDef Detection HRP Polymer System (Cell Marque, 954D-30) with antibodies against p21^{CIP1} (SCBT, sc-6246; 1:200), IL-8 (Abcam, ab18672; 1:200), H3K9me3

(Abcam, ab8898; 1:2,000), BCL2L2 (Abcam, ab190952; 1:1,000) and CD86 (Antibodies-online, ABIN736701; 1:100).

Original scans of the immunoblots presented in Figs. 1f, 4a, with molecular mass markers and crop area indicated, are shown in the [Supplementary Information](#).

In situ hybridization

In situ hybridization was performed as previously described⁴⁶ using a ViewRNA Tissue Assay Core kit (Invitrogen, 19931) and a ViewRNA Tissue Assay Blue Module (Invitrogen, 19932) according to the manufacturer's instructions. For the detection of SARS-CoV-2, ViewRNA Type 1 Probe Set COVID19 polyprotein (Invitrogen, CVX-06, Assay ID VPNKRHH) and ViewRNA Type 6 Probe Set Human ACTB (Invitrogen, VX-06, Assay ID VA6-10506) were used. Following hybridization, sections were counterstained with haematoxylin and mounted with ProLong Glass Antifade Mountant (Invitrogen, P36982). Images were taken using an Olympus Slide Scanner VS200.

Quantification of gene transcription

RT-qPCR

RNA isolated from cell pellets using TRIzol (Invitrogen) was transcribed to cDNA using SuperScript II reverse transcriptase (Invitrogen). Individual gene expression was analysed by RT-qPCR using Taqman assays from Applied Biosystems. A list of the Taqman assays used is available in the [Supplementary Information](#).

RNA-seq

Total RNA was isolated using a RNAeasy Mini kit (Qiagen) and sequenced at BGI Genomics. scRNA-seq was conducted as previously described⁵⁹. Further processing of the raw sequencing data is described in the section 'Statistics and data analysis'.

Oligonucleotide-hybridization-based transcriptome profiling

RNA was extracted from FFPE tissue sections using a PureLink FFPE RNA Isolation kit (Thermo Fisher Scientific, K156002). RNA was then hybridized with the probe set of the NanoString nCounter Human Tumor Signaling 360 Panel (XT-CSPS-H-T360-12) and analysed on a NanoString nCounter SPRINT.

Quantification of protein expression

Multiplex bead-based protein detection (MAGPIX)

MAGPIX assays were conducted according to the manufacturer's manual with following bead panels: custom Procortaplex 19-plex (Thermo Fisher Scientific, PPX-19, Assay ID MXAACDR), custom Procortaplex 4-plex (Thermo Fisher Scientific, PPX-04, Assay ID MXCE4XN) and Bio-Plex Pro Rat Cytokine 23-Plex Assay (Bio-Rad, 12005641). The assay was measured using a BioPlex MAGPIX multiplex reader (Bio-Rad) and analysed with a 5PL algorithm provided by the Bio-Plex Manager software (v.6.1). Detailed procedures for sample preparation and measurement are described in the [Supplementary Information](#). Note that owing to a different normalization procedure, values cannot be cross-read between different panels (for example, Fig. 1d compared with Fig. 3b).

Mass-spectrometry-based proteomics

Detailed protocols of sample preparation, mass spectrometry and data processing have been previously described³⁴; for further details see the [Supplementary Information](#). In brief, serum samples were reduced, alkylated, digested and conditioned on a Biomek i7 workstation, and approximately 5 µg of peptides per injection was used for the gradient liquid chromatography–tandem mass spectrometry analysis. The raw data were processed using DIA-NN 1.7.12.

VIS assays in vitro

Growth curve analysis

The HDF IMR90, WI38 or Tig3 cells were infected with MSCV retrovirus at day 0 and day 3, and SA-β-gal activity was measured at day 5. For growth curve analyses, 2 × 10⁴ cells were seeded into 12-well plates and cell numbers were counted at days 3, 6 and 9.

2'3'-cGAMP ELISA assay

Cell cytoplasmic 2'3'-cGAMP concentration was measured using a Caymanchem ELISA kit. In brief, cells were lysed in M-PER extraction reagent (Thermo Fisher) and 10 µg protein lysate was used to determine the 2'3'-cGAMP content.

Analysis of cell viability and senescence

Viability and cell numbers were analysed by Trypan blue dye exclusion or Guava Viacount (Millipore). SA-β-gal activity at pH 6.0 (for human cells) or pH 5.5 (for

rodent cells) as a senescence marker in fresh or cryopreserved cells was assessed as previously described⁶⁰. In situ detection of lipofuscin as a senescence marker in FFPE samples was carried out using SenTraGor reagent (Lab Supplies Scientific; provided by V. G. Gorgoulis) according to the manufacturer's instructions.

ROS detection

Dihydroethidium (20 µM, MedChemExpress) was directly added to cells and incubated at 37 °C for 20 min. Dihydroethidium was then washed away with PBS. Cells were fixed in 4% paraformaldehyde and staining intensity was analysed using a Nikon fluorescence microscope.

VIS supernatant transfer and secondary, paracrine senescence

Conditioned medium was collected from proliferating and VIS cells after 24 h of incubation and centrifuged at 5,000 r.p.m. for 5 min. The supernatant (SN_{prol.} or SN_{VIS}, respectively) was transferred to HUVEC or THP-1 cells for further analysis. For the supernatant transfer from SARS-CoV-2-infected HNEpC cells, custom-made neutralizing antibodies against SARS-CoV-2 (provided by the H.S. laboratory) were mixed in to block secondary infection.

NET formation assay

NET formation was measured according to the concentration of NET DNA bound to myeloperoxidase (MPO). Neutrophils were isolated from whole blood of four healthy donors. NET formation was quantified as previously described⁶¹. In brief, 10 µg ml⁻¹ anti-MPO antibody (Abcam, ab25989) was immobilized on the surface of black MaxiSorp-treated plates (Thermo Scientific). The plate was subsequently washed with PBS and blocked with 5% non-fat milk for 2 h at room temperature. Neutrophils incubated for 4 h at 37 °C in RPMI medium from proliferating or VIS WI-38 or IMR-90 cells were pipetted onto the MPO-coated plate and incubated for 1 h at room temperature. NET formation quantification was performed using a MPO-DNA PicoGreen assay according to the manufacturer's instructions (Quant-iT PicoGreen dsDNA Assay kit, Invitrogen). Sample fluorescence was measured using a GloMax Discover microplate reader (Promega).

Rotational thromboelastometry

To measure clotting time, a rotational thromboelastometry assay was performed on a ROTEM delta (Werfen) device according to the manufacturer's instructions. INTEM captures intrinsic, platelet-dependent clotting and EXTEM extrinsic, non-platelet-

dependent clotting. Whole-blood samples from healthy donors were spiked with the supernatant from WI38 cells in proliferation or VIS. Exclusion criteria for the healthy donors were coagulation disorders and clotting-affecting medication. Sex distribution was equal among the donors.

Platelet activation and ADP release measurement by VIS supernatant

Platelet activation was measured by flow cytometry as the percentage of CD62/P-selectin-positive cells in whole blood. To measure VIS-induced ADP release, 2×10^6 platelets from healthy donors were resuspended in 200 μl conditioned medium and incubated at 37 °C for 1 h. Supernatant was collected by centrifugation at 2,000g for 5 min, and the ADP concentration was measured using an ADP Colorimetric Assay Kit II (BioVision) according to the manufacturer's instruction.

Complement-mediated cytotoxicity in HUVEC endothelial cells

Serum from healthy donors (500 μl) was incubated with proliferating or VIS HDF (Fig. 3*i,j*) or HNEpC cells (Fig. 4*f*, Extended Data Fig. 5*h*) in 5 ml medium at 37 °C for 30 min. Heat-inactivated (56 °C for 30 min) serum was used as a control. Supernatant was collected and incubated with HUVEC endothelial cells at 37 °C. After 2 h of incubation, HUVEC cells were fixed in 4% paraformaldehyde, and C5b–C9 immunofluorescence staining was carried out. Alternatively, 24 h after incubation, a cytotoxicity assay was performed using a CyQUANT LDH Cytotoxicity kit (Invitrogen).

Senolytic treatment in vitro and secondary viral infection

VIS cells were treated with venetoclax (1 µM), navitoclax (1 µM), fisetin (20 µM), D/Q (20 µM, reflecting 2 µM dasatinib plus 20 µM quercetin) or AT-101 (1 µM) for 48 h, and cell viability was determined by Trypan blue staining using a Countess II FL Automated Cell Counter (Thermo Fisher). To generate the supernatant used for secondary viral infection, wild-type mouse embryo fibroblasts were infected with VSV for 6 h and treated with 1 µM navitoclax for 24 h. Supernatant was centrifuged and filtered through a 0.22-µm PVDF filter and added to THP-1 cells. After 24 h, secondary infectivity was measured by counting GFP⁺ THP-1 cells.

SARS-CoV-2-driven COVID-19 animal models

In vitro and in vivo studies related to hamsters were conducted under appropriate biosafety conditions in the BSL-3 facility at the Institute for Virology, Freie Universität Berlin, Germany. All hamster experimentation was approved by the relevant state authority (Landesamt für Gesundheit und Soziales Berlin, Germany; permit number 0086/20), and performed in compliance with national and international guidelines for the care and humane use of animals. Preparation of SARS-CoV-2 virus stock and intranasal infection of Syrian hamsters (*Mesocricetus auratus*) as a faithful in vivo model of COVID-19 lung disease have been previously described⁴⁶. In brief, a SARS-CoV-2 wild-type isolate (BetaCoV/Munich/BavPat2-ChVir984-ChVir1017/2020) was grown in Vero E6 cells. To ensure genetic integrity, passage 3 stocks were genome-sequenced, and results showed conformity with the published sequence (GenBank [MT270112.1](#)) and confirmed the presence of the furin cleavage site essential for in vivo pathogenesis. Anaesthetized male and female hamsters at 6–10 weeks of age were inoculated with 1×10^5 PFU SARS-CoV-2 in a total volume of 60 µl cell culture medium. Control animals were mock-infected with the same volume of cell culture medium. One day after infection, animals were randomized and half of the animals ($n = 5$) received a single 85 mg kg⁻¹ body-weight dose of navitoclax in solvent (60% Phosal PG, 30% PEG 300, 20% ethanol) intraperitoneally every day for 6 consecutive days. The other

half of infected animals ($n = 5$) received the same volume of solvent only. The control group ($n = 3$) did not receive virus or treatment. On day 7 after infection, 1 day after the last treatment, all hamsters were euthanized, and tissue and peripheral blood samples were prepared for further analyses.

The Roborovski dwarf hamster (*Phodopus roborovskii*), a species highly susceptible to a severe course of SARS-CoV-2 infection, was used under the permit mentioned above. Infections were performed as previously described⁴⁸. Female Roborovski dwarf hamsters at 5–7 weeks of age underwent the procedure described above for Syrian hamsters with the exception that the total volume of the inoculum was reduced to 20 µl. The same virus stock was used. Animals were randomly distributed into three treatment groups ($n = 5$) and one non-infected, non-treated group ($n = 2$). After 6 h of infection, animals were treated orally once a day with navitoclax (85 mg kg⁻¹) or D/Q (5/50 mg kg⁻¹) dissolved in 60% Phosal PG, 30% PEG 300, 20% ethanol and mixed 1:1 with strawberry syrup. The placebo-treatment group received the same solvent/syrup combination without drug. On day 4 after infection, animals were killed, and tissue and peripheral blood specimens were collected for downstream analyses.

Infection of *K18-hACE2* mice (Jackson Laboratory strain 034860) with SARS-CoV-2 was performed according to approval by the Institutional Animal Care and Use Committee of the Icahn School of Medicine at Mount Sinai as previously reported⁶². In brief, 6-week-old female mice were infected with 1×10^4 PFU SARS-CoV-2 (USA-WA1/2020, BEI resources NR-52281) grown in Vero E6 cells and validated by genome sequencing, and randomly distributed into three treatment groups ($n = 5$ each) and one solvent-only control group ($n = 5$). From 1 day after infection, randomly chosen animals were orally treated with oral navitoclax (85 mg kg⁻¹), D/Q (5/50 mg kg⁻¹) or fisetin (100 mg kg⁻¹) dissolved in 60% Phosal PG, 30% PEG 300, 20% ethanol every other day. On day 6 after infection (1 day after the last treatment), animals were killed, and tissue specimens were collected for histopathological analyses.

Hamster and mouse lung tissues were processed for histopathology as previously described⁴⁷ and analysed by board-certified veterinary pathologists (blinded about the treatment) following suggested standard

criteria⁶³. Transmission electron microscopy was performed with trachea tissue from infected and treated Syrian golden hamsters. Fixation and further processing of the samples and image acquisition procedures are described in the [Supplementary Information](#).

Statistics and data analysis

Based on previous experience^{22,24,41,47,50,53,54,57}, sample sizes typically reflected three to five replicates. In some experiments, much higher numbers of individual primary material were used as biological replicates. All quantifications from staining reactions were carried out by an independent and blinded second examiner and reflect at least 3 samples with at least 100 events counted (typically in 3 different areas) each. For patients and for animal models, IHA quantification was carried out in SARS-CoV-2-affected areas. Regarding Fig. 5, Extended Data Figs. 6 and 7, quantification of the indicated features was based on the following numbers of individual photomicrographs from animals as indicated in the legends and text: Fig. 5a: nasopharynx H3K9me3 ($n = 3$ for mock, $n = 6$ for solvent and navitoclax), lung H3K9me3 and lipofuscin ($n = 3$ for mock, $n = 5$ for solvent and navitoclax); Fig. 5b: H3K9me3 ($n = 5$ for solvent and navitoclax, $n = 6$ for D/Q), lipofuscin ($n = 5$ for all three groups); Extended Data Fig. 7e: p16^{INK4A} ($n = 5$ for solvent, navitoclax and D/Q, $n = 4$ for fisetin), H3K9me3 ($n = 4$ for solvent and navitoclax, $n = 5$ for fisetin and D/Q), lipofuscin ($n = 5$ for solvent and navitoclax, $n = 4$ for fisetin, $n = 7$ for D/Q).

Data analysis was performed with GraphPad Prism 9. For statistical comparisons, a *t*-test was applied. Unless otherwise stated, a *P* value of <0.05 was considered statistically significant. For multiple-testing corrections, the Benjamini–Hochberg method was used to control for the false discovery rate⁶⁴. Bioinformatics analysis was performed in R, v.4.0.3, and Bioconductor 3.12 using various R packages as described in the [Supplementary Information](#) in greater detail. High-performance computation was performed in the Research/Clinic cluster of the Berlin Institute of Health. For further analyses of the clinical data from patients with COVID-19 (refs. ^{51,52}) as presented in Fig. 5f and Extended Data Fig. 8a,b, JMP Pro 14 (SAS Institute) was used for agglomerative hierarchical

clustering, GraphPad Prism 9 was used for Fisher's exact test for *P* values, and a Haldane–Anscombe correction was applied to calculate relative risks. Lipofuscin (SenTraGor) staining was quantified with the pixel counting function of the ImageJ program (bundled with Java 1.8.0_172, NIH)⁶⁵. No statistical methods were used to predetermine sample size.

Reporting summary

Further information on research design is available in the [Nature Research Reporting Summary](#) linked to this paper.

Data availability

The WI38 VIS- and OIS-derived raw RNA-seq data (Fig. 1b and Extended Data Fig. 1b) were deposited at the Gene Expression Omnibus (GEO) repository of the National Center for Biotechnology Information (NCBI) under accession number [GSE165532](#). Gene expression data of human AECs infected with SARS-CoV-2 (Fig. 1k) are publicly available from at the GEO under the accession number [GSE148729](#). Raw sequencing data of NHBE, Calu-3 and A549 cells infected with SARS-CoV-2 (Extended Data Fig. 2k) are publicly available at the GEO under the accession number [GSE147507](#) (ref. ⁴). Seurat objects comprising scRNA-seq datasets of nasopharyngeal, protected specimen brush and bronchial lavage samples of 19 patients with COVID-19 and 5 healthy donors³⁰, constituting a total of 36 samples that was analysed in this study (Fig. 2b), are available at FigShare (<https://doi.org/10.6084/m9.figshare.12436517>; covid_nbt_main.rds, covid_nct_loc.rds). The mass-spectrometry-based proteomics data of serum from patients with COVID-19 and healthy donors in Fig. 2f are described in ref. ³⁴. Patient proteomics data (Fig. 2g, Extended Data Fig. 3e) are publicly available at <https://www.who.int/teams/blueprint/covid-19>, in which disease severity was defined as follows: g3, hospitalized, no oxygen therapy; g4, oxygen by mask or nasal prongs; g5, noninvasive ventilation or high-flow oxygen; g6, intubation and mechanical ventilation; g7, ventilation and additional organ support. scRNA-seq data of hamsters infected with SARS-CoV-2 (Extended Data Fig. 6a, b) are available at the GEO ([GSE162208](#))⁵⁹. All information

related to the two randomized trials on early quercetin intervention in patients with COVID-19 ([NCT04578158](#) and [NCT04861298](#)) can be found in the respective publications^{51,52} and in Extended Data Table 2.

References

1. 1.
Zhang, X. et al. Viral and host factors related to the clinical outcome of COVID-19. *Nature* **583**, 437–440 (2020).
2. 2.
Mehta, P. et al. COVID-19: consider cytokine storm syndromes and immunosuppression. *Lancet* **395**, 1033–1034 (2020).
3. 3.
Merad, M. & Martin, J. C. Pathological inflammation in patients with COVID-19: a key role for monocytes and macrophages. *Nat. Rev. Immunol.* **20**, 355–362 (2020).
4. 4.
Blanco-Melo, D. et al. Imbalanced host response to SARS-CoV-2 drives development of COVID-19. *Cell* **181**, 1036–1045.e9 (2020).
5. 5.
Coppe, J. P., Desprez, P. Y., Krtolica, A. & Campisi, J. The senescence-associated secretory phenotype: the dark side of tumor suppression. *Annu. Rev. Pathol.* **5**, 99–118 (2010).
6. 6.
Lee, S. & Schmitt, C. A. The dynamic nature of senescence in cancer. *Nat. Cell Biol.* **21**, 94–101 (2019).

7. 7.

Wiley, C. D. et al. SILAC analysis reveals increased secretion of hemostasis-related factors by senescent cells. *Cell Rep.* **28**, 3329–3337.e5 (2019).

8. 8.

Ackermann, M. et al. Pulmonary vascular endothelialitis, thrombosis, and angiogenesis in Covid-19. *N. Engl. J. Med.* **383**, 120–128 (2020).

9. 9.

Middleton, E. A. et al. Neutrophil extracellular traps contribute to immunothrombosis in COVID-19 acute respiratory distress syndrome. *Blood* **136**, 1169–1179 (2020).

10. 10.

Berlin, D. A., Gulick, R. M. & Martinez, F. J. Severe Covid-19. *N. Engl. J. Med.* **383**, 2451–2460 (2020).

11. 11.

Wolfel, R. et al. Virological assessment of hospitalized patients with COVID-2019. *Nature* **581**, 465–469 (2020).

12. 12.

Hoffmann, M. et al. SARS-CoV-2 cell entry depends on ACE2 and TMPRSS2 and is blocked by a clinically proven protease inhibitor. *Cell* **181**, 271–280.e8 (2020).

13. 13.

Ju, B. et al. Human neutralizing antibodies elicited by SARS-CoV-2 infection. *Nature* **584**, 115–119 (2020).

14. 14.

Horby, P. et al. Dexamethasone in hospitalized patients with Covid-19. *N. Engl. J. Med.* **384**, 693–704 (2021).

15. 15.

Xu, X. et al. Effective treatment of severe COVID-19 patients with tocilizumab. *Proc. Natl Acad. Sci. USA* **117**, 10970–10975 (2020).

16. 16.

Chuprin, A. et al. Cell fusion induced by ERVWE1 or measles virus causes cellular senescence. *Genes Dev.* **27**, 2356–2366 (2013).

17. 17.

Martínez, I. et al. Induction of DNA double-strand breaks and cellular senescence by human respiratory syncytial virus. *Virulence* **7**, 427–442 (2016).

18. 18.

Baz-Martinez, M. et al. Cell senescence is an antiviral defense mechanism. *Sci. Rep.* **6**, 37007 (2016).

19. 19.

Hsieh, T. H. et al. Senescence in monocytes facilitates dengue virus infection by increasing infectivity. *Front. Cell. Infect. Microbiol.* **10**, 375 (2020).

20. 20.

Dimri, G. P. et al. A biomarker that identifies senescent human cells in culture and in aging skin in vivo. *Proc. Natl Acad. Sci. USA* **92**, 9363–9367 (1995).

21. 21.

Narita, M. et al. Rb-mediated heterochromatin formation and silencing of E2F target genes during cellular senescence. *Cell* **113**, 703–716 (2003).

22. 22.

Yu, Y. et al. Targeting the senescence-overriding cooperative activity of structurally unrelated H3K9 demethylases in melanoma. *Cancer Cell* **33**, 322–336 (2018).

23. 23.

Kuilman, T. et al. Oncogene-induced senescence relayed by an interleukin-dependent inflammatory network. *Cell* **133**, 1019–1031 (2008).

24. 24.

Jing, H. et al. Opposing roles of NF-κB in anti-cancer treatment outcome unveiled by cross-species investigations. *Genes Dev.* **25**, 2137–2146 (2011).

25. 25.

Serrano, M., Lin, A. W., McCurrach, M. E., Beach, D. & Lowe, S. W. Oncogenic ras provokes premature cell senescence associated with accumulation of p53 and p16INK4a. *Cell* **88**, 593–602 (1997).

26. 26.

Dou, Z. et al. Cytoplasmic chromatin triggers inflammation in senescence and cancer. *Nature* **550**, 402–406 (2017).

27. 27.

Liu, S. et al. Phosphorylation of innate immune adaptor proteins MAVS, STING, and TRIF induces IRF3 activation. *Science* **347**, aaa2630 (2015).

28. 28.

Buss, H. et al. Constitutive and interleukin-1-inducible phosphorylation of p65 NF- κ B at serine 536 is mediated by multiple protein kinases including I κ B kinase (IKK)- α , IKK β , IKK ϵ , TRAF family member-associated (TANK)-binding kinase 1 (TBK1), and an unknown kinase and couples p65 to TATA-binding protein-associated factor II31-mediated interleukin-8 transcription. *J. Biol. Chem.* **279**, 55633–55643 (2004).

29. 29.

Wang, P. et al. Expression cloning of functional receptor used by SARS coronavirus. *Biochem. Biophys. Res. Commun.* **315**, 439–444 (2004).

30. 30.

Chua, R. L. et al. COVID-19 severity correlates with airway epithelium–immune cell interactions identified by single-cell analysis. *Nat. Biotechnol.* **38**, 970–979 (2020).

31. 31.

Acosta, J. C. et al. A complex secretory program orchestrated by the inflammasome controls paracrine senescence. *Nat. Cell Biol.* **15**, 978–990 (2013).

32. 32.

Roussel, M. et al. Mass cytometry deep phenotyping of human mononuclear phagocytes and myeloid-derived suppressor cells from human blood and bone marrow. *J. Leukoc. Biol.* **102**, 437–447 (2017).

33. 33.

Li, X. et al. The flavonoid quercetin ameliorates liver inflammation and fibrosis by regulating hepatic macrophages activation and polarization in mice. *Front. Pharmacol.* **9**, 72 (2018).

34. 34.

Messner, C. B. et al. Ultra-high-throughput clinical proteomics reveals classifiers of COVID-19 infection. *Cell Syst.* **11**, 11–24.e4 (2020).

35. 35.

Demichev, V. et al. A time-resolved proteomic and prognostic map of COVID-19. *Cell Syst.* **12**, 780–794.e7 (2021).

36. 36.

Kang, S. et al. IL-6 trans-signaling induces plasminogen activator inhibitor-1 from vascular endothelial cells in cytokine release syndrome. *Proc. Natl Acad. Sci. USA* **117**, 22351–22356 (2020).

37. 37.

Beigi, R., Kobatake, E., Aizawa, M. & Dubyak, G. R. Detection of local ATP release from activated platelets using cell surface-attached firefly luciferase. *Am. J. Physiol.* **276**, C267–C278 (1999).

38. 38.

Zhu, Y. et al. The Achilles' heel of senescent cells: from transcriptome to senolytic drugs. *Aging Cell* **14**, 644–658 (2015).

39. 39.

Xu, M. et al. Senolytics improve physical function and increase lifespan in old age. *Nat. Med.* **24**, 1246–1256 (2018).

40. 40.

Dorr, J. R. et al. Synthetic lethal metabolic targeting of cellular senescence in cancer therapy. *Nature* **501**, 421–425 (2013).

41. 41.

Chang, J. et al. Clearance of senescent cells by ABT263 rejuvenates aged hematopoietic stem cells in mice. *Nat. Med.* **22**, 78–83 (2016).

42. 42.

Kirkland, J. L. & Tchkonia, T. Senolytic drugs: from discovery to translation. *J. Intern. Med.* **288**, 518–536 (2020).

43. 43.

Freund, A., Patil, C. K. & Campisi, J. p38MAPK is a novel DNA damage response-independent regulator of the senescence-associated secretory phenotype. *EMBO J.* **30**, 1536–1548 (2011).

44. 44.

Bent, E. H., Gilbert, L. A. & Hemann, M. T. A senescence secretory switch mediated by PI3K/AKT/mTOR activation controls chemoprotective endothelial secretory responses. *Genes Dev.* **30**, 1811–1821 (2016).

45. 45.

Jung, S. H. et al. Integrin $\alpha 6\beta 4$ –Src–AKT signaling induces cellular senescence by counteracting apoptosis in irradiated tumor cells and tissues. *Cell Death Differ.* **26**, 245–259 (2019).

46. 46.

Kreye, J. et al. A therapeutic non-self-reactive SARS-CoV-2 antibody protects from lung pathology in a COVID-19 hamster model. *Cell* **183**, 1058–1069.e19 (2020).

47. 47.

Osterrieder, N. et al. Age-dependent progression of SARS-CoV-2 infection in Syrian hamsters. *Viruses* **12**, 779 (2020).

48. 48.

Trimpert, J. et al. The Roborovski dwarf hamster is a highly susceptible model for a rapid and fatal course of SARS-CoV-2 infection. *Cell Rep.* **33**, 108488 (2020).

49. 49.

Winkler, E. S. et al. SARS-CoV-2 infection of human ACE2-transgenic mice causes severe lung inflammation and impaired function. *Nat. Immunol.* **21**, 1327–1335 (2020).

50. 50.

White, K. M. et al. Plitidepsin has potent preclinical efficacy against SARS-CoV-2 by targeting the host protein eEF1A. *Science* **371**, 926–931 (2021).

51. 51.

Di Pierro, F. et al. Possible therapeutic effects of adjuvant quercetin supplementation against early-stage COVID-19 infection: a prospective, randomized, controlled, and open-label study. *Int. J. Gen. Med.* **14**, 2359–2366 (2021).

52. 52.

Di Pierro, F. et al. Potential clinical benefits of quercetin in the early stage of COVID-19: results of a second, pilot, randomized, controlled and open-label clinical trial. *Int. J. Gen. Med.* **14**, 2807–2816 (2021).

53. 53.

Camell, C. D. et al. Senolytics reduce coronavirus-related mortality in old mice. *Science* **373**, eabe4832 (2021).

54. 54.

Nalbandian, A. et al. Post-acute COVID-19 syndrome. *Nat. Med.* **27**, 601–615 (2021).

55. 55.

Milanovic, M. et al. Senescence-associated reprogramming promotes cancer stemness. *Nature* **553**, 96–100 (2018).

56. 56.

Schmitt, C. A., Rosenthal, C. T. & Lowe, S. W. Genetic analysis of chemoresistance in primary murine lymphomas. *Nat. Med.* **6**, 1029–1035 (2000).

57. 57.

Corman, V. M. et al. Detection of 2019 novel coronavirus (2019-nCoV) by real-time RT–PCR. *Euro Surveill.* **25**, 2000045 (2020).

58. 58.

Schmitt, C. A., McCurrach, M. E., de Stanchina, E., Wallace-Brodeur, R. R. & Lowe, S. W. *INK4a/ARF* mutations accelerate lymphomagenesis and promote chemoresistance by disabling p53. *Genes Dev.* **13**, 2670–2677 (1999).

59. 59.

Nouailles, G. et al. Longitudinal omics in Syrian hamsters integrated with human data unravel complexity of moderate immune responses to SARS-CoV-2. Preprint at <https://doi.org/10.1101/2020.12.18.423524> (2020).

60. 60.

Reimann, M. et al. Tumor stroma-derived TGF- β limits Myc-driven lymphomagenesis via Suv39h1-dependent senescence. *Cancer Cell* **17**, 262–272 (2010).

61. 61.

Veras, F. P. et al. SARS-CoV-2-triggered neutrophil extracellular traps mediate COVID-19 pathology. *J. Exp. Med.* **217**, e20201129 (2020).

62. 62.

Rathnasinghe, R. et al. Comparison of transgenic and adenovirus hACE2 mouse models for SARS-CoV-2 infection. *Emerg. Microbes Infect.* **9**, 2433–2445 (2020).

63. 63.

Gruber, A. D. et al. Standardization of reporting criteria for lung pathology in SARS-CoV-2-infected hamsters: what matters? *Am. J. Respir. Cell Mol. Biol.* **63**, 856–859 (2020).

64. 64.

Hochberg, Y. & Benjamini, Y. More powerful procedures for multiple significance testing. *Stat. Med.* **9**, 811–818 (1990).

65. 65.

Schneider, C. A., Rasband, W. S. & Eliceiri, K. W. NIH Image to ImageJ: 25 years of image analysis. *Nat. Methods* **9**, 671–675 (2012).

66. 66.

Fridman, A. L. & Tainsky, M. A. Critical pathways in cellular senescence and immortalization revealed by gene expression profiling. *Oncogene* **27**, 5975–5987 (2008).

67. 67.

Hari, P. et al. The innate immune sensor Toll-like receptor 2 controls the senescence-associated secretory phenotype. *Sci. Adv.* **5**, eaaw0254 (2019).

68. 68.

Schleich, K. et al. H3K9me3-mediated epigenetic regulation of senescence in mice predicts outcome of lymphoma patients. *Nat. Commun.* **11**, 3651 (2020).

Acknowledgements

We thank S. Fukushi and M. Saijo, C. Ratswohl and K. de la Rosa, V. G. Gorgoulis, K. Hoffman and W. Brune, E. Schiebel for materials; F. Walper for their support in the BSL-3 facility; F. Kurth, P. Tauber-Lau, V. Demichev and L. E. Sander on behalf of the Charité PA–COVID-19 study group as well as members of the Charité Core Facility High-throughput Proteomics for data and measurements; S. Jangra, R. Rathnasinghe and R. Albrecht for support in the BSL-3 facility and procedures, and R. Cadagan for technical assistance; M. Almeder for handling patient samples; M. Recchia for the statistical analysis of the data from clinical trials; and members of the collaborating laboratories for discussions and editorial advice. This work was supported by grants to C.A.S. from the Medical Faculty of the Johannes Kepler University, Linz, Austria, the Deutsche Krebshilfe (no. 7011377629), the Deutsche Forschungsgemeinschaft DFG (GO 2688/1-1 | SCHM 1633/11-1, SCHM 1633/9-1), and the Förderverein Hämatologie und internistische Onkologie (Tyle Private Foundation, Linz, Austria), and to S.L. and C.A.S. by the German BMBF e:Med programme project SeneSys (no. 031L0189A). J. Trimpert and A.D.G. were funded by the German Research Council (grant SFB-TR84 Z01b). This interdisciplinary work was further made possible by the Berlin School of Integrative Oncology (BSIO) graduate programme funded within the German Excellence Initiative (with D.B. as a member of this programme) and the German Cancer Consortium (GCC). This research was also partly funded by CRIP (Center for Research on Influenza Pathogenesis), a NIAID funded Center of Excellence for Influenza Research and Surveillance (CEIRS, contract no. HHSN272201400008C) and CRIPT (Center for Research on Influenza Pathogenesis and Transmission), a NIAID-funded Center of Excellence for Influenza Research and Response (CEIRR, contract no. 75N93021C00014), by DARPA grant HR0011-19-2-0020, by supplements to NIAID grant U19AI142733, U19AI135972 and DoD grant W81XWH-20-1-0270, by a Fast Grant of the Mercatus Center and by the support of the JPB

Foundation, the Open Philanthropy Project (research grant 2020-215611 (5384)) and anonymous donors to A.G.-S. M. Rasler is partly funded by the Francis Crick Institute, which receives its core funding from Cancer Research UK (FC001134), the UK Medical Research Council (FC001134) and the Wellcome Trust (FC001134).

Author information

Author notes

1. Melissa Uccellini

Present address: Regeneron Pharmaceuticals, New York, NY, USA

2. These authors contributed equally: Soyoung Lee, Yong Yu

Affiliations

1. Medical Department of Hematology, Oncology and Tumor Immunology, Molekulares Krebsforschungszentrum (MKFZ), Charité - Universitätsmedizin, Berlin, Germany

Soyoung Lee, Paulina Richter-Pechanska, Dimitri Belenki, Lea Kausche, Andrea Lau, Martin Schönlein, Maurice Reimann, Dorothy N. Y. Fan & Clemens A. Schmitt

2. Max-Delbrück-Center for Molecular Medicine in the Helmholtz Association, Berlin, Germany

Soyoung Lee, Emanuel Wyler, Dimitri Belenki, Séverine Kunz, Bettina Purfürst, Markus Landthaler & Clemens A. Schmitt

3. Deutsches Konsortium für Translationale Krebsforschung (German Cancer Consortium), Partner Site Berlin, Berlin, Germany

Soyoung Lee, Dorothy N. Y. Fan & Clemens A. Schmitt

4. Medical Faculty, Johannes Kepler University, Linz, Austria

Yong Yu, Fahad Benthani, Mario Mairhofer, Sabine Kaltenbrunner, Maria Pammer, Susanne Kimeswenger, Wolfram Hoetzenegger, Bernd Lamprecht, Rupert Langer & Clemens A. Schmitt

5. Institute of Virology, Freie Universität Berlin, Berlin, Germany

Jakob Trimpert, Julia M. Adler & Nikolaus Osterrieder

6. Department of Hematology and Oncology, Kepler University Hospital, Linz, Austria

Lea Kausche, Riad Ghanem & Clemens A. Schmitt

7. Institute of Veterinary Pathology, Freie Universität Berlin, Berlin, Germany

Theresa C. Firsching, Kristina Dietert & Achim D. Gruber

8. Veterinary Centre for Resistance Research, Freie Universität Berlin, Berlin, Germany

Kristina Dietert

9. Department of Microbiology, Icahn School of Medicine at Mount Sinai, New York, NY, USA

Michael Schotsaert, Carles Martínez-Romero, Gagandeep Singh, Melissa Uccellini & Adolfo García-Sastre

10. Global Health and Emerging Pathogens Institute, Icahn School of Medicine at Mount Sinai, New York, NY, USA

Michael Schotsaert, Carles Martínez-Romero, Gagandeep Singh, Melissa Uccellini & Adolfo García-Sastre

11. Institute of Virology, German Center for Infection Research (DZIF), Charité—Universitätsmedizin, Berlin, Germany

Daniela Niemeyer & Christian Drosten

12. Department of Pulmonology, Kepler University Hospital, Linz, Austria

Helmut J. F. Salzer & Bernd Lamprecht

13. Laboratory Medicine, Kepler University Hospital, Linz, Austria

Christian Paar, Anna Habringer & Josef Tomasits

14. Core Facility – High-Throughput Mass Spectrometry and Department of Biochemistry, Charité - Universitätsmedizin, Berlin, Germany

Michael Mülleder & Markus Ralser

15. Institute of Pathology, Charité - Universitätsmedizin, Berlin, Germany

Edward G. Michaelis

16. Department of Chemistry, University of Oxford, Oxford, UK

Amjad Khan

17. Department of Oncology, Hematology and Bone Marrow Transplantation with Section of Pneumology, University Medical Center Hamburg-Eppendorf, Hamburg, Germany

Martin Schönlein

18. Department of Dermatology, Kepler University Hospital, Linz, Austria

Wolfram Hoetzenegger

19. Department of Applied Genetics and Cell Biology, University of Natural Resources and Life Sciences, Vienna, Austria

Herta Steinkellner

20. Institute of Pathology, Kepler University Hospital, Linz, Austria

Reinhard Motz & Rupert Langer

21. Scientific and Research Department, Velleja Research, Milan, Italy

Francesco Di Pierro

22. Digestive Endoscopy, Fondazione Poliambulanza, Brescia, Italy

Francesco Di Pierro

23. Department of Infectious Diseases and Public Health, City University of Hong Kong, Kowloon Tong, Hong Kong

Nikolaus Osterrieder

24. Department of Medicine, Division of Infectious Diseases, Icahn School of Medicine at Mount Sinai, New York, NY, USA

Adolfo García-Sastre

25. The Tisch Cancer Institute, Icahn School of Medicine at Mount Sinai, New York, NY, USA

Adolfo García-Sastre

26. The Molecular Biology of Metabolism Laboratory, The Francis Crick Institute, London, UK

Markus Ralser

27. Center for Digital Health, Charité - Universitätsmedizin and Berlin Institute of Health (BIH), Berlin, Germany

Roland Eils

Contributions

S.L., Y.Y., F.B., M. Mairhofer, D.B., S. Kaltenbrunner, A.L., M. Schönlein, M. Reimann and D.N.Y.F. outlined and performed the molecular genetic,

biochemical and cell biological experiments in cell lines, primary human and hamster material. J. Trimpert, J.M.A. and N.O. conceptualized and conducted the hamster experiments. P.R.-P. carried out the bioinformatics analyses. E.W., M.L. and R.E. conceptualized and generated the scRNA-seq data. M.P., S. Kunz, B.P., R.M. and R.L. analysed the tissue specimens from patients with COVID-19 and healthy donors. L.K., M. Mairhofer and J. Tomasits conceptualized and conducted the clotting-related experiments. T.C.F., K.D., E.G.M. and A.D.G. analysed the histopathology of hamster and mouse tissues. M. Schotsaert, C.M.-R., G.S., M.U. and A.G.-S. conceptualized and conducted the mouse experiments. D.N. and C.D. enabled SARS-CoV-2 infections of human cells and contributed to the experimental design. R.G., H.J.F.S. and B.L. provided clinical insights and blood samples from patients with COVID-19. C.P. and A.H. processed blood samples and carried out SARS-CoV-2 PCR testing. M. Mülleider and M. Ralser conducted the proteome data analysis and interpretation. S. Kimeswenger and W.H. contributed conceptual input and logistical support regarding specimen collection and virus-based experiments. A.K. and F.D.P. designed and conducted clinical trials on quercetin in patients with COVID-19. H.S. provided neutralizing antibodies targeting the spike protein of the SARS-CoV-2 virus and gave experimental recommendations in this regard. S.L. and C.A.S. designed the project, supervised the data analysis and wrote the manuscript.

Corresponding author

Correspondence to [Clemens A. Schmitt](#).

Ethics declarations

Competing interests

M.U. contributed to this Article as an employee of Mount Sinai and the views expressed do not necessarily represent the views of Regeneron Pharmaceuticals. F.D.P. is a member of the Scientific Board of Pharmextracta, the vendor of Quevir, a dietary supplement containing quercetin in a sunflower lecithin formulation. The laboratory of A.G.-S. has

received research support from Pfizer, Senhwa Biosciences, Kenall Manufacturing, Avimex, Johnson & Johnson, Dynavax, 7Hills Pharma, Pharmamar, ImmunityBio, Accurius, Nanocomposix, and Merck. A.G.-S. has consulting agreements with the following companies involving cash and/or stock: Vivaldi Biosciences, Contraflect, 7Hills Pharma, Avimex, Vaxalto, Pagoda, Accurius, Esperovax, Farmak, and Pfizer. A.G.-S. is an inventor on patents and patent applications on the use of antivirals and vaccines for the treatment and prevention of virus infections owned by the Icahn School of Medicine at Mount Sinai, New York. C.A.S. received travel support, honoraria and consulting fees from Abbvie, AstraZeneca, Bayer, Bristol-Myers Squibb/Celgene, Gilead/Kite, Janssen-Cilag, MSD, Novartis, Octapharma, Pierre Fabre, Roche, Sanofi, Takeda and TissUse.

Additional information

Peer review information *Nature* thanks Jesus Gill, Stanley Perlman and David Sinclair for their contribution to the peer review of this work. Peer review reports are available.

Publisher's note Springer Nature remains neutral with regard to jurisdictional claims in published maps and institutional affiliations.

Extended data figures and tables

[Extended Data Fig. 1 Additional biological properties of retroviral VIS.](#)

a, SA- β -gal staining, SAHF formation by DAPI, and p16^{INK4A} staining of HDFs (Tig3 and WI38) five days after retroviral infection or mock control. Representative photomicrographs of $n = 3$ independent experiments. **b**, Gene set enrichment analysis (GSEA) of virus infection-relevant GO terms probing RNA-seq datasets of WI38 HDF in VIS and OIS. Positive normalized enrichment scores (NES) indicate enrichment in VIS (dark grey bars) or OIS (light grey bars) compared to proliferating counterparts (mock infection for VIS, or empty vector control for OIS). NES with FDR $q \leq 0.1$ are considered statistically significant and presented (for individual q -

values, see [Supplementary Information](#)); $n = 3$ biological replicates each. **c**, Gene expression analysis for core senescence and SASP genes by RT-qPCR in WI38 and Tig3 as in **a**. Mean relative transcript level compared to mock control + s.d. of $n = 3$ independent experiments are shown. **d**, Growth curve analyses of HDF infected with retrovirus at different MOI as indicated, showing that high-titer virus induced VIS, reflected by stable cell numbers over time, while lower virus titer remained compatible with exponential cell growth. $n = 3$ independent experiments are presented as mean cell numbers \pm s.d. **e**, SA- β -gal staining (left) and gene expression analysis of the indicated transcripts by RT-qPCR (right) in wild-type (WT) or senescence-defective $p53^{-/-}$ MEF, five days after infection with high-titer retrovirus or mock as a control. Representative photomicrographs with fractions of SA- β -gal-positive cells, and mean relative transcript levels normalized to mock control \pm s.d. of $n = 4$ independent experiments are shown. **f**, Gene expression analysis of the indicated transcripts by RT-qPCR in IMR90 cells expressing JMJD2C, $p53$ shRNA (*shp53*), or control vector as in Fig. [1e](#). **g**, Multiplex bead-based protein analysis of SN of senescence-incapable IMR90 as in Fig. [1e](#). $SN_{mock} = SN$ of mock-infected cells; $SN_{virus} = SN$ of retrovirus-infected cells. Mean expression levels of $n = 3$ biological replicates are shown. **h**, cGAS/STING activation upon viral infection, as evidenced by a higher induction of cyclic guanosine monophosphate-adenosine monophosphate (2'3'-cGAMP) by ELISA analysis in matched pairs of HDF after either mock or retrovirus infection (mean of $n = 4$ independent experiments for each cell line, upper panel). Mean cGAMP levels + s.d. for senescence-incapable IMR90 as in Fig. [1e](#) ($n = 4$ independent experiments, lower panel). **i**, SA- β -gal staining of IMR90 cells, treated with reverse transcriptase inhibitor azidothymidine Zidovudine (50 μ M), cGAS inhibitor G150 (5 μ M), STING inhibitor H-151 (1 μ M), or DMSO. Mock infection and DMSO solvent treatment as negative controls. Representative photomicrographs and quantification of positively stained cells as mean \pm s.d. of $n = 3$ independent experiments are shown. **j**, 2'3'-cGAMP ELISA analysis of VIS IMR90 cells as in **i**.

[Extended Data Fig. 2 Additional biological properties of VIS exerted by a variety of viruses.](#)

a, SA- β -gal staining in human cell lines (RPE1, A549) infected with AAV, lentivirus, HCoV-NL63, and VSV as in Fig. 1g. **b**, SA- β -gal staining of human primary bronchial or nasal epithelial cells (HBEpC and HNEpC, respectively) infected with HCoV-NL63 and VSV. Mock infected cells as negative control. Quantification of positive cells for $n = 3$ independent experiments is shown as mean \pm s.d.; scale bar = 100 μ m. **c**, Quantification result of SA- β -gal-positive cells (RPE1, A549) after lentiviral infection at MOI as indicated are shown as mean percentage \pm s.d. for $n = 3$ independent experiments. Note that MOI 50 was chosen for VIS induction. **d**, Quantification result of SA- β -gal-positive RPE1 cells after infection with VSV- Δ G*-CoV-S or VSV- Δ G*-CoV-2-S at MOI as indicated are shown as mean percentage \pm s.d. for $n = 3$ independent experiments. Note that MOI 10 was chosen for VIS induction. **e**, SA- β -gal staining in human cell lines (RPE1, A549) and primary HNEpC infected with VSV- Δ G*-CoV-S, VSV- Δ G*-CoV-2-S, or VSV- Δ G*/empty vector (VSV- Δ G*-emp) as in Fig. 1g. NIH3T3 as ACE2-negative, infection-resistant control. **f**, Fluorescence detection of ROS in IMR90 after infection with retrovirus or VSV and treatment with NAC as indicated (upper panels). SA- β -gal staining and quantification of corresponding samples (lower panels). Mock infection or solvent treatment controls (UT) are shown. Representative photomicrographs and quantification are shown as mean percentages \pm s.d. for $n = 3$ independent experiments. Scale bar for ROS and SA- β -gal = 100 μ m; for γ H2A.X (insets; pink dots reflect foci) 5 μ m. **g**, Quantification of γ H2A.X-positive IMR90 cells as in f. $n = 3$ independent experiments is shown as mean \pm s.d. **h**, 2'3'-cGAMP ELISA analysis of IMR90 infected and treated with GS-441524 as in g. $n = 8$ independent experiments is shown as mean \pm s.d. **i**, Viral RNA detection in the supernatant of primary nasal epithelial cells with exogenous hACE2 expression (HNEpC-hACE2) infected with SARS-CoV-2, at the indicated time-points. p53 shRNA (*shp53*) renders cells senescence-incapable, but, unlike treatment with 10 μ M GS-441524 (GS), does not block viral replication. Data are shown as mean values \pm s.d. for $n = 3$ independent experiments. **j**, Relative viability of the indicated conditions, each compared to the corresponding untreated (UT) control of SARS-CoV-2-infected or mock-infected cells as in i, 72 h after infection. Data are shown as mean values \pm s.d. for $n = 3$ independent experiments. **k**, GSEA probing selected senescence-related gene sets⁶⁶ by RNA-seq (GSE147507) analysis of NHBE, Calu-3, and A549 cells infected

with SARS-CoV-2, compared to corresponding mock-infected controls. Positive NES indicates enrichment in virus-infected cells (dark grey bars), negative NES indicates downregulation in virus-infected cells (light grey bars). NES of FDR $q < 0.05$ are considered statistically significant and presented (for individual q -values, see [Supplementary Information](#)). Biological replicates comprise $n = 7$ control and $n = 3$ infected regarding NHBE, $n = 3$ for each condition regarding Calu-3, and $n = 5$ control and $n = 3$ infected regarding A549.

Extended Data Fig. 3 Vignettes of VIS in human COVID-19 lung specimens.

a, IHA of senescence markers in autopsy lung specimens from individuals without COVID-19 (non-COVID-19; with no obvious airway pathology) *vs.* patients with SARS-CoV-2-PCR-proven COVID-19. Representative photomicrographs and quantification of affected area as mean percentages of positive cells \pm s.d. or mean percentage of positive area \pm s.d (only for lipofuscin) of patients with COVID-19 (lipofuscin, p21^{CIP1}, H3K9me3, *BCL2L2*, $n = 5$; IL-8, $n = 9$; SARS-CoV-2 RNA, $n = 4$) and individuals without COVID-19 ($n = 2$). Note that *in situ* hybridization of SARS-CoV-2 RNA was occasionally, but not consistently positive in COVID-19 samples at autopsy (2/4). Scale bars represent 50 μ m. **b**, scRNA-sequencing-based expression analysis of *CDKN2A* and targets of navitoclax (*BCL2L1* and *BCL2L2*) in bronchiolar protected specimen brushes (PS), and bronchoalveolar lavages (BL) of patients with COVID-19 with critical course of the disease ($n = 4$). UMAPs of cell types (top). Orange color code marks cells expressing *CDKN2A*, purple *BCL2L1* (lower left) or *BCL2L2* (lower right), and red for both. **c**, Gene expression profile (GEP) indicating elevated transcript expression of cytokines and markers related to M1 macrophage polarization and activation^{32,33} by oligonucleotide-based transcript hybridization of lung specimens as in **a** ($n = 3$ each). **d**, CD62/P-selectin-marked platelet activation by flow cytometry in whole blood samples of healthy donors ($n = 7$) or COVID-19 patients ($n = 10$). Mean \pm s.d. with individual values as dots. * $p = 0.0368$ by unpaired t-test (two-tailed). **e**, Volcano plot of proteins differentially ($p < 0.05$) expressed in COVID-19 patient serum; SASP factor SERPINA3⁶⁷ highlighted in red as presented in Fig. 2g. Combined clinical COVID-19 severity WHO grade 3

and grade 4 ($n = 86$ patients) vs. grade 7 ($n = 52$ patients) are compared. The \log_2 -transformed fold changes are plotted against \log_{10} adjusted (Benjamini-Hochberg) p -values. Vertical red lines indicate \log_2 -transformed fold change cutoffs $-0.5/0.5$, horizontal red line indicates a significance cutoff $p = 0.05$. Analysis was performed using the DEqMS software package. **f**, Scatter plot showing average level of 16 SASP factors measured as in Fig. 2e and fibrinogen concentration in the serum (y-axis) of the same individual patients. $n = 3$ severe, $n = 5$ moderate, and $n = 18$ mild COVID-19 patients and healthy control ($n = 6$) are shown as color-coded dots. Correlation coefficient (Pearson) $r = 0.4139$ with $p = 0.0103$. **g**, Expression levels of senescence-related transcripts (gene sets: Reactome_SASP and SASP_Schleich⁶⁸) by oligonucleotide-based transcript hybridization of nasopharyngeal and lung specimens of patients with COVID-19 ($n = 3$) separated by their histopathological microthrombosis status. Shown are genes with fold-change > 1.5 . **h**, Percentages of IL-8-positive cells in COVID-19 lung specimens as in a, now stratified by their microthrombosis status (positive, $n = 4$; negative $n = 5$), are shown as mean values + s.d.. $p = 0.0397$ by unpaired t-test (two-tailed).

Extended Data Fig. 4 Additional COVID-19-relevant biological features evoked by the VIS-associated secretome.

a, Percentage of CD13⁺ THP-1 macrophages exposed to SN from retroviral VIS vs. proliferating HDF as indicated and shown in Fig. 3a. $n = 3$ ($n = 4$ for medium control) independent experiments; shown are mean percentages + s.d. * $p = 0.0017$ for IMR90 and 0.0029 for WI38 by unpaired t-test (two-tailed). **b**, GSEA of SN_{VIS}-primed macrophages unveiled vignettes of senescence and inflammation in the CD86⁺ population by probing of selected senescence- or macrophage activation-related GO terms and gene sets^{66,68} in RNA-seq analyses of THP-1 macrophages incubated with IMR90 SN_{VIS} and sorted by CD86 expression status (as in Fig. 3c, left). $n = 2$ for each condition. Gene sets with FDR $q \leq 0.05$ are shown. **c**, SA- β -gal staining (left) and gene expression analysis by RT-qPCR (right) of HUVEC endothelial cells that entered secondary, paracrine senescence upon exposure to SN_{VIS} of WI38 as indicated. Representative photomicrographs

and quantification of $n = 3$ independent experiments; shown are mean percentages \pm s.d. Relative expression levels of core senescence-related transcripts (left panel) and SASP transcripts (right panel) are shown as mean values \pm s.d.

Extended Data Fig. 5 Targets of senolytic drugs are induced after viral infection and render VIS cells sensitive to senolytics.

a, Gene expression analysis of BCL2 family transcripts by RT-qPCR in VIS HDF, with mock infection as a control, as indicated. $n = 3$ independent experiments for each cell line and infection. **b**, STITCH plot showing interactions between senolytic drugs (navitoclax, fisetin, dasatinib, quercetin) and their potential targets. Protein-protein interactions are shown in grey, chemical-protein interactions in green and interactions between chemicals in red. Modified from <http://stitch.embl.de>. Note that all senolytics shown are working in close proximity and have overlapping targets at the level of kinase networks and BCL2-family members. **c**, Relative viability of proliferating or VIS (retrovirus) WI38 and Tig3 HDFs as in Extended Data Fig. [1a](#), 24 h after treatment with 1 μ M venetoclax, 1 μ M navitoclax, or solvent-only (DMSO). $n = 3$ independent experiments. **d**, Relative viability of senescence-incapable IMR90 cells (as in Fig. [1e](#), [4b](#)) infected with VSV, and 24 h after treatment with 1 μ M venetoclax, 1 μ M navitoclax, 20 μ M fisetin, 20 μ M D/Q or solvent-only (DMSO). $n = 3$ independent experiments. **e**, Relative viability of proliferating or VIS IMR90 HDF compared to solvent-only (DMSO) control, two days after treatments with 1 μ M navitoclax, 1 μ M MCL1 inhibitor AT101, or both. Results shown as mean relative viability \pm s.d. for $n = 3$ independent experiments. Of note, strongly MCL-1-expressing IMR90 VIS cells (see Fig. [4a](#)) were not more susceptible to combined treatment with navitoclax plus an MCL-1 inhibitor as compared to navitoclax alone. **f**, Secondary viral infectivity by SN transfer. Wild-type MEF that entered VIS in response to replication-competent VSV/GFP (or mock) were treated with 1 μ M navitoclax before transferring the SN to uninfected THP-1 macrophages, here used as an infectivity reporter line. SA- β -gal staining to illustrate VIS, and GFP detection to visualize VSV infection of MEF. Secondary infectivity was measured as the GFP-positive fraction of THP-1 cells exposed to SN from MEF after navitoclax or solvent-only treatment

(bar plot). Senescence-dependent killing of VIS MEF did not increase GFP-positive THP-1 cells, thereby demonstrating that non-assembled cytoplasmic virus material potentially released upon senolysis does not add to infectivity. $n = 3$ independent experiments. **g**, Secondary viral infectivity (% GFP) and relative viability (Rel. viability) of THP-1 cells after SN transfer from VSV- or mock-infected MEFs. Dilution of VIS SN as indicated below decreases secondary infection and increases viability. $n = 3$ independent experiments. **h**, Viability of HUVEC endothelial cells after exposure to human serum and SN of proliferating ($\text{SN}_{\text{prol.}}$) or VIS (SN_{VIS}) primary nasal epithelial cells (HNEpC-ACE2) as in Fig. 4f. $n = 3$ independent experiments. **i – l**, SARS-CoV-2 spike protein-pseudotyped VSV- ΔG^* /CoV-2-S system to probe VIS in response to spike protein-affecting mutations. **i**, SA- β -gal staining of human cell line RPE1 infected with VSV- ΔG^* -CoV-2-S (WT), VSV- ΔG^* -CoV-2-S variant B.1.1.7 (Alpha), VSV- ΔG^* -CoV-2-S variant B.1.351 (Beta), or mock infection as control. No obvious difference in the ability to drive VIS was detected. Representative photomicrographs and quantifications are shown as mean percentages \pm s.d. for $n = 3$ independent experiments. Scale bar represents 100 μm . **j**, CD86-marked activation of THP-1 cells exposed to SN of RPE1 cells in VIS after infection with VSV- ΔG^* pseudotypes as indicated, or mock infection, as in **i**. Fractions of CD86 $^+$ cells relative to mock are shown. SN of cells infected with either mutant- or wild-type-pseudotyped virus equally enhance the fraction of CD86 $^+$ THP-1 cells. $n = 3$ independent experiments. **k**, Viability of cells as in **i**, after senolytic treatments as indicated. $n = 3$ independent experiments. All senolytic regimens, navitoclax, fisetin and D/Q proved equally effective in selectively eliminating VIS cells induced by the wild-type or the alpha or beta mutants. **l**, Gene expression analysis of senescence-related genes by RT-qPCR in RPE1 cells as in **i**. While transcript profiles of cell-autonomous senescence markers and pro-coagulatory SASP factors were similar between wild-type and mutants, pro-inflammatory cytokines and extracellular matrix-active factors appeared to be significantly higher expressed in the two mutant scenarios compared to wild-type. $n = 3$ independent experiments. All bar plots in this figure show mean results \pm s.d. with individual values as dots.
 $*p < 0.05$ by unpaired t-test (two-tailed) in all panels of this figure.

Extended Data Fig. 6 Senolysis as a novel treatment concept in the COVID-19 golden hamster model.

a, scRNA-seq-based expression analysis of viral RNA and senescence-associated genes in SARS-CoV-2-infected Syrian golden hamster lungs ($n = 3$ per time-point). UMAPs of cell types (top left, cell types of special interest in red), core senescence genes (top right), *Cdkn2a* (bottom left), SASP genes (bottom second from left), and *Src* (bottom right) on the indicated day after infection.; orange color code marks cells expressing senescence-associated genes, purple viral RNA, and red both. **b**, scRNA-seq-based expression analysis of *Bcl-w*, *Bcl2* and *Mcl1* transcripts in the indicated cell types in SARS-CoV-2-infected Syrian golden hamster lungs ($n = 3$ per time-point) at the indicated days after infection.; average-scaled (z-scores) expression levels are shown in color code. Note that *Bcl-2* and *M-1* transcript levels followed no clear trend, while *Bcl-w* transcripts were induced at day 5 after infection in all cell types presented. **c**, Daily body weight assessment of Syrian golden hamsters infected with SARS-CoV-2 (or uninfected healthy controls), and subsequently treated with navitoclax or solvent-only as in Fig. 5a. $n = 5$ each for SARS-CoV-2-infected solvent-only- and navitoclax-treated animals; $n = 3$ for the healthy control group. **d**, Number of platelets per 500 erythrocytes in blood smears of golden hamsters infected with SARS-CoV-2 and treated as in c, on day 7 after infection. Mean counts \pm s.d. of $n = 5$ hamsters per treatment group. $*p = 0.0127$ by unpaired t-test (two-tailed). Note for c and d: Although the navitoclax group presented with relative weight loss of around nine percent and a reduction of nearly 40% of the initial thrombocyte concentration compared to the infection-only group at the end of therapy, a prominent adverse effect of navitoclax, no obvious external or internal signs of enhanced hemorrhage was observed. **e**, Transmission electron microscopy analysis of trachea epithelial cells from hamsters as in b and c. In infected and solvent treated animals (with the enlarged photomicrograph of a nucleus on the right), ciliated epithelial cells show senescent features as dilated endoplasmic reticulum (*), disrupted and dilated nuclear envelope (N = nucleus), vacuolization and altered mitochondria. Scale bar = 1 μ m. $n = 4$ for SARS-CoV-2 infected groups and $n = 3$ for the mock infection group. **f**, Representative photomicrographs of H/E-stained lung tissue of Syrian golden hamsters as in Fig. 5a and c–e at day 7 after infection.. Lung

sections for overview (i, v, ix) with active inflammation (arrow), signs of necrosis (inset, arrowhead), and hyperplasia (arrowheads) of alveolar epithelial cells (AEC) II (ii, vi). Vascular endothelialitis (iii, vii) with sloughing of endothelial cells (arrow), and subendothelial infiltration by lymphocytes (arrowhead). Regeneration of bronchial epithelium (iv, viii; double-headed arrow). Lung of mock-infected, untreated animals as control (ix, x, xi, xii). General signs of inflammation and AEC II hyperplasia in the navitoclax group were rather similar to untreated animals. while the navitoclax group presented with a less extensive patchy pneumonia pattern when compared to the solvent-only group (compare f-v to f-i). $n = 5$ each for SARS-CoV-2-infected solvent-only- and navitoclax-treated animals. $n = 3$ for the healthy control group. Scale bars in i, v, ix = 1 mm, ii-iv, vi-viii, x-xii = 50 μ m, insets ii, vi, x = 20 μ m. **g**, Quantification of the findings shown in f. * $p = 0.0042$ by unpaired t-test (two-tailed). **h**, Multiplex bead-based protein analysis of golden hamster serum samples at day 7 after infection.; hamsters as in **c-g**. All bar plots in this figure show mean results + s.d. with individual values as dots.

Extended Data Fig. 7 Senolysis as a novel treatment concept in COVID-19 in additional animal models.

a, Daily body weight assessment of dwarf hamsters and *K18-hACE2* mice infected with SARS-CoV-2 (or uninfected healthy controls), and subsequently treated with senolytics as in **b-e** and Fig. [5b-e](#). Dwarf hamsters: $n = 5$ each for SARS-CoV-2-infected solvent-only-, navitoclax- or D/Q-treated; $n = 2$ for the healthy control group. *K18-hACE2*-transgenic mice: $n = 5$ for solvent, navitoclax, and D/Q; $n = 4$ for fisetin. **b**, Survival rate of *K18-hACE2*-transgenic mice on day 6d after infection with SARS-CoV-2 and subsequent senolytic treatment as in **a**. **c**, Histological scoring of H/E-stained lung tissue of *K18-hACE2* mice as in **a** and **b**. **d**, Viral load in hamster and mouse tissues on day 6 (mouse, as in **a-c**), day 7 (golden hamster, as in Fig. [5a](#) and Extended Data Fig [6](#)), and day 4 (dwarf hamster, as in Fig. [5b-e](#)) after infection. **e**, IHA of senescence markers ($p16^{INK4A}$, H3K9me3) and lipofuscin-staining in lung specimens of *K18-hACE2*-transgenic mice as in **a-d**. All bar plots in this figure show mean results + s.d. with individual values as dots.

Extended Data Fig. 8 Senolysis as a novel treatment concept in COVID-19 patients.

a, Frequency (bars) and risk (odds ratio) of COVID-19 patients to be hospitalized or in need of oxygen support after either standard care (SC) or quercetin plus standard care (Quercetin). $n = 97$ for each group, based on two randomized trials combined and re-analysed here^{51,52}. **b**, Days of hospitalization (left) of COVID-19 patients (left; * $p < 0.0001$ by unpaired t-test, two-tailed), the fraction of patients admitted to the intensive care unit (ICU; middle) or deceased in the course of the disease (right). Note that there was no patient in ICU or deceased in the quercetin group. Patients as in **a**; $n = 97$ for each group.

Extended Data Table 1 Histological scoring of COVID-19 features in the SARS-CoV-2-infected hamsters

Extended Data Table 2 Input data for Figure 5f

Supplementary information

Supplementary Information

This file contains details of the experimental procedures, Supplementary Tables 1 and 2, Supplementary References and Supplementary Figs. 1 and 2.

Reporting Summary

Peer Review File

Rights and permissions

Reprints and Permissions

About this article

Cite this article

Lee, S., Yu, Y., Trimpert, J. *et al.* Virus-induced senescence is a driver and therapeutic target in COVID-19. *Nature* **599**, 283–289 (2021).
<https://doi.org/10.1038/s41586-021-03995-1>

- Received: 10 January 2021
- Accepted: 03 September 2021
- Published: 13 September 2021
- Issue Date: 11 November 2021
- DOI: <https://doi.org/10.1038/s41586-021-03995-1>

Share this article

Anyone you share the following link with will be able to read this content:

[Get shareable link](#)

Sorry, a shareable link is not currently available for this article.

[Copy to clipboard](#)

Provided by the Springer Nature SharedIt content-sharing initiative

This article was downloaded by **calibre** from <https://www.nature.com/articles/s41586-021-03995-1>

- Article
- [Published: 20 October 2021](#)

Shigella evades pyroptosis by arginine ADP-ribosylation of caspase-11

- [Zilin Li](#) ORCID: orcid.org/0000-0003-3410-8231^{1,2},
- [Wang Liu](#)^{1,2},
- [Jiaqi Fu](#)³,
- [Sen Cheng](#)^{2,3},
- [Yue Xu](#)^{1,2},
- [Zhiqiang Wang](#)²,
- [Xiaofan Liu](#)²,
- [Xuyan Shi](#)²,
- [Yixin Liu](#)²,
- [Xiangbing Qi](#) ORCID: orcid.org/0000-0002-7139-5164²,
- [Xiaoyun Liu](#) ORCID: orcid.org/0001-7083-5263^{3,4},
- [Jingjin Ding](#)^{2,5} &
- [Feng Shao](#) ORCID: orcid.org/0000-0002-9562-7791^{1,2,5,6}

Nature volume 599, pages 290–295 (2021)

- 10k Accesses
- 32 Altmetric
- [Metrics details](#)

Subjects

- [Cell death and immune response](#)
- [Pathogens](#)
- [Post-translational modifications](#)

Abstract

Mouse caspase-11 and human caspase-4 and caspase-5 recognize cytosolic lipopolysaccharide (LPS) to induce pyroptosis by cleaving the pore-forming protein GSDMD^{1,2,3,4,5}. This non-canonical inflammasome defends against Gram-negative bacteria^{6,7}. *Shigella flexneri*, which causes bacillary dysentery, lives freely within the host cytosol where these caspases reside. However, the role of caspase-11-mediated pyroptosis in *S. flexneri* infection is unknown. Here we show that caspase-11 did not protect mice from *S. flexneri* infection, in contrast to infection with another cytosolic bacterium, *Burkholderia thailandensis*⁸. *S. flexneri* evaded pyroptosis mediated by caspase-11 or caspase 4 (hereafter referred to as caspase-11/4) using a type III secretion system (T3SS) effector, OspC3. OspC3, but not its paralogues OspC1 and 2, covalently modified caspase-11/4; although it used the NAD⁺ donor, this modification was not ADP-ribosylation. Biochemical dissections uncovered an ADP-riboxanation modification on Arg314 and Arg310 in caspase-4 and caspase-11, respectively. The enzymatic activity was shared by OspC1 and 2, whose ankyrin-repeat domains, unlike that of OspC3, could not recognize caspase-11/4. ADP-riboxanation of the arginine blocked autoprocessing of caspase-4/11 as well as their recognition and cleavage of GSDMD. ADP-riboxanation of caspase-11 paralysed pyroptosis-mediated defence in *Shigella*-infected mice and mutation of *ospC3* stimulated caspase-11- and GSDMD-dependent anti-*Shigella* humoral immunity, generating a vaccine-like protective effect. Our study establishes ADP-riboxanation of arginine as a bacterial virulence mechanism that prevents LPS-induced pyroptosis.

[Download PDF](#)

Main

Intracellular *S. flexneri* infection causes shigellosis in humans. Although most intracellular bacteria reside in vacuoles, *S. flexneri*, like *Burkholderia* spp., live freely in the host cytosol, inevitably exposing their LPS to caspase-11/4. Wild-type (WT) mice, unlike *Casp11*^{-/-} mice, survived *B. thailandensis* infection⁸ (Fig. 1a, Extended Data Fig. 1a). Mice are increasingly being used as a surrogate host for *S. flexneri*. Unexpectedly, both WT and *Casp11*^{-/-} mice succumbed to lethal *S. flexneri* infection (Fig. 1a) and tolerated similarly the low-dose challenge (Extended Data Fig. 1a). Given the absence of caspase-11-mediated protection, we assayed non-canonical inflammasome activation upon *S. flexneri* infection. *Casp1*^{-/-} immortalized bone marrow-derived macrophages (iBMDMs) were used to avoid interference by the canonical inflammasome. Although *B. thailandensis* and *S. Typhimurium* Δ *sisfA* induced *Casp11*-dependent GSDMD cleavage and pyroptosis⁸, *S. flexneri* triggered little pyroptosis (Fig. 1b) despite a higher infection efficiency (Extended Data Fig. 1b). In epithelium-derived human SiHa and A431 cells, *S. flexneri*, unlike *S. Typhimurium* Δ *sisfA*, also did not activate the caspase-4–GSDMD pyroptosis pathway (Fig. 1b,

Extended Data Fig. 1c, d). Purified LPS from *S. flexneri* was highly pro-pyroptotic (Extended Data Fig. 1e). Thus, *S. flexneri* evaded caspase-11/4-mediated pyroptosis.

Fig. 1: *S. flexneri* blocks cytosolic LPS-induced pyroptosis through OspC3.

 figure1

a, Survival curves of WT or *Casp11*^{-/-} mice intraperitoneally infected with *S. flexneri* or *B. thailandensis* (2×10^7 CFU per mouse); two-tailed log-rank (Mantel–Cox) test. **b, c**, Indicated SiHa cells or iBMDMs were infected with *S. flexneri* (S.f., WT or an *ospC3* deletion/complementation strain), *B. thailandensis* (B.t.) or *S. Typhimurium* (S.T.) *ΔsifA*. LDH release-based cell death data are means (bars) of three individual replicates (circles). Cell supernatants were blotted with anti-cleaved GSDMD-C antibody. Data are representative of two (a) or three (b, c) independent experiments. For gel source data, see [Supplementary Fig. 1](#).

[Source data](#)

The guanylate-binding protein (GBP) family promotes the release of LPS from intracellular bacteria and its presentation to caspase-11/4 (refs. 9,10). IpaH9.8, a *Shigella* ubiquitin-ligase T3SS effector, targets multiple GBPs for degradation^{11,12,13,14}. A 2013 report proposed that *S. flexneri* uses the T3SS effector OspC3 to target caspase-4 but, notably, not caspase-11 (ref. 15). We examined whether IpaH9.8, OspC3 or another factor underlies evasion of pyroptosis by *S. flexneri* using SiHa, A431 and iBMDM cells (Fig. 1c, Extended Data Fig. 1d, f, g). Infection with *ΔipaH9.8*, compared to WT bacteria, caused negligibly increased pyroptosis. By contrast, *ΔospC3* induced extensive pyroptosis with evident GSDMD cleavage, which was diminished by re-expression of OspC3 in the bacteria or deletion of *CASP4/11* deletion in the host cells. Deletion of all seven GBPs from A431 cells affected pyroptosis during early but not late infection (Extended Data Fig. 1h). This is consistent with the notion that GBPs, having little LPS-binding activity (Extended Data Fig. 1i), are not absolutely required for bacteria-induced caspase-4 activation. Thus, *S. flexneri* requires OspC3 to evade LPS-stimulated pyroptosis.

OspC3 expression in host cells blocked the induction of pyroptosis by *S. flexneri* *ΔospC3*, *S. Typhimurium* and even LPS alone (Extended Data Fig. 1j), suggesting that

it has a bacteria-independent function. OspC3 co-immunoprecipitated with the p20/p10 form of caspase-4(C258A) (protease-deficient; C/A hereafter) in 293T cells (Extended Data Fig. [2a](#)). The interaction did not cause p20–p10 dissociation, in contrast to earlier findings^{[15](#)}. OspC3 also co-immunoprecipitated with inactive p20- and-p10-unprocessed caspase-4/11 (Fig. [2a](#), Extended Data Fig. [2b](#)). OspC3 did not affect the proteolytic activity of caspase-4/11-p20/p10 (Extended Data Fig. [2c–e](#)). Purified OspC3 also did not inhibit LPS-induced activation of pro-caspase-4 to cleave GSDMD, but it blocked pyroptosis when electroporated into cells (Extended Data Fig. [2f,g](#)). Thus, hijacking of caspase-4/11 by OspC3 involves a cell-dependent mechanism.

Fig. 2: OspC3 catalyses an NAD⁺-dependent modification of caspase-4/11.



a, b, Co-immunoprecipitation of caspase-4/11-p30-C/A with OspC3 and modification of caspase-4-p20/p10 by OspC3 in 293T cells. **c–e**, Caspase-4/11-p30-C/A, expressed alone or with OspC3 in bacteria (**c, d**) or reacted with OspC3 with or without NAD⁺ in vitro (**e**), was analysed by native/SDS-PAGE (**c, e**) or ESI-MS (**d**). Control, OspC3-modified caspase-4-p30-C/A. **f**, *CASP4*^{−/−} HeLa cells expressing Flag–caspase-4-p30-C/A were infected as indicated. Anti-Flag immunoprecipitates were analysed as shown. Data are representative of three (**a–e**) or two (**f**) independent experiments. For gel source data, see Supplementary Fig. 1.

In 293T cells, OspC3 induced slower migration of caspase-4-p10 on an SDS gel (Fig. 2b, Extended Data Fig. 2a). Caspase-4/11-p30, co-expressed with OspC3 in *Escherichia coli*, exhibited a marked shift on a native gel (Fig. 2c), indicating a post-translational modification (PTM). Electrospray ionization–mass spectrometry (ESI–MS) identified a 524-Da modification, which was located to $_{314}\text{RDSTMGSIF}_{322}$ within caspase-4-p10 by collision-induced dissociation (CID)–MS (Fig. 2d, Extended Data Fig. 2h,i). MS/MS detected fragment ions with mass-to-charge ratios of 136.06, 348.07 and 428.04, matching the mass of adenine, AMP and ADP, respectively (Extended Data Fig. 2j). This reminded us of ADP-ribosylation, in which ADP-ribose (ADPR) from nicotinamide adenine dinucleotide (NAD⁺) is usually transferred to serine, arginine, asparagine, aspartate, glutamate or glutamine. Although the OspC3-induced PTM is 17 Da smaller than ADP-ribosylation, NAD⁺ enabled recombinant OspC3 to modify caspase-4/11-p30 by 524 Da (Fig. 2e, Extended Data Fig. 2k,l). In *S. flexneri* infection, the $_{314}\text{RDSTMGSIF}_{322}$ peptide and the corresponding caspase-11 peptide showed the 524-Da modification in an *ospC3*-dependent manner (Extended Data Fig. 2m). Consistently, caspase-4-p30-C/A from cells infected with WT *S. flexneri* but not ΔospC3 had a mobility shift similar to that in the in vitro assay (Fig. 2f). Thus, OspC3 catalyses an NAD⁺-mediated PTM on caspase-4/11.

Electron-transfer/higher-energy collision dissociation (EThcD)–MS showed that Arg314 and Arg310 in caspase-4 and -11, respectively, harboured the modification (Fig. 3a, Extended Data Fig. 3a). Replacing these residues with lysine or asparagine abolished the modification (Fig. 3b, Extended Data Fig. 3b–e). Quantitative high-performance liquid chromatography (HPLC)–MS analyses of the reaction (Extended Data Fig. 4a) revealed that one molecule of free nicotinamide (Nam) was released upon modification of one molecule of caspase-4 by one molecule of NAD⁺. Thus, the OspC3-catalysed PTM may contain an initial ADP-ribosylation and an additional 17-Da mass reduction reaction.

Fig. 3: OspC3 catalyses ADP-riboxanation on an arginine in caspase-4/11.

 **figure3**

a, EThcD–tandem mass spectrum of the Arg314-containing peptide from OspC3-modified caspase-4-p30-C/A in bacteria. **b**, Caspase-4-p30-C/A was reacted with OspC3 with or without NAD⁺, followed by native/SDS-PAGE analyses. **c**, Mass changes of OspC3-modified caspase-4-p30 by NAD⁺ analogues. **d**, OspC3-induced mass changes on caspase-4 Arg314-containing peptide from normal or ¹³C₆, ¹⁵N₄-labeled arginine–labelled 293T cells. **e**, Quantification of release of ammonia/ammonium from the OspC3-modification reaction; data are means (bars) of three individual replicates (circles). **f**, Caspase-4-p30-C/A was reacted with OspC3 and a ribosyl 2'-substituted NAD⁺ analogue. Control, OspC3-modified caspase-4-p30-C/A. **g**, Chemical structures of ADP-riboxanated and ADP-ribosylated arginine. Data are representative of three (**a–c**, **e**, **f**) or two (**d**) independent experiments. For gel source data, see Supplementary Fig. 1.

Source data

Fourteen NAD⁺ analogues or derivatives were assayed in OspC3 modification of caspase-4 (Extended Data Fig. 4b). NAD⁺ fragments (ADPR, cyclic-ADPR (cADPR) and nicotinamide mononucleotide (NMN)), α-NAD⁺, nicotinic acid adenine dinucleotide (NAAD⁺), nicotinamide adenine dinucleotide phosphate (NADP⁺) and NADPH were inactive. By contrast, NADH, thio-NAD⁺ and thio-NADH, altered in the Nam part, supported the 524-Da modification (Fig. 3c, Extended Data Fig. 4b,c). Deamino-NAD⁺, biotin-NAD⁺, ε-NAD⁺ or nicotinamide guanine dinucleotide (NGD⁺) allowed modifications that preserved the mass difference between the cognate analogue and NAD⁺. These confirm the transfer of ADPR to caspase-4/11 with Nam being the leaving group. Indeed, OspC3-modified caspase-4 was recognized by an anti-ADP-ribose antibody¹⁶ (Fig. 2f, Extended Data Fig. 4d).

NGD⁺-mediated modification also had a 17-Da mass reduction from the ‘GDP-ribosylation’. A non-specific pyrophosphohydrolase, NUDT16 (ref. 17), removed an AMP from OspC3-modified caspase-4 (Extended Data Fig. 4d,e). These data suggest that the 17-Da loss occurs on the phosphoribosylated arginine. We performed stable isotope labelling by amino acids in cell culture (SILAC), using ¹³C₆, ¹⁵N₄-l-arginine to label Flagcaspase-4-p20/p10 expressed alone or with OspC3 in 293T cells. MS detected a 523-Da (not 524-Da) increase on a caspase-4 Arg314-containing peptide (Fig. 3d, Extended Data Fig. 5a). The 1-Da change suggests that one N^ω atom in ADP-ribosylated arginine is removed via internal deamination, explaining the 17-Da reduction. Consistent with this, free NH₃/NH₄⁺ was detected in the modification reaction (Fig. 3e).

The above analyses predict that a nucleophile adjacent to the ADP-ribosylated arginine guanidino performs the deamination. Studies of ADP-ribosylation-based elimination¹⁸ suggest that the ribosyl-2'-OH could be a candidate nucleophile. β-2'-Deoxy-2'-H-NAD⁺ (2'-H-NAD⁺) and 2'-fluoro-NAD⁺ were assayed in the OspC3-catalysed modification (Extended Data Fig. 5b). 2'-Fluoro-NAD⁺, which is incompetent for canonical ADP-ribosylation¹⁹, could not support OspC3 modification of caspase-4. OspC3 could use 2'-H-NAD⁺; notably, the modification was merely the transfer of 2'-deoxy-ADPR without further deamination (Fig. 3f, Extended Data Fig. 5c). The remaining puzzle is the atom on which the initial ADP-ribosylation occurs. Both N^ω and N^δ in arginine can accept ADPR from NAD⁺. Ninhydrin could bond simultaneously with the two N^ω in native arginine, as noted with Arg314 in unmodified caspase-4 (Extended Data Fig. 5d,e). For canonical arginine N^ω-ADP-ribosylation (Rab4a by ExoS²⁰), the modified arginine resisted conjugation by ninhydrin (Extended Data Fig. 5f). For 2'-H-NAD⁺-mediated modification, the 2'-deoxy-ADP-ribosylated Arg314 could react with ninhydrin (Extended Data Fig. 5e). We propose that OspC3 modifies Arg314/Arg310 of caspase-4/11 by two steps (Extended Data Fig. 5g). First, the arginine N^δ (rather than N^ω) performs nucleophilic substitution of the Nam in NAD⁺. Second, the ribosyl-2'-OH of ADPR initiates a deamination to remove one N^ω, forming an oxazolidine ring. We designate this arginine ADP-2'-imine-ribofuran[1',2':4,5]oxazolidination modification as ADP-riboboxanation (Fig. 3g), catalysed by arginine ADP-riboboxanase activity in OspC3.

S. flexneri harbours *ospC1*, *ospC2* and a pseudogene *ospC4* in the *ospC3* locus. OspC1, OspC2 and OspC3 (>60% sequence identity; Extended Data Fig. 6a) share a C-terminal ankyrin-repeat domain (ARD) and an N-terminal (N) domain (Fig. 4a). Δ*ospC1* or Δ*ospC2* caused no increase in pyroptosis in infected cells (Extended Data Fig. 1f). OspC1/2 could not block cytosolic LPS-induced pyroptosis (Extended Data Fig. 6b). Purified OspC1/2 barely modified caspase-4 (Fig. 4b). Notably, the ARD of OspC3, but neither OspC1/2 nor their ARDs, readily co-immunoprecipitated with

caspase-4-p30 (Fig. 4c, Extended Data Fig. 6c). Replacing the ARD in OspC3 with that of OspC1/2 diminished its caspase-4-modification and pyroptosis-blocking activity (Fig. 4b, Extended Data Fig. 6b). Conversely, chimeric proteins with the OspC1/2 N-domain and OspC3 ARD were highly active. Thus, the ARD of OspC3 determines caspase-4/11 recognition; OspC1/2 use their ARDs to target other host proteins for ADP-ribosylation.

Fig. 4: Analyses of the OspC family and mechanisms of OspC3 inactivation of caspase-4/11.

 figure4

a, Domain structure of OspC3 (red, residues essential for its ADP-ribosylating activity). **b**, Caspase-4-p30-C/A was reacted with OspC or a chimeric OspC protein, followed by native/SDS-PAGE analyses. **c**, Co-immunoprecipitation of caspase-4-p30-C/A with the ARD of an OspC in 293T cells. **d**, **e**, Caspase-4-p30-C/A modified by OspC3 (WT or D177A) in vitro (**d**) or in *E. coli* (**e**) was analysed by native/SDS-PAGE or MS, respectively. **f**, Extracted ion chromatograms of the Arg314-containing peptide. **g**, **h**, Indicated SiHa or A431 cells expressing OspC3 or caspase-4 (WT or R314A) were electroporated with LPS or muramyl dipeptide (MDP). **g**, **h**, GSDMD was subjected to cleavage by an indicated form of caspase-4/11-p20/p10. Control (**b**, **d**), OspC3-modified caspase-4-p30-C/A. Data are representative of two (**e**, **f**) or three (**b–d**, **g**, **h**) independent experiments. For gel source data, see Supplementary Fig. 1.

Random mutagenesis identified Phe141, Phe186, Glu192, Glu326 and His328 in OspC3 (Fig. 4a, Extended Data Fig. 6a) as essential for ADP-ribosylating caspase-4/11 and blocking pyroptosis (Extended Data Fig. 6d–g). Another D177A mutation supported ADP-ribosylation but blocked subsequent deamination (Fig. 4d, e). Although OspC3(D177A)-modified caspase-4 was sensitive to ADP-ribosylarginine

hydrolase (ADPRH), WT OspC3-catalysed ADP-riboxanation resisted demodification by ADPRH and other known host ADP-ribosylhydrolases (Extended Data Fig. 6*h,i*). Thus, hijacking of caspase-4/11 by ADP-riboxanation is more advantageous to bacterial virulence.

OspC3 blocked LPS-induced caspase-4 autoprocessing (Fig. 4*f*). This was recapitulated by mutations of Arg314 that also inhibited infection or LPS-induced pyroptosis (Fig. 4*f*, Extended Data Fig. 7*a,b*). Mutations of Arg310 in caspase-11 had the same effect (Extended Data Fig. 7*c–e*). OspC3 could also ADP-riboxanate already activated caspase-4/11 (Fig. 2*b*); the modified caspase-4/11-p20/p10, like their Arg314/Arg310 mutants, failed to target GSDMD (Fig. 4*g,h*, Extended Data Fig. 7*f,g*) owing to structural interference with the GSDMD-binding exosite²¹. Arg314/Arg310, which are conserved in caspases (Extended Data Fig. 7*h*), coordinate substrate P1 aspartate; caspase-4/11-p20/p10 R314/R310 mutants could not cleave the peptide substrate (Extended Data Fig. 7*i*). Thus, ADP-riboxanation blocked caspase-4/11 activation and cleavage of their substrate.

We used the inactive OspC3 E192A/H328A mutant (EH/AA) (Extended Data Fig. 6*d–g*) and assessed the function of caspase-11 ADP-riboxanation in *Shigella* infection. WT mice survived *S. flexneri* ΔospC3 infection, and this effect was reversed by complementation with OspC3 WT but not the EH/AA mutant (Fig. 5*a*). Accordingly, mice infected with ΔospC3 alone or ΔospC3 expressing OspC3 EH/AA had lower bacterial burdens than mice infected with WT OspC3-expressing strain (Fig. 5*b*). Unlike WT mice, Casp11^{–/–} mice succumbed equally to *S. flexneri* WT and ΔospC3, which replicated to a similarly high level. Notably, *S. flexneri* ΔospC3-infected mice produced much more anti-*Shigella* IgG than WT bacteria-infected mice at the 10% LD₅₀-normalized dose (the burden of ΔospC3 was not higher than WT bacteria at 24 h after infection), but this effect was abolished in Casp11^{–/–} and Gsdmd^{–/–} mice (Fig. 5*c*, Extended Data Fig. 8*a*). ΔospC3-infected mice were more resistant to lethal *S. flexneri* re-infection, and this increased resistance was also absent in Casp11^{–/–} mice (Fig. 5*d*). Such effects occurred at multiple inoculation doses (Extended Data Fig. 8*b,c*). These findings suggest that caspase-11-mediated pyroptosis has an intrinsic function of activating humoral immunity and also highlight the importance of OspC3-catalysed ADP-riboxanation for evasion of caspase-11-mediated pyroptosis by *Shigella*.

Fig. 5: OspC3 underlies evasion by *Shigella* of pyroptosis-mediated defence that promotes anti-*Shigella* humoral immunity.

 **figure5**

a, b, WT and *Casp11*^{-/-} mice were infected intraperitoneally with *S. flexneri* WT or an *ospC3* deletion/complementation strain (2×10^7 CFU per mouse). **a**, Survival curves. Top, $n = 16$ for WT/WT and WT/ $\Delta ospC3$ + pOspC3, $n = 17$ for WT/ $\Delta ospC3$ and $n = 15$ for WT/ $\Delta ospC3$ + pOspC3-EH/AA. Bottom, $n = 6$ for all groups. **b**, Bacterial loads. $n = 5$ for *S. flexneri* WT-infected *Casp11*^{-/-} mice, $n = 7$ for *S. flexneri* $\Delta ospC3$ + pOspC3-infected WT mice and $n = 6$ for all other groups. **c–f**, Indicated mice were immunized with *S. flexneri* WT or $\Delta ospC3$ (1.2×10^6 and 4×10^6 CFU per mouse in WT mice, respectively (both 10% LD₅₀); both 2×10^6 CFU per mouse in *Casp11*^{-/-} and *Gsdmd*^{-/-} mice) (**c, d**) or other deletion strains (2×10^6 CFU per mouse) (**e, f**). **c, e**, Anti-*Shigella* antibody in the sera of immunized mice. **d, f**, Indicated immunized mice were re-challenged with WT *S. flexneri* (1.5×10^8 CFU per mouse in **d** and the upper panel of **f** and 1×10^8 CFU per mouse in the lower panel of **f**). **a, d, f**, Two-tailed log-rank (Mantel–Cox) test ($****P \leq 0.0001$, $***P \leq 0.001$, $**P \leq 0.01$). **b, c, e**, Median values, two-tailed Mann–Whitney *U*-test. All data are representative of two independent experiments.

Source data

Development of a *Shigella* vaccine has been challenging. $\Delta icsA$ and $\Delta guaBA$ mutants are being developed as live-attenuated vaccines²². Compared to $\Delta icsA$ and $\Delta guaBA$, *S. flexneri* $\Delta ospC3$ induced a higher level of anti-*Shigella* IgG (Extended Data Fig. 8d). Deletion of *ospC3* on either $\Delta icsA$ or $\Delta guaBA$ background further boosted antibody production and conferred better protection from WT *S. flexneri* re-challenge (Fig. 5e,f). The better immunization of $\Delta icsA\Delta ospC3$ over $\Delta icsA$ also occurred at

lower or higher inoculation doses in both C57BL/6 and BALB/c mice (Extended Data Fig. 8e–h). These findings are valuable for *Shigella* vaccine development, although with the limitation of the mouse model.

A BLAST search identified 27 OspC homologues in diverse bacteria, including *Vibrio*, *Salmonella*, *Erwinia* and *Chromobacterium* (Extended Data Fig. 9a). Homology of their catalytic domains and ARDs to those of OspC3 ranges from 99% to 56% and from 100% to 27%, respectively. Certain homologues readily ADP-ribosylate caspase-4/11 and blocked LPS-induced pyroptosis, and this effect was abolished by the corresponding EH/AA mutations (Extended Data Fig. 9b,c). For homologues that could not modify caspase-4/11, replacing their ARDs with that of OspC3 enabled the modification (Extended Data Fig. 9c). CopC from *Chromobacterium violaceum*, a deadly bacterium that causes hepatic abscesses in humans, could ADP-ribosylate caspase-4 and inhibit LPS-induced pyroptosis, less potently than OspC3 (Extended Data Fig. 10a–c). CopC could also modify caspase-4/11 during infections, and *C. violaceum* ΔcopC showed decreased replication in infected mouse liver (Extended Data Fig. 10d–f). Thus, OspC-like ADP-ribosylases are widely used by bacteria for various functions, including blocking pyroptosis.

In summary, *Shigella* uses OspC3 to modify caspase-11/4 and thereby thwart the inflammasome/pyroptosis-mediated defence. This differs from known bacterial inflammasome-modulating strategies that are self-alterations or indirect, such as inhibition of the Pyrin inflammasome by *Yersinia* YopM²³. Future studies will uncover other inflammasome/pyroptosis-targeting effectors. OspC3 catalyses arginine ADP-ribosylation; the activity is shared by the OspC family in bacteria. Arginine ADP-ribosylation might also exist in eukaryotes, and could be identified by mining ADP-ribosylome proteomic data.

Methods

No statistical methods were used to predetermine sample size. The experiments were not randomized, and investigators were not blinded to allocation during experiments and outcome assessment.

Plasmids, antibodies and reagents

DNAs for *ospC1*, *ospC2* and *ospC3* were amplified from *S. flexneri* 2a strain 2457T. DNA for *exoS* was amplified from *Pseudomonas aeruginosa* strain PAO1. DNA for *sdeA* was amplified from *Legionella pneumophila* strain Lp02. DNA for *copC* was amplified from the genomic DNA of *C. violaceum* strain 12472. Complementary DNA (cDNA) for NUDT16 was from an ORF library of Invitrogen (clone ID: IOH61424). cDNAs for human caspase-4, GSDMD, Rab4A, YWHAB and caspase-11 were

described previously^{2,24,25}. The DNAs were ligated into pCS2-Flag, pCS2-3×Flag, pCS2-3×Flag-GST, pCS2-3×HA, pLVX-3×Flag or FUIGW-Flag vectors for transient or stable expression in mammalian cells. For recombinant protein expression in *E. coli*, the DNAs were inserted into pGEX-6p-2, pET28a-6×His, pET28a-6×His-SUMO, pET21a, pACYCDuet-1, pQE-30 or pAC-SUMO (generated by replacing the replication origin of pET28a-6×His-SUMO with the p15A replicon derived from the pACYC vector). For complementation in the *S. flexneri* Δ*ospC3* strain, C-terminal Flag-tagged DNAs for *ospC3* and its mutants, together with its native promoter sequence, were cloned into the pET28a vector. The pSpCas9(BB)-2A-GFP plasmid (PX458) used for generating knockout cells was obtained from Addgene (48138). All truncations and point mutations were generated by the standard polymerase chain reaction (PCR) cloning method. All plasmids were verified by DNA sequencing.

Monoclonal antibodies against human GSDMD (ab210070/EPR19829), mouse GSDMD (ab219800/EPR20859), human cleaved GSDMD-C domain (ab227821/EPR20885-203)²¹ and mouse cleaved GSDMD-C domain (ab255603/EPR20859-147)²¹ were from Abcam. Antibodies against Flag (F3165/M2 and F7425/polyclonal) and tubulin (T5168/B-5-1-2) were from Sigma-Aldrich. The anti-HA antibody (3724/C29F4) was from Cell Signaling Technology, and rabbit Fc-fused mono-ADP-ribose binding reagent (MABE1076) was from Sigma-Aldrich. The monoclonal antibody for caspase-4 and polyclonal antibody for caspase-11 were generated by the in-house facility at the National Institute of Biological Sciences (NIBS) in Beijing, China. For western blot, horseradish peroxidase (HRP)-conjugated anti-mouse IgG (NA931/polyclonal) and HRP-conjugated anti-rabbit IgG (NA934/polyclonal) were purchased from GE Healthcare Life Sciences. For enzyme-linked immunosorbent assay (ELISA), HRP-conjugated goat anti-mouse IgG (1036-05/polyclonal) was purchased from SouthernBiotech (lot no. D4913-WJ86H). Antibodies for Flag and tubulin were used at 1:5,000 dilution, and all other primary antibodies were used at 1:1,000 dilution for western blot. Secondary antibodies were used at 1:5,000 and 1:6,000 dilutions for western blot and ELISA, respectively.

The following chemical reagents were purchased from Sigma-Aldrich: NAD⁺ (N1636), NADH (N8129), NADPH (N7505), NGD⁺ (N5131), ε-NAD⁺ (N2630), Thio-NAD⁺ (T7375), Deamino-NAD⁺ (N6506), NAAD⁺ (N4256), α-NAD⁺ (N6754), α-NADH (N6879), NMN⁺ (N3501), ADPR (A0752) and ninhydrin (N4876). The ammonia assay kit (MAK310) was also from Sigma-Aldrich. 2'-F-NAD⁺ (D148) was from the BIOLOG Life Science Institute. Biotin-NAD⁺ (4670-500-01) was from Trevigen. Thio-NADH (BIB5005) was from Apollo Scientific. NADP⁺ (432216) was from J&K Scientific. Cyclic-ADPR (21417) was from Cayman Chemical. 2'-H-NAD⁺ was synthesized at the chemical centre of our institute. All other chemical reagents used were from Sigma-Aldrich unless otherwise noted.

Bacterial strains and infection

S. flexneri 2a strain 2457T, *B. thailandensis* E264, *C. violaceum* 12472 and *S. Typhimurium* SL1344 were used in cell culture infections, and the first three were used to infect mice. *S. flexneri* $\Delta ospC1$, $\Delta ospC2$ and $\Delta ospC3$ mutants were generated by using the λ Red recombineering method²⁶. *C. violaceum* $\Delta copC$ was generated by homologous recombination using the suicide vector pDM4-SacB. *S. flexneri* $\Delta ipaH9.8$ and *S. Typhimurium* $\Delta sifA$ have been described previously^{1,11}. For infection in epithelial cells, *S. flexneri* strains were transformed with an afimbral adhesin (Afa) locus to achieve high infection efficiency. For in vivo infection, the mouse-passaged *B. thailandensis* strain was used⁸.

Cultured cells were seeded in 24-well plates 12–16 h before infection. iBMDMs were primed with 0.1 $\mu\text{g ml}^{-1}$ of LPS for 16 h to stimulate caspase-11 expression. The bacteria were cultured overnight at 37 °C in 2 \times YT medium with shaking at 220 rpm. Overnight bacterial cultures were diluted 1:50 (1:20 for *B. thailandensis*) in fresh 2 \times YT medium and cultured at 37 °C with shaking for about 3.5 h (4.5 h for *B. thailandensis*) when OD₆₀₀ reached about 1.7. Bacteria were diluted in serum-free Dulbecco's modified Eagle's medium (DMEM) to achieve the desired multiplicity of infection (MOI: 25 for *S. flexneri*; 50 for *S. Typhimurium*; 100 for *B. thailandensis*; and 10 for *C. violaceum*). Infection was started by centrifugation at 800g for 5 min at room temperature followed by incubation at 37 °C in a 5% CO₂ incubator. After 1 h of infection (0.5 h for *S. Typhimurium* in iBMDMs, 1.5 h for *B. thailandensis*), cell culture media were replaced with fresh serum-free DMEM supplemented with appropriate antibiotics (100 $\mu\text{g ml}^{-1}$ of gentamycin and 34 $\mu\text{g ml}^{-1}$ of chloramphenicol for *S. flexneri* and *S. Typhimurium*, 100 $\mu\text{g ml}^{-1}$ of gentamycin for *B. thailandensis*). Infected cells were further incubated for different time durations dependent upon the context of infection. Specifically, iBMDMs were incubated for 1 h (*S. Typhimurium*), 2.5 h (*S. flexneri*) and 6.5 h (*B. thailandensis*); SiHa and A431 cells were incubated for 3.5 h. The cell culture media were collected and subjected to LDH release assay or trichloroacetic acid precipitation to obtain released protein samples. Infection of A431 cells with *S. flexneri* was performed in the presence of 4 μM human α -defensin 5 (kindly provided by Dr. Dan Xu, Xi'an Jiaotong University, China). The LDH assay was performed using the CytoTox 96 Non-Radioactive Cytotoxicity Assay Kit (Promega).

WT C57BL/6 mice, purchased from Beijing Vital River Laboratory Animal Technology, and *Casp11*^{−/−} C57BL/6 mice⁶, were used for infection in animals. All mice were maintained in the specific pathogen-free facility at NIBS under standard housing conditions (12-h dark/light cycle, 20–26 °C, 40–70% humidity, noise \leq 60 dB) in accordance with the national guidelines for housing and care of laboratory animals.

(National Health Commission, China). Mice were transferred to a Biosafety Level 2 facility with the same housing conditions to conduct infections. The protocols for mouse experiments are in accordance with institutional regulations after review and approval by the Institutional Animal Care and Use Committee of NIBS. The bacteria were cultured overnight at 37 °C in 2× YT medium with shaking at 220 rpm.

Overnight cultures were diluted 1:100 in fresh 2× YT medium and grown until OD₆₀₀ reached 1.5. The bacteria were collected by centrifugation (4,000 rpm. for 5 min) and re-suspended in PBS. Next, 8–10-week-old female mice were infected intraperitoneally with 200 µl of bacteria suspension (2×10^7 colony-forming units (CFU) for each mouse). For infection of *C. violaceum*, 7-week-old female mice were infected intravenously with 5×10^3 *C. violaceum* (in 200 µl of PBS). Survival of mice was checked daily for 10 d. To measure bacterial burden, livers and spleens of infected mice were collected 13–16 h after infection and homogenized in sterile PBS. The CFU numbers in the tissue were measured by plating serial-diluted homogenates on 2× YT agar plates.

Mice immunisation and ELISA

Female C57BL/6 and BALB/c mice (8 weeks old) were immunized by intraperitoneal injection of bacteria (1.2×10^6 CFU for WT *S. flexneri*, 4×10^6 CFU for $\Delta ospC3$ mutant and 2×10^6 CFU for all candidate vaccine strains unless specifically indicated) re-suspended in 200 µl of PBS. Owing to the more efficient clearance of the $\Delta ospC3$ strain in mice, the doses of immunization for WT and the $\Delta ospC3$ mutant were normalized by their virulence, and 10% of the median lethal dose (LD₅₀) of each strain was used. Sera samples were collected 14 d after the immunisation, and *Shigella*-specific antibody levels were assessed by standard ELISA assay. In brief, 96-well ELISA plates (Nunc MaxiSorp) were coated with 2×10^7 CFU of live *S. flexneri* re-suspended in 100 µl of carbonate-bicarbonate buffer (pH 9.6) at 4 °C overnight. The *Shigella*-coated plates were washed three times with PBST buffer (0.05% Tween 20 in PBS) before blocking with 200 µl of the buffer (2% BSA in PBST) for 2 h at 37 °C. After washing with PBST three times, twofold serial dilutions of the sera (diluted in the blocking buffer) were added to the plates (100 µl per well) and incubated for 2 h at 37 °C. The plates were then washed four times with PBST before adding HRP-conjugated goat anti-mouse IgG antibody (1:6,000 diluted in the blocking buffer, 100 µl per well) for 1 h at 37 °C. After washing with PBST four times, peroxidase substrate *o*-phenylenediamine (0.4 mg ml⁻¹, dissolved in 0.15 M phosphate-citrate buffer supplemented with 0.03% H₂O₂, pH 5.0) was added to the plates (100 µl per well) and incubated for 15 min at room temperature. The reaction was then stopped by adding 2 M H₂SO₄ (50 µl per well), and OD₄₉₂ was measured. Antibody titres were defined as the reciprocal of the last dilution having an OD₄₉₂ value at least twofold higher than

that obtained in the control wells; the blocking buffer was used as the mock serum sample.

Cell culture, transfection and immunoprecipitation

HeLa, SiHa, A431, 293T and iBMDM cells were grown in DMEM supplemented with 10% (v/v) FBS and 2 mM l-glutamine. All cell lines were obtained from the American Type Culture Collection except for the previously described iBMDMs¹. Cells were maintained at 37 °C in a humidified 5% CO₂ incubator. All cells were tested for mycoplasma using the standard PCR method. Cell identity was checked frequently by morphological features but was not authenticated by short tandem repeat profiling. Knockout cell lines were generated by the CRISPR–Cas9 method as previously described¹. In brief, PX458 plasmids containing the guide RNAs targeting *Casp1*, *Casp11* or *CASP4* were electroporated into the cells (1 µg of DNA per 1 × 10⁶ cells). Three days later, GFP-positive cells were sorted into single clones on 96-well plates by flow cytometry. Single clones were screened and verified by sequencing of the PCR fragments and confirmed by western blot. Sequences for the guide RNAs used are 5'-GGAATTCTGGAGCTTCAATC-3' for *CASP1*, 5'-GGTCCACACTGAAGAATGTC-3' for *Casp11* and 5'-CAAGAGAAGCAACGTATGGC-3' for *CASP4*. The HeLa *CASP4*^{-/-} cell line was described previously¹. Transient transfection was performed using jetPRIME (Polyplus-transfection) following the manufacturer's instructions. Cell lines with stable gene expression were generated by lentiviral infection as previously described¹. For immunoprecipitation, 293T cells grown to 60% confluence were transfected with indicated plasmids. Twenty-four hours after transfection, cell pellets were harvested and lysed in the lysis buffer (50 mM Tris-HCl, pH 7.6, 150 mM NaCl, 1 mM CaCl₂, 1% Triton X-100 and a protease inhibitor cocktail) for 0.5 h followed by centrifugation at 4 °C (15,000 rpm for 10 min). The lysates were incubated with anti-Flag M2 affinity beads at 4 °C with gentle rotation for 2 h. The beads were washed five times with the lysis buffer, and the immunoprecipitants were eluted from the beads with Flag or 3×Flag peptides.

Recombinant protein purification

The *E. coli* BL21 (DE3) strain was used for all recombinant protein expression. Induction of protein expression (18 °C for 16 h) was achieved with 0.4 mM isopropyl β-D-1-thiogalactopyranoside after OD₆₀₀ of bacterial culture reached 1.0. Bacterial cells were harvested and lysed by an ultrasonic homogenizer in buffer containing 20 mM HEPES (pH 7.0), 300 mM NaCl, 5 mM CaCl₂ and 5 mM dithiothreitol. GST-fusion OspC or OspC chimeric proteins were purified by glutathione sepharose affinity chromatography. The GST tag was removed by overnight digestion with homemade

PreScission Protease (PPase) at 4 °C. The untagged proteins were further purified by HiTrap SP HP cation exchange chromatography and Superdex G75 gel filtration chromatography (GE Healthcare Life Sciences). The purified proteins were concentrated and stored at –80 °C in buffer containing 20 mM HEPES (pH 7.0), 150 mM NaCl, 2 mM CaCl₂ and 5 mM dithiothreitol. pAC-SUMO-CASP4-p30-C/A plasmid was used to express caspase-4-p30-C/A protein. Bacteria cells were harvested and lysed in the buffer containing 20 mM Tris-HCl (pH 8.0), 300 mM NaCl, 20 mM imidazole and 10 mM 2-mercaptoethanol. The His₆-SUMO-tagged protein was first purified by affinity chromatography using Ni-chelating sepharose resin, and the tag was removed by overnight digestion at 4 °C with homemade ULP1 protease. The untagged protein was further purified by HiTrap Q HP anion exchange and Superdex G75 gel filtration chromatography. Purified caspase-4 proteins were concentrated and stored at –80 °C in buffer containing 20 mM Tris-HCl (pH 8.0), 150 mM NaCl and 5 mM dithiothreitol. A similar procedure was followed to purify other His₆-SUMO-tagged proteins, including caspase-11-p30-C/A, GSDMD, NUDT16, ExoS (ADP-ribosyltransferase domain starting from Ala233), Rab4a, 14-3-3β, ADPRH, ADPRS, OARD1, MACROD2 and His₆-tagged MACROD1 (starting from Thr91). Accession numbers (for the NCBI protein database, <https://www.ncbi.nlm.nih.gov/protein/>) of the proteins used in this study are: OspC3 (WP_015683184.1), OspC2 (WP_000701108.1), OspC1 (WP_001026857.1), CASP4 (NP_001216.1), CASP11 (NP_031635.2), GSDMD (NP_001159709.1), NUDT16 (NP_689608.2), ExoS (WP_003113791.1), RAB4A (NP_004569.2), 14-3-3β (NP_647539.1), ADPRH (NP_001116.1), ADPRS (NP_060295.1), OARD1 (NP_001316613.1), MACROD2 (NP_542407.2) and MACROD1 (NP_054786.2).

OspC3-catalysed modification reaction and native-PAGE

The reaction was carried out in a buffer containing 20 mM HEPES (pH 7.0), 150 mM NaCl, 1 mM CaCl₂ and 5 mM dithiothreitol. Purified caspase-4/11-p30-C/A and OspC3 proteins (molar ratio: 1:1) were incubated at 16 °C for 12 h in the presence of 1 mM NAD⁺. Native-PAGE was used to analyse OspC3-catalysed modification of caspase-4/11. Samples of the in vitro reaction or the purified protein were separated on a 4–20% gradient non-denaturing polyacrylamide gel in a buffer containing 25 mM Tris (pH 8.3) and 192 mM glycine. The electrophoresis was started at a voltage of 90 V; the voltage was gradually increased to 180 V, and the electrophoresis was stopped until the dyes in the loading buffer (bromophenol blue and xylene cyanol FF) migrated out of the gel. The gel was stained with Coomassie Brilliant Blue R-250 to visualize the mobility shift of the modified caspase-4/11 protein.

Stable isotope labelling by amino acids in cell culture experiment

293T cells were first adapted to SILAC DMEM medium in which l-arginine was replaced by heavy isotope labelled arginine (l-arginine-¹³C₆, ¹⁵N₄), and regular FBS was replaced by dialysed FBS. The cells were cultured in SILAC DMEM medium and passaged at a ratio of 1:10 for five times to ensure complete incorporation, which was further checked by LC–MS analysis before the experiment. Flag–caspase-4 p20/p10 complexes were expressed alone or co-expressed with OspC3 by transient transfection in the adapted 293T cells. Thirty-six hours after transfection, cell pellets were harvested and lysed in a buffer containing 50 mM Tris-HCl (pH 7.6), 150 mM NaCl, 1% Triton X-100 and a protease inhibitor cocktail. Standard immunoprecipitation was performed to purify caspase-4 p20/p10 proteins that were subjected to subsequent LC–MS analyses.

MS

For LC–MS/MS identification of the modified peptides, samples were separated on an SDS-PAGE gel, and the protein bands of interest were reduced and alkylated using dithiothreitol and iodoacetamide, respectively. The protein samples were digested overnight with chymotrypsin. The resulting peptides were dried on a SpeedVac vacuum concentrator and then re-suspended in an aqueous buffer before LC–MS/MS analysis. A Hybrid Ion Trap Orbitrap mass spectrometer (LTQ Orbitrap Velos, Thermo Fisher Scientific) was used to identify and analyse the modified peptides, and profiling of the modification sites was performed on the Orbitrap Fusion Lumos mass spectrometer (Thermo Fisher Scientific).

For CID–MS and EThcD–MS analyses, a capillary column (75 µm × 150 mm) with a laser-pulled electrospray tip (Model P-2000, Sutter Instrument) was home-packed with 4-mm, 100-Å Magic C18AQ silica-based particles. The LC mobile phase comprised solvent A (97% H₂O, 3% acetonitrile and 0.1% formic acid) and solvent B (80% acetonitrile, 20% H₂O and 0.1% formic acid). An EASY-nLC 1200 HPLC system (Thermo Fisher Scientific) was used to generate the following HPLC gradient: solvent B was increased from 7% to 40% in 40 min and then raised to 95% in 2 min and kept for 10 min followed by 100% solvent A for column equilibration. A data-dependent acquisition mode was enabled for peptide fragmentation with one full MS scan (*m/z* range 350.00–1,200.00, resolution 60,000) followed by CID. To identify the modification site, precursor ions were subjected to EThcD for peptide fragmentation. Raw MS files were processed using Mascot (version 2.3.02, Matrix Science). The following settings were used for database search: 20 ppm precursor mass error tolerance and 0.8-Da fragment mass error tolerance for LTQ Orbitrap Velos and 10 p.p.m. precursor mass error tolerance and 0.02-Da fragment mass error tolerance for Orbitrap Fusion Lumos. Carbamidomethylation of cysteine residues was set as a fixed modification, and oxidation of methionine was set as a variable modification. A maximum of two missed cleavage sites was allowed. Peptide and protein

identifications were filtered at less than 1% false discovery rates. The corresponding peptide peaks were obtained from Thermo Xcalibur 2.2 (Thermo Fisher Scientific).

To measure the total molecular weight of caspase-4 or -11, the purified proteins were separated on a C₁₈ reversed-phase column. The EASY-nLC 1200 HPLC system was used to generate the following gradient: 20–50% B in 20 min, 50–70% B in 3 min and maintained at 70% B for 20 min. MS data were processed using Thermo Scientific Protein Deconvolution software. The parameters were specified according to the mass spectrometer setting. Deconvoluted mass of the most abundant ion was selected as the mass of the target protein with a mass tolerance of 30 ppm.

Reporting summary

Further information on research design is available in the [Nature Research Reporting Summary](#) linked to this paper.

Data availability

All data supporting the findings of this study are included in this manuscript and its [Supplementary Information](#). [Source data](#) are provided with this paper.

References

1. 1. Shi, J. et al. Inflammatory caspases are innate immune receptors for intracellular LPS. *Nature* **514**, 187–192 (2014).
2. 2. Shi, J. et al. Cleavage of GSDMD by inflammatory caspases determines pyroptotic cell death. *Nature* **526**, 660–665 (2015).
3. 3. Kayagaki, N. et al. Caspase-11 cleaves gasdermin D for non-canonical inflammasome signalling. *Nature* **526**, 666–671 (2015).
4. 4. Ding, J. et al. Pore-forming activity and structural autoinhibition of the gasdermin family. *Nature* **535**, 111–116 (2016).

5. 5.

Broz, P., Pelegrin, P. & Shao, F. The gasdermins, a protein family executing cell death and inflammation. *Nat. Rev. Immunol.* **20**, 143–157 (2020).

6. 6.

Kayagaki, N. et al. Non-canonical inflammasome activation targets caspase-11. *Nature* **479**, 117–121 (2011).

7. 7.

Rathinam, V. A. K., Zhao, Y. & Shao, F. Innate immunity to intracellular LPS. *Nat. Immunol.* **20**, 527–533 (2019).

8. 8.

Aachoui, Y. et al. Caspase-11 protects against bacteria that escape the vacuole. *Science* **339**, 975–978 (2013).

9. 9.

Pilla, D. M. et al. Guanylate binding proteins promote caspase-11-dependent pyroptosis in response to cytoplasmic LPS. *Proc. Natl Acad. Sci. USA* **111**, 6046–6051 (2014).

10. 10.

Tretina, K., Park, E. S., Maminska, A. & MacMicking, J. D. Interferon-induced guanylate-binding proteins: guardians of host defense in health and disease. *J. Exp. Med.* **216**, 482–500 (2019).

11. 11.

Li, P. et al. Ubiquitination and degradation of GBPs by a *Shigella* effector to suppress host defence. *Nature* **551**, 378–383 (2017).

12. 12.

Wandel, M. P. et al. GBPs inhibit motility of *Shigella flexneri* but are targeted for degradation by the bacterial ubiquitin ligase IpaH9.8. *Cell Host Microbe* **22**, 507–518 (2017).

13. 13.

Ji, C. et al. Structural mechanism for guanylate-binding proteins (GBPs) targeting by the *Shigella* E3 ligase IpaH9.8. *PLoS Pathog.* **15**, e1007876 (2019).

14. 14.

Wandel, M. P. et al. Guanylate-binding proteins convert cytosolic bacteria into caspase-4 signaling platforms. *Nat. Immunol.* **21**, 880–891 (2020).

15. 15.

Kobayashi, T. et al. The *Shigella* OspC3 effector inhibits caspase-4, antagonizes inflammatory cell death, and promotes epithelial infection. *Cell Host Microbe* **13**, 570–583 (2013).

16. 16.

Xu, Y. et al. A bacterial effector reveals the V-ATPase–ATG16L1 axis that initiates xenophagy. *Cell* **178**, 552–566 (2019).

17. 17.

Palazzo, L. et al. Processing of protein ADP-ribosylation by Nudix hydrolases. *Biochem. J.* **468**, 293–301 (2015).

18. 18.

Sauve, A. A. & Schramm, V. L. SIR2: The biochemical mechanism of NAD⁺-dependent protein deacetylation and ADP-ribosyl enzyme intermediates. *Curr. Med. Chem.* **11**, 807–826 (2004).

19. 19.

Handlon, A. L., Xu, C., Muller-Steffner, H. M., Schuber, F. & Oppenheimer, N. J. 2'-Ribose substituent effects on the chemical and enzymic hydrolysis of NAD⁺. *JACS* **116**, 12087–12088 (1994).

20. 20.

Bette-Bobillo, P., Giro, P., Sainte-Marie, J. & Vidal, M. Exoenzyme S from *P. aeruginosa* ADP ribosylates rab4 and inhibits transferrin recycling in SLO-permeabilized reticulocytes. *Biochem. Biophys. Res. Commun.* **244**, 336–341 (1998).

21. 21.

Wang, K. et al. Structural mechanism for GSDMD targeting by autoprocessed caspases in pyroptosis. *Cell* **180**, 941–955 (2020).

22. 22.

Mani, S., Wierzba, T. & Walker, R. I. Status of vaccine research and development for *Shigella*. *Vaccine* **34**, 2887–2894 (2016).

23. 23.

Chung, L. K. et al. The *Yersinia* virulence factor YopM hijacks host kinases to inhibit type III effector-triggered activation of the pyrin inflammasome. *Cell Host Microbe* **20**, 296–306 (2016).

24. 24.

Dong, N. et al. Structurally distinct bacterial TBC-like GAPs link Arf GTPase to Rab1 inactivation to counteract host defenses. *Cell* **150**, 1029–1041 (2012).

25. 25.

Gao, W., Yang, J., Liu, W., Wang, Y. & Shao, F. Site-specific phosphorylation and microtubule dynamics control Pyrin inflammasome activation. *Proc. Natl Acad. Sci. USA* **113**, E4857–E4866 (2016).

26. 26.

Murphy, K. C. & Campellone, K. G. Lambda Red-mediated recombinogenic engineering of enterohemorrhagic and enteropathogenic *E. coli*. *BMC Mol. Biol.* **4**, 11 (2003).

Acknowledgements

We thank L. Li and S. Chen for mass spectrometry, P. Li and H. He for technical assistance and C. Li for advice. The work was supported by National Key Research and Development Programs of China (2017YFA0505900 and 2016YFA0501500), the Strategic Priority Research Program of the Chinese Academy of Sciences (XDB37030202 and XDB29020202), the National Natural Science Foundation of China (81788104, 81922043, 21622501 and 21974002) and the Chinese Academy of Medical Sciences Innovation Fund for Medical Sciences (2019-I2M-5-084).

Author information

Affiliations

1. Research Unit of Pyroptosis and Immunity, Chinese Academy of Medical Sciences and National Institute of Biological Sciences, Beijing, China

Zilin Li, Wang Liu, Yue Xu & Feng Shao

2. National Institute of Biological Sciences, Beijing, China

Zilin Li, Wang Liu, Sen Cheng, Yue Xu, Zhiqiang Wang, Xiaofan Liu, Xuyan Shi, Yaxin Liu, Xiangbing Qi, Jingjin Ding & Feng Shao

3. Institute of Analytical Chemistry & Synthetic and Functional Biomolecules Center, College of Chemistry and Molecular Engineering, Peking University, Beijing, China

Jiaqi Fu, Sen Cheng & Xiaoyun Liu

4. Department of Microbiology, School of Basic Medical Sciences, Peking University Health Science Center, Beijing, China

Xiaoyun Liu

5. National Laboratory of Biomacromolecules, Institute of Biophysics, Chinese Academy of Sciences, Beijing, China

Jingjin Ding & Feng Shao

6. Tsinghua Institute of Multidisciplinary Biomedical Research, Tsinghua University, Beijing, China

Feng Shao

Contributions

Z.L., W.L. and F.S. conceived the study. Z.L. performed most of the biochemical and functional experiments. W.L. made the initial observation of a possible new PTM on caspase-11 by OspC3. J.F., S.C. and X.L. were responsible for mass spectrometry and data analyses. Z.W. and X.Q. synthesized 2'-H-NAD⁺. Y.X., Y.L., X.L., X.S. and J.D. provided technical assistance and valuable suggestions. Z.L. and F.S. analysed the data and wrote the manuscript, with input from all authors. All authors discussed the results and commented on the manuscript.

Corresponding authors

Correspondence to [Xiaoyun Liu](#) or [Feng Shao](#).

Ethics declarations

Competing interests

The authors declare no competing interests.

Additional information

Peer review information *Nature* thanks Klaus Aktories and the other, anonymous, reviewer(s) for their contribution to the peer review of this work.

Publisher's note Springer Nature remains neutral with regard to jurisdictional claims in published maps and institutional affiliations.

Extended data figures and tables

[Extended Data Fig. 1 *S. flexneri* suppresses cytosolic LPS-induced host defense through the OspC3 effector.](#)

a, Survival curves of WT or *Casp11*^{-/-} mice infected intraperitoneally with *S. flexneri* or *B. thailandensis* (5×10^6 CFU per mouse, $n = 10$ for each group; two-tailed log-rank (Mantel-Cox) test). **b**, *Casp1*^{-/-}*Casp11*^{-/-} iBMDMs were infected with *S. flexneri* (*S.f.*) or *B. thailandensis* (*B.t.*) at the indicated MOIs for 1.5 h. Extracellular bacteria were killed by gentamycin. Intracellular bacteria were stained by anti-*Shigella* or anti-*Burkholderia* antibodies (scale bar, 20 μ m). The numbers of bacteria/cell (mean values) were calculated from 5 randomly selected images. **c, g**, WT or *CASP4*^{-/-} A431 cells were infected with *S. flexneri* (WT, an *ospC3* deletion or complementation (pOspC3) strain) or *S. Typhimurium* Δ *sifA*. **d**, WT or *CASP4*^{-/-} SiHa cells were infected with *S. flexneri* WT or Δ *ospC3* at the indicated MOIs. **e**, Indicated cells were electroporated with LPS purified from *S. flexneri*, *B. thailandensis* or *E. coli* (*E.c.*). **f**, WT or *CASP4*^{-/-} SiHa cells and *Casp1*^{-/-} or *Casp1*^{-/-}*Casp11*^{-/-} iBMDMs were infected with *S. flexneri* WT or an indicated mutant. **h**, WT or *CASP4*^{-/-} or *GBPs*^{-/-} (lacking all seven human GBPs) A431 cells were infected with indicated bacteria strains; cell death was assayed at the indicated time points post-infection. **i**, Streptavidin pull-down assay of the binding of biotin-conjugated LPS or Pam3CSK4 to Flag-tagged caspase-4/11-C/A and GBP1 in transfected 293T cell lysates. **j**, WT,

CASP4^{-/-}, or OspC3-expressing SiHa cells were infected with *S. flexneri* Δ ospC3 or *S. Typhimurium* Δ sifA, or electroporated with LPS. **c, g, j**, Cell lysates were immunoblotted as shown and supernatants were blotted with the anti-cleaved GSDMD-C antibody. **f, h**, Cells were primed with 100 ng ml⁻¹ IFN γ overnight prior to infection. Cell death (**c, d, f–h, j**) was quantified by LDH release at 3.5 h post-infection unless noted and ATP-based cell viability (**e**) was measured 2 h post-electroporation; data are means (bars) of three individual replicates (circles). Data are pooled from two experiments (**a**) and representative of three independent experiments (**b–i**). For gel source data, see Supplementary Fig. 1.

[Source data](#)

Extended Data Fig. 2 OspC3 catalyzes an NAD⁺-dependent modification of caspase-4/11.

a, b, Co-immunoprecipitation of OspC3 with caspase-4-p20/p10 (**a**) or full-length caspase-4/11 (**b**). C/A, the catalytic-cysteine mutant. **c–e**, GSDMD (**c, d**) or the fluorescent peptide substrate Ac-WEHD-AFC (**e**) were assayed for in vitro cleavage by caspase-4/11-p20/p10 in the presence of OspC3 at indicated concentrations. **f**, Cleavage of GSDMD by LPS-activated caspase-4 in the presence or absence of OspC3. **g**, LPS alone or mixed with purified OspC3 or EGFP was electroporated into HeLa cells or iBMDMs. ATP-based cell viability was measured. **h, k**, Caspase-11-p30-C/A, expressed alone/with OspC3 in bacteria (**h**) or reacted with OspC3 \pm NAD⁺ in vitro (**k**), was analysed by ESI-MS (**h**) or native/SDS-PAGE (**k**). Control, OspC3-modified caspase-11-p30-C/A. **i, j**, CID-tandem mass spectrum of a chymotryptic caspase-4 peptide bearing the 524-Da modification. Purified caspase-4-p30-C/A, modified by OspC3 in *E. coli*, was subjected to mass spectrometry analyses. **j**, The upper and lower panels show the tandem mass spectra of a fragment ion ($m/z = 428.04$) from the modified peptide in **i** and the ADP standard, respectively. *, OspC3-modified; M_{ox}, oxidized methionine. **l**, ESI-MS determination of the molecular mass of caspase-4/11-p30-C/A that had been reacted with OspC3 in the presence or absence of NAD⁺. **m**, EThcD-MS of purified caspase-4/11; extracted ion chromatograms of the R314/R310-containing peptides or a control peptide. *, OspC3-modified; M_{ox}, oxidized methionine. **e, g**, Data are means (bars) of three individual replicates (circles). Data are representative of three (**a–k**) or two (**l, m**) independent experiments. For gel source data, see Supplementary Fig. 1.

[Source data](#)

Extended Data Fig. 3 OspC3 modifies Arg314 in caspase-4 and the equivalent Arg310 in caspase-11.

a, EThcD-tandem mass spectrum of the Arg310-containing chymotryptic peptide from modified caspase-4/11-p30-C/A obtained by co-expression with OspC3 in bacteria. Fragmentation patterns generating the observed c/z and b/y ions are indicated along the peptide sequence. **b, d**, Caspase-4/11-p30-C/A or an Arg314/R310 mutant were expressed alone or together with OspC3 in 293T cells. Immunopurified caspase-4/11-p30 were analysed by ESI-MS to determine the total molecular mass. ♦, a contamination ion that only appeared in the particular experiment. **c, e**, Caspase-4/11-p30-C/A or an R314/R310 mutant protein were reacted with OspC3 in the presence or absence of NAD⁺. The reactions were analysed by native/SDS-PAGE (**c**). Chymotrypsin-digested caspase-4/11-p30 proteins were analysed by mass spectrometry (**e**). Shown are the extracted ion chromatograms of the R314/R310-containing peptides. **a, e**, M_{ox}, oxidized methionine. Data are representative of three (**a, c, e**) or two (**b, d**) independent experiments. For gel source data, see Supplementary Fig. 1.

Extended Data Fig. 4 OspC3 modification of caspase-4/11 contains a step of ADP-ribosylation.

a, HPLC-MS quantification of small-molecule products present in indicated in vitro caspase-4 modification reactions. Mean values ± s.d., n = 3 (independent experiments), two-tailed unpaired Student's t-test (**P < 0.001, **P < 0.01, ns, non-significant). **b, c**, Assessing the ability of various NAD⁺ analogues or derivatives to support in vitro modification of caspase-4-p30-C/A by OspC3. **b**, The reactions were subjected to native/SDS-PAGE analyses. Control, OspC3-modified caspase-4-p30-C/A in bacteria. **c**, Following the modification, caspase-4-p30 was digested with chymotrypsin and analysed by mass spectrometry. Shown are the extracted ion chromatograms of the R314-containing peptides. Mass changes of each analogue from NAD⁺ are illustrated underneath the corresponding chromatograms. A, adenine; N, nicotinamide; P, phosphate; R, ribose. **d, e**, Caspase-4/11-p30-C/A modified by OspC3 in bacteria was treated with SdeA or NUDT16 overnight. **d**, The caspase-4 samples were then immunoblotted with an anti-ADP-ribosylation antibody. **e**, Caspase-4/11 after NUDT16 treatment was digested with chymotrypsin and analysed by mass spectrometry. Shown are extracted ion chromatograms of the R314/R310-containing peptides. All data are representative of three independent experiments. For gel source data, see Supplementary Fig. 1.

[Source data](#)

Extended Data Fig. 5 OspC3-catalyzed modification involves ADP-ribosylation-dependent arginine deamination.

a, Caspase-4-p20/p10-C/A was expressed alone or co-expressed with OspC3 in 293T cells metabolically labeled with $^{13}\text{C}_6$, $^{15}\text{N}_4$ -L arginine. Immunopurified caspase-4 was analysed by mass spectrometry. **b**, Structural illustration of 2'-H-NAD $^+$ and 2'-F-NAD $^+$. **c**, Caspase-4-p30-C/A was reacted with OspC3 in the absence or presence of 2'-H-NAD $^+$, and then analysed by mass spectrometry. **d**, Chemical scheme of ninhydrin modification of an arginine. **e**, Unmodified caspase-4-p30-C/A or OspC3-modified caspase-4-p30-C/A using NAD $^+$ or 2'-H-NAD $^+$ were incubated with 5 mM ninhydrin for 8 h at room temperature, and then digested with chymotrypsin and analysed by mass spectrometry. **f**, Purified Rab4a was ADP-ribosylated by ExoS (activated by 14-3-3 protein). ADP-ribosylated and native Rab4a was incubated with 5 mM ninhydrin, followed by mass spectrometry analyses. **g**, A proposed scheme of OspC3-catalyzed arginine ADP-riboboxanation. **a, c, e, f**, Extracted ion chromatograms of caspase-4 R314-containing peptides (**a, c, e**) or Rab4a R84-containing peptide (**f**). Data are representative of two (**a**) or three (**c, e, f**) independent experiments.

Extended Data Fig. 6 Domain architecture and enzymatic properties of the OspC family.

a, Multiple sequence alignment of OspC1, OspC2 and OspC3. The alignment was performed using the ClustalW2 algorithm and illustrated using ESPript 3.0 (<http://escript.ibcp.fr/ESPript/cgi-bin/ESPript.cgi>). Identical residues are in red background and conserved residues are colored in red. The N-terminal putative ADP-riboboxanase domain and the C-terminal ARD are marked along the sequence. Residues required for OspC3 ADP-riboboxanase activity are highlighted by black rectangle. **b**, HeLa cells were electroporated with LPS together with recombinant OspC or an indicated chimeric protein. Cell viability was determined by the ATP assay. **c**, Co-immunoprecipitation of caspase-4-p30-C/A with an OspC-family member. **d, e**, Caspase-4/11-p30-C/A was reacted with OspC3 or an indicated mutant in the presence of NAD $^+$. The reactions were subjected to native/SDS-PAGE analyses. Control, OspC3-modified caspase-11/4-p30-C/A in bacteria. EH/AA, OspC3 E326A/H328A. **f, g**, SiHa cells and *CaspI* $^{-/-}$ or *CaspI* $^{-/-}$ *CaspII* $^{-/-}$ iBMDMs were infected with WT *S. flexneri* or an *ospC3* deletion/complementation strain. Cell death was measured by the LDH-release assay. **h**, Flag-caspase-4-p30-C/A was co-expressed with OspC3 or an indicated mutant in 293T cells. **i**, Caspase-4-p30-C/A was left unmodified (Unmod.) or pre-modified by OspC3 (WT or D177A) in vitro. Anti-Flag immunoprecipitates (**h**) or caspase-4-p30-C/A (**i**) were left untreated or treated with ADP-ribosylarginine hydrolase (ADPRH) or other indicated ADP-ribosylhydrolases. The samples were subjected to anti-ADPR immunoblotting. **b, f, g**, Data are means (bars) of three individual replicates (circles). Data are representative of three (**b–h**) or two (**i**) independent experiments. For gel source data, see Supplementary Fig. [1](#).

[Source data](#)

[**Extended Data Fig. 7 R314/R310 ADP-riboxanation of caspase-4/11 blocks their autoprocessing and also cleaving of GSDMD.**](#)

a, c, *CASP4*^{-/-} A431 cells (**a**) or *CaspI*^{-/-}*CaspII*^{-/-} iBMDMs (**c**) stably expressing an Arg314 or Arg310 mutant caspase-4 or -11, respectively, were electroporated with LPS. Cell viability was measured 2 h post-electroporation. **b, d, e**, *CASP4*^{-/-} A431 cells stably expressing caspase-4 (WT or an indicated R310 mutant) or *CaspI*^{-/-}*CaspII*^{-/-} iBMDMs stably expressing caspase-11 (WT or an indicated R314 mutant) were infected with *S. Typhimurium* Δ *sifA* (**b**), or *S. flexneri* Δ *ospC3* (**d**) or *B. thailandensis* (**e**), respectively. Pyroptosis was measured by the LDH-release assay. **b, d**, Cell lysates were immunoblotted as shown and supernatants were blotted with the anti-cleaved GSDMD-C antibody. **f**, WT or R314/R310-mutant caspase-4/11-p20/p10 proteins were purified from bacteria and analysed by SDS-PAGE. **g**, Gel-filtration chromatography analyses of caspase-4-p20/p10 (WT or R314A)-GSDMD-C complex formation. Caspase-4-p20/p10-A, R314-ADP-riboxanated form obtained by co-expression with OspC3 in bacteria. **h**, Alignment of caspase sequences around Arg314 in caspase-4. The alignment was performed using the ClustalW2 algorithm and presented using ESPript 3.0 (<http://escript.ibcp.fr/EScript/cgi-bin/EScript.cgi>). Identical residues are colored in red background and conserved residues are in red. The invariant arginine is highlighted by a black rectangle. Sequence numbers of the starting residues are indicated on the left. **i**, Cleavage of the fluorescent peptide substrate Ac-WEHD-AFC by WT or R314/R310-mutant caspase-4/11-p20/p10 proteins at the indicated concentrations. **a–e**, Data are means (bars) of three individual replicates (circles). All data are representative of three independent experiments. For gel source data, see Supplementary Fig. 1.

[Source data](#)

[**Extended Data Fig. 8 *S. flexneri* \$\Delta\$ *ospC3* promotes adaptive anti-*Shigella* immunity.**](#)

a–c, C57BL/6 mice were infected intraperitoneally with *S. flexneri* WT or Δ *ospC3* at the indicated doses ($n = 12$ for each group). 1%, 2.5%, 5%, 10% and 15% LD₅₀ equal 1.2×10^5 , 3×10^5 , 6×10^5 , 1.2×10^6 , and 1.8×10^6 CFU, respectively, for *S. flexneri* WT, and 4×10^5 , 1×10^6 , 2×10^6 , 4×10^6 , and 6×10^6 CFU, respectively, for *S. flexneri* Δ *ospC3*. **a**, Bacterial loads (CFU per gram of tissue) were determined 24 h post-infection. **b, c**, Fourteen days after immunization, serum anti-*Shigella* antibodies were determined (**b**); two additional days later, mice were re-challenged intraperitoneally with WT *S. flexneri* (1.5×10^8 CFU per mouse) and survival was

monitored daily (**c**). **d–h**, C57BL/6 (**d, e, f**) or BALB/c (**d, g, h**) mice were immunized with an indicated *S. flexneri* deletion strain at the indicated CFUs. Fourteen days after immunization, serum anti-*Shigella* antibodies were determined (**d, e, g**); two additional days later, mice immunized in **e** and **g** were re-challenged intraperitoneally with WT *S. flexneri* (1.5×10^8 and 8×10^7 CFU per mouse for **e** and **g**, respectively) and survival was monitored daily (**f, h**). **d**, $n = 12$ for $\Delta ospC3$ groups in C57BL/6 and BALB/c mice, $n = 18$ for $\Delta icsA$ and $\Delta guaBA$ groups in C57BL/6 mice, and $n = 15$ for $\Delta icsA$ and $\Delta guaBA$ groups in BALB/c mice. The data in C57BL/6 mice are representations from those in **b** for $\Delta ospC3$ and in Fig. [5e](#) for $\Delta icsA$ and $\Delta guaBA$. **e–h**, $n = 11$ for the $\Delta icsA$ (4×10^6 CFU) group in **f**, and $n = 12$ for all other groups. **a, b, d, e, g**, Median values; two-tailed Mann-Whitney *U*-test ($****P \leq 0.0001$). **c, f, h**, Two-tailed log-rank (Mantel-Cox) test. All data are representative of two independent experiments.

[Source data](#)

[Extended Data Fig. 9 The wide presence of OspC-like arginine ADP-riboboxanase in bacteria.](#)

a, Domain organization of OspC homologs identified through BLAST searches. The source of bacterial species and the accession number of the homologs are indicated on the left of the diagram. Sequence similarity of each homolog to OspC3 within the ADP-riboboxanase domain and the ARD are indicated. **b**, *CASP4*^{−/−} HeLa cells stably expressing Flag-caspase-4/11 were transfected with an indicated OspC3 homolog. LPS was electroporated into the cells and ATP-based cell viability was measured 2 h post-electroporation. Data are means (bars) of three individual replicates (circles). Cell lysates prepared prior to LPS electroporation were subjected to anti-Flag immunoprecipitation. EH/AA, mutations corresponding to the E326A/H328A double mutation in OspC3. **c**, Lysates of 293T cells co-transfected with Flag-caspase-4-C/A and a chimeric OspC-family protein (replacing the ARD with that of OspC3) were subjected to immunoprecipitation. The homolog from *C. amalonaticus* used is WP_103774980.1. **b, c**, Anti-Flag, anti-HA or anti-ADPR immunoblotting. Data are representative of two independent experiments. For gel source data, see Supplementary Fig. [1](#).

[Source data](#)

[Extended Data Fig. 10 Functional analyses of the CopC effector from *C. violaceum*.](#)

a, b, Purified caspase-4-p20/p10-C/A (**a**) or caspase-4-p30-C/A (**b**) was reacted with recombinant CopC or OspC protein (CopC $\Delta N50$ and OspC3 $\Delta N52$ were used in **a**) at

the indicated molar ratio in the presence of NAD⁺. Reactions were analysed by SDS-PAGE (**a**) or native-PAGE (**b**). Red * indicates ADP-riboxanation of caspase-4-p10. **c**, HeLa cells expressing CopC or an empty vector were electroporated with LPS. Cell death was measured by the LDH-release assay. Data are means (bars) of three individual replicates (circles). **d, e**, 3xFlag-caspase-4/11-expressing 293T cells were infected with *S. Typhimurium* SL1344 harboring CopC WT or E325A (**d**) or *C. violaceum* WT, Δ cviC or Δ copC (**e**). Immunoprecipitated Flag-caspase-4/11 was subjected to anti-Flag or anti-ADPR immunoblotting. **f**, C57BL/6 mice ($n = 14$ for each group) were intravenously infected with *C. violaceum* WT or Δ copC (5×10^3 CFU per mouse). Seventy-two h later, bacterial burden in the mouse liver (CFU per gram) was determined (median values, two-tailed Mann-Whitney *U*-test). Data are representative of three (**a–c**) or two (**d–f**) independent experiments. For gel source data, see Supplementary Fig. [1](#).

[Source data](#)

Supplementary information

[Supplementary Fig. 1](#)

Figures of the uncropped immunoblots for key data are presented in the main text and Extended Data section of the manuscript.

[Reporting Summary](#)

Source data

[Source Data Fig. 1](#)

[Source Data Fig. 3](#)

[Source Data Fig. 5](#)

[Source Data Extended Data Fig. 1](#)

[Source Data Extended Data Fig. 2](#)

[Source Data Extended Data Fig. 4](#)

[Source Data Extended Data Fig. 6](#)

[Source Data Extended Data Fig. 7](#)

[Source Data Extended Data Fig. 8](#)

[Source Data Extended Data Fig. 9](#)

[Source Data Extended Data Fig. 10](#)

Rights and permissions

[Reprints and Permissions](#)

About this article

Cite this article

Li, Z., Liu, W., Fu, J. *et al.* *Shigella* evades pyroptosis by arginine ADP-ribosylation of caspase-11. *Nature* **599**, 290–295 (2021). <https://doi.org/10.1038/s41586-021-04020-1>

- Received: 29 July 2020
- Accepted: 14 September 2021
- Published: 20 October 2021
- Issue Date: 11 November 2021
- DOI: <https://doi.org/10.1038/s41586-021-04020-1>

Share this article

Anyone you share the following link with will be able to read this content:

[Get shareable link](#)

Sorry, a shareable link is not currently available for this article.

[Copy to clipboard](#)

Provided by the Springer Nature SharedIt content-sharing initiative

This article was downloaded by **calibre** from <https://www.nature.com/articles/s41586-021-04020-1>

| [Section menu](#) | [Main menu](#) |

- Article
- [Published: 27 October 2021](#)

Glycogen metabolism links glucose homeostasis to thermogenesis in adipocytes

- [Omer Keinan](#)¹,
- [Joseph M. Valentine](#)¹,
- [Haopeng Xiao](#) [ORCID: orcid.org/0000-0002-4166-647X](#)^{2,3},
- [Sushil K. Mahata](#)⁴,
- [Shannon M. Reilly](#) [ORCID: orcid.org/0000-0003-0412-2446](#)¹,
- [Mohammad Abu-Odeh](#)¹,
- [Julia H. Deluca](#)¹,
- [Benyamin Dadpey](#) [ORCID: orcid.org/0000-0002-6253-7167](#)¹,
- [Leslie Cho](#)¹,
- [Austin Pan](#)¹,
- [Ruth T. Yu](#) [ORCID: orcid.org/0000-0002-9527-9627](#)⁵,
- [Yang Dai](#)⁵,
- [Christopher Liddle](#) [ORCID: orcid.org/0000-0003-3936-6790](#)⁶,
- [Michael Downes](#)⁵,
- [Ronald M. Evans](#) [ORCID: orcid.org/0000-0002-9986-5965](#)⁵,
- [Aldons J. Lusis](#) [ORCID: orcid.org/0000-0001-9013-0228](#)⁷,
- [Markku Laakso](#) [ORCID: orcid.org/0000-0002-3394-7749](#)⁸,
- [Edward T. Chouchani](#) [ORCID: orcid.org/0000-0002-9776-8790](#)^{2,3},
- [Mikael Ryde'n](#) [ORCID: orcid.org/0000-0003-4785-1876](#)⁹ &
- [Alan R. Saltiel](#) [ORCID: orcid.org/0000-0002-9726-9828](#)^{1,10}

[Nature](#) volume 599, pages 296–301 (2021)

- 6808 Accesses
- 203 Altmetric
- [Metrics details](#)

Subjects

- [Fat metabolism](#)
- [Obesity](#)

Abstract

Adipocytes increase energy expenditure in response to prolonged sympathetic activation via persistent expression of uncoupling protein 1 (UCP1)^{1,2}. Here we report that the regulation of glycogen metabolism by catecholamines is critical for UCP1 expression. Chronic β -adrenergic activation leads to increased glycogen accumulation in adipocytes expressing UCP1. Adipocyte-specific deletion of a scaffolding protein, protein targeting to glycogen (PTG), reduces glycogen levels in beige adipocytes, attenuating UCP1 expression and responsiveness to cold or β -adrenergic receptor-stimulated weight loss in obese mice. Unexpectedly, we observed that glycogen synthesis and degradation are increased in response to catecholamines, and that glycogen turnover is required to produce reactive oxygen species leading to the activation of p38 MAPK, which drives UCP1 expression. Thus, glycogen has a key regulatory role in adipocytes, linking glucose metabolism to thermogenesis.

Access options

Subscribe to Journal

Get full journal access for 1 year

\$199.00

only \$3.90 per issue

Subscribe

All prices are NET prices.

VAT will be added later in the checkout.

Tax calculation will be finalised during checkout.

Rent or Buy article

Get time limited or full article access on ReadCube.

from \$8.99

Rent or Buy

All prices are NET prices.

Additional access options:

- [Log in](#)
- [Access through your institution](#)
- [Learn about institutional subscriptions](#)

Fig. 1: PTG-KO reduces the expression of UCP1 in beige adipocytes.

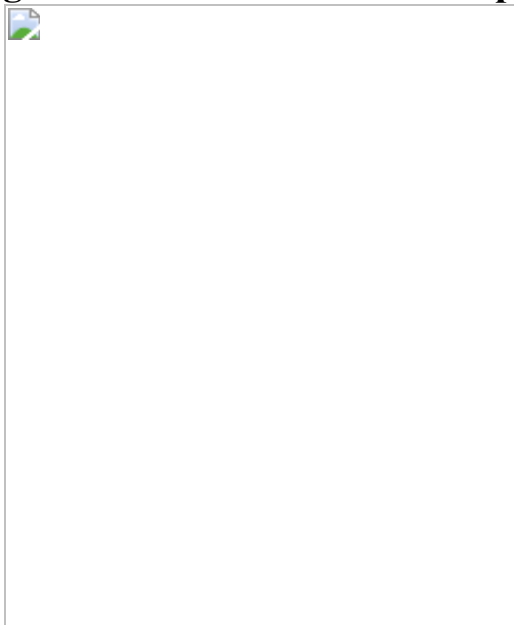


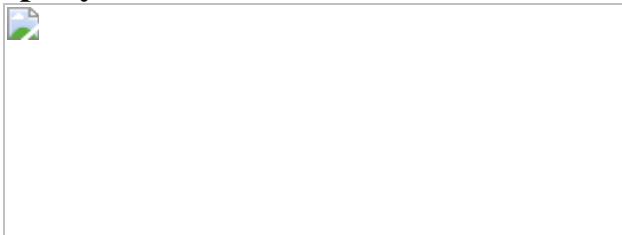
Fig. 2: Adipose-specific PTG knockout reduces UCP1 expression and energy expenditure.



Fig. 3: Attenuation of glycogen metabolism reduces the activation of p38.



Fig. 4: Glycogen metabolism contributes to ROS production in adipocytes.



Data availability

RNA-seq data reported in this paper have been deposited in the National Center for Biotechnology Information (NCBI) Sequence Read Archive⁴⁸ database under BioProject [PRJNA752350](#).

References

1. 1.
Ikeda, K. & Yamada, T. UCP1 dependent and independent thermogenesis in brown and beige adipocytes. *Front. Endocrinol.* **11**, 498 (2020).
2. 2.
Wu, J. et al. Beige adipocytes are a distinct type of thermogenic fat cell in mouse and human. *Cell* **150**, 366–376 (2012).
3. 3.
Kusminski, C. M., Bickel, P. E. & Scherer, P. E. Targeting adipose tissue in the treatment of obesity-associated diabetes. *Nat. Rev. Drug Discov.* **15**, 639–660 (2016).
4. 4.
Saltiel, A. R. New therapeutic approaches for the treatment of obesity. *Sci. Transl. Med.* **8**, 323rv2 (2016).
5. 5.
Dobin, A. et al. STAR: ultrafast universal RNA-seq aligner. *Bioinformatics* **29**, 15–21 (2013).
6. 6.
Oelkrug, R., Polymeropoulos, E. T. & Jastroch, M. Brown adipose tissue: physiological function and evolutionary significance. *J. Comp. Physiol. B* **185**, 587–606 (2015).

7. 7.

Thyagarajan, B. & Foster, M. T. Beiging of white adipose tissue as a therapeutic strategy for weight loss in humans. *Horm. Mol. Biol. Clin. Investig.* **31**, 0016 (2017).

8. 8.

Ikeda, K. et al. UCP1-independent signaling involving SERCA2b-mediated calcium cycling regulates beige fat thermogenesis and systemic glucose homeostasis. *Nat. Med.* **23**, 1454–1465 (2017).

9. 9.

Kazak, L. et al. A creatine-driven substrate cycle enhances energy expenditure and thermogenesis in beige fat. *Cell* **163**, 643–655 (2015).

10. 10.

Roach, P. J., Depaoli-Roach, A. A., Hurley, T. D. & Tagliabracci, V. S. Glycogen and its metabolism: some new developments and old themes. *Biochem. J.* **441**, 763–787 (2012).

11. 11.

Brady, M. J., Nairn, A. C. & Saltiel, A. R. The regulation of glycogen synthase by protein phosphatase 1 in 3T3-L1 adipocytes. Evidence for a potential role for DARPP-32 in insulin action. *J. Biol. Chem.* **272**, 29698–29703 (1997).

12. 12.

Brady, M. J. & Saltiel, A. R. The role of protein phosphatase-1 in insulin action. *Recent Prog. Horm. Res.* **56**, 157–173 (2001).

13. 13.

Newgard, C. B., Brady, M. J., O'Doherty, R. M. & Saltiel, A. R. Organizing glucose disposal: emerging roles of the glycogen targeting

subunits of protein phosphatase-1. *Diabetes* **49**, 1967–1977 (2000).

14. 14.

Printen, J. A., Brady, M. J. & Saltiel, A. R. PTG, a protein phosphatase 1-binding protein with a role in glycogen metabolism. *Science* **275**, 1475–1478 (1997).

15. 15.

Chandler, A. M. & Moore, R. O. Glycogen deposition in adipose tissue: variations in levels of glycogen-cycle enzymes during fasting and refeeding. *Arch. Biochem. Biophys.* **108**, 183–192 (1964).

16. 16.

Carmean, C. M., Bobe, A. M., Yu, J. C., Volden, P. A. & Brady, M. J. Refeeding-induced brown adipose tissue glycogen hyper-accumulation in mice is mediated by insulin and catecholamines. *PLoS ONE* **8**, e67807 (2013).

17. 17.

Min, S. Y. et al. Diverse repertoire of human adipocyte subtypes develops from transcriptionally distinct mesenchymal progenitor cells. *Proc. Natl Acad. Sci. USA* **116**, 17970–17979 (2019).

18. 18.

Arner, E. et al. Adipose tissue microRNAs as regulators of CCL2 production in human obesity. *Diabetes* **61**, 1986–1993 (2012).

19. 19.

Civelek, M. et al. Genetic regulation of adipose gene expression and cardio-metabolic traits. *Am. J. Hum. Genet.* **100**, 428–443 (2017).

20. 20.

Cao, W. et al. p38 mitogen-activated protein kinase is the central regulator of cyclic AMP-dependent transcription of the brown fat uncoupling protein 1 gene. *Mol. Cell. Biol.* **24**, 3057–3067 (2004).

21. 21.

Ito, K. et al. Reactive oxygen species act through p38 MAPK to limit the lifespan of hematopoietic stem cells. *Nat. Med.* **12**, 446–451 (2006).

22. 22.

Noguchi, T. et al. Requirement of reactive oxygen species-dependent activation of ASK1-p38 MAPK pathway for extracellular ATP-induced apoptosis in macrophage. *J. Biol. Chem.* **283**, 7657–7665 (2008).

23. 23.

Thomas, S. A. & Palmiter, R. D. Thermoregulatory and metabolic phenotypes of mice lacking noradrenaline and adrenaline. *Nature* **387**, 94–97 (1997).

24. 24.

Markan, K. R., Jurczak, M. J. & Brady, M. J. Stranger in a strange land: roles of glycogen turnover in adipose tissue metabolism. *Mol. Cell. Endocrinol.* **318**, 54–60 (2010).

25. 25.

Wertheimer, E. Glycogen in adipose tissue. *J. Physiol.* **103**, 359–366 (1945).

26. 26.

Kobayashi, M., Soman, G. & Graves, D. J. A comparison of the activator sites of liver and muscle glycogen phosphorylase b. *J. Biol. Chem.* **257**, 14041–14047 (1982).

27. 27.

Merlin, J. et al. The PPAR γ agonist rosiglitazone promotes the induction of brite adipocytes, increasing beta-adrenoceptor-mediated mitochondrial function and glucose uptake. *Cell Signal.* **42**, 54–66 (2018).

28. 28.

Jia, Y. T. et al. Activation of p38 MAPK by reactive oxygen species is essential in a rat model of stress-induced gastric mucosal injury. *J. Immunol.* **179**, 7808–7819 (2007).

29. 29.

Emerling, B. M. et al. Mitochondrial reactive oxygen species activation of p38 mitogen-activated protein kinase is required for hypoxia signaling. *Mol. Cell. Biol.* **25**, 4853–4862 (2005).

30. 30.

Ro, S. H. et al. Sestrin2 inhibits uncoupling protein 1 expression through suppressing reactive oxygen species. *Proc. Natl Acad. Sci. USA* **111**, 7849–7854 (2014).

31. 31.

Cao, W., Medvedev, A. V., Daniel, K. W. & Collins, S. β -Adrenergic activation of p38 MAP kinase in adipocytes: cAMP induction of the uncoupling protein 1 (UCP1) gene requires p38 MAP kinase. *J. Biol. Chem.* **276**, 27077–27082 (2001).

32. 32.

Hattori, K. et al. ASK1 signalling regulates brown and beige adipocyte function. *Nat. Commun.* **7**, 11158 (2016).

33. 33.

Forrester, S. J., Kikuchi, D. S., Hernandes, M. S., Xu, Q. & Griendling, K. K. Reactive oxygen species in metabolic and inflammatory signaling. *Circ. Res.* **122**, 877–902 (2018).

34. 34.

Jastroch, M. Uncoupling protein 1 controls reactive oxygen species in brown adipose tissue. *Proc. Natl Acad. Sci. USA* **114**, 7744–7746 (2017).

35. 35.

Chouchani, E. T. et al. Mitochondrial ROS regulate thermogenic energy expenditure and sulfenylation of UCP1. *Nature* **532**, 112–116 (2016).

36. 36.

Crosson, S. M., Khan, A., Printen, J., Pessin, J. E. & Saltiel, A. R. PTG gene deletion causes impaired glycogen synthesis and developmental insulin resistance. *J. Clin. Invest.* **111**, 1423–1432 (2003).

37. 37.

Reilly, S. M. et al. Catecholamines suppress fatty acid re-esterification and increase oxidation in white adipocytes via STAT3. *Nat. Metab.* **2**, 620–634 (2020).

38. 38.

Smets, F. N., Chen, Y., Wang, L. J. & Soriano, H. E. Loss of cell anchorage triggers apoptosis (anoikis) in primary mouse hepatocytes. *Mol. Genet. Metab.* **75**, 344–352 (2002).

39. 39.

Lu, B., et al. Metabolic crosstalk: molecular links between glycogen and lipid metabolism in obesity. *Diabetes* **63**, 2935–2948 (2014).

40. 40.

Xiao, H. et al. A quantitative tissue-specific landscape of protein redox regulation during aging. *Cell* **180**, 968–83.e24 (2020).

41. 41.

Navarrete-Perea, J., Yu, Q., Gygi, S. P. & Paulo, J. A. Streamlined tandem mass tag (SL-TMT) protocol: an efficient strategy for quantitative (phospho)proteome profiling using tandem mass tag-synchronous precursor selection-MS3. *J. Proteome Res.* **17**, 2226–2236 (2018).

42. 42.

Schwepppe, D. K. et al. Characterization and optimization of multiplexed quantitative analyses using high-field asymmetric-waveform ion mobility mass spectrometry. *Anal. Chem.* **91**, 4010–4016 (2019).

43. 43.

McAlister, G. C. et al. MultiNotch MS3 enables accurate, sensitive, and multiplexed detection of differential expression across cancer cell line proteomes. *Anal. Chem.* **86**, 7150–7158 (2014).

44. 44.

Eng, J. K., Jahan, T. A. & Hoopmann, M. R. Comet: an open-source MS/MS sequence database search tool. *Proteomics* **13**, 22–24 (2013).

45. 45.

Elias, J. E. & Gygi, S. P. Target-decoy search strategy for increased confidence in large-scale protein identifications by mass spectrometry. *Nat. Methods* **4**, 207–214 (2007).

46. 46.

Hutlin, E. L. et al. A tissue-specific atlas of mouse protein phosphorylation and expression. *Cell* **143**, 1174–1189 (2010).

47. 47.

Peng, J., Elias, J. E., Thoreen, C. C., Licklider, L. J. & Gygi, S. P. Evaluation of multidimensional chromatography coupled with tandem mass spectrometry (LC/LC-MS/MS) for large-scale protein analysis: the yeast proteome. *J. Proteome Res.* **2**, 43–50 (2003).

48. 48.

Orian, A. et al Structural motifs involved in ubiquitin-mediated processing of the NF-κB precursor p105: roles of the glycine-rich region and a downstream ubiquitination domain. *Mol. Cell. Biol.* **19**, 3664–3673 (1999).

Acknowledgements

We thank members of Saltiel laboratory at UCSD for helpful discussions, comments and suggestions and the UCSD histology core for tissue sectioning and staining. The authors are supported by 1R01 DK117850 and 1R01 HL147883 (A.J.L.); American Diabetes Association no. 1-19-PDF-177 (M.A.-O.); American Diabetes Association grant no. 1-19-JDF-012 (S.M.R.); F32DK124947 (J.M.V.); DK057978 and DK120480 (R.M.E.); R01DK117551, R01DK125820 and R01DK076906 (A.R.S.); and P30 DK063491 (R.M.E. and A.R.S.). E.T.C. is supported by Claudia Adams Barr Program, the Lavine Family Fund and NIH DK123095. H.X. is supported by a postdoctoral fellowship from the National Cancer Center.

Author information

Affiliations

1. Department of Medicine, University of California San Diego, San Diego, CA, USA

Omer Keinan, Joseph M. Valentine, Shannon M. Reilly, Mohammad Abu-Odeh, Julia H. Deluca, Benyamin Dadpey, Leslie Cho, Austin Pan & Alan R. Saltiel

2. Department of Cancer Biology, Dana–Farber Cancer Institute, Boston, MA, USA

Haopeng Xiao & Edward T. Chouchani

3. Department of Cell Biology, Harvard Medical School, Boston, MA, USA

Haopeng Xiao & Edward T. Chouchani

4. VA San Diego Healthcare System and University of California San Diego, San Diego, CA, USA

Sushil K. Mahata

5. Gene Expression Laboratory, Salk Institute for Biological Sciences, La Jolla, CA, USA

Ruth T. Yu, Yang Dai, Michael Downes & Ronald M. Evans

6. Storr Liver Centre, Westmead Institute for Medical Research and Sydney Medical School, University of Sydney, Westmead, New South Wales, Australia

Christopher Liddle

7. Department of Microbiology, Immunology, and Molecular Genetics, University of California, Los Angeles, CA, USA

Aldons J. Lusis

8. Institute of Clinical Medicine, Internal Medicine, University of Eastern Finland, Kuopio, Finland

Markku Laakso

9. Department of Medicine (H7), Karolinska Institutet, Karolinska University Hospital, Stockholm, 86, Sweden

Mikael Ryde'n

10. Department of Pharmacology, University of California, San Diego, San Diego, CA, USA

Alan R. Saltiel

Contributions

O.K. performed experimental design, experiments, data acquisition and interpretation, and wrote the manuscript. J.M.V. performed experimental design, analysis of data from human studies and wrote the manuscript. H.X. and E.T.C. performed and analysed the global assessment of cysteine oxidation. S.K.M. performed electron microscopy experiments and image acquisition and provided critical edits to the text. S.M.R. performed experimental design and provided critical edits to the text. M.A.-O. performed experiments and interpretation. J.H.D, B.D., L.C. and A.P. performed experiments. R.T.Y., Y.D., C.L., M.D. and R.M.E. performed and analysed RNA-seq experiments. A.J.L. and M.L. provided human gene expression data from the METSIM study and provided edits to the text. M.R. provided human gene expression data and provided critical edits to the text. A.R.S. conceptualized the study, performed data interpretation and wrote the manuscript.

Corresponding author

Correspondence to [Alan R. Saltiel](#).

Ethics declarations

Competing interests

The authors declare no competing interests.

Additional information

Peer review information *Nature* thanks the anonymous reviewer(s) for their contribution to the peer review of this work.

Publisher's note Springer Nature remains neutral with regard to jurisdictional claims in published maps and institutional affiliations.

Extended data figures and tables

Extended Data Fig. 1 Glycogen metabolism is enhanced in beige adipocytes.

a, b, Gene expression in iWAT from mice treated with either vehicle or CL-316,243 for 7 days. $n = 5$ mice (vehicle) and 6 mice (CL-316,243). **c**, Protein expression in mice treated as in **a**, $n = 5$ mice (vehicle) and 6 mice (CL-316,243). **d**, Glycogen levels in iWAT of vehicle or CL-316,243 treated mice, $n = 4$ mice (vehicle) and 5 mice (CL-316,243). **e**, Electron micrographs of iWAT from vehicle or CL-316,243 treated mice. Arrows point to glycogen granules. Scale bar, Left two images – 1 μm , right two images – 260 nm. Shown are representative images of tissues from 6 different mice (3 vehicle and 3 CL-316,243). **f**, Periodic acid-Schiff (PAS) staining for glycogen and UCP1 immunostaining in iWAT of vehicle or CL-316,243 treated mice. Right panels show a higher magnification of areas marked by a square. Scale bars, 4 left images – 2 mm, high magnification images – 100 μm . Shown are representative images of tissues from 6 different mice (3 vehicle and 3 CL-316,243). **g**, Gene expression in iWAT-derived stromal-vascular fraction and primary mature adipocytes from vehicle or CL-316,243 treated mice $n = 4$ biological replicates per treatment. Data are presented as mean \pm s.e.m. * $P < 0.05$, ** $P < 0.01$, *** $P < 0.001$. # $P < 0.05$, ## $P < 0.01$. *Significance between vehicle and CL-316,243 treatment. #Significance between SVF and vehicle treated mature adipocytes. Statistical significance for **a, b** and **d** was determined by two-sided *t*-test, two-way ANOVA with adjustments for multiple comparisons was used for **g**.

Extended Data Fig. 2 CL-316,243 treatment does not affect the expression of glycogen metabolizing genes in BAT.

a, gene expression in human preadipocytes, differentiated adipocytes or differentiated adipocytes treated with forskolin for 3 days. $n = 52$ biological replicates per treatment. Statistical significance was determined using two-way ANOVA with adjustments for multiple comparisons, ***- $p < 0.001$. **b**, Mice were treated with either vehicle or CL-316,243 for 7 days. Gene expression in BAT was determined using qPCR, $n = 5$ mice per treatment. **c**, Quantification of protein expression data shown in Extended Data Fig. 1C (main text), expression was normalized to HSP90. $n = 5$ mice (Vehicle), $n = 6$ mice (CL-316,243). Statistical significance was determined using two-sided *t*-test. **d**, Protein expression in BAT from mice treated as in **b** was determined by SDS-PAGE, $n = 5$ mice (vehicle), $n = 6$ mice (CL-316,243). No statistical significance detected. Data in **a–c** are presented as mean \pm s.e.m.

Extended Data Fig. 3 PTG-KO does not affect the response to CL-316,243.

a–e, RNAseq data from iWAT-derived mature adipocytes of WT and PTG-KO mice treated with either vehicle or CL-316,243, $n = 3$. **a**, Differential gene expression analyses of RNAseq data. **b**, Log₂ of fold change of gene expression of CL-316,243 treated WT mice versus vehicle-treated WT mice. Statistical significance was determined using two-sided *t*-test. **c**, Log₂ of fold change of gene expression of CL-316,243 treated PTG-KO mice versus vehicle treated PTG-KO mice. Statistical significance was determined using two-sided *t*-test. **d, e**, Pathway analyses of RNAseq were conducted using Gene Set Enrichment Analysis. **f**, Quantification of UCP1 protein expression data shown in Fig. 1f (main text), expression was normalized to RalA. $n = 4$ mice per treatment. Statistical significance was determined using two-sided *t*-test. **g**, Serum FFA levels in WT and PTG-KO mice treated with either vehicle or CL-316,243 for 20 min, $n = 5$ mice per genotype per treatment. Statistical significance was determined using two-way ANOVA with adjustments for multiple comparisons. Data are

presented as mean \pm s.e.m. * $p < 0.05$. *** $p < 0.001$. Accession number to cite these SRA data: PRJNA752350.

Extended Data Fig. 4 Adipose specific PTG-KO reduces energy expenditure.

a, Quantification of protein expression data shown in Fig. 2a (main text), expression was normalized to HSP90. $n = 5$ mice per treatment per genotype. **b, c**, Carbon dioxide production (VCO_2) in WT and PTG-AKO mice treated with CL-316,243. $n = 4$ mice per treatment per genotype. **b**, Average VCO_2 over the first three days of CL-316,243 treatment. **c**, Average VCO_2 during days 4-7 of CL-316,243 treatment. **d**, Quantification of UCP1 protein expression data shown in Fig. 2e (main text), expression was normalized to HSP90. $n = 4$ mice per treatment per genotype. **e**, Gene expression in iWAT of WT and PTG-AKO mice fed HFD for three months and then treated with either vehicle or CL-316,243 for 7 days. $n = 6$ mice per treatment per genotype. **f**, Body weight of WT and PTG-AKO mice fed HFD for three months before (day 0) and after 7 days (day 6) daily injections of Cl-316,243. $n = 7$ mice (WT), $n = 6$ mice (PTG-AKO). **g**, Weight of the inguinal white adipose tissue of WT and PTG-AKO mice fed HFD for three months and then treated for 7 days with either vehicle or Cl-316,243. $n = 7$ mice (WT), $n = 6$ mice (PTG-AKO). **h**, Linear regression analysis on anthropometric measurements in relation to gene expression from adipose tissue of 770 men. Data are presented as mean \pm s.e.m. Statistical significance determined by two-way ANOVA with adjustments for multiple comparisons. * $P < 0.05$, ** $P < 0.01$, *** $P < 0.001$. # $P < 0.05$. * - significance between vehicle and Cl-316-243 treatment within the same genotype. # - significance between WT and PTG-AKO mice treated with CL-316,243.

Extended Data Fig. 5 Overexpression of PTG increases UCP1 expression *in vitro*.

a, Glycogen levels in mouse primary hepatocytes treated with either vehicle or glucagon (10nM). $n = 2$ biological replicates per treatment. **b, c**, HEK-293t cells transfected with a *Ucp1*-promoter-driven turbo-GFP (*Ucp1*-GFP)

alone or with FLAG tagged PTG (PTG-FLAG). **b**, Images of transfected cells were acquired using the Nikon eclipse Ts2R microscope. Shown are representative images from 3 independent experiments. Scale bar – 1 μ m. **c**, GFP expression levels were determined by western blot. **d**, Preadipocytes were treated with either Cl-316,243 alone or in combination with Tautomycin. Protein expression was determined by western blot. $n = 3$ biological replicates per treatment. **e**, Quantification of protein expression data shown in D. $n = 3$ biological replicates per treatment. **f**, Quantification of protein expression data shown in Fig. 3e (main text). $n = 2$ biological replicates per treatment per genotype. **g**, Quantification of protein expression data shown in Fig. 3g (main text). $n = 3$ biological replicates per treatment. Data are presented as mean \pm s.e.m. Statistical significance was determined using two-way ANOVA with adjustments for multiple comparisons. * $P < 0.05$, ** $P < 0.01$. # $P < 0.05$. * - Significance between the zero time point and Glucagon/Cl-316,243 treatment within the same genotype. # - Significance between genotypes within the same time point.

Extended Data Fig. 6 Glycogen metabolism affects ROS production in response to Cl-316,243.

a, Quantification of protein expression data shown in Fig. 4c (main text). $n = 2$ biological replicates per treatment. Data are presented as mean \pm s.e.m. Statistical significance was determined using two-way ANOVA with adjustments for multiple comparisons. * $P < 0.05$, ** $P < 0.01$, *** $P < 0.001$. # $P < 0.05$. * - Significance between the zero time point and the assigned time point within the same treatment. # - Significance between different vehicle and NAC treatments within the same time point. **b** and **c**, Global cysteine oxidation in preadipocytes treated with either vehicle or Cl-316,243 (**b**) or Cl-316,243 alone or in combination with GPI (**c**), was determined as described in the methods section. **b**, Blue dots represent proteins with higher cysteine oxidation in vehicle-treated cells, red dots represent proteins with higher cysteine oxidation in Cl-316,243 treated cells. **c**, Blue dots represent proteins with higher cysteine oxidation in Cl-316,243 treated cells, red dots represent proteins with higher cysteine oxidation in cells treated with Cl-316,243 in combination with GPI.

Statistical significance was determined using two-sided t test, cysteine sites shown had at least 5% change between treatments with a $p < 0.05$.

Extended Data Fig. 7 PTG-KO reduces energy expenditure during long term cold adaptation.

a, Core body temperature of WT and PTG-KO mice measured every 90 min during an acute cold exposure (4 °C), $n = 8$ mice per genotype. **b**, Brown adipose tissue glycogen levels in WT and PTG-KO mice at room temperature (RT) or cold exposed for 6 h and allowed to recover for 4 h at RT (4 °C-RT), $n = 3$ mice per genotype per condition. **c**, Core body temperature during a second cold exposure in WT and PTG-KO mice that were first cold exposed for 6 h and allowed to recover at room temperature for 4 h, $n = 8$ mice per genotype. **d**, **e** and **f**, gene expression in iWAT of WT and PTG-BKO mice housed either at room temperature or subjected to prolonged cold adaptation (7 days at 18 °C followed by 14 days at 4 °C), $n = 8$ mice per genotype. **g**, Protein expression in iWAT of the mice described in **d**, $n = 5$ mice per genotype. **h**, Oxygen consumption (VO_2) in WT and PTG-BKO mice before and during prolonged cold adaptation $n = 8$ mice per genotype. **i**, Working model. Acute activation of the $\beta 3$ -adrenergic receptor in white adipocytes results in lipolysis and glycogenolysis through the activation of PKA and subsequent activation of HSL and GP respectively. Prolonged $\beta 3$ -adrenergic receptor activation results in enhanced glycogen accumulation turnover which is required for ROS-dependent p38 activation and the subsequent expression of Ucp1. Data are presented as mean \pm s.e.m. Statistical significance was determined two-way ANOVA with adjustments for multiple comparisons. * $P < 0.05$, ** $P < 0.01$. # $P < 0.05$. * - significance between room temperature and cold exposure within the same genotype. # - significance between WT and PTG-KO/PTG-BKO with the same treatment.

Extended Data Fig. 8 Increased expression of BAT-Ucp1 following long-term cold exposure does not require PTG.

a, Quantification of protein expression data shown in Extended Data Fig. 7 (main text). $n = 5$ mice per genotype. **b**, Protein expression levels in BAT of

WT and PTG-BKO mice housed either at room temperature or subjected to prolonged cold adaptation was determined by SDS-PAGE, n (22 °C) = 4, n (4 °C) = 5 . c carbon dioxide production (VCO₂) in WT and PTG-BKO mice before and during prolonged cold adaptation. n = 8 mice per genotype. Data are presented as mean ± s.e.m. Statistical significance was determined using two-sided t test (A) or two way ANOVA with adjustments for multiple comparisons (C). *P < 0.05. #P < 0.05. * - Significance between 4 °C and 22 °C within the same genotype. # - Significance between different genotypes within the same time point.

Supplementary information

Supplementary Figure

This file contains the uncropped Western blots used in the main figures and extended data figures.

Reporting Summary

Supplementary Table 1

This file contains the qPCR primers used in the study.

Rights and permissions

Reprints and Permissions

About this article

Cite this article

Keinan, O., Valentine, J.M., Xiao, H. *et al.* Glycogen metabolism links glucose homeostasis to thermogenesis in adipocytes. *Nature* **599**, 296–301 (2021). <https://doi.org/10.1038/s41586-021-04019-8>

- Received: 15 November 2020
- Accepted: 13 September 2021
- Published: 27 October 2021
- Issue Date: 11 November 2021
- DOI: <https://doi.org/10.1038/s41586-021-04019-8>

Share this article

Anyone you share the following link with will be able to read this content:

[Get shareable link](#)

Sorry, a shareable link is not currently available for this article.

[Copy to clipboard](#)

Provided by the Springer Nature SharedIt content-sharing initiative

[Glycogen involved in browning of adipocytes](#)

- Claire Greenhill

Research Highlight 10 Nov 2021

This article was downloaded by **calibre** from <https://www.nature.com/articles/s41586-021-04019-8>

- Article
- [Published: 20 October 2021](#)

Low glycaemic diets alter lipid metabolism to influence tumour growth

- [Evan C. Lien](#)¹,
- [Anna M. Westermark](#)¹,
- [Yin Zhang](#) [ORCID: orcid.org/0000-0001-6367-6583](#)^{2,3},
- [Chen Yuan](#)²,
- [Zhaoqi Li](#)^{1,4},
- [Allison N. Lau](#)¹,
- [Kiera M. Sapp](#) [ORCID: orcid.org/0000-0002-5523-1223](#)^{1,4},
- [Brian M. Wolpin](#)² &
- [Matthew G. Vander Heiden](#) [ORCID: orcid.org/0000-0002-6702-4192](#)^{1,2,4}

[Nature](#) volume **599**, pages 302–307 (2021)

- 18k Accesses
- 1 Citations
- 419 Altmetric
- [Metrics details](#)

Subjects

- [Cancer metabolism](#)

- [Fatty acids](#)
- [Metabolomics](#)

Abstract

Dietary interventions can change metabolite levels in the tumour microenvironment, which might then affect cancer cell metabolism to alter tumour growth^{1,2,3,4,5}. Although caloric restriction (CR) and a ketogenic diet (KD) are often thought to limit tumour progression by lowering blood glucose and insulin levels^{6,7,8}, we found that only CR inhibits the growth of select tumour allografts in mice, suggesting that other mechanisms contribute to tumour growth inhibition. A change in nutrient availability observed with CR, but not with KD, is lower lipid levels in the plasma and tumours. Upregulation of stearoyl-CoA desaturase (SCD), which synthesises monounsaturated fatty acids, is required for cancer cells to proliferate in a lipid-depleted environment, and CR also impairs tumour SCD activity to cause an imbalance between unsaturated and saturated fatty acids to slow tumour growth. Enforcing cancer cell SCD expression or raising circulating lipid levels through a higher-fat CR diet confers resistance to the effects of CR. By contrast, although KD also impairs tumour SCD activity, KD-driven increases in lipid availability maintain the unsaturated to saturated fatty acid ratios in tumours, and changing the KD fat composition to increase tumour saturated fatty acid levels cooperates with decreased tumour SCD activity to slow tumour growth. These data suggest that diet-induced mismatches between tumour fatty acid desaturation activity and the availability of specific fatty acid species determine whether low glycaemic diets impair tumour growth.

Access options

Subscribe to Journal

Get full journal access for 1 year

\$199.00

only \$3.90 per issue

Subscribe

All prices are NET prices.

VAT will be added later in the checkout.

Tax calculation will be finalised during checkout.

Rent or Buy article

Get time limited or full article access on ReadCube.

from \$8.99

Rent or Buy

All prices are NET prices.

Additional access options:

- [Log in](#)
- [Access through your institution](#)
- [Learn about institutional subscriptions](#)

Fig. 1: CR, but not the KD, impairs growth of PDAC allograft tumours.

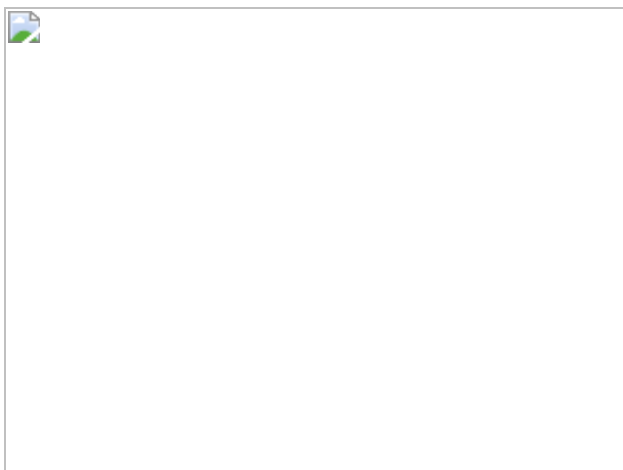


Fig. 2: CR and the KD differentially alter nutrient levels in the plasma and TIF.

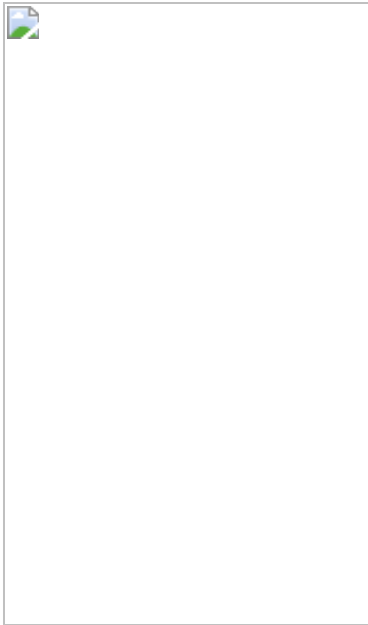


Fig. 3: Increased SCD activity is required for cancer cells to adapt to exogenous lipid limitation.

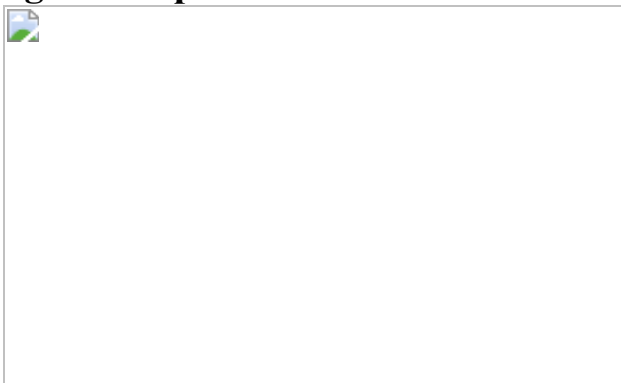
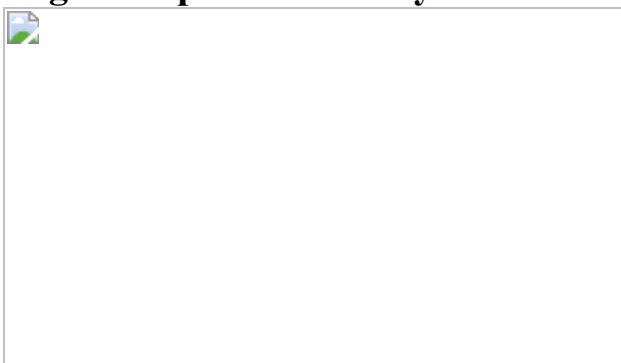


Fig. 4: Low glycaemic diets impair tumour SCD, which interacts with changes in lipid availability to affect tumour growth.



Data availability

All data generated or analysed in this study are included in the published article and in Supplementary Table 1, Supplementary Figs. 1–23 and Source Data for Figs. 1–4 and Extended Data Figs. 1–8. Correspondence and requests for materials should be addressed to Matthew G. Vander Heiden (m vh@mit.edu). [Source data](#) are provided with this paper.

References

1. 1.
Lien, E. C. & Vander Heiden, M. G. A framework for examining how diet impacts tumour metabolism. *Nat. Rev. Cancer* **19**, 651–661 (2019).
2. 2.
Sullivan, M. R. et al. Increased serine synthesis provides an advantage for tumors arising in tissues where serine levels are limiting. *Cell Metab.* **29**, 1410–1421 (2019).
3. 3.
Sullivan, M. R. et al. Quantification of microenvironmental metabolites in murine cancers reveals determinants of tumor nutrient availability. *Elife* **8**, e44235 (2019).
4. 4.
Maddock, O. D. K. et al. Modulating the therapeutic response of tumours to dietary serine and glycine starvation. *Nature* **544**, 372–376 (2017).
5. 5.
Gao, X. et al. Dietary methionine influences therapy in mouse cancer models and alters human metabolism. *Nature* **572**, 397–401 (2019).
6. 6.

Kalaany, N. Y. & Sabatini, D. M. Tumours with PI3K activation are resistant to dietary restriction. *Nature* **458**, 725–731 (2009).

7. 7.

Hopkins, B. D. et al. Suppression of insulin feedback enhances the efficacy of PI3K inhibitors. *Nature* **560**, 499–503 (2018).

8. 8.

Nencioni, A., Caffa, I., Cortellino, S. & Longo, V. D. Fasting and cancer: molecular mechanisms and clinical application. *Nat. Rev. Cancer* **18**, 707–719 (2018).

9. 9.

Danai, L. V. et al. Altered exocrine function can drive adipose wasting in early pancreatic cancer. *Nature* **558**, 600–604 (2018).

10. 10.

Gocheva, V. et al. Quantitative proteomics identify Tenascin-C as a promoter of lung cancer progression and contributor to a signature prognostic of patient survival. *Proc. Natl Acad. Sci. USA* **114**, E5625–E5634 (2017).

11. 11.

Kennedy, A. R. et al. A high-fat, ketogenic diet induces a unique metabolic state in mice. *Am. J. Physiol. Endocrinol. Metab.* **292**, E1724–E1739 (2007).

12. 12.

Mukherjee, P., El-Abbadi, M. M., Kasperzyk, J. L., Ranes, M. K. & Seyfried, T. N. Dietary restriction reduces angiogenesis and growth in an orthotopic mouse brain tumour model. *Br. J. Cancer* **86**, 1615–1621 (2002).

13. 13.

Zhang, J. et al. Low ketolytic enzyme levels in tumors predict ketogenic diet responses in cancer cell lines in vitro and in vivo. *J. Lipid Res.* **59**, 625–634 (2018).

14. 14.

Hosios, A. M., Li, Z., Lien, E. C. & Vander Heiden, M. G. Preparation of lipid-stripped serum for the study of lipid metabolism in cell culture. *Bio Protoc.* **8**, e2876 (2018).

15. 15.

Peck, B. & Schulze, A. Lipid desaturation—the next step in targeting lipogenesis in cancer. *FEBS J.* **283**, 2767–2778 (2016).

16. 16.

Vriens, K. et al. Evidence for an alternative fatty acid desaturation pathway increasing cancer plasticity. *Nature* **566**, 403–406 (2019).

17. 17.

Kim, W. et al. Polyunsaturated fatty acid desaturation is a mechanism for glycolytic NAD⁺ recycling. *Cell Metab.* **29**, 856–870 (2019).

18. 18.

Sullivan, L. B. et al. Supporting aspartate biosynthesis is an essential function of respiration in proliferating cells. *Cell* **162**, 552–563 (2015).

19. 19.

Birsoy, K. et al. An essential role of the mitochondrial electron transport chain in cell proliferation is to enable aspartate synthesis. *Cell* **162**, 540–551 (2015).

20. 20.

Titov, D. V. et al. Complementation of mitochondrial electron transport chain by manipulation of the NAD⁺/NADH ratio. *Science* **352**, 231–235 (2016).

21. 21.

Diehl, F. F., Lewis, C. A., Fiske, B. P. & Vander Heiden, M. G. Cellular redox state constrains serine synthesis and nucleotide production to impact cell proliferation. *Nat. Metab.* **1**, 861–867 (2019).

22. 22.

Piccolis, M. et al. Probing the global cellular responses to lipotoxicity caused by saturated fatty acids. *Mol. Cell* **74**, 32–44 (2019).

23. 23.

Mauvoisin, D. & Mounier, C. Hormonal and nutritional regulation of SCD1 gene expression. *Biochimie* **93**, 78–86 (2011).

24. 24.

Young, R. M. et al. Dysregulated mTORC1 renders cells critically dependent on desaturated lipids for survival under tumor-like stress. *Genes Dev.* **27**, 1115–1131 (2013).

25. 25.

Ackerman, D. et al. Triglycerides promote lipid homeostasis during hypoxic stress by balancing fatty acid saturation. *Cell Rep.* **24**, 2596–2605 (2018).

26. 26.

Kamphorst, J. J. et al. Hypoxic and Ras-transformed cells support growth by scavenging unsaturated fatty acids from lysophospholipids. *Proc. Natl Acad. Sci. USA* **110**, 8882–8887 (2013).

27. 27.

Coulston, A. M. The role of dietary fats in plant-based diets. *Am. J. Clin. Nutr.* **70**, 512S–515S (1999).

28. 28.

Pascual, G. et al. Targeting metastasis-initiating cells through the fatty acid receptor CD36. *Nature* **541**, 41–45 (2017).

29. 29.

Siri-Tarino, P. W., Chiu, S., Bergeron, N. & Krauss, R. M. Saturated fats versus polyunsaturated fats versus carbohydrates for cardiovascular disease prevention and treatment. *Annu. Rev. Nutr.* **35**, 517–543 (2015).

30. 30.

Mayers, J. R. et al. Tissue of origin dictates branched-chain amino acid metabolism in mutant Kras-driven cancers. *Science* **353**, 1161–1165 (2016).

31. 31.

Lewis, C. A. et al. Tracing compartmentalized NADPH metabolism in the cytosol and mitochondria of mammalian cells. *Mol. Cell* **55**, 253–263 (2014).

32. 32.

Heinrich, P. et al. Correcting for natural isotope abundance and tracer impurity in MS-, MS/MS- and high-resolution-multiple-tracer-data from stable isotope labeling experiments with IsoCorrectoR. *Sci. Rep.* **8**, 17910 (2018).

33. 33.

Antoniewicz, M. R., Kelleher, J. K. & Stephanopoulos, G. Measuring deuterium enrichment of glucose hydrogen atoms by gas

chromatography/mass spectrometry. *Anal. Chem.* **83**, 3211–3216 (2011).

34. 34.

Argus, J. P. et al. Development and application of FASA, a model for quantifying fatty acid metabolism using stable isotope labeling. *Cell Rep.* **25**, 2919–2934 (2018).

35. 35.

Vichai, V. & Kirtikara, K. Sulforhodamine B colorimetric assay for cytotoxicity screening. *Nat. Protoc.* **1**, 1112–1116 (2006).

36. 36.

Colditz, G. A. & Hankinson, S. E. The Nurses' Health Study: lifestyle and health among women. *Nat. Rev. Cancer* **5**, 388–396 (2005).

37. 37.

Belanger, C. F., Hennekens, C. H., Rosner, B. & Speizer, F. E. The nurses' health study. *Am. J. Nurs.* **78**, 1039–1040 (1978).

38. 38.

Health Professionals Follow-Up Study (Harvard T. H. Chan School of Public Health, 2020); <https://sites.sph.harvard.edu/hpfs/>

39. 39.

Hu, F. B. et al. Reproducibility and validity of dietary patterns assessed with a food-frequency questionnaire. *Am. J. Clin. Nutr.* **69**, 243–249 (1999).

40. 40.

Feskanich, D. et al. Reproducibility and validity of food intake measurements from a semiquantitative food frequency questionnaire.

J. Am. Diet Assoc. **93**, 790–796 (1993).

41. 41.

Willett, W. C. et al. Reproducibility and validity of a semiquantitative food frequency questionnaire. *Am. J. Epidemiol.* **122**, 51–65 (1985).

42. 42.

Rimm, E. B. et al. Reproducibility and validity of an expanded self-administered semiquantitative food frequency questionnaire among male health professionals. *Am. J. Epidemiol.* **135**, 1114–1126 (1992).

43. 43.

Willett, W. C. *Nutritional Epidemiology* (Oxford University Press, 2012).

44. 44.

Yuan, C. et al. Validity of a dietary questionnaire assessed by comparison with multiple weighed dietary records or 24-hour recalls. *Am. J. Epidemiol.* **185**, 570–584 (2017).

45. 45.

Yuan, C. et al. Relative validity of nutrient intakes assessed by questionnaire, 24-hour recalls, and diet records as compared with urinary recovery and plasma concentration biomarkers: findings for women. *Am. J. Epidemiol.* **187**, 1051–1063 (2018).

46. 46.

Halton, T. L., Liu, S., Manson, J. E. & Hu, F. B. Low-carbohydrate-diet score and risk of type 2 diabetes in women. *Am. J. Clin. Nutr.* **87**, 339–346 (2008).

47. 47.

Halton, T. L. et al. Low-carbohydrate-diet score and the risk of coronary heart disease in women. *N. Engl. J. Med.* **355**, 1991–2002 (2006).

48. 48.

Liu, Y. et al. Plant-based and animal-based low-carbohydrate diets and risk of hepatocellular carcinoma among US men and women. *Hepatology* **73**, 175–185 (2020).

49. 49.

Stampfer, M. J. et al. Test of the National Death Index. *Am. J. Epidemiol.* **119**, 837–839 (1984).

50. 50.

Rich-Edwards, J. W., Corsano, K. A. & Stampfer, M. J. Test of the National Death Index and Equifax Nationwide Death Search. *Am. J. Epidemiol.* **140**, 1016–1019 (1994).

51. 51.

Colditz, G. A. et al. Validation of questionnaire information on risk factors and disease outcomes in a prospective cohort study of women. *Am. J. Epidemiol.* **123**, 894–900 (1986).

Acknowledgements

We thank members of the Vander Heiden laboratory for useful discussions and experimental advice. E.C.L. was supported by the Damon Runyon Cancer Research Foundation (DRG-2299-17). A.N.L. was a Robert Black Fellow of the Damon Runyon Cancer Research Foundation (DRG-2241-15) and was supported by an NIH Pathway to Independence Award (K99CA234221). Z.L. and K.M.S. were supported by NIH training grant T32GM007287. B.M.W. was supported by the Lustgarten Foundation, the Dana-Farber Cancer Institute Hale Family Center for Pancreatic Cancer Research, the NIH (U01CA210171 and P50CA127003), Stand Up To

Cancer, the Pancreatic Cancer Action Network, the Noble Effort Fund, the Wexler Family Fund, Promises for Purple and the Bob Parsons Fund. M.G.V.H. acknowledges support from the Emerald Foundation, the Lustgarten Foundation, a Faculty Scholar grant from the Howard Hughes Medical Institute, Stand Up To Cancer, the MIT Center for Precision Cancer Medicine, the Ludwig Center at MIT and the NIH (R35CA242379, R01CA168653, R01CA201276 and P30CA14051). The Nurses' Health Study and the Health Professionals Follow-up Study were supported by grants UM1 CA186107, U01 CA176726, P01 CA87969, U01 CA167552 and R03 CA223619 from the NIH. The authors thank all participants and staff of the Nurses' Health Study and the Health Professionals Follow-Up Study for their contributions to this research. We are grateful for help from the following state cancer registries: Alabama, Arizona, Arkansas, California, Colorado, Connecticut, Delaware, Florida, Georgia, Idaho, Illinois, Indiana, Iowa, Kentucky, Louisiana, Maine, Maryland, Massachusetts, Michigan, Nebraska, New Hampshire, New Jersey, New York, North Carolina, North Dakota, Ohio, Oklahoma, Oregon, Pennsylvania, Rhode Island, South Carolina, Tennessee, Texas, Virginia, Washington and Wyoming. The authors also thank the Channing Division of Network Medicine, Brigham and Women's Hospital and Harvard Medical School for leading the Nurses' Health Study and the Harvard T.H. Chan School of Public Health for leading the Health Professionals Follow-Up Study. The authors assume full responsibility for analyses and interpretation of these data.

Author information

Affiliations

1. Koch Institute for Integrative Cancer Research, Massachusetts Institute of Technology, Cambridge, MA, USA

Evan C. Lien, Anna M. Westerman, Zhaoqi Li, Allison N. Lau, Kiera M. Sapp & Matthew G. Vander Heiden

2. Department of Medical Oncology, Dana-Farber Cancer Institute, Boston, MA, USA

Yin Zhang, Chen Yuan, Brian M. Wolpin & Matthew G. Vander Heiden

3. Department of Epidemiology, Harvard T. H. Chan School of Public Health, Boston, MA, USA

Yin Zhang

4. Department of Biology, Massachusetts Institute of Technology, Cambridge, MA, USA

Zhaoqi Li, Kiera M. Sapp & Matthew G. Vander Heiden

Contributions

E.C.L. and M.G.V.H. conceived the project. E.C.L. performed the experiments and analysed data. A.M.W. and A.N.L. assisted with animal experiments and interpreted data. A.M.W., Z.L. and K.M.S. assisted with fatty acid profiling experiments and interpreted data. Y.Z., C.Y. and B.M.W. performed analyses of patient population data from the Nurses' Health Study and the Health Professionals Follow-up Study. E.C.L. and M.G.V.H. wrote the manuscript, with input from all authors.

Corresponding author

Correspondence to [Matthew G. Vander Heiden](#).

Ethics declarations

Competing interests

M.G.V.H. is a scientific advisor for Agios Pharmaceuticals, Aeglea Biotherapeutics, iTeos Therapeutics and Auron Therapeutics. B.M.W. declares research funding from Celgene and Eli Lilly and consulting for BioLineRx, Celgene and GRAIL. E.C.L., A.M.W., Y.Z., C.Y., Z.L., A.N.L. and K.M.S. declare no competing interests.

Additional information

Peer review information *Nature* thanks Valter Longo, Costas Lyssiotis, Stephan Herzig and the other, anonymous, reviewer(s) for their contribution to the peer review of this work .

Publisher's note Springer Nature remains neutral with regard to jurisdictional claims in published maps and institutional affiliations.

Extended data figures and tables

[Extended Data Fig. 1 Caloric restriction, but not the ketogenic diet, impairs growth of tumor allografts.](#)

a–d, Normalized tumor volumes (**a, c**) and normalized tumor weights (**b, d**) of subcutaneous AL1376 PDAC allografts in male mice exposed to CR or a control diet (**a, b**), or the KD or a control diet (**c, d**). Tumor volumes and weights normalized to animal body weight are shown. (**a, b**) Control n = 5 mice, CR n = 4 mice; (**c, d**) Control n = 5 mice, KD n = 5 mice. **e–h**, Tumor volumes (**e, g**) and tumor weights (**f, h**) of subcutaneous AL1376 PDAC allografts in female mice exposed to CR or a control diet (**e, f**), or the KD or a control diet (**g, h**). (**e, f**) Control n = 8 mice, CR n = 8 mice; (**g, h**) Control n = 4 mice, KD n = 4 mice. **i–l**, Tumor volumes (**i, k**) and tumor weights (**j, l**) of subcutaneous LGSP non-small cell lung cancer (NSCLC) allografts in male (**i, j**) and female (**k, l**) mice exposed to CR or a control diet. (**i, j**) Control n = 10 mice, CR n = 11 mice; (**k, l**) Control n = 5 mice, CR n = 5 mice. **m–p**, Tumor volumes (**m, o**) and tumor weights (**n, p**) of subcutaneous LGSP NSCLC allografts in male (**m, n**) and female (**o, p**) mice exposed to KD or a control diet. (**m, n**) Control n = 5 mice, KD n = 5 mice; (**o, p**) Control n = 3 mice, KD n = 3 mice. Data are presented as box-and-whisker plots displaying median, interquartile range (boxes), and minima and maxima (whiskers) (**b, d, f, h, j, l, n, p**) or mean ± SEM (**a, c, e, g, i, k, m, o**). Comparisons were made using a two-tailed Student's t-test (**b, d, f, h, j, l, n, p**) or two-way repeated measures analysis of variance (ANOVA) (**a, c, e, g, i, k, m, o**)

[Source data](#).

Extended Data Fig. 2 Caloric restriction and the ketogenic diet have distinct effects on whole-body physiology.

a, b, Daily food consumption by weight (**a**) and daily caloric consumption (**b**) of the control diet and CR by male and female mice. **c**, Body weights of male and female mice exposed to CR or a control diet. Male Control n = 10, Male CR n = 11, Female Control n = 5, Female CR n = 5. **d, e**, Ki67 (**d**) and cleaved caspase 3 (CC3) (**e**) immunohistochemical staining in subcutaneous AL1376 tumors from mice exposed to a control or CR diet. n = 3 tumors per group. 5-8 independent fields from each tumor were quantified: Control n = 23, CR n = 18 (**d**); n = 17 per group (**e**). **f**, Weights of gastrocnemius muscle (Gastroc) and white adipose tissue (WAT) in male and female mice exposed to CR or a control diet. Tissue weights normalized to animal body weight are shown. n = 5 per group. **g–i**, Plasma glucagon (**g**), FGF21 (**h**), and corticosterone (**i**) levels in male mice exposed to CR or a control diet. Control n = 6, CR n = 5. **j, k**, Daily food consumption by weight (**j**) and daily caloric consumption (**k**) of the control diet and KD by male and female mice. Male Control n = 5, Male KD n = 5, Female Control n = 4, Female KD n = 5. **l**, Body weights of male and female mice exposed to KD or a control diet. Male Control n = 5, Male KD n = 5, Female Control n = 3, Female KD n = 3. **m, n**, Ki67 (**m**) and CC3 (**n**) immunohistochemical staining in subcutaneous AL1376 tumors from mice exposed to a control diet or the KD. n = 3 tumors per group. 5-8 independent fields from each tumor were quantified: n = 24 per group (**m, n**). **o**, Weights of Gastroc and WAT in male and female mice exposed to KD or a control diet. Tissue weights normalized to animal body weight are shown. Male Control n = 5, Male KD n = 5, Female Control n = 6, Female KD n = 6. **p–r**, Plasma glucagon (**p**), FGF21 (**q**), and corticosterone (**r**) levels in male mice exposed to KD or a control diet. (**p**) n = 4 per group; (**q–r**) n = 5 per group. Data are presented as mean \pm SEM (**a–c, f–l, o–r**) or box-and-whisker plots displaying median, interquartile range (boxes), and minima and maxima (whiskers) (**d, e, m, n**). Comparisons were made using a two-tailed Student's t-test

[Source data](#).

Extended Data Fig. 3 β-OHB is metabolized by PDAC cells.

a, Concentrations of β-OHB in plasma and tumor interstitial fluid (TIF) from mice implanted with subcutaneous AL1376 tumors exposed to a control diet, CR, or the KD. Plasma Control (CR cohort) n = 8, Plasma CR n = 8, Plasma Control (KD cohort) n = 10, Plasma KD n = 9, TIF Control (CR cohort) n = 16, TIF CR n = 13, TIF Control (KD cohort) n = 5, TIF KD n = 6. **b**, Doubling times of AL1376 cells cultured in media with or without 5 mM β-OHB. **c**, Fractional labeling of [M+2] TCA cycle metabolites from AL1376 cells cultured in the presence of 5 mM [U-¹³C]-β-OHB for 24 h. **d**, Mass isotopologue distribution of labeled palmitate from AL1376 cells cultured in the presence of 5 mM [U-¹³C]-β-OHB for 24 h. **e**, **f**, The indicated fatty acid levels (**e**) and MUFA/SFA ratios (**f**) measured in AL1376 cells cultured in media with or without 5 mM β-OHB for 24 h. Data are presented as box-and-whisker plots displaying median, interquartile range (boxes), and minima and maxima (whiskers) (**a**) or mean ± SEM (**b–f**). Unless otherwise indicated, n = 3 biologically independent replicates, and comparisons were made using a two-tailed Student's t-test

[Source data](#).

Extended Data Fig. 4 Increased stearoyl-CoA desaturase activity is required for cancer cells to adapt to exogenous lipid limitation.

a, Levels of the indicated fatty acids in lipidated and de-lipidated fetal bovine serum (FBS). **b**, Doubling times of the specified cells cultured in media containing lipidated versus de-lipidated serum. **c**, Fold changes in levels of the indicated fatty acids in cells cultured in de-lipidated versus lipidated media for 24 h. **d**, Relative fatty acid synthesis rates in the indicated cells cultured in lipidated versus de-lipidated media. A one-tailed Student's t-test was used for comparison between groups. **e**, **f**, Representative mass isotopologue distributions (MIDs) of 16:0 (**e**) and 18:0 (**f**) from AL1376 cells labeled with [U-¹³C]-glucose and [U-¹³C]-glutamine for 24 h in lipidated versus de-lipidated media. **g**, **h**, Representative MIDs of 16:1(n-7) (**g**) and 18:1(n-9) (**h**) from AL1376 cells labeled with [U-¹³C]-

glucose and [$^{\text{U}}\text{-}{}^{13}\text{C}$]-glutamine for 24 h in lipidated versus de-lipidated media containing 50 nM A939572. MIDs above M+12 are predominantly observed, consistent with a majority of lipogenic acetyl-CoA being derived from glucose and glutamine. **i**, Immunoblot for the mature activated form of SREBP1 (m-SREBP1) and β -actin in lysates from AL1376 cells cultured in lipidated versus de-lipidated media for 24 h, with or without 50 nM A939572, 50 μM 18:1(n-9), or 50 μM 18:2(n-6). Data is representative of three biologically independent experiments. **j**, Absolute fatty acid concentrations in AL1376 and LGSP cells cultured in lipidated media. **k**, **l**, Ratios of 16:1(n-7)/16:0 (**k**) and 18:1(n-9)/18:0 (**l**) in cells cultured in lipidated versus de-lipidated media with or without the SCD inhibitor A939572 (LGSP: 50 nM; HeLa, Panc1, A549: 200 nM) for 24 h. **m**, **n**, 16:1(n-7) (**m**) and 18:1(n-9) (**n**) synthesis rates in cells cultured in lipidated versus de-lipidated media with or without A939572 (LGSP: 50 nM; HeLa, Panc1, A549: 200 nM) for 24 h as indicated. A one-tailed ratio paired t-test was used for comparison between groups. **o**, Doubling times of the specified cells cultured in lipidated versus de-lipidated media with the indicated concentrations of A939572. **p**, Doubling times of LGSP cells cultured in de-lipidated media with or without 50 nM A939572, BSA, 100 μM 18:1(n-9), 100 μM 18:2(n-6), or 15 μM 16:0. **q**, Doubling times of cells cultured in de-lipidated media containing 200 nM A939572, BSA, or 25 μM 18:2(n-6). **r**–**v**, 18:1(n-9) (**r**), 16:1(n-7) (**s**), 18:1(n-9)/18:0 (**t**), 16:1(n-7)/16:0 (**u**), and 16:0 (**v**) levels in LGSP cells cultured in de-lipidated media with or without 50 nM A939572, BSA, 100 μM 18:1(n-9), 100 μM 18:2(n-6), or 15 μM 16:0 for 48 h. **w**, Relative fatty acid synthesis rates in LGSP cells cultured in de-lipidated media containing 50 nM A939572, BSA, 100 μM 18:1(n-9), or 100 μM 18:2(n-6). **x**, Doubling times of cells cultured in de-lipidated media containing A939572 (LGSP: 50 nM; HeLa, Panc1, A549: 200 nM), the FASN inhibitor GSK2194069 (LGSP: 0.3 μM ; HeLa, A549: 0.015 μM ; Panc1: 0.05 μM), or the ACC inhibitor PF-05175157 (LGSP: 10 μM ; HeLa: 0.3 μM ; Panc1: 1 μM ; A549: 0.5 μM). A paired two-tailed Student's t-test was used for comparison between groups in Panc1 and A549 cells. All data are presented as mean \pm SEM; unless otherwise indicated, $n = 3$ biologically independent replicates, and a two-tailed Student's t-test was used for comparison between groups unless otherwise noted above

[Source data.](#)

Extended Data Fig. 5 Determining whether SCD inhibition affects cancer cell proliferation via NAD⁺ limitation or changes to cellular fatty acid levels.

a, Doubling times of the indicated cell lines cultured in de-lipidated media with or without 1 mM pyruvate and rotenone (AL1376: 400 nM; LGSP, A549: 100 nM; HeLa, Panc1: 50 nM). **b**, Doubling times of the indicated cell lines cultured in de-lipidated media containing the indicated concentrations of the SCD inhibitor A939572 and 1 mM pyruvate. **c**, Doubling times of the indicated cell lines cultured in de-lipidated media with or without 50 nM A939572. **d–i**, Relative levels of 16:0 (**d**), 18:0 (**e**), 16:1(n-7) (**f**), 18:1(n-9) (**g**), 16:1(n-7)/16:0 (**h**), and 18:1(n-9)/18:0 (**i**) in the indicated cell lines cultured in de-lipidated media with or without 50 nM A939572. **j–l**, Relative levels of 16:1(n-10) (**j**), normalized levels of 16:1(n-10)/16:0 (**k**), and relative levels of 16:1(n-10)/16:0 (**l**) in the indicated cell lines cultured in de-lipidated media with or without 50 nM A939572. All data are presented as mean ± SEM; n = 3 biologically independent replicates. A two-tailed Student's t-test was used for comparison between groups

[Source data.](#)

Extended Data Fig. 6 Caloric restriction and the ketogenic diet alter fatty acid composition and SCD activity in tumors.

a, The indicated fatty acid levels measured in subcutaneous AL1376 tumors from mice exposed to a control or CR diet. Control n = 10, CR n = 8. **b–d**, The indicated fatty acid levels (**b**, **d**) and MUFA/SFA ratios (**c**) measured in subcutaneous AL1376 tumors from male or female mice exposed to a control or CR diet. Male Control n = 6, Male CR n = 4, Female Control n = 4, Female CR n = 4. **e–g**, The indicated fatty acid levels (**e**, **g**) and MUFA/SFA ratios (**f**) measured in subcutaneous LGSP tumors from male mice exposed to a control or CR diet. Control n = 6, CR n = 6. **h–i**, Immunoblot and quantification for mouse Scd1 (mSCD1) and vinculin in

subcutaneous AL1376 tumors from female mice (**h**, n = 7 per group) or subcutaneous LGSP tumors from male mice (**i**, n = 6 per group) exposed to a control or CR diet. **j**, The indicated fatty acid levels measured in subcutaneous AL1376 tumors from mice exposed to a control diet or KD. Control n = 8, KD n = 9. **k–m**, The indicated fatty acid levels (**k**, **m**) and MUFA/SFA ratios (**l**) measured in subcutaneous AL1376 tumors from male or female mice exposed to a control diet or KD. Male Control n = 5, Male KD n = 5, Female Control n = 3, Female KD n = 4. **n–p**, The indicated fatty acid levels (**n**, **p**) and MUFA/SFA ratios (**o**) measured in subcutaneous LGSP tumors from male mice exposed to a control diet or KD. Control n = 6, KD n = 6. **q–r**, Immunoblot and quantification for mSCD1 and vinculin in subcutaneous AL1376 tumors from female mice (**q**, Control n = 3, KD n = 4) or subcutaneous LGSP tumors from male mice (**r**, n = 6 per group) exposed to a control diet or KD. **s**, AL1376 and LGSP cells were serum-starved in the presence of 1% Lipid Mixture for 16 h followed by insulin stimulation (100 nM) for 3 h. Lysates were immunoblotted for mSCD1, p-AKT S473, AKT, and vinculin. Data is representative of three biologically independent experiments. Data are presented as box-and-whisker plots displaying median, interquartile range (boxes), and minima and maxima (whiskers) (**a**, **e–g**, **j**, **n–p**) or mean ± SEM (**b–d**, **h**, **i**, **k–m**, **q–r**). Comparisons were made using a two-tailed Student's t-test

[Source data](#).

[Extended Data Fig. 7 Exogenous SCD expression partially rescues tumor growth inhibition by caloric restriction.](#)

a, b, Tumor volumes (**a**) and tumor weights (**b**) normalized to animal body weight of subcutaneous AL1376 tumors expressing EV or SCD-HA in male mice exposed to a control or CR diet. EV: Control n = 4 mice, EV: CR n = 4 mice, SCD-HA: Control n = 4 mice, SCD-HA: CR n = 4 mice. **c, d**, Tumor volumes (**c**) and tumor weights (**d**) of subcutaneous AL1376 tumors expressing EV or SCD-HA in female mice exposed to a control or CR diet. EV: Control n = 4 mice, EV: CR n = 4 mice, SCD-HA: Control n = 4 mice, SCD-HA: CR n = 4 mice. **e, f**, Tumor volumes (**e**) and tumor weights (**f**) normalized to animal body weight of subcutaneous AL1376 tumors expressing EV or SCD-HA in female mice exposed to a control or CR diet.

EV: Control n = 4 mice, EV: CR n = 4 mice, SCD-HA: Control n = 4 mice, SCD-HA: CR n = 4 mice. **g, h**, Daily food consumption by weight (**g**) and daily caloric consumption (**h**) of the control diet and CR by male and female mice. **i, j**, Tumor weights (**i**) and tumor weights normalized to animal body weight (**j**) of subcutaneous LGSP tumors expressing EV or SCD-HA in mice exposed to a control or CR diet. EV: Control n = 6 mice, EV: CR n = 5 mice, SCD-HA: Control n = 6 mice, SCD-HA: CR n = 6 mice. **k**, Immunoblot for HA, human SCD (hSCD), mouse Scd1 (mSCD1), and vinculin in subcutaneous AL1376 tumors expressing an empty vector (EV) or SCD-HA from mice exposed to a control or CR diet for 18 days. **l–n**, The indicated MUFA/SFA ratios (**l**) and fatty acid levels (**m, n**) measured in subcutaneous AL1376 tumors expressing EV or SCD-HA from mice exposed to a control or CR diet for 18 days. EV: Control n = 6, EV: CR n = 6, SCD-HA: Control n = 6, SCD-HA: CR n = 6. **o**, Immunoblot for HA, hSCD, mSCD1, and vinculin in subcutaneous AL1376 tumors expressing an empty vector (EV) or SCD-HA from mice exposed to a control or CR diet for 7 days. **p–r**, The indicated MUFA/SFA ratios (**p**) and fatty acid levels (**q–r**) measured in subcutaneous AL1376 tumors expressing EV or SCD-HA from mice exposed to a control or CR diet for 7 days. EV: Control n = 6, EV: CR n = 6, SCD-HA: Control n = 6, SCD-HA: CR n = 6. Data are presented as box-and-whisker plots displaying median, interquartile range (boxes), and minima and maxima (whiskers) (**b, d, f, i, j, l–n, p–r**) or mean \pm SEM (**a, c, e, g, h**). Comparisons were made using two-way repeated measures analysis of variance (ANOVA) (**a, c, e**) or a two-tailed Student's t-test (**b, d, f, i, j, l–n, p–r**)

[Source data](#).

Extended Data Fig. 8 Changing the fat composition of caloric restriction and the ketogenic diet alters tumor growth and tumor fatty acid composition.

a, b, The indicated fatty acid levels measured in plasma from mice exposed to a control diet, CR, high fat caloric restriction diet consisting of soybean oil (HFCR-Soybean), and high fat caloric restriction diet consisting of palm oil (HFCR-Palm). Control n = 6, CR n = 5, HFCR-Soybean n = 5, HFCR-Palm n = 5. **c–e**, The indicated fatty acid levels (**c, e**) and MUFA/SFA ratios

(d) measured in subcutaneous AL1376 tumors from mice exposed to a control diet, CR, HFCR-Soybean, or HFCR-Palm. Control n = 7, CR n = 7, HFCR-Soybean n = 7, HFCR-Palm n = 7. **f, g**, Tumor volumes (**f**) and tumor weights (**g**) of subcutaneous LGSP tumors in mice exposed to a control diet, CR, HFCR-Soybean, or HFCR-Palm. Control n = 5 mice, CR n = 6 mice, HFCR-Soybean n = 5 mice, HFCR-Palm n = 6 mice. **h–j**, The indicated fatty acid levels (**h, j**) and MUFA/SFA ratios (**i**) measured in subcutaneous LGSP tumors from mice exposed to a control diet, CR, HFCR-Soybean, or HFCR-Palm. Control n = 6, CR n = 6, HFCR-Soybean n = 6, HFCR-Palm n = 6. **k**, Tumor weights of subcutaneous LGSP tumors expressing an empty vector (EV) or SCD-HA in mice exposed to a control or KD diet consisting of palm oil (KD-Palm). EV: Control n = 6 mice, EV: KD-Palm n = 6 mice, SCD-HA: Control n = 6 mice, SCD-HA: KD-Palm n = 6 mice. **l–n**, The indicated fatty acid levels measured in plasma from mice exposed to a control diet or KD-Palm. Control n = 12, KD-Palm n = 12. **o–r**, The indicated fatty acid levels (**o, p, r**) and MUFA/SFA ratios (**q**) measured in subcutaneous AL1376 tumors expressing an EV or SCD-HA from mice exposed to a control diet or KD-Palm. EV: Control n = 6, EV: KD-Palm n = 7, SCD-HA: Control n = 6, SCD-HA: KD-Palm n = 6. Data are presented as box-and-whisker plots displaying median, interquartile range (boxes), and minima and maxima (whiskers) (**a–e, g–r**) or mean ± SEM (**f**). Comparisons were made using a two-tailed Student's t-test (**a–e, h–r**), a two-way repeated measures analysis of variance (ANOVA) (**f**), or a one-way ANOVA (**g**)

Source data.

Extended Data Table 1 Compositions of diets used in this study

Extended Data Table 2 Low-carbohydrate dietary pattern or macronutrient intake and overall survival among 1,165 pancreatic cancer patients in two large cohorts

Supplementary information

Supplementary Figs.

Supplementary Figs. 1–23, containing uncropped scans of western blots.

Reporting Summary

Peer Review File

Supplementary Table 1

Raw data used for fatty acid source analysis (FASA) synthesis rate calculations in Fig. 3 and Extended Data Fig. 4 .

Source data

Source Data Fig. 1

Source Data Fig. 2

Source Data Fig. 3

Source Data Fig. 4

Source Data Extended Data Fig. 1

Source Data Extended Data Fig. 2

Source Data Extended Data Fig. 3

Source Data Extended Data Fig. 4

Source Data Extended Data Fig. 5

Source Data Extended Data Fig. 6

Source Data Extended Data Fig. 7

Source Data Extended Data Fig. 8

Rights and permissions

[Reprints and Permissions](#)

About this article

Cite this article

Lien, E.C., Westermark, A.M., Zhang, Y. *et al.* Low glycaemic diets alter lipid metabolism to influence tumour growth. *Nature* **599**, 302–307 (2021). <https://doi.org/10.1038/s41586-021-04049-2>

- Received: 20 March 2020
- Accepted: 17 September 2021
- Published: 20 October 2021
- Issue Date: 11 November 2021
- DOI: <https://doi.org/10.1038/s41586-021-04049-2>

Share this article

Anyone you share the following link with will be able to read this content:

[Get shareable link](#)

Sorry, a shareable link is not currently available for this article.

[Copy to clipboard](#)

Provided by the Springer Nature SharedIt content-sharing initiative

Further reading

- **Diet comparison suggests a lipid imbalance can slow tumour growth**

- Giulia Salvadori
- & Valter D. Longo

Nature (2021)

Diet comparison suggests a lipid imbalance can slow tumour growth

- Giulia Salvadori
- Valter D. Longo

News & Views 20 Oct 2021

This article was downloaded by **calibre** from <https://www.nature.com/articles/s41586-021-04049-2>

| [Section menu](#) | [Main menu](#) |

- Article
- [Published: 20 October 2021](#)

eccDNAs are apoptotic products with high innate immunostimulatory activity

- [Yuangao Wang^{1,2}](#),
- [Meng Wang](#) ORCID: [orcid.org/0000-0002-1072-7073^{1,2}](https://orcid.org/0000-0002-1072-7073),
- [Mohamed Nadhir Djekidel](#) ORCID: [orcid.org/0000-0001-5361-1858^{1,2}](https://orcid.org/0000-0001-5361-1858),
- [Huan Chen^{1,2}](#),
- [Di Liu^{3,4}](#),
- [Frederick W. Alt](#) ORCID: [orcid.org/0000-0002-0583-1271^{1,2,5}](https://orcid.org/0000-0002-0583-1271) &
- [Yi Zhang](#) ORCID: [orcid.org/0000-0002-2789-0811^{1,2,5,6}](https://orcid.org/0000-0002-2789-0811)

Nature volume 599, pages 308–314 (2021)

- 13k Accesses
- 52 Altmetric
- [Metrics details](#)

Subjects

- [DNA](#)
- [DNA metabolism](#)
- [Innate immunity](#)

Abstract

Extrachromosomal circular DNA elements (eccDNAs) have been described in the literature for several decades, and are known for their broad existence across different species^{1,2}. However, their biogenesis and functions are largely unknown. By developing a new circular DNA enrichment method, here we purified and sequenced full-length eccDNAs with Nanopore sequencing. We found that eccDNAs map across the entire genome in a close to random manner, suggesting a biogenesis mechanism of random ligation of genomic DNA fragments. Consistent with this idea, we found that

apoptosis inducers can increase eccDNA generation, which is dependent on apoptotic DNA fragmentation followed by ligation by DNA ligase 3. Importantly, we demonstrated that eccDNAs can function as potent innate immunostimulants in a manner that is independent of eccDNA sequence but dependent on eccDNA circularity and the cytosolic DNA sensor Sting. Collectively, our study not only revealed the origin, biogenesis and immunostimulant function of eccDNAs but also uncovered their sensing pathway and potential clinical implications in immune response.

[Download PDF](#)

Main

Since its first description in wheat embryos and boar sperm in 1964 (ref. ³), extrachromosomal circular DNA (eccDNA) has been reported in almost all cell lines and tissues⁴ across different species, although its abundance is highly variable^{1,2}. Unlike the independently existing circular DNA in organelles, such as mitochondrial DNA (mtDNA), eccDNAs are derived from genomic DNA and range in size from a few hundred bases to megabases¹. Although some studies have suggested that eccDNA generation might be linked to DNA damage repair⁵, hypertranscription^{5,6}, homologous recombination⁷ and replication stress⁵, how exactly eccDNAs are generated is largely unknown. Similarly, it is also unclear whether eccDNA has any function, although some studies have suggested that eccDNAs might contribute to gene amplification in cancer¹ or might be linked to ageing^{6,7,8}.

To understand eccDNA biogenesis, efficient and robust methods that allow purification and sequencing of eccDNAs are needed. Most existing eccDNA purification procedures involve two sequential steps, isolation of crude extrachromosomal DNA followed by removal of contaminating linear DNA through exonuclease digestion^{5,6,9} and rolling circle amplification (RCA) for profiling^{5,9,10}. However, most eccDNA samples prepared in this way contain a high level of linear DNA before RCA, as revealed by electron microscopy^{5,9}, indicating that exonuclease digestion alone is not sufficient to eliminate all contaminating linear DNA.

An efficient eccDNA purification method

We have developed a new three-step eccDNA enrichment method that allows efficient eccDNA purification (Fig. [1a](#)). In the first step, to minimize eccDNA loss, we replaced the conventional unbuffered sodium hydroxide lysis, which may cause irreversible denaturation or breakage of DNA circles¹¹, with a modified alkaline buffer at pH 11.8 to lyse the whole cells. In the second step, we used the rare cutter PacI restriction enzyme to linearize mtDNA before addition of an exonuclease (Plasmid-

Safe ATP-dependent DNase) to digest linear DNA. In the third step, solution A, which could selectively recover circular DNA, but not linear DNA, on silica beads (Extended Data Fig. 1a), was used to exclude any linear DNA that escaped exonuclease digestion (Fig. 1a). Additionally, vertical agarose gel electrophoresis was used to increase the sensitivity of eccDNA detection (Extended Data Fig. 1b). Using this three-step purification procedure, we purified eccDNA from 10 million HeLa cells growing at confluence, a stress condition known to increase eccDNA abundance¹². The purified eccDNAs exhibited a discrete banded pattern (Fig. 1b). Furthermore, mtDNA could be removed by PacI treatment (Fig. 1b, compare lanes 1 and 2). We further confirmed the circularity of the purified eccDNAs using scanning atomic-force microscopy (SAFM) (Fig. 1c). To determine whether eccDNAs occur in non-cancer cells, mouse embryonic stem cells (mESCs) were used, and mESC-derived eccDNAs exhibited a similar banded pattern (Fig. 1d), and their purity and circularity were also verified by SAFM (Fig. 1e).

Fig. 1: Development of a three-step eccDNA purification procedure.

 figure1

a. Schematic of the three-step eccDNA purification and sequencing procedure. Step 1, extract crude DNA circles from whole cells in a buffered alkaline lysis solution and

bind them to a silica column; step 2, linearize mtDNA with PacI and reduce overall linear DNA levels with Plasmid-Safe (PS) DNase; step 3, selectively recover eccDNAs by excluding residual linear DNA in solution A. eccDNAs are then sequenced by Oxford Nanopore sequencing after RCA (left) or by Illumina sequencing after Tn5 fragmentation on eccDNAs (right). **b**, Agarose gel showing eccDNAs purified from over-confluent HeLa cells without (–) or with (+) PacI treatment. M, linear DNA marker; Mt, mtDNA. **c**, eccDNAs in **b** (lane 2: top image; lane 3: bottom image) scanned with SAFM. **d**, Agarose gel showing eccDNAs purified from normal cultured mESCs. Red arrowheads indicate distinct DNA bands. **e**, eccDNAs in **d** (lane 2: top image; lane 3: bottom image) scanned with SAFM. In **b** and **d**, representative gels are shown from three independent experiments. In **c** and **e**, two representative fields are shown.

eccDNAs map to the entire genome

To gain insights into the potential mechanism of eccDNA biogenesis, we determined the genomic source of eccDNAs. HeLa cells are notorious for their aberrant genome, including aneuploidy and numerous structural variations, such as deletions, duplications, inversions, translocations and rearrangements, etc.¹³, making interpretation of sequencing data and dissection of the eccDNA biogenesis mechanism difficult. Thus, we performed eccDNA sequencing and mapping using mESCs, whose genetic integrity is maintained during culture¹⁴. To obtain full-length eccDNA sequences, we performed RCA and subsequent long-read Nanopore sequencing of the multiple tandem copies of individual eccDNA molecules (Fig. [1a](#) and Extended Data Fig. [2a](#)). Repeated sequencing of the same eccDNA with long reads allows generation of a consensus sequence matching the full-length sequence of the original eccDNA by a computational threading method (Fig. [2a](#) and Extended Data Fig. [2c](#)). We obtained 4 million long reads with a mean size of 3.7 kb (Extended Data Fig. [2b](#)). To reduce false positives due to RCA artefacts and sequencing errors from the Nanopore technique¹⁵, we only used the 1.9 million long reads that each contained at least two full passes covering their original eccDNA molecule to identify high-confidence eccDNAs, resulting in the identification of 1.6 million unique eccDNAs with a median size of 1 kb (Extended Data Fig. [2b](#)). Interestingly, the eccDNAs exhibited a regular average size interval of 188 bp (Fig. [2b](#)). The great majority (89%) of unique eccDNAs were sequenced from a single long read (single-event eccDNA), with less than 1.5% of unique eccDNAs sequenced from more than three unique long molecules (Fig. [2c](#)); no dominant eccDNA was identified. Such large numbers of single-event eccDNAs coupled with the lack of dominant eccDNA molecules suggest that eccDNAs are unlikely to be derived from specific genome regions.

Fig. 2: eccDNAs are circularized genomic DNA fragments that map across the genome.

 **figure2**

a, Integrative Genomics Viewer (IGV) alignments showing eccDNA examples from two genomic loci on chromosomes 17 and 18. Individual horizontal bars in the same colour represent subreads from a unique Nanopore long read that was repeatedly aligned to the same genomic locus or loci. ecc-1, ecc-2 and ecc-4 are single-fragment

circles. ecc-1 partially overlaps ecc-2; ecc-4 partially overlaps one fragment of ecc-3, which is a two-fragment circle (2f eccDNA) aligned to two loci on chromosomes 17 and 18. **b**, Histogram showing eccDNA size distribution and relative abundance. **c**, Pie chart showing the percentages of eccDNAs with the indicated event numbers among the total unique eccDNAs identified. **d**, Bar graph showing eccDNA counts with the indicated number of fragments (1–7) in each circle. **e**, Circle plot showing the chromosomal origin of all two-fragments eccDNAs. Sub-reads from the same chromosome are in the same colour. **f**, Overall chromosomal distribution of eccDNAs across the genome.

Genome mapping of full-length eccDNAs revealed their various genomic alignment patterns, including at adjacent, overlapped or nested positions on the same chromosome or even across different chromosomes (Fig. 2a). We found that a great majority of eccDNAs originated from single continuous genomic loci (continuous eccDNAs, self-circularization of a single genomic fragment), and only a relatively small number of eccDNAs were formed from multiple genomic fragments (non-continuous eccDNAs, circularization of multiple genomic fragments) (Fig. 2d and Extended Data Fig. 2c), including three eccDNAs each with seven genomic fragments joined together to form a circle (7f eccDNA) (Fig. 2d). To determine whether the physical distance between genomic fragments affects the frequency of eccDNA formation, we analysed the genomic origin of two-fragment eccDNAs (2f eccDNAs). A circle plot clearly showed that paired fragments of 2f eccDNAs are not restricted to the same chromosome (Fig. 2e), but rather are randomly bridged between chromosomes, indicating that eccDNAs can be formed by joining genomic fragments from different chromosomes. Consistent with this, genome mapping of all eccDNAs revealed that eccDNAs are widespread across the entire genome (Fig. 2f).

To rule out potential biases caused by uneven amplification by RCA¹⁶, we purified another batch of eccDNAs and directly tagged them with Tn5 transposase without RCA for Illumina sequencing (Fig. 1a and Extended Data Fig. 3a). eccDNA sequences obtained in this way should faithfully reveal their genomic location and relative abundance. Consistent with the Nanopore sequencing results, Illumina sequencing showed widespread alignment of eccDNAs across the entire genome (Extended Data Fig. 3b). We noticed that the eccDNA density on the X chromosome was about half that of the autosomes (Fig. 2f and Extended Data Fig. 3b), consistent with the fact that the diploid male genome of mESC/E14 cells carries one copy of the X chromosome but two copies of each autosome (Fig. 2f and Extended Data Fig. 3b). The lack of eccDNAs mapped to the Y chromosome is largely due to the many undetermined sequences and repeat sequences on the Y chromosome¹⁷. Collectively, these data suggest that eccDNAs are widespread across the entire genome and their abundance is correlated with genomic copy numbers.

DNase γ is required for eccDNA generation

The great diversity, randomness and nucleosome ‘ladder’ size (Fig. 2) suggest that eccDNAs might be generated by random ligation (including self-ligation) of oligonucleosomal DNA fragments, which can be visualized as ‘ladders’ in agarose gel and are a known feature of apoptosis¹⁸. To determine whether apoptotic cells are the source of eccDNAs, mESCs were treated with the apoptosis inducers staurosporine, etoposide or UV light. Successful induction of apoptosis was confirmed by the typical nucleosomal ladder pattern of genomic DNA (Fig. 3a). When equal amounts of control (DMSO-treated) cells and apoptosis inducer-treated cells were subjected to the three-step eccDNA purification procedure and visualized on an agarose gel, all three treatments induced eccDNA production, although UV treatment resulted in the strongest induction (Fig. 3b and Extended Data Fig. 4a).

Fig. 3: Apoptotic DNA fragmentation and subsequent ligation by Lig3 are required for eccDNA production in mESCs.

 **figure3**

a, b, eccDNA production is induced by apoptosis. mESCs were treated with the indicated apoptosis inducers, and total DNA (**a**) and eccDNAs (**b**) were purified. ETO, etoposide; STS, staurosporine. **c, d**, Deficiency of oligonucleosomal DNA fragmentation abolishes apoptosis-induced eccDNA production. Knockout of *Dnase1l3*, but not *Endog* (encoding endonuclease G), abolishes UV-induced oligonucleosomal DNA fragmentation (**c**) and eccDNA production (**d**) in mESCs. mtDNA was kept as an internal control. **e**, Confirmation of DNA ligase-deficient CH12F3 cell lines. Top, immunoblotting confirming knockout of DNA ligases in CH12F3 cell lines. Bottom, genomic structure of *Lig3* with CRISPR–Cas9 specifically

targeting (Δ) *NucLig3* but retaining *MtLig3* for cell viability. **f, g**, Lig3 is the major DNA ligase for eccDNA generation. Shown are staurosporine-induced oligonucleosomal DNA fragmentation (**f**) and eccDNA (**g**) from the indicated CH12F3 cell lines. In **a–d**, **f** and **g**, the amount of input cells and elution and loading volumes were equal among the samples on each agarose gel. Shown are representatives of three independent experiments.

We next determined whether eccDNA generation requires apoptotic DNA fragmentation (ADF), which is mediated by caspase-activated DNase (CAD)¹⁹, endonuclease G (EndoG)²⁰ or DNase γ ²¹ in a cell-type-specific manner. Genetic manipulation (Extended Data Fig. [4b, c](#)) indicated that DNase γ , but not EndoG, mediates ADF in mESCs, as indicated by the lack of a ladder pattern with DNase γ (encoded by *DnaseII3*) knockout²¹ (Fig. [3c](#)). *DnaseII3* knockout did not affect cell viability under either normal culture conditions or UV treatment (Extended Data Fig. [4d, e](#)). Purification of the eccDNAs from UV-treated cells demonstrated that abrogation of ADF prevented eccDNA generation (Fig. [3d](#) and Extended Data Fig. [4f](#)). We intentionally skipped PacI digestion to retain mtDNA as an internal control for equal cell input and circular DNA recovery (Fig. [3d](#)). These results demonstrate that ADF is a prerequisite for eccDNA generation.

Lig3 is required for eccDNA generation

Next, we attempted to identify the DNA ligase responsible for circularizing the fragmented DNA. Mammals have three DNA ligase genes (*Lig1*, *Lig3* and *Lig4*), each of which has a specific function, although they also function redundantly in DNA metabolism²². The functions of these ligases have been well studied in the CH12F3 mouse B-lymphocyte cell line²³. To determine which of the three DNA ligases is responsible for ADF circularization, individual DNA ligases and their combinations were knocked out in CH12F3 cells by CRISPR–Cas9 with knockout confirmed by western blotting (Fig. [3e](#)). Lig3 has both nuclear and mitochondrial isoforms, the later of which is essential for mitochondria maintenance and, consequently, cell viability²⁴. Thus, the *Lig3*-knockout cell line was generated by specifically targeting the nuclear isoform (*NucLig3*^{−/−}) without interfering with the mitochondrial isoform (*MtLig3*; Fig. [3e](#), lower diagram). Equal numbers of wild-type (WT) and mutant cells were treated with staurosporine to induce ADF (Fig. [3f](#)), and eccDNAs were purified and visualized in agarose gel (Fig. [3g](#)). The results indicated that knockout of *Lig1* or *Lig4* alone or in combination did not significantly affect eccDNA generation. In contrast, knockout of *Lig3* greatly reduced eccDNA generation (Fig. [3g](#) and Extended Data Fig. [4g](#)). Because double knockout of *Lig1* and *Lig3* is lethal to cells^{23,24}, it is unknown whether double knockout could completely abrogate eccDNA generation.

Nevertheless, these data support Lig3 as the main ligase for eccDNA generation in CH12F3 cells.

Fig. 4: eccDNAs are potent immunostimulants.

 figure4

a, eccDNAs induce *Ifna* (encoding IFN α) and *Ifnb1* (encoding IFN β) expression in BMDCs. Equal amounts of the indicated DNA were transfected into BMDCs at increasing concentrations for RT-qPCR analysis. Data are presented as relative mRNA fold change (y axis) with respect to that in mock transfected cells (without DNA). Li-DNA, sonicated genomic linear DNA with sizes similar to those of eccDNAs. **b**, ELISA analysis of IFN α and IFN β production in medium from **a**. **c**, Confirmation of eccDNA linearization. A representative gel shows equal amounts of the indicated DNA digested with Plasmid-Safe DNase or left undigested. Li-ecc, linearized eccDNA. **d**, Linearized eccDNAs lose their immunostimulatory activities. The DNAs from lanes 1–3 in **c** were transfected into BMDCs at 30 ng ml $^{-1}$ and mRNA levels were evaluated as in **a**. **e**, **f**, Synthetic small DNA circles are potent immunostimulants. The same experiments were performed as in **a** and **b**, except that the linear DNA and eccDNA were replaced by synthetic linear (Syn-linear) and circular (Syn-circular) DNAs with the same sequence. **g**, eccDNAs are present in apoptotic medium from WT cells but not *Dnase1l3* $^{+/-}$ ($-/-$) cells. A representative gel of eccDNA (left) and quantification (right; $n = 3$) are shown; ND, not detected. **h**, Exonuclease-resistant DNA (not mtDNA) in apoptotic medium activates *Ifna* and

Ifnb1 expression. Supernatants from apoptotic WT or *Dnase1l3*^{-/-} (^{-/-}) cells were treated as indicated, then incubated with BMDCs for RT–qPCR analysis as in **a**. Benz, benzonase. In **a**, **b**, **d–f** and **h**, data are shown as the mean ± s.e.m. of replicates ($n = 4$ per group) of a representative from three independent experiments. Statistics were calculated on biological replicates with ordinary one-way ANOVA with Tukey’s multiple-comparison test (**a**, **b**, **d–f**, **h**) or two-tailed unpaired *t*-tests (**g**): * $P < 0.05$, ** $P < 0.01$, *** $P < 0.001$, **** $P < 0.0001$; NS, not significant.

eccDNAs are potent innate immunostimulants

The above results demonstrate that eccDNAs are ligation products of fragmented genomic DNA from apoptotic cells. DNA released from dying cells has previously been reported to promote immune responses¹⁸. Two important mediators of immune response, Toll-like receptor 9 (TLR9)²⁵ and high-mobility-group box 1 (HMGB1)²⁶, have been reported to preferentially bind to DNA curvatures. These observations suggest that eccDNAs may serve as immunostimulants. To test this idea, we generated bone marrow-derived dendritic cells (BMDCs) (Extended Data Fig. [5a](#)) and compared the immunostimulant activity of sheared linear genomic DNA, eccDNAs and the widely used potent DNA ligand of cytosolic DNA sensors poly(dG:dC)²⁷ (Extended Data Fig. [5b](#)). We transfected BMDCs with different amounts of the three forms of DNA and then collected cells for RT–qPCR assays. Compared with transfection with linear DNA, type I interferons (IFN α , IFN β), interleukin-6 (IL-6) and tumour necrosis factor (TNF) were all significantly induced by eccDNAs at a wide range of concentrations (10–240 ng ml⁻¹) (Fig. [4a](#) and Extended Data Fig. [5c](#)). Surprisingly, the widely regarded ‘potent’ cytokine inducer poly(dG:dC) was not nearly as potent as eccDNAs at lower concentrations, and the linear DNA triggered only a mild response, even at the highest concentration, when compared with mock transfection, indicating that dendritic cells are much more sensitive to eccDNA treatment than that with linear DNA or poly(dG:dC). Consistent with this, enzyme-linked immunosorbent assays (ELISAs) confirmed the strong potency of eccDNAs in cytokine induction (Fig. [4b](#) and Extended Data Fig. [5d](#)).

In addition to dendritic cells, macrophages are also known to respond to immunostimulants²⁸. To determine whether macrophages behave like dendritic cells upon eccDNA transfection, we generated bone marrow-derived macrophages (BMDMs) (Extended Data Fig. [6a](#)). Similarly to the observations in BMDCs, eccDNAs also displayed much higher immunostimulant activities in BMDMs than linear DNA or poly(dG:dC), particularly at lower concentrations (10 and 30 ng ml⁻¹) (Extended Data Fig. [6b,c](#)). These data indicate that eccDNAs are very potent immunostimulants in activating both BMDCs and BMDMs. Furthermore, pretreatment of eccDNA with DNase I before transfection completely abrogated the capacity of

eccDNA to induce cytokine production (Extended Data Fig. 5e,f), demonstrating that eccDNA, rather than potential concomitants of eccDNA, is responsible for the immune activation.

Circularization confers eccDNA potency

To determine whether the circular nature of eccDNAs is critical for their strong immunostimulatory activity, purified eccDNAs were first treated with FnoCas12a (Cpf1), which introduces one nick per circular DNA in the presence of Mn²⁺ and the absence of guide RNA²⁹. The nicked eccDNAs were then treated with the single-strand-specific endonuclease nuclease S1, which cleaved the intact circular strand at the site opposite to the nick to generate linearized eccDNA. Linearization of eccDNAs was confirmed by their sensitivity to exonuclease digestion while intact eccDNAs were resistant (Fig. 4c, compare lanes 5 and 6). When equal amounts of linear DNAs, eccDNAs and linear eccDNAs were transfected into BMDCs, linear eccDNAs behaved like linear DNAs and failed to activate IFN α , IFN β , IL-6 or TNF (Fig. 4d and Extended Data Fig. 7a). These results demonstrated that the circular nature of eccDNAs is critical for their strong immunostimulant activity. Because eccDNAs are derived from randomly ligated genomic fragments, their sequences are unlikely to significantly contribute to their potency. This notion was confirmed by the ability of a synthetic 200-bp circular DNA, but not its linear counterpart, to greatly induce cytokine genes transcription in BMDCs (Fig. 4e and Extended Data Fig. 7b). Similarly to native eccDNAs, synthetic circular DNA also showed higher potency in cytokine gene activation than poly(dG:dC) (Fig. 4e and Extended Data Fig. 7b). Consistent with these findings, ELISAs confirmed the strong cytokine induction capacity of synthetic circular DNA (Fig. 4f and Extended Data Fig. 7c).

To rule out the possibility that the increased immunostimulatory potency of circular DNA is due to increased stability and transfection efficiency, and to minimize the effects of exonuclease activity on linear DNA, we added phosphorothioate³⁰ bonds on both ends of the synthetic 200-bp linear DNA. To exclude potential effects from the phosphorothioate bonds on transfection and immune stimulation, equal numbers of phosphorothioate bonds were also added in the circular counterpart. Linear and circular DNAs were separately transfected into BMDCs, and cell lysates and culture media were collected for qPCR and ELISA to compare transfection efficiency (1 h after transfection), stability and cytokine induction (12 h after transfection) (Extended Data Fig. 7d). We found no significant difference in transfection efficiency or stability between the linear and circular 200-bp DNAs (Extended Data Fig. 7e). Yet, the circular DNA induced a high level of cytokine production while its linear counterpart did not (Extended Data Fig. 7f). Collectively, these data support the idea that the circularity but not the sequence of eccDNAs confers the high potency of their immunostimulant activity.

BMDCs sense eccDNAs in medium from apoptotic cells

Because eccDNAs are generated in apoptotic cells, they could be released into the culture medium. Indeed, a substantial amount of eccDNAs could be detected in the cell-free supernatant of UV-treated mESCs undergoing apoptosis (Fig. 4g). To determine whether eccDNAs from the supernatant of apoptotic cells can be actively sensed by BMDCs without transfection, BMDCs were co-incubated with cell-free apoptotic supernatant from WT or *Dnase1l3*^{-/-} mESCs. RT-qPCR analysis indicated that the supernatant from WT, but not *Dnase1l3*^{-/-}, apoptotic cells stimulated IFN α and IFN β expression (Fig. 4h). Importantly, this stimulation was not sensitive to pretreatment of the supernatant with Plasmid-Safe DNase, PacI restriction enzyme or RNases, which digest linear DNA, mtDNA and RNA, respectively (Fig. 4h), but was sensitive to pretreatment with benzonase, a nuclease that destroys all forms of DNA and RNA without proteolytic activity (Fig. 4h). These data indicate that eccDNAs, but not linear DNAs, mtDNAs or RNAs, in the supernatant of apoptotic cells are responsible for the induced immune response. Furthermore, these results also indicate that eccDNAs can be actively sensed by BMDCs without transfection. Collectively, our results indicate that eccDNAs are potent damage-associated molecular patterns of the innate immune system²⁸.

eccDNA-triggered immune response requires Sting

To assess the global transcriptional effect of eccDNA, we performed RNA-seq analysis of BMDCs transfected with purified eccDNAs or sonicated with genomic DNA of similar size (Extended Data Fig. 8a–c). Comparative analysis indicated that eccDNAs, but not the linear DNA control, significantly increased the expression of 290 genes (fold change ≥ 5 , $P < 0.001$), including 34 cytokines and chemokines (Fig. 5a and Supplementary Table 4), under our experimental conditions (30 ng ml^{-1} DNA transfected). Importantly, 9 of the top 20 most upregulated genes belong to the family of type I interferons (Fig. 5b). Gene ontology (GO) enrichment analysis revealed that the upregulated genes were enriched in terms relevant to immune response and related signalling pathways (Fig. 5c), supporting our conclusion that eccDNA is a potent innate immunostimulant that can generally increase the innate immune response. Parallel experiments further demonstrated a similar effect of eccDNAs in BMDMs (Extended Data Fig. 9a–f and Supplementary Table 5). Collectively, these data support a higher capacity and potency of eccDNA in triggering a general immune response than linear genomic DNA fragments (Fig. 5b). Importantly, this eccDNA property depends on eccDNA circularization, but not sequence, as transfection of the 200-bp synthetic circular DNA into BMDCs triggered a similar transcriptional response as purified eccDNAs (Fig. 5d and Extended Data Fig. 10a).

Fig. 5: Sting is required for eccDNA-induced gene expression.

 figure5

a, Scatterplot showing 290 genes (left, red dots) that are significantly induced by eccDNA, but not linear DNA, in BMDCs. Thirty-four significantly induced cytokine genes are indicated (right, red dots). FC, fold change. **b**, Heatmap representation of the top 20 most strongly induced genes. **c**, GO terms enriched in the genes activated by eccDNA treatment in BMDCs. The number of genes in each term and the *P* values of enrichment are indicated. **d**, Scatterplot indicating that the transcriptomes of BMDCs treated with eccDNAs and BMDCs treated with synthetic circular DNA are highly similar. **e**, Heatmap representation of the eccDNA-responsive genes in control and eccDNA-treated BMDCs of the indicated genotype. **f**, Scatterplots comparing the transcriptome affected by eccDNA in BMDCs from WT, *Sting*^{−/−} and *Myd88*^{−/−} mice. eccDNA-responsive genes in WT BMDCs are indicated by red dots (upregulated, *n* =

365) and blue dots (downregulated, $n = 79$). In **a**, **d** and **f**, the x and y axes are log₂-transformed normalized read counts; P values were generated using DESeq2 (ref. ⁴²) and adjusted by IHW⁴³. FC ≥ 5 , adjusted $P < 0.001$ in **a** and **f**; FC ≥ 2 , adjusted $P < 0.01$ in **d**.

To determine how eccDNA is sensed, two well-known mouse lines deficient in DNA sensing, with knockout of *Sting1* (stimulator of interferon genes)³¹ or *Myd88* (myeloid differentiation primary response 88)³², were used to generate BMDCs (Extended Data Fig. **10b**), which were then subjected to eccDNA transfection. Comparative RNA-seq analysis demonstrated that, while loss of function of Myd88 did not affect BMDC responses to eccDNAs, loss of Sting function completely abrogated the capacity of BMDCs to respond to eccDNAs, as almost all the genes normally induced by eccDNA were not induced in the absence of Sting (Fig. **5e,f**, Extended Data Fig. **10c** and Supplementary Table **6**). These data strongly suggest that the Sting pathway is responsible for sensing eccDNA to mediate its immune response.

Our data indicate that apoptotic oligonucleosomal DNA fragmentation (ODF) is directly linked to eccDNA generation, as blocking ADF abolishes eccDNA production (Fig. **3c,d**). This notion challenges the assumption that eccDNAs isolated from a cell population or tissue are equally contributed by each cell⁹. On the contrary, our data suggest that eccDNAs are mostly derived from cells that undergo genomic DNA fragmentation. During apoptosis, genomic DNA is first broken into high-molecular-weight (HMW) fragments (>50 kb) and subsequently undergoes ODF to generate oligonucleosomal fragments^{19,33}. Similarly to ODF in myoblasts²¹ and neuroblastomas under differentiation conditions³⁴, we showed that DNase γ is required for ODF and subsequent eccDNA generation in mESCs (Fig. **3c,d**). This suggests that the eccDNAs that we purified are generated in the late stage of apoptosis when ODF occurs³³, which is consistent with our observation that the great majority (99.5%) of eccDNAs are within 3 kb in size (Fig. **2b**), although we identified eccDNAs as long as 10 kb. Although random ligation by Lig3 of nucleosome-sized DNA fragments in the late stage of apoptosis explains the predominantly oligonucleosomal sizes and the absence of abundant individual eccDNAs in our study and previous studies^{5,9}, it is possible that rare ligation of HMW fragments in the early stage of apoptosis might also occur. Our demonstration that Lig3 is responsible for nucleosome-sized eccDNA generation is consistent with the ability of Lig3 to circularize DNA fragments *in vitro*³⁵. Whether Lig3 is also involved in the biogenesis of larger eccDNAs, double minutes³⁶ and extrachromosomal DNAs³⁷ remains to be determined. Although this study mainly focused on eccDNA generation under apoptotic conditions, we do not rule out the possibility that eccDNAs can also be generated under other conditions that cause genomic DNA fragmentation (for example, replication stress, double-strand DNA breaks, V(D)J recombination, etc.) with subsequent circularization.

We demonstrated that purified eccDNAs or synthetic circular DNA, but not their linear counterparts, have strong immunostimulatory activity (Figs. 4 and 5a–c). Importantly, Sting, but not Myd88, is required to mediate this process (Fig. 5e,f). cGAS–Sting is a well-known intracellular DNA sensing pathway³⁸, and DNA sensing by cGAS has been reported to be enhanced by the host factors HMGB1 and TFAM, which facilitate DNA bending or form U-shaped structures³⁹. Whether these factors are involved in eccDNA-mediated immune stimulation remains to be determined. In addition to the immunostimulatory activity of eccDNA we showed in this study, it is not clear whether eccDNAs from apoptotic cells are linked to the oncogene amplification and tumour progression shown for large extrachromosomal DNAs³⁷.

Our demonstration that eccDNAs can dramatically induce type I interferon expression (Figs. 4 and 5), combined with previous observations that type I interferons possess adjuvant activity⁴⁰ and that DNA released from dying cells mediates aluminum adjuvant activity¹⁸, prompt us to propose that eccDNAs possess high adjuvant activity. In addition, the existence of eccDNAs in plasma¹⁰ suggests that eccDNA is highly mobile. Given that increased levels of cell-free DNA and serum IL-6 and TNF are good predictors of disease severity leading to a cytokine storm⁴¹, we suspect that apoptosis-driven eccDNA generation and subsequent induction of cytokines might underlie the cytokine storm observed in diseases such as severe sepsis and coronavirus disease 2019 (COVID-19), as these diseases can involve massive cell death. If future studies confirm this notion, the eccDNA biogenesis and sensing pathway revealed in this study could serve as the basis for therapeutic interventions.

In summary, by providing answers to three key questions regarding the origin, biogenesis and biological function of eccDNAs, our study substantially advances understanding of eccDNAs. Further characterization of the molecular basis of eccDNA-mediated immune responses can provide new insight into innate immunity as well as vaccine design and immunotherapy.

Methods

Cell culture and apoptosis induction

mESC/E14 cells were cultured on dishes coated with 0.1% gelatin in standard LIF/serum medium containing mouse LIF (1,000 U ml⁻¹), 15% foetal bovine serum (FBS), 0.1 mM non-essential amino acids, 0.055 mM β-mercaptoethanol (BME), 2 mM GlutaMAX, 1 mM sodium pyruvate and penicillin-streptomycin. HeLa S3 cells were grown in DMEM supplemented with 10% FBS and 100 U ml⁻¹ penicillin-streptomycin. CH12F3 cells were cultured in RPMI 1640 supplemented with 10% heat-inactivated FBS, 100 U ml⁻¹ penicillin-streptomycin, 2 mM BME and 2 mM

GlutaMAX. L929 cells were cultured in DMEM supplemented with 10% heat-inactivated FBS and 100 U ml⁻¹ penicillin-streptomycin.

Apoptotic cell death of mESCs was induced with 0.5 µM etoposide (Selleck) or 2 µM staurosporine (Selleck) for 24 h or by irradiation at 3 mJ using UV-C light in a Stratagene Stratalinker 2400 without medium and continued culture for 16 h.

Apoptotic cell death was induced in CH12F3 cells by treatment with 2 µM staurosporine for 16 h. Cell viability was analysed with a BD FACSCanto II instrument after staining with the Live/Dead Fixable Far Red Dead Cell Stain Kit. FSC-A and SSC-A gates were used to exclude debris, and FSC-A and FSC-H were used to gate on singlets and then gate on APC⁺ cells as dead cells. Data were analysed with FlowJo v.10.8.0.

Knockout cell line generation

Dnase1l3- and *Endog*-knockout mESC cell lines were generated by CRISPR–Cas9 through transient transfection with px330-mCherry (Addgene, 98750). mCherry⁺ cells were sorted by flow cytometry. Guide RNAs targeting sequences and PCR genotyping primers for *Dnase1l3* and *Endog* are listed in Supplementary Table 1. The *Lig1*^{−/−} CH12F3 cell line was generated using CRISPR–Cas9 guide RNAs targeting introns 17 and 19 to delete exons 18 and 19, which encode the conserved ligase catalytic site. Deletion resulted in a premature stop codon. The *NucLig3*^{−/−} CH12F3 cell line was generated by specifically deleting the sequences encoding the nucLig3 start codon and the two subsequent methionine residues (Met89-Met144) with CRISPR–Cas9 guide RNAs while keeping mtLig3 in frame and functional. *Lig4* is a single-exon gene, and two pairs of guide RNAs were used for two rounds of targeting to obtain homozygous deletion of the entire 2.7-kb exon. Guide RNA sequences are listed in Supplementary Table 1. Knockout cell lines were confirmed by immunoblotting.

eccDNA purification and visualization on agarose gels

To purify eccDNAs, cells were first dehydrated in >90% methanol before crude extrachromosomal DNA was extracted in an alkaline lysis buffer at pH 11.8. After neutralization and precipitation, crude extrachromosomal DNA was bound to a silica column (QIAGEN Plasmid Plus Midi Kit) in binding buffer (buffer BB from the QIAGEN Plasmid Plus Midi Kit). Bound DNA was eluted, digested with PacI (NEB) and Plasmid-Safe ATP-dependent DNase (Lucigen) for 4–16 h, then extracted with phenol:chloroform:isoamyl alcohol (PCI) solution (25:24:1) in a Phase Lock Gel tube (QuantaBio) to minimize DNA loss. After precipitation with carrier glycogen (Roche) and 1/10 volume of 3 M sodium acetate (pH 5.5), the precipitated crude eccDNAs were resuspended in solution A (One-Step Max Plasmid DNAout, TIANDZ). eccDNAs were selectively bound to magnetic silica beads in this solution and were

then eluted with $0.1\times$ elution buffer (1 mM Tris-HCl, pH 8.0), and the concentration was measured by Qubit dsDNA HS Assay kit (Thermo Fisher). A detailed eccDNA purification protocol is in preparation for publication.

For comparisons of eccDNA production among treatments or genotypes, both total DNA (Quick-DNA microPrep Plus Kit, Zymo) and eccDNA were purified from equal numbers of cells, eluted and loaded onto an agarose gel with equal volume. All DNA, except for in PCR genotyping, was resolved with vertical agarose gel electrophoresis and visualized by staining with SYBR Gold (Fisher Scientific; 1:10,000).

Synthetic small DNA circle preparation

Synthetic small DNA circles were prepared by the procedure of ligase-assisted minicircle accumulation (LAMA)⁴⁴. Random DNA sequences were generated (<https://faculty.ucr.edu/~mmaduro/random.htm>) with 50% G+C content. The isomers of single-strand templates as well as their amplification primer sets were synthesized by IDT, and their sequences are listed in Supplementary Table 3. Products with a 5'-end phosphate were prepared with 2 \times Q5 DNA polymerase (NEB). Equal amounts of isomers were added to generate 100- μ l HiFi Taq DNA ligase reaction mixtures and placed in thermocyclers using the following cycles: 95 °C for 3 min, 60 °C for 10 min and 37 °C for 5 min for at least 10 cycles. Circularized products were recovered with a PCR Purification Kit (Qiagen) and digested with Plasmid-Safe ATP-dependent DNase (Lucigen) before being recovered with a PCR Purification Kit.

SAFM imaging

SAFM imaging of DNA was performed in dry mode⁴⁵. Briefly, 1/10 volume of 10 \times imaging buffer (100 mM NiCl₂ and 100 mM Tris-HCl, pH 8.0) was added to the sample to reach a final DNA concentration of 0.6–1.0 ng μ l⁻¹, and 2–5 μ l of the mixture was then spread on a freshly cleaved mica (Ted Pella) surface. After 2 min of incubation, the specimen was rinsed twice with 30 μ l of 2 mM magnesium acetate, drying before and after the rinses with compressed air. Images were acquired by using tip C of an SNL-10 probe on a Veeco MultiMode atomic-force microscope with a Nanoscope V Controller in ‘ScanAsyst in Air mode’ and processed with Gwyddion 2.50.

Library preparation and eccDNA sequencing

The Nanopore sequencing library for eccDNA was prepared with the Ligation Sequencing Kit (Oxford Nanopore) according to the manufacturer’s instructions after RCA and debranching. RCA was performed with phi29 DNA polymerase (NEB) with some modifications to ensure efficient amplification from 100 pg of template per

reaction. Briefly, each 20- μ l reaction mixture contained 2 μ l of 10 \times phi29 DNA polymerase buffer (NEB), 2 μ l of 25 mM dNTPs, 1 μ l Exo-Resistant Random Primer (Thermo Fisher) and \geq 100 pg of eccDNA, with ultra-pure water added to a maximum volume of 17.6 μ l. Reactions were mixed and incubated at 95 °C for 5 min before ramping the temperature down to 30 °C at a 1% ramp rate. Then, 1 μ l of phi29 DNA polymerase, 0.6 μ l of inorganic pyrophosphatase (yeast, NEB), 0.4 μ l of 0.1 M DTT (NEB) and 0.4 μ l of 20 mg ml⁻¹ BSA (NEB) were added. The reaction mixture was incubated at 30 °C for 10–16 h. Because high branch structure in RCA products can block nanopores and abolish sequencing, RCA products for eccDNAs were further debranched with T7 endonuclease I (NEB) before being used for sequencing library construction with the Ligation Sequencing Kit (Oxford Nanopore, SQK-LSK109). The library was sequenced in a flow cell (R9.4.1, FL-MIN106D) on a MinION instrument according to the manufacturer’s instructions.

Illumina sequencing libraries for eccDNA were prepared by Tn5-transposon-based tagmentation with the Nextera XT DNA Sample Preparation Kit according to the manufacturer’s instructions. Briefly, after validating the purity of the eccDNAs with SAFM imaging, 0.5 ng of pure eccDNAs was directly tagmented with Tn5 transposase, followed by 12–14 cycles of PCR amplification with Illumina sequencing adaptors. Barcoded libraries were pooled and sequenced with the Illumina 2500 platform in 150-bp paired-end mode.

eccDNA sequencing data analyses

Nanopore base calling and reads mapping

The fast5 files generated by Nanopore MinION were fed to Guppy (version 3.5.2) for base calling. The parameters used for Guppy were as follows: -flowcell FLO-MIN106 --kit SQK-LSK109 --qscore_filtering --calib_detect --trim_barcodes --trim_strategy dna --disable_pings --device auto --num_callers 16. The generated reads in fastq format were further processed by porechop (version 0.2.4) to remove adaptor sequences for each read with the following parameters: --extra_end_trim 0 --discard_middle. To reduce artefacts due to misalignment during read mapping, we compiled a customized reference mouse genome (mm10combine) based on mm10 reference sequences. Briefly, we downloaded all the nucleotide sequences from the NCBI NT database (30 October 2018), and R/Bioconductor genbankr (version 1.10.0) was then used to distinguish mouse contigs from the contigs of other species. On the basis of each contig’s description and manual inspection, we removed all gene-related contigs, retaining only 15,984. The selected fasta sequences were extracted using the command ‘blastdbcmd -db nt_db -entry_batch selected_ids.txt -out selected_ids.fa -outfmt %f’. The fasta sequences were mapped to the mm10 genome. Finally, we selected contigs that could not be mapped, contigs for which less than 50% of the

sequence mapped uniquely and contigs that were uniquely mapped but with a sequencing quality score of <10. In total, 103 contig sequences were added to mm10 to build the mm10combine reference genome. Cleaned reads were then aligned to mm10combine using minimap2 (version 2.17)⁴⁶ with the following parameters: -x map-ont -c --secondary=no -t 16. The alignments for each read were stored in PAF format.

Consensus eccDNA generation

To obtain the consensus boundary and sequence of each eccDNA from the mapped RCA long reads, we developed a tool (https://github.com/YiZhang-lab/eccDNA_RCA_nanopore) that uses the alignments in PAF files as input and outputs eccDNA fragment composition (chromosome and genomic start and end positions of each fragment), successive fragment coverage (number of passes) and the consensus sequence derived from each RCA long read. The subreads of each RCA long read could be mapped to one genomic location or multiple locations. Subreads with mapping quality lower than 30 were discarded. The tool performed bootstrapping of successive subreads in each RCA long read to check whether the order of the mapped genomic locations for each subread was concordant with the order in the RCA long read. Because of the inaccuracy and gap-prone nature of Nanopore reads, we allowed a maximum of 20 bp offset of the mapped genomic positions (start and end positions) for two subreads to be considered as mapping to the same location. Reads with discordant subread order, location or strand were discarded. The exact boundaries of eccDNA fragments were determined by voting from the subreads' start and end positions. Boundary positions were further refined by threading the subreads to ensure no gaps or overlaps between any successive subreads. The number of passes for each eccDNA fragment was calculated as the number of concordant subreads mapped to that location. Only eccDNAs with at least two passes were kept for downstream analysis. Each eccDNA sequence was derived from the reference genome sequence to which it mapped, with sequence variants incorporated. Sequence variants were called from subreads mapped to the corresponding location, requiring a minimum depth of 4 and a minimum allele frequency of 0.75.

Genomic distribution of eccDNAs

The eccDNA fragments were piled up across the genome. To remove PCR duplicates, eccDNA fragments on the same chromosome with the same start and end positions were treated as duplicates and only one was retained. The coverage of unique eccDNA fragments at each base of the genome was obtained using bedtools (version 2.29.2)⁴⁷ and stored in bigwig files. The distribution of eccDNA fragments across each

chromosome was plotted using karyoploteR (version 1.14.1)⁴⁸ with the bigwig file as input.

Mapping of Illumina sequencing reads

Raw Illumina sequence reads were first processed by Trimmomatic (version 0.39)⁴⁹ to remove sequencing adaptors and low-quality reads, using the following parameters: ILLUMINACLIP:adapters/NexteraPE-PE.fa:2:30:10:1:true LEADING:3 TRAILING:3 SLIDINGWINDOW:4:15 MINLEN:75 TOPHRED33. BWA⁵⁰ MEM (version 0.7.17) was used with default parameters. Then, the reads were mapped to our customized mm10combine reference genome. Duplicated reads were removed by Picard (version 2.23.4). Reads with a mapping quality score of at least 60 were considered as uniquely mapped and used for downstream analysis. The genomic coverage was calculated using bamCoverage from deeptools (version 3.5.0)⁵¹ with binSize 1.

Western blot analysis

Equal numbers of cells were lysed in NuPAGE LDS sample buffer (Thermo Fisher), and protein extracts were resolved by SDS–PAGE and transferred to PVDF membrane. Antibodies against Lig1 (Proteintech; 1:1,000), Lig3 (BD Biosciences; 1:1,000), Lig4 (a gift from D. Schatz (Yale University); 1:1,000), Myd88 (ProSci; 1:1,000), Sting (Proteintech; 1:1,000) and Gapdh (Thermo Fisher; 1:20,000) were used. Uncropped and unprocessed scans of blots are provided in Supplementary Fig. 1.

BMDC and BMDM preparation and stimulation

Male mice, including WT C57BL/6, *Sting*^{I^{-/-}} (Tmem173gt, stock no. 017537) and *Myd88*^{I^{-/-}} (Myd88tm1.1Defr, stock no. 009088) mice, were purchased from Jackson Labs and were housed on a 12-h light/dark cycle at 23 °C with 45–55% humidity. After at least 7 days of habituation, mice between 8 and 12 weeks old were used to collect bone marrow cells for BMDC and BMDM differentiation. BMDCs were differentiated in RPMI 1640 supplemented with 10% heat-inactivated FBS (Sigma), 10 mM HEPES, 1 mM sodium pyruvate, 100 U ml⁻¹ penicillin-streptomycin, 2 mM GlutaMAX and 20 ng ml⁻¹ mouse granulocyte and macrophage colony-stimulating factor (GM-CSF; Peprotech). BMDMs were differentiated in DMEM supplemented with 10% heat-inactivated FBS, 100 U ml⁻¹ penicillin-streptomycin and 20% L929 conditioned medium. Half of the medium was replaced at day 3 and day 6. BMDCs and BMDMs were confirmed to be CD11c⁺MHC II⁺ and F4/80⁺CD11b⁺, respectively, after excluding debris with FSC-A and SSC-A gates and subsequent FSC-A and FSC-H gates on singlets. Data were analysed with FlowJo v.10.8.0. For cell stimulation,

cells at days 7–9 were seeded in 96-well plates at 3.5×10^4 cells per well. DNA was transfected into cells with FuGENE HD (Promega) in Opti-MEM (Gibco) according to the manufacturer’s instructions after measuring its concentration with a Qubit dsDNA HS Assay Kit (Thermo Fisher). All transfections were performed for 12 h except as indicated, media were collected for ELISA and cells were lysed with TRIzol (Thermo Fisher) for RNA isolation.

Transfection efficiency assays

To determine the transfection efficiency for linear and circular DNA, a set of primers (for sequences, see Supplementary Table 2) with five phosphorothioate bonds at their 5' end were used to prepare end-protected linear DNA by PCR. To balance the effects of the phosphorothioate bonds, the circular form was prepared with the same number of phosphorothioate bonds as the linear one. Then, DNA concentration was determined by Qubit dsDNA HS Assay Kit (Thermo Fisher), and DNA was transfected into BMDCs as described above with FuGENE HD (Promega). After transfection, cells were rinsed three times with PBS and lysed in 100 µl of lysis buffer (50 mM Tris-HCl pH 8.0, 1 mM EDTA, 0.5% Tween-20, 3 U ml⁻¹ thermolabile proteinase K (NEB, P8111S)) and incubated at 37 °C for 2 h followed by incubation for 15 min at 55 °C to inactivate proteinase K. Four microlitres of cell lysate was used for qPCR with a set of primers targeting both linear and circular DNA to determine the amount of transfected DNA.

Incubation of BMDCs with supernatant from apoptotic cells

WT and *Dnase1l3*^{-/-} cells in 10-cm dishes that were 80–100% confluent were washed three times with PBS and irradiated with 3 mJ of UV-C light in a Stratagene Stratalinker 2400, 10 ml Opti-MEM (Gibco) was added and cells were cultured for another 48 h. Medium was centrifuged at 650g for 5 min, and the supernatant was filtered through a 0.45-µm filter. Four hundred microlitres of supernatant was left untreated or treated with enzyme (PacI, Plasmid-Safe ATP-dependent DNase, RNase A/T1 or benzonase, as indicated) in a 500-µl reaction volume at 37 °C for 2 h and then dialyzed (molecular weight cut-off (MWCO), 10 kDa) with fresh Opti-MEM at 4 °C overnight to deplete ATP, which is required for the activity of Plasmid-Safe ATP-dependent DNase. Then, 100 µl per well of dialyzed supernatant was added to BMDCs in 96-well plates, and an equal volume of fresh Opti-MEM was added in parallel to separate wells as a mock control; 12 h later, cells were collected for RT-qPCR analysis, and data are presented as relative mRNA levels with respect to those of mock controls after normalizing to *Gapdh*.

RNA isolation, RT–qPCR, RNA-seq and ELISA analyses

Cellular RNA was isolated with a Zymo Direct-zol RNA Miniprep kit. cDNA was synthesized with SuperScript III, and qPCR was performed with Fast SYBR Green Master Mix (Thermo Fisher). The primer sequences for qPCR of each gene are listed in Supplementary Table 2. Gene induction levels are presented as the relative fold change with respect to mock treatment after normalizing to *Gapdh*. Bulk RNA-seq libraries were prepared by following the manufacturer's instructions for the NEBNext Ultra Directional RNA Library Prep Kit for Illumina (NEB, E7420S). For ELISA analysis, ELISA kits for IFN β , IL-6 and TNF were obtained from BioLegend, and IFN α ELISA kits were obtained from PBL Assay Science. Assays were performed according to the manufacturers' instructions. Appropriate volumes of culture medium were used to ensure that the readouts were within the range of the standard curve.

RNA-seq data analysis

For RNA-seq data, adaptors and low-quality reads were trimmed using Trimmomatic (version 0.39)⁴⁹ with the following parameters: ILLUMINACLIP:adapters/TruSeq3-PE.fa:2:30:10:1:true LEADING:3 TRAILING:3 SLIDINGWINDOW:4:15 MINLEN:50 TOPHRED33. Cleaned paired-end reads were aligned to the mm10 reference genome with GENCODE⁵² mouse gene set M24, using STAR (version 2.7.6a)⁵³ with the following parameters: --outSAMunmapped Within --outFilterType BySJout --outSAMattributes NH HI AS NM MD --outFilterMultimapNmax 20 --outFilterMismatchNmax 999 --outFilterMismatchNoverReadLmax 0.04 --alignIntronMin 20 --alignIntronMax 1000000 --alignMatesGapMax 1000000 --alignSJoverhangMin 8 --alignSJDBoverhangMin 1 --sjdbScore 1 --outSAMtype BAM SortedByCoordinate --quantMode TranscriptomeSAM. RSEM (version 1.3.3)⁵⁴ was used to quantify gene expression levels using the reads aligned to the transcriptome in the bam file as input, with the following parameters: --alignments --estimate-rspd --calc-ci --no-bam-output --seed 12345 --ci-memory 30000 --paired-end --strandedness reverse. Differentially expressed genes were identified using the DESeq2 package⁴².

eccDNA linearization

eccDNA linearization was performed by sequential treatment of eccDNAs with the nickase fnCpf1 (Applied Biological Materials)³⁷ and single-strand DNA-specific nuclease. Fifty nanograms of eccDNAs was nicked in a 20- μ l reaction that contained 1/8 volume of 8 \times fnCpf1 linearization buffer (160 mM HEPES pH 7.5, 1.2 M KCl, 4 mM DTT, 0.8 M EDTA, 80 mM MnCl₂) and 1 μ l fnCpf1. After incubating at 37 °C for 1 h, the treated eccDNAs were extracted with PCI solution (25:24:1) in a Phase Lock Gel tube (QuantaBio) and precipitated at -80 °C with carrier glycogen (Roche) and 1/10 volume of 3 M sodium acetate (pH 5.5). Nicked eccDNAs were linearized in 10- μ l reactions that contained 2 μ l of 5 \times buffer (0.25 M sodium acetate pH 5.2, 1.4 M

NaCl, 25 mM ZnSO₄) and 1 µl S1 nuclease (Thermo Fisher) and were incubated at 37 °C for 5 min. Reactions were stopped by adding 40 µl of 10 mM Tris-HCl (pH 8.0), and linear eccDNAs were immediately recovered with 75 µl of SPRIselect beads (Beckman Coulter). Successful linearization of eccDNAs was confirmed by efficient digestion with Plasmid-Safe ATP-dependent DNase (Lucigen).

Statistics

Ordinary one-way ANOVA and two-tailed unpaired *t*-tests were performed with GraphPad Prism 9.

Ethics statement

All procedures on animals involved in this study were conducted according to protocols approved by the Harvard Medical School IACUC.

Reporting summary

Further information on research design is available in the [Nature Research Reporting Summary](#) linked to this paper.

Data availability

The eccDNA sequencing data and RNA-seq data have been deposited in the Gene Expression Omnibus (GEO) with accession number [GSE165919](#).

Code availability

The code used to analyse eccDNA sequencing data is available at GitHub (https://github.com/YiZhang-lab/eccDNA_RCA_nanopore).

References

1. 1.

Paulsen, T., Kumar, P., Koseoglu, M. M. & Dutta, A. Discoveries of extrachromosomal circles of DNA in normal and tumor cells. *Trends Genet.* **34**, 270–278 (2018).

2. 2.

Gaubatz, J. W. Extrachromosomal circular DNAs and genomic sequence plasticity in eukaryotic cells. *Mutat. Res.* **237**, 271–292 (1990).

3. 3.

Hotta, Y. & Bassel, A. Molecular size and circularity of DNA in cells of mammals and higher plants. *Proc. Natl Acad. Sci. USA* **53**, 356–362 (1965).

4. 4.

Moller, H. D. et al. Circular DNA elements of chromosomal origin are common in healthy human somatic tissue. *Nat. Commun.* **9**, 1069 (2018).

5. 5.

Dillon, L. W. et al. Production of extrachromosomal microDNAs is linked to mismatch repair pathways and transcriptional activity. *Cell Rep.* **11**, 1749–1759 (2015).

6. 6.

Hull, R. M. et al. Transcription-induced formation of extrachromosomal DNA during yeast ageing. *PLoS Biol.* **17**, e3000471 (2019).

7. 7.

Gresham, D. et al. Adaptation to diverse nitrogen-limited environments by deletion or extrachromosomal element formation of the *GAP1* locus. *Proc. Natl Acad. Sci. USA* **107**, 18551–18556 (2010).

8. 8.

Sinclair, D. A. & Guarente, L. Extrachromosomal rDNA circles—a cause of aging in yeast. *Cell* **91**, 1033–1042, (1997).

9. 9.

Shibata, Y. et al. Extrachromosomal microDNAs and chromosomal microdeletions in normal tissues. *Science* **336**, 82–86 (2012).

10. 10.

Zhu, J. et al. Molecular characterization of cell-free eccDNAs in human plasma. *Sci. Rep.* **7**, 10968 (2017).

11. 11.
Cloninger, C., Felton, M., Paul, B., Hirakawa, Y. & Metzenberg, S. Control of pH during plasmid preparation by alkaline lysis of *Escherichia coli*. *Anal. Biochem.* **378**, 224–225 (2008).
12. 12.
DeLap, R. J., Rush, M. G., Zouzias, D. & Khan, S. Isolation and preliminary characterization of the small circular DNA present in African green monkey kidney (BSC-1) cells. *Plasmid* **1**, 508–521 (1978).
13. 13.
Landry, J. J. et al. The genomic and transcriptomic landscape of a HeLa cell line. *G3* **3**, 1213–1224 (2013).
14. 14.
Tichy, E. D. Mechanisms maintaining genomic integrity in embryonic stem cells and induced pluripotent stem cells. *Exp. Biol. Med.* **236**, 987–996 (2011).
15. 15.
Rang, F. J., Kloosterman, W. P. & de Ridder, J. From squiggle to basepair: computational approaches for improving nanopore sequencing read accuracy. *Genome Biol.* **19**, 90 (2018).
16. 16.
Joffroy, B., Uca, Y. O., Presern, D., Doye, J. P. K. & Schmidt, T. L. Rolling circle amplification shows a sinusoidal template length-dependent amplification bias. *Nucleic Acids Res.* **46**, 538–545 (2018).
17. 17.
Soh, Y. Q. et al. Sequencing the mouse Y chromosome reveals convergent gene acquisition and amplification on both sex chromosomes. *Cell* **159**, 800–813 (2014).
18. 18.
Marichal, T. et al. DNA released from dying host cells mediates aluminum adjuvant activity. *Nat. Med.* **17**, 996–1002 (2011).

19. 19. Sakahira, H., Enari, M. & Nagata, S. Cleavage of CAD inhibitor in CAD activation and DNA degradation during apoptosis. *Nature* **391**, 96–99 (1998).
20. 20. Li, L. Y., Luo, X. & Wang, X. Endonuclease G is an apoptotic DNase when released from mitochondria. *Nature* **412**, 95–99 (2001).
21. 21. Shiokawa, D., Kobayashi, T. & Tanuma, S. Involvement of DNase γ in apoptosis associated with myogenic differentiation of C2C12 cells. *J. Biol. Chem.* **277**, 31031–31037 (2002).
22. 22. Arakawa, H. et al. Functional redundancy between DNA ligases I and III in DNA replication in vertebrate cells. *Nucleic Acids Res.* **40**, 2599–2610, (2012).
23. 23. Lu, G. et al. Ligase I and ligase III mediate the DNA double-strand break ligation in alternative end-joining. *Proc. Natl Acad. Sci. USA* **113**, 1256–1260 (2016).
24. 24. Simsek, D. et al. Crucial role for DNA ligase III in mitochondria but not in Xrcc1-dependent repair. *Nature* **471**, 245–248 (2011).
25. 25. Li, Y., Berke, I. C. & Modis, Y. DNA binding to proteolytically activated TLR9 is sequence-independent and enhanced by DNA curvature. *EMBO J.* **31**, 919–931 (2012).
26. 26. Lange, S. S. & Vasquez, K. M. HMGB1: the jack-of-all-trades protein is a master DNA repair mechanic. *Mol. Carcinog.* **48**, 571–580 (2009).
27. 27.

Wang, Z. et al. Regulation of innate immune responses by DAI (DLM-1/ZBP1) and other DNA-sensing molecules. *Proc. Natl Acad. Sci. USA* **105**, 5477–5482 (2008).

28. 28.

Green, D. R., Ferguson, T., Zitvogel, L. & Kroemer, G. Immunogenic and tolerogenic cell death. *Nat. Rev. Immunol.* **9**, 353–363 (2009).

29. 29.

Sundaresan, R., Parameshwaran, H. P., Yogesha, S. D., Keilbarth, M. W. & Rajan, R. RNA-independent DNA cleavage activities of Cas9 and Cas12a. *Cell Rep.* **21**, 3728–3739 (2017).

30. 30.

Putney, S. D., Benkovic, S. J. & Schimmel, P. R. A DNA fragment with an α -phosphorothioate nucleotide at one end is asymmetrically blocked from digestion by exonuclease III and can be replicated in vivo. *Proc. Natl Acad. Sci. USA* **78**, 7350–7354 (1981).

31. 31.

Sauer, J. D. et al. The *N*-ethyl-*N*-nitrosourea-induced Goldenticket mouse mutant reveals an essential function of Sting in the in vivo interferon response to *Listeria monocytogenes* and cyclic dinucleotides. *Infect. Immun.* **79**, 688–694 (2011).

32. 32.

Hou, B., Reizis, B. & DeFranco, A. L. Toll-like receptors activate innate and adaptive immunity by using dendritic cell-intrinsic and -extrinsic mechanisms. *Immunity* **29**, 272–282 (2008).

33. 33.

Oberhammer, F. et al. Apoptotic death in epithelial cells: cleavage of DNA to 300 and/or 50 kb fragments prior to or in the absence of internucleosomal fragmentation. *EMBO J.* **12**, 3679–3684 (1993).

34. 34.

Shiokawa, D. & Tanuma, S. Differential DNases are selectively used in neuronal apoptosis depending on the differentiation state. *Cell Death Differ.* **11**, 1112–1120

(2004).

35. 35.

Wang, H. et al. DNA ligase III as a candidate component of backup pathways of nonhomologous end joining. *Cancer Res.* **65**, 4020–4030 (2005).

36. 36.

Cox, D., Yuncken, C. & Spriggs, A. I. Minute chromatin bodies in malignant tumours of childhood. *Lancet* **1**, 55–58 (1965).

37. 37.

Turner, K. M. et al. Extrachromosomal oncogene amplification drives tumour evolution and genetic heterogeneity. *Nature* **543**, 122–125 (2017).

38. 38.

Li, X. D. et al. Pivotal roles of cGAS–cGAMP signaling in antiviral defense and immune adjuvant effects. *Science* **341**, 1390–1394 (2013).

39. 39.

Andreeva, L. et al. cGAS senses long and HMGB/TFAM-bound U-turn DNA by forming protein–DNA ladders. *Nature* **549**, 394–398 (2017).

40. 40.

Tovey, M. G., Lallemand, C. & Thyphronitis, G. Adjuvant activity of type I interferons. *Biol. Chem.* **389**, 541–545 (2008).

41. 41.

Moore, J. B. & June, C. H. Cytokine release syndrome in severe COVID-19. *Science* **368**, 473–474 (2020).

42. 42.

Love, M. I., Huber, W. & Anders, S. Moderated estimation of fold change and dispersion for RNA-seq data with DESeq2. *Genome Biol.* **15**, 550 (2014).

43. 43.

Ignatiadis, N., Klaus, B., Zaugg, J. B. & Huber, W. Data-driven hypothesis weighting increases detection power in genome-scale multiple testing. *Nat. Methods* **13**, 577–580 (2016).

44. 44.

Du, Q., Kotlyar, A. & Vologodskii, A. Kinking the double helix by bending deformation. *Nucleic Acids Res.* **36**, 1120–1128 (2008).

45. 45.

Liu, D. et al. Branched kissing loops for the construction of diverse RNA homooligomeric nanostructures. *Nat. Chem.* **12**, 249–259 (2020).

46. 46.

Li, H. Minimap2: pairwise alignment for nucleotide sequences. *Bioinformatics* **34**, 3094–3100 (2018).

47. 47.

Quinlan, A. R. & Hall, I. M. BEDTools: a flexible suite of utilities for comparing genomic features. *Bioinformatics* **26**, 841–842 (2010).

48. 48.

Gel, B. & Serra, E. karyoploteR: an R/Bioconductor package to plot customizable genomes displaying arbitrary data. *Bioinformatics* **33**, 3088–3090 (2017).

49. 49.

Bolger, A. M., Lohse, M. & Usadel, B. Trimmomatic: a flexible trimmer for Illumina sequence data. *Bioinformatics* **30**, 2114–2120 (2014).

50. 50.

Li, H. & Durbin, R. Fast and accurate short read alignment with Burrows–Wheeler transform. *Bioinformatics* **25**, 1754–1760 (2009).

51. 51.

Ramirez, F. et al. deepTools2: a next generation web server for deep-sequencing data analysis. *Nucleic Acids Res.* **44**, W160–W165 (2016).

52. 52.

Frankish, A. et al. GENCODE reference annotation for the human and mouse genomes. *Nucleic Acids Res.* **47**, D766–D773 (2019).

53. 53.

Dobin, A. et al. STAR: ultrafast universal RNA-seq aligner. *Bioinformatics* **29**, 15–21 (2013).

54. 54.

Li, B. & Dewey, C. N. RSEM: accurate transcript quantification from RNA-Seq data with or without a reference genome. *BMC Bioinformatics* **12**, 323 (2011).

Acknowledgements

We thank D. Schatz (Yale University) for the antibody to mouse Lig4, R. Rajan (University of Oklahoma) for the initial gift of FnoCas protein, X. Zhang for help in BMDC preparation, P. Yin for allowing us to use the AFM instrument and J. Lieberman for critical reading of the manuscript. H.C. was supported by a Leukemia and Lymphoma Society Fellow Award. D.L. is a Merck Fellow of the Life Sciences Research Foundation. This work was supported by the Howard Hughes Medical Institute. F.W.A. and Y.Z. are Investigators of the Howard Hughes Medical Institute.

Author information

Affiliations

1. Howard Hughes Medical Institute, Boston, MA, USA

Yuangao Wang, Meng Wang, Mohamed Nadhir Djekidel, Huan Chen, Frederick W. Alt & Yi Zhang

2. Program in Cellular and Molecular Medicine, Boston Children's Hospital, Boston, MA, USA

Yuangao Wang, Meng Wang, Mohamed Nadhir Djekidel, Huan Chen, Frederick W. Alt & Yi Zhang

3. Wyss Institute for Biologically Inspired Engineering, Harvard University, Boston, MA, USA

Di Liu

4. Department of Systems Biology, Harvard Medical School, Boston, MA, USA

Di Liu

5. Department of Genetics, Harvard University, Boston, MA, USA

Frederick W. Alt & Yi Zhang

6. Harvard Stem Cell Institute WAB-149G, Boston, MA, USA

Yi Zhang

Contributions

Y.Z. conceived the project; Y.W. and Y.Z. designed the experiments; Y.W. performed the majority of the experiments; H.C. generated the ligase-knockout cell lines; M.W. developed the method to call eccDNA from Nanopore data and performed all bioinformatics analyses; M.N.D. performed pilot analysis of eccDNA sequencing data; D.L. helped with the SAFM imaging; F.W.A. supervised the work by H.C.; Y.W. and Y.Z. wrote the manuscript.

Corresponding author

Correspondence to [Yi Zhang](#).

Ethics declarations

Competing interests

A patent application (with the patent agency Wolf, Greenfield & Sacks) covering the eccDNA purification method and the application of eccDNA as an immunostimulant has been filed by the Boston Children's Medical Center Corporation.

Additional information

Peer review information *Nature* thanks Birgitte Regenberg and the other, anonymous, reviewer(s) for their contribution to the peer review of this work. Peer reviewer reports are available.

Publisher's note Springer Nature remains neutral with regard to jurisdictional claims in published maps and institutional affiliations.

Extended data figures and tables

Extended Data Fig. 1 Selective binding of eccDNAs to beads and high sensitivity of DNA detection by SYBR Gold staining.

a, Representative gel image showing selective binding of circular DNA to magnetic silica beads in solution A. The assay was tested with 200 \times (mass) linear DNA (lane 4 and 6) and 1X (mass) DNA circles (lane 5 and 6). Lanes 1-3 indicate the input DNAs. Lane 1, 0.5% of input linear DNA for lane 4 was loaded; lane 2, equal amount of input circular DNAs for lane 5 were loaded; lane 3, 0.5% of input linear DNA and equal amount of input circular DNAs for lane 6 were loaded. Lanes 4-6 were DNAs recovered from Solution A. lane 4, 200 \times (mass) linear DNA alone undergone purification by solution A; lane 5, 1 \times (mass) DNA circles undergone purification by solution A; lane 6 mixture of 200 \times (mass) linear DNA and 1 \times (mass) DNA circles undergone purification by solution A. Note, only circular DNAs were recovered. The recovery rate was very high, particularly for the smaller circular DNAs, C2: a 200 bp circle, C5: a 525 bp circle. **b**, High sensitivity of DNA detection using vertical agarose gel electrophoresis and SYBR Gold staining. 0.2 μ l commercial DNA ladder (total of 10 ng) was undergone 5 \times series dilutions and fractionated by 1% vertical agarose gel electrophoresis, stained by SYBR Gold, DNA in lane-4 were 125 \times diluted of that in lane-1, and could still be visualized. The detection limit is estimated as 5-10 pg/band. Results in **a–b** are representative of three independent experiments.

Extended Data Fig. 2 Summary of the nanopore sequencing data.

a, Diagram of nanopore long read sequencing of eccDNA. Tandem copies of eccDNAs were self-concatenated to long molecule by rolling cycle amplification (RCA), and directly read through by Oxford Nanopore. Each copy of eccDNA molecule in a single long molecule was sequenced multiple times. “S”: split site. **b**, Summary of mESC eccDNA long reads from an Oxford Nanopore MinION flow cell. **c**, Diagram showing how the eccDNA full-length sequence is called and categorized. Nanopore reads from **(a)**, the dashed box, were aligned to a single locus (Continuous) or to multiple loci (Non-continuous) in genome. Continuous: an example of six sub-regions of a long nanopore read repeatedly aligned to a single locus, where full length sequence of eccDNA was presented with only one split site (S); Non-continuous: an example of eight sub-regions of a single long read sequentially aligned to two separate loci (Locus-1 and Locus-2), representing an eccDNA ligated by two genomic fragments (2f ecc) with two split sites (S1 and S2). **d**, Criteria for eccDNA calling.

EccDNAs were called based on their number of full passes aligned to the genome. Long reads with less than two full passes were discarded (left and middle panel). Left, Nanopore read that hits genome only once either fails to designate the genomic start and end site of eccDNA (up panel), or miss the middle region (bottom panel) that may or may not include in the original eccDNA molecule (Uncertain); Middle, because of potential sequencing error of Oxford Nanopore, reads that hit genome more than once but less than twice (1 full pass) were also discarded due to the lack of confirmation in eccDNA calling, particularly on designating the start and end site of eccDNA. Right, eccDNA molecules were called from long reads when covered at least twice (≥ 2 full pass) on their aligned loci.

Extended Data Fig. 3 Summary of Illumina short read sequencing and Chromosomal distribution of eccDNA fragments.

a, Summary of eccDNA short read sequencing without RCA. Purified eccDNA was directly fragmented with Tn5 (Illumina Nextera), and sequenced with Illumina Hiseq 2500 in PE150 mode. **b**, Chromosomal distribution of eccDNA short reads.

Extended Data Fig. 4 Effects of Endonuclease G, DNase γ , and DNA ligases knockout on apoptosis and eccDNA generation.

a, Quantification of eccDNA from cells of the indicated treatment. EccDNA production was presented as nanogram per 10 million cells; ud, under detection limit. Bars indicate mean \pm s.e.m. of three independent experiments. **b**, Diagram illustration and PCR confirmation of the *EndoG* knockout mESC line. Gene structure of *EndoG*, sgRNAs (red arrows), two sets of screen primers for internal sites (black arrowhead, “n” =negative knockout cell line) and external sites (red arrowhead, “p” =positive knockout cell line) were shown. **c**, Diagram illustration and PCR confirmation of the *DNase γ* knockout mESC lines. Gene structure of *DNase γ* , sgRNAs (red arrows), two sets of screen primers for internal sites (black arrowhead, “n” =negative knockout cell line) and external sites (red arrowhead, “p” =positive knockout cell line) were shown. **d**, Cell viability is not affected by *EndoG* or *DNase γ* KO. Cell viability was evaluated by flow cytometry, after staining with Far Red Live/Dead Cell Stain Kit, FSC-A/SSC-A and FSC-A/FSC-H were sequentially used to exclude debris and gate on singlets, respectively, then gate on APC+ as dead cells. Bars indicate mean \pm s.e.m. of dead cell ratio from three independent experiments. **e**, Deficiency of *DNase γ* or *EndoG* in mESC do not significantly alter UV-induced cell death. Cell death was measured by flow cytometry, after staining with Far Red Live/Dead Cell Stain Kit, FSC-A/SSC-A and FSC-A/FSC-H were sequentially used to exclude debris and gate on singlets, respectively, then gate on APC+ as dead cells. Bar indicate mean \pm s.e.m. of dead cell ratio of 3 independent experiments. **f**, Quantification of eccDNAs presented in Fig. 3d. EccDNAs below the mtDNA band were quantified by densitometry (by Image J

1.53e) and presented as relative levels to that in WT cells of parallel eccDNA purifications. Bars indicate mean \pm s.e.m. of three independent experiments. **g**, Quantification of eccDNA below the mtDNA band by densitometry (by Image J 1.53e). Data are presented as relative levels to that purified from WT cells of parallel eccDNA purifications (Fig. 3g), bars indicate mean \pm s.e.m. of three independent experiments. Ordinary one-way ANOVA with Tukey's multiple comparison test was used for multiple comparisons in **e**, **f**, **g**. **, $p < 0.01$; ns, no significant.

Extended Data Fig. 5 EccDNAs are potent immunostimulants for BMDCs.

a, Confirmation of BMDC identity by flow cytometry. After differentiating bone marrow cells with 20 ng/ml GM-CSF for 7 days, cell debris (left) were first excluded and singlets (middle) were then phenotyped on the basis of their CD11c and major histocompatibility complex II (MHCII) expression (right) to define BMDC, the numbers indicate the percentage of gated cells. Data were further analyzed with FlowJo. V10.8.0 and shown as representative of 2 independent experiments. **b**, Various DNAs were resolved by agarose gel electrophoresis. Li-DNA: sheared linear genomic DNA; poly(dG:dC), poly(deoxyguanylic-deoxycytidylic). Representative gel of three independent experiments was shown. **c**, **d**, Bar graphs showing the relative mRNA (**c**) and protein (ELISA) (**d**) levels of *IL-6* and *TNF- α* . Data is shown as mean \pm s.e.m. of replicates ($n=4$ per group) of a representative experiment in three independent experiments. **e**, **f**, DNase I pretreatment abolishes *IL-6* and *TNF- α* induction by eccDNA. Equal amount of DNA (120 ng/ml) used to prepare transfection mixtures were pre-treated with or without DNase I as indicated, then transfected to BMDCs. 12 h later, total RNA was extracted for RT-qPCR (**e**) and medium was collected for ELISA (**f**). Data are shown as mean \pm s.e.m. of replicates ($n=4$ per group) of a representative experiment in three independent experiments. Comparisons in **c–f** were done on biological replicates by Ordinary one-way ANOVA with Tukey's multiple comparison test. *, $p < 0.05$; **, $p < 0.01$; ***, $p < 0.001$; ****, $p < 0.0001$; ns, no significant; nd, not detected.

Extended Data Fig. 6 EccDNAs are potent immunostimulants for BMDMs.

a, Confirmation of BMDMs identify by flow cytometry. After differentiating bone marrow cells with L929 conditioned medium for 7 days, cells debris (left) were first excluded and singlets (middle) were phenotyped on the basis of F4/80 and CD11b expression (right) to define BMDM, the numbers indicate the percentage of gated cells. Data were further analyzed with FlowJo. V10.8.0 and shown as representative of 2 independent experiments. **b**, **c**, EccDNAs induce cytokine genes in BMDMs. Bar graphs showing the induction of mRNA (**b**) and protein (**c**) of *IL-6* and *TNF- α* in

BMDMs that transfected with varying levels of eccDNA, compared with fragmented linear DNA, and poly(dG:dC). RT-qPCR were performed after 12-hours transfection. ELISA analysis (**c**) was performed after 24-hours transfection. Data are shown as mean \pm s.e.m. of replicates (n=4 per group) of a representative experiment of three independent experiments. Comparisons were performed on biological replicates with equal amount of DNA transfection by Ordinary one-way ANOVA with Tukey's multiple comparison test. *, $p<0.05$; **, $p<0.01$; ***, $p<0.001$; ****, $p<0.0001$; ns, no significant; nd, not detected.

Extended Data Fig. 7 The circularity of eccDNAs, but not the sequence, is critical for their immunostimulant activity.

a, Bar graphs showing the relative *IL-6* and *TNF- α* mRNA levels. Data is shown as mean \pm s.e.m. of replicates (n=4 per group) of a representative experiment in three independent experiments. **b**, **c**, Bar graphs showing the relative *IL-6* and *TNF- α* mRNA levels (**b**), and protein (ELISA) levels (**c**). Data is shown as mean \pm s.e.m. of replicates (n=4 per group) of a representative experiment in three independent experiments. **d**, Diagram of DNA transfection efficiency and stability assay. Step-1: 5 Phosphorothioate (purple “*”) end-protected synthetic linear DNA (PS-syn-linear) and its circular form with equal number of phosphorothioate bonds (PS-Syn-circular) were transfected to BMDCs in the same way as in Fig. 5 for either 1 or 12 h. Step-2: cells were lysed in 100 μ l lysis buffer and treated with Thermolabile Proteinase K to prepare total DNA. Step-3: 4 μ l total DNA was used for qPCR with a set of primers that amplify a 117 bp fragment in both linear and circular DNA. **e**, qPCR analysis of the samples prepared as described in (**d**). Transfected DNA level was normalized to that of 10 ng/ml PS-syn-linear transfection (n= 4 or 6, as indicated by dots). Bars indicate mean \pm s.e.m. of three independent experiments. **f**, 12 h after transfection of indicated DNA at 30 ng/ml, medium was collected for ELISA essay, Data are shown as mean \pm s.e.m. of replicates (n=4 per group) of a representative experiment in three independent experiments. Comparisons in **a–c** were performed on biological replicates by Ordinary one-way ANOVA with Tukey's multiple comparison test; two-tailed unpaired *t* tests (**e**, **f**). *, $p<0.05$; **, $p<0.01$; ***, $p<0.001$; ****, $p<0.0001$; ns, no significant.

Extended Data Fig. 8 Reproducibility of the BMDC transcriptomes.

a–c, Scatter plot of pair-wise comparison of the transcriptomes of three independent BMDC samples of untreated (**a**), treated with eccDNA (**b**) or linear DNA (**c**). The x and y-axis are log2(FPKM+0.1).

Extended Data Fig. 9 Global transcriptional response to eccDNA in BMDMs.

a–c, Scatter plot of pair-wise comparison of the transcriptomes of three independent BMDM samples of untreated (**a**), treated with eccDNA (**b**) or linear DNA (Extended Data Fig. 6). The x and y-axis are $\log_2(\text{FPKM}+0.1)$. **d**, Scatter plot showing 380 genes (left panel, red dots) that are significantly induced ($\text{FC} \geq 5$, adjusted p-value < 0.001; FC and p-value were generated using DESeq2⁴² and p-values were adjusted by IHW⁴³) by eccDNA, but not linear DNA, in BMDMs. 24 significantly induced cytokine genes are indicated (right panel, red dots). The x and y-axis are \log_2 -transformed normalized read counts. **e**, Heatmap presentation of the top 20 induced genes. **f**, GO terms enriched in the genes activated by eccDNA treatment in BMDMs. The number of genes in each term and the p-value of the enrichment is indicated.

Extended Data Fig. 10 Analysis of the eccDNA sensing pathway.

a, Scatter plot indicates the transcriptomes of the two replicates of synthetic circular DNA treated BMDCs are highly similar. The x and y-axis are $\log_2(\text{FPKM}+0.1)$. **b**, Western blot confirmation of the Sting-/- and Myd88-/- cells. Blots were performed once, but cell genotypes were further confirmed by mRNA sequences from RNA-seq data (data not shown). **c**, Correlation of the transcriptomes of 2 replicates eccDNA treated Sting-/- and Myd88-/- BMDC. The x and y-axis are $\log_2(\text{FPKM}+0.1)$.

Supplementary information

Supplementary Fig. 1

This file contains uncropped images of agarose gels and scan images of immunoblotting.

Reporting Summary

Supplementary Table 1

List of CRISPR–Cas9 guide RNA and genotyping PCR primer sequences for the different knockout cell lines

Supplementary Table 2

List of RT–qPCR primer sequences for the various cytokine genes analysed

Supplementary Table 3

List of synthetic small DNAs and their PCR amplification primer sequences

Supplementary Table 4

List of the differentially expressed genes in eccDNA-treated BMDCs

Supplementary Table 5

List of the differentially expressed genes in eccDNA-treated BMDMs

Supplementary Table 6

List of the differentially expressed genes in eccDNA-treated BMDCs in response to *Sting1* or *Myd88* knockout

Peer Review File

Rights and permissions

Reprints and Permissions

About this article

Cite this article

Wang, Y., Wang, M., Djekidel, M.N. *et al.* eccDNAs are apoptotic products with high innate immunostimulatory activity. *Nature* **599**, 308–314 (2021).

<https://doi.org/10.1038/s41586-021-04009-w>

- Received: 16 February 2021
- Accepted: 07 September 2021
- Published: 20 October 2021
- Issue Date: 11 November 2021
- DOI: <https://doi.org/10.1038/s41586-021-04009-w>

Share this article

Anyone you share the following link with will be able to read this content:

[Get shareable link](#)

Sorry, a shareable link is not currently available for this article.

[Copy to clipboard](#)

Provided by the Springer Nature SharedIt content-sharing initiative

This article was downloaded by **calibre** from <https://www.nature.com/articles/s41586-021-04009-w>

| [Section menu](#) | [Main menu](#) |

- Article
- Open Access
- [Published: 27 October 2021](#)

The structure of neurofibromin isoform 2 reveals different functional states

- [Andreas Naschberger^{1,2}](#) [ORCID: orcid.org/0000-0002-6096-9169](#),
- [Rozbeh Baradaran](#) [ORCID: orcid.org/0000-0002-6096-9169](#),
- [Bernhard Rupp](#) [ORCID: orcid.org/0000-0002-3300-6965](#)^{2,3} &
- [Marta Carroni](#) [ORCID: orcid.org/0000-0002-7697-6427](#)

Nature volume **599**, pages 315–319 (2021)

- 4787 Accesses
- 79 Altmetric
- [Metrics details](#)

Subjects

- [Cryoelectron microscopy](#)
- [Growth factor signalling](#)
- [Tumour-suppressor proteins](#)

Abstract

The autosomal dominant monogenetic disease neurofibromatosis type 1 (NF1) affects approximately one in 3,000 individuals and is caused by mutations in the *NF1* tumour suppressor gene, leading to dysfunction in the protein neurofibromin (Nfl)^{1,2}. As a GTPase-activating protein, a key function of Nfl is repression of the Ras oncogene signalling cascade. We determined the human Nfl dimer structure at an overall resolution of 3.3 Å. The cryo-electron microscopy structure reveals domain organization and structural details of the Nfl exon 23a splicing³ isoform 2 in a closed, self-inhibited, Zn-stabilized state and an open state. In the closed conformation, HEAT/ARM core domains shield the GTPase-activating protein-related domain

(GRD) so that Ras binding is sterically inhibited. In a distinctly different, open conformation of one protomer, a large-scale movement of the GRD occurs, which is necessary to access Ras, whereas Sec14-PH reorients to allow interaction with the cellular membrane⁴. Zn incubation of Nf1 leads to reduced Ras-GAP activity with both protomers in the self-inhibited, closed conformation stabilized by a Zn binding site between the N-HEAT/ARM domain and the GRD–Sec14-PH linker. The transition between closed, self-inhibited states of Nf1 and open states provides guidance for targeted studies deciphering the complex molecular mechanism behind the widespread neurofibromatosis syndrome and Nf1 dysfunction in carcinogenesis.

[Download PDF](#)

Main

Nf1^{5,6} is a multifunctional tumour suppressor protein forming an obligate high-affinity dimer⁷ of about 640-kDa molecular weight. As a GTPase-activating protein (GAP), its primary function is suppression of the Ras signalling cascade by accelerating the GTP hydrolysis rate of Ras, which returns Ras to its inactive GDP bound form^{4,8}. Consequently, mutated Nf1 shows altered Ras-GAP activity and leads to uncontrolled signalling in multiple cell signalling pathways. The resulting syndrome NF1 presents diverse phenotypes⁹, ranging from benign lesions to cognitive impairment and psychological retardation^{1,2}. Patients with NF1 carry a higher overall lifetime risk for developing cancer. The *NF1* disease mutations are distributed over the entire protein^{1,4}, with slightly higher occurrence in the catalytic GRD. About half of all cases of NF1 are inherited, whereas the remaining cases result from de novo mutations¹⁰. Somatic Nf1 mutations are also present in 5–10% of cancers, demonstrating the role of Nf1 as a tumour suppressor¹.

The ubiquitous Nf1 isoform-2 splice variant Nf1-23a (2839aa) is, together with Nf1 isoform 1, which lacks the 23a insertion (2818aa), one of the two biologically relevant alternative Nf1 isoforms. Inclusion of exon 23a is found in most human tissues but predominately skipped in neurons of the central nervous system³, and variation of the isoform 1/2 splicing ratio leads to disturbed neuronal differentiation¹¹. The 23a insertion, located within the GRD, leads to about tenfold less GAP activity¹² than Nf1 isoform 1. The presence or absence of 23a regulates Ras/ERK signalling and affects memory and learning behaviour¹².

Of the many proteins interacting with Nf1, only the interaction with Ras and Sprouty-related protein with an EVH1 domain (SPRED1) is well characterized^{4,13}. SPRED1 recruits Nf1 from the cytosol to the plasma membrane where Ras resides, and Nf1 subsequently can downregulate GTP-bound Ras¹⁴.

Domain organization of the Nf1-23a dimer

Our high-resolution single particle cryo-electron microscopy (EM) structures reveal the domain organization and structural details of the full-length Nf1-23a isoform 2 dimer (Fig. 1a–c, Extended Data Figs. 1–3). Contrasting an unpublished low-resolution, symmetric Nf1 model¹⁵, two distinct populations of the Nf1-23a dimer are present: (1) a major population with both protomers showing a closed, auto-inhibited conformation (closed Nf1 state) stabilized by Zn and (2) a second population (open Nf1 state) with one protomer in the auto-inhibited conformation and the other protomer in an open configuration necessary for Ras binding (Fig. 1d).

Fig. 1: Structure of the neurofibromin homodimer.

 **figure1**

a, Overview of the Nf1 dimer with one protomer yellow and one pink. Dimer interaction regions are green. **b**, Domain organization of Nf1-23a. N-HEAT/ARM and C-HEAT/ARM domains are grey, GRD light blue and the Sec14-PH domain yellow. Locations of the interdomain linkers, exon 23a insert and S-rich region are annotated.

c, Composite density map (left) and ribbon model (right) of the Nf1-23a homodimer in double-auto-inhibited conformation, coloured as in **b**. **d**, Nf1 double-auto-inhibited, closed state (left) and open state (right). The boxed insert (bottom left) shows that, in auto-inhibited, closed conformation, Ras, docked from the crystal structure complex with GRD (PDB entry 6ob3), cannot bind. In the open protomer conformation (right insert), GRD can bind Ras.

An asymmetric, homodimeric core of 27 ordered HEAT-repeats and four ARM-repeats forms the molecular framework into which the GRD, including its non-catalytic GAPex subdomain¹³, and the membrane-associated Sec14-PH domain are centrally linked (Extended Data Fig. 4). Three major dimer interfaces between the protomers exist in both states. The N-terminal HEAT helices contact the terminal C-HEAT helices at the other protomer (Fig. 1a), each contact burying about 950 Å² of surface area. The resulting dimer is connected in the centre, forming a core that buries almost 3,000 Å² of surface area. The GRD and Sec14-PH domain extend out from the N-HEAT/ARM core, and the chain returns to the C-HEAT/ARM core near where it branched out. In the closed state, additional contacts between the last helix α63 of the GRD and the core bury another ~240 Å² of surface. The linker between GRD and the Sec14-PH domain is in the closed conformation part of a Zn binding site, contributing a stabilising contact to the N-HEAT/ARM core. The dimer interfaces are detailed in Extended Data Fig. 5. The disordered, S-rich region branching out from C-HEAT helix α103 and returning into the core at C-HEAT helix α104 could not be traced. Flexibility and solvent access are consistent with the reported target for phosphorylation⁴.

Open state

In the open Nf1 state, one protomer presents a closed conformation, where binding of Ras or a Ras dimer¹⁶ by the Nf1 GRD¹⁷ is sterically inhibited, with access of the Nf1 GRD to Ras completely blocked by the HEAT/ARM-repeat core. The conformation of the other protomer presents a distinctly different, open conformation, with the GRD and Sec14-PH domains reoriented and almost reversed in position compared to the closed conformation (Figs. 1d, 2a). The density maps reveal the linkages between the domains, including L1 between the N-HEAT/ARM and the GRD; the (in X-ray models absent) linker L2 between the GRD and the lipid-binding Sec14-PH domain; and L3, the linkage from Sec14-PH to the core C-HEAT/ARM domain (Extended Data Fig. 6). In the transition to the open conformation, these linkers undergo significant conformational rearrangement, which is crucial for the large-scale movement of the GRD necessary to bind Ras and for Sec14-PH to access the cellular membrane.

Fig. 2: Conformational rearrangement between closed and open Nf1 states.

 **figure2**

a, Comparison of closed (pink, left panels) and open (green, right panels) conformation of the Nf1 protomers. Illustrated are the massive conformational rearrangement of the GRD (light blue), its GAPex domain (magenta) and its Sec14-PH domain (yellow). **b**, View of both states along the principal direction of the Nf1 dimer core. **c**, Detail of the Zn metal binding site stabilising the closed Nf1 conformation. Superposition of open and closed state on the last three helices of GAPex illustrates the large movement of the Sec14-PH domain against the GRD/GAPex domain.

Conformation changes between states

Supplementary Video 1 illustrates the rearrangement from the auto-inhibited, closed Nf1 state to the open state (Fig. 2a, b), in which Nf1 can access Ras and associate with the membrane. From the closed conformation blocking Ras access, the GRD and Sec14-PH domain rotate $\sim 130^\circ$ and $\sim 90^\circ$, respectively, with the active Ras binding and

the lipid binding site of the respective domains facing away from the core and facilitating membrane access.

Connecting loop L1 (G1190 to L1196) between the N-HEAT core helix α 48 (L1173 to G1190) and GRD helix α 49 (L1196 to M1215) rearranges completely and then forms an extension of the two almost aligned helices, with G1190 as a plausible hinge point. To accommodate relocation of the GRD, the Sec14-PH domain also undergoes a $\sim 90^\circ$ rotation, and its linker L3 to the C-HEAT/ARM domain completely changes conformation in proline-rich region Q1835 to G1852. The proximity of L1 and L3 to each other, at the centre of the overall rotation, is of fundamental importance, because modest local conformational changes suffice to accommodate the large rotation and long-range relocation of the two domains. Were L1 and L3 far distant from each other, both domains would remain clamped to the core, unable to undergo the large rotational rearrangement.

The relative movement of the GRD and Sec14-PH domain against each other also requires a conformational change of the long L2 interdomain linker. Extending from the last helix α 63 of the GRD, the L2 linker hinges at a proline-rich loop beginning around G1547 (G1526 in Nf1 isoform 1 X-ray models) to T1565, continuing into a three-turn helix that becomes part of the Sec14 domain and connects with a short loop to the first helix α 65 of the Sec14 domain (Extended Data Fig. [6](#)). This connecting loop and the last helix α 73 are not present in the Sec14-PH domain X-ray models.

Metal binding site

The closed conformation of native Nf1 is stabilized by a cysteine- and histidine-coordinated transition metal binding site between the N-HEAT/ARM domain and the GRD-Sec14-PH linker L2 and is formed by the triade C1032, H1558 and H1576 (Fig. [2c](#)), with the fourth coordination partner a solvent accessible water molecule (Fig. [3b](#)). The tetrahedral site coordination is clear in map density and typical for Zn^{2+} . The His₂Cys motif presents the most preferred binding site coordination for Zn^{2+} in proteins^{[18](#)}. After domain rotation to the open conformation, C1032 of the N-HEAT/ARM core is separated by 30 Å from the two histidine residues of the relocated GRD-Sec14-PH linker, and the metal binding site is lost (Fig. [2c](#)). X-ray fluorescence scans confirmed the presence of Zn in native Nf1 (Extended Data Fig. [7c](#)).

Fig. 3: Zn site and conformation of Nf1 and SPRED1 binding.

 **figure3**

Colour scheme as in Fig. 2. **a**, A conformational state with both protomers in the open conformation was not observed and is impeded by severe steric interference (indicated by the asterisk) between the two respective GRDs. **b**, Insert: density around the metal binding site, with tetrahedral His₂Cys-water coordination and distances typical for Zn²⁺. Right panel: Nf1-23a accelerates the rate of GTP hydrolysis by KRas. Error bars represent the mean \pm s.e.m. of $n = 5$ or $n = 8$ independent assays of the same sample as indicated in each bar by individual data points. Significance calculated by one-way ANOVA followed by pairwise two-sided *t*-tests, applying Bonferroni correction with $\alpha = 0.01$. * $P = 0.0016$, *** $P < 0.000052$; NS, not significant. **c**, Top: concomitant SPRED1 and Ras binding is possible only to the protomer in open conformation. Bottom: In the closed conformation, SPRED1 can bind, whereas Ras cannot bind. **d**, Superposition of all available GRD and Sec14-PH domains onto the Protein Data Bank (PDB) model 1nf1. The backbone traces of GRD X-ray models are shown light blue, and the X-ray Sec14-PH domains are shown in yellow. The GRD loop C1486-

D1490, not visible in the X-ray structures, must undergo rearrangement upon SPRED1 binding in both conformations because it interferes with bound SPRED1.

Zn stabilizes the closed conformation

Upon addition of Zn to native Nf1, structural analysis revealed a stabilized Nf1 state with both protomers in the closed conformation and their Zn sites occupied. In contrast, Nf1 stripped with 1 mM EDTA destabilized the protein significantly, as shown by the higher void peak in the size exclusion chromatogram (Extended Data Fig. 7a). Zn-stabilized Nf1 yielded high-resolution maps, particularly of the GRD-Sec14-PH region, corroborating a stabilising role of Zn (Extended Data Figs. 2, 3). Ras-GAP activity assays (Fig. 3b, Extended Data Fig. 7d) confirmed that Zn-Nf1 shows concentration-dependent, significantly lower activity than the native, mixed-state Nf1. In contrast, 3d transition metal ions of Mn, Fe, Ni, Cu and Ca did not suppress Ras-GAP activity (Extended Data Fig. 7e).

Exon 23a loop insert

The 63-nucleotide exon 23a inserts 21 amino acids into the Nf1 GRD between residues Q1370 and V1371, extending helix α 56 by one turn before it loops back into helix α 57, with residues A1380 to R1396 remaining disordered at the lysine-rich loop apex. Based on the SPRED1-GRD-Sec14-PH X-ray complex models¹⁹, no immediate direct interference of this flexible 23a insert is evident with either Ras or SPRED1 bound to the GRD (Fig. 3). Any structural role causal to reduced Ras-GAP activity is, therefore, likely indirect. However, in the open conformation, the 23a insertion loop points towards the membrane where access to the membrane-anchored Ras or to SPRED1 for Nf1 recruiting¹³ is crucial. Interference by the partly disordered, basic and hydrophilic 23a insertion could thus be contributing to diminished Ras-GAP activity of Nf1-23a¹².

Sec-14-PH lipid-binding domain

In the closed protomer conformation, access to the hydrophobic core of the Sec14-PH domain that, in the X-ray models^{20,21}, harbours a phosphatidylethanolamine representing a membrane lipid component, is largely blocked by the GRD. In Zn-Nf1 maps with 3.0 Å local resolution, the lipid could be modelled as phosphatidylethanolamine (Extended Data Fig. 8e). In the open state, the hydrophobic cavity of Sec14-PH is readily accessible and exposed. No major conformational rearrangements in the Nf1-23a Sec14-PH domain core relative to the X-ray models were observed (Fig. 3d).

EM GRD domains differ from X-ray models

Although the X-ray models of GRD and Ras-bound GRD differ in detail (Fig. 3d), they are conformationally similar overall, with a modest backbone root-mean-square deviation (RMSD) of ~1.0 Å. The Nf1-23a GRD RMSD to the X-ray models and between open and closed form is around ~2.5 Å, but shifts of secondary structure elements up to ~7 Å occur (Fig. 3d). The well-defined linker L2 connecting the GRD with the Sec14-PH domain is unique to the cryo-EM model. In closed conformation, the GRD arginine finger R1276, critical for Ras binding^{22,23}, is not accessible. Reorientation of the GRD in the open conformation exposes the arginine finger, which becomes accessible for Ras binding.

SPRED1 binding to Nf1

SPRED1 recruits Nf1 by the GAPex domain from the cytosol to the membrane, where Nf1 can interact and downregulate Ras^{14,24}. Mutations in SPRED1 were linked to the distinct rasopathy legius syndrome, related to NF1²⁵. These diseases can be largely explained by impaired SPRED1-mediated membrane recruiting of Nf1. The structure reveals that, unlike Ras, SPRED1 can bind to both Nf1 conformations (Fig 3c), indicating that SPRED1 can bind cytosolic Nf1 also in its closed state and recruit it to the membrane. However, SPRED1 bound to the open, GAP-active conformer has a different orientation relative to the membrane than SPRED1 bound to the closed protomer (Fig 3c). It is possible that SPRED1 bound to the closed conformer suffices to recruit Nf1 to the membrane where the open conformer then downregulates Ras activity (Fig. 4a). The role of a second SPRED1 possibly bound to the open conformer remains unresolved.

Fig. 4: Postulated neurofibromin action.

 **figure4**

a, In the closed state, inactivated Nf1 cannot downregulate Ras. In the active, open Nf1 state, SPRED1 can bring Nf1 to the cell membrane where Nf1 can bind and downregulate monomeric Ras \times GTP to Ras \times GDP. The open Nf1 state could also regulate a Ras \times GTP dimer. **b**, Hypothetical model of a not-observed Nf1 state with two partially open GRDs that would allow downregulation of one Ras \times GTP dimer at the same time in one cycle.

Implications for NF1 function

The full-length Nf1-23a dimer structures highlight the complexity of Nf1 function, pointing towards a network of allosteric regulatory effects. The Nf1 HEAT/ARM dimer framework is rigid in its core, providing a stable platform for the GRD-Sec14-PH domain rearrangement while retaining high mobility at the peripheral tips of the two lobes. The resulting structural complexity and involvement of massive

rearrangements of the GRD and Sec14-PH domain against the core can explain the wide variety of disease-relevant mutations⁴.

The exact reason for the flexibility and dimerization is unknown but is likely required to trigger or facilitate transition between closed inactive and open active conformations. If both states are energetically similar, thermal motion might provide enough torque to trigger or support a transition between states. Active NTP-dependent mechanisms cannot be ruled out, but a nucleotide-binding pocket in the structure remains to be discovered. The role of the unobserved, mobile S-rich domain in triggering domain rearrangements remains unresolved.

Because both Nf1 protomers in the dimer cannot assume the open conformation at the same time (Fig. 3a), Ras-GAP regulation would have to occur with one Nf1 dimer regulating one Ras×GTP monomer or Ras×GTP dimer at the time (Fig. 4a). However, the existence of structurally different open states that could accommodate binding of a Ras×GTP dimer by two structurally different open conformer protomers is possible. Binding and regulation of Ras dimers by Nf1 remains an open line of investigation (Fig. 4b), and it is uncertain how many SPRED1 will bind in this process. For an isolated open–closed conformation Nf1 dimer, two SPRED1 domains could bind without interference, but their relative orientations differ, and it is unknown which configuration is causal in membrane recruiting. The Sec-14-PH domain might play a role as a membrane sensor and might impart additional regulatory function on Nf1. Lipid exchange function was established²⁰ for Sec14-PH, indicating that Sec14-PH can sense the membrane environment before Nf1 transitions into the open state.

High levels of intracellular Zn ('Zn wave') were reported, dependent on calcium and MAPK signalling activity²⁶, and the presence of a cysteine-coordinated Zn binding site²⁷ suggests involvement of a secondary regulatory element in the Nf1 Ras-GAP activity.^{26,27} Zn stabilizes the auto-inhibited conformation of Nf1, and, consequently, Ras is upregulated, which, in turn, would lead to higher MAPK signalling. However, our concentration-dependent Zn assays indicate that, to suppress Nf1 activity, Zn concentrations must be significantly higher than presumed cytosolic steady-state concentrations. Given the complexity of the cellular Zn metallome and unknown spatiotemporal Zn concentrations²⁸, we cannot presently draw firm conclusions about a regulatory role of Zn as a second messenger. Additional studies should clarify the exact role of Zn in the Ras signalling pathway, especially whether Nf1 can be regulated in vivo by Zn and how Zn release into the cytosol is triggered and regulated.

The dynamics of Nf1 might be additionally modulated by the many described, but not well-characterized, Nf1 interaction partners⁴. Regulation of Nf1 likely occurs in many layers, and our study sets the stage for research aiming to clarify the exact mechanism of Nf1 action and its related, multifaceted disease, NF1.

Methods

Cloning, expression and purification of human Nf1-23a

Full-length human Nf1-23a (Nf1 isoform 2, UniProt accession no. P21359), including an N-terminal strep tag followed by a TEV cleavage site, was designed and generated synthetically (GeneArt) and cloned into pACEBac1 baculovirus transfer vector²⁹. Nf1-23a was expressed in *Sf21* insect cells for 2 d after baculovirus infection (Bac-to-Bac, Invitrogen). All subsequent steps were carried out at 4 °C. Cells (~0.6 ml at ~1 million cells per ml) were harvested by centrifugation (1,000g for 10 min) and resuspended in 20 ml of lysis buffer containing 50 mM Tris pH 8.0, 300 mM NaCl, 2 mM DTT, 1 mg ml⁻¹ of DNase I and a protease inhibitor cocktail tablet (EDTA-free, Sigma-Aldrich). Suspended cells were lysed by 20 strokes with a Dounce homogenizer on ice. Cell debris was removed by centrifugation (20,000g for 1 h), and the supernatant was filtered through a 0.8-μm polystyrene membrane (Millipore). The sample was loaded onto a Strep-Tactin column (5 ml), washed with 10 column volumes (CV) of wash buffer (50 mM Tris pH 8.0, 300 mM NaCl and 2 mM DTT), and the protein was eluted with 5 CV of wash buffer containing 5 mM desthiobiotin. The eluate was concentrated to ~5 mg ml⁻¹ using a 100-kDa concentrator (Amicon Ultra, EMD Millipore) and run on a Superose 6 Increase 10/300 size-exclusion chromatography (SEC) GL column, equilibrated with gel filtration buffer (20 mM Tris pH 8.0, 300 mM NaCl and 2 mM DTT). Elution fractions containing Nf1-23a were pooled and concentrated to ~4 mg ml⁻¹ using a 100-kDa concentrator (Amicon Ultra, EMD Millipore). Purified protein was flash-frozen in liquid nitrogen until further use.

For the second dataset containing Zn, freshly purified Nf1-23a at ~0.5 mg ml⁻¹ was incubated for 90 min with a final concentration of 50 μM ZnCl₂ before freezing grids. Sample preparation and data collection were carried out as described for native Nf1-23a.

To determine the stability of Nf1-23a in the absence of metals, the protein was purified in the presence of 1 mM EDTA throughout the preparation. This resulted in a higher void peak (~9 ml) in the final gel filtration column profile (Extended Data Fig. 7a), indicating that the protein is less stable in the absence of metals.

Cloning, expression and purification of human KRas

Wild-type human KRas (amino acids 1–169, UniProt accession no. P01116) with amino terminal 6×His tag was purchased from Addgene and expressed overnight in *Escherichia coli* cells at 18 °C. All subsequent steps were carried out at 4 °C. Cells were harvested by centrifugation (3,000g for 20 min) and lysed twice by sonication on

ice in a buffer containing 50 mM HEPES pH 8.0, 300 mM NaCl, 0.1 mM GTP (Sigma-Aldrich), 1 mM MgCl₂, 2 mM TCEP, 1 mg ml⁻¹ of DNase I and a protease inhibitor cocktail tablet. Cell debris was removed by centrifugation (20,000g for 1 h), and the supernatant was filtered through a 0.8-μm polystyrene membrane (Millipore). The sample was loaded onto a HisTrap column (5 ml), washed with 10 CV of wash buffer (50 mM HEPES pH 8.0, 300 mM NaCl, 1 mM MgCl₂ and 20 mM imidazole), and the protein was eluted with 5 CV of elution buffer (50 mM HEPES pH 8.0, 300 mM NaCl, 1 mM MgCl₂ and 200 mM imidazole). The eluate was supplemented with 0.1 mM GTP, concentrated to ~5 mg ml⁻¹ using a 10-kDa concentrator (Amicon Ultra, EMD Millipore) and run on a HiLoad 16/60 Superdex 200 SEC GL column, equilibrated with gel filtration buffer (20 mM HEPES pH 8.0, 300 mM NaCl, 0.1 mM GTP, 1 mM MgCl₂ and 2 mM DTT). Elution fractions containing KRas were pooled and concentrated to ~4 mg ml⁻¹ using a 10-kDa concentrator (Amicon Ultra, EMD Millipore). Purified protein was flash-frozen in liquid nitrogen until further use.

Cryo-EM sample preparation and data acquisition

Quantifoil R2/1 holey carbon grids (Au 300 mesh, Electron Microscopy Sciences) were glow-discharged for 60 s at 20 mA using a GloQube (Quorum) instrument. Purified Nf1-23a was thawed, centrifuged (14,000g for 5 min at 4 °C) and diluted to ~0.5 mg ml⁻¹ with gel filtration buffer. Protein was loaded into the freshly glow-discharged grids and plunge-frozen in LN₂-cooled liquid ethane using a Vitrobot Mark IV (Thermo Fisher Scientific) with a blot force of -2 for 2.5 s. Temperature and relative humidity were maintained at 4 °C and 100%, respectively. Grids were clipped and loaded into a 300-kV Titan Krios G2 microscope (Thermo Fisher Scientific, EPU 2.8.1 software) equipped with a Gatan BioQuantum energy filter and a K3 Summit direct electron detector (AMETEK). Grids were screened for quality control based on particle distribution and density, and images from the best grid were recorded. Micrographs were recorded at a nominal magnification of ×105,000, corresponding to a calibrated pixel size of 0.86 Å. The dose rate was 12 electron physical pixels per second, and images were recorded for 3.3 s divided into 40 frames, corresponding to a total dose of 40 electrons per Å². Defocus range was set between -0.5 μm and -4 μm. Gain-corrected image data were acquired.

Cryo-EM data processing

Extended Data Fig. 1 illustrates the data processing workflow for the native Nf1-23a dataset. The following pre-processing steps were performed with cryoSPARC Live v3.1.0 (ref. 30). Movie stacks were motion-corrected and dose-weighted using MotionCor2 v2.1.1 (ref. 31). Contrast transfer function (CTF) estimates for the motion-

corrected micrographs were calculated with CTFFIND4 v4.1.13 (ref. [32](#)). Poor-quality micrographs were discarded. Particles were initially picked with a blob-picker using subset-selected micrographs, and these were used for reference-free two-dimensional (2D) classification to generate picking templates. Auto-picking (using 23 of the representative 2D classes containing different orientations as templates) from 7,848 micrographs yielded ~1.4 million particles. An initial model was generated without imposing symmetry (C1) using stochastic gradient descent in cryoSPARC Live. Subsequent image processing was carried out with cryoSPARC v3.1.0 (ref. [33](#)). Particles were classified with three-dimensional (3D) heterogenous refinement using four classes, resulting in 714,512 particles. Further classification using reference-free 2D classification with 100 classes yielded 582,742 particles. Particles were converted into a STAR file and input into RELION v3.1.1 (ref. [34](#)) for further processing.

To generate a consensus reconstruction, particles were re-extracted in 470 pixels ($1.7 \times$ binned) followed by 3D refinement with local angular search using the cryoSPARC map as the starting model. ‘Polished’ particle images, which were corrected for individual particle movements, were generated using aligned movie frames that were output from MotionCor2. 3D refinement on the polished particles, followed by CTF refinement and another round of 3D refinement, yielded a reconstruction to ~3.4 Å overall resolution with C1 symmetry.

Using the polished particles and the consensus reconstruction, signal subtraction was carried out on each lobe separately with reboxing to 235 pixels and recentring on the mask. 3D refinement followed by CTF refinement and another round of 3D refinement improved the reconstruction of each lobe to ~3.1 Å overall resolution with C1 symmetry (Extended Data Fig. [1](#)).

To generate reconstructions for the different conformations of Nf1-23a, the unpolished 582,742 images were used in RELION v3.1.1. Particles were re-extracted in 400 pixels ($2 \times$ binned) followed by 3D refinement. Polished particle images were first generated, followed by three rounds of 3D refinement and CTF refinement (without 4th-order aberrations), in an alternative manner. This yielded a reconstruction to ~3.5 Å overall resolution in C1 symmetry. To generate the closed (auto-inhibited) conformation reconstruction, signal subtraction was carried out on the particles using a mask on lobe 2, with reboxing to 200 pixels and recentring on the mask. After 3D refinement, 3D classification (with three classes) without alignment to generate a class with 130,329 particles representing the closed conformation was performed. Signals for these particles were reverted to the original unsubtracted images, and 3D refinement yielded the auto-inhibited reconstruction at overall resolution of ~4 Å (Extended Data Fig. [1](#)).

One of the classes from the above 3D classification with 189,570 particles had a lobe in the open conformation. Another round of 3D classification (with three classes)

without alignment yielded a class with 51,951 particles that had a better resolution for the open conformation. Signals for these particles were reverted to the original, and 3D refinement yielded the open reconstruction at an overall resolution of ~4.8 Å (Extended Data Fig. 1).

The 582,742 particles polished above with an overall resolution of ~3.5 Å were used to improve the resolution on the GRD-Sec14-PH domain. A mask was generated on this region in lobe 1, and the signal outside of the mask was subtracted with reboxing to 200 pixels and recentring on the mask. After 3D refinement, 3D classification was performed (with three classes) without alignment to generate a class with 100,684 particles that had a better overall resolution. 3D refinement on these particles yielded a reconstruction to ~3.5 Å resolution (Extended Data Fig. 1).

Extended Data Fig. 2 illustrates the data processing workflow for the dataset from Zn-Nf1. The pre-processing steps were performed with cryoSPARC Live v3.1.0 as described above. Auto-picking (using 33 of the representative 2D classes containing different orientations as templates) from 18,882 micrographs yielded ~2.3 million particles. Subsequent image processing was carried out with cryoSPARC v3.1.0. Particles were classified with 3D heterogenous refinement using four classes, resulting in 1,046,333 particles. Further classification using reference-free 2D classification with 100 classes yielded 843,857 particles. Particles were refined to ~3.6 Å resolution with homogenous refinement and re-extracted in 384 pixels (1.56× binned) using the refined coordinates. Further refinement of the particles using non-uniform refinement yielded a reconstruction to ~3.3 Å resolution. The refined particles were converted into a STAR file and input into RELION v3.1.1 for further processing.

To generate a consensus reconstruction, particles were re-extracted in 400 pixels (1.5× binned) followed by 3D refinement with local angular search using the consensus map generated from the first dataset as the starting model. After CTF refinement (without the 4th-order aberrations) and 3D refinement, particle images were polished to correct for individual particle movements, using aligned movie frames that were output from MotionCor2. 3D refinement on the polished particles yielded a reconstruction to ~3.3 Å overall resolution with C1 symmetry. However, there was some anisotropy in the reconstructed map, likely due to the presence of different conformations of the particles. To improve the reconstruction, the polished particles were classified using 3D classification (with five classes) without alignment. One class containing 300,087 particles had GRD-Sec14-PH domains on both lobes that were well defined. 3D refinement, followed by CTF refinement (without 4th-order aberrations) and 3D refinement on these particles yielded a consensus reconstruction to ~3.3 Å, which did not show anisotropy artefacts.

Using the 300,087 particles from the above 3D classification, signal subtraction was carried out on each lobe separately with reboxing to 270 pixels and recentring on the

mask, and the subtracted particles were then combined. 3D refinement followed by CTF refinement and another round of 3D refinement using a mask on the core improved the reconstruction in this region of each lobe to \sim 2.9 Å overall resolution with C1 symmetry (Extended Data Fig. 2). Using another mask for the tip of each lobe improved the reconstruction in this region for each lobe to \sim 3.1 Å overall resolution with C1 symmetry.

To improve the resolution for the GRD-Sec14-PH domain on each lobe, the 843,857 polished particles were used to subtract signal outside of this domain in each lobe separately, with reboxing to 270 pixels and recentring on the mask. 3D classification (three classes) without alignment was carried out on each GRD-Sec14-PH domain. The GRD-Sec14-PH domain in each lobe contained one class (356,665 particles in lobe 1 and 309,370 particles in lobe 2), which had a better resolution. These classes were combined, and, subsequently, 3D refinement, CTF refinement and another round of 3D refinement were performed to yield a reconstruction for the GRD-Sec14-PH domain to \sim 3.0 Å resolution with C1 symmetry.

All final reconstructions were sharpened using either RELION post-processing or DeepEMhancer³⁵. The local resolution estimations in Extended Data Fig. 3 were performed using Resmap v1.1.4 (ref. 36).

Model building and refinement

A partial starting model for the Nf1-23a core was built ab initio by Buccaneer v1.6.10 (ref. 37) and manually completed and real-space refined into the highest resolution map (3.2 Å) with Coot 0.9.4.1 (refs. 38,39). The GRD of 1nf1 (ref. 17) and the 2e2x Sec14-PH domain²⁰ were rigid body fitted using Chimera^{40,41} into the best GRD-Sec14-PH map and manually corrected and completed by real-space refinement in Coot. Additional linker regions were built manually in Coot. The core model as well as the GRD-Sec14-PH model were real-space refined with PHENIX v1.19-4092 real-space-refine⁴² into the corresponding domain maps. The resulting refined models were then fitted into the consensus map using UCSF Chimera v1.15 and refined by PHENIX real-space-refine. Similarly, for the closed conformation, the model of the core and the model of the GRD-Sec14-PH domains were fitted into the density and real-space refined in Coot, followed by connecting the different domains of the model. For the open conformation, the GRD and Sec14-PH domains were rigid body fitted in Chimera followed by manual modelling of the linker regions in Coot. The closed and opened state models were refined by PHENIX real-space-refine using maps generated by DeepEMhancer³⁵. All structure models were validated using the PDB validation service⁴³. Dimer interfaces and buried surface areas were computed with ePISA v1.52 (ref. 44). Data collection, refinement and model quality statistics are summarized in Extended Data Table 1.

For the Zn-stabilized structure, the Nf1 closed state of the native dataset was rigid body fitted into a composite map that was generated with PHENIX combine-focused-maps out of all high-resolution maps for the different parts (tip, core and GAP-Sec14-PH region). The model was real-space refined using Coot and refined with PHENIX real-space-refine.

PDB deposition codes of X-ray structure models used in analysis and modelling were 2d4q⁴⁵, 2e2x²⁰, 3peg, 3pg7, 3p7z²¹, 1nf1 (ref. ¹⁷), 6ob2, 6ob3 (ref. ⁴⁶), 6v65 and 6v6f¹⁹ (Supplementary Table ¹).

GAP activity assays

Assays for GAP-stimulated GTP hydrolysis were performed using a GTPase assay kit (Abcam), according to the manufacturer's instructions. The assay uses a malachite photometrically green reagent to measure the concentration of phosphate ions (P_i) in solution. In brief, KRas (wild-type) was first buffer exchanged into buffer A (50 mM HEPES pH 8.0 and 300 mM NaCl) to remove any excess of free nucleotides and P_i and then added to white opaque 96-well plates (Corning) at a final concentration of 0.5 μ M. GTPase reactions were initiated by the addition of Nf1 (buffer exchanged into buffer A) at a final concentration of 0.5 μ M (final volume 100 μ l with 0.5 mM GTP and 2.5 mM MgCl₂ added to the assay buffer). Samples were incubated for 90 min at room temperature, and the absorbance was measured at 600 nm using a SpectraMax i3x plate reader (Molecular Devices). To test the effect of divalent cations, ZnCl₂, MnCl₂, FeCl₂, CaCl₂, CuCl₂ and NiCl₂ were added to each assay buffer at a final concentration of 50 μ M. The effect of different concentration of ZnCl₂ (10–100 μ M) on the rate of Nf1-23a GTP hydrolysis by KRas was also measured. A standard curve of absorbance for known concentrations of P_i was generated and used to estimate the concentration of P_i in each sample. Each assay was repeated by three, five or eight independent experiments. Data are expressed as the mean \pm s.e.m. Significance was calculated by one-way ANOVA followed by pairwise two-sided *t*-tests, applying Bonferroni correction⁴⁷. The high concentration of protein used in the assays and the long incubation periods were necessary to measure μ M concentrations of P_i in a relatively large volume in each assay. Raw assay data and analysis are available in Supplementary Data ¹.

Total reflection X-ray fluorescence

The elemental nature of the bound metal cation in native Nf1-23a, purified without any Zn addition, was determined using total reflection X-ray fluorescence (TXRF) analysis on a Bruker PICOFOX S2 instrument. Both sample and buffer were measured

in the presence of a gallium internal standard at 2 mg l⁻¹ added to the samples (1:1, v/v) before the measurements. TXRF spectra were analysed using the Bruker PICOFOX Super Bayes Quantification software provided with the spectrometer. The highest metal peak was clearly identified as Zn (Extended Data Fig. 7c).

Sequence alignment

Homologous sequences of established and candidate HEAT/ARM proteins were identified through PSI-BLAST searches in the MPI Bioinformatics Toolkit (three iterations, default parameters)⁴⁸. Sequences with unusual insertions and/or deletions were removed, as were sequences that aligned very poorly. Each set of retrieved sequences, as well as the sequences for Nf1-23a residues 1–1,193 and 1,850–2,839, were submitted for alignment to the threefold prediction server HHpred (<https://toolkit.tuebingen.mpg.de/tools/hhpred>)^{49,50}. The server was run with default parameters with three iterations of global alignment against PDB_mmCIF70_3_Mar and PDB_mmCIF30_3_Mar databases. The alignments with the highest probabilities (>93%) and the lowest *E* values (<0.25) were used for representation in Extended Data Fig. 4, with multiple sequence alignments done in Jalview⁵¹ using Clustal W colouring⁵².

Extended Data Fig. 6 with secondary structure depiction of Nf1 was generated with <https://escript.ibcp.fr> (ref.⁵³). Figure panels were created with UCSF Chimera⁴⁰ and UCSF ChimeraX⁴¹. All graphs were made with Prism v8.3.0 (GraphPad Software, www.graphpad.com) and Biorender (<https://biorender.com/>).

Reporting summary

Further information on research design is available in the [Nature Research Reporting Summary](#) linked to this paper.

Data availability

All cryo-EM density maps, half maps, masks, Fourier shell correlation curves and composite maps were deposited into the Electron Microscopy Data Bank (<https://www.ebi.ac.uk/pdbe/emdb/>) under accession codes [EMD-13394](#), [EMD-13391](#), [EMD-13392](#), [EMD-13393](#), [EMD-13395](#) and [EMD-13396](#). The corresponding model coordinates were deposited in the Protein Data Bank (<https://www.ebi.ac.uk/pdbe>) under accession codes [7PGS](#), [7PGP](#), [7PGQ](#), [7PGR](#), [7PGT](#) and [7PGU](#). Local map reconstructions without fitted models were deposited under codes [EMD-13397](#) (Zn-Nf1 tip), [EMD-13398](#) (Zn-Nf1 core) and [EMD-13399](#) (Zn-Nf1 GRD-Sec14-PH). All assay data are supplied as Supplementary Data.

References

1. 1.

Ratner, N. & Miller, S. J. A RASopathy gene commonly mutated in cancer: the neurofibromatosis type 1 tumour suppressor. *Nat. Rev. Cancer* **15**, 290–301 (2015).

2. 2.

Gutmann, D. H. et al. Neurofibromatosis type 1. *Nat. Rev. Dis. Primers* **3**, 17004 (2017).

3. 3.

Barron, V. A. & Lou, H. Alternative splicing of the neurofibromatosis type I pre-mRNA. *Biosci. Rep.* **32**, 131–138 (2012).

4. 4.

Scheffzek, K. & Welti, S. In: *Neurofibromatosis Type 1: Molecular and Cellular Biology* (eds Upadhyaya, M. & Cooper, D. N.) 305–326 (Springer, 2012).

5. 5.

Gutmann, D. H., Wood, D. L. & Collins, F. S. Identification of the neurofibromatosis type 1 gene product. *Proc. Natl Acad. Sci. USA* **88**, 9658–9662 (1991).

6. 6.

Marchuk, D. A. et al. cDNA cloning of the type 1 neurofibromatosis gene: complete sequence of the *NF1* gene product. *Genomics* **11**, 931–940 (1991).

7. 7.

Sherekar, M. et al. Biochemical and structural analyses reveal that the tumor suppressor neurofibromin (NF1) forms a high-affinity dimer. *J. Biol. Chem.* **295**, 1105–1119 (2020).

8. 8.

Cichowski, K. & Jacks, T. NF1 tumor suppressor gene function: narrowing the GAP. *Cell* **104**, 593–604 (2001).

9. 9.

Larizza, L., Gervasini, C., Natacci, F. & Riva, P. Developmental abnormalities and cancer predisposition in neurofibromatosis type 1. *Curr. Mol. Med.* **9**, 634–653 (2009).

10. 10.

Evans, D. G. et al. Birth incidence and prevalence of tumor-prone syndromes: estimates from a UK family genetic register service. *Am. J. Med. Genet. A* **152A**, 327–332 (2010).

11. 11.

Biayna, J. et al. Using antisense oligonucleotides for the physiological modulation of the alternative splicing of *NF1* exon 23a during PC12 neuronal differentiation. *Sci. Rep.* **11**, 3661 (2021).

12. 12.

Nguyen, H. T. et al. Neurofibromatosis type 1 alternative splicing is a key regulator of Ras/ERK signaling and learning behaviors in mice. *Hum. Mol. Genet.* **26**, 3797–3807 (2017).

13. 13.

Dunzendorfer-Matt, T., Mercado, E. L., Maly, K., McCormick, F. & Scheffzek, K. The neurofibromin recruitment factor Spred1 binds to the GAP related domain without affecting Ras inactivation. *Proc. Natl Acad. Sci. USA* **113**, 7497–7502 (2016).

14. 14.

Stowe, I. B. et al. A shared molecular mechanism underlies the human rasopathies Legius syndrome and Neurofibromatosis-1. *Genes Dev.* **26**, 1421–1426 (2012).

15. 15.

Lupton, C. J. et al. The cryo-EM structure of the neurofibromin dimer reveals the molecular basis for von Recklinghausen disease. Preprint at <https://www.biorxiv.org/content/10.1101/2021.02.18.431788v1> (2021).

16. 16.

Muratcioglu, S. et al. GTP-dependent K-Ras dimerization. *Structure* **23**, 1325–1335 (2015).

17. 17.

Scheffzek, K. et al. Structural analysis of the GAP-related domain from neurofibromin and its implications. *EMBO J.* **17**, 4313–4327 (1998).

18. 18.

Ebert, J. C. & Altman, R. B. Robust recognition of zinc binding sites in proteins. *Protein Sci.* **17**, 54–65 (2008).

19. 19.

Yan, W. et al. Structural insights into the SPRED1-neurofibromin-KRAS complex and disruption of SPRED1-neurofibromin interaction by oncogenic EGFR. *Cell Rep.* **32**, 107909 (2020).

20. 20.

Welti, S., Fraterman, S., D'Angelo, I., Wilm, M. & Scheffzek, K. The Sec14 homology module of neurofibromin binds cellular glycerophospholipids: mass spectrometry and structure of a lipid complex. *J. Mol. Biol.* **366**, 551–562 (2007).

21. 21.

Welti, S. et al. Structural and biochemical consequences of NF1 associated nontruncating mutations in the Sec14-PH module of neurofibromin. *Hum. Mutat.* **32**, 191–197 (2011).

22. 22.

Bourne, H. R. The arginine finger strikes again. *Nature* **389**, 673–674 (1997).

23. 23.

Scheffzek, K. et al. The Ras-RasGAP complex: structural basis for GTPase activation and its loss in oncogenic Ras mutants. *Science* **277**, 333–338 (1997).

24. 24.

Dunzendorfer-Matt, T., Mercado, E. L., Maly, K., McCormick, F. & Scheffzek, K. The neurofibromin recruitment factor Spred1 binds to the GAP related domain

without affecting Ras inactivation. *Proc. Natl Acad. Sci. USA* **113**, 7497–7502 (2016).

25. 25.

Brems, H. et al. Germline loss-of-function mutations in SPRED1 cause a neurofibromatosis 1-like phenotype. *Nat. Genet.* **39**, 1120–1126 (2007).

26. 26.

Yamasaki, S. et al. Zinc is a novel intracellular second messenger. *J. Cell Biol.* **177**, 637–645 (2007).

27. 27.

Pace, N. J. & Weerapana, E. Zinc-binding cysteines: diverse functions and structural motifs. *Biomolecules* **4**, 419–434 (2014).

28. 28.

Colvin, R. A., Holmes, W. R., Fontaine, C. P. & Maret, W. Cytosolic zinc buffering and muffling: their role in intracellular zinc homeostasis. *Metalloomics* **2**, 306–317 (2010).

29. 29.

Bieniossek, C., Imasaki, T., Takagi, Y. & Berger, I. MultiBac: expanding the research toolbox for multiprotein complexes. *Trends Biochem. Sci.* **37**, 49–57 (2012).

30. 30.

Punjani, A., Zhang, H. & Fleet, D. J. Non-uniform refinement: adaptive regularization improves single-particle cryo-EM reconstruction. *Nat. Methods* **17**, 1214–1221 (2020).

31. 31.

Zheng, S. Q. et al. MotionCor2: anisotropic correction of beam-induced motion for improved cryo-electron microscopy. *Nat. Methods* **14**, 331–332 (2017).

32. 32.

Grant, T., Rohou, A. & Grigorieff, N. cisTEM, user-friendly software for single-particle image processing. *eLife* **7**, e35383 (2018).

33. 33.

Punjani, A. Algorithmic advances in single particle cryo-EM data processing using CryoSPARC. *Microsc. Microanal.* **26**, 2322–2323 (2020).

34. 34.

Zivanov, J. et al. New tools for automated high-resolution cryo-EM structure determination in RELION-3. *eLife* **7**, e42166 (2018).

35. 35.

Sanchez-Garcia, R. et al. DeepEMhancer: a deep learning solution for cryo-EM volume post-processing. *Commun. Biol.* **4**, 874 (2021).

36. 36.

Kucukelbir, A., Sigworth, F. J. & Tagare, H. D. Quantifying the local resolution of cryo-EM density maps. *Nat. Methods* **11**, 63–65 (2014).

37. 37.

Cowtan, K. The Buccaneer software for automated model building. 1. Tracing protein chains. *Acta Crystallogr. D Biol. Crystallogr.* **62**, 1002–1011 (2006).

38. 38.

Casañal, A., Lohkamp, B. & Emsley, P. Current developments in Coot for macromolecular model building of electron cryo-microscopy and crystallographic data. *Protein Sci.* **29**, 1069–1078 (2020).

39. 39.

Emsley, P., Lohkamp, B., Scott, W. G. & Cowtan, K. Features and development of Coot. *Acta Crystallogr. D Biol. Crystallogr.* **66**, 486–501 (2010).

40. 40.

Pettersen, E. F. et al. UCSF Chimera—a visualization system for exploratory research and analysis. *J. Comput. Chem.* **25**, 1605–1612 (2004).

41. 41.

Goddard, T. D. et al. UCSF ChimeraX: meeting modern challenges in visualization and analysis. *Protein Sci.* **27**, 14–25 (2018).

42. 42.

Afonine, P. V. et al. Real-space refinement in PHENIX for cryo-EM and crystallography. *Acta Crystallogr. D Struct. Biol.* **74**, 531–544 (2018).

43. 43.

Velankar, S. et al. PDBe: improved accessibility of macromolecular structure data from PDB and EMDB. *Nucleic Acids. Res.* **44**, D385–D395 (2016).

44. 44.

Krissinel, E. & Henrick, K. Inference of macromolecular assemblies from crystalline state. *J. Mol. Biol.* **372**, 774–797 (2007).

45. 45.

D’angelo, I., Welti, S., Bonneau, F. & Scheffzek, K. A novel bipartite phospholipid-binding module in the neurofibromatosis type 1 protein. *EMBO Rep.* **7**, 174–179 (2006).

46. 46.

Rabara, D. et al. KRAS G13D sensitivity to neurofibromin-mediated GTP hydrolysis. *Proc. Natl Acad. Sci. USA* **116**, 22122–22131 (2019).

47. 47.

Noble, W. S. How does multiple testing correction work? *Nat. Biotechnol.* **27**, 1135–1137 (2009).

48. 48.

Gabler, F. et al. Protein sequence analysis using the MPI Bioinformatics Toolkit. *Curr. Protoc. Bioinformatics* **72**, e108 (2020).

49. 49.

Hildebrand, A., Remmert, M., Biegert, A. & Soding, J. Fast and accurate automatic structure prediction with HHpred. *Proteins* **77**, 128–132 (2009).

50. 50.

Söding, J. Protein homology detection by HMM–HMM comparison. *Bioinformatics* **21**, 951–960 (2005).

51. 51.

Troshin, P. V. et al. JABAWS 2.2 distributed web services for Bioinformatics: protein disorder, conservation and RNA secondary structure. *Bioinformatics* **34**, 1939–1940 (2018).

52. 52.

Larkin, M. A. et al. Clustal W and Clustal X version 2.0. *Bioinformatics* **23**, 2947–2948 (2007).

53. 53.

Robert, X. & Gouet, P. Deciphering key features in protein structures with the new ENDscript server. *Nucleic Acids Res.* **42**, W320–W324 (2014).

Acknowledgements

B.R. acknowledges partial funding through the Austrian Science Fund (grants P28395 and I5152). B.R. and A.N. thank S. Lechner for assistance with *Sf21* insect cell expression. M.C. acknowledges partial funding from the Knut and Alice Wallenberg Foundation (KAW project 431042) and SciLifeLab project 1243867. Data were collected at the Cryo-EM Swedish National Facility funded by the Knut and Alice Wallenberg Foundation, the Family Erling Persson and Kempe Foundations, SciLifeLab, Stockholm University and Umeå University. M.C., A.N. and R.B. thank S. Fleischmann for IT support. We thank A. Amunts for equipment use, J. John for assistance with X-ray fluorescence experiments and P. Hudson for use of a plate reader. Computational models of K-Ras dimers were kindly provided by H. Jang of the Nussinov laboratory at the National Institutes of Health/National Cancer Institute.

Author information

Author notes

1. These authors contributed equally: Andreas Naschberger, Rozbeh Baradaran

Affiliations

1. SciLifeLab, Department of Biochemistry and Biophysics, Stockholm University, Solna, Sweden

Andreas Naschberger, Rozbeh Baradaran & Marta Carroni

2. Institute of Genetic Epidemiology, Medical University Innsbruck, Innsbruck, Austria

Andreas Naschberger & Bernhard Rupp

3. k.-k. Hofkristallamt, San Diego, CA, USA

Bernhard Rupp

Contributions

A.N. conceived and designed the project. A.N. designed the clone of Nf1-23a. A.N. and R.B. prepared the Nf1-23a samples. A.N., R.B. and M.C. collected, processed and refined the data. R.B. performed the GAP activity assays. M.C. collected TXRF data. A.N. and B.R. built the models. All authors analysed models and data and jointly prepared the manuscript.

Corresponding authors

Correspondence to [Bernhard Rupp](#) or [Marta Carroni](#).

Ethics declarations

Competing interests

The authors declare no competing interests.

Additional information

Peer review information *Nature* thanks Ken Westover and the other, anonymous, reviewer(s) for their contribution to the peer review of this work.

Publisher's note Springer Nature remains neutral with regard to jurisdictional claims in published maps and institutional affiliations.

Extended data figures and tables

Extended Data Fig. 1 Flowchart illustrating cryo-EM data processing of native Nf1-23a in the absence of Zn.

Details are described in the Methods section.

Extended Data Fig. 2 Flowchart illustrating cryo-EM data processing of Nf1-23a incubated with Zn.

Details are described in the Methods section.

Extended Data Fig. 3 Local resolution of final reconstructions in the absence (a-c) and presence (d-f) of Zn.

a, d, Final 3D reconstructions coloured according to local resolution estimation calculated by Resmap. **b, e**, Solvent-corrected “gold-standard” Fourier Shell Correlation (FSC) curves of the final 3D reconstructions. The estimated resolution (FSC = 0.143) for each reconstruction is indicated. **c, f**, Model-to-map FSCs. The estimated resolution (FSC = 0.5) for each model is indicated.

Extended Data Fig. 4 Structure-based sequence alignment of the core domains of Nf1-23a.

Multiple sequence alignments of residues 1-1193 and 1850-2839 of Nf1-23a were performed in HHpred (<https://toolkit.tuebingen.mpg.de/tools/hhpred>) against PDB_mmCIF70_3_Mar and PDB_mmCIF30_3_Mar databases using default parameter settings with the exception of global alignment mode. The PDB codes and their corresponding chains that have aligned to Nf1-23a are shown. The amino acid sequences are coloured according to the ClustalW convention. Regions predicted to have HEAT- and ARM-repeats are indicated by rectangular boxes. The alpha-helices are highlighted by zig-zag grey lines and labelled according to Extended Data Fig. 6.

Extended Data Fig. 5 Details of Nf1 dimer interface interactions.

Contact regions indicated in boxes (**a-d**) are detailed in the large panels. Participating protomer residues are coloured pink and yellow, respectively. Interactions are shown

between **a**, GRD and C-HEAT/ARM core; **b, c**, the N-HEAT/ARM and C-HEAT/ARM core; **d**, the N-terminal tip of the N-HEAT/ARM domain and the C-terminal end of the C-HEAT/ARM domain. Hydrogen bonds/charged interactions are indicated by dashed lines.

Extended Data Fig. 6 Sequence and model-based secondary structure assignment of neurofibromin isoform 2 (Nf1-23a) and neurofibromin isoform 1.

Regions are boxed in grey for N-HEAT and C-HEAT domains, black for L1 and L3, red for L2, light blue for GRD and gold for Sec14-PH. The 23a insertion in isoform 2 is highlighted in yellow. Metal-coordinating residues C1032, H1558, and H1576 are labelled with arrows. Contact regions between protomer termini and between the protomer cores are highlighted green, the contacts between GRD in closed conformation and the protomer core are highlighted cyan.

Extended Data Fig. 7 Purification, characterization, and activity assays of Nf1-23a.

a, Size-exclusion chromatography purification of Nf1-23a in the absence (blue line) and presence (red line) of EDTA. In both preparations, Nf1-23a purified as a single peak, but with a higher void peak (~9 mL) in the presence of EDTA in comparison to without. **b**, SDS-PAGE analysis of corresponding fractions from the size-exclusion chromatography. Nf1-23a is highly pure by SDS-PAGE. For gel source data see Supplementary Figure 1. **c**, Total reflection X-ray fluorescence (TXRF) spectrum of purified Nf1-23a identified the presence of Zn in native Nf1. Measurements on both sample and buffer were done in presence of a gallium internal standard at 2 mg L^{-1} , added to the samples (1:1, v/v) before measurements. Buffer subtracted difference spectrum normalized by internal standard. $\text{K}\alpha$ X-ray emission lines for different metals are indicated with arrows. **d**, The effect of different concentration of Zn on the rate of Nf1-23a GTP hydrolysis by KRas. Each assay was measured with 3 independent replications. The concentration of P_i in each assay was normalized against both the buffer + Zn and Nf1 + Zn control. Error bars represent the mean \pm s.e.m. of $n = 3$ independent assays of the same sample. Significance calculated by one-way ANOVA followed by pairwise 2-sided t-tests, applying Bonferroni correction with $\alpha = 0.05$. *** $p < 0.00009$; n.s. not significant. **e**, Nf1-23a GTP hydrolysis by KRas is only inhibited by Zn. Hydrolysis was measured in the presence of $50 \mu\text{M}$ metal using a GTPase assay kit (Abcam) to detect the amount of phosphate ions (P_i) in solution, with 3 independent replications. The concentration of P_i in each assay was normalized against both the buffer + metal and Nf1 + metal control. Error bars represent the mean \pm s.e.m. of $n = 3$ independent assays of the same sample. Significance calculated by

one-way ANOVA followed by pairwise 2-sided t-tests, applying Bonferroni correction with $\alpha = 0.05$. ** $p = 0.0023$; n.s. not significant.

Extended Data Fig. 8 Quality of cryo-EM density maps. Different regions are shown starting from N- to C-terminus of Nf1.

The labels of the panels correspond to regions and residue ranges in the central overview panel and the domain scheme. Coulomb potential density of **a**, the N-HEAT/ARM in the Nf1 tip region, **b**, the N-HEAT/ARM in the Nf1 core region, **c**, the GRD, **d**, the L2 linker between GRD and Sec14-PH, **e**, the lipid bound to Sec14-PH, **f**, resolved beta-strands of Sec14-PH, **g**, the C-HEAT/ARM in the Nf1 core region, **h**, the C-HEAT/ARM at the C-terminus.

Extended Data Table 1 Cryo-EM data collection, model refinement, and validation statistics summary

Supplementary information

Supplementary Information

This file contains Supplementary Fig. 1 (the uncropped blots) and Supplementary Table 1, which shows the compilation of Nf1 domain X-ray structure models.

Reporting Summary

Supplementary Data 1

GAP assay data and statistical analysis. Original assay data measurements and analysis are described in the Methods, ‘GAP activity assays’ section.

Supplementary Video 1

Morphing video of Nf1 from closed to open state. The video shows the transition from the closed, auto-inhibited, inactive state of Nf1-23a to its open, active state. Content was created with Chimera X, edited in Microsoft Movie Maker.

Rights and permissions

Open Access This article is licensed under a Creative Commons Attribution 4.0 International License, which permits use, sharing, adaptation, distribution and reproduction in any medium or format, as long as you give appropriate credit to the

original author(s) and the source, provide a link to the Creative Commons license, and indicate if changes were made. The images or other third party material in this article are included in the article's Creative Commons license, unless indicated otherwise in a credit line to the material. If material is not included in the article's Creative Commons license and your intended use is not permitted by statutory regulation or exceeds the permitted use, you will need to obtain permission directly from the copyright holder. To view a copy of this license, visit <http://creativecommons.org/licenses/by/4.0/>.

Reprints and Permissions

About this article

Cite this article

Naschberger, A., Baradaran, R., Rupp, B. *et al.* The structure of neurofibromin isoform 2 reveals different functional states. *Nature* **599**, 315–319 (2021).
<https://doi.org/10.1038/s41586-021-04024-x>

- Received: 14 April 2021
- Accepted: 13 September 2021
- Published: 27 October 2021
- Issue Date: 11 November 2021
- DOI: <https://doi.org/10.1038/s41586-021-04024-x>

Share this article

Anyone you share the following link with will be able to read this content:

[Get shareable link](#)

Sorry, a shareable link is not currently available for this article.

[Copy to clipboard](#)

Provided by the Springer Nature SharedIt content-sharing initiative

| [Section menu](#) | [Main menu](#) |

- Article
- [Published: 27 October 2021](#)

Dispatched uses Na⁺ flux to power release of lipid-modified Hedgehog

- [Qianqian Wang](#) [ORCID: orcid.org/0000-0003-2498-9442](#)^{1 na1},
- [Daniel E. Asarnow](#) [ORCID: orcid.org/0000-0001-7870-5308](#)^{2 na1},
- [Ke Ding](#)¹,
- [Randall K. Mann](#) [ORCID: orcid.org/0000-0002-0590-9737](#)¹,
- [Jason Hatakeyama](#) [ORCID: orcid.org/0000-0001-8690-5107](#)¹,
- [Yunxiao Zhang](#) [ORCID: orcid.org/0000-0003-2145-4151](#)^{1 nAff6},
- [Yong Ma](#)^{3 nAff7},
- [Yifan Cheng](#) [ORCID: orcid.org/0000-0001-9535-0369](#)^{2,4} &
- [Philip A. Beachy](#) [ORCID: orcid.org/0000-0003-1098-9046](#)^{1,5}

[Nature](#) volume **599**, pages 320–324 (2021)

- 4424 Accesses
- 8 Altmetric
- [Metrics details](#)

Subjects

- [Cryoelectron microscopy](#)
- [Embryonic induction](#)
- [Morphogen signalling](#)
- [Permeation and transport](#)
- [Sodium](#)

Abstract

The Dispatched protein, which is related to the NPC1 and PTCH1 cholesterol transporters^{1,2} and to H⁺-driven transporters of the RND family^{3,4}, enables tissue-patterning activity of the lipid-modified Hedgehog protein by releasing it from tightly -localized sites of embryonic expression^{5,6,7,8,9,10}. Here we determine a cryo-electron microscopy structure of the mouse protein Dispatched homologue 1 (DISP1), revealing three Na⁺ ions coordinated within a channel that traverses its transmembrane domain. We find that the rate of Hedgehog export is dependent on the Na⁺ gradient across the plasma membrane. The transmembrane channel and Na⁺ binding are disrupted in DISP1-NNN, a variant with asparagine substitutions for three intramembrane aspartate residues that each coordinate and neutralize the charge of one of the three Na⁺ ions. DISP1-NNN and variants that disrupt single Na⁺ sites retain binding to, but are impaired in export of the lipid-modified Hedgehog protein to the SCUBE2 acceptor. Interaction of the amino-terminal signalling domain of the Sonic hedgehog protein (ShhN) with DISP1 occurs via an extensive buried surface area and contacts with an extended furin-cleaved DISP1 arm. Variability analysis reveals that ShhN binding is restricted to one extreme of a continuous series of DISP1 conformations. The bound and unbound DISP1 conformations display distinct Na⁺-site occupancies, which suggests a mechanism by which transmembrane Na⁺ flux may power extraction of the lipid-linked Hedgehog signal from the membrane. Na⁺-coordinating residues in DISP1 are conserved in PTCH1 and other metazoan RND family members, suggesting that Na⁺ flux powers their conformationally driven activities.

Access options

Subscribe to Journal

Get full journal access for 1 year

\$199.00

only \$3.90 per issue

[Subscribe](#)

All prices are NET prices.

VAT will be added later in the checkout.

Tax calculation will be finalised during checkout.

Rent or Buy article

Get time limited or full article access on ReadCube.

from \$8.99

[Rent or Buy](#)

All prices are NET prices.

Additional access options:

- [Log in](#)
- [Access through your institution](#)
- [Learn about institutional subscriptions](#)

Fig. 1: Structure and lipid binding sites of DISP1.

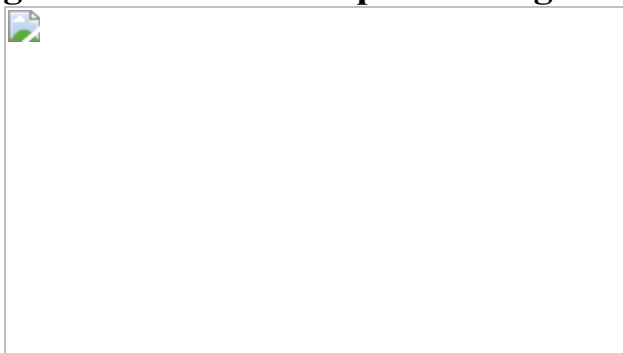


Fig. 2: Three Na⁺ densities in the transmembrane domain.



Fig. 3: A transmembrane Na^+ permeation channel is disrupted in the structure of DISP1-A-NNN.

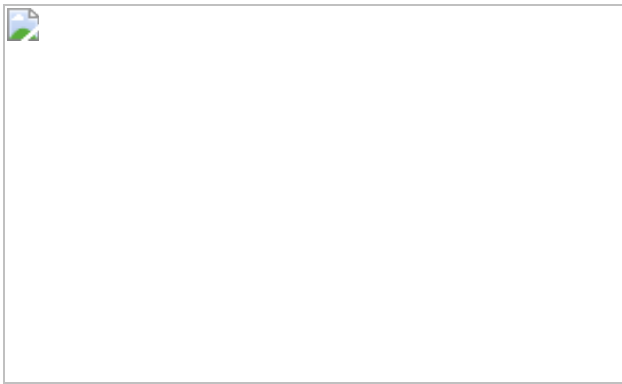


Fig. 4: DISP1-A binds ShhN between its distal ECDs.



Data availability

Coordinates for the DISP1-A R conformation, DISP1-A T conformation, DISP1-A-NNN, and ShhN–DISP1-A complex models reported in this paper have been deposited in the Protein Data Bank under accessions [7RPH](#), [7RP1](#), [7RPJ](#) and [7RPK](#), respectively. The maps of DISP1-A R conformation, DISP1-A T conformation, DISP1-A-NNN and ShhN–DISP1-A complex have been deposited in the Electron Microscopy Data Bank under accession codes [EMD-24614](#), [EMD-24615](#), [EMD-24616](#) and [EMD-24617](#), respectively. Further information and requests for data should be directed to the corresponding authors. PDB IDs of cited structures are provided either in the related figure legends or in the Methods.

References

1. 1.

Zhang, Y. et al. Structural basis for cholesterol transport-like activity of the Hedgehog receptor Patched. *Cell* **175**, 1352–1364.e14 (2018).

2. 2.

Carstea, E. D. et al. Niemann-Pick C1 disease gene: homology to mediators of cholesterol homeostasis. *Science* **277**, 228–231 (1997).

3. 3.

Nikaido, H. & Takatsuka, Y. Mechanisms of RND multidrug efflux pumps. *Biochim. Biophys. Acta* **1794**, 769–781 (2009).

4. 4.

Yamaguchi, A., Nakashima, R. & Sakurai, K. Structural basis of RND-type multidrug exporters. *Front. Microbiol.* **6**, 327 (2015).

5. 5.

Burke, R. et al. Dispatched, a novel sterol-sensing domain protein dedicated to the release of cholesterol-modified Hedgehog from signaling cells. *Cell* **99**, 803–815 (1999).

6. 6.

Ma, Y. et al. Hedgehog-mediated patterning of the mammalian embryo requires transporter-like function of Dispatched. *Cell* **111**, 63–75 (2002).

7. 7.

Kawakami, T. et al. Mouse dispatched mutants fail to distribute hedgehog proteins and are defective in hedgehog signaling. *Development* **129**, 5753–5765 (2002).

8. 8.

Roessler, E. et al. Truncating loss-of-function mutations of DISP1 contribute to holoprosencephaly-like microform features in humans. *Hum. Genet.* **125**, 393–400 (2009).

9. 9.

Caspary, T. et al. Mouse dispatched homolog1 is required for long-range, but not juxtacrine, Hh signaling. *Curr. Biol.* **12**, 1628–1632 (2002).

10. 10.

Nakano, Y. et al. Inactivation of dispatched 1 by the chameleon mutation disrupts Hedgehog signalling in the zebrafish embryo. *Dev. Biol.* **269**, 381–392 (2004).

11. 11.

Riddle, R. D., Johnson, R. L., Laufer, E. & Tabin, C. Sonic hedgehog mediates the polarizing activity of the ZPA. *Cell* **75**, 1401–1416 (1993).

12. 12.

Echelard, Y. et al. Sonic hedgehog, a member of a family of putative signaling molecules, is implicated in the regulation of CNS polarity. *Cell* **75**, 1417–1430 (1993).

13. 13.

Krauss, S., Concordet, J.-P. & Ingham, P. W. A functionally conserved homolog of the Drosophila segment polarity gene hh is expressed in tissues with polarizing activity in Zebrafish embryos. *Cell* **75**, 1431–1444 (1993).

14. 14.

Chiang, C. et al. Cyclopia and defective axial patterning in mice lacking Sonic hedgehog gene function. *Nature* **383**, 407–413 (1996).

15. 15.

Mann, R. K. & Beachy, P. A. Novel lipid modifications of secreted protein signals. *Annu. Rev. Biochem.* **73**, 891–923 (2004).

16. 16.

Porter, J. A., Young, K. E. & Beachy, P. A. Cholesterol modification of Hedgehog signaling proteins in animal development. *Science* **274**, 255–260 (1996).

17. 17.

Pepinsky, R. B. et al. Identification of a palmitic acid-modified form of human sonic Hedgehog. *J. Biol. Chem.* **273**, 14037–14045 (1998).

18. 18.

Chamoun, Z. et al. Skinny Hedgehog, an acyltransferase required for palmitoylation and activity of the Hedgehog signal. *Science* **293**, 2080–2085 (2001).

19. 19.

Woods, I. G. & Talbot, W. S. The you gene encodes an EGF-CUB protein essential for Hedgehog signaling in Zebrafish. *PLoS Biol.* **3**, e66 (2005).

20. 20.

Creanga, A. et al. Hedgehog signal in soluble form Scube/You activity mediates release of dually lipid-modified Hedgehog signal in soluble form. *Genes Dev.* **26**, 1312–1325 (2012).

21. 21.

Tukachinsky, H., Kuzmickas, R. P., Jao, C. Y., Liu, J. & Salic, A. Dispatched and Scube mediate the efficient secretion of the cholesterol-modified Hedgehog ligand. *Cell Rep.* **2**, 308–320 (2012).

22. 22.

Stewart, D. P. et al. Cleavage activates Dispatched for Sonic Hedgehog ligand release. *eLife* **7**, e31678 (2018).

23. 23.

Punjani, A. & Fleet, D. J. 3D variability analysis: resolving continuous flexibility and discrete heterogeneity from single particle cryo-EM. *J. Struct. Biol.* **213**, 107702 (2021).

24. 24.

Cannac, F. et al. Cryo-EM structure of the Hedgehog release protein Dispatched. *Sci. Adv.* **6**, eaay7928 (2020).

25. 25.

Chen, H., Liu, Y. & Li, X. Structure of human Dispatched-1 provides insights into Hedgehog ligand biogenesis. *Life Sci. Alliance* **3**, e202000776 (2020).

26. 26.

Zheng, H. et al. CheckMyMetal: a macromolecular metal-binding validation tool. *Acta Crystallogr. D* **73**, 223–233 (2017).

27. 27.

Myers, B. R., Neahring, L., Zhang, Y. & Roberts, K. J. Rapid, direct activity assays for Smoothened reveal Hedgehog pathway regulation by membrane cholesterol and extracellular sodium. *Proc. Natl Acad. Sci. USA* **114**, E11141–E11150 (2017).

28. 28.

Petrov, K., Wierbowski, B. M., Liu, J. & Salic, A. Distinct cation gradients power cholesterol transport at different key points in the Hedgehog signaling pathway. *Dev. Cell* **55**, 314–327.e7 (2020).

29. 29.

Chovancova, E. et al. CAVER 3.0: a tool for the analysis of transport pathways in dynamic protein structures. *PLoS Comput. Biol.* **8**, e1002708 (2012).

30. 30.

Hall, T. M. T., Porter, J. A., Beachy, P. A. & Leahy, D. J. A potential catalytic site revealed by the 1.7-Å crystal structure of the amino-terminal signalling domain of Sonic hedgehog. *Nature* **378**, 212–216 (1995).

31. 31.

McLellan, J. S. et al. The mode of Hedgehog binding to Ihog homologues is not conserved across different phyla. *Nature* **455**, 979–983 (2008).

32. 32.

Zhulyn, O., Nieuwenhuis, E., Liu, C. Y., Angers, S. & Hui, C. Ptch2 shares overlapping functions with Ptch1 in Smo regulation and limb development. *Dev. Biol.* **397**, 191–202 (2015).

33. 33.

Deshpande, I. et al. Smoothed stimulation by membrane sterols drives Hedgehog pathway activity. *Nature* **571**, 284–288 (2019).

34. 34.

Qi, X. et al. Cryo-EM structure of oxysterol-bound human Smoothed coupled to a heterotrimeric Gi. *Nature* **571**, 279–283 (2019).

35. 35.

Qi, C., et al Structural basis of sterol recognition by human hedgehog receptor PTCH1. *Sci. Adv.* **5**, eaaw6490 (2019).

36. 36.

Whalen, D. M., Malinauskas, T., Gilbert, R. J. C. & Siebold, C. Structural insights into proteoglycan-shaped Hedgehog signaling. *Proc. Natl Acad. Sci. USA* **110**, 16420–16425 (2013).

37. 37.

Mastronarde, D. N. Automated electron microscope tomography using robust prediction of specimen movements. *J. Struct. Biol.* **152**, 36–51 (2005).

38. 38.

Zheng, S. Q. et al. MotionCor2: anisotropic correction of beam-induced motion for improved cryo-electron microscopy. *Nat. Methods* **14**, 331–332 (2017).

39. 39.

Punjani, A., Rubinstein, J. L., Fleet, D. J. & Brubaker, M. A. cryoSPARC: algorithms for rapid unsupervised cryo-EM structure determination. *Nat. Methods* **14**, 290–296 (2017).

40. 40.

Zivanov, J. et al. New tools for automated high-resolution cryo-EM structure determination in RELION-3. *eLife* **7**, e42166 (2018).

41. 41.

Asarnow, D., Palovcak, E. & Cheng, Y.
<https://doi.org/10.5281/zenodo.3576630> (2019).

42. 42.

Dang, S. et al. Cryo-EM structures of the TMEM16A calcium-activated chloride channel. *Nature* **552**, 426–429 (2017).

43. 43.

Emsley, P., Lohkamp, B., Scott, W. G. & Cowtan, K. Features and development of Coot. *Acta Crystallogr. D* **D66**, 486–501 (2010).

44. 44.

Adams, P. D. et al. PHENIX: a comprehensive Python-based system for macromolecular structure solution. *Acta Crystallogr. D* **D66**, 213–221 (2010).

45. 45.

Croll, T. I. ISOLDE: a physically realistic environment for model building into low-resolution electron-density maps. *Acta Crystallogr. D* **D74**, 519–530 (2018).

46. 46.

Kelley, L. A., Mezulis, S., Yates, C. M., Wass, M. N. & Sternberg, M. J. E. The Phyre2 web portal for protein modelling, prediction and analysis. *Nat. Protoc.* **10**, 845–858 (2015).

47. 47.

Berman, H., Henrick, K. & Nakamura, H. Announcing the worldwide Protein Data Bank. *Nat. Struct. Biol.* **10**, 980 (2003).

48. 48.

Pettersen, E. F. et al. UCSF Chimera—A visualization system for exploratory research and analysis. *J. Comput. Chem.* **25**, 1605–1612 (2004).

49. 49.

Goddard, T. D. et al. UCSF ChimeraX: meeting modern challenges in visualization and analysis. *Protein Sci.* **27**, 14–25 (2018).

50. 50.

Krissinel, E. & Henrick, K. Inference of macromolecular assemblies from crystalline state. *J. Mol. Biol.* **372**, 774–797 (2007).

51. 51.

Sievers, F. et al. Fast, scalable generation of high-quality protein multiple sequence alignments using Clustal Omega. *Mol. Syst. Biol.* **7**, 539 (2011).

52. 52.

Robert, X. & Gouet, P. Deciphering key features in protein structures with the new ENDscript server. *Nucleic Acids Res.* **42**, W320–W324 (2014).

53. 53.

Goodrich, L. V., Milenkovic, L., Higgins, K. M. & Scott, M. P. Altered neural cell fates and medulloblastoma in mouse patched mutants. *Science* **277**, 1109–1113 (1997).

54. 54.

Zhang, X. M., Ramalho-santos, M. & McMahon, A. P. Smoothened mutants reveal redundant roles for Shh and Ihh signaling including regulation of L/R asymmetry by the mouse node. *Cell* **105**, 781–792 (2001).

55. 55.

Zhang, Y. et al. Hedgehog pathway activation through nanobody-mediated conformational blockade of the Patched sterol conduit. *Proc. Natl Acad. Sci. USA* **117**, 28838–28846 (2020).

56. 56.

McLellan, J. S. et al. Structure of a heparin-dependent complex of Hedgehog and Ihog. *Proc. Natl Acad. Sci. USA* **103**, 17208–17213 (2006).

57. 57.

Qi, X., Hassan, A., Liang, Q., Brabander, J. K. D. & Li, X. Structural basis for itraconazole-mediated NPC1 inhibition. *Nat. Commun.* **11**, 152 (2020).

58. 58.

Wang, X. et al. TPC proteins are phosphoinositide-activated sodium-selective ion channels in endosomes and lysosomes. *Cell* **151**, 372–383 (2012).

59. 59.

Altmann, S. W. et al. Niemann-Pick C1 like 1 protein is critical for intestinal cholesterol absorption. *Science* **303**, 1201–1204 (2004).

60. 60. Chaudhry, A. et al. Phenotypic spectrum associated with PTCHD1 deletions and truncating mutations includes intellectual disability and autism spectrum disorder. *Clin. Genet.* **88**, 224–233 (2015).
61. 61. Fan, J. et al. Male germ cell-specific expression of a novel Patched-domain containing gene Ptchd3. *Biochem. Biophys. Res. Commun.* **363**, 757–761 (2007).
62. 62. Chung, J. H., Larsen, A. R., Chen, E. & Bunz, F. A PTCH1 homolog transcriptionally activated by p53 suppresses Hedgehog signaling. *J. Biol. Chem.* **289**, 33020–33031 (2014).
63. 63. Seeger, M. A. et al. Structural asymmetry of AcrB trimer suggests a peristaltic pump mechanism. *Science* **313**, 1295–1298 (2006).
64. 64. Sennhauser, G., Bukowska, M. A., Briand, C. & Grütter, M. G. Crystal structure of the multidrug exporter MexB from *Pseudomonas aeruginosa*. *J. Mol. Biol.* **389**, 134–145 (2009).
65. 65. Su, C. et al. Structures and transport dynamics of a *Campylobacter jejuni* multidrug efflux pump. *Nat. Commun.* **8**, 171 (2017).
66. 66. Su, C. et al. Cryo-electron microscopy structure of an *Acinetobacter baumannii* multidrug efflux pump. *mBio* **10**, e01295-19 (2019).

67. 67.

Su, C. et al. Crystal structure of the CusBA heavy-metal efflux complex of *Escherichia coli*. *Nature* **470**, 558–562 (2011).

68. 68.

Su, C. et al. MmpL3 is a lipid transporter that binds trehalose monomycolate and phosphatidylethanolamine. *Proc. Natl Acad. Sci. USA* **116**, 11241–11246 (2019).

69. 69.

Kumar, N., Su, C., Chou, T., Radhakrishnan, A. & Delmar, J. A. Crystal structures of the *Burkholderia multivorans* hopanoid transporter HpN. *Proc. Natl Acad. Sci. USA* **114**, 6557–6562 (2017).

70. 70.

Tsukazaki, T. et al. Structure and function of a membrane component SecDF that enhances protein export. *Nature* **474**, 235–238 (2011).

71. 71.

Ishii, E. et al. Nascent chain-monitored remodeling of the Sec machinery for salinity adaptation of marine bacteria. *Proc. Natl Acad. Sci. USA* **112**, E5513-E5522 (2015).

Acknowledgements

We thank K. Roberts and A. Kershner for technical assistance and advice, and V. Korkhov and X. Li for sharing data and information prior to publication. Y.C. is an investigator of the Howard Hughes Medical Institute. Supported by NIH grants R01GM102498, Stanford Department of Urology, and Ludwig Cancer Institute (to P.A.B.) and R35GM140847, S10OD020054 and S10OD021741 (to Y.C.).

Author information

Author notes

1. Yunxiao Zhang

Present address: Howard Hughes Medical Institute, Neuroscience Department, The Scripps Research Institute, La Jolla, CA, USA

2. Yong Ma

Present address: Suzhou Institute of Biomedical Engineering and Technology, Chinese Academy of Sciences, Suzhou, China

3. These authors contributed equally: Qianqian Wang and Daniel E. Asarnow

Affiliations

1. Institute for Stem Cell Biology and Regenerative Medicine, Stanford University School of Medicine, Stanford, CA, USA

Qianqian Wang, Ke Ding, Randall K. Mann, Jason Hatakeyama, Yunxiao Zhang & Philip A. Beachy

2. Department of Biochemistry and Biophysics, University of California, San Francisco, CA, USA

Daniel E. Asarnow & Yifan Cheng

3. Department of Molecular Biology and Genetics, Johns Hopkins University School of Medicine, Baltimore, MD, USA

Yong Ma

4. Howard Hughes Medical Institute, University of California, San Francisco, CA, USA

Yifan Cheng

5. Departments of Urology, and Developmental Biology, Stanford University School of Medicine, Stanford, CA, USA

Philip A. Beachy

Contributions

Q.W. purified and characterized DISP1-A, DISP1-A-NNN and ShhN–DISP1-A complex and SCUBE2 protein, and developed and performed ShhNp binding and release assays. D.E.A. prepared cryo-EM grids, collected and processed cryo-EM data, and performed the 3DVA. R.M. devised and aided in the SCUBE2 purification. J.H. performed ShhNp release assays. K.D., D.E.A., Y.Z. and Q.W. built the models. Y.M. provided mouse genetic epistasis analysis while in the laboratory of P.A.B. at Johns Hopkins University School of Medicine. All authors participated in discussion and analysis of the data. P.A.B., Q.W., D.E.A., K.D., Y.C. and Y.Z. prepared the manuscript.

Corresponding authors

Correspondence to [Yifan Cheng](#) or [Philip A. Beachy](#).

Ethics declarations

Competing interests

The authors declare no competing interests.

Additional information

Peer review information *Nature* thanks Philip Ingham, Poul Nissen and the other, anonymous, reviewer(s) for their contribution to the peer review of this work.

Publisher's note Springer Nature remains neutral with regard to jurisdictional claims in published maps and institutional affiliations.

Extended data figures and tables

Extended Data Fig. 1 Structurally related transporters Dispatched and Patched in Hedgehog signalling.

a, b, Opposing functions of Dispatched and Patched in Hedgehog signalling. **a**, The HH protein signal, covalently modified by cholesterol and palmitate, requires the action of DISP1 and SCUBE for release from the membrane of producing cells. HH then uses its palmitoyl adduct to clog the sterol transport conduit and block the function of its receptor PTCH1 in responding cells. The loss of PTCH1 sterol transport activity permits accumulation of cholesterol within the inner leaflet to levels that activate SMO by binding within its seven transmembrane helix bundle, resulting in activation of the GLI transcriptional effector of Hedgehog signalling. **b**, As *Ptch1* is a target for GLI activation, the X-Gal staining of a *Ptch1*^{LacZ} knock-in allele⁵³ provides an indication of Hedgehog pathway activity (leftmost embryo). Homozygous mutation of *Disp1*^{6,7,8,9,10} causes a loss of nearly all embryonic Hedgehog pathway activity (2nd embryo from left)⁵⁴, whereas homozygous disruption of *Ptch1* leads to unregulated ectopic pathway activity, regardless of the functional status of *Disp1* (rightmost two embryos)⁵³. **c–f**, Truncated DISP1 protein. As murine full-length DISP1 protein was poorly expressed in HEK293 cells, we tested a variety of constructs, and ultimately settled on an N-terminal truncation. Although its export activity was partially reduced, truncated DISP1-A protein nevertheless mediated efficient release of ShhNp (autoprocessed, lipid-modified Shh protein) into cell culture medium containing SCUBE2 (mouse SCUBE2, lacking amino acids 30–281) upon transfection into *Disp*^{-/-} mouse embryonic fibroblasts^{6,20} (MEFs), indicating preservation of its function. **c**, DISP1-mEGFP and DISP1-A-mEGFP in HEK293T cells with magnified insets showing expression on the cell membrane. **d**, Western blot showing high level of DISP1-A expression relative to DISP1 (both proteins were SBP and HA-tagged at the C-terminus). **e**, Functional assay ([Methods](#), ShhNp release endpoint assay) in *Disp*^{-/-} MEFs. Culture media and cell

lysates from transiently transfected *Disp*^{-/-} MEFs were probed by immunoblotting for expression of DISP-mEGFP (SBP, HA and mEGFP tagged at the C-terminus, see panel **c**), ShhNp, and SCUBE2. DISP1 and DISP1-A both released ShhNp in the presence of SCUBE2. β-ACTIN, loading control. **f**, Size exclusion chromatography of purified DISP1-A, together with the SDS-PAGE of the indicated fraction, corresponding to monomeric DISP1-A. Panels **c–f**, show representative results ($n = 4$ biologically independent replicates). **g**, Structural comparison between DISP1-A and mouse PTCH1⁵⁵ (PDB ID: 7K65). The ECDs, closely apposed in PTCH1 to form a conduit for sterol transport, in DISP1-A are splayed apart. Conserved ferredoxin-like $\alpha + \beta$ open-faced sandwich folds are highlighted (lime for ECD1 and pink for ECD2). Magnified views in spectral sequence from N to C termini of the $\alpha + \beta$ open-faced sandwich folds in DISP1-A ECD1 (bottom left) and ECD2 (bottom right). Distal structures inserted into the peripheral loops of the ferredoxin-like folds are structurally unrelated to each other or to distal PTCH1 ECD structures. Red symbols indicate the five N-linked glycosylation sites, three in ECD1 (N362, N390 and N475) and two in ECD2 (N834 and N915), which can be inferred from additional densities that extend from N-X-S/T sequences in the extracellular loops. Panels **d, e, f**, see Supplementary Fig. 1 for gel source data.

[Extended Data Fig. 2 Dispatched protein sequence alignment and structural features.](#)

Sequence alignment of Dispatched proteins from *Mus musculus* (mouse), *Homo sapiens* (human), *Danio rerio* (zebrafish) and *Drosophila melanogaster* (fruit fly). Secondary structure elements and other features are indicated above the sequence, with subdomains coloured according to Fig. 1a. Protein sequences were aligned using Clustal Omega⁵¹ and the ESPript server⁵². TM, transmembrane helix.

[Extended Data Fig. 3 Cryo-EM data and image processing flow for DISP1-A and DISP1-A-NNN.](#)

a, A representative cryo-EM micrograph ($n = 4487$ for DISP1-A, $n = 4467$ for DISP1-A-NNN) and several highly-populated, reference-free 2D class averages are shown for DISP1-A (left) and DISP1-A-NNN (right). The micrograph for DISP1-A-NNN has been contrast-stretched for display in order to account for the presence of a gold edge in the upper left corner of the image (the DISP1-A-NNN particle distribution on this grid necessitated targeting of the gold edge). **b**, Schematic flow-chart representing the image processing approach for DISP1-A. Thumbnail images of each 3D class or refinement are shown along with global GS-FSC resolution in black, particle counts in red, and dashed black boxes to indicate selected 3D classes. After separation of the R and T conformations in the first round of 3D classification, the identical processing flows for the two conformations are shown in parallel. Cryo-EM map (Red box) and atomic model of R conformation are used in main figures to present DISP1-A features. Subclasses of R and T conformations, R_1 , R_2 , T_1 and T_3 , are labeled.

Extended Data Fig. 4 Cryo-EM density and atomic model quality.

Fourier shell correlation curves (**a**), particle orientation distributions (**b**), and local resolution maps (**c, d**) are shown for R and T conformations of DISP1-A, DISP1-A-NNN, and for ShhN–DISP1-A complex. The ‘gold-standard’ independent half-map FSC curves and orientation distributions were determined during refinement in cryoSPARC, map-to-model FSC curves were calculated in PHENIX using protein chains only, and directional FSC curves were estimated as in ref. ⁴². The orientation distributions are plotted such that an elevation angle of 0° corresponds to a ‘side-view’ perpendicular to the transmembrane helices; in each case the predominant views are ‘side-views’ at a wide range of azimuthal angles. Local resolution estimates were computed using the BLOCRES algorithm as implemented in cryoSPARC.

Extended Data Fig. 5 Coincident modes of DISP1 conformational flexibility revealed by 3D classification and 3D variability analysis (3DVA).

a, Overlay comparing front view of R and T conformations (khaki and salmon, respectively) from 3D classification. Major conformational changes are localized to the extracellular domains. **b**, Cut-away view showing the formation of a ‘kink’ in the back-side linker of the T conformation, with an accompanying shift of about one helix turn that breaks a hydrogen bond between linker residue H777 and the backbone carbonyl of K767. **c**, Extracellular view of the R and T conformations, highlighting the movement of secondary structure elements in ECD1 ($> 5 \text{ \AA}$) and ECD2 ($\sim 2 \text{ \AA}$). The shift of ECD1 and the formation of the inter-ECD linker ‘kink’ appear intimately related. Numbers indicate distances (\AA) between the Ca of F772 in R and T (marked by \blacktriangle in **b**) and R382 and S898 (marked by \bullet and \circ , respectively, in **c**). **d**, Comparison of the most extreme R and T conformations from 3D classification (right) and the two extreme ends of PC2, PC2+ (R-like) and PC2- (T-like), from 3DVA left) shows that a nearly identical mode of motion is captured by both techniques. **e**, Distributions of DISP1-A particles stratified by their 3D class along the PC2 axis of 3DVA, demonstrating colinearity between the 3DVA trajectory and the 3D subclasses ordered by apparent conformation. T_1 and T_3 , and R_1 and R_2 , respectively, are subclasses of T and R conformations resolved by 3D classification (Extended Data Fig. 3).

Extended Data Fig. 6 Representative cryo-EM densities from selected structural features.

a–d, Representative cryo-EM densities from 3D reconstruction of DISP1-A, conformation R. **a**, Densities of all transmembrane helices. **b**, Representative densities of beta-sheets from ECD1 and ECD2. **c**, Cryo-EM densities of three representative disulfide bonds. **d**, Cryo-EM densities of five representative CHS molecules. **e**, Representative cryo-EM densities in ShhN from 3D reconstruction of ShhN–DISP1-A complex. **f**, **g**, Representation of surface hydrophobicity, viewed from top (**f**, left) or a top-front position of DISP1-A (**g**, left). Close-up views of hydrophobic cavities in both ECD1 (**f**, right) and ECD2 (**g**, right). A hydrophobic track beginning near the front-side lifted sterol (cyan) extends outward from the membrane (dotted shape). The enclosed hydrophobic conduit employed by the PTCH1 protein for sterol movement away from the membrane is formed by the juxtaposition of ECD1 and ECD2. In DISP1, although ECD1 and ECD2 are

split apart in a manner that would bisect this conduit, the ECD2 portion retains a series of hydrophobic residues that line its inner surface, which could perhaps form a partial hydrophobic conduit to the hydrophobic cavities near the distal tips of ECD1 and ECD2, analogous to the sterol conduit within the center of the conjoined ECDs of PTCH1.

Extended Data Fig. 7 Na⁺-coordinating amino acid residues in DISP1, and conformational rearrangements within the transmembrane Na⁺ pathway in DISP1-A-NNN.

a, b, Side (**a**) and extracellular (**b**) views of three Na⁺ ion binding sites within the transmembrane domain, each labeled with its associated charge-neutralizing intra-membrane Asp. **c**, Residues in DISP1 with carbonyl oxygens or side-chain residues that coordinate Na⁺ and carboxylate residues that neutralize Na⁺ charge are conserved in PTCH1 (see also Extended Data Fig. 11). **d**, Solvent excluded surfaces (1.4 Å probe radius) reveal transmembrane cavities within DISP1-A (left) that are altered in DISP1-A-NNN (right). Two extracellular branches (upper insets) that provide access to the central channel can be individually opened or closed depending on alternate conformations of M557 ('A' and 'B' in DISP1-A) and alternate conformations of L1035 ('A' and 'B' in DISP1-A-NNN). Significant rearrangements also take place around a mid-membrane water-filled cavity containing the three ion coordination sites (lower insets). In DISP1-A, short kinks in TM4 and TM10 position I568 above this cavity. In DISP1-A-NNN, however, TM4 and TM10 straighten, rotating I568 and D571N and D1049N into this cavity, dramatically reducing its volume and isolating the channel from its intracellular exit (see [Supplementary Discussion](#)).

Extended Data Fig. 8 Quantitative luciferase-based assay of ShhNp release.

a, Inserting Nanoluciferase coding sequence between E131 and D132 of Shh does not affect Shh autoprocessing and associated lipid modification. Immunoblotting of ShhNp detects both precursor and processed forms of the protein. Most of the expressed nanoluciferase-inserted Shh is in the

processed form. **b**, Coomassie blue staining of purified SCUBE2 (Δ 30-281) protein. **c**, Composition of buffers used in this study (see Fig. [2b,c](#)). **d**, Time course of NanoLuc-ShhNp release at different Na^+ concentrations (see panel **c**) with or without SCUBE2 (Δ 30-281, 1 μM). One representative set of normalized data (see [Methods](#)) with linear regression (dashed lines) is shown for each condition ($n = 4$ biologically independent experiments). The release rate determined as the slope of the linear regression line is presented in Fig. [2b](#). **e**, Western blot-based ShhNp release assay ([Methods](#), ShhNp release endpoint assay). Culture media and cell lysates from transiently transfected Disp-/- MEFs were probed by immunoblotting for DISP-HA (SBP and HA-tagged at the C-terminus), ShhNp, and SCUBE2. β -ACTIN, loading control. **f**, DISP-ShhNp binding assay using HEK293 with stably integrated constructs for doxycycline-inducible expression of full-length Shh²⁰. DISP1-A variants tagged with SBP and HA at the C-terminus (DISP-HA) were immunoprecipitated with Streptavidin resin, and ShhNp detected by Western blot. Alterations in ion site residues as follows: DISP1-A-NNN, D571N/D572N/D1049N; DISP1-A-VVVVVA, T613V/T614V/T1087V/T1088V/T610V/S611A; Site I (NVV), D1049N/T613V/T614V; Site II (NVV), D571N/T1087V/T1088V; Site III (NVA), D572N/T610V/S611A; Site I (LVV), D1049L/T613V/T614V; Site II (LVV), D571L/T1087V/T1088V; Site III (LVA), D572L/T610V/S611A. Panels **a**, **b**, **e**, **f**, show representative results ($n = 3$ biologically independent replicates, see Supplementary Fig. [1](#) for gel source data).

[Extended Data Fig. 9 Cryo-EM data and image processing flow for ShhN–DISP1-A complex, and comparison to *Drosophila* HhNDisp complex.](#)

a, A representative cryo-EM micrograph ($n = 1687$) and highly populated reference-free 2D class averages for ShhN–DISP1-A. **b**, Schematic flow-chart illustrating the image processing used for ShhN–DISP1-A data. Thumbnail images are shown for reference-based 3D classes and high resolution refinements. Dashed black boxes indicate 3D classes selected for the next processing step, with class particle counts in red and refinement GS-FSC resolutions in black. The label, ‘3D classification with references’ indicates that explicit ‘apo’ and ‘complex’ references were used to seed the

classification. **c**, Left, the cryo-EM density from our ShhN–DISP1-A complex (transparent grey), overlaid on a ribbon diagram of ShhN (goldenrod). Right, cryo-EM density from the *Drosophila* HhNDisp complex in Cannac et al²⁴ (transparent grey, EMD: 10464), overlaid on the ribbon diagram of HhN (orchid, model extracted from PDB ID: 6TD6). Middle, superimposition of the ShhN–DISP1-A and HhNDisp complex models reported here and in Cannac et al²⁴, with mouse DISP1-A and ShhN in khaki and goldenrod, and *Drosophila* Disp and HhN in pink and orchid. The model of *Drosophila* HhN was based on docking of a *Drosophila* HhN structure⁵⁶ within a 4.8 Å density map. Relative to *Drosophila* HhN, murine ShhN is translated upwards, away from the membrane, and rotated towards the right. Asterisks indicate corresponding positions near the N termini of ShhN and HhN proteins. This difference is somewhat puzzling in light of the ability of mammalian DISP1 to rescue *Drosophila* disp mutant function⁶, and we cannot definitively account for it. One functional difference is that mammalian DISP1 cooperates with SCUBE2 for its Hedgehog-releasing activity, whereas *Drosophila* lacks a Scube orthologue. The ECD domain split and the Hedgehog interaction with the furin-cleaved linker arm together help explain the requirement for furin cleavage²² in DISP1 function.

Extended Data Fig. 10 Conformational dynamics link intramembrane Na⁺ site occupancy to Hedgehog release.

a, Three-dimensional variability analysis (3DVA) of the ShhN–DISP1-A complex dataset reveals a conformational series with ShhN bound or absent at opposite ends of the first principal component (PC1). Front (first line) and top (second line) views of reconstructed densities from the extremes of PC1 (unbound, khaki; bound, salmon) are shown, with a superimposed view of these extremes in the centre. The overall changes in ECD position are illustrated by lines drawn atop the reconstructed densities and by schematized diagrams to the left. Reconstructed densities at the Na⁺ coordination sites in the transmembrane domain indicate that these sites change from fully occupied in the unbound state to site I only occupied in the bound state. See also Supplementary Video 4. **b**, 3DVA analysis of the

apoprotein preparation shows a similar conformational series along PC1, along with similar shifts in Na⁺ site occupancy.

Extended Data Fig. 11 Na⁺ ion utilization by DISP1, PTCH1, and other members of the RND transporter family.

a, Close-up views of Na⁺ ion sites I, II, and III in DISP1, showing the locations of liganding oxygens from amino acid side chains and main-chain carbonyls (see main text), and of the corresponding locations in PTCH1³⁵ (PDB ID: 6RMG), based on structural alignment of the two proteins. Note the presence in both proteins of a charge-neutralizing acidic residue at each site, and the conservation of side-chain oxygens as ligands. **b**, Structural alignment, using Chimera Matchmaker, of RND family members, including DISP1, PTCH1, NPC1, and several prokaryotic RND transporters. **c**, Tabulated conservation of charge-neutralizing residues (3 total) or oxygen ligands from amino acid side-chains (10 total) in the indicated proteins, aligned from structure (**b**, see PDB IDs from the second right column) or, if possible without ambiguity, aligned from sequence. References to specific sequences, structures, or background information are given within the table, including refs [1](#),[2](#),[6](#),[24](#),[27](#),[32](#),[35](#),[57](#),[58](#),[59](#),[60](#),[61](#),[62](#),[63](#),[64](#),[65](#),[66](#),[67](#),[68](#),[69](#),[70](#),[71](#). Note the close conservation of Na⁺-liganding side-chains and charge-neutralizing residues in PTCH1, known to require Na⁺ for its activity, and in Disp from *Drosophila melanogaster*. The prokaryotic Na⁺-utilizing SecD1/SecF1 peptide translocator from *Vibrio alginolyticus* (encoded as two peptides; aligned by homology to *Thermus thermophilus* SecDF), in contrast, appears to have evolved a distinct mode of Na⁺ interaction. See [Supplementary Discussion](#). Abbreviations: Mmus, *Mus musculus*; Dmel, *Drosophila melanogaster*; Hsap, *Homo sapiens*; Ecol, *Escherichia coli*; Paer, *Pseudomonas aeruginosa*; Cjej, *Campylobacter jejuni*; Abau, *Acinetobacter baumannii*; Msme, *Mycobacterium smegmatis*; Bmul, *Burkholderia multivorans*; Tthe2, *Thermus thermophilus*; Valg, *Vibrio alginolyticus*.

Extended Data Table 1 Cryo-EM data collection, refinement and validation statistics

Supplementary information

Supplementary Information

This file contains Supplementary Discussion, Supplementary Fig. 1, and legends of Supplementary Videos 1–4.

Reporting Summary

Supplementary Video 1

Conformational dynamics associated with R–T transition (PC2). The structural changes associated with the transition between DISP1-A R and T subclasses are visualized using PC2 of 3DVA in cryoSPARC. The inset histogram of PC scores (*x*-axis) for normalized number of particles (*y*-axis) assigned to R₁, R₂ or T₁, T₃ shows the quantitative relationship between this variance component and the standard 3D classification of particles presented in Extended Data Fig. 5.

Supplementary Video 2

Overview of the 28 lipids or detergent molecules associated with DISP1-A. A movie displaying DISP1-A (pale ribbon) with 26 CHS (blue or cyan) and 2 LMNG molecules (magenta) resolved in the structure. The front lifted CHS is coloured cyan (see text).

Supplementary Video 3

Identification of a Na⁺ permeation channel in DISP1-A. Using the CAVER 3 PyMOL plugin with a probe of radius 1.0 Å, we identified a continuous pathway through the transmembrane domain of DISP1-A (blue surface). This channel is occupied by resolved water molecules (red spheres), and provides access to the transmembrane cavity that contains the Na⁺ ions and water. Finally, inspection of the exterior solvent-excluded surface of DISP1-A, computed with 1.4 Å probe radius in ChimeraX and shown in khaki,

shows the extra- and intracellular openings through which water (and Na⁺) may pass through the transmembrane domain.

Supplementary Video 4

DISP1 protein conformation and Hedgehog binding/release are linked to Na⁺ site occupancy. Animation of PC1 identified by 3DVA of ShhN–DISP1-A cryo-EM data. In synchronization, the left shows a wide-angle view from the front of DISP1 (khaki), with bound ShhN (goldenrod) appearing in coordination with tensing of DISP1 ECDs. The centre view highlights at a lower density threshold the DISP1 residues preceding the furin site, which form a one-armed embrace of ShhN upon binding (hot pink). At right, a tilted, cut-away top view illustrating loss of density in Na⁺ sites II & III, again coincident with bound ShhN.

Rights and permissions

Reprints and Permissions

About this article

Cite this article

Wang, Q., Asarnow, D.E., Ding, K. *et al.* Dispatched uses Na⁺ flux to power release of lipid-modified Hedgehog. *Nature* **599**, 320–324 (2021). <https://doi.org/10.1038/s41586-021-03996-0>

- Received: 06 May 2020
- Accepted: 06 September 2021
- Published: 27 October 2021
- Issue Date: 11 November 2021
- DOI: <https://doi.org/10.1038/s41586-021-03996-0>

Share this article

Anyone you share the following link with will be able to read this content:

[Get shareable link](#)

Sorry, a shareable link is not currently available for this article.

[Copy to clipboard](#)

Provided by the Springer Nature SharedIt content-sharing initiative

This article was downloaded by **calibre** from <https://www.nature.com/articles/s41586-021-03996-0>

| [Section menu](#) | [Main menu](#) |

- Article
- [Published: 22 September 2021](#)

Kainate receptor modulation by NETO2

- [Lingli He^{1,2,3} na1](#),
- [Jiahui Sun^{4,5} na1](#),
- [Yiwei Gao](#) [ORCID: orcid.org/0000-0001-8169-9332](#)^{1,3} na1,
- [Bin Li^{1,3}](#),
- [Yuhang Wang^{1,3}](#),
- [Yanli Dong](#) [ORCID: orcid.org/0000-0002-7919-3276](#)^{1,2,3},
- [Weidong An^{1,3}](#),
- [Hang Li^{1,3}](#),
- [Bei Yang^{1,2,3}](#),
- [Yuhan Ge^{4,5}](#),
- [Xuejun Cai Zhang](#) [ORCID: orcid.org/0000-0001-6726-3698](#)^{1,3},
- [Yun Stone Shi](#) [ORCID: orcid.org/0000-0002-8842-9818](#)^{4,5,6,7} &
- [Yan Zhao](#) [ORCID: orcid.org/0000-0002-4348-256X](#)^{1,2,3}

[Nature](#) volume 599, pages 325–329 (2021)

- 3909 Accesses
- 1 Citations
- 30 Altmetric
- [Metrics details](#)

Subjects

- [Cryoelectron microscopy](#)
- [Neurological disorders](#)
- [Neurotransmitters](#)

This article has been [updated](#)

Abstract

Glutamate-gated kainate receptors are ubiquitous in the central nervous system of vertebrates, mediate synaptic transmission at the postsynapse and modulate transmitter release at the presynapse^{1,2,3,4,5,6,7}. In the brain, the trafficking, gating kinetics and pharmacology of kainate receptors are tightly regulated by neuropilin and tolloid-like (NETO) proteins^{8,9,10,11}. Here we report cryo-electron microscopy structures of homotetrameric GluK2 in complex with NETO2 at inhibited and desensitized states, illustrating variable stoichiometry of GluK2–NETO2 complexes, with one or two NETO2 subunits associating with GluK2. We find that NETO2 accesses only two broad faces of kainate receptors, intermolecularly crosslinking the lower lobe of ATD^{A/C}, the upper lobe of LBD^{B/D} and the lower lobe of LBD^{A/C}, illustrating how NETO2 regulates receptor-gating kinetics. The transmembrane helix of NETO2 is positioned proximal to the selectivity filter and competes with the amphiphilic H1 helix after M4 for interaction with an intracellular cap domain formed by the M1–M2 linkers of the receptor, revealing how rectification is regulated by NETO2.

Access options

Subscribe to Journal

Get full journal access for 1 year

\$199.00

only \$3.90 per issue

Subscribe

All prices are NET prices.

VAT will be added later in the checkout.

Tax calculation will be finalised during checkout.

Rent or Buy article

Get time limited or full article access on ReadCube.

from \$8.99

Rent or Buy

All prices are NET prices.

Additional access options:

- [Log in](#)
- [Access through your institution](#)
- [Learn about institutional subscriptions](#)

Fig. 1: Architectures of the GluK2–NETO2 complexes.



Fig. 2: Extracellular interactions between GluK2 and NETO2.

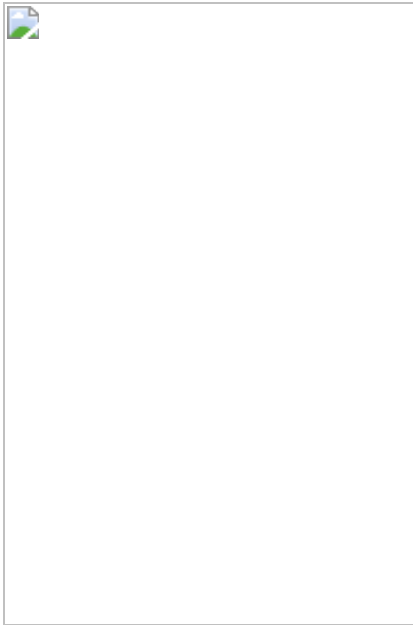
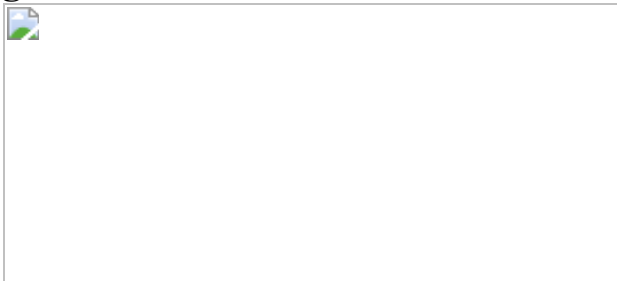


Fig. 3: Ion conduction pore of GluK2 and the modulation mechanism of inward rectification.



Fig. 4: Architecture of the desensitized GluK2–NETO2 complex.



Data availability

The 3D cryo-EM density maps of the antagonist DNQX-bound GluK2-1 \times NETO2, LBD-TMD of the GluK2-1 \times NETO2, GluK2-2 \times NETO2, GluK2-1 \times NETO2^{asymLBD} complex and the agonist kainate-bound desensitized GluK2-1 \times NETO2^{des} complex have been deposited in the Electron Microscopy Database under the accession codes [EMD-31462](#), [EMD-31464](#), [EMD-31463](#), [EMD-31459](#) and [EMD-31460](#), respectively. The cryo-EM map of LBD-TMD of the GluK2-2 \times NETO2 complexes have been deposited as an additional map under entry [EMD-31463](#). The coordinates

for the structures have been deposited in the PDB under accession codes [7F59](#), [7F5B](#), [7F5A](#), [7F56](#) and [7F57](#), respectively. [Source data](#) are provided with this paper.

Change history

- 27 September 2021

The linking to some of the Supplementary Information files was originally incorrect and has now been amended.

References

1. 1.
Herb, A. et al. The KA-2 subunit of excitatory amino acid receptors shows widespread expression in brain and forms ion channels with distantly related subunits. *Neuron* **8**, 775–785 (1992).
2. 2.
Bettler, B. et al. Cloning of a novel glutamate receptor subunit, GluR5: expression in the nervous system during development. *Neuron* **5**, 583–595 (1990).
3. 3.
Traynelis, S. F. et al. Glutamate receptor ion channels: structure, regulation, and function. *Pharmacol. Rev.* **62**, 405–496 (2010).
4. 4.
Castillo, P. E., Malenka, R. C. & Nicoll, R. A. Kainate receptors mediate a slow postsynaptic current in hippocampal CA3 neurons. *Nature* **388**, 182–186 (1997).
5. 5.

Vignes, M. & Collingridge, G. L. The synaptic activation of kainate receptors. *Nature* **388**, 179–182 (1997).

6. 6.

MacDermott, A. B., Role, L. W. & Siegelbaum, S. A. Presynaptic ionotropic receptors and the control of transmitter release. *Annu. Rev. Neurosci.* **22**, 443–485 (1999).

7. 7.

Chittajallu, R. et al. Regulation of glutamate release by presynaptic kainate receptors in the hippocampus. *Nature* **379**, 78–81 (1996).

8. 8.

Zhang, W. et al. A transmembrane accessory subunit that modulates kainate-type glutamate receptors. *Neuron* **61**, 385–396 (2009).

9. 9.

Copits, B. A., Robbins, J. S., Frausto, S. & Swanson, G. T. Synaptic targeting and functional modulation of GluK1 kainate receptors by the auxiliary neuropilin and toll-like (NETO) proteins. *J. Neurosci.* **31**, 7334–7340 (2011).

10. 10.

Tang, M. et al. Neto1 is an auxiliary subunit of native synaptic kainate receptors. *J. Neurosci.* **31**, 10009–10018 (2011).

11. 11.

Tomita, S. & Castillo, P. E. Neto1 and Neto2: auxiliary subunits that determine key properties of native kainate receptors. *J. Physiol.* **590**, 2217–2223 (2012).

12. 12.

Straub, C., Zhang, W. & Howe, J. R. Neto2 modulation of kainate receptors with different subunit compositions. *J. Neurosci.* **31**, 8078–8082 (2011).

13. 13.

Fisher, J. L. & Mott, D. D. The auxiliary subunits Neto1 and Neto2 reduce voltage-dependent inhibition of recombinant kainate receptors. *J. Neurosci.* **32**, 12928–12933 (2012).

14. 14.

Meyerson, J. R. et al. Structural mechanism of glutamate receptor activation and desensitization. *Nature* **514**, 328–334 (2014).

15. 15.

Mayer, M. L. Crystal structures of the GluR5 and GluR6 ligand binding cores: molecular mechanisms underlying kainate receptor selectivity. *Neuron* **45**, 539–552 (2005).

16. 16.

Kumari, J., Vinnakota, R. & Kumar, J. Structural and functional insights into GluK3–kainate receptor desensitization and recovery. *Sci. Rep.* **9**, 1–16 (2019).

17. 17.

Khanra, N., Brown, P. M., Perazzo, A. M., Bowie, D. & Meyerson, J. R. Architecture and structural dynamics of the heteromeric GluK2/K5 kainate receptor. *Elife* **10**, e66097 (2021).

18. 18.

Meyerson, J. R. et al. Structural basis of kainate subtype glutamate receptor desensitization. *Nature* **537**, 567–571 (2016).

19. 19.

Honore, T. et al. Quinoxalinediones: potent competitive non-NMDA glutamate receptor antagonists. *Science* **241**, 701–703 (1988).

20. 20.

Zhao, Y., Chen, S., Yoshioka, C., Baconguis, I. & Gouaux, E. Architecture of fully occupied GluA2 AMPA receptor–TARP complex elucidated by cryo-EM. *Nature* **536**, 108–111 (2016).

21. 21.

Copits, B. A. & Swanson, G. T. Dancing partners at the synapse: auxiliary subunits that shape kainate receptor function. *Nat. Rev. Neurosci.* **13**, 675–686 (2012).

22. 22.

Kumar, J., Schuck, P. & Mayer, M. L. Structure and assembly mechanism for heteromeric kainate receptors. *Neuron* **71**, 319–331 (2011).

23. 23.

Pinheiro, P. S. et al. Selective block of postsynaptic kainate receptors reveals their function at hippocampal mossy fiber synapses. *Cereb. Cortex* **23**, 323–331 (2013).

24. 24.

Li, Y.-J. et al. Neto proteins regulate gating of the kainate-type glutamate receptor GluK2 through two binding sites. *J. Biol. Chem.* **294**, 17889–17902 (2019).

25. 25.

Köhler, M., Burnashev, N., Sakmann, B. & Seeburg, P. H. Determinants of Ca^{2+} permeability in both TM1 and TM2 of high affinity kainate receptor channels: diversity by RNA editing. *Neuron* **10**, 491–500 (1993).

26. 26.

Chen, S. et al. Activation and desensitization mechanism of AMPA receptor–TARP complex by cryo-EM. *Cell* **170**, 1234–1246.e14 (2017).

27. 27.

Zhang, D., Watson, J. F., Matthews, P. M., Cais, O. & Greger, I. H. Gating and modulation of a hetero-octameric AMPA glutamate receptor. *Nature* **594**, 454–458 (2021).

28. 28.

Bowie, D. & Mayer, M. L. Inward rectification of both AMPA and kainate subtype glutamate receptors generated by polyamine-mediated ion channel block. *Neuron* **15**, 453–462 (1995).

29. 29.

Kamboj, S. K., Swanson, G. T. & Cull-Candy, S. G. Intracellular spermine confers rectification on rat calcium-permeable AMPA and kainate receptors. *J. Physiol.* **486**, 297–303 (1995).

30. 30.

Nayeem, N., Mayans, O. & Green, T. Correlating efficacy and desensitization with GluK2 ligand-binding domain movements. *Open Biol.* **3**, 130051 (2013).

31. 31.

Goehring, A. et al. Screening and large-scale expression of membrane proteins in mammalian cells for structural studies. *Nat. Protoc.* **9**, 2574–2585 (2014).

32. 32.

Zheng, S. Q. et al. MotionCor2: anisotropic correction of beam-induced motion for improved cryo-electron microscopy. *Nat. Methods* **14**, 331–332 (2017).

33. 33.

Zhang, K. Getf: real-time CTF determination and correction. *J. Struct. Biol.* **193**, 1–12 (2016).

34. 34.

Bepler, T., Kelley, K., Noble, A. J. & Berger, B. Topaz-Denoise: general deep denoising models for cryoEM and cryoET. *Nat. Commun.* **11**, 5208 (2020).

35. 35.

Zivanov, J. et al. New tools for automated high-resolution cryo-EM structure determination in RELION-3. *Elife* **7**, e42166 (2018).

36. 36.

Punjani, A., Rubinstein, J. L., Fleet, D. J. & Brubaker, M. A. cryoSPARC: algorithms for rapid unsupervised cryo-EM structure determination. *Nat. Methods* **14**, 290–296 (2017).

37. 37.

Scheres, S. H. & Chen, S. Prevention of overfitting in cryo-EM structure determination. *Nat. Methods* **9**, 853–854 (2012).

38. 38.

Bordoli, L. et al. Protein structure homology modeling using SWISS-MODEL workspace. *Nat. Protoc.* **4**, 1–13 (2009).

39. 39.

Briggs, D. C. et al. Metal ion-dependent heavy chain transfer activity of TSG-6 mediates assembly of the cumulus-oocyte matrix. *J. Biol. Chem.* **290**, 28708–28723 (2015).

40. 40.

Emsley, P. & Cowtan, K. Coot: model-building tools for molecular graphics. *Acta Crystallogr. D Biol. Crystallogr.* **60**, 2126–2132 (2004).

41. 41.

Afonine, P. V. et al. Real-space refinement in PHENIX for cryo-EM and crystallography. *Acta Crystallogr. D Struct. Biol.* **74**, 531–544 (2018).

42. 42.

Appleton, B. A. et al. Structural studies of neuropilin/antibody complexes provide insights into semaphorin and VEGF binding. *EMBO J.* **26**, 4902–4912 (2007).

43. 43.

Goddard, T. D. et al. UCSF ChimeraX: meeting modern challenges in visualization and analysis. *Protein Sci.* **27**, 14–25 (2018).

44. 44.

DeLano, W. L. Pymol: an open-source molecular graphics tool. *CCP4 Newsletter on Protein Crystallography*
http://148.79.162.84/newsletters/newsletter40/11_pymol.html (2002).

Acknowledgements

We thank X. Huang, B. Zhu, X. Li, L. Chen and other staff members at the Center for Biological Imaging (CBI), Core Facilities for Protein Science at the Institute of Biophysics, Chinese Academy of Science (IBP, CAS) for the support in cryo-EM data collection; N. Sheng for providing the cDNAs of

GluK2 and NETO2; and Y. Wu for his research assistant service. This work is funded by the Chinese Academy of Sciences Strategic Priority Research Program (grant XDB37030304 to Y.Z. and grant XDB37030301 to X.C.Z.), the National Key R & D Program of China (2019YFA0801603 to Y.S.S.), the National Natural Science Foundation of China (91849112 to Y.S.S. and 31971134 to X.C.Z.), the Natural Science Foundation of Jiangsu Province (BE2019707 to Y.S.S.) and the Fundamental Research Funds for the Central Universities (0903-14380029 to Y.S.S.).

Author information

Author notes

1. These authors contributed equally: Lingli He, Jiahui Sun, Yiwei Gao

Affiliations

1. National Laboratory of Biomacromolecules, CAS Center for Excellence in Biomacromolecules, Institute of Biophysics, Chinese Academy of Sciences, Beijing, China

Lingli He, Yiwei Gao, Bin Li, Yuhang Wang, Yanli Dong, Weidong An, Hang Li, Bei Yang, Xuejun Cai Zhang & Yan Zhao

2. State Key Laboratory of Brain and Cognitive Science, Institute of Biophysics, Chinese Academy of Sciences, Beijing, China

Lingli He, Yanli Dong, Bei Yang & Yan Zhao

3. College of Life Sciences, University of Chinese Academy of Sciences, Beijing, China

Lingli He, Yiwei Gao, Bin Li, Yuhang Wang, Yanli Dong, Weidong An, Hang Li, Bei Yang, Xuejun Cai Zhang & Yan Zhao

4. Ministry of Education Key Laboratory of Model Animal for Disease Study, Model Animal Research Center, Medical School, Nanjing

University, Nanjing, China

Jiahui Sun, Yuhan Ge & Yun Stone Shi

5. State Key Laboratory of Pharmaceutical Biotechnology, Department of Neurology, Affiliated Drum Tower Hospital of Nanjing University Medical School, Nanjing University, Nanjing, China

Jiahui Sun, Yuhan Ge & Yun Stone Shi

6. Institute for Brain Sciences, Nanjing University, Nanjing, China

Yun Stone Shi

7. Chemistry and Biomedicine Innovation Center, Nanjing University, Nanjing, China

Yun Stone Shi

Contributions

Y.Z. conceived the project and supervised the research. L.H., J.S., W.A. and B.Y. carried out molecular cloning and the cell biology experiments. L.H. expressed and purified the protein complex sample. L.H., Y.D. and Y.W. prepared the sample for the cryo-EM study. Y. Gao. L.H., Y.W. and Y.D. carried out cryo-EM data collection. Y. Gao and Y.Z. processed the cryo-EM data and prepared the figures. B.L. and H.L. built and refined the atomic model. Y.Z. and X.C.Z. analysed the structure. Y.Z. and Y.S.S. designed the electrophysiological study. J.S. and Y. Ge performed the electrophysiological analysis. Y.Z. prepared the initial draft of the manuscript. X.C.Z., Y.S.S. and Y.Z. edited the manuscript with input from all authors in the final version.

Corresponding authors

Correspondence to [Xuejun Cai Zhang](#), [Yun Stone Shi](#) or [Yan Zhao](#).

Ethics declarations

Competing interests

The authors declare no competing interests.

Additional information

Peer review information *Nature* thanks Ingo Greger and Geoffrey Swanson for their contribution to the peer review of this work. Peer reviewer reports are available.

Publisher's note Springer Nature remains neutral with regard to jurisdictional claims in published maps and institutional affiliations.

Extended data figures and tables

Extended Data Fig. 1 Functional study and purification of GluK2-Neto2 complex.

a, b, Outside-out recording of the WT GluK2 and GluK2^{F107L}, in the absence or presence of Neto2. **c**, Statistical analysis of the desensitization time constant of the WT GluK2 and GluK2^{F107L}, with or without Neto2 (GluK2, $n = 12$; GluK2 + Neto2, $n = 14$; GluK2^{F107L}, $n = 10$; GluK2^{F107L} + Neto2, $n = 10$). Each symbol represents a single cell recording, and n value represents biologically independent cells for statistical analysis.

Significances were determined using two-sided unpaired t-test. ****, $P < 0.0001$. Similar results were reproduced from two independent experiments. Error bars stand for S.E.M. **d**, Fluorescence-detection size-exclusion chromatography (FSEC) analysis of the co-expressed GluK2-mCherry (red) and Neto2-GFP (green). The experiments were repeated independently with more than three times with similar results. **e**, Size-exclusion chromatography (SEC) profile of the purified GluK2-Neto2 complex. Fractions within the dashed lines were pooled for cryo-EM sample preparation. The experiments were repeated independently with more than

three times with similar results. (f) Coomassie blue-stained SDS-PAGE gel of the pooled fractions. The gel was repeated three times from different batches of purification with similar results. The uncropped gel can be found in Supplementary Fig. 1.

[Source data](#)

[Extended Data Fig. 2 Cryo-EM data analysis of GluK2-1×Neto2, GluK2-2×Neto2, and GluK2-1×Neto2^{asymLBD} complex.](#)

a, Flowchart of cryo-EM data processing. A total of 5,448 movie stacks were collected and motion-corrected, followed by CTF estimation and particle picking. A representative motion-corrected micrograph of this dataset is shown here (Scale bar = 40 nm). The experiments were repeated three times with similar results. Particles were cleaned and classified using several rounds of 2D and 3D classifications, which generated 3 classes, representing GluK2-1×Neto2, GluK2-2×Neto2, and GluK2-1×Neto2^{asymLBD}, respectively. Particles were then submitted to further 3D classifications separately to improve resolutions. Focused classification and refinement of LBD-TMD were conducted on the particles of GluK2-1×Neto2 complex. Masks used in focused processing were overlaid on GluK2 map (green) as transparent grey surfaces alongside the arrows. **b, e, h, k**, Angular distribution of the particles contributing the final reconstruction for GluK2-1×Neto2^{asymLBD} complex (**b**), GluK2-2×Neto2 complex (**e**), GluK2-1×Neto2 complex (**h**), and LBD-TMD (**k**). The length of each spike indicates of the number of particles in the designated orientation. **c, f, i, l**, Sharpened map of GluK2-1×Neto2^{asymLBD} complex (**c**), GluK2-2×Neto2 complex (**f**), GluK2-1×Neto2 complex (**i**), and LBD-TMD (**l**), colored according to local resolution estimation. **d, g, j, m**, The half-map (red) and model-map (black) Fourier shell correlation (FSC) of GluK2-1×Neto2^{asymLBD} complex (**d**), GluK2-2×Neto2 complex (**g**), GluK2-1×Neto2 complex (**j**), and LBD-TMD (**m**).

[Source data](#)

Extended Data Fig. 3 EM maps for transmembrane helices and the LBD-TMD.

a, Transmembrane helices M1–M4, and the M1-M2 loop. EM maps are shown as transparent grey surfaces. Some sidechains are shown as sticks. **b**, EM maps for LBD and TMD layers. CUB2 and LDL_a of Neto2 are colored in orange. Receptor is colored in purple. N-glycans and a lipid tail are shown in sticks.

Extended Data Fig. 4 Structural comparison of ATD and LBD layers.

a, Superimposition of antagonist bound LBDs of 5KUH (grey) and GluK2-1×Neto2 (red). **b**, Comparison of the ATD^A-LBD^B and ATD^C-LBD^D segments between subunit A (grey) and C (blue) of the GluK2-1×Neto2, GluK2-2×Neto2 and GluK2-1×Neto2^{asymLBD} complexes, using LBD as a reference. The COMs of the ATD R1/R2-lobe of subunits A and C are depicted as rectangles or triangles, respectively. The COMs of the LBD layer is marked as a circle. **c**, Superimposition of ATD-CUB1 interactions between GluK2-1×Neto2^{asymLBD} (grey) and GluK2-1×Neto2 (red, orange and blue).

Extended Data Fig. 5 Sequence alignments and structural comparison of the KARs.

a–d, Sequence alignments of the GluK members in *Rat norvegicus*, numbered according to full-length subunits. Secondary structures of GluK2 are marked above the sequence alignment. Dashes represent gaps. Conserved residues are shaded in grey. Residues which are involved in Neto2 interaction are indicated by triangle symbol. **e**, Structural comparison of the LBD of GluK2 with GluK1 (3FUZ, green), GluK3 (3U92, cyan), GluK4 (5IKB, magenta), and GluK5 (7KS0, yellow), respectively. D1- and D2- lobes and Loop 1 are indicated.

Extended Data Fig. 6 Representative desensitization and rectification traces.

a, Representative desensitization traces of GluK2 and mutants responded to 60 ms application of 10 mM glutamate were normalized and aligned to the peak. Superimposed responses of the receptor alone and the receptor-Neto2 complex were shown in black and green traces, respectively. **b**, Normalized current-voltage relationship of GluK2 mutants in the absence and presence of Neto2. *n* value represents independent cells for analysis. **c**, Representative desensitization traces and related statistical analysis (GluA2, *n* = 16; GluA2^{K2ICD}, *n* = 12). Each symbol represents a single cell recording, and *n* value represents biologically independent cells for statistical analysis. Significances were determined using two-sided unpaired t-test. Not significant (ns), P = 0.0755. No adjustments were made for multiple comparisons. Error bars stand for S.E.M. The H1-helix is composed of residues ⁸⁵⁷FCSAMVEELRMSLK⁸⁷⁰ and removed in GluK2^{ΔH1} construct. The amino acid sequence of the ICD of GluK2 and GluA2 between M1-M2 helices are ⁵⁸⁷YEWYNPHPCNPDSDVEN⁶⁰⁴ and ⁵⁷⁰YEWHTEEFEDGRETQSSESTNE⁵⁹¹, respectively, which are involved in the ICD swapping constructs of GluA2^{K2ICD} and GluK2^{A2ICD}. **d**, I-V relationship for GluA2, GluK2 and related mutants. Desensitization curves (10 mM glutamate for 200 ms) were recorded at holding potential ranging from -100 to +100 mV in 20 mV increase. Traces were normalized to the peak value at -100 mV.

[Source data](#)

[**Extended Data Fig. 7 Interactions stabilizing the pore helix M2.**](#)

a, EM density map of the LBD and TMD layers of the GluK2-1×Neto2 complex. Subunits A/C and B/D of GluK2 are colored in blue and red, respectively. The Neto2 protein is colored in orange. N-glycans are colored in yellow. **b**, The ion conduction pore and its profile of the GluK2-Neto2 complex. Pore loops are colored in green. A cation ion is shown as a grey sphere, overlaid with corresponding EM density colored in marine. Q621, T652, A656, and T660 are shown in sticks. Constriction sites are indicated in the pore profile. **c**, The TM helices of the GluK2 (red and blue) and the Neto2 (yellow) are shown as cartoon. The EM density of M2 helix are shown as transparent grey surface. Critical residues involved in interactions

are shown as sticks. **d**, “Top-down” view of M2 helices and the pore loops. Q621 residues are shown in sticks.

Extended Data Fig. 8 Cryo-EM data analysis of GluK2-1×Neto2^{des} complex.

a, Flowchart of cryo-EM data processing. A total of 2,957 movie stacks were collected and motion-corrected, followed by CTF estimation and particle picking. A representative motion-corrected micrograph of this dataset is shown here (Scale bar = 40 nm). The experiments were repeated three times with similar results. Three-dimensional classification generated 8 classes, 4 of which displayed classical structures of kainate receptors. Another round of 3D classification was then performed, followed by *Ab-initio* Reconstruction and Heterologous Refinement to furtherly improve the quality of map. **b**, Angular distribution of the particles contributing the final reconstruction of GluK2-1×Neto2^{des} complex. The length of each spike indicates of the number of particles in the designated orientation. **c**, Sharpened map of GluK2-1×Neto2^{des} complex, colored according to local resolution estimation. **d**, The half-map (red) and model-map (black) Fourier shell correlation.

Source data

Extended Data Fig. 9 Conformational change of GluK2-Neto2 complex upon desensitization.

a, Superimposition of agonist bound LBDs of 4BDM (grey) and GluK2-1×Neto2^{des} (red). **b**, Superimposition of ATD-CUB1-LBD interactions between GluK2-1×Neto2^{asymLBD} (grey) and GluK2-1×Neto2^{des} (red, orange and blue). **c**, Organization of the D1 lobe of the GluK2-1×Neto2^{des} (red and blue) and desensitized GluK2 alone (grey). COMs of the lobes are depicted as black dots. Distances and angles are indicated. **d**, The LBD rearrangement between GluK2-1×Neto2 and GluK2-1×Neto2^{des} upon desensitization. **e**, Displacement of LBD at B-position of GluK2-1×Neto2^{des} complex (red, blue and orange) compared with desensitized GluK2 (5KUF, grey).

Extended Data Table 1 Cryo-EM data collection, refinement and validation statistics

Supplementary information

[**Supplementary Information.**](#)

[**Reporting Summary**](#)

[**Peer Review File**](#)

Source data

[**Source Data Fig. 2**](#)

[**Source Data Fig. 3**](#)

[**Source Data Extended Data Fig. 1**](#)

[**Source Data Extended Data Fig. 2**](#)

[**Source Data Extended Data Fig. 6**](#)

[**Source Data Extended Data Fig. 8**](#)

Rights and permissions

[**Reprints and Permissions**](#)

About this article

Cite this article

He, L., Sun, J., Gao, Y. *et al.* Kainate receptor modulation by NETO2. *Nature* **599**, 325–329 (2021). <https://doi.org/10.1038/s41586-021-03936-y>

- Received: 12 May 2021
- Accepted: 20 August 2021
- Published: 22 September 2021
- Issue Date: 11 November 2021
- DOI: <https://doi.org/10.1038/s41586-021-03936-y>

Share this article

Anyone you share the following link with will be able to read this content:

[Get shareable link](#)

Sorry, a shareable link is not currently available for this article.

[Copy to clipboard](#)

Provided by the Springer Nature SharedIt content-sharing initiative

This article was downloaded by **calibre** from <https://www.nature.com/articles/s41586-021-03936-y>.

Collections